europhysics
conference
abstracts

15th European Conference on

Controlled Fusion and Plasma Heating

Dubrovnik, May 16—20, 1988

Editors: S. Pešić, J. Jacquinot

Contributed Papers
Part II

Published by: European Physical Society

Editor: Dr. J. Heijn, Petten

ing Editor: G. Thomas, Geneva

VOLUME 12B Part II

XV
FUSION
DUBROVNIK
1988

B
C
D
E

15th European Conference on

Controlled Fusion and Plasma Heating

Dubrovnik, May 16—20, 1988

Editors: S. Pešić, J. Jacquinot

Contributed Papers
Part II

EUROPHYSICS CONFERENCE ABSTRACTS is published by the
European Physical Society, © 1988

Preface

The 15th European Conference on Controlled Fusion and Plasma Heating was organized by the Boris Kidrič Institute of Nuclear Sciences, Belgrade, Yugoslavia, on behalf of the Plasma Physics Division of the European Physical Society (EPS). It was held in Cavtat, near Dubrovnik, from 16 to 22 May 1988.

The 15th Conference concentrates on experimental and theoretical aspects of Plasma Confinement and Plasma Heating. The programme, format and schedule of the meeting was determined by the International Programme Committee, which was appointed by the Plasma Physics Division Board of the EPS. The Programme Committee selected 19 invited and 24 oral contributed papers.

This volume contains all accepted contributed papers received in due time by the Organizers. It is published in the Europhysics Conference Abstracts Series and it follows the rules for publication of the EPS. The 4–page extended abstracts were reproduced photographically using the camera ready manuscripts submitted by the authors who are therefore responsible for the quality of the presentation. Post-deadline papers are not included in this volume.

All invited papers will be published in a special issue of the journal "Plasma Physics and Controlled Fusion". This journal may also publish rapidly an extended version of contributed papers, following an accelerated refereeing procedure.

The Organizers would like to acknowledge the support of the Serbian Science Research Council and the technical assistance of the Publishing Department of the Boris Kidrič Institute of Nuclear Sciences. The Conference has been organized under the general sponsorship of the Union of Yugoslav Societies of Mathematicians, Physicists and Astronomers, member of EPS.

April 1988 — The Editors

International Programme Committee

J. Jacquinot (Chairman), JET, Abingdon, United Kingdom
S. Pešić (Vice–Chairman), IBK, Belgrade, Yugoslavia
K. Appert, CRPP, Lausanne, Switzerland
H. Bodin, Culham Lab., Abingdon, United Kingdom
G. Briffod, CENG, Grenoble, France
F. Engelmann, NET, Garching, F. R. Germany
L. Kovrizhnykh, GPI, Moscow, USSR
K. Lackner, IPP, Garching, F. R. Germany
E. Sindoni, University of Milan, Milan, Italy
M. M. Škorić, IBK, Belgrade, Yugoslavia

Organizing Committee

M. M. Škorić (Chairman), IBK, Belgrade
S. Pešić, IBK, Belgrade
Đ. Jović, IBK, Belgrade
Đ. Miljanić, IBK, Belgrade
Lj. Hadžievski, IBK, Belgrade
S. Pavićević, Yugotours, Belgrade

Contents

Paper Identification

Each paper is identified with a 6 character code printed on the top right corner of the first page. The code *u v wx yz* has the following structure:

- *u* — type of contribution; *u* = I, O, P for invited paper, oral and poster contributed paper
- *v* — the day of event; *v* = 0, 1, 2,...,9 for Monday morning, Monday afternoon, Tuesday morning,..., to Friday afternoon
- *wx* — the topic and subtopic of the contribution
- *yz* — the poster board number: *yz* = 01, 02,...,99

Note that the authors of oral contributed papers are given the possibility to post their contributions. Therefore, the data in the code refer to the corresponding poster presentation.

Example

P 8 E2 47

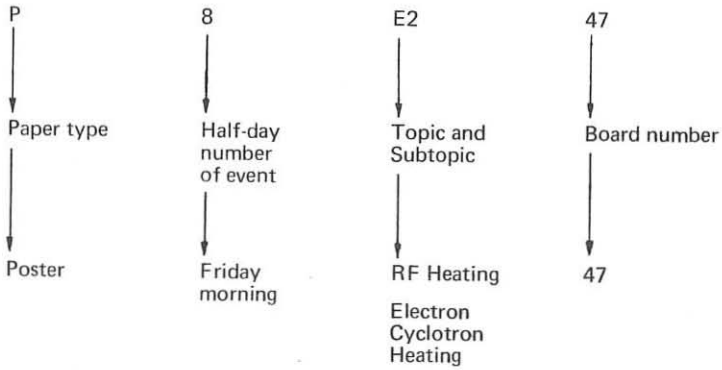

Title List of Contributed Papers

A. TOKAMAKS

E1. Experiments

A2. H Mode

A3. Theory

B. STELLARATORS

C. ALTERNATIVE CONFINEMENT SCHEMES

C1. Reverse Field Pinch

C2. Other Alternative Magnetic Confinement Schemes

D. PLASMA EDGE PHYSICS

E. RF HEATING

E1. Ion Cyclotron Heating

E2. Electron Cyclotron Heating

E3. Lower Hybrid Heating

E4. Alfven Wave and Other RF Heating Methods

F. CURRENT DRIVE AND PROFILE CONTROL

F1. Lower Hybrid Current Drive

F2. Other Profile Control Methods

G. NEUTRAL BEAM INJECTION HEATING

J. INERTIAL CONFINEMENT PHYSICS

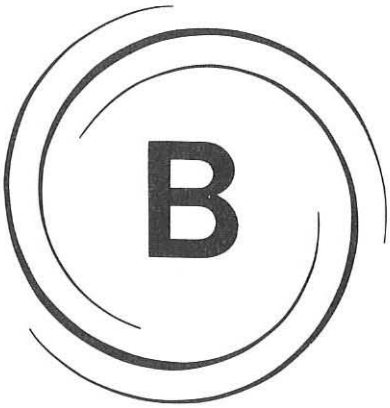

Stellarators

ELECTRON CYCLOTRON HEATING (ECH) OF THE CURRENTLESS AND "TARGET" CURRENT PLASMAS BY AN ORDINARY WAVE IN THE L-2 STELLARATOR

E.D.Andryukhina, D.K.Akulina, G.M.Batanov, M.S.Berezhetskii, G.S.Voronov, N.P.Donskaya, K.S.Dyabilin, L.V.Kolik, L.M.Kovrizhnykh, N.F.Larionova, K.M.Likin, A.I.Meshcheryakov, A.E.Petrov, S.N.Popov, V.I.Roshchin, A.V.Sapozhnikov, K.A.Sarksyan, N.N.Skvortsova, I.S.Sbitnikova, O.I.Fedyanin, Yu.V.Khol'nov, M.G.Shats, I.S.Spigel'

General Physics Institute, Academy of Sciences of the USSR
117942 Moscow, Vavilov street, 38. USSR

During the last time the experiments on ECH (ECR at the fundamental harmonic of the electron gyrofrequency $\omega_o = \omega_{He}$) of plasma by an ordinary wave have been carried out in the L-2 stellarator [1] (R = 100 cm, a_p = 11.5 cm, l = 2, m = 14).

The results of ECH of "target" current plasma by an ordinary wave were published in [2] . In the present report the main results of experiments on ECR production and heating of currentless plasma by an ordinary wave in the L-2 stellarator are given. The comparison with ECH current plasma is carried out.

The Gaussian microwave beam parameters and conditions of the beam launching in the vacuum vessel from the low field side were the same as in [2] . Wave power was injected in L-2 P_o = 100 kW in one experimental series and in the other series the power reached P_o = 160÷180 kW.

At first let us consider the results of currentless plasma production and heating at P_o = 100 kW which is the same as in [2] .

In Fig.1 temporal evolutions of the main plasma parameters is shown: the average density $\overline{n}_e$(4 mm interferometer), the central electron temperature $T_e(0)$(laser Thomson scattering), plasma energy content W (diamagnetic measurements) and the radiation power P_{rad} (piroelectric detector). From the dependence on $\overline{n}_e(t)$ (see Fig.1b) it follows that after the gas (hydrogen) breakdown and plasma buildup the density is nearly constant during the heating pulse and it is equal to $\overline{n}_e \simeq 7.5 \ 10^{12} cm^{-3}$. The electron temperature $T_e(0)$ and plasma energy W grow with time (see Fig.1d,c).

The maximum values of $T_e(0)$ and W achieved at the end of the heating pulse are accordingly equal $T_e(0) \simeq 0.8 \div 1.0$keV,

$W \simeq 180 \div 200$ J.

The ion temperature T_i is measured by the neutral particle analyser. The rate of ion heating changes in time: for the first 0.5 ms fast collisionless heating up to 50 eV occur, then the rate decreases so that at the end of the pulse $T_i \simeq 80$ eV. The ion distribution is nonmaxwellian only during the first 1-2 ms of the heating pulse. At the same time the burst of the density fluctuation intensity at frequences close to ion cyclotron and lower-hybrid is observed [3].

The energy confinement time τ_E defined by diamagnetic measurements at the time of the switching-off the heating pulse is equal to $\tau_E = 3$ ms. The value of the absorption power calculated at the same time is $P_{abs} \simeq 70$ kW, that gives the absorption coefficient $\alpha = \frac{P_{abs}}{P_o} \cdot 100\% \simeq 70\%$. This value occurs to be in good agreement with the calculated one-pass absorption coefficient that is equal to $\alpha = 75\%$ [4].

At last we note that currentless plasma heating efficiency is close to $\eta = 10 \div 12$ eV/kW/10^{13}cm^3.

The comparison of these experimental data with the results of current plasma ECH [2] shows that in the case of ECH of currentless plasma higher values of $T_e(0)$, W, τ_E and η are achieved. In particular value τ_E is 1.5 times more and η is 2 times more than in current plasma.

Now we consider the experiments of ECH of currentless plasma by ordinary wave with higher power $P_o = 160 \div 180$ kW.

In Fig.2 temporal evolutions of the same plasma parameters are presented. From the dependence $\overline{n_e}(t)$ (see Fig.2b) it follows that the density is nearly constant during the heating pulse and it is equal to $\overline{n_e} \simeq 7.5\ 10^{12}$cm^{-3}as at power $P_o \simeq 100$ kW. With the increase of the wave power the radiation power slightly rises up to $P_{rad} \simeq 12 \div 15$ kW. As it follows from Fig.2c,d $T_e(0)$ and W did not essentially grow in spite of the launched wave power is more than 1.5 times higher. So, maximum values of $T_e(0)$ and W are equal to: $T_e(0) = 1 \div 1.2$ keV and $W = 190 \div 230$ J. One can see from Fig.2c,d that temporal evolutions of $T_e(0)$ and W noticeably changed in contrast with Fig.1c,d. The maximum of $T_e(0)$ is reached about 3 ms and then the temperature is constant or slightly decreased. The saturation is observed in the temporal evolution of W.

At present we have preliminary results about electron temperature and plasma density radial profile. The profiles are broadening by the end of the heating pulse.

The energy confinement time τ_E is the same as in the experiments with a lower waves power and is close to $\tau_E \simeq 3$ms. The energy confinement time is obtained by means of the diamagnetic measurements at the heating pulse switch-off time. At this time the absorbed power P_{abs} = 70÷80 kW that corresponds to $\mathcal{A}$ = 40÷45% although the calculated one-pass absorption coefficient is $\mathcal{A}$ = 75%.

Thus, with the increase of wave power following peculiarities are observed in the experiment:

1. The saturation was observed in the dependencies $T_e(t)$ and $W(t)$ in the second half of the heating pulse;
2. A weak growth of the maximum values of $T_e(0)$ and W took place.

What were the reasons of these peculiarities?

It can be proposed that the absence of the temperature and energy linear growth with the increase of P_o can be connected with the entry into " superbanana " region for L-2, when $T_e \simeq 1$ keV. In this case the absorption power must rise, but it is not observed in the experiment.

It is possible that the quasilinear relaxation [5] is developed at the introduced power. This process must lead to the decrease of the real absorption coefficient in contrast with the linear one-pass coefficient.

It is also possible that the local energy deposit takes place near the wave introduce region. This part of the absorbed energy can not be measured in the present experiments.

At last it should be noted that in the peripheral plasma region the absorbed energy cannot be measured either, because the confinement time of the peripheral energy is less than the resolving time of diamagnetic measurements (< 0.5 ms).

References

1 Andryukhina, E.D., Berezhetskii, M.S., Voronov, G.S. et al., "Stellarator L-2". Preprint Lebedev Institute (1977), Moscow, No 154.

2 Andryukhina, E.D., Akulina, D.K., Batanov, G.M., et al., XI Int. Conf. on Pl. Phys. on Contr. Nucl. Fusion Res. Kyoto (1986) CN-471d-III-3.

3 Batanov, G.M., Kolik, L.V., Sapozhnikov, A.V. et al. Report at this conference P 1 B 03

4 Likin, K.M., Ochirov, B.D., Skvortsova, N.N. Report at this conference P 1 B 02

5 Alikaev, V.V., Litvak, A.G., Suvorov, E.V., Fraiman, A.A. "HF Plasma heating" Gor'kii (1983), p.6.

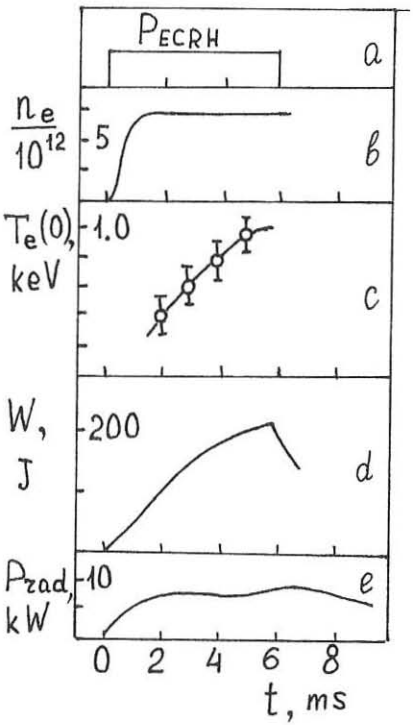

Fig.1. The temporal evolutions of the plasma parameters.
P_o = 100 kW.

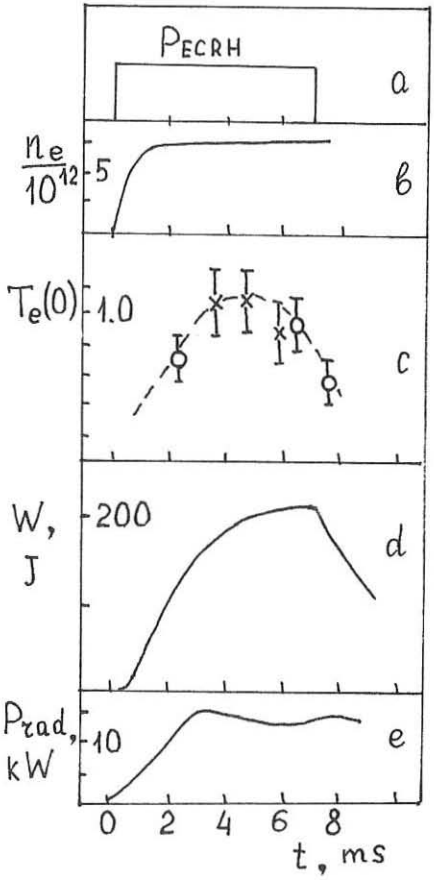

Fig.2. The temporal evolutions of the plasma parameters.
P_o = 160-180 kW.
° - laser, × - SX-ray.

ENERGY DEPOSITION PROFILES OF SIMULATION OF ECRH IN THE L-2 STELLARATOR.

Likin K.M., Ochirov B.D.*, Skvortsova N.N.

General Physics Institute, USSR Academy of Sciences, 117924, Moscow, Vavilov street, 38, USSR

*Institute of Automation and Electrometry. 630090, Novosibirsk, USSR

The determination of energy deposition profiles is of some interest in the electron-cyclotron resonance heating (ECRH) experiments in the magnetic traps. As experimental measurements of energy deposition profiles are connected with certain difficulties, it is necessary to carry out the simulation of propagation and absorption electromagnetic waves in plasma for the representation of these profiles.

This work is the continuation of our earlier published papers [1,2] . Numerical calculations were made in the geometrical optics approximation. Ray tracing equations are as follows [3] : $dx_i/dt = \partial G/\partial k_i$, $dk_i/dt = -\partial G/\partial x_i$, where x_i - unspecified spatial coordinates, k_i - components of phase gradient along ray trajectory, G - dispersion relation for the defined wave type.

The power varied along ray trajectory is defined by the equation: $dP_j/d\ell = -P_j \cdot 2 \cdot Im k_j \cos\alpha_j$, where P_j - the power emitted by the antenna in the j-ray; ℓ - the coordinate along the ray trajectory; $Im k_j$ - cyclotron damping coefficient, α_j - angle between ray and wave vectors. The deposition energy is averaged over magnetic surfaces of the stellarator.

Numerical modelling was carried out for the calculation of deposition energy profiles during ECRH by the ordinary wave in the L-2 stellarator. Some characteristic parameters of this device are: R_o = 1 m, a_o = 0.175 m , magnetic field B_o = 13.4 kG. The magnetic field in the L-2 stellarator has rather complicated configuration (Fig.1). Magnetic surfaces are assumed as follows: $r_\psi = \bar{r} + \delta(r)\cos\Theta + \varepsilon_2 \cos 2(\Theta - N\varphi)$, where ε_2 - the peak amplitude of the basic toroidal harmonic; $\delta(r) = B_\perp/B_0 \cdot R_0/\iota(r)$; $N\varphi$ = 7.

Temperature and density distributions are varying due to the stellarator regimes. The ordinary wave was launched in plasma as the Gaussian beam from the low magnetic field side. Generator frequency was the first harmonic of the electron cyclotron frequency. Microwave power was at the level

150 kW.

The ray trajectories for the currentless plasma are shown in Fig.2. Energy deposition profile is shown in Fig.3 for this regime (R is the average plasma redius). The total absorption coefficient is equal to 0.43 in this case.

The next regime is represented in Fig.4. It is the ohmic heating (OH) and ECRH of plasma. The parameters of plasma are the same as for the previous regime, but the centre of the magnetic surfaces is shifted by 3 cm outside from the stellarator axis. It can be seen that the energy deposition profile becomes wider while the total absorption coefficient is the same as for the currentless plasma. The electron temperature as the function of R may be expected wider in this experimental regime. Our simulations demonstrate that the energy deposition profiles depend very little on the temperature profiles (central electron temperature is equal to 0.4 keV). In varying plasma density profiles the energy deposition profiles are changed. The average plasma density is constant in these calculations.

The energy deposition profile is represented in Fig.5 for the electron density profile: $n_e(R) = n_e(0)(1-R^6)$. Comparing with the regime where $n_e(R) = n_e(0)(1-R^2)$ (Fig.1), it can be seen that this profile became narrower. The energy deposition profile for higher central electron temperature ($T_e(0) = 1$ keV) is shown in Fig.6. Total absorption coefficient in this regime is equal to 0.74.

The most interesting results are obtained for the Gaussian beam slope in the minor section plane of the stellarator. Total absorption coefficient increases up to 0.49 if the beam is sloped towards the "saddle" region of the magnetic field ($\alpha = +3^\circ$), but the energy deposition profile becomes wider (Fig.7) in the comparison with the regime in Fig.1 ($\alpha = 0^\circ$). The total absorption coefficient decreases up to 0.22 if the beam is sloped to the opposite side ($\alpha = -5^\circ$). In this case the energy deposition profile becomes narrower and energy density is near 10 W/ cm^3 at the first magnetic surface which radius is equal to 1 cm. Quasilinear effects have to be taken into account during ECRH for this high energy density.

In the launching Gaussian beam from the high magnetic field side the energy deposition profiles are close to the same profiles when the beam is launched from the low magnetic field side. The total absorption coefficient does not exceed 0.5 for the plasma regime: $n_e(0) = 1.125 \cdot 10^{13} cm^{-3}$, $n_e(R) = n_e(0)(1-R^2)$, $T_e(0) = 0.4$ keV, $T_e(R) = T_e(0)(1-R^2)$, $B_o = 13.4$ kG.

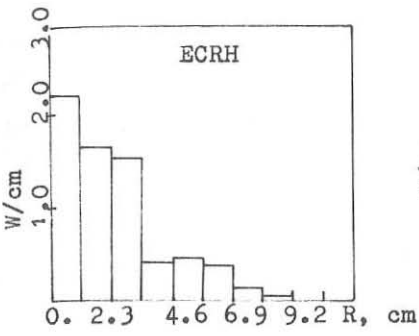

Fig.3. $n_e(0) = 1.125 \cdot 10^{13}\,cm^{-3}$, $\alpha = 0^\circ$
$T_e(0) = 0.4$ keV, $B_o(0) = 13.4$kG

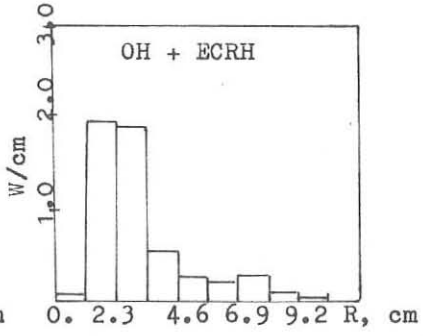

Fig.4. $n_e(0) = 1.125 \cdot 10^{13}\,cm^{-3}$
$\alpha = 0^\circ$, $T_e(0) = 0.4$keV, $B_o(0) = 13.4$kG

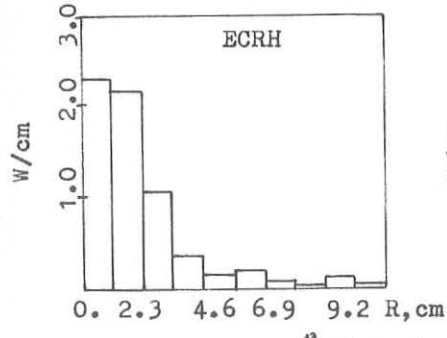

Fig.5. $n_e(0) = 0.875 \cdot 10^{13}\,cm^{-3}$, $\alpha = 0^\circ$
$T_e(0) = 0.4$keV, $B_o(0) = 13.4$kG

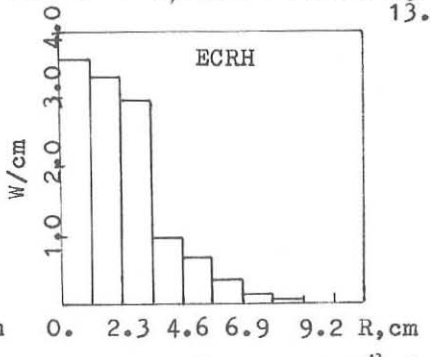

Fig.6. $n_e(0) = 1.125 \cdot 10^{13}\,cm^{-3}$
$\alpha = 0^\circ$, $T(0) = 1.0$keV, $B_o(0) = 13.4$kG

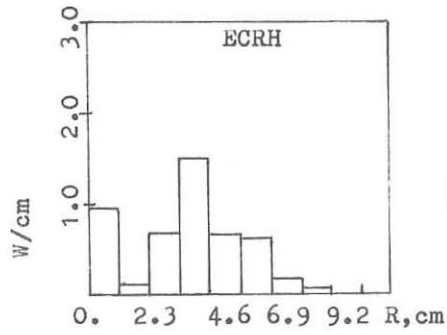

Fig.7. $n_e(0) = 1.125 \cdot 10^{13}\,cm^{-3}$, $\alpha = +3^\circ$
$T_e(0) = 0.4$keV, $B_o(0) = 13.4$kG

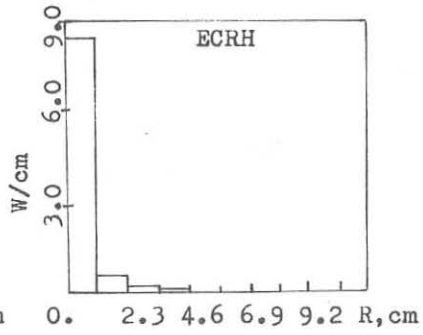

Fig.8. $n_e(0) = 1.125 \cdot 10^{13}\,cm^{-3}$
$\alpha = -5^\circ$, $T_e(0) = 0.4$keV, $B_o(0) = 13.4$kG

References

1 Ochirov, B.D., Skvortsova,N.N. Preprint No 71, General Physics Institute, Moscow, 1987.
2 Ochirov,B.D., Skvortsova,N.N. Proceeding of XVIII Conf. on ionised gases. v.4, 1987, p.590.
3 Ochirov,B.D., Preprint No 124, Inst. of Automation and Electrometry, Novosibirsk, 1986.
4 Danilkin,I.S., Hadin,O.E. Preprint No 343, General Physics Institute, Moscow, 1985.

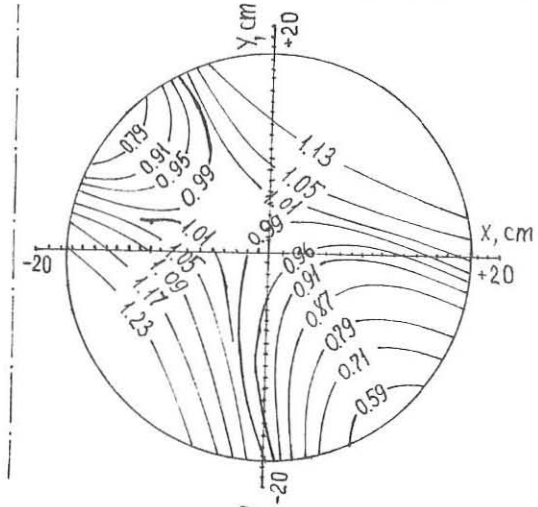

Fig.1.

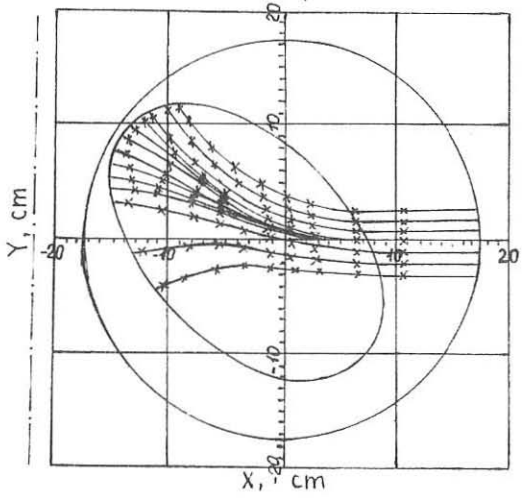

Fig.2. Ray trajectories $n_e(0)=1.125\cdot10^{13}cm^{-3}$

MICROWAVE SCATTERING ON PLASMA DENSITY FLUCTUATIONS IN THE L-2 STELLARATOR

Batanov,G.M., Kolik L.V., Sapozchnikov A.V., Sarksyan K.A., Khol'nov Yu.V., Shats M.G.

General Physics Institute, USSR Academy of Sciences, 117942 Moscow, Vavilov street, 38, USSR

In this report the results of investigations of low-frequency (in the range of 4-50 kHz) plasma waves for OH and ECH regimes in the L-2 stellarator are presented. The collective scattering diagnostics (incident wavelength λ_i = 2.5 mm) was used to measure the scattered radiation (the linear dimension of the scattering volume L_s = 4 cm) at the angles θ_s = 15°, 30° and 45° with the respect to the incident beam. This corresponds to the scattering from the waves with wavenumbers $k_\perp$ = 6, 13 and 20 cm^{-1} in the poloidal plane. The angle resolution corresponds to the wavenumber resolution $\Delta k_\perp$ = 4 cm^{-1} . After the homodyne detection of the scattered wave low-frequency signals were amplified and digitized. Then the autocorrelation function (AF) and the Fourier transform of AF (with the fast Fourier transform algorithm) were calculated. The instruments applied allow to obtain the frequency spectra in the range of f = 4-500kHz with the resolution Δf = 2 kHz for three angle channels simultaneously. Besides, the development of the scattered signals was studied using selective voltmeters with the bandwidth of Δf ($\Delta f/f$ = const. = 0.1).

In Fig.1 the oscillograms of the scattered wave at the separated frequencies are presented. Figs.1a,d show that the signals have a "burst" character. The frequency and the duration of the "bursts" depend upon signal frequency. Such nature of the waves in the drift wave frequency range was already noted in the TFR tokamak [1] . It is also noteworthy that the oscillations at the frequencies f = 20 kHz (Fig.1a) and f = 100 kHz (Fig.1b) have totally different behaviour. The oscillograms shown in Fig.1 were obtained during ECH of currentless plasma ($\bar{n}_e = 8 \cdot 10^{12}$ cm^{-3}, $T_e(0)$ = 900 eV, B = 13.4 kG). At the end of microwave power pulse (P_{ECH} = 180 kW, Fig.1c) the intensity of the oscillations at the frequency f = 20 kHz (Fig.1a) decays over 10 milliseconds whereas the oscillations at the frequency f = 100 kHz (Fig.1b) decay over 3-4 ms (corresponding to the estimation of the $\tau_E \approx 3.5$ ms).

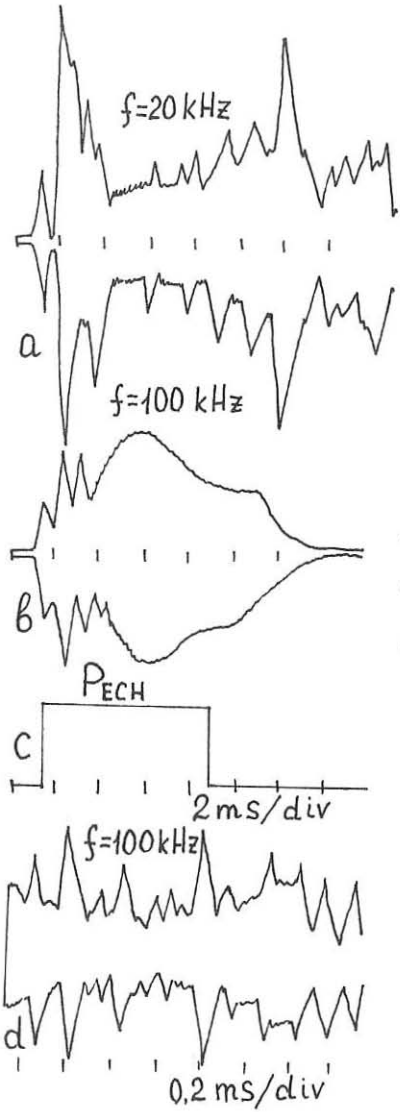
f=20 kHz
a
f=100 kHz
в
P ECH
c
2 ms/div
f=100kHz
d
0,2 ms/div

Fig.1.

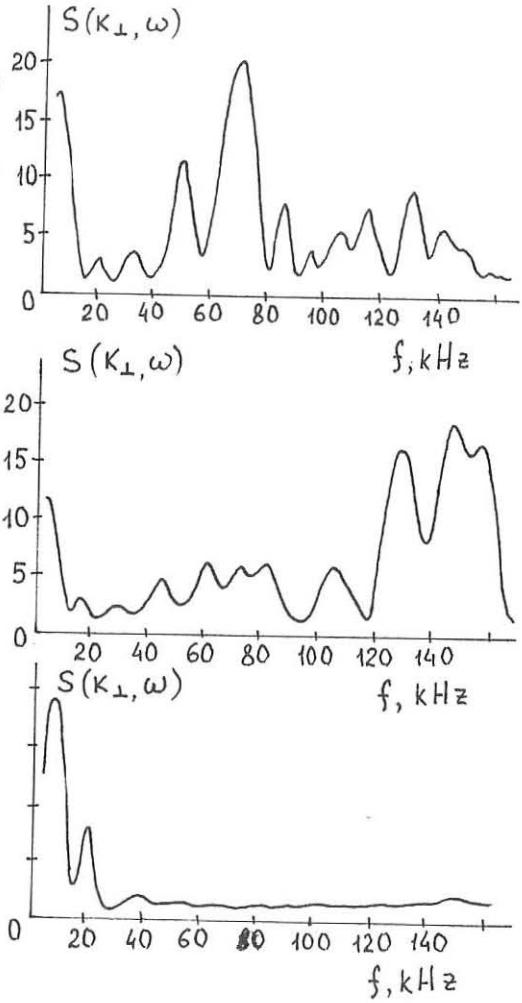
S(K⊥, ω)
20
15
10
5
0
20 40 60 80 100 120 140
f, kHz
S(K⊥, ω)
f, kHz
S(K⊥, ω)
f, kHz

Fig.2.

The frequency spectra of plasma waves with the poloidal wavenumber $k_\perp = 6$ cm^{-1} are presented in Fig.2. These spectra were obtained during the time interval T = 0.5 ms. In OH regime (Fig.2a) plasma had the following parameters: I_p = 14 kA, B = 12 kG, $\bar{n}_e = 10^{13}$cm^{-3}, $T_e(0)$ = 400 eV, the density profile $n_e(r) = n_o(1-(r/a)^2)$, the working gas- hydrogen. During the ECH of currentless plasma (Fig.2b) the parameters were: P_{ECH} = 100 kW, B = 13.4 kG, $\bar{n}_e = 7\cdot10^{12}$cm^{-3}, $T_e(0)$ = 800eV, $n_e(r) = n_o(1-(r/a)^2)$, the working gas - helium (a = 11.5cm- the mean plasma radius). In the ECH regime of currentless hydrogenium plasma (the spectrum in Fig.2c) parameters of plasma were as follows: $n_e(r) = n_o(1-(r/a)^6)$, P_{ECH} = 100 kW, B = 13.4 kG, $\bar{n}_e = 8\cdot10^{12}$cm^{-3}, $T_e(0)$ = 550 eV. The comparison of the spectra shown in Fig.2 reveals the following features: frequency range corresponding to the maximum of the spectral density $S(k_\perp, \omega)$ depends greatly on the density profiles and weakly depends on the electron temperature. The spectral density maximum corresponds to the frequency $\omega/2\pi$ = 130kHz in the case of the parabolic profile of $n_e(r)$ and relatively high electron temperature (Fig.2b). At the same time when the density profile is broadened (Fig.2c) the major part of the spectral density lies in the frequency range f≤20 kHz. It should be noted that the frequency spectra obtained at the different values of $k_\perp$ are not distinguished from each other.

Such behaviour of the spectra is in agreement with the expression for the spectrum of short-wavelength drift waves ($k_\perp \rho_i > 1$) [2] :

$$\omega = -\frac{T_e k_y v_{Ti}}{T_e + T_i(1+k^2 r_{De}^2)} \frac{1}{\sqrt{2\pi}\, k_\perp} \frac{\partial}{\partial x} \ln \frac{n_e}{\sqrt{T_e}}$$

An estimation for the parameters in the scattering volume T_e = 200 eV, T_i = 40 eV gives a value f = 60 kHz.

The spectral density $S(k_\perp) = \int S(k_\perp, \omega)\, d\omega$ as a function of the wavenumber $k_\perp$ in OH regime is shown in Fig.3. The intensity of the waves in the range of wavenumber from $k_\perp$ = 6 cm^{-1} to $k_\perp$ = 20 cm^{-1} decreases by the order of magnitude.

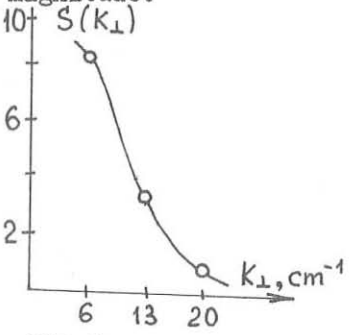

Fig.3.

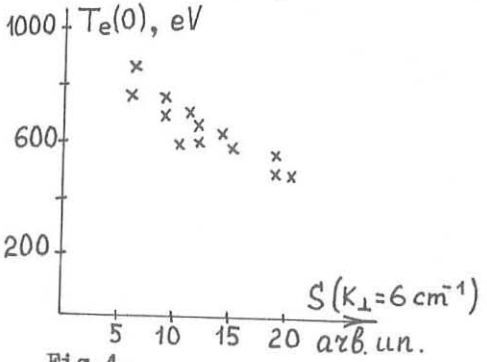

Fig.4.

In different heating regimes the wave intensity can change several times. The lowest relative level of fluctuations was observed during ECH of currentless plasma: $\delta n/n_e = 2 \cdot 10^{-2}$, whereas in the OH regime $\delta n/n_e$ is equal to $5 \cdot 10^{-2}$. The values of spectral density $S(k_\perp)$ for $k_\perp = 6$ cm^{-1} and electron temperature in the centre of plasma for different heating regimes in the L-2 stellarator (OH, ECH of current plasma, ECH of currentless plasma) are shown in Fig.4. As it is shown the temperature achieved during the heating pulse is higher when the fluctuation level is lower. The dependence of $T_e = f\ ((\delta n/n_e)^2)$ can show the connection of the drift waves intensity with the transport phenomena.

References

1 Barkley,H., Andreoletti,J., Gervais,F., et al., Int. Conf. on Plasma Physics, Kiev, 1987, v.3, p.24.
2 Alexandrov, A.F., Bogdankevich,L.S., Rukhadze,A.A. The principles of plasma electrodynamics. Moscow, 1978, p. 270.

CURRENTLESS PLASMA HEAT TRANSPORT IN THE L-2 STELLARATOR.

Andryukhina E.D., Dyabilin K.S., Fedyanin O.I.

General Physics Institute, Academy of Sciences of the USSR, 117942 Moscow, Vavilov street, 38.

Experiments in the L-2 stellarator have shown [1,2] that it is possible to create currentless plasma with $n_e = 10^{13} cm^{-3}$, $T_e(0) \sim 1$ keV, $T_i(0) \sim 0.1$ keV by ECRH. In these conditions the confining magnetic field structure is determined by external windings only and there is no drift motions in plasma due to the heating current. These circumstances allow to make the comparison of experimental results with the neoclassical heat transport theory in the stellarator.

Electron temperature profiles, mean plasma density, diamagnetic signal, radiation losses, absorbed microwave power, ion temperature were measured in our experiments. Numerical simulations were made for plasma energy balance by using neoclassical heat transport theory. The calculations were carried out in the frame of the model proposed in paper [3] . These calculations allowed us to follow the behavior of the measured plasma parameters during the heating pulse.

The L-2 parameters are: R = 100 cm, $r_p = 11.5$ cm (separatrix); helical windings: l = 2, m = 14, rotational transform $\iota(0) = 0.2$, $\iota(r_p) = 0.8$; ECRH: $\lambda = 8$ mm, $P_o = 200$ kW, t = 10 ms.

The microwaves of the ordinary polarization were launched into the vacuum chamber from weak field side via waveguide or quasi-optical system. The heating showed resonant behavior with the magnetic field; there was an optimal heating depending on plasma density. We present here the results which correspond to the optimal heating conditions.

The results obtained for one set of experimental conditions (depending on the microwave power value and the transmition method) are shown in Fig.1. One can see from these Figs. that after breakdown the mean electron density grows during 0.5 ms up to its maximal value and then remains constant. The electron temperature in the plasma core increases during 2÷3 ms and then smoothly saturates. The absorbed power has a similar behaviour, sometimes it even decreases to the end of the heating pulse. We will not present here the details of ion heating mentioning only that after 2 ms $T_i(0)$ reaches

its limit value. The radiation losses in these experiments are only a small fraction of the absorbed power (~ 15%) and therefore do not play a significant role in the plasma energy balance.

Comparing numerical calculations of plasma energy balance with the experimental results we consider two important features: the dynamics of heating and radial temperature profiles and the dependences of central electron temperature and plasma energy content W on the value of the absorbed power. The dynamics of heating has to show that the used functional dependence of the heat transport coefficient on temperature and density is correct. The radial profiles depend more on the magnetic field structure.

Fig.2 shows the calculated (solid line) T_e profile for P_{ab} = 60 kW , t = 4 ms. In calculations $P_{ab}(t) = 60(1-e^{-\frac{t}{\tau}})$, τ = 2 ms, and $P_{ab}(r)$is uniformly distributed inside the volume with $r \leqslant 0.4\ r_p$, which correspond to the experimental data (see Fig.1) and one-path absorption simulations [4] . The experimental data were taken from Thomson-scattering measurements at the end of the heating pulse.

Fig.3a shows the diamagnetic signal (solid line) and the calculated plasma energy (dashed line), Fig.3b shows experimental data for $T_e(0)$ and the calculated curve (dashed line) $T_e(0)$ during the heating pulse. Good agreement of the calculated curves with the experimental results shows that the used model seems to be correct.

Making a final conclusion from the comparison of experimental and calculated data let us consider two curves shown in Figs.4a and 4b. These curves represent dependences $T_e(0)$ and W on the value of the absorbed microwave power P_{ab} for the end of the heating pulse. In fact the launched microwave power is changed in the experiment and that causes the chenge of the absorbed power. The electron temperature for small P_{ab} increases very fast with the power input increase but then this increase slows down due to strong dependence of the heat transport coefficient on the temperature. The energy content W still increases more rapidly. The calculations show that it can be due to broadening of the electron temperature profile, but it is difficult to estimate this fact experimentally from Thomson scattering measurements. By the way it is clearly seen from Fig.4 that the experimental data (dashed area) are in good agreement with both calculated dependences T_e and W on the absorbed power.

Summary. The numerical simulation of currentless plasma energy balance in the L-2 stellarator based on the neoclassical theory of the heat transport makes it possible to describe the dynamics of plasma heating by ECRH method. Time dependence

of the electron temperature, its profiles and plasma energy containment during the heating pulse were calculated. The experimental data are rather well described by the calculated curves. The experimental dependence of electron temperature and diamagnetic signal on the input power do not contradict the results obtained from the proposed theoretical model.

Acknowledgements. The authors are grateful to ECRH team, Dr. Larionova,N.F. who made Thomson-scattering measurements and Dr. Shpigel',I.S. for the helpful discussion.

References

1 Andryukhina,E.D., Agapov, L.N., Batanov,G.M., et al., Pys'ma ZhETF, Vol. 40, No 9, (1984) 377.
2 Andryukhina,E.D., Akulina,D.K., Batanov,G.M., et al., Electron Cyclotron Heating (ECH) of the Currentless and "Target" Current Plasmas by an Ordinary Wave in the L-2 Stellarator. The report of this conference O 1 B 01
3 Dyabilin,K.S., Kovrizhnykh,L.M., in Plasma Phys. and CNFR 1984 (Proc. 10th Int. Conf. London, 1984), Vol.2, Vienna (1985) 47.
4 Likin,K.M., Ochirov,B.D., Skvortsova,N.N. Energy Deposition Profile at Simulation of the ECRH in the L-2 Stellarator. The report of this conference P 1 B 02

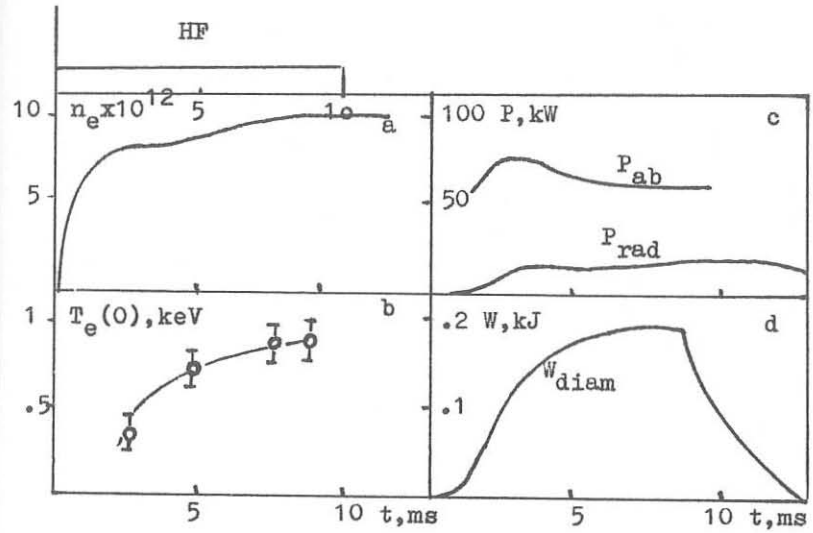

Fig.1

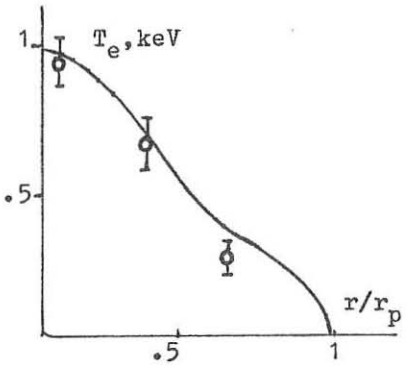

Fig.2

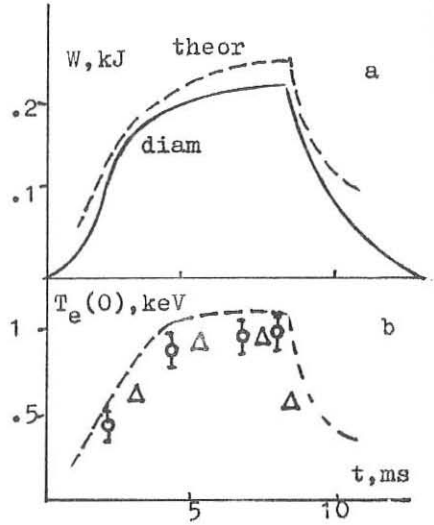

Fig.3

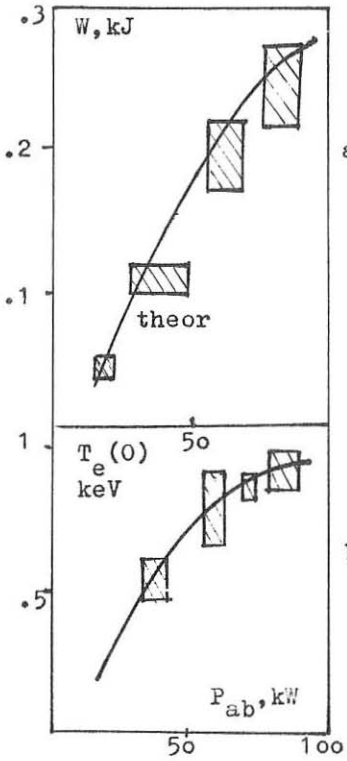

Fig.4

L-2 STELLARATOR PLASMA ROTATION IN OHMIC HEATING REGIME

Voronov G.S., Donskaya N.P.

General Physics Institute, Academy of Sciences of the USSR
117942 Moscow, Vavilov street, 38, USSR

The interest in the subject of plasma rotation has grown up in the recent years as a result of understanding the important role of electric field in transport processes.

Plasma rotation in L-2 stellarator was measured from the Doppler shift of lines emitted by the main gas He and oxygen and carbon impurities ions. Two channel monochromator with high quality plane grating 1200gr/mm was used in the first and second orders (the inverse dispersion - 13 and 6.5 Å/mm). The apparatus function is Gaussian with half-width 0.5Å. Quartz window limits the available spectral range above 2000Å. Two space channels were created by opaque screens at the entrance and exit slits. Radiation from each part of exit slit is directed by mirrors to separate photomultiplier. Plasma radiation is directed to the entrance slit by a system of mirrors. Toroidal rotation was measured along tangent line of the magnetic axis, parallel and antiparallel to the direction of toroidal magnetic field. Poloidal velocity was measured by comparing spectral profiles of impurity lines viewing along two tangentials to the same magnetic surface. Such measurements are independent on an exact wave length setting of spectrometer. It needs usually 15-20 shots to measure the line counter. The wave length changes from shot to shot for both channels simultaniously.

To collect experimental data we use a computer working on-line with the experiment. The Doppler line contour and the constant back ground are determined by four parameters C, F , T, λ_0:

$$F = C + F_0 \exp\left\{-mc^2(\lambda-\lambda_0)^2/2\kappa T\lambda_0^2\right\}$$

The special code was used to fit the optimal values for these parameters from experimental data by the nonlinear minimization mean-squares method. The accuracy of temperature T and wavelength λ_0 (the contour center) are determined mainly by discharge reproducibility and was $T \sim 10$ eV, $\lambda_0 \sim 0.02$Å. Corresponding uncertainty in rotation velocity is 1 km/s.

Experimental results are shown in Fig.1 and 2. The direction of plasma poloidal rotation coincides with that of the electron diamagnetic drift. The maximum value of poloidal

velocity $V_p \sim 1.5$ km/s occurs in the middle part of the plasma radius. The direction of plasma poloidal rotation changes its sign at the plasma edge ($r > 10$ cm). The direction of toroidal velocity coincides with that of the plasma current and toroidal magnetic field. Its magnitude is 4 km/s. The direction of toroidal magnetic field and ohmic current are the same as usual in the L-2 stellarator, since in other case the discharge becomes unstable when the total rotational transform comes to zero. So we can change the direction of magnetic field and ohmic current only simultaniously.

We expected that in that case both components of the rotation velocity should change their signs while their values should stay the same. But the situation is more complicated. Poloidal velocity is reversed as we expected, but its value changed and the radial profile of V_p altered (Fig.1). Toroidal velocity decreased, but its direction did not change. So, the direction of V_t became opposite to magnetic field and current (Fig.2).

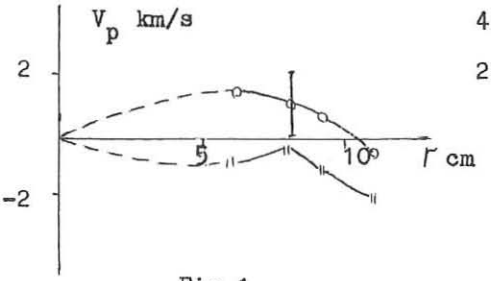

Fig.1.

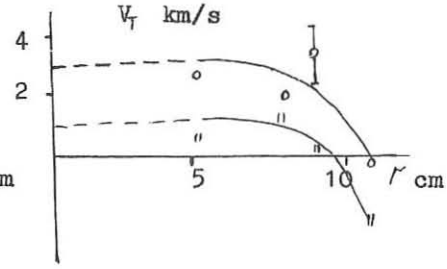

Fig.2.

It looks like if we have two parts of rotation velocity: one, which changes its sign when magnetic field and current are reversed, and the second one whose direction does not change. This constant rotation velocity value is 2 km/s. The reason of that asymmetry is not yet understood. Probably, this is connected with asymmetric stray fields that could change the magnetic field structure. Some asymmetry in electron and ion temperature profiles and radiation losses has been observed too.

We can estimate the value of radial electric field in plasma from the experimental values of toroidal and poloidal rotation velocities:

$$E_r = B_p \frac{v_T}{c} - B_0 \frac{v_p}{c} + \frac{T_i}{eZ}\left(\frac{n_i'}{n_i} + \frac{T_i'}{T_i}\right) \qquad (1)$$

This equation was obtained from the radial force balance and it includes no assumption. We suppose that ion density profile is similar to electron density profile $n_e(r)$ which

was measured by multichannel submillimeter interferometer and occured to be parabolic. $T_i(r)$ profile is taken from Doppler measurements.

The radial electric field is negative. Its value reaches -30 V/ cm (Fig.3). The sign of electric field does not change when the magnetic field is reversed and its value changes slightly.

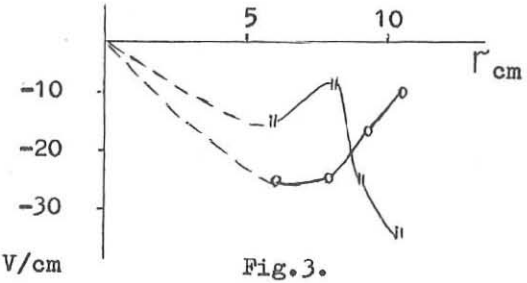

Fig.3.

In accordance with neoclassical theory [1], poloidal and toroidal rotation velocities are:

$$v_p^{n.c.} = K \frac{c\,T_i'}{e Z B_\theta}, \qquad v_t^{n.c.} = \frac{c\,T_i}{e Z B_p}\left[\frac{e Z E}{T_i} - (1-K)\frac{T_i'}{T_i} - \frac{n'}{n}\right] \qquad (2)$$

The coefficient K depends on collision frequency changing from K = ±5 on the plateau to K = -2.1 in Pfirsh-Slütter regime. Experimental values of rotation velocities considerably differ from neoclassical predictions poloidal velocity is 3-4 times more, but toroidal component is an order less. The decrease of the magnetic field leads to the increase of rotation in accordance with (2).

References

1 Hazeltine,R.D., Phys. Fluids 17, (1974), 961.

ANALYSIS OF ECRH IN THE TJ-II FLEXIBLE HELIAC USING RAYS

C. Alejaldre and F. Castejón

Asociación **EURATOM/CIEMAT** para Fusión
C.I.E.M.A.T.
28040 Madrid, Spain

R.C. Goldfinger and D.B. Batchelor

Oak Ridge National Laboratory
Tennessee , U.S.A.

Introduction

Previous studies assuming linear propagation of microwaves in the range of the first or second electron cyclotron frequency, launched into a slab stratified plasma confined by the magnetic configuration of the TJ-II Heliac to be built in Madrid, have shown ECRH as an efficient way of heating and controlling the temperature profile in this device[1]. Unfortunately the particularly difficult TJ-II geometry, questions any study that does not take into consideration the full 3-D geometry of the device . The 3-dimensional , ray-tracing code RAYS[2,3] developed at Oak Ridge National Laboratory has been adapted to the geometry of the TJ-II flexible heliac. Using RAYS a study ,taking into consideration the limitations of the actual vacuum chamber for access to the plasma, has been conducted to obtain the optimum position of ray launching from the point of view of maximizing power deposition and controlling the temperature profile. The power absorbed by the plasma in "one-pass" is shown to have maximum values of the order of 40% for first harmonic propagation in the O-mode and 90% for X-mode propagation in the 2^{cd} Harmonic. The spatial absorption region is of the order of 2-3 cms. and therefore ECRH still looks as a very convenient way of temperature profile control in this device.

RAYS code

The ray tracing is carried out by integrating the Hamiltonian form of the geometrical optics equations using the two-component, cold plasma dispersion relations

$$\frac{dr}{ds} = \frac{1}{|V_g|}\frac{dr}{dt} = -\,\mathrm{sgn}\left(\frac{\partial D}{\partial \omega}\right)\frac{\partial D/\partial k}{|\partial D/\partial k|} \qquad \frac{dk}{ds} = \frac{1}{|V_g|}\frac{dk}{dt} = -\,\mathrm{sgn}\left(\frac{\partial D}{\partial \omega}\right)\frac{\partial D/\partial r}{|\partial D/\partial k|}$$

where the dispersion relation is,

$$D = \left[\left(\varepsilon_1 - n_{\parallel}^2\right)\left(\varepsilon_1 - n_{\parallel}^2\right) - \varepsilon_2^2\right]\left(\varepsilon_3 - n_{\perp}^2\right) - \left[n_{\parallel}^2 n_{\perp}^2\right]\left(\varepsilon_1 - n^2\right) = 0$$

and the coefficients ε_1, ε_2, ε_3 are defined as

$$\varepsilon_1 = 1 - \frac{\omega_{pe}^2}{\omega^2 - \omega_{ce}^2} - \frac{\omega_{pi}^2}{\omega^2 - \omega_{ci}^2} \qquad \varepsilon_2 = -\frac{\omega_{pe}^2}{\omega^2}\frac{\omega_{ce}}{\omega^2 - \omega_{ce}^2} - \frac{\omega_{pi}^2}{\omega^2}\frac{\omega_{ci}}{\omega^2 - \omega_{ci}^2}$$

$$\varepsilon_3 = 1 - \frac{\omega_{pe}^2}{\omega^2} - \frac{\omega_{pi}^2}{\omega^2} \qquad \omega_{pe,\,i} = \left(\frac{4\pi n_e^2}{m_{e,\,i}}\right)^{\frac{1}{2}}, \quad \omega_{ce,\,i} = \frac{eB}{m_{e,\,i}}.$$

The TJ-II vacuum magnetic field is obtained using the code AVAC[4] with two vertical field coils, thirty two helically distributed coils and a helical coil wrapped around a

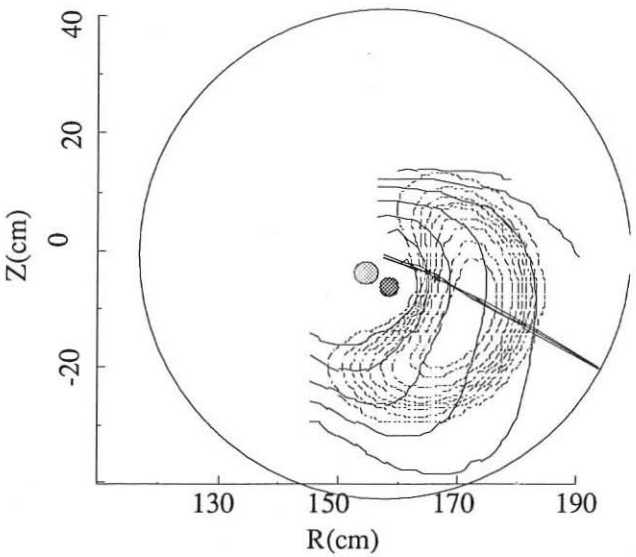

Figure 1
Poloidal projection of four O-mode rays launched at Ψ=5.6°, θ=-20°. *The magnetic surfaces and the mod-B curves are also shown.*

circular one to form the so-called hard core in a configuration appropriate for TJ-II. The toroidal magnetic flux function ψ was obtained from a fourier representation of the three-dimensional flux surfaces[5]. The plasma density and electron temperature are assumed to be constant at the flux surfaces and given by the function:

$$d(\psi) = \frac{d_c - \tanh \frac{\psi - \psi_0}{\Delta^2}}{d_c + d_0} \qquad d_0 = \tanh \frac{\psi_0}{\Delta^2} \qquad d_c = 1 + d_\infty \frac{1 + d_0}{1 - d_\infty}$$

In the TJ-II Heliac, plasma breakdown and heating will be initially based upon an ECRH system consisting of a 200 kW, 28 GHz. gyrotron. To obtain more relevant plasmas two 56 GHz gyrotrons able to deliver 400 kW will be provided.

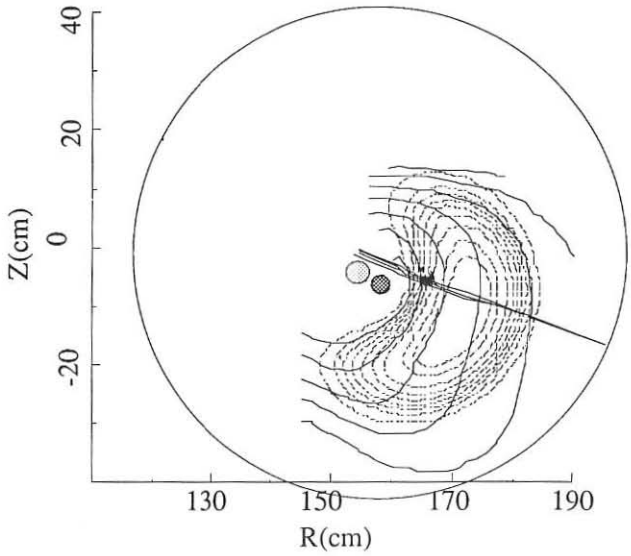

Figure 2
Poloidal projection of X-mode rays for the same situation of fig.1.
ω=56 GHz.

Taking into consideration the physical location of the windows and the situation of the cut-offs and resonances, a study has been conducted to determine the optimum position for ECRH heating from the point of view of this linear theory. In figs. 1,2 the trajectories for rays coming from the window corresponding to the toroidal position 5.625° are shown. At this toroidal position the resonance region is accessible for rays coming from

the "low field" direction and they reach it in regions of high plasma density. Fig. 1 corresponds to propagation in the O-mode of the first harmonic with a central plasma density of .65 x 10^{13} cm^{-3} and a central temperature of 1.8 keV. Fig. 2 shows the trajectories for rays propagating in the X-mode at 56 GHz into a plasma of central density 1.5 x 10^{13} cm^{-3}, $T_e(0)$=1 keV

A fully relativistic absorption module is used in the code to evaluate the fractional absorption of wave energy given by

$$\eta(s) = 1 - \exp\left(-2\int_0^s \mathbf{k}_i \cdot ds\right)$$

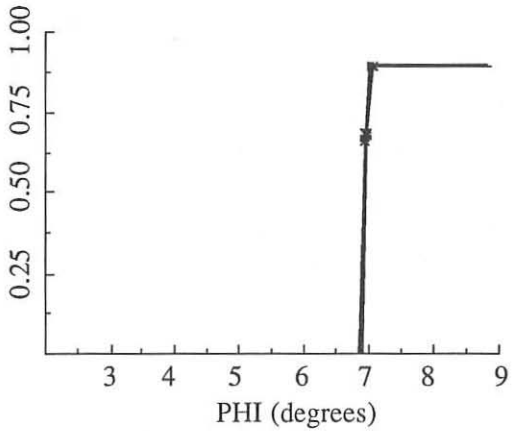

Figure 3

Fractional power absorbed for propagation in the x-mode.
$n_e(0)$=1.5 x 10^{13}, $T_e(0)$=0.8 keV.,ω = 56 GHz.

Typical one-pass power absorption values , for the same conditions of figs. 2-3 are in the order of 40% for heating in the ordinary mode of the first harmonic and ≈ 90% for the x-mode of the second harmonic, see figure 3, that agree well with those found in Ref.1. The toroidal position shown, $\Phi = 5.625°$ has been chosen for ECRH heating for both:accessibility and power absorption, although considerations for quasi-linear effects have not been taken into consideration in the present analysis.

References:

1 C. Alejaldre and J. Guasp, Nucl. Fusion **27** (1987) 2153
2 Batchelor,D.B., Goldfinger,R.C., RAYS:A Geometrical Optics Code for EBT, Oak Ridge National Lab., Rep. ORNL/TM-6844(1982)
3 Goldfinger,R.C., Batchelor,D.B., Nucl.Fusion **27** (1987) 31
4 Lynch, V.E. et al., J. Comput. Phys. **66** (1986) 411
5 Harris, J. et al., private communication

EXPERIMENTAL STUDIES OF ENERGY TRANSPORT OF ECRH PLASMA ON HELIOTRON E.

M.Sato, H.Zushi S.Sudo, K.Itoh, N.Noda, T.Mutoh, S.Morimoto, F.Sano, K.Kondo, H.Kaneko, T.Mizuuchi, Y.Takeiri, H.Okada, Y.Nakamura, S.Kobayashi, M.Iima, O.Motojima, A.Iiyoshi, K.Uo

Plasma Physics Laboratory Kyoto University
Gokasho, Uji, Kyoto, Japan

1. Introduction

The energy transport has been investigating on ECRH currentless plasma in the nested magnetic field with high rotational transform and high ripple produced by helical windings[1]~[3]. The radial profiles of electron and ion temperatures, electron density and microwave power deposition profiles were measured to evaluate the energy flux and transport coefficients. The polarity of radial electric field, Er, are observed by the measurement of poloidal rotation of plasma. The impurity ion particle confinement time are also observed by the blow off silicon injection method. The informations from the plasma boundary are obtained by the poloidal array of thermocouplers.

The energy transport near the half radius can be explained mainly by neoclassical theory in the trapped particle region with radial electric field. The anomalous transport is dominant on the out of the half radius. The energy transport in the center and particle transport have not been clear yet.

2. Plasma parameters and radial profiles

The microwave frequency, radiative mode of antenna and power are 53.2GH$_z$, TE$_{02}$ mode and 150 kw~650 kw, respectively. The almost all the plasma parameters, such as electron and ion temperatures, electron density, intensities of soft x-ray, VUV impurity line emissions and bolometric signals reach to the steady state values in the beginning of 10 to 20 m sec of rf pulse. During rest of the pulse, the parameters can be kept constant only by control of gas puffing. Here, steady state means that the pulse length is much longer than the characteristic time of the parameters. The electron density profiles are measured by 6ch FIR interferometer. The line average density can be changed from 0.6×10^{19} m^{-3} to 3.3×10^{19} m^{-3}. The electron temperature (Te(r))and it's time evolution (dTe(r)/dt) are detected by electron cyclotron emission along the longer axis of magnetic surface.

Fig.1 shows the electron and ion temperatures and density profiles of low density plasma at the power levels of 150 kw and 650 kw. If we assume that the electron energy transport does not change with and without rf pulse, the power deposition profile can be estimated at the pulse end as

$$Pabs(r)=1.6 \times 10^{19}\frac{d}{dt}(Te(r)\cdot ne(r)) \quad (w/m^3).$$

The deposition profiles are also evaluated by rf pulse modulation as shown by dashed line in the figure. The estimated power by this method is about two times larger than that of pulse end. The reason of the discrepancy has not been clear. The error bars on q_{eEXP} include this uncertainty in Fig.2.

3. Energy transport

The electron heat flux can be obtained experimentally as

$$q_{eEXP} = 1/r \int_0^r rdr \left\{ P_{abs}(r) - P_{ei}(r) - P_{rad}(r) \right\},$$

where, $T_e(r)$, $n_e(r)$, $P_{abs}(r)$, $P_{ei}(r)$ and $P_{rad}(r)$ are averaged over the calculated magnetic surfaces.

$T_e(0)$ and line average density n_e are varied from 0.9 to 1.7 keV and from 0.6 to 3.3 x $10^{19}m^{-3}$, respectively by rf power and gas puffing. Fig.2 a,b show the comparison of q_{eEXP} with that of neoclassical theory for $n_e \simeq 1 \times 10^{19}m^{-3}$ plasma. The radiation loss $P_{rad}(r)$ is negligible small in such low density plasma. Using experimentally obtained $T_e(r)$ and $n_e(r)$, we estimate the neoclassical values of q_{ePL} and $q_{eRipple}$[3], which are large enough to explain the heat transport by the theory at 0.3 $\leq$ r/a $\leq$ 0.6. If the transport is mainly governed by neoclassical theory, $q_{e\ EXP}$ and heat conductivity $\chi_{e\ EXP}$ should be close to the theoretical prediction including the parameter dependence on $n_e(r)$, $T_e(r)$, ∇T_e and ν_{**}.

Fig.3 shows $\chi_{eEXP}(=q_{eEXP}/1.6 \times 10^{19} \times n_e(r)\ {}_r T_e)$ versus T_e, including all the data obtained by the series of experiment. χ_e has the dependence close to $T_e^{3\sim 3.5}$ which correspond well with rippled transport of $T_e^{3.5}$.

As for the collision frequency $\nu_{**}(=\nu_e/w_h\varepsilon_h)$, if $0.1 < \nu_{**}$, the normalized heat flux q_{eEXP}/q_{ePL} increase with $1/\nu_{**}$. (Fig.4)

However, in the low collision regime $\nu_{**} < 0.1$, the heat flux does not increase so rapidly as $1/\nu_{**}$.

The direction of poloidal rotation of impurity ions shows that radial electric potential is positive in the low collision regime. The electric fields are estimated to be $100\sim 200$ V/cm at $0.6 \leq r/a$. Unfortunately, we

do not know the velocity of rotation in the central part of plasma. The particle flux balance calculation, based on the data of neutral particle density $n_o(r)$, can also suggest positive potential within the half radius.

The parameter dependence and absolute values of electron heat flux can be explained well by neoclassical theory in the wide collision frequency range, especially if we consider the radial electric field in the low collision regime.

The heat flux out of the half radius is governed by anomalies transport, since the absolute values and parameter dependence are completely different from neoclassical theory as shown in Fig.3. Plotting q_{eEXP} to $n_e(r)\nabla_r T$, we know that the effective heat conductivity χ_e exist in $0.8 \sim 2\ m^2/s$ at r/a=0.8, which are almost the same order of the other ECRH experiments on toroidal devices.

The gross energy confinement time τ_E^G is fitted to,

$$\tau_E^G = 4.1 \times 10^{-8}\ P_{abs}^{-0.56}\ n_e^{-0.45} \qquad \text{(sec)}$$

as shown in fig 5.

The particle transports are now under investigation. The density decrease in the plasma center can not be explained only by neoclassical theory.

Reference

[1]K.Uo et al., Proc. 11th Int. Conf. on Plasma Phys. and Controlled Nucl. Fusion Research (kyoto, 1986), IAEA-CN-47/D-I-1.

[2]A.Iiyoshi, M.Sato, O.Motojima, T.Mutoh, S.Sudo, M.Iima, S.Kinoshita, H.Kaneko, K.Uo, et al., "Confinement of a Currentless Plasma in the Heliotron-E.", Physical Review Letters, Vol. 48, (1982)p. 745.

[3]K.Itoh; Proc. US-Japan Workshop Anomalous transport in toroidal fusion devices, Feb 1987, p.73.
Will be contributed to Plasm: Phys. and Controlled Fusion

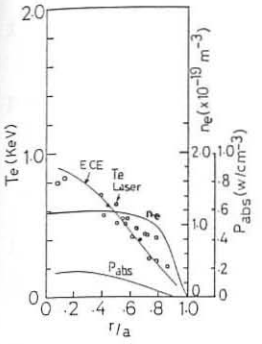

Fig. 1(a)

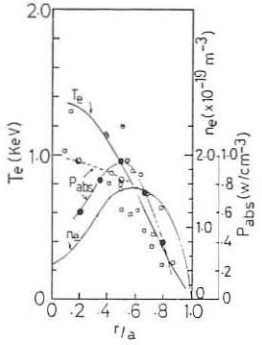

Fig. 1(b)

Radial Profiels of Te, ne Pabs
white circles; Te by laser
Black circles; Pabs at pulse end

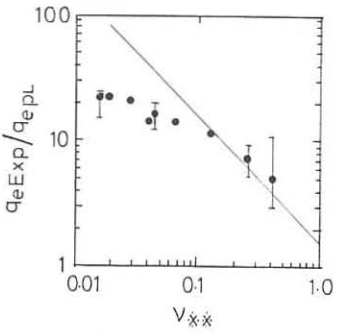

Fig. 4
V_{xx} dependence of q_{eEXP}/q_{ePL}

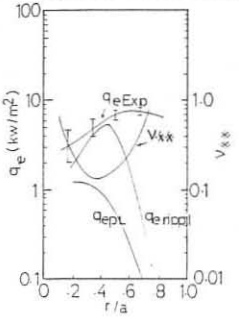

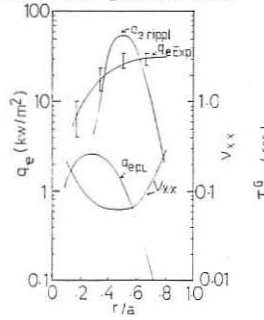

Fig. 2(a) Fig. 2(b)
Comparisons of electron heat flux with neoclassical theory

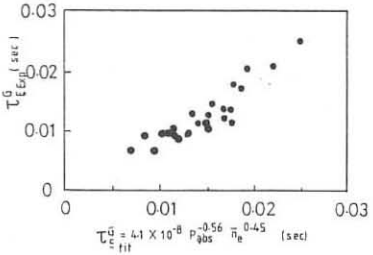

Fig. 5
Scaling of Gross energy confiment time

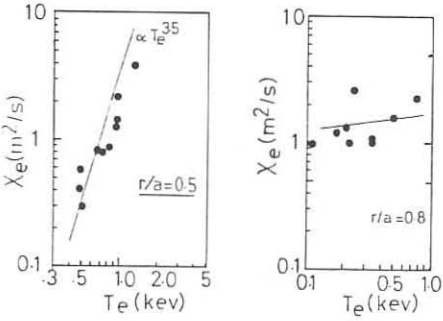

Fig. 3
χ_{eEXP} v.s Te

FINITE-BETA EFFECT ON NEOCLASSICAL TRANSPORT IN TORSATRONS

V.E.Bykov, D.L.Grekov, A.A.Shishkin,
Institute of Physics and Technology, the Ukrainian Academy of Sciences, Kharkov 310108, USSR
L.Garcia, J.H.Harris, and J.A.Rome
Oak Ridge National Laboratory, Oak Ridge, Tennessee, USA

For reduction of the neoclassical transport coefficients in the regime where $D_\perp, \chi_\perp \propto 1/\nu$ in torsatrons, a special winding law can be used, as described in refs. /1,2/. The helical conductors must be arranged so that the winding pitch angle is steeper on the inside than on the outside of the torus. This requirement can be fulfilled by choosing a negative modulation coefficient $\alpha < 0$ in a helical winding law of the form $(m/l)\varphi = \vartheta - \alpha \sin \vartheta$. Here m is the number of magnetic field periods on the torus, l is the poloidal multipolarity of the helical field, φ and ϑ are, respectively, the poloidal and toroidal angles, with ϑ measured from the direction opposite to the principal normal to the circular axis of a torus.

For a winding law with $\alpha < 0$, the amplitude of the helical ripple in $|B|$ along the field lines is increased on the inside of the torus and is decreased on the outside of the torus. Such a spatial variation in $|B|$ results in a weakening of the ∇B drift of particles trapped in the helical ripple wells /3/ and thus reduces the plasma transport coefficients in the $1/\nu$ regime. The signs and amplitudes of satellite harmonics of the main helical field harmonic play a crucial role in determining the magnitude of this effect.

The presence of equilibrium plasma currents, however, can significantly alter the harmonic content of the magnetic field variation along the lines of force, principally because of the outward shift of the magnetic surfaces at finite plasma pressure with the result that the transport coef-

ficients increase /4,5/.

Therefore, it is important to establish whether the apparent transport improvement seen in vacuum field configurations with $\alpha < 0$ (in comparison with configurations having $\alpha > 0$) is retained at finite $\beta = 8\pi P/B_0^2$.

The present study concerns the behaviour of the geometric factor D, which determines the magnitude of the transport coefficients $D_\perp$, $\chi_\perp \propto 1/\nu$, at finite plasma pressure. Two l=2 torsatron configurations with the same coil aspect ratio ($R/a \simeq 3.4$) and number of field periods (m=8) but with differing modulation coefficients $\alpha \simeq a/R$ and $\alpha = -a/R$ are compared. The two configurations differ in the angles of rotational transfer on the outermost closed magnetic surface of the vacuum approximation, i.e., at the plasma boundary $\iota(a_0) = 0.65$ and 1.2 for $\alpha = -a/R$ and a/R, respectively. Hence, the β_{eq} values determined by $2\,\iota^2(a_0)\,a_0/R$ turn out to be different for the systems considered. To perform a correct comparison between the two traps (at as most equal conditions as possible), the $\beta(0)$ values were chosen such that the $\beta(0)/\beta_{eq}$ ratios were close for the two torsatrons. To have outermost magnetic surfaces of nearly the same size, the transverse magnetic fields (averaged along the circular axis of the torus) were chosen to be $B_\perp/B_0 = 2\%$ and -2% for $\alpha = a/R$ and $-a/R$, respectively, /2/. These configurations were chosen only as an example of the torsatrons with the satellite harmonic content of the magnetic field differing in sign, and should not be considered as optimum with respect to other parameters.

Plasma equilibrium and variations in the $|B|$ distribution along magnetic field lines due to finite beta were studied using a three-dimensional equilibrium code NEAR (with a fixed plasma boundary). As seen from fig. 1, the $|B|$ modulation along the field lines does not change its behaviour with the plasma presence: the bumps of the helical magnetic field in

$|B|$ are localized on the inside of the torus at $\alpha = -a/R$ and on the outside at $\alpha = a/R$. For the analysis we have chosen the surfaces with $r_c/a = 0.22 - 0.25$ at $t\,(r_0) = 0.7$ and 0.4 for $\alpha = a/R$ and $\alpha = -a/R$, respectively, i.e., the surfaces whose size is approximately half the plasma radius. The nearest satellites ε_{l-1} and ε_{l+1} retain their signs relative to the main helical harmonic ε_l (fig. 1). In the $\alpha = -a/R$ torsatron, the $\varepsilon_{l\pm1}/\varepsilon_l$ ratio decreases as β increases and this proves to be a negative effect because the nearest satellites at $\varepsilon_{l\pm1}/\varepsilon_l < 0$ reduce the geometric factor in $D_\perp, \chi_\perp \sim 1/\nu$.

The geometric factor D is expressed in terms of the field harmonic parameters as /1, 2/

$$D = \varepsilon_t^2 \varepsilon_l^{3/2} \frac{a^2}{r_c^2} \left[\gamma_1 - \frac{\varepsilon_l}{\varepsilon_t} \gamma_2 + \left(\frac{\varepsilon_l}{\varepsilon_t} \right)^2 \gamma_3 \right],$$

where γ_1, γ_2, γ_3 are the functions of $\varepsilon_{l\pm1}/\varepsilon_l$, $\varepsilon_{l\pm2}/\varepsilon_l$ /2/. The comparison of D values for the same $\beta(0)/\beta_{eq}$ values at fixed r_c/a ratios shows them to be by a factor of 1.5 - 2 lower in the torsatrons with $\alpha = -a/R$ than in the $\alpha \simeq a/R$ torsatrons (fig. 2).

The results obtained lead to the following conclusions.

1) At finite plasma pressure, as in the case of a vacuum configuration, the proper choice of the modulation coefficient of helical conductors can efficiently change the modulation and harmonic content of $|B|$ and thus decrease neoclassical transport coefficients in the $1/\nu$ regime.

2) From the analysis of the configurations considered above as an example it may be seen that the finite $\beta(0)/\beta_{eq}$ value does not actually alter the reduction factor $D_\perp, \chi_\perp \sim 1/\nu$ calculated in the vacuum approximation to be between 1.5 and 2. The reduction factor could be much more essential (by 5-8 times, including the finite beta case), if the D value were determined only by the satellites nearest to the main harmonic ($l \pm 1$, m), i.e., if the distant satellites were suppressed.

3) Further efforts are required to develop such a configuration with $\alpha < 0$, which would combine the improved transport with good MHD properties.

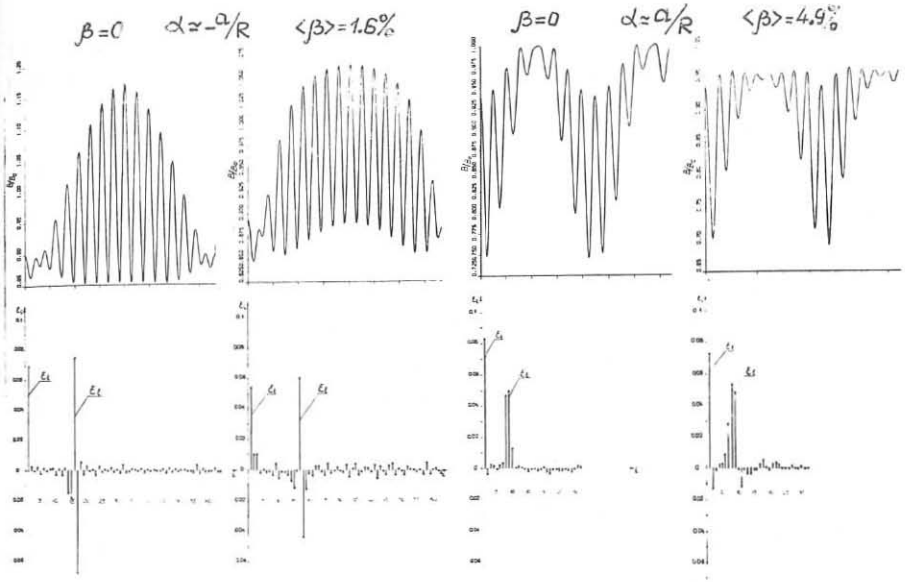

Fig. 1

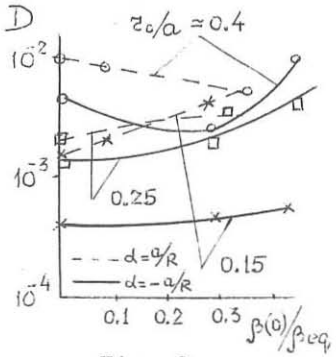

Fig. 2

References

1. Volkov, E.D., Suprunenko, V.A., Shishkin, A.A., Stellarator (Naukova dumka, Kiev, 1983).
2. Bykov, V.E. et al., Nucl. Fusion 24 (1984) 1195.
3. Mynick, H.E. et al. Phys. Rev. Letters 48 (1982) 322.
4. Shaing, K.C., Hokin, S.A., Phys. Fluids 26 (1983) 2136.
5. Mynick, H.E., Phys. Fluids 28 (1985) 1139.
6. Hender, T.C. et al., J. Comp. Phys. 60 (1985) 76.

MAGNETIC SURFACE DESTRUCTION DUE TO EQUILIBRIUM PLASMA CURRENTS IN TORSATRONS

A.A.Shishkin, V.E.Bykov, V.G.Peletminskaya, A.V.Khodyachikh

Institute of Physics and Technology, the Ukrainian Academy of Sciences, Kharkov 310108, USSR

Equilibrium plasma currents create the magnetic fields that disturb the vacuum magnetic configuration. The most dangerous effect produced by these equilibrium currents in stellarator-type traps is the interruption of the magnetic surfaces and a rapid escape of the field lines from the confinement volume, i.e., the magnetic surface destruction. To find out the β values ($\beta = 8\pi P/B_0^2$), at which this effect occurs, is one of the most important practical goals of the theory of plasma equilibrium in stellarators.

The problem has been studied in this work for $l=3$ and $l=2$ torsatrons with different winding laws of helical conductors on the basis of a new procedure involving an analytical calculation of equilibrium current magnetic field components and a numerical solution of field line equations for the total magnetic field that includes the vacuum field and the field from equilibrium plasma currents. Our approach differs from the previous one /1/ in two points. Firstly, the analytical components of the equilibrium current-induced magnetic field comprise the basic characteristics of a three-dimensional geometry of torsatron configurations, in particular, the satellite harmonic content of the magnetic field and the magnetic surface functions /2/. This circumstance allows one to judge to which extent this or that trap is adequate to the M & S configuration /3/. Secondly, the present procedure is iterative and self-consistent at each step as β increases. The changes in the configuration occurring at a preceding step, i.e., at a lower β value, are introduced into the equi-

librium current field components at which the magnetic surfaces are calculated at a subsequent step when β is higher. In this respect our approach is close to that developed in /4/.

Figure 1 displays the results obtained with our procedure for two torsatron configurations (l=3, m=8, $R/a \simeq 3.6$). These have the same dimensions of the last closed magnetic surfaces, $a_0 \simeq 0.39$, and nearly the same angles of rotational transform at the plasma boundary, $t\,(a_0) \simeq 0.52 - 0.57$, but differ in modulation coefficients α in a helical winding law $(m/l)\varphi = \vartheta - \alpha \sin\vartheta$, where φ and ϑ are, respectively, the angular variables along major and minor circumferences of the torus. The modulation coefficients were chosen to be $\alpha \simeq 3a/R$ for one torsatron configuration and $\alpha = -a/R$ for another. This difference is responsible for the different satellite harmonic content of the magnetic field, in particular, $\varepsilon_{l\pm1}/\varepsilon_l < 0$ for $\alpha = -a/R$ and $\varepsilon_{l\pm1}/\varepsilon_l > 0$ for $\alpha \simeq 3a/R$, where $\varepsilon_l, \varepsilon_{l\pm1}$ are the $|B|$ expansion Fourier coefficients at $(l,m)(l\pm1,m)$ harmonics.

A significant effect caused by equilibrium currents is the stripping of the magnetic surfaces and splitting of the family of nested surfaces into two independent regions of essentially smaller dimensions. In the example considered, the destruction caused by a plasma with $\beta\,(0) = 5\%$ in the torsatron with $\alpha = -a/R$ is nearly the same as that in the $\alpha = 3a/R$ torsatron with a $\beta\,(0) = 3\%$ plasma. In other words, torsatrons with $\varepsilon_{l\pm1}/\varepsilon_l < 0$ ensure higher β values (by a factor of 1.7) than torsatrons with $\varepsilon_{l\pm1}/\varepsilon_l > 0$ do.

Similar effects are observed in l=2 torsatrons. In the Uragan-2M (m=4, $R/a \simeq 3.8$) a plasma with $\beta\,(0) \simeq 0.5\%$ causes a reduction by 1/6 in the mean radius of the last closed magnetic surface, whereas in the ATF-1 torsatron a destruction by 1/3 of the plasma radius is caused by a $\beta\,(0) \simeq 3\%$ plasma. (Fig.2) The limiting equilibrium β value can be enhanced in each specific case through correcting the surfaces by

ying external transverse magnetic fields.

The undertaken study leads to the following conclusions.

An essential effect of equilibrium currents is the magnetic surface destruction (reduction of the plasma confinement volume and, hence, a reduced plasma lifetime). It is this effect that restricts most strongly the permissible critical plasma pressure (β_{eq}) in stellarator traps, in particular, torsatrons.

2) The extent of magnetic surface destruction due to finite β can be controlled by choosing an appropriate helical winding law for a torsatron. This is a consequence of the reduction of equilibrium current $\propto \cos \vartheta$ and current-induced transverse magnetic field values by means of a proper choice of the satellite harmonic content of the magnetic field.

References

1. Gorbachov N.S., Kuznetsov Yu.K., Pinos I.B., Nucl. Fusion 20 (1980) 341.
2. Shishkin A.A., Vopr. Atomn. Nauki i Tekhn. Ser. Termoyad. sintez n2 (1987) 15.
3. Mynick H.E., Chu T.K., Boozer A.H., Phys. Rev. Letters 48 (1982) 322.
4. Kisslinger J., Wobig H., Proc. 12th Europ. Conf. on Contr. Fus. and Plasma Physics (Budapest, 1985). Part 1, p.453.

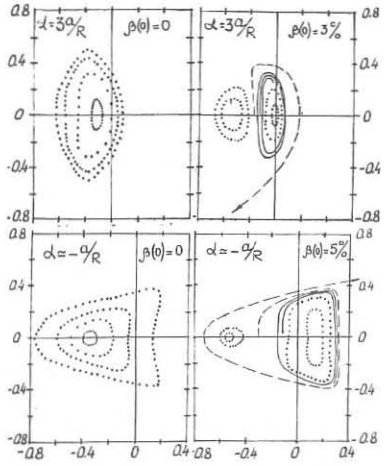
α=3%R
β(0)=0
α=3%R
β(0)=3%
α=-%R
β(0)=0
α=-%R
β(0)=5%
0.8
0.4
0
-0.4
-0.8

Fig. 1

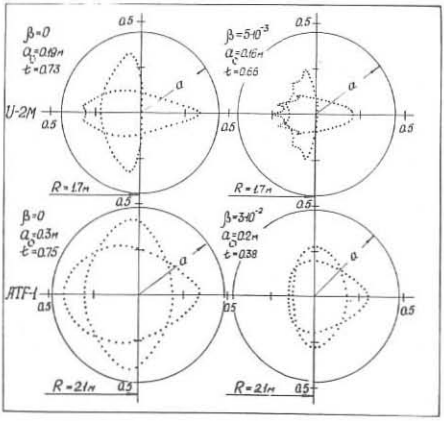
β=0
a=0.19m
ε=0.73
β=5·10⁻³
a=0.16m
ε=0.66
U-2M
R=1.7m
β=0
a=0.3m
ε=0.75
β=3·10⁻²
a=0.2m
ε=0.38
ATF-I
R=2.1m
0.5

Fig. 2

A COMPACT TORSATRON FOR DEMONSTRATING THE FEASIBILITY OF A TWO-COMPONENT BURNING REGIME

V.Z.Amelin, V.E.Bykov, E.D.Volkov, A.V.Georgievskij, Yu.N.Kuznetsov, S.A.Lebed', A.V.Longinov, S.A.Martynov, S.S.Pavlov, V.A.Rudakov, Yu.F.Sergeev, K.N.Stepanov, A.V.Khodyachikh

Institute of Physics and Technology, the Ukrainian Academy of Sciences, Kharkov 310108, USSR

Calculations of reactor-stellarator parameters give rather large dimensions of these devices /1,2/. The minor radius a_n of the plasma in such a reactor generally ranges from 1 to 2 m, and the aspect ratio $A = R/a_n \geq 10$. To ensure the proper plasma confinement, it is necessary to have rather high magnetic fields $B \sim 5$ T. The construction of such a reactor would be rather costly. Even with the parameters satisfying the demonstration experiment, where the power enhancement factor $Q = P_{TN}/P_H \sim 1$ (P_{TN} is the thermonuclear fusion power (neutrons + α -particles), P_H is the power of additional heating), the reactor size and costs would be too great.

In the early seventies there appeared an idea of creating a compact reactor using a two-component burning regime which can be realized by injecting a beam of fast neutrals /3,4/. The present work studies the possibility of a demonstration experiment in a stellarator system, where the two-component burning regime is achieved with a cyclotron absorption of slow waves by ions of one of the D-T plasma components /5/. In this case, a major portion of particles of the "hot" component acquires the energies sufficiently high to promote the D-T reaction, thereby facilitating the attainment of the regimes with $Q \geq 1$. The transport theory for stellarators predicts essential losses in a hot thermonuclear plasma /6/, and this determines large dimensions of a reactor-stellarator. Note that the greatest energy transfer occurs in the region where the collisional frequency is close to the frequency of plasma rotation in the ambipolar electric field. Because of an essential difference in collisional frequencies for electron and ion components at typical reactor plasma parameters, the losses are proportional to ν_e^{-1} in the electron channel, and to $\nu_i^{1/2}$ in the ion channel.

Taking from /6/ the expressions for the fluxes in the energy balance with due account of bremsstrahlung, and also assuming that all RF power needed to heat the "hot" component should be transferred to the cold part of the plasma via Coulomb interactions, the characteristic parameters of the device can be related to plasma parameters and the heating absorbed power. This relation has the form

$$A^2 = \frac{3.19\cdot10^7 T_e^{9/2}\varepsilon_h^{3/2}(5.5-K_e) + D^3\,\frac{3.8\cdot10^5 T_i^{3/4}(328+K_i)}{\varkappa_i^{3/2}|K_i|^{3/2}}}{D^4\left(\frac{7\cdot10^{18}\langle\sigma v\rangle_{RF}}{W+1} - 9.5\,T_e^{1/2} + \frac{617\,\rho_h}{N^2}\right)} \qquad (1)$$

where T_j is the temperature in 10 keV units, ε_h is the amplitude of the helical magnetic-field inhomogeneity, $\langle\sigma v\rangle_{RF}$ is the DT-reaction rate, $\varkappa_j = (\nabla T_j/T_j)a_n$, $K_j = \nabla\Phi/\nabla T_j$, $W = E/T$, E is the average "hot" component energy, N is the plasma density in 10^{14} cm^{-3}, ρ_h is the specific RF heating power, $D = B^{1/2}N^{1/2}a_n$, j = e, i.

It follows from /5/ that $Q \geq 1$ at $T_e \geq 5$ keV can be achieved by the use of a two-component burning regime with a deuterium minority in a tritium plasma at $n \sim 10^{14}$ cm^{-3}.

Figure 1 shows demonstration device parameters versus plasma concentration (N_e) at $T_e = T_i = 5$ keV and the optimum concentration of deuterium ions (9.5%). Shaded are the regions associated with inhomogeneity in ambipolar potential values ($-2.3 \leq K \leq 4.5$). The parameters were calculated assuming that $a_n = 0.6$ m, B = 6 T, $\varepsilon_h = 0.15$. As seen from the figure, the low density region is characterized by relatively low heating power levels and small β -values, while the aspect ratios are rather great in this region. The latter adds to the device cost and increases energy consumption to generate the magnetic field. The high density region ($N_e > 1.5$) typically shows high levels of the power required for additional heating, relatively low aspect ratios and high β values. Thus, the region of N between 0.7 and 1, where $A \approx 10$, P_H = 30 to 40 MW and the values are within permissible limits, is best suited to our purposes. Yet, the high density region ($N > 1.5$) seems attractive from the standpoint of performing a demonstration experiment in a relatively small device, though in this case, the problem of high input power levels has to be solved.

It seems most convenient to carry out the demonstration experiment in the regime with tritium as an ion minority. In this case, the $Q \geq 1$ regimes can be attained at a plasma temperature $T_e \geq 6.4$ keV. Figure 2 shows the device parameters versus the plasma density with tritium being the "hot" minority. It may be easily seen that here the required RF heating absorbed powers and device dimensions are somewhat greater.

Note that P_H is proportional to N^2 and to the plasma volume. It follows from (1) that A does not change if $D = B^{1/2}N^{1/2}a_n$ remains constant. It is then evident that P_H may be reduced either by proportionally increasing the device dimensions or by enhancing the magnetic field. The analysis of various magnetic system designs and reasonable parameters of the demonstration device shows that the feasibility of the two-component burning regime can be demonstrated using a relatively small torsatron with a plasma radius of 0.5 - 0.6 m

and an aspect ratio ranging between 5 and 10, the heating power reaching several tens MW. The magnetic field value should be sufficiently high (5-6 T) in this case.

The improvement of confinement properties by increasing the minor cross section of the trap or by raising the magnetic field value may lead to a more compact system with lower aspect ratios and reduced input power levels for RF heating.

Two types of steeply bent torsatrons with helical winding (HW) periods m_b = 1 and m_b = 2 have been considered as possible variants of the design. The m_b=1 type was a rather easy for fabrication compact torsatron /7/ with a very low HW aspect ratio ($A_h = R/a_h$ = 1.3-1.5, A = 1.5 - 2.5). With these low A_b values the HW was a set of current coils (ℓ = 2, 3, 4) deformed in accordance with a special law and arranged on the torus with a circular or elliptic minor cross section. The coils are mechanically linked with each other. The design admits a modification with planar circular coils /8,9/. It has been demonstrated that the variation of the magnetic system parameters gives ι (a_n) = 0.1 - 0.3, a_n/a_h = 0.4-0.5 and the ellipticity Λ = 1-4. Thus, there is a hope that the proper β values and good confinement properties for the demonstration device can be attained. According to /7/, the magnetic configuration of some modifications of the design shows a peculiar behaviour, namely, owing to the plasma column shift to the centre of the torus, the actual toroidal inhomogeneity ε_t is approximately by a factor of 2 lower than the a_n/R ratio. Thus, in its confinement properties this system may be equivalent to the device with the aspect ratio twice as large.

The second type was a magnetic configuration of an l=2 torsatron with four field periods. It has been established that in this system at A_h = 1.6 there exist closed surfaces with A = 2.6 and the transform angle ι = 0.4, and this allows us to consider this system as a suitable device for the demonstration experiment.

References

1. Komin, A.B., Maneev, A.B., Engineering problems of controlled fusion (Trudy II Vsesoyuzn. konf., Leningrad, 1982), V. 1 (1982), dokl. 31. 32.
2. Volkov, E.D., Rudakov, V.A., Suprunenko, V.A., in Vopr. Atomn. Nauki i Tekhn., ser. Termoyad. sintez, Is. 2(15) (1984) 36.
3. Dawson, I.M., Furth, H.P. and Tenney, F.H., Phys. Rev. Lett. 26 (1971) 1157.
4. Pistunovich, V.N., Atomn. Ehnergiya 35 (1973) 11.
5. Longinov, A.V., Pavlov, S.S., Stepanov, K.N., in Vopr. Atomn. Nauki i Tekhn., ser. Termoyad. sintez, Is. 2 (1987) 3.
6. Kovrizhnykh, L.M., Nucl. Fusion 24 (1984) 435.

7. Bykov, V.E. et al., in Vopr. Atomn. Nauki i Tekhn., ser. Termoyad. sintez, Moscow, IAEh, Is. 2 (1987) 19.
8. Gourdon, C., Marty, O., Vuillemin, M.,DPh-PFC/SRAC/STGT, EUR-CEA-FC-411.
9. Romanov, S.S., Preprint KhFTI 74-22, Kharkov, 1974.

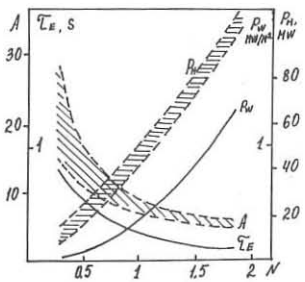

Fig. 1. Demonstration device parameters for hot deuterium. B=6 T, a_n = 0.6 m, T = 5 keV, ε_h = 0.15.

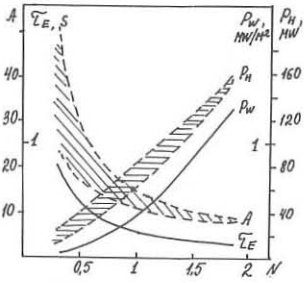

Fig. 2. Demonstration device parameters for hot tritium. B=6 T, a_n =0.6 m, T=6.4 keV, ε_h = 0.15.

CURRENTLESS PLASMA GENERATION AND HEATING IN THE ATF TORSATRON *

G. H. Neilson, F. S. B. Anderson[1], D. B. Batchelor, G. L. Bell[2], J. D. Bell, T. S. Bigelow, M. D. Carter, R. J. Colchin, E. C. Crume, J. L. Dunlap, G. R. Dyer, A. C. England, J. C. Glowienka, R. C. Goldfinger, J. W. Halliwell, J. H. Harris, G. R. Haste, D. L. Hillis, S. Hiroe, L. D. Horton, H. C. Howe, R. C. Isler, T. C. Jernigan, R. R. Kindsfather, R. A. Langley, J. F. Lyon, M. M. Menon, P. K. Mioduszewski, T. Mizuuchi[3], O. Motojima[3], M. Murakami, V. K. Paré, D. A. Rasmussen, M. J. Saltmarsh, F. Sano[3], J. E. Simpkins, T. Uckan, T. L. White, J. B. Wilgen, and W. R. Wing

Oak Ridge National Laboratory
Oak Ridge, Tennessee 37831, U.S.A.

Introduction

Experimental operation of the Advanced Toroidal Facility (ATF) [1] began in January 1988. The device is a continuous-coil, ℓ=2 torsatron with major radius $R_0 = 2.1$ m, average minor radius $\bar{a} = 0.27$ m, plasma volume $V = 3.1$ m^3, average magnetic field on axis $B_0 \leq 2$ T, rotational transform $0.3 < \iota < 1.0$ (typically), and an MHD-stability-optimized, flexible magnetic configuration. It will be used to investigate a number of toroidal confinement physics topics, mainly finite-beta stability limits, low-collisionality transport, electric field effects, particle and energy control, and long-pulse operation. Results from the initial operation of ATF at $B_0 \approx 0.95$ T are presented in terms of (1) general operating characteristics, (2) second-harmonic 53-GHz electron cyclotron plasma initiation, and (3) heating with $\leq$200 kW of electron cyclotron heating (ECH) and $\leq$350 kW of neutral beam injection (NBI). The main objective in this brief phase was to establish basic operating capabilities of the facility, so the results do not reflect optimized performance.

General Operating Characteristics

A cross section of ATF with the coils, typical calculated magnetic surfaces, and constant-$|B|$ contours is shown in Fig. 1. In these experiments the magnetic configuration is established about 1 s before discharge initiation and held constant for about 2.5 s. The plasma is produced by injecting a $\leq$ 0.5 torr · L puff of H_2 gas into the vacuum vessel (volume 10^4 L) about 100 ms before applying the microwave (ECH) power, as shown in Fig. 2(a). The line density $n_e\ell$ is measured by a 2-mm interferometer along a 0.65-m horizontal chord. Toroidal plasma currents measured during the discharge are $\leq$1.5 kA, so their calculated effect on the configuration is small (e.g., $\Delta\iota(0) < 0.04$). Two wall conditioning methods have been used to date: glow discharge cleaning and fundamental electron cyclotron resonance (ECR) discharge cleaning. Typically, these procedures are applied daily for periods of 12–24 hours per day. Pulsed experimental

*Research sponsored by the Office of Fusion Energy, U.S. Department of Energy, under contract DE-AC05-84OR21400 with Martin Marietta Energy Systems, Inc.

[1]University of Wisconsin, Madison, WI, U.S.A.
[2]Auburn University, Auburn, AL, U.S.A.
[3]Kyoto University, Kyoto, Japan.

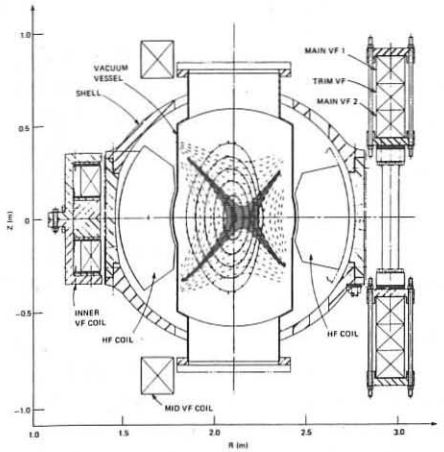

FIG. 1. Cross section of ATF in the plane of the ECH launcher, showing magnetic surfaces and constant-$|B|$ surfaces.

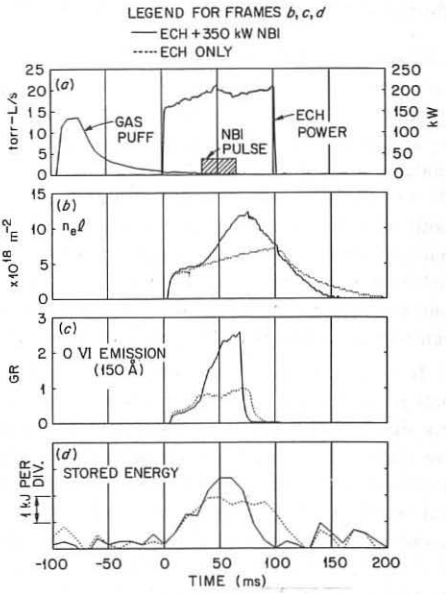

FIG. 2. Experimental signals for ECH and ECH+NBI discharges. The gas puff and ECH power signals in (a) apply to both cases.

operation with ECH plus NBI is also found to be an effective conditioning technique, as explained below.

Electron Cyclotron Plasma Initiation

Microwave power $P_{\mathrm{ECH}} \leq 200$ kW is supplied by a single gyrotron and transmitted to the device via a 6.35-cm-diam evacuated waveguide system (with no window at the device interface) operating in the TE_{02}^{0} mode. The power is radiated in a wide-angle (11° half-angle) pattern from an open-waveguide launch point located on the low-field side about 1.2 m above the midplane. Plasma breakdown is optimal when the initial H_2 fill pressure is about 5×10^{-5} torr and the second-harmonic resonance layer is close to the saddle point in $|B|$, in general agreement with the nonlinear theory of Carter et al. [2]. To confirm the $|B|$-dependence, systematic scans of the magnetic field strength were made by varying the helical winding current to determine the range over which breakdown could be obtained. The range was found to be quite narrow—$0.93 \leq B_0 \leq 0.96$ T (3.2%)—similar to that found in Heliotron-E [3]. Over this range, the second-harmonic resonant surface ($|B| = 0.947$ T) sweeps through the shaded region shown in Fig. 1, which depicts the toroidal plane in which the ECH launcher is located. The initial rate of density buildup depends on P_{ECH}, H_2 fill pressure, and wall conditioning history, but in the best cases to date, $\bar{n}_e$ rises to 5×10^{18} m^{-3} in < 10 ms.

Electron Cyclotron and Neutral Beam Injection Heating

After the breakdown phase, with the discharge still sustained by ECH power alone, the density continues to rise as shown in Fig. 2(b), despite the fact that, typically, no further gas puffing is added. Spectroscopic measurements of absolute line intensities show a steady influx of light impurities, principally C and O, as exemplified by the O VI emission signal shown in Fig. 2(c). Analysis of the exhaust gas from the system after a discharge indicates ~10% concentrations of CO and H_2O. Furthermore, the rate of density rise after the breakdown tends to decrease as a result of wall conditioning, as shown in Fig. 3, consistent with the long-term buildup being due to impurities from the wall. Comparing the density behaviors obtained with normal gas puff and with no gas puff (Fig. 4) shows that the initial density contributed by the H_2 gas puff produces a constant pedestal on the subsequent density evolution. The achievable density rise in this initial transient increases with the general cleanup of the machine through wall conditioning.

In regard to the power balance, a bolometer located ~0.5 m from the ECH launcher detects power fluxes equivalent to several times the total input power. The interpretation is that this signal is dominated by microwave power undergoing multiple reflections; thus, the effective single-pass plasma absorption is small, consistent with the non-optimal launch geometry described above. The microwave power losses from the system are also estimated to be small, so that nearly 100% of the power is calculated to be absorbed in multiple passes. The spectroscopic measurements are consistent with most of the power being radiated in partially stripped stages of C and O, subject to some uncertainties in the absolute calibration and the axisymmetry of the radiation. Ion temperatures determined by impurity Doppler broadening steadily decrease as the density rises, and similar trends are seen in the electron temperatures estimated from line excitation levels and from fundamental electron cyclotron emission. In the late stages, a peaking and subsequent gradual decrease in the density frequently occurs as well, as in the NBI case in Fig. 2(b). These experimental observations, as well as supporting time-dependent transport modeling, are all consistent with a gradual impurity buildup combined with insufficient power (at present) to overcome the resulting radiative losses. Similar behavior has been observed in

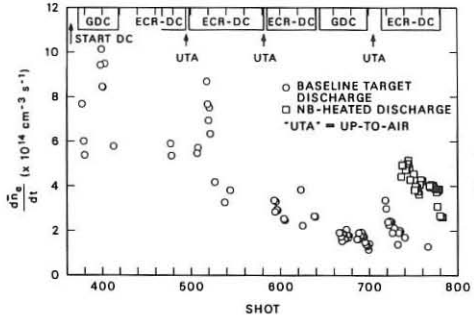

FIG. 3. Performance improvements, as measured by the decrease in $d\bar{n}_e/dt$, due to wall conditioning and pulsed ECH+NBI operation.

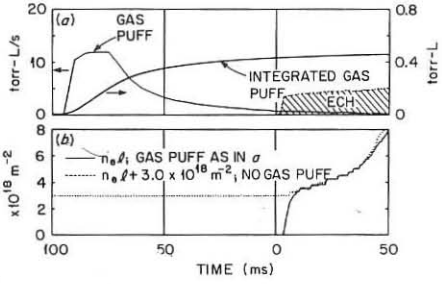

FIG. 4. Early density evolution with and without usual gas puff.

Heliotron-E, as well as in tokamaks where it is typically associated with disruptions. In a stellarator such as ATF, however, the magnetic configuration remains intact, and the slow density decay ($\tau_n \leq 50$ ms) after the power is turned off is indicative that good particle confinement still exists. Electron-beam measurements of the magnetic surface quality are in progress.

The behavior is qualitatively similar when NBI heating is applied at low power (typically 350 kW) and moderate energy (25 kV) for short pulse lengths (35 ms). Tangential co-injection is used, and $\bar{n}_e \geq 8 \times 10^{18}$ m^{-3}, so the calculated shinethrough loss is $< 15\%$. Despite the added power, the final collapse is not avoided because the impurity levels increase with NBI, the density rises at a faster rate (Fig. 2(b)), and X-mode cutoff near the center begins to reduce the ECH power absorption. On the other hand, ECH-only shots after ~50 ECH+NBI shots showed evidence of improved behavior (slower density rise, as shown in Fig. 3, and no collapse), indicating that even short-pulse NBI may condition the walls in a way that leads to reduced impurity influx. Diamagnetic measurements (Fig. 2(d)) show that the stored energy (W_d) peaks at 2.5 ± 0.7 kJ within 20 ms after beam turn-on, making it possible to estimate the global energy confinement time, $\tau_E^* \equiv W_\mathrm{d}/P_\mathrm{abs} \approx 7$ ms. The total absorbed power P_abs is calculated to be 365 kW, taking beam shinethrough and microwave cutoff into account. The equivalent average temperature estimated from the diamagnetic flux, $kT_d \equiv W_d/(3\bar{n}_e V)$, is about 140 eV. This is consistent with temperatures inferred from other diagnostics; for example, $T_i(0) = 260 \pm 40$ eV is obtained from charge-exchange spectroscopic measurements.

Conclusions

The initial, low-power experiments on ATF have established some basic operating characteristics of the device. Second-harmonic plasma initiation successfully produces target plasmas with densities sufficient for NBI, using only 200 kW of ECH and a non-optimized launch configuration. Following the initial breakdown phase, the discharge behavior is strongly affected by light impurities, which dominate the particle sources and the energy losses and frequently lead to a radiative collapse. However, there are indications that the good particle confinement typically seen in stellarator devices exists in ATF as well and evidence that impurity levels can be reduced through extended wall conditioning and experimental operation. In future operation, the wall conditioning procedures will be augmented with the addition of vessel baking and gettering capabilities, and a more directed ECH launch scheme will be implemented.

References

[1] J. F. Lyon, B. A. Carreras, et al., Fusion Technol. **10** (1986) 179.

[2] M. D. Carter, D. B. Batchelor, and A. C. England, Nucl. Fusion **27** (1987) 985.

[3] A. Iiyoshi et al., in Plasma Physics and Controlled Nuclear Fusion Research 1984 (Proc. 10th Int. Conf., London, 12–19 Sept., 1984), Nucl. Fusion Suppl., Vienna (1985) 453.

EFFECT OF TRANSVERSAL MULTIPOLE FIELDS ON THE STELLARATOR CONFIGURATION

Pustovitov V.D.
I.V.Kurchatov Institute of Atomic Energy, Moscow, USSR

A magnetic system in torsatrons includes the coils of two types. The main coils are helical with unidirectional currents providing longitudinal and helical magnetic fields necessary for plasma confinement. The second type includes circular conductors. Their objective is to compensate a transversal field produced by the currents through the helical coils. Combinding the currents through circular conductors, one can also solve another problem: to produce an axially-symmetric poloidal field necessary for the plasma shape and position control. The first large-scale experiments of such a kind are planned to be performed on the ATF-torsatron [1].

Let us consider an effect of a separate harmonic of an external field:

$$\vec{B}_m = -\frac{B_m}{mb^{m-1}}\left[\nabla(\rho^m \cos m u)\,\vec{e}_\zeta\right] \qquad (1)$$

on a stellarator (torsatron) configuration. Here (ρ, u, ζ) are the quasi-cylindrical coordinates connected with a geometrical axis of the system, b is the characteristic transversal dimension.

Let us assume that averaged vacuum magnetic surfaces are circular in the absence of the fields (1). Under the field (1) their form (Ψ=const) is changed :

$$\Psi = \frac{2}{b^2}\int \rho\, \mu_h(\rho)\, d\rho + 2A\,\frac{B_m}{mB_0}\,\frac{\rho^m}{b^m}\cos m u \,. \qquad (2)$$

Here $\mu_h(\rho)$ is the vacuum rotational transform at $B_m=0$, B_0 is the longitudinal field strength at the geometrical axis of the system; $A=R/b$, R is the radius of the axis. We didn't take account of toroidal corrections in (2) which can affect the geometry of magnetic surfaces near the axis $\rho=0$, see [2], at low B_m - magnitudes.

The configuration of the surfaces Ψ = const, number and positions of singular points depend on the profile $\mu_h(\rho)$ and on the multipolarity of an external field. For a wide range of stellarators μ_h can be represented by a formula

$$\mu_h = \mu_0 + (\mu_b - \mu_0) \rho^2/b^2 . \qquad (3)$$

When $\mu_0 \neq 0$, as seen from (2), only harmonics of (1) with $m \leqslant 2$ can affect the near-axial surfaces. An effect of higher order harmonics is manifested at the periphery: the greater m, the less their effect on a central region.

A homogeneous vertical field, $\vec{B}_1$ „ in our model shifts the surfaces Ψ = const towards $[\vec{e}_\zeta \vec{B}_1]$ and slightly distorts them. One can effectively control the plasma shape via a quadrupole (m=2) and a hexapole (m=3) fields. It can be necessary to provide the stability of a high-pressure plasma in stellarators. One can easely find the limits within which such application of multipole fields is possible:

$$\begin{aligned} |B_2| &< B_2^{cr} = \mu_0 B_0/A , \\ |B_3| &< B_3^{cr} = 2\sqrt{\mu_0(\mu_b - \mu_0)}\, B_0/A . \end{aligned} \qquad (4)$$

An excess over a critical value, B_2^{cr}, is accompanied by splitting of the axis and by the emergence of an internal figure-eight separatrix. When the magnitude of the hexapole field exceeds B_3^{cr}, a triangular separatrix with islands near its vertices emerges.

A critical value B_2^{cr} corresponds to a maximal elongation, E, of a magnetic surface passing through the points ρ =b, u = $0,\pi$, which is obtained without splitting the axis:

$$E^4 = 1 + 4\mu_0/(\mu_b - \mu_0) . \qquad (5)$$

The quantity E turns out to be rather low: E = 1.35 for ATF, E = 1.2 for LIVEN'-2. Singleaxis configurations with highly-elongated cross-sections can be obtained in the stellarators with a low shear ($E \geqslant 3$ at $\mu_b/\mu_0 \leqslant 1.05$). When $B_3 = B_3^{cr}$ singularities emerge at a distance

$$d = b\sqrt{\mu_0/(\mu_b - \mu_0)}\ . \qquad (6)$$

When $B_3 > B_3^{cr}$, they are splitted into a hyperbolic and an elliptic axes:

$$\rho_e - \rho_h = 2d\sqrt{(B_3/B_3^{cr})^2 - 1}\ . \qquad (7)$$

A hyperbolic point rapidly moves towards the centre with a rise in B_3: $\rho_h = d/2$ at $B_3^{cr}/B_3^{cr} = 1.25$.

Note that in the l=3 stellarator ($\mu_0=0$) $B_2^{cr}=B_3^{cr}=0$. It means that the single-axis configuration in the l=3 stellarator can be obtained only in the absence of quadrupole and hexapole fields. In the stellarators with $\mu_0 = 0$ an octupole field at $|B_4| > B_0\mu_b/A$ can also cause the emergence of an internal separatrix.

Let us obtain a dependence of a plasma column displacement, Δ_b, as a whole, on B_1 at a finite plasma pressure. This problem was considered in [3-5] on the basis of extremely - simplified approaches. The general solution to this problem can be found with the virtual casing principle [6]. For a plasma column with circular (on average) boundary at the parabolic profile μ_h it can be obtained analytically:

$$B_1 = -\frac{b}{2R}\left\{ B_J\left(\ln\frac{8R}{b} - \frac{3}{2}\right) - B_0\left[\mu\Delta' + \right.\right.$$
$$\left.\left. + (a^2\mu_h)'/a^2 + 2(\mu_b - \mu_0)\Delta^3/b^3\right]\right\}_{a=b}\ . \qquad (8)$$

Here $B_J = J/2\pi b$ is the field of a longitudinal current, J, at the plasma column boundary; μ is the rotational transform, $\Delta(a)$ is the toroidal displacement of magnetic surfaces, a = const, respective to the axis $\rho = 0$, $\Delta' = d\Delta/da$. In derivation of (8) it has been assumed that $|\Delta'| \ll 1$ near the boundary.

Determination of a derivative Δ' included into (8) needs a solution to the internal equilibrium problem. In a shearless stellarator of the WVII-A type $\Delta'(b) = -\beta/\beta_{eq}$ at any pressure profile, where $\beta_{eq} = \mu_0^2/A$. In this case, when $B_J = 0$, it follows from (8) that

$$\frac{\Delta_b}{b} = \frac{B_1}{B_0}\frac{A}{\mu_0} + \frac{\beta}{2\beta_{eq}} . \qquad (9)$$

From this it follows that the plasma column, at high β close to β_{eq}, should be displaced to a distance of the order of a half of the minor radius in the absence of B_1. It is clear that it is possible to reach such β without plasma column collapse on the wall (limiter) only when a displacement Δ_b is compensated by a vertical field B_1. This conclusion about the role of a vertical field in the shearless stellarator contradicts the statement made in [3] disclaiming the necessity in B_1 within such a system.

One cannot succeed in obtaining a simple relationship like (9) in the high-shear stellarators because of a more complicated dependence of $\Delta'(b)$ on β. In this case, however, one can see that at high β, when $\Delta'(b) \approx -1$, the displacement Δ_b turns out to be intolerably large in the absence of B_1.

REFERENCES

[1] Lyon J.F., Carreras B.A., Chipley K.K. et al. Preprint ORNL/TM-9831. Oak Ridge, 1986.

[2] Volkov E.D., Suprunenko V.A., Shishkin A.A. Stellarator. Kiev, Naukova Dumka, 1983 (in Russian).

[3] Hitchon W.N.G., Fielding P.J., Nucl. Fusion 21 (1981), 775.

[4] Kuznetsov Yu.K., Mikhailov M.I., Pashnev V.K., Tonkopryad V.M., Nucl. Fusion 23 (1983), 15.

[5] Friedberg J.P., Politzer P.A., Rosenau P., Phys. Fluids 27 (1984), 2093.

[6] Pustovitov V.D., Virtual Casing Principle for Stellarators, paper No. , this conference.

BOOTSTRAP CURRENT IN STELLARATOR CONFIGURATIONS

E. Harmayer, J. Kisslinger, A. Montvai*, F.Rau, H. Wobig
Max-Planck-Institut für Plasmaphysik, EURATOM Association
D-8046 Garching, Fed. Rep. Germany
* guest from CRIP, Budapest, Hungary.

Neoclassical transport theory predicts the existence of a net toroidal current, the so-called bootstrap current. The presence of this current in stellarators of the next generation (WENDELSTEIN VII X, LHS, etc.) can affect the stability behaviour and the confinement properties of these systems. Therefore it is desirable to reduce its value in order to attain a nearly currentless regime of operation.

The theory of bootstrap currents has been established in several papers [1], [2], [3]. In the present paper a numerical evaluation of the geometrical coefficient C_b characterising the effect of the geometry of magnetic surfaces on the bootstrap current is given for several advanced stellarators with reduced Pfirsch-Schlüter currents.

If the magnetic field $B(\eta,\varsigma)$ on a magnetic surface is given in terms of a Fourier series:

$$B = \sum a_{l,m}\, cos(l\eta - m\varsigma) + b_{l,m}\,(l\eta + m\varsigma)$$

where (η,ς) are the poloidal and toroidal Hamada coordinates, the coefficient C_b depends on the rotational transform ι and the coefficients $a_{l,m}, b_{l,m}$. C_b will be normalized to an axisymmetric configuration with the same aspect ratio and the same rotational transform.

As has been pointed out in [1] the driving term for the bootstrap current is the parallel viscosity $< \mathbf{B}\cdot\nabla\cdot\pi_>$ with $\pi_{i,k} \sim (p_\parallel - p_{p\perp})(n_i n_k - \frac{1}{3}\delta_{ik})$, $n_i = B_i/B$. π is the anisotropic pressure tensor in the Chew-Goldberg-Low form.

$$p_\parallel - p_\perp \sim \int f_1 (v_\parallel^2 - \frac{1}{2} v_\perp^2) d^3\mathrm{v} \qquad (1)$$

The relevant term h_1 of the perturbed distribution function f_1 has to be calculated from the drift kinetic equation (see Ref. 4)

$$L\,h_1 =: v_\parallel \frac{\mathbf{B}}{B}\cdot\nabla h_1 - C[h_1] = \frac{(v_\parallel^2 - \frac{1}{2}v_\perp^2)}{v_{th}^2}\left(\frac{\mathrm{V}_j\cdot\nabla B}{B}\right) f_o \qquad (2)$$

f_o = local Maxwellian, C = collision operator, $\mathbf{V}_j$ is the lowest order plasma flow of each particle species j within the magnetic surface.

$$\mathbf{V}_j = \left[\frac{kT}{q_j}\frac{N_j'}{N_j} + \Phi'(\psi)\right]\mathbf{V}_o + \Lambda_j \mathbf{B} \tag{3}$$

$N_j(\psi)$ = plasma density,$\Phi(\psi)$ = electric potential, $\mathbf{V}_o$ is a poloidal vector with $\mathbf{V}_o \times \mathbf{B} = \nabla\psi$ and $\nabla \cdot \mathbf{V}_o = 0$. The vector $\mathbf{V}_o$ is proportional to $\mathbf{B}_p$, see in [1].

After evaluating $< \mathbf{B} \cdot \nabla \cdot \pi_j >$ and using eqs. (1), (2) and (3), the geometrical bootstrap factor C_b is:

$$C_b \sim \Big\langle \int (v_\parallel^2 - \frac{1}{2}v_\perp^2)\frac{\mathbf{B}\cdot\nabla B}{B} L^{-1}\{(v_\parallel^2 - \frac{1}{2}v_\perp^2) f_o \frac{\mathbf{V}_o \cdot \nabla B}{B}\} d^3\mathbf{v} \Big\rangle \tag{4}$$

In the collision dominated regime this reduces to:

$$C_b \sim \Big\langle (\frac{\mathbf{B}\cdot\nabla B}{B})(\frac{\mathbf{V}_o \cdot \nabla B}{B}) \Big\rangle \tag{5}$$

which can also be obtained from Braginskii's form of the bulk viscosity [5]. In the plateau limit eq. (4) coincides with the equations given by Shaing, Solano [3].

In the long-mean-free path regime the coefficient has been given by Shaing et al. [2]. A numerical investigation of it has been done by Ohkawa ($C_b = (\frac{f_t}{f_c})G_b$) [6].

It can be shown, that the bootstrap current is zero if the Pfirsch-Schlüter currents vanish ($j_\parallel = 0 \rightarrow C_b = 0$) therefore it is expected, that stellarators with low Pfirsch - Schlüter currents also exhibit small bootstrap current.

In Helias configurations [7] the parallel plasma currents $j_\parallel$ are as large as the diamagnetic currents $j_\perp$. A 4-period configuration is shown in Fig. 1. Locally the bootstrap current is not zero, however, integration over a magnetic surface yields nearly zero toroidal current (see table I) In table I the normalized geometrical bootstrap factor C_b (*or* G_b) is given for several Stellarator configurations, beginning with Wendelstein VII-A. $C_b = 1$ corrsponds to the equivalent axisymmetric device.

As shown in table I the bootstrap factor in the Pfirsch-Schlüter regime is negative in most cases and differs appreciably from unity. However, the absolute value of the bootstrap curent is negligible in the collisional regime. In the plateau regime circulating particles carry the bootstrap current. In W VII - A the factor C_b is of the order one, but in the W VII - AS already a smaller C_b arises. In Helias configurations (last three cases in table. I) various cases with large or very small bootstrap factors can be realized.

In the loong-mean-free-path regime (last column in table I.) the three Helias cases show low bootstrap current too.

As has been pointed out by Shaing, Callen [1] the bootstrap current in conventional stellarators or torsatrons can change sign across the plasma radius, thus making the integral bootstrap current very small. The analysis presented here proves the existence of Helias type configurations with vanishing bootstrap current on every magnetic surface.

References

/1/ K.C. Shaing, J.D. Callen, Phys. Fluids. **26**, 3315, (1983)

/2/ K.C. Shaing, S.P. Hirshman, J.S. Tolliver. Phys. Fluids, **29**, 2548, (1986)

/3/ E. Rodriguez-Solano, K.C. Shaing. Phys. Fluids, **30**,9 462, (1967)

/4/ M. Coronado, H. Wobig. Phys. Fluids. **29**, 527, (1986)

/5/ S.I. Braginskii. Rev. of Plasma Physics. **1**, 527, (1969)

/6/ T. Ohkawa, M.S. Chu. Report GA-A 18688, (1986)

/7/ J. Nührenberg, R. Zille. Phys. Letters.**114**(A), 129, (1986)

/8/ A. Montvai. Proc of Workshop on W-VII-X, EUR 11058, (1986)

	Regime→	Pfirsch -	Schlüter	Plateau	Banana
	Method→	direct	Fourier	Ref. 3.	Ref.8.
System	Radius[cm]				
W-VII A	1.1	0.0005 ...	-0.12 ...	1.0	~ 0
	5.6	-0.274	-0.3	0.99	-0.12
	10.1	-0.88	-0.94	0.96	-0.25
W-VII AS	5	2.77	2.05	0.72 ...	-0.03
	10	0.86	0.11	0.6	-0.11
	20	-1.53	-1.78	0.2	-0.2
HC5E1	9	-8.64	-4.6	-2.2 ...	-2.16
	27	-8.65	-4.8	-2.2	-1.1
	45	-8.83	-5.3	-2.4	-3
BSX52	11	7.4	10	0.18 ...	-0.03
	21	8.4	15.3	0.31	-0.15
	30	11.3	23	0.29	-0.06
HELIASK	3	-9.7	-9.1	-1.33 ..	-0.08
	15	-9.3	-8.8	-1.43	-0.11
	31	-7.7	-7.7	-1.30	-0.2
HS4E8	13	-0.1	-0.056 ..	.....	-0.02
	30	-0.1	-0.03	0.	-0.22
	42	-0.15	-0.072		0.1
HSV11	10	-0.056 ...	-0.056 ..	-0.02 ..	-0.04
	27	-0.6	-0.64	-0.03	-0.09
	45	-0.36	-0.85	-0.04	-0.09

TABLE I Bootstrap coefficients C_b *or* G_b of different stellarators.

HELIAS - Configuration HS-4-11

Modular Coil System of HS-4-11

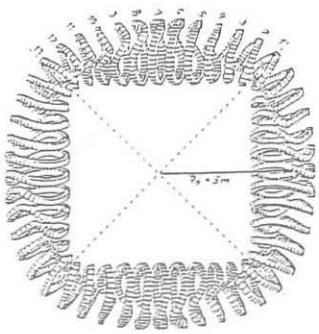

Magnetic Surface of HS-4-11

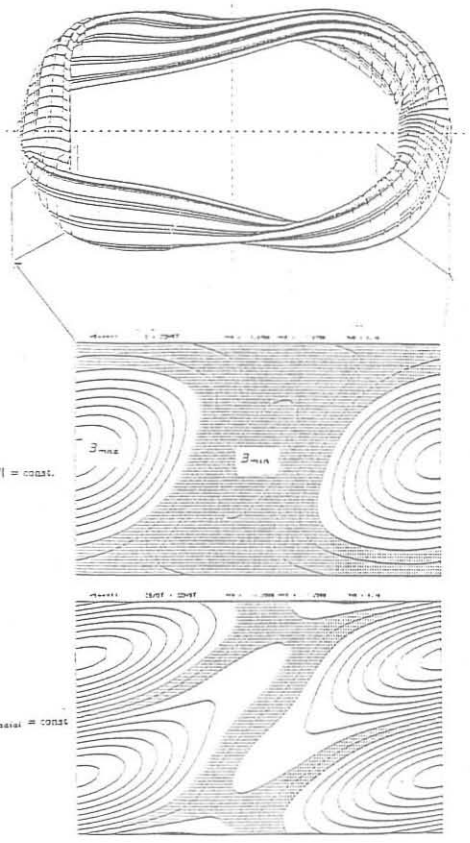

Fig. 1.

This figure shows a magnetic surface of a 4-period Helias configuration with reduced Pfirsch-Schlüter currents. The $|B|$ = const. plot (middle) indicates the region of localistaion for trapped particles. On the last figure the local radial drift velocity is shown, which is particularly small in the region of trapped particles. Small radial drift velocity reduces all neoclassical effects including the bootstrap current too.

MHD STABLE $\beta-$ REGIONS IN $\ell = 2,3$ STELLARATORS

F. HERRNEGGER
Max-Planck-Institut für Plasmaphysik
IPP-EURATOM Association
D-8046 Garching bei München

1. Introduction

An average magnetic well ($V'' < 0$) of the vacuum fields of small shear is one mechanism to stabilize[1,2] MHD-unstable free-boundary modes. In the present study, a class of $\ell = 2,3$ stellarator configurations, which are characterized by an average magnetic hill or well and small shear, are analysed with respect to free-boundary MHD modes. The analysis is performed by using the stellarator expansion procedure STEP[3].

The various vacuum field configurations are given in terms of Dommaschk potentials[4] and the notation of Refs.2,5 is used. Table 1 gives two examples of $l = 2,3$ vacuum fields. These configurations consist of $M = 5$ field periods of period length L_P and aspect ratio $A \approx 10$ ($A = R_T/a = ML_P/2\pi a$, a is the average minor plasma radius, R_T is the major torus radius). The value of the twist (angle of rotational transform divided by 2π) is in the range of $0.56 \leq \iota \leq 0.67$ (see Fig.2). The specific volume V' can be varied by changing the axisymmetric dipole and quadrupole fields[2,5] (resulting in a displacement of the magnetic axis with respect to the outermost magnetic surface) or by adjusting the $\ell = 3$ fields having 5 or 10 field periods around the torus (see Fig.1).

By these means the dependence of the MHD stability of global modes with low values of the toroidal mode number n on the magnetic well of the associated vacuum fields can be studied. In all cases the the pressure profile is approximately a parabolic function of the minor radius r, $p \simeq p_o(1-(r/a)^2)$, and the pressure p_o (measured by β_o on the magnetic axis) is varied (stability parameter). The finite-β equilibria are net-current free. As examples, the Figs. 1 and 2 show the magnetic surfaces, the twist ι and the specific volume V' as functions of r/R_T of two configurations with magnetic well and hill. The configuration FZH207B has a very small aspect ratio of $A \simeq 5$.

2. Stability Results

For the stability computations the equilibrium mass density ρ is assumed to be $\rho \sim \sqrt{p}$ and the plasma region is surrounded by a vacuum region with an electrically conducting wall at infinity. In the STEP procedure the mode number n is a free input parameter ($1 \leq n \leq 6$ for the present study) whereas the various poloidal Fourier modes associated with each n-value result from the computations. The m-numbers given in the Figures correspond to the resonant Fourier mode with the dominant amplitude. In all cases, about ten Fourier modes in the neighborhood of the resonant mode are sufficient.

In Fig.3 the normalized eigenvalues are plotted as functions of β_0 for several unstable free-boundary modes where the corresponding magnetic vacuum field has a magnetic hill of $(\Delta V'/V'_o)_{vac} = 2.81\%$. The modes are characterized by the mode numbers n, m and the node number in radial direction. All modes shown here have no radial nodes except those of the curve with bold squares ($n = 3, m = 5$) which have smaller absolute eigenvalues and are more localized than the corresponding modes without radial nodes.

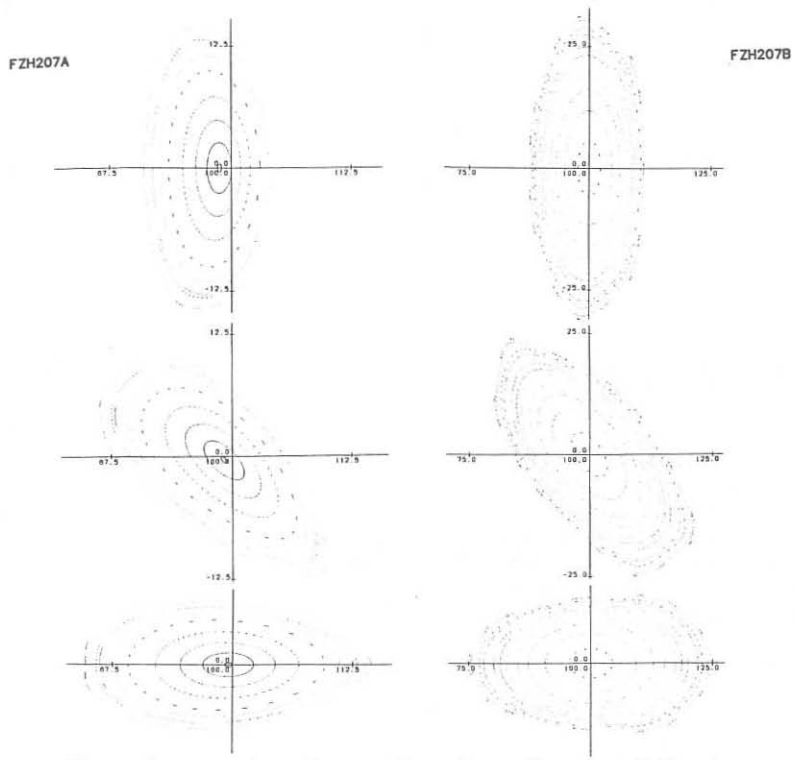

Fig.1. Contour plots of magnetic surfaces of vacuum fields at 0, $L_P/4$, $L_P/2$ of a field period with period lenth L_P;
left: $\iota_o = 0.57$, $\iota_b = 0.65$, $A = 10.3$, $\Delta V'/V_o' = -2.3\%$, $\langle j_\parallel / j_\perp \rangle_{ax} = 2.75$, $J_{ax}^* = 8.54$;
right: $\iota_o = 0.41$, $\iota_b = 0.67$, $A = 5$, $\Delta V'/V_o' = 14.3\%$, $\langle j_\parallel / j_\perp \rangle_{ax} = 2.95$, $J_{ax}^* = 9.73$.

Reducing the magnetic hill of the vacuum field to $(\Delta V'/V_o')_{vac} = 1.38\%$, the absolute eigenvalues are becoming smaller (see Fig.4). One observes that the $n = 3$ and $n = 6$ modes show a resonance feature, are unstable for small β_o-values (i.e. $-(\gamma R_T/v_A)^2 > 0$) and are stabilized at higher β_o-values ($\beta_o \geq 2.6\%$, second stability region for those modes). However modes with different n ($n = 4$, $n = 5$) appear which are localized very close to the magnetic axis or the plasma boundary. The stable β_o-window is very narrow in this case. For equilibrium configurations with $(\Delta V'/V_o')_{vac} = 0.96\%$ (and smaller, see Fig.5), the absolute eigenvalues of the unstable modes decrease further and a small stable region around $\beta_o = 2.3\%$ can be observed where no unstable free-boundary modes with $n = 1, 2, ..., 6$ investigated so far have been found. Another stable β-region is found for $3.3\% \leq \beta_o \leq 5\%$, the width of which depends on the magnetic well depth. In case of a magnetic well $(\Delta V'/V_o')_{vac} = -0.2\%$, no unstable global modes are observed for $\beta_o \leq 3.5\%$.

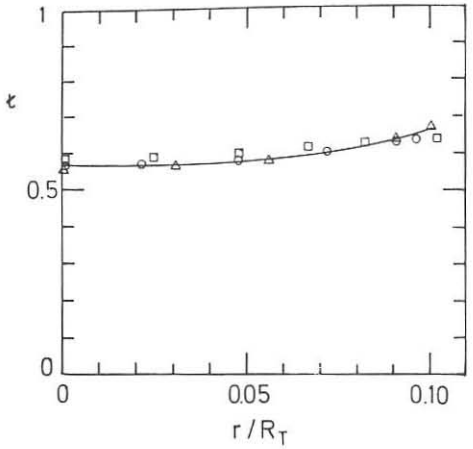

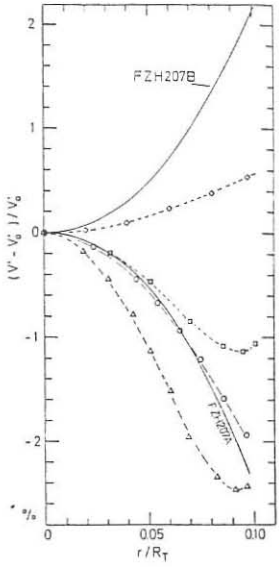

Fig.2. Twist ι and normalized specific volume $(V'-V_o')/V_o'$ as functions of r/R_T for various vacuum fields. The solid curves are for the configuration FZH207A from a field line tracing code and the corresponding values from STEP are indicated by open circles. The additional curves (squares and triangles) obtained by STEP show the variety of vacuum fields (V'' positive and negative) used for the stability computations.

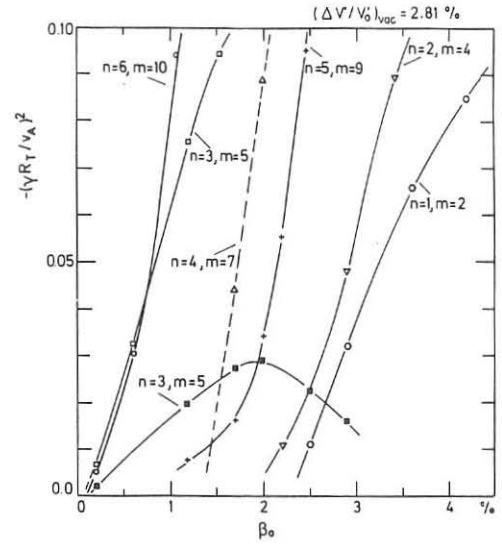

Fig.3. Normalized eigenvalues as functions of β_o for $n = 1, 2, ...6$ free-boundary modes with no or one radial node ($\iota_{o,vac} = 0.59$, $\iota_{b,vac} = 0.61$). The mode structure is changed if β_o increases. There are many other modes with smaller absolute eigenvalues.

Table 1 a
FIELD CONFIG. FZH207A CC=1.0, 3/88

MPER	IANP	RA	BZO/ IDN	M	L	ANP
5	21	1.00E+00	-6.160E-03			
	1	0	3	-2.800E-01		
	1	5	1	-3.240E-02		
	2	5	1	3.240E-02		
	1	5	2	-1.550E+00		
	2	5	2	-1.550E+00		
	1	5	3	-1.500E-01		
	2	5	3	5.000E+00		
	1	5	4	-4.450E+01		
	2	5	4	-2.440E+01		
	1	5	5	-1.000E+02		
	2	5	5	1.100E+02		
	1	5	6	-4.810E+02		
	2	5	6	1.120E+02		
	1	10	3	-4.500E-00		
	2	10	3	4.500E-00		
	1	10	4	4.630E+01		
	2	10	4	4.580E+01		
	1	10	5	2.640E+02		
	2	10	5	-2.350E+02		
	1	10	6	3.000E+03		
	2	10	6	1.500E+03		

Table 1 b
FIELD CONFIG. FZH207B CC=0.9, 3/88

MPER	IANP	RA	BZO/ IDN	M	L	ANP
5	25	1.00E+00	6.161E-04			
	2	0	2	1.080E-01		
	1	0	3	-4.876E-04		
	2	0	4	-6.638E-04		
	1	0	5	7.005E+01		
	2	0	6	6.599E-01		
	1	5	1	2.238E-03		
	2	5	1	-2.239E-03		
	1	5	2	-1.544E+00		
	2	5	2	-1.546E+00		
	1	5	3	-2.152E+00		
	2	5	3	2.950E+00		
	1	5	4	-3.452E+01		
	2	5	4	-1.437E+01		
	1	5	5	-1.008E+02		
	2	5	5	1.106E+02		
	1	5	6	-4.813E+02		
	2	5	6	1.119E+02		
	1	10	3	8.502E-01		
	2	10	3	-8.507E-01		
	1	10	4	2.631E+01		
	2	10	4	2.584E+01		
	1	10	5	2.638E+02		
	2	10	5	-2.346E+02		
	1	10	6	2.991E+03		
	2	10	6	1.505E+03		

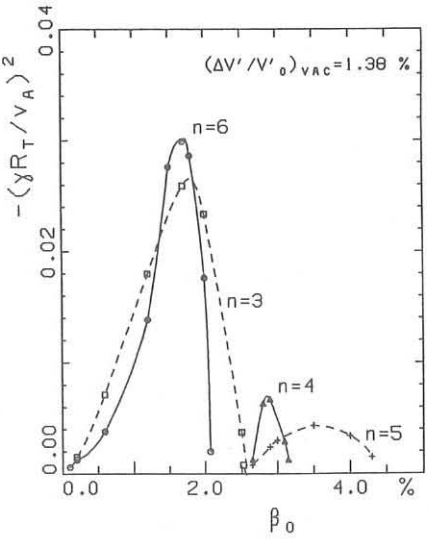

Fig.4. Eigenvalues vs β_o for $n/m = 6/10,\ 3/5,\ 5/9,\ 4/7$ free-boundary modes.

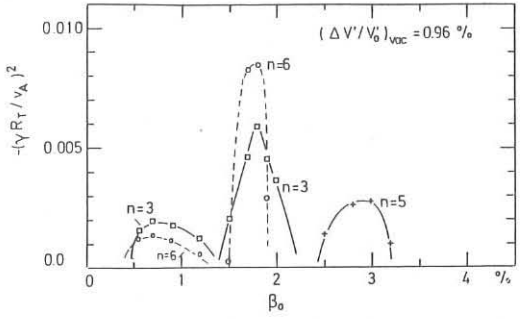

Fig.5. Eigenvalues vs β_o for $n/m = 6/10,\ 3/5,\ 5/8$ free-boundary modes.

References

1 F. Herrnegger, P. Merkel, J. L. Johnson, J. Comput. Physics **66**, 445 (1986).

2 F. Herrnegger, Z. Naturforsch. **42a**, 1085 (1987).

3 G. Anania, J.L. Johnson, K. E. Weimer, Phys. Fluids **26**, 3070 (1983).
G. Anania and J.L. Johnson, Phys. Fluids **26**, 3070 (1983).

4 W. Dommaschk, Z. Naturforsch. **36a**, 251 (1981).

5 F. Herrnegger, 14th Europ. Conf. on Contr. Fusion and Plasma Physics, ECA Vol. **11D**, Pt. I, p. 419 (22-26 June 1987, Madrid, Spain; Europ. Phys. Soc., F. Engelmann and J.L. Alvarez Rivas, Eds.).

VIRTUAL CASING PRINCIPLE FOR STELLARATORS

Pustovitov V.D.

I.V.Kurchatov Institute of Atomic Energy, Moscow, USSR

In the sharp plasma-boundary model the general equilibrium problem is naturally splitted into internal and external ones. They can be solved independently, when the boundary is known. This simplifies the solution of equilibrium and stability problems in which radial distributions of equilibrium quantities is of importance. In this case the external problem is solved after finding a configuration with desired properties and serves for determining the external magnetic fields necessary for its formation. The confining field in tokamaks is calculated from the known internal solution with a simple and effective virtual casing principle [1] . It is based on the idea of replacing external currents by the current

$$\vec{i} = [\vec{B}\,\vec{n}] \qquad (1)$$

which flows on the surface coinciding with the plasma boundary. Here $\vec{B}$ is the equilibrium field strength at the plasma boundary, $\vec{n}$ is the external normal. It is not difficult to find a field produced by the currents (1) in tokamaks. However, this problem becomes complicated for the systems which do not possess an axial symmetry, see [2] . For stellarators with a plane circular axis it is convenient to use a simpler approach based on the possibility of describing these systems by two-dimensional (averaged) equations.It is well known that such an approach is rather precise [3] . It is also important that a two-dimensional image of a stellarator does not differ in its geometry

from a tokamak. Let us show how one can determine an external confining field by the known field at the plasma boundary, using this model. Here and then we mean average quantities independent of a longitudinal coordinate ζ and a smoothed axially symmetric boundary.

A poloidal field averaged over ζ in a stellarator can be represented in the form [4]:

$$\vec{B}_p = \frac{1}{2\pi} [\nabla(\psi - \psi_v)\nabla\zeta] , \qquad (2)$$

where ψ_v is the averaged poloidal flux of helical field ($\psi_v = 0$ in tokamaks). The field (2) has a normal component not equal to zero, when $\psi_v \neq 0$, on the surface $\psi = \text{const}$ coinciding with isobars. Due to this, a direct transfer of the results [1] to our case is impossible. In order to reduce our problem to that solved in [1] let us consider an auxiliary vector field $\vec{b}$ instead of $\vec{B}_p$

$$\vec{b} = \vec{B}_p + \vec{b}^* , \qquad (3)$$

where $\vec{b}^*$ is the poloidal field determined in the plasma by a formula

$$\vec{b}^* = \frac{1}{2\pi} [\nabla\psi_v \nabla\zeta] , \qquad (4)$$

It should satisfy the equation $\mathrm{div}\vec{b}^* = 0$, $\mathrm{rot}\vec{b}^* = 0$ and the same boundary conditions as those for $\vec{B}$ in a vacuum. For the field $\vec{b}$ the problem of finding its component $\vec{b}_{ext}$ produced by external "currents" is stated in the same way as that for a tokamak [1]. Assume, as in [1], that an ideally conducting casing is placed at the plasma boundary, and a current passes through it:

$$\vec{i}_c = [\vec{b}\,\vec{n}] . \qquad (5)$$

Together with a volume current $\mathrm{rot}\vec{b}$ it is a source for the field $\vec{b}$ in the plasma. The total field of these currents equals zero in a vacuum. In other words:

$$\vec{b}_c = \begin{cases} \vec{b}_{ext} = \vec{B}_{ext} + \vec{b}^*_{ext} & \text{in plasma} \\ -\vec{b}_{pl} = -(\vec{B}_{pl} + \vec{b}^*_{pl}) & \text{in vacuum} \end{cases} \qquad (6)$$

where $\vec{b}_c$ - is the field produced by a surface current $\vec{i}_c$. Introducing a vector-potential $\vec{A}=A\vec{e}_s=r\,A\nabla\zeta$ for each component of the field, one finally gets

$$rA_c = \begin{cases} rA_{ext} + \Psi_v/2\pi - rA_{j*} & \text{in plasma} \\ -rA_{pl} - rA_{j*} & \text{in vacuum} \end{cases} \qquad (7)$$

Here we have taken account of the fact that, by definition, $\vec{b}^*_{pl}=\vec{b}_{j*}$ - is the field produced by the volume current, $\vec{j}^*=\mathrm{rot}\,\vec{b}^*$, and $\vec{b}^*_{ext}=\vec{b}^*-\vec{b}_{j*}$. A circular current j_s, distributed across a cross-section ζ=const within an area produces a field $[\nabla(rA)\,\nabla\zeta]$:

$$rA = \int G(\vec{r},\vec{r}')\, j(\vec{r}')\, dS' , \qquad (8)$$

where G is the source function. For the surface current (5) flowing along the boundary, l, of this area $j_s dS$ should be replaced by $i_\zeta dl$:

$$rA_c = -\oint G\,(\vec{B} + \vec{b}^*)\,\vec{dl} , \qquad (9)$$

Here $\vec{dl} = [\vec{e}'\,\vec{n}']\,dl'$. An integral of the type (8) for rA_{j*} can be reduced to contour integrals via the second Green's formula

$$rA_{j*} = \oint G\,\vec{b}^*\,\vec{dl} + \frac{1}{2\pi}\oint \frac{\Psi_v}{r'}\frac{\partial G}{\partial n'}\,dl' + \eta\,\frac{\Psi_v}{2\pi} , \qquad (10)$$

η =1 in plasma, η =0 in vacuum. Substituting these expressions A_c and A_{j*} into (7), one obtains an explicit expression of unknown quantities in terms of an equilibrium field $\vec{B}$ at the plasma boundary and the function Ψ_v, representing averaged vacuum surfaces in the stellarator:

$$-\oint G\,\vec{B}\,\vec{dl} + \frac{1}{2\pi}\oint \frac{\Psi_v}{r'}\frac{\partial G}{\partial n'}\,dl' = \begin{cases} rA_{ext} & \text{in plasma} \\ -rA_{pl} & \text{in vacuum} \end{cases} \qquad (11)$$

When Ψ_v=0, Eq.(11) coincides with the known result[1]for a

tokamak.

The equality (11) completely determines the confining field necessary for creating a desired plasma configuration. In the simplest case of circular (on average) boundary, Eq.(11) gives

$$rA_{ext} = - B_{\perp} R\varrho\cos u - \sum_{n=2}^{\infty} \left[\frac{bR}{2n} H_n + \frac{\Psi_n}{4\pi} \right] \frac{\varrho^n}{b^n} \cos nu \,, \quad (12)$$

Here b - is the average radius of a transversal plasma cross-section; (ϱ, u - are quasi-cylindrical coordinates connected with its centre, R is the radius of a geometrical stellarator axis, H_n and Ψ_n are the coefficients of the Fourier series for the functions $\vec{Be}_u$ and Ψ_v at $\varrho = b$;

$$B_{\perp} = - \frac{b}{2R} \left[H_0 \left(\ln \frac{8R}{b} - 1/2 \right) - \left(\frac{R}{b} H_1 + \frac{\Psi_1}{2\pi b^2} \right) \right] . \quad (13)$$

One can see from (12) that $B_{\perp}$ is the external homogeneous vertical field. The relationship (13) allows one to find a displacement of the plasma column respective to a geometrical axis in a stellarator after solving an internal equilibrium problem.

The relationship (13) is applicable to both stellarators and tokamaks. In tokamaks $\Psi_1 = 0$, $H_1 \sim H_0 = J/2\pi b$, where J is the total plasma current. From (13) one obtains $B_{\perp} \sim J$ in this case. As known, the plasma equilibrium in a tokamak is impossible without such a field. In stellarators the dependence of $B_{\perp}$ on equilibrium parameters has entirely different nature because of a term Ψ_1, in the right-hand side of Eq.(13) and auxiliary terms in H_1, which are proportional to the plasma column displacement. The equality (13) can be realized in a stellarator even at $B_{\perp} = 0$ too.

REFERENCES

1 Shafranov V.D., Zakharov L.E., Nucl.Fusion, 12 (1972), 599.

2 Hitchon W.N.G., Fielding P.J., Preprint CLM-P605 (1980), Culham.

3 Carreras B.A., Hicks H.R., Holmes J.A. et al. Phys.Fluids, 26 (1983), 3569.

4 Pustovitov V.D. Nucl.Fusion, 26 (1983), 1079.

GUIDING CENTER STUDIES AND MONTE CARLO CALCULATIONS FOR A MODULAR HELIAS

E. Harmeyer, J. Kißlinger, W. Lotz, A. Montvai*, F. Rau , and H. Wobig

Max-Planck Institut für Plasmaphysik, D-8046 Garching, FRG,
EURATOM-Association.
* Guest from: Central Research Institute for Physics, H-1525 Budapest, Hungary.

Abstract . *Collisionless guiding center orbits are calculated for D^+ ions at 80 keV in a modular Helias system with $a/\rho \approx 30$, where a is the minor radius, and ρ is the ion Larmor radius. Most particles are circulating and well confined. Various orbits of trapped particles are seen. Deeply trapped particles are lost after typically 100 oscillations, those with reflection points close to the local B_{max} stay in the system for times up to 15 ms. Pitch angle scattering or a radial electric field can reduce these losses.*

Monte Carlo calculations show the expected improvement of particle and energy confinement of the Helias topology, compared to that of a classical stellarator. A radial electric field improves the neoclassical ion confinement at low collisionalities. Estimated confinement times are $\tau_p \approx 360$ and $\tau_E \approx 170$ ms for a system with low effective ripple at $a/\rho \approx 100$.

Introduction . The future experiment WENDELSTEIN VII-X, the next step [1] in the Garching stellarator program will use a HELIAS configuration = *Heli*cal *A*dvanced *S*tellarator. Such configurations have reduced Pfirsch-Schlüter currents, improved confinement and stability properties, e.g. the prospect to achieve a reactor relevant $\langle\beta\rangle \geq 5\%$ [2]. For a typical modular coil set with 48 non-planar coils, M = 4 field periods, R = 5 m, aspect ratio $A = 10$, average induction $\langle B\rangle = 4$ T along the helical magnetic axis, the rotational transform is $\iota = 0.74 \ldots 0.78$ between the axis and the edge.

The main reasons for studying collisionless guiding center orbits is to estimate the effect of trapped particles on neoclassical transport, and the problem of α-particle losses in stellarator reactors. Three different Helias coil configurations have been analyzed in a recent study [3], the magnetic field being the vacuum field generated by the modular coils:

HS5R4 : a reactor-size system with R = 20 m, a = 1.6 m, $B = 6$ T, 5 field periods, and a maximum $1/2 \cdot \delta B/B$ on the magnetic surfaces between 2 % (magnetic axis) and 15 % (edge).

The other two systems are in the size of a 'next-generation' experiment:
HS5K : R = 5 m, a = 0.4 m, $B = 4$ T, 5 field periods, $1/2 \cdot \delta B/B = 15 - 30\,\%$;
HS4V : R = 5 m, a = 0.5 m, $B = 4$ T, 4 field periods, $1/2 \cdot \delta B/B = 3.5 - 15.3\,\%$.

Owing to the difference in $\delta B/B$, these configurations differ in the fraction of trapped particles, which is a maximum in HS5K. On a magnetic surface the contours $|B| = const.$ determine the accessible regions for trapped particles with fixed E/μ. Local minima of B caused by the modular ripple, see Fig. 1, are particularly dangerous for particle losses. The dotted areas in the middle and lower parts of the figure indicate regions of nearly vanishing drift velocities. Their gross structure is similar to that of the $|B|$-contours, hence particles which are reflected at these locations can stay in the system for long times.

Guiding center orbits are calculated in the absence of electric fields. The local effective drift velocity is obtained in order to estimate the particle confinement at low collisionality.

In the HS5R4, 3.5 MeV fusion alpha particles (velocity $v = 1.3 \cdot 10^7$ m/s, Larmor radius $\rho = 4.5$ cm) are investigated. In the two other cases the ratio $\rho/a \approx 1/30$ is kept constant by choosing 80 keV D^+ ions with velocity $v = 2.8 \cdot 10^6$ m/s and a Larmor radius $\rho = 1.6$ cm. The guiding center orbits are launched at the local field minimum on magnetic surfaces with average minor radii $r = 1/16 \ldots 1/3 \cdot a$. This corresponds to peaked profiles of alpha particle production in a 'burning' plasma, and to a central deposition of high energy particles produced by neutral injection or by ion cyclotron heating in the next-generation experiments.

General results :

For a Maxwellian distribution function most of the particles circulate and are well confined. Their drift surfaces deviate from the magnetic surfaces less than the value $\Delta_c = \rho/\iota$ of a classical stellarator. This is caused by the 'drift optimization' of the Helias topology. The observed improvement factors range between values of 2 to 10.

A large variety of orbits is seen for trapped particles, nearly all of them are lost eventually. Deeply trapped particles are lost in ripples between the modular coils. Moderately trapped particles with $E/\mu \lesssim B_{Sep}$ stay within a field period. Their average drift velocity is reduced below $v_{tor} = v \cdot \rho/R$, which is that of an equivalent axisymmetric toroidal field $B \sim 1/R$. The magnitude and sign depend on the pitch and starting point. Particles with $E/\mu \gtrsim B_{sep}$ can overcome the helical ripple, extend their path through several field periods, and increase their 'lifetime'. Collisionless trapping and detrapping processes lead to frequent transitions among various states of trapping. Then the second adiabatic invariant changes its value, and there are large deviations from the magnetic surface given by the starting point. Particles reflected at a mirror field $B_{mirror} \lesssim B_{Max}$ behave nearly like circulating particles and stay within the system until the end of the computation, or they are finally lost in a local ripple of the coils. Trapped particles are influenced either by pitch angle scattering or by the effect of a radial electric field with potential ϕ. Both polarities are beneficial: since the energy $\frac{m}{2} v_{||}^2 + \mu B + e\phi$ is constant, an increase of $v_{||}$ can transfer trapped particles to circulating ones; a reduction of $v_{||}$ restricts the accessible range in minor radius for the particle.

Quantitative details for HS4V :

In the recent study [3] the particles were launched close to the point of B_{Min}, the local field minimum, see Fig. 1. All types of orbits are covered in scans of $v_\perp/v$. Particles starting at $r/a = 1/3$ are circulating for $v_\perp/v \lesssim 0.942$, and have $\Delta_c/\rho = 0.3$ to 1.3 (improvement factor ≈ 2). There are fewer trapped particles in this system than in HS5K.

Trapped 80 keV D^+ ions are lost in modular ripples at $v_\perp/v \gtrsim 0.98$. Near a ratio $v_\perp/v \approx 0.99$ the vertical drift changes sign. These particles stay in the system for a rather long time. Moderately trapped particles at values $v_\perp/v \approx 0.96$ oscillate within nearly the whole length of the field period. They show an average vertical drift velocity $v_d = 0.13$ cm/μs which is small compared to $v_{tor} = 0.8$ cm/μs. Trapped particles at $v_\perp/v \lesssim 0.96$ leave the initial field period with a radial 'banana width' of $\Delta_b/\rho \approx 2.4$ and show large deviations from the magnetic surface given by the starting point. These particles are lost in a modular ripple within $t \approx 1$ ms. Nearly circulating particles with $v_\perp/v \lesssim 0.947$ are followed up to a time $t \leq 7.7$ ms without getting lost. They behave approximately like a pair of circulating particles with velocity directions parallel and opposite to $\vec{B}$ and show small deviations from magnetic surfaces.

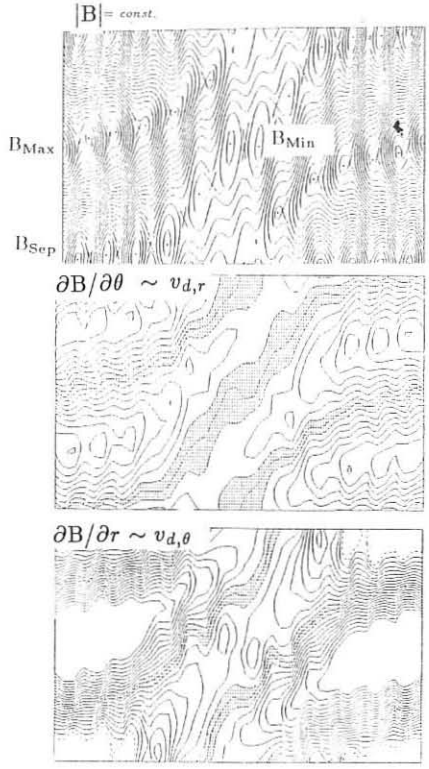

Fig. 1 : Angular distribution of |B|, as well as the derivatives $\partial B/\partial\theta \sim v_{d,r}$ and $\partial B/\partial r \sim v_{d,\theta}$ obtained from the Fourier coefficients of |B| for HS4V11 at r/a = 0.4.

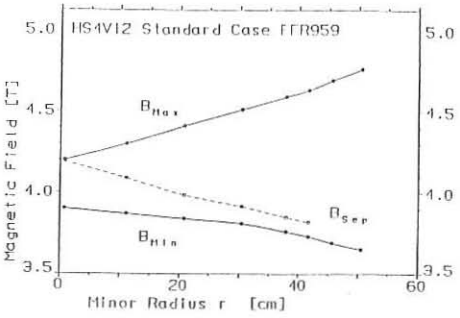

Fig. 2 : Radial dependence of the magnetic induction for the 'Standard Case' of HS4V12.

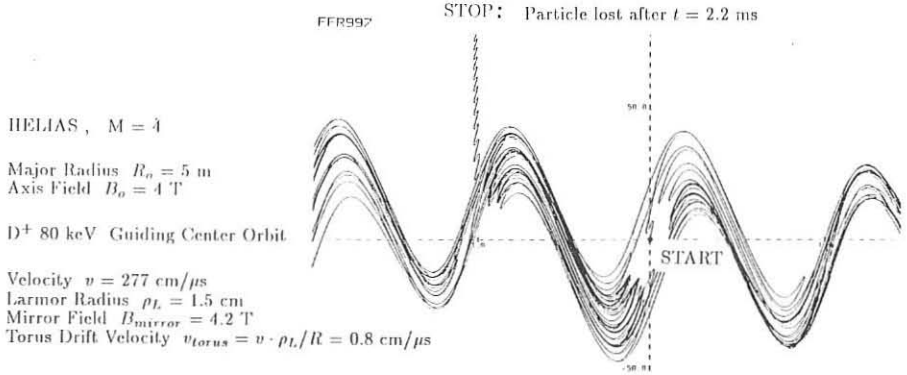

Fig. 3 Guiding center orbit with many reflections and final loss in modular ripple, shown in the Z , φ plane.

In the present paper we concentrate on the most recent configuration, HS4V12. Fig. 2 shows the radial distribution of the magnetic field. Close to the magnetic axis the ripple ratio is small, hence there is a low number of trapped particles. Slightly different numbers of $v_\perp/v$ are valid for circulating and trapped particles, especially when they are started near the locations of the neutral injection beams foreseen for WENDELSTEIN VII-X, i.e. at values above B_{Sep}. High-energy ions produced by neutral injection have $v_\perp/v \lesssim 1$, and there is the danger that the particle gets lost in a local ripple between two of the modular coils. Such a loss is shown in Fig. 3, and occurs at $t = 2.2$ ms. The longest time of a similar orbit observed so far is $t = 15$ ms, which is long compared to a typical pitch angle scattering time. More detailed investigations are required to estimate the efficiency of neutral injection for this system.

Monte Carlo calculations were performed [4] in stellarators of general geometry and in tokamaks with and without ripple. Neoclassical transport coefficients and confinement times are computed over wide ranges of mean free paths, ratios of plasma to Larmor radius, and radial electric fields. The results for monoenergetic particles can be represented by simple formulas using a transport coefficient normalized to the tokamak plateau value and a mean free path normalized to half the connection length. Transport coefficients obtained with monoenergetic particles subjected to pitch angle scattering and energy relaxation are convoluted with a Maxwellian energy distribution. A radial electric field increases the neoclassical ion confinement at low collisionalities.

The Helias system used for these calculations is similar to that for the guiding center studies, but has a smaller effective ripple amplitude of ≈ 1 %. The analysis is done for an average induction $\langle B \rangle = 4$ T, at a surface with aspect ratio $A = 20$ for D^+ ions at $kT_i = kT_e = 6.4$ keV, i.e. for a ratio $a/\rho \approx 100$. For a radial electric field with potential $e\phi/kT = 1.5$ we estimate in the lmfp regime for $\tau_{p,i} \approx \tau_{p,e}$ particle and energy confinement times $\tau_p \approx 360$ and $\tau_E \approx 170$ ms. These values are much larger than the respective numbers for a classical stellarator, $\tau_p \approx 80$ and $\tau_E = 34$ ms. The relevant data for HS4V12 are being investigated.

Conclusions : In contrast to circulating particles, which in Helias configurations clearly exhibit the effect of drift optimization and are well confined, deeply trapped high-energy particles tend to be lost after about 100 reflections. Moderately trapped to nearly circulating particles stay in the system for longer times, but trapping in the modular ripple appreciably enhances losses. The longest time observed so far for a trapped 80 keV D^+ ion is $t = 15$ ms, in the field of a modular coil set. Pitch angle scattering or electric fields can reduce the loss of trapped high energy ions, but trapped α-particles in a stellarator reactor will not experience the confining effect of the E-field. A basic requirement is the fraction of trapped particles be minimized by minimizing the ripple $\delta\, B/B$ in an otherwise optimized configuration.

Monte Carlo calculations show the expected improvement of particle and energy confinement of the Helias topology, compared to that of a classical stellarator. A radial electric field improves the neoclassical ion confinement at low collisionalities. Estimated confinement times are $\tau_p \approx 360$ and $\tau_E \approx 170$ ms for a Helias system with low effective ripple at $a/\rho \approx 100$.

References

/1/ E. Harmeyer, F. Herrnegger, J. Kißlinger, A. Montvai, F. Rau, and H. Wobig, Proc. 14^{th} Eur. Conf. on Contr. Fus. and Plasma Phys., Madrid, Spain, 11 D, 411 (1987).

/2/ J. Nührenberg and R. Zille, Physics Letters, 114A, 129 (1986).

/3/ E. Harmeyer, J. Kisslinger, A. Montvai, F. Rau, H. Wobig, Poster P-41, 2^{nd} Europ. Fus. Theory Meeting, Varenna, Italy (1987), see also IPP Annual Report 1987 (in press).

/4/ W. Lotz and J. Nührenberg, IPP-Report 0/49 (1987), Phys. Fluids (1988).

ION HEAT CONDUCTION IN THE l=2 STELLARATOR

Yu.V.Gott
I.V.Kurchatov Institute of Atomic Energy, Moscow, USSR

Stellarator is one of the condidates for a fusion reactor prototype at present. Therefore, the problems related with ion heat conduction in the facilities of such a type are of great interest.

As known [1] nobody has managed yet to find a solution applicable to any frequency of collisions, ν_{ii}, for the kinetic equation representing the behaviour of particles in a stellarator.

An analysis of this equation shows that the diffusion and heat conduction coefficients for ions are proportional to $\nu_{ii}^{3/4}$ in the range of low collisional frequencies [1] or to ν_{ii} [2]; meanwhile they are proportional to $1/\nu_{ii}$ in the range of high collisional frequencies and to $\nu_{ii}^{1/2}$ in the intermediate one. One should add that the boundaries among these ranges have not been precisely determined, and the behaviour of these coefficients within transition zones is unknown.

In 1982 L.M.Kovrizhnykh found a solution to the kinetic equation (in the so-called τ -or Krook's approximation) which is true for any frequency of collisions [3]. This distribution function for calculations of thermal ion fluxes in the l=2 stellarator is used in a given paper.

Let us consider an ideal stellarator, i.e. such a trap, where the magnetic field is determined by one helical harmonics

$$B \approx B_0 \left(1 - \varepsilon_t(\bar{r}) \cos\bar{\varphi} - \varepsilon_h(\bar{r}) \cos l(\bar{\varphi} - \alpha\bar{z})\right) \quad (1)$$

Here, $\varepsilon_h(\bar{r}) = \varepsilon I_l'(\alpha l \bar{r})$, is the number characterizing the helical field magnitude, $I_l(x)$ is the modified Bessel's function, l is the multipolarity, $\alpha = 2\pi/\lambda$, λ is the period of helical winding, $\varepsilon_t = \bar{r}/R$, $\bar{r}$ and R are the minor and major radii of the torus.

A solution to the kinetic equation is found in terms of the variables r and φ which are related with the ordinary variables $\bar{r}$ and $\bar{\varphi}$ (with respect to $\mathcal{E}_h$ in the first approximation) by the following relationships:

$$z = \bar{z} - \frac{\mathcal{E}_0}{(\alpha l)^2} \frac{\partial \bar{J}_{\parallel}}{\partial \bar{z}} \cos l(\bar{\varphi} - \alpha \bar{z})$$
$$\varphi = \bar{\varphi} + \frac{\mathcal{E}_0 \bar{J}_{\parallel}}{l(\alpha \bar{z})^2} \sin l(\bar{\varphi} - \alpha \bar{z}) \qquad (2)$$

In this case, the distribution function for ions trapped by a helical field has the form:

$$F(z, \varphi) = \frac{1}{1 - e^{-\tilde{\gamma}}} \int_{\varphi - 2\pi \hat{\alpha}/|\hat{\alpha}|}^{\varphi} \hat{\alpha} F_M e^{\int_{\varphi}^{\varphi'} \hat{\alpha} d\varphi''} d\varphi' \qquad (3)$$

where $r_0 = r(\mathcal{J})$ - is the integral of a drift equation, $\mathcal{J} = \oint v_{\parallel} ds$ - is the longitudinal invariant, $v_{\parallel} = \sqrt{\frac{2}{m}(E - \mu B - e\Phi)}$ is the longitudinal component of velocity, Φ is the electric plasma potential, μ is the magnetic moment of a particle,

$$\hat{\alpha}(z, \varphi) = \tau \nu_{ii}(E) / (\varepsilon_h V_\varphi) \Big| z = z(z, \varphi) ;$$
$$\tilde{\gamma} = \int_0^{2\pi} |\hat{\alpha}| d\varphi ;$$
$$V_\varphi = -\frac{\partial \mathcal{J}}{\partial z} / \left(m \omega_B \frac{\partial \mathcal{J}}{\partial E}\right) ; \quad \omega_B = \frac{eB}{mc} \qquad (4)$$
$$\mathcal{J} \sim \sqrt{\varepsilon_h} \left(E(\kappa) - (1 - \kappa^2) K(\kappa)\right) ;$$
$$2\kappa^2 = 1 + (E - \mu B_0 - e\Phi + \varepsilon_t \mu B_0 \cos\varphi) / (\varepsilon_h \mu B_0) ,$$

E(k) and K(k) are the full elliptical integrals of the first and second kinds,

$\nu_{ii}(E) = \frac{\sqrt{2}\pi}{\sqrt{m}} \frac{n e^4 \lambda}{(\omega \tau)^{3/2}} \psi(\omega)$ is the frequency of ion-ion collisions,

$$\psi(\omega) = \frac{2}{\pi} \left(\sqrt{\omega}\, e^{-\omega} + (1 + 1/2\omega) \int_0^{\omega} \sqrt{x}\, e^{-x} dx\right) ;$$

$\omega = (E - e\Phi) / T(z)$; $F_M = \frac{n}{(2\pi T)^{3/2}} e^{-\omega}$ is the Maxwellian distribution function.

Later on, all the linear dimensions will be normalized to the plasma radius, a.

Using the distribution function (3), let us find an energy flux through a magnetic surface with the radius r:

$$Q = \int_{-\pi}^{\pi} \frac{d\varphi}{2\pi} \int d^3v \, v_r \, (E - e\Phi) \, F \qquad (5)$$

where $v_r = \frac{c}{eZB_0} \frac{\partial \gamma}{\partial \varphi} \Big/ \frac{\partial \gamma}{\partial E}$ is the radial component of a drift velocity,

$$d^3v = 8 (\gamma \bar{\iota})^{3/2} \sqrt{\varepsilon_n} \, K(k) \, dw \, dk^2 / w \quad ;$$

$$\gamma = w / (1 - (2k^2 - 1)\varepsilon_n - \varepsilon_t \cos\varphi) ,$$

The results of numerical calculations for the energy fluxes, using the formula (5), show that these fluxes do not exceed a value

$$\tilde{Q} = Q / Q_{pl} = \frac{60 \varepsilon_n^{3/2} \varepsilon_t}{S_0 q z t^2} \cdot \frac{\hat{\nu}}{1 + 3.7\hat{\nu} + 1.2\hat{\nu}^2} \qquad (6)$$

(at $-1.5 \leq \Phi/T \leq 1.5$, $\Phi = 0$ included) in a wide range of variations in the plasma parameters and in the parameters of the facility. Here

$$Q_{pl} = \frac{3\sqrt{2}}{\pi} \frac{\rho_c^2 t q v_T n \bar{T}}{R} \left| \frac{\partial \ln \bar{T}}{\partial z} \right| ;$$

$$\hat{\nu} = \frac{zt}{10 \rho_c q} \cdot \frac{\varepsilon_t^{5/2}}{\varepsilon_n^2} \nu_* = \frac{\sqrt{2}}{10} \frac{z^2 t}{v_T \rho_c \varepsilon_n^2 \tau_{ii}} ; \qquad (7)$$

$v_T = \sqrt{2T/m}$ is the thermal velocity of a particle. ρ_c - is the Larmor radius of a particle with $E = T(o)$; $T(r) = T_o t(r)$; $\nu_* = \frac{\sqrt{2}}{v_T} \cdot \frac{Rq}{\varepsilon_t^{3/2} \tau_{ii}}$ - is the ratio between the frequency of collisions and the frequency of motion along the banana trajectory in the toroidal field; $\tau_{ii} = \frac{3\sqrt{m} \, T^{3/2}}{4\sqrt{\pi} \, n e^4 \lambda}$; $q = 1/\iota$ - is the safety factor; ι is the angle of rotational transform. The formula (7) is true for $\varepsilon_t / \varepsilon_n \leq 0.1$. In the opposite case, a considerable number of trajectories along which the particles trapped within a helical field are moved intersect the wall of the chamber and the particle losses cease to have a purely-diffusive nature.

It is of interest to compare the energy losses from the

plasma due to the particles trapped within the helical and toroidal fields.

Let us asseume that $\nu_* \ll 1$. Then, the energy losses related with the particles trapped within the toroidal field are equal [4] to $\tilde{Q}_t = 0.36\,\nu_*\left(1 + \frac{0.3\,x^2}{1+x^4}(z_t^{1/2} + z_n)\right) + 0.53\,\nu_*\varepsilon_t^{3/2}(1.5 + 1/q^2)$ (8)

where $z_t = \left|\frac{\partial \ln T}{\partial r}\right|$; $z_n = \left|\frac{\partial \ln n}{\partial r}\right|$;

when $\varepsilon_t = 0.02$; $\varepsilon_h = 0.2$; $\rho_0 = 0.015$; $q = 5$; $t = 1 - r^2 = 0.6$; $\tilde{Q}/\tilde{Q}_t = 10^{-2}$.

Thus, one can see that it is possible reach a state, when an energy flux through an ion channel determined by the helical magnetic field will be less than a flux determined by the toroidal field, by choosing a combination of such parameters as ε_t, ε_h, ρ_0, q.

In conclusion the author would like to express his gratitude to L.M.Kovrizhnykh and E.I.Yurchenko for useful discussions.

References

1 L.M.Kovrizhnykh, Nucl. Fus., 1984, 24, 851.

2 W.N.Hitchon, C.D.Beidler, H.E.Mynick, J.L.Shohet, J.Plasma Phys., 1985, 34, 327.

3 L.M.Kovrizhnykh, Fizika Plasmy 1982, 8, 1105.

4 Yu.V.Gott, E.I.Yurchenko, Fizika Plasmy, 1987, 13, 131.

OPTIMIZATION OF COILS FOR STELLARATORS

P. MERKEL

Max-Planck-Institut für Plasmaphysik
IPP-EURATOM Association
D-8046 Garching bei München
Federal Republic of Germany

1. Introduction

In stellarator configuration studies the optimization of plasma equilibrium properties and the realization of the magnetic field geometry by external currents can be treated separately. The Helias class of MHD stable stellarators has been obtained by studying fixed boundary equilibria [1]. The equilibria are characterized by strongly reduced parallel current density and a magnetic well. In order to realize these equilibria experimentally a method has been developed to determine external coils which will produce the appropriate magnetic field (NESCOIL code). In [2], [3] one finds a detailed description: On a closed surface surrounding the plasma equilibrium a surface current distribution is determined such that the field, $\vec{B}$, produced approximates the vacuum field of the plasma configuration. This is achieved by requiring that the normal component of $\vec{B}$ is minimized on the plasma surface

$$F \equiv \int_{\partial R} (\vec{B} \cdot \vec{n})^2 \mathrm{d}f = \min! \tag{1.1}$$

The outer surface is given by mapping the unit square $0 \leq u < 1$, $0 \leq v < 1$ of the two angle-like variables, u and v, onto one period of the surface:

$$\begin{aligned} r &= \sum_{m=0,n=-n_b}^{m_b,n_b} \hat{r}_{mn} \cos 2\pi(mu + nv) \ , \\ z &= \sum_{m=0,n=-n_b}^{m_b,n_b} \hat{z}_{mn} \sin 2\pi(mu + nv) \ , \\ \varphi &= \frac{2\pi}{n_p} v, \end{aligned} \tag{1.2}$$

where (r, φ, z) are cylindrical coordinates and the usual stellarator symmetry is assumed. The surface current density with the same periodicity can be expressed by a potential $\Psi(u, v)$ defined on the surface:

$$\vec{j} = \vec{n} \times \mathrm{Grad}\ \Psi(u, v) \ , \tag{1.3}$$

where Grad is the gradient operator on the surface ($\vec{x}_u \cdot \mathrm{Grad}\ \Psi = \Psi_u$, $\vec{x}_v \cdot \mathrm{Grad}\ \Psi = \Psi_v$), $\vec{n}$ is the exterior normal to ∂D, and $\vec{x}_u, \vec{x}_v$ are the derivatives with respect to u and v respectively (Fig. 1). The general ansatz for $\Psi(u,v)$ can be written as

$$\Psi(u,v) = \sum_{m=0,n=-N}^{M,N} \hat{\Psi}_{mn} \sin 2\pi(mu + nv) - \frac{I_p}{n_p} v - I_t u \ , \tag{1.4}$$

where I_p and I_t are the net poloidal and toroidal surface currents, respectively.

If the closed contours of the surface current are sufficiently simple then the current may be discretized into a finite number of infinitely thin filaments, which will approximate the external coils of the configuration. However, the coils for a realistic device have to satisfy a number of additional conditions: The minimal (maximal) plasma – coil distance must be prescribed. The curvature of the coils and the current density in the coils must not exceed certain limits.

For this purpose a further optimization step has been added: The outer current carrying surface is varied systematically by varying the Fourier coefficients $\hat{r}_{mn}$, $\hat{z}_{mn}$. Again, F is minimized, but this time the above mentioned side-conditions are expressed as constraints (penalty functions) in the minimization.

2. Applications

The Helias configuration is considered to be the most promising candidate for the W VII-X device [4]. Preliminary data for the W VII-X are: major radius 5 m, aspect ratio $A \approx 10$, magnetic field $B = 4$ Tesla, minimal coil – plasma distance $d_{\min} \geq 0.2$ m, maximal coil curvature $\kappa_{\max} = 0.2$ m and maximal coil current density $j_{\max} = 40\ \mathrm{MA/m^2}$.

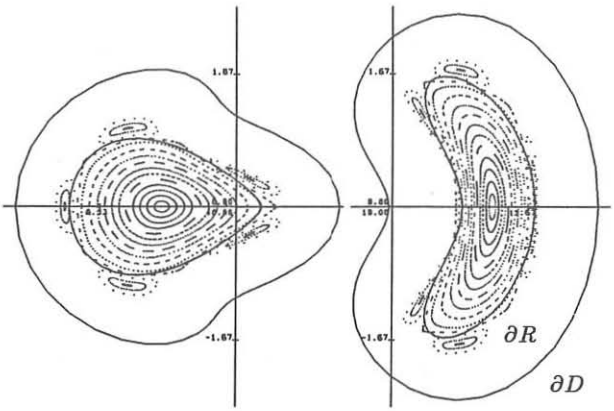

Fig.1 Poincaré plot of the 5081 Helias field. Fourier harmonics $\hat{\Psi}_{mn}$ of the potential taken into account have $m \leq 4$, $|n| \leq 4$. Fourier coefficients $\hat{r}_{mn}$, $\hat{z}_{mn}$ of optimized current carrying boundary have $m \leq 4$, $|n| \leq 4$.

Two optimized coil configurations which have been computed for the Helias cases 5081 and 5099 are presented here [5]. Characteristic properties of the 5081 Helias are: number of periods $n_p = 5$, aspect ratio $A = 10$, rotational transform $0.8 \lesssim \iota \lesssim 1$, ballooning stable up to $\langle\beta\rangle = 0.05$. In Fig. 2 one period of a coil system is shown. Fig. 1 shows the Poincaré plot of the magnetic field produced by 10 coils per period. A magnetic well of 1.9 % is obtained. The configuration may also be of interest as a candidate for an island-divertor concept with divertor regions at the tips of the bean-shaped and the triangular cross-sections.

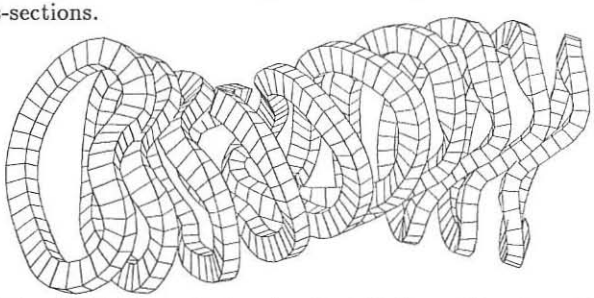

Fig.2 One period of modular coils for the 5081 Helias stellarator. Coils per period $N_c = 10$, major radius $R = 5$ m, minimal and maximal distance of coils to plasma $d_{\min} = 0.19$ m, and $d_{\max} = 0.32$ m, maximal curvature at coil boundary $\kappa = 5\ \mathrm{m}^{-1}$, coil cross-section $q = 0.18 \times 0.28\ \mathrm{m}^2$.

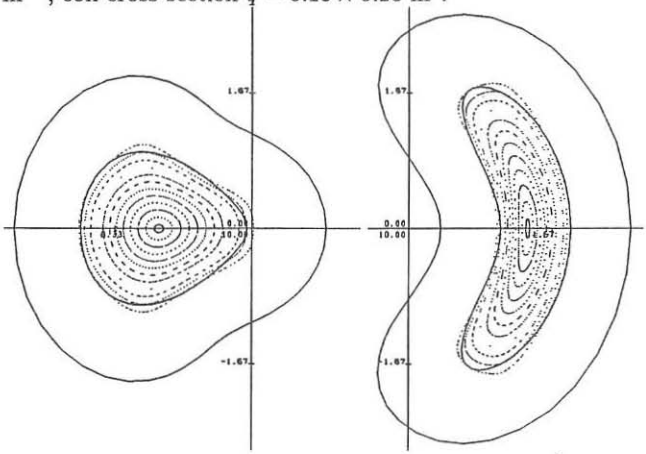

Fig.3 Poincaré plot of the 5099 Helias field. Fourier harmonics $\hat{\Psi}_{mn}$, of the potential taken into account have $m \leq 4$, $|n| \leq 3$. Fourier coefficients $\hat{r}_{mn}$, $\hat{z}_{mn}$ of optimized current carrying boundary have $m \leq 4$, $|n| \leq 4$.

The 5099 Helias case differs from the 5081 case only with respect to the rotational transform, which is almost constant with $\iota = 0.9$. The magnetic well is 1.8 %. Figure 3 shows the Poincaré plot for this case which is produced by the coils shown in Fig. 4. There are 10 coils per period each carrying the same current.

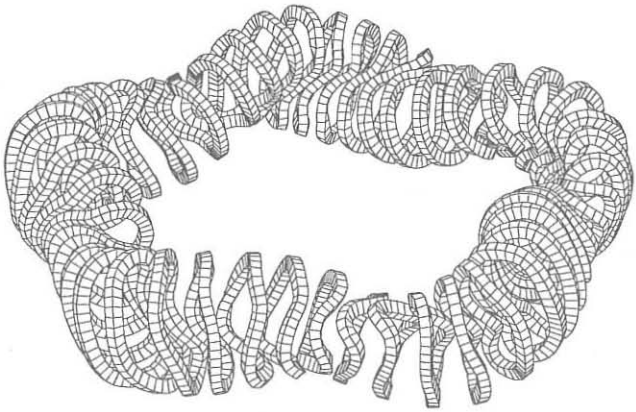

Fig.4 Modular coils for the 5099 Helias stellarator. Coils per period $N_c = 10$, major radius $R = 5$ m, minimal and maximal distance of coils to plasma $d_{\min} = 0.22$ m, and $d_{\max} = 0.34$ m, maximal curvature at coil boundary $\kappa = 4$ m^{-1}, coil cross-section $q = 0.2 \times 0.25$ m^2. A magnetic field $B = 4$ Tesla is achievable with current density $j = 40$ MA/m^2.

3. Summary

The NESCOIL code has been extended to take into account important practical constraints on the properties of stellarator coils. The code has been used to compute coil configurations for some possible W VII-X designs. Having found the coils producing the external field, one can study free boundary plasma equilibrium using the NEMEC code [6], [7]. In particular, the change in plasma properties with $\langle\beta\rangle$ and with the superposition of a vertical B_z-field can be studied.

4. References

[1] W. Dommaschk, F. Herrnegger, W. Lotz, P. Merkel, J. Nührenberg, A. Schlüter, U. Schwenn, and R. Zille, Plasma Physics and Contr. Nucl. Fusion Res. 1986, Vol. 2, p.383-390 (IAEA 1987, Vienna, Proc. 11th Intern. Conf., 13-20 Nov. 1987 Kyoto).

[2] P. Merkel, Nucl. Fusion **27** (1987) 867.

[3] P. Merkel, In: Theory of Fusion Plasmas, Eds. A. Bondeson E. Sindoni, and F. Troyon, Varenna, Italy, EUR 11336 EN, 25-46.

[4] Proc. Workshop on W VII-X (18-20 March 1987, Schloß Ringberg, Germany; EUR 11058 EN; Eds. F. Rau and G.G. Leotta; CEC Brussels, Belgium).

[5] IPP Annual Report 1987; J. Nührenberg, private communication.

[6] S.P. Hirshman, W.I. Van Rij, P. Merkel, Comput. Phys. Comm. **43** (1986) 143.

[7] P. Merkel, J. Comput. Physics **66** (1986) 83.

EQUILIBRIUM STUDIES FOR HELICAL AXIS STELLARATORS†

L. Garcia
Universidad Complutense. 28040 Madrid. Spain.

B.A. Carreras, N. Dominguez
Oak Ridge National Laboratory. Oak Ridge. Tennessee. USA.

† Supported in part by the association EURATOM/CIEMAT

MHD equilibrium studies in stellarator-type configurations are very complex because their intrinsic 3-D character. Although very efficient 3-D equilibrium codes have been developed, the computational time inverted in their calculation renders them inadequate for data analysis. For certain type of configurations, MHD equilibrium studies can be reduced to a 2-D problem by the method of averaging.

Greene and Johnson[1] proposed an averaged method based in the expansion of the equilibrium equations in powers of the inverse aspect ratio ε. This method has been very successful in explaining stellarator properties, and has been tested versus 3-D codes. However, due to its assumptions, the approach is inadequate for helical axis systems.

Hender and Carreras[2] proposed a method that uses vacuum flux coordinates. The zero-order approximation is the vacuum field. The main restriction is that the method is only valid in the case of toroidally or helically dominated shift. In the case of realistic helical axis configurations, as in the TJ–II flexible heliac, the helical shift can be significant for some magnetic configurations, but it is clearly dominated by the toroidal shift, rendering the method suitable for equilibrium calculations.

The specific vacuum flux coordinates employed are those described by Boozer[3]. For a vacuum, the magnetic field may be written in contravariant or covariant form as $\mathbf{B}_v = B_0\ \rho \nabla\rho \times \nabla(\theta - \iota_v \varphi) = g_B \nabla\varphi$, where $\iota_v(\rho)$ is the rotational transform, g_B is a constant, and $B_0 \pi \rho^2 = \Phi$ is the toroidal flux. The radial variable is ρ, while θ and φ are, respectively, poloidal and toroidal-like angles.

The ordering of the metric elements and different magnetic field components is discussed in Ref. 2. To lowest order, the averaged equilibrium equations yields a Grad-Shafranov-type equation for the averaged poloidal

flux:

$$\frac{1}{\rho}\frac{\partial}{\partial\rho}\left[\rho\left(\bar{g}^{\rho\rho}\frac{\partial\psi}{\partial\rho}+\bar{g}^{\rho\theta}\frac{1}{\rho}\frac{\partial\psi}{\partial\theta}\right)\right]+\frac{1}{\rho}\frac{\partial}{\partial\theta}\left(\bar{g}^{\rho\theta}\frac{\partial\psi}{\partial\rho}+\bar{g}^{\theta\theta}\frac{1}{\rho}\frac{\partial\psi}{\partial\theta}\right)=$$

$$-\frac{F}{g_B}\left[\frac{1}{\rho}\frac{\partial}{\partial\rho}\left(\rho^2\iota_v\bar{g}^{\rho\rho}\right)+\frac{1}{\rho^2}\frac{\partial}{\partial\theta}\left(\rho^2\iota_v\bar{g}^{\rho\theta}\right)\right]-\mu_0 g_B^2\left\langle\frac{B_0^2}{B_v^2}\right\rangle\frac{dp}{d\psi}-\frac{1}{\alpha}F\frac{dF}{d\psi}$$

where $\alpha=1+\dfrac{\rho^2\iota_v^2}{g_B^2}\langle g^{\rho\rho}\rangle$ and

$$\bar{g}^{\rho\rho}=\frac{\langle g^{\rho\rho}\rangle}{\alpha},\qquad \bar{g}^{\rho\theta}=\rho\frac{\langle g^{\rho\theta}\rangle}{\alpha},\qquad \bar{g}^{\theta\theta}=\rho^2\left[\frac{\langle g^{\theta\theta}\rangle}{\alpha}-\frac{\rho}{g_B}\iota_v^2(\langle D\rangle-\bar{D})\right],\ \text{with}$$

$$\langle D\rangle=\frac{1}{\rho g_B}\left\langle\frac{B_v^2}{B_0^2}\right\rangle,\qquad \bar{D}=\frac{\rho}{g_B}\frac{\langle g^{\rho\rho}\rangle\langle g^{\theta\theta}\rangle-\langle g^{\rho\theta}\rangle^2}{\alpha}$$

D is the Jacobian of the coordinates transformation, g^{ij} are the metric elements, and $\langle\ \rangle$ denotes average over the toroidal angle φ. The averaged plasma pressure is p, and F the covariant component of the magnetic field in the toroidal direction.

The Grad-Shafranov equation is solved numerically using the vacuum magnetic information as input, and a given $p(\psi)$ profile. The averaged equilibrium flux is then calculated by imposing either flux conservation ($\iota=\iota_v$) or zero toroidal current on each flux surface. The last condition is the most relevant for stellarator operation, and can be written in the vacuum flux surface coordinates as

$$\mu_0 g_B\frac{dp}{d\psi}+F\frac{dF}{d\psi}\frac{d}{dV}\int\int\frac{1}{\alpha}\rho\,d\rho\,d\theta-\frac{dF}{d\psi}\frac{d}{dV}\int\int\frac{\rho}{g_B}\iota_v\left(\bar{g}^{\rho\rho}\frac{\partial\psi}{\partial\rho}+\bar{g}^{\rho\theta}\frac{1}{\rho}\frac{\partial\psi}{\partial\theta}\right)\rho\,d\rho\,d\theta=0$$

where the integrals are calculated over contours of constant ψ, and $2\pi V$ is the volume enclosed by each flux surface.

To calculate ψ, the Grad-Shafranov equation is solved first by assuming a given dependence $F=F(\psi)$. This problem is solved iteratively in the vacuum flux coordinates system with the boundary conditions $p=B^\rho=0$ at the edge. Once ψ has been obtained, we solve the ordinary differential equation for the $F(\psi)$ required to give zero net current within each flux surface. The value of F is, in general, different from that which was used to solve the Grad-Shafranov

equation, and it is necessary to iterate the solutions of both equations until F converges.

Finally, we present the numerical results. Fig. 1 shows the comparison of the shift obtained for the so-called CT6 configuration. CT6 is a 6-field period l=2 torsatron with plasma aspect ratio 4, and ι ranging from 0.32 at the center to 0.95 at the edge, described elsewhere[4]. This is a planar axis configuration, and is a appropriated test for the code. We compare this method (CHAV) with three-dimensional calculations using VMEC[5] and calculations using RSTEQ[6]. The later solves the equations of the Greene and Johnson stellarator expansion. The pressure is proportional to ψ^2, and the value of peak beta is normalized to the critical beta value $\beta_c = \iota_e^2/A$, where ι_e denotes the value of the rotational transform at the edge, and A the aspect ratio. The results obtained by using the three codes are very similar.

The results shown in Fig. 2 correspond to the "standard" TJ-II configuration[7]. For this case, ι is almost flat, ranging from 1.46 at the center to 1.49 at the edge. The RSTEQ code has not been used in this case, because the classical average method cannot be applied to configurations with helical magnetic axis. The comparison between CHAV and the three-dimensional code VMEC shows an error close to 20%, consistent with the ordering assumed in the expansion.

Fig. 3 shows the flux surfaces reconstruction in real space of the vacuum and $\beta_0 = 12.92\%$ cases for the CT6 configuration. Fig. 4 shows the flux surfaces of the vaccum and $\beta_0 = 10.32\%$ for the standard TJ-II configuration. In this case, the shift is more marked in the toroidal cut corresponding to a fourth of field period.

REFERENCES

1. J.M. Greene and J.L. Johnson, *Phys. Fluids* **4**, 875 (1961)
2. T.C. Hender and B.A. Carreras, *Phys. Fluids* **27**, 2101 (1984)
3. A.H. Boozer, *Phys. Fluids* **25**, 520 (1982).
4. B.A. Carreras, et al. Compact Torsatron Configurations, Oak Ridge National Laboratory Rep. ORNL/TM-10030 (1987).
5. S.P. Hirshman, W. van Rij, and P. Merkel, *Comput. Phys. Commun.* **43**, 163 (1986).
6. V.E. Lynch, et al., *J. Comput. Phys.* **66**, 411 (1986).
7. J. Guasp, et al. Controlled Fusion and Plasma Physics (Proc. 12th Europ. Conf. Budapest, 1985) Vol. 1, European Physical Society 441,1985.

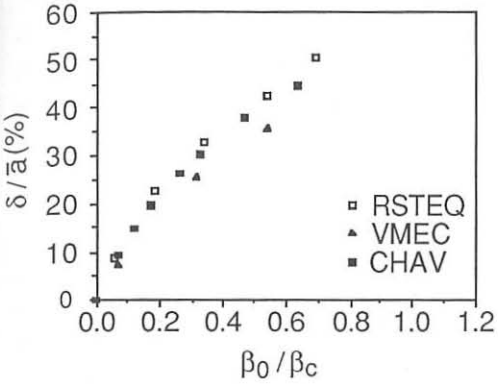

Fig. 1. The equilibrium shift as a function of β_0 for the CT6 configuration.

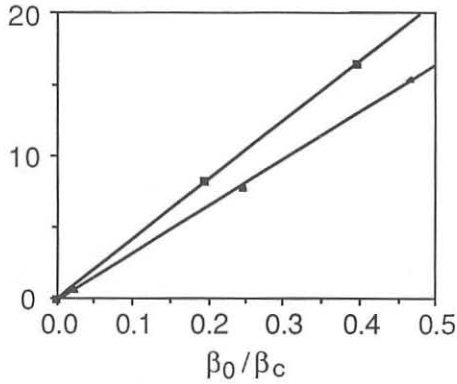

Fig. 2. The same as Fig. 1 for the standard TJ-II configuration

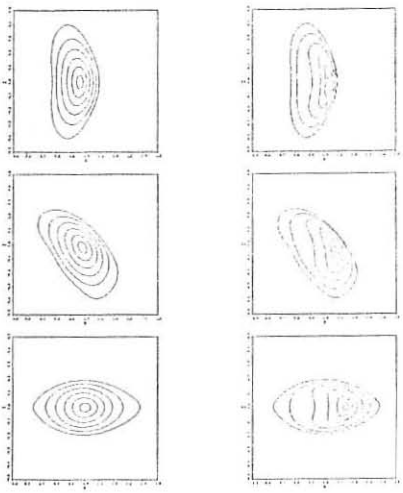

Fig. 3. Flux surfaces for the CT6 torsatron at β_0=0 and 12.92%.

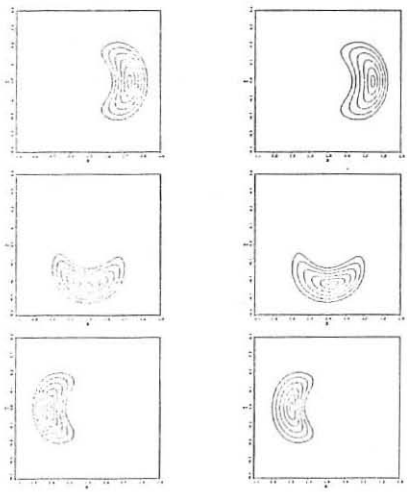

Fig. 4. Flux surfaces for theTJ-II heliac at β_0=0 and 10.32%.

DRIFT LOSSES OF ALPHA PARTICLES IN A STELLARATOR WITH LOW ASPECT RATIO

V.P.Nagornyj, V.A.Yavorskij

Institute for Nuclear Research, Ukrainian SSR Academy of Sciences, Kiev, USSR

The conception of low-aspect-ratio stellarator with a simple coil configuration has been propozed recently in Ref./1/. An important feature of this stellarator is low amplitude of the helical field ripple (ϵ_h), so that $A\epsilon_{ha} \ll 1$, where A is the aspect ratio, ϵ_{ha} is the ripple amplitude at the plasma edge.

The purpose of the present work is to examine the confinement of bulk alpha particles (trapped and untrapped) in the low-aspect-ratio stellarator. The drift losses (particle confinement time $\tau \leq A a^2/(\rho_L v)$, with a being the plasma minor radius, v and ρ_L the particle velocity and gyroradius, respectively) are considered only.

Let us consider the model magnetic field

$$b = B/B_0 = 1 - \epsilon_t \cos\theta - \epsilon_h \cos(N\varphi - \ell\theta), \qquad (1)$$

with $B_0 = B(\rho=0)$, $\epsilon_t = \rho/(aA)$, ℓ and N the multipolarity and the number of field periods. A toroidal system of coordinates ρ, θ, φ is used, where ρ the flux surface radius, θ and φ the poloidal and toroidal angles. To compute orbits of both trapped and circulating particles we use conservation of the action J /2/:

$$J = \psi - \sigma(2^{3/2}/\pi)(\lambda\epsilon_h)^{1/2}\rho_L \varkappa E(\varkappa^{-1}). \qquad (2)$$

Here $\lambda = v_\perp^2/(v^2 b)$, $\sigma = \mathrm{sgn}(v_\parallel/v)$, ψ is the flux function

$$\psi = (aA)^{-1}\int \iota\rho\, d\rho, \qquad (3)$$

ι is the rotational transform, and $\varkappa^2=(\epsilon_h+\lambda^{-1}-1+\epsilon_t\cos\theta)/(2\epsilon_h)\geq 1$. As the majority of alphas will be produced at the central region of the plasma column the first to be considered are the orbits of the particles passing through the neighbourhood of the magnetic axis. An orbit equation of these particles is given by

$$x^{4\ell-5}-4(\ell-1)\chi\delta A x^{2\ell-3}-4(\ell-1)^2(1+\chi^2)\delta^2\cos\theta=0 \quad (4)$$

with $x=\rho/a$, $\delta=\rho_{L0}A/(\iota_a a)$, $\chi=\sigma\sqrt{1-\lambda}$ the cosine of the local pitch angle on the axis. It follows from Eq.(4) that particles with $0>\chi>\chi_*=C_\ell A^{-1/2}\delta^{1/(4\ell-5)}$ ($C_2=0.94$, $C_3=0.99$) are toroidally trapped and all the rest particles are untrapped. The largest radial excursion (x_M) has the trapped particle with $\chi=\chi_*+0$. To a high degree of accuracy this excursion can be approximated by

$$x_M=(\ell^2\delta)^{2/4\ell-5}. \quad (5)$$

Fig.1 shows the maximal radial excursions (x_m) of the particles under consideration, as a function of χ, for $\ell=2$ and $\ell=3$ stellarators. It follows from Fig.1 that the dependence of ρ_m on χ in $\ell=3$ stellarator is sufficiently weaker compared to that in $\ell=2$ stellarator. Hence, in $\ell=3$ stellarator the untrapped particles make a more sufficient contribution to transport processes. It follows from Eq.(5) that the confinement criteria for the particles passing the axis is

$$\rho_L/a<\ell^{-2}\iota_a A^{-1/2}. \quad (6)$$

This criteria makes the serious demands for the stellarator parameters. In particular, for $\ell=3$, $\iota_a=0.2$, $A=4$ /1/ the condition (6) gives $\rho_L/a<10^{-2}$.

Let us now assume that condition (6) is satisfied and the losses of alphas in the first bounce period are negligible. Obviously, in this case the trapped particle losses are caused by the orbit transformation of the toroidally trapped particles into the unconfined helically trapped ones. A pro-

bability of the transformation is /2/

$$W_{t\to\ell} = -\sigma_\theta \frac{2\sqrt{2}}{\pi} \frac{\ell \rho_L \sqrt{\epsilon_h}}{\rho\, \iota\, \epsilon_t} \left(1 + O\left(\iota \epsilon_t (N\epsilon_h)^{-1} ctg|\theta|\right)\right), \quad (7)$$

where $\sigma_\theta = \mathrm{sgn} \sin\theta$. Except the narrow region in the vicinity of $\theta = \pi$ $W_{t\to\ell}$ is positive below the plasma midplane (a toroidal drift being directed down) and equals 0.2 at the plasma edge for the stellarator with $\rho_L/a = 0.02$, $\ell = 3$, $\epsilon_{ha} = 0.05$, $A = 4$, $\iota_a = 0.3$ as in Ref.1. It follows from Eq.(7) that $W(\rho<a) > W(a)$, and thus, after a few bounces $n \lesssim W^{-1}(a)$ the trapped particle would be transformed into localized one.

The behaviour of the localized particles can be derived from the following invariant /3/

$$J_{||} = \sqrt{\epsilon_h}\, f(\varkappa^2), \quad (8)$$

where $f(\varkappa^2) = E(\varkappa) - (1-\varkappa^2) K(\varkappa)$, $K(\varkappa)$ and $E(\varkappa)$ are the complete elliptic integrals of the first and second kind, $\varkappa^2 \leq 1$.

Taking into account that $\varkappa^2(\rho_*, \theta_*) = 1$ and $f(1) = 1$, with ρ_*, θ_* the the coordinates of the point where the orbit transformation takes place we find the transformed orbit. The elementary analysis of the equation $J_{||}(a, \pi) = \sqrt{\epsilon_{h*}}$ shows that all transformed particles are lost if $\epsilon_{ta}/\epsilon_{ha} > 1$ and 1.2 for $\ell = 2$ and $\ell = 3$, respectively. Thus, in the low-aspect-ratio stellarator all the trapped particles escape from the plasma column except the narrow region $|\pi - \theta| \lesssim \iota/N \ll 1$ defined by the condition $\sigma_\theta W_{t\to\ell} > 0$.

Integrating over the loss region we find that more than 90% of all trapped particles are lost when $\epsilon_{ta}/\epsilon_{ha} > 1$. Since 30-35% (for A=4) of all born particles are trapped ones the fraction of lost alphas is about 30%.

An important question to discuss is the influence of the field's harmonic structure on the particle confinement. One can show that at least in the case of the superposition of

of the harmonics with $\ell=2$ and $\ell=3$ the drift losses do not change. Therefore, one can hardly hope to improve the confinement by the field coil optimization.

Evidently, the losses may be influenced by the electric field induced by the alpha particle losses. Hence, the electric field should be taken into account to get the self-consistent solution of the problem.

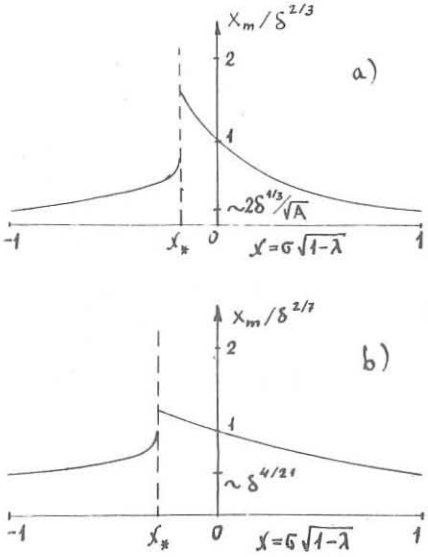

Fig.1. The maximal radial excursions (x_m) of the particles crossing the axis versus x (the cosine of the local pitch-angle on the axis) for l=2 (curve "a") and l=3 (curve "b").

REFERENCES:

/1/ Bykov, V.E., Volkov, E.D., Georgievskij, A.V. et al., in "Voprosy atomnoj nauki i tekhniki", Termoyadernij sintez, 1980,No.2, p.19.

/2/ Nagornyj, V.P., Yavorskij, V.A. Preprint KINR 87-14, Kiev Institute of Nuclear Research (1987).

/3/ Galeev, A.A., Sagdeev, R.Z., in "Vopr. Teor. Plazmy", 1973, 7, p.205.

EXPERIMENTAL RESULTS FROM A FLEXIBLE HELIAC

X.H. Shi, B.D. Blackwell S.M. Hamberger

Plasma Research Laboratory
Research School of Physical Sciences
The Australian National University
Canberra, ACT, 2601, Australia

The original heliac SHEILA[1], which had three field periods, major radius R=18.75cm and mean radius of its outer (bean-shaped)magnetic surface a = 3.1cm, has been converted into a so-called 'flexible' heliac[2] by adding an ℓ=1 helical winding around the poloidal ring. Highly reproducible plasma configurations are obtained in the range of $0.7 \leq \iota(0) \leq 1.86$ when the current ratio $C = I_h/I_r$ is varied from -0.13 to 0.25, where I_h,I_r are the currents in helical winding and poloidal ring respectively. Adverse effects of the low-order resonances on particle confinement have been observed experimentally and reported in [3].

In this paper we show detailed comparisons between the plasma pressure profiles measured by Langmuir probes and the computed vacuum magnetic surfaces and show that we can account for some apparent disparities which appear for configurations with $\iota(0)$ close to unity by including the effect of known error fields.

The experiments are conducted in highly ionized argon plasma produced by a weak oscillatory discharge. Typical parameters are listed in Table I. Plasma density and electron temperature profiles are measured at two toroidal positions, at $\phi = 60^0$ by a Langmuir probe which scans horizontal chord 16mm above the median plane, and at $\phi = 120^0$ by a second movable probe which can reach most of the plasma cross-section. The pressure profiles are obtained from the product $n_e T_e$ by assuming the ions to be cold.

As the field due to the oscillatory ohmic heating current in the plasma is much smaller than that due to the quasi-steady currents flowing in the external coils, and the plasma beta is very low, plasma pressure distributions can be directly compared with the computed vacuum configurations. The data taken from pressure profiles have been ploted against a parameter X which labels each magnetic surface[1]. Two examples, for C=0.15 and 0.25 which correspond to configurations with $\iota(0) = 1.62$ and $\iota(0) = 1.86$ respectively, are shown in Fig.1. In most cases, as shown in Fig.1, the pressure values are very close to each other at any given magnetic flux surface as calculated from the ideal coil currents and locations, and their dependence on the different flux surfaces lies within experimental uncertainty on a single smooth curve. However, for configurations with $\iota(0)$ close to unity some obvious discrepancies can be seen, e.g. in the positions of the magnetic axes and in

the lack of 3-fold symmetry with ϕ. A careful check has revealed a small error in the poloidal ring position. Vacuum field calculations which include this geometrical effect confirm that the error fields caused by the horizontal displacement (about 1.5mm) of the poloidal ring break the three-fold heliac symmetry by adding a predominantly m=1,n=1 field harmonic which has most effect on configurations which include an $\iota = 1$ surface. Their effects on magnetic axis locations are shown in Fig.2, where we compare the measured peak pressure positions for different values of C, at the two nominally symmetric planes $\phi = 0$ and $\phi = 120^0$.

The magnetic islands which result from the resonance between the surface $\iota = 3/2$ and the m=2, n=3 vacuum field harmonics inherent in the heliac geometry can be experimentally identified with certain features observed in profiles of both the plasma pressure and the floating potential. An example is given in Fig.3 in which islands appear on both sides of the main closed surface region when the $\iota = 3/2$ surface is near the edge. The measured pressure profiles show that the pressure gradient is generally larger inside the closed surface regions, including those inside the small islands, while the profiles are significantly flatter in the ergodic regions. The floating potential also changes noticeably at the boundaries between 'closed' and 'open' field line regions.

Low frequency ($10 - 20$kHz) density and magnetic field fluctuations in Langmuir probe ion saturation current signals and in magnetic probe signals are observed and studied. When the magnetic field is decreased below a critical value corresponding to $\rho_i \sim a$, where ρ_i is the ion Larmor radius evaluated at T_e, the plasma becomes very quiet. This dependence of the density fluctuations on magnetic field strength is similar to that seen in early drift wave studies in Q machines[4]. As the threshold is exceeded, the fluctuation first appears as a single, coherent mode. When the magnetic field is increased further more frequencies appear.

The structure of the coherent mode and the dependence of its levels on radial and poloidal positions are measured in configurations with different rotational transform ranges. The toroidal and poloidal mode numbers n and m, measured and expressed in terms of straight-field-line coordinates, and the wave numbers directly measured along the field lines both indicate that the wave propagates nearly perpendicular to the field lines in every case, i.e.$n/m \approx \iota$. The fluctuations are present throughout the plasma, but the relative fluctuation level peaks towards the plasma edge. It also varies by a factor of up to 7 to 8 around a given surface cross-section, whose cause is uncertain.

The magnetic field fluctuations perpendicular to the field lines, which have the same frequency component, are smaller than the density fluctuations by a factor of $O(\beta)$. This is consistent with the nature of the fluctuations being electrostatic rather than magnetohydrodynamic[5].

REFERENCES

1: Blackwell, B.D., Hamberger, S.M., Sharp, L.E., and Shi, X.H., Nucl. Fusion. 25 (1985)1485.

2: Harris, J.H., Cantrell, J.L., Hender, T.C., Carreras, B.A., and Morris, R.N., Nucl. Fusion. 25 (1985)623.

3: Blackwell, B.D., Dewar, R.L., Gardner, H.J., Hamberger, S.M., Sharp, L.E., Shi, X.H., Vance, C.F., Zhou, D.F., in Plasma Physics and Controlled Nuclear Fusion Research (Proc. 11th Int. Conf. Kyoto, 1986), Vol.2, IAEA, Vienna(1987)511.

4: Hendel, H.W., Chu, T.K., Politzer, P.A., Phys. Fluids. 11 (1968)2426.

5: Kadomtsev, B.B., Plasma Turbulence(Academic, New York, 1965),pp. 82-83; Callen, J.D., Phys. Rev. Lett. 39 (1977)1540.

Table I. Typical parameters

Working gas	argon
Filling pressure (Torr)	9×10^{-5}
Magnetic field strength (T)	$0.15 \leq B \leq 0.19$
Magnetic field duration (ms)	$30 - 45$ ms
Plasma duration (ms)	$10 - 15$ ms
Equivalent plasma radius (m)	0.035 m
Plasma density (m^{-3})	$1 - 3 \times 10^{18}$
Electron temperature (eV)	$6 - 8$

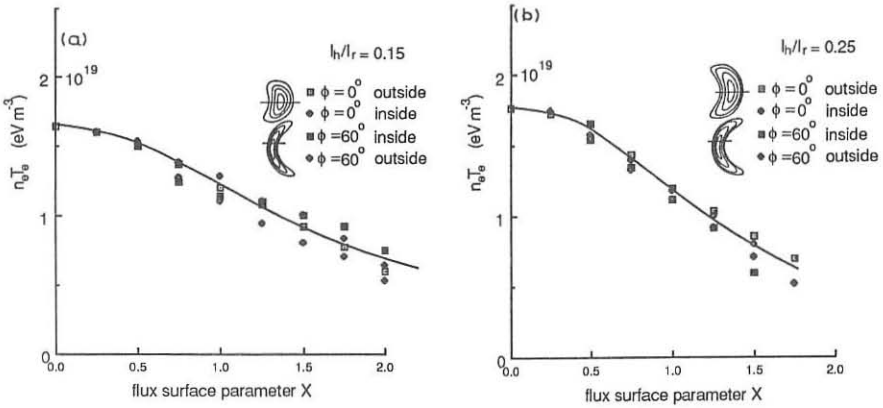

Fig.1: Pressure taken from profiles at two toroidal locations $\phi = 60^0$ and $\phi = 120^0$ plotted as functions of flux surface parameter X. 'Inside/outside' refers to the position of the plasma with respect to the minor axis.

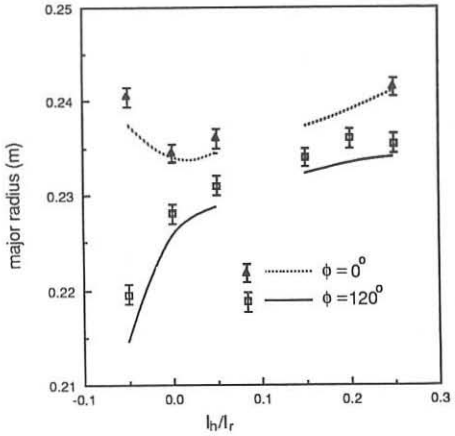

Fig.2: The positions of peak pressure measured along mid-plane chords at $\phi = 0$ and $\phi = 120^0$ for various I_h/I_r, compared with the magnetic axes computed to include the field error.

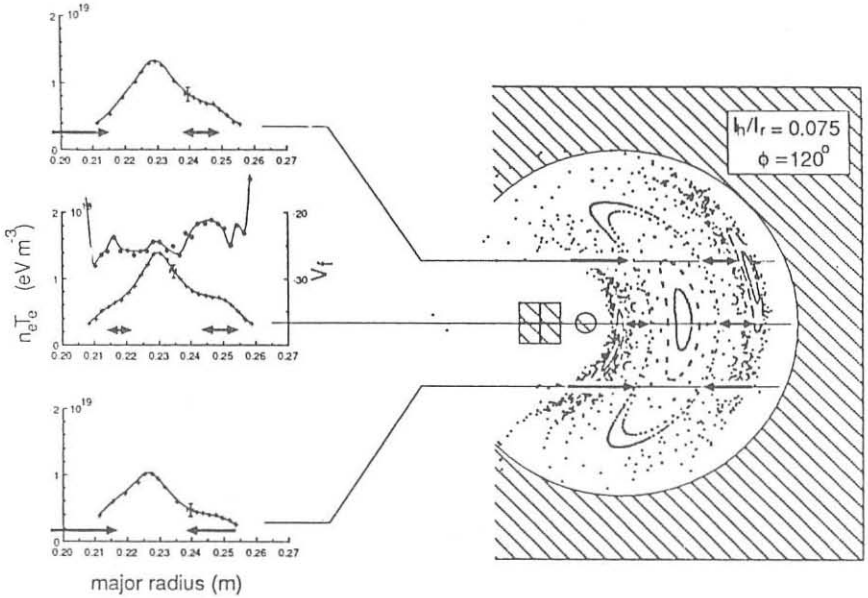

Fig.3: Three chordal pressure scans for $I_h/I_r = 0.075$, along mid-plane and 20 mm above and below the mid-plane, at $\phi = 120^0$. The appropriate vacuum configurations are shown on the right. The heavy lines indicate the ergodic regions and the arrow heads correspond to the boundaries between closed surface and ergodic regions.

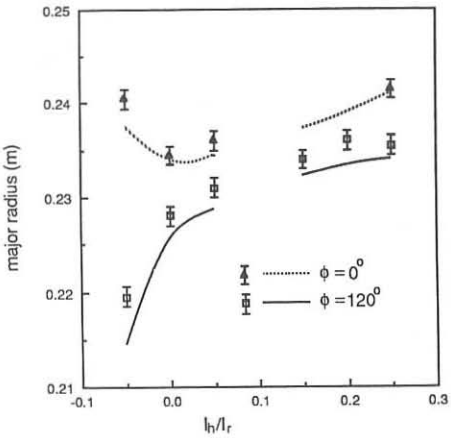

Fig.2: The positions of peak pressure measured along mid-plane chords at $\phi = 0$ and $\phi = 120^0$ for various I_h/I_r, compared with the magnetic axes computed to include the field error.

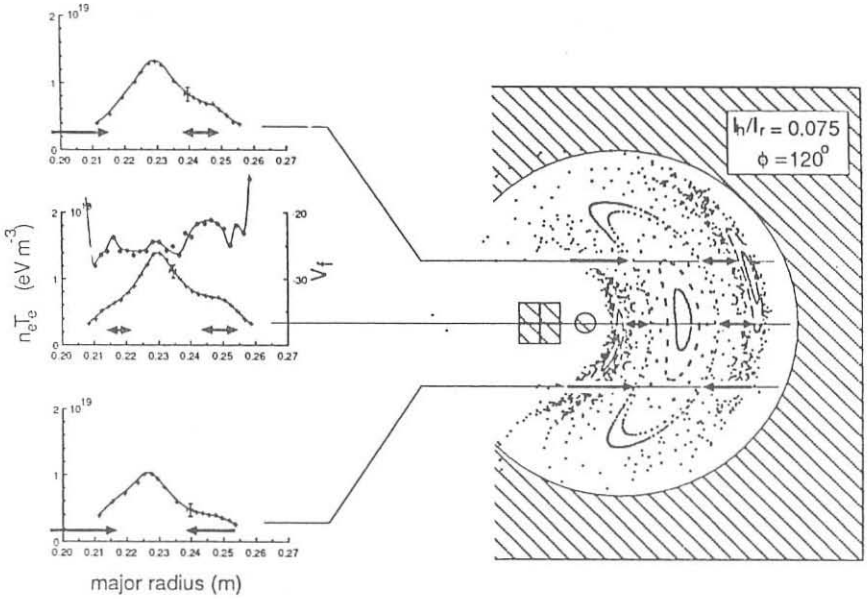

Fig.3: Three chordal pressure scans for $I_h/I_r = 0.075$, along mid-plane and 20 mm above and below the mid-plane, at $\phi = 120^0$. The appropriate vacuum configurations are shown on the right. The heavy lines indicate the ergodic regions and the arrow heads correspond to the boundaries between closed surface and ergodic regions.

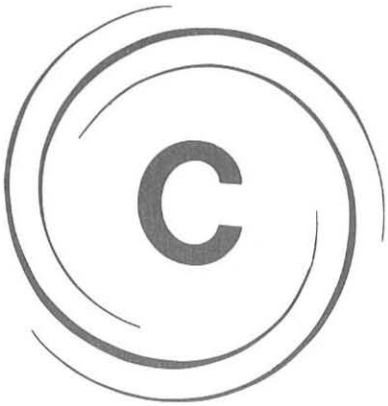

Alternative Confinement Schemes

ION HEATING STUDIES IN THE ZT-40M REVERSED FIELD PINCH

G. A. Wurden, P. G. Weber, K. F. Schoenberg, A. E. Schofield,
J. A. Phillips, C. P. Munson, G. Miller, J. C. Ingraham,
R. B. Howell, J. N. Downing, R. E. Chrien, T. E. Cayton,
L. C. Burkhardt, R. J. Bastasz*, S. E. Walker†,
A. M. Preszler†, P. G. Carolan‡, and C. A. Bunting‡

Los Alamos National Laboratory, Los Alamos, NM 87545, USA

*Sandia National Laboratory, Livermore, CA
† Phillips Petroleum Co., Bartlesville, OK
‡ Culham Laboratory, United Kingdom

Introduction: Heating of ions to levels $T_i \sim T_e$ is a common feature of the ohmically driven reversed field pinch.[1,2] Because of the several millisecond electron-ion equilibration time, a non-ohmic ion heating mechanism is indicated.[3] Departures from $T_i \simeq T_e$ have been observed to $T_i \sim 3 - 4 \times T_e$ in ZT–40M,[4] and also to the opposite extreme of $T_i \sim 0.3\ T_e$ on HBTX–1B.[5] An understanding of the mechanisms of ion heating in the RFP is a key ingredient to basic understanding of the RFP configuration. We present measurements of ion energy distributions and temperatures, over a range of experimental conditions, to build an experimental basis for theoretical interpretation. In cooperation with several laboratories, we have assembled on ZT–40M the most complete set of ion energy and supporting diagnostics yet employed on a modern RFP. These include a low energy time of flight (TOF) neutral particle spectrometer, Doppler broadening spectrometers,[6,1] neutron activation counters, time-resolved neutron rate detectors, silicon sample implantation edge probes,[7] a time of flight neutron spectrometer,[8] and a charge exchange neutral particle analyzer (NPA).[9] The results reported here are an initial survey of ion measurements under two non-standard plasma conditions: deep-reversal ramped current discharges, and limiter insertion into standard 120 kA flattops.

Hot Ion Mode: In ZT-40M, it has been previously observed that neutron rates of order 1×10^{10} n/s are produced in deeply reversed 100-200 kA ramping discharges. The neutron emission is not associated with startup, but occurs during the last two-thirds of the plasma lifetime.[4] Neutron emission has been observed in high-Θ flattops, F-Θ pumping shots, and high-Θ ramping discharges. Running similar deuterium discharges with the same current ramping rate, but at shallow reversal, drops the neutron rate below the detectable threshhold ($\sim 1 \times 10^7$ n/s), while also reducing the general fluctuation levels. We have used the NPA and TOF to measure the emitted deuterium neutral flux, perpendicular to field lines, for two high neutron flux conditions. The 5-channel NPA is set to three successive energy ranges to cover the neutral flux spectrum in three bands on a shot to shot basis. Figure 1 shows the slope obtained from the $\ln(dN/\sqrt{E}dE)$ vs. E, referred to as T_i^*, for three energy bands: 0.5-1.3keV, 1-2.7 keV, and 2-5.5keV during 100-190 kA ramping shots, as well as the electron density and loop voltage time dependence. For slightly different plasma conditions ("slow-start" ramping[10]), we fit a composite NPA spectrum in Figure 2 (data points are solid circles) to a theoretical spectrum (shown as a solid line)

modelled with the code NEUCG2.[11] The fit assumes $T_i(0) = 1.0$ keV, $T_e(0) = 350$ eV, $n_e(0) = 2.7 \times 10^{19} m^{-3}$, 20 eV edge temperatures, and functional forms of $(1-(r/a)^2)^2$ for ion temperature (similar to HBTX[3]), and $(1-(r/a)^4)$ for electron temperature and density. A recalibration check of the NPA will be done at Culham to verify the older calibrations presently in use. Neutron rate Maxwellian equivalent temperature for the profile above is estimated at $T_i^{neut} = 1.4 \pm 0.3$ keV. Macroscopic fluctuation activity is seen in nearly all time resolved diagnostics, and both m=1 and m=0 activity is present in the plasma. The NPA shows periodic flux bursts, with brightness changing by a factor of 20-40x on a timescale of 100 μsec, simultaneously with bursts on D_α and CrI light monitors in the same toroidal section. These disturbances rotate toroidally with velocities of $0.5 - 3 \times 10^4 m/s$, in the electron diamagnetic direction.[12] The NPA spectra indicate a 20% decrease in T_i^* during flux maxima relative to the minima.

Neutron activity is measured by a number of techniques. Three independently calibrated, absolute neutron yield activation measurements are used: Arsenic, Silver, and Indium. Arsenic[13] and Indium[14] measure fast neutrons, while Silver responds to thermalized neutrons. All three measurements agree to better than a factor of two. Time dependent neutron rate is obtained from a Li^6I crystal, and a detailed comparison of the NPA and neutron rate temperature is in progress. The neutron emission is grossly symmetric around the torus, as measured by five thermoluminescent dosimeters. A crude neutron energy spectrum has been obtained from the Phillips Petroleum Co. time of flight neutron spectrometer, indicating that the neutrons are 2.5 MeV in origin. Further measurements with better statistics, perhaps resulting in a direct neutron spectral measurement, are being planned.

Limiter Insertion: Single limiters of different designs have been inserted into both ZT-40M[15] and HBTX-1B,[5] with a significant difference in plasma response. In ZT-40M both the electron and ion temperatures remained constant with limiter insertion (up to 6 cm) whereas in HBTX-1B T_i increased from 300 to 400 eV for a 6 cm insertion depth while T_e fell from 300 to 200 eV. As a cross-check, the HBTX-1B paddle was therefore installed on ZT-40M at the same time as the NPA. The usual orientation was with the paddle face perpendicular to the major radius. Up to an insertion of 2.5 cm (relative to the local vacuum vessel wall), the location of the paddle was shadowed by poloidal ring limiters located at each side of the diagnostic section. Insertion experiments were performed at a nominal 120 kA plasma current.

The paddle perturbed the local plasma, causing the equilibrium there to shift away from the tile. An increase of 3-4x in the radial magnetic field at the midplane port in the paddle section, also indicates the plasma moved radially, locally. However the global equilibrium positions were not affected, while the poloidal gap positions were feedback controlled. Similarly, F and Θ, measured some 90° toroidally from the paddle location, showed no significant change.

The paddle edge surface temperature was determined using an infra-red camera. At a 7.5 cm insertion the edge reaches the graphite sublimation temperature after 2 ms. As a result, deuterium and impurities are released from the paddle, causing an increase in the line average electron density as measured at 3 ms for deep insertions. Concomitantly the electron temperature on axis (Thomson scattering) drops from 140 eV without the paddle to 80 eV. The ion temperature from Doppler broadening of CV drops from 140 to 120 eV, setting T_i^{CV}/T_e at unity for insertions to 10 cm and at about 1.4 at 15 cm insertion. Core ion temperatures estimated from the NPA and

TOF are higher, and remain near 200 eV for all insertion depths. Increasing loop voltage with limiter insertion, and the T_i/T_e ratios are shown in Figure 3. We note that insertion depths of greater than 9 cm exposed some of the stainless steel paddle support structure to the plasma, although the trends seen in Figure 3 are established before this is a potential problem.

Discussion: The quantity $(1-\eta_k/\eta_w)$, where η_k (η_w) is the global plasma resistivity determined from magnetic helicity (energy) balance respectively, indicates the fraction of ohmic input power absorbed by fluctuations in the discharge.[16] In principle, the power absorbed by fluctuations is available to drive the RFP dynamo and/or ion heating.[3] This quantity is a strong function of the plasma parameter Θ and, independently, of the rate of current rise as seen in Figure 4. The hot ion mode shots have $\Theta \simeq 1.7-1.8$ and a ramping rate of $14-19\ kA/ms$, with $(1-\eta_k/\eta_w) \simeq 0.4-0.5$ at 5 ms. The limiter insertion series of discharges had the lowest possible theta values (to scrape off as much of a field pitch length as possible), and the current was flat to within 2 kA/ms. These shots have $(1-\eta_k/\eta_w) \simeq 0.25$ for limiter insertions to 15 cm, and show weaker ion heating. The strong experimental correlation of $(1-\eta_k/\eta_w)$ with ion temperature is indicative of fluctuation-driven ion heating. The mechanism may be self-limited by large sawtoothing modes which appear for high values of Θ, causing periodic energy dumps to the wall.

Summary: A neutral particle analyzer (NPA) has been used on ZT-40M to measure the neutral deuterium spectra to an energy of 8 keV. The NPA has confirmed the existence of a hot ion population during deeply reversed ramped discharges. Preliminary neutral flux modelling is consistent with $\bar{n}_e = 2.2 \times 10^{19} m^{-3}$, $T_e(0) \sim 300-400$ eV, and a strongly peaked ion temperature profile, with $T_i(0) \sim 800-1100$ eV, though the neutron yield indicates a higher energy tail may be present. The extra ion heating is attributed to fluctuations driven in the plasma under deep reversal and/or current ramping conditions. With insertion of a paddle limiter into normal discharges, we confirm the HBTX result that $T_i(0)/T_e(0)$ increases with insertion depth, although apparently due to a decrease in T_e rather than an increase in T_i. Global energy confinement is degraded with limiter insertion, as is the electron energy confinement, while ion power balance details require further study.

This work is supported by the USDOE, PPC, UKAEA, and EURATOM.

[1]R. B. Howell and Y. Nagayama, Physics of Fluids **28**, 743 (1985).
[2]K. Ogawa, Y. Maejima, et. al., Nuclear Fusion **25**, 1295 (1985).
[3]P. G. Carolan, A. R. Field, et. al., in *14th European Conference on Controlled Fusion and Plasma Physics*, Vol. IID, p. 469 (European Physical Society, Madrid, 1987).
[4]G. A. Wurden, K. F. Schoenberg, et. al., in *International School of Plasma Physics, Course and Workshop on Physics of Mirrors, RFP's and Compact Tori* (Varenna, Italy, 1987).
[5]H. A. Bodin and the HBTX Team, *ibid.*
[6]P. G. Weber, Review of Scientific Instruments **54**, 1331 (1983).
[7]R. J. Bastasz and T. E. Cayton, Journal of Nuclear Materials **145-147**, 476 (1987).
[8]S. E. Walker, A. M. Preszler, and W. A. Millard, Review of Scientific Instruments **57**, 1740 (1986).
[9]C. A. Bunting, P. G. Carolan, and A. R. Field, Review of Scientific Instruments **56**, 1103 (1985).
[10]J. A. Phillips, D. A. Baker, et. al., LA-UR-87-3321, submitted to Nuclear Fusion.
[11]K. H. Burrell, Journal of Computational Physics **27**, 88 (1978)[modified by Bob Stockdale, GA].
[12]R. B. Howell, J. C. Ingraham, et. al., Physics of Fluids **30**, 1828 (1987).
[13]E. L. Jacobs, S. D. Bonaparte, and P. D. Thacher, Nuc. Instr. and Methods **213**, 387 (1983).
[14]G. Zankl, J. D. Strachan, et. al., Nuc. Instr. and Methods **185**, 321 (1981).
[15]J. C. Ingraham, Bulletin of the American Physical Society **32**, 1785 (1987).
[16]K. F. Schoenberg, R. W. Moses, Jr., and R. L. Hagenson, Physics of Fluids **27**, 1671 (1984).

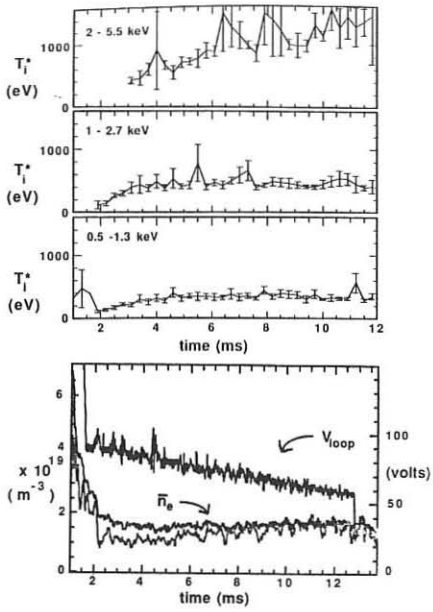

Figure 1: (a). NPA measurement of emitted neutral flux during deep reversal ramping shots. T_i^* from three energy ranges for the NPA. (b) Corresponding loop voltage, and two chords (+4 cm and +16 cm) of electron density.

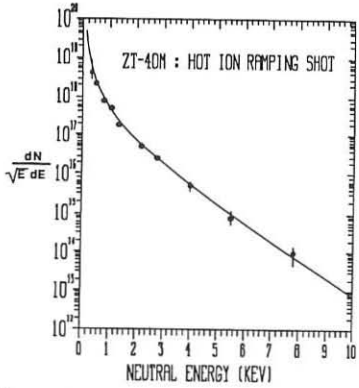

Figure 2: Composite NPA spectrum fitted by theoretical curve, using a peaked ion temperature profile. $T_i(0) = 1000$ eV.

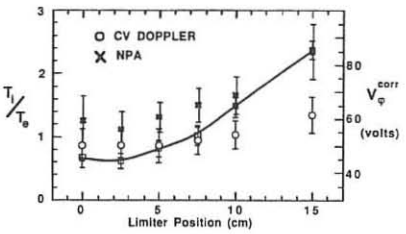

Figure 3: Loop voltage (solid curve) and T_i/T_e, vs. paddle limiter insertion depth, at 3 msec into 120 kA discharges. Error bars indicate standard deviation due to shot variation. T_i CV Doppler (o), and $T_i(0)$ NPA (x), are ratioed against $T_e(0)$ from Thomson scattering. The liner bellows are at 1.2 cm, and the fixed ring limiters are at 2.5 cm.

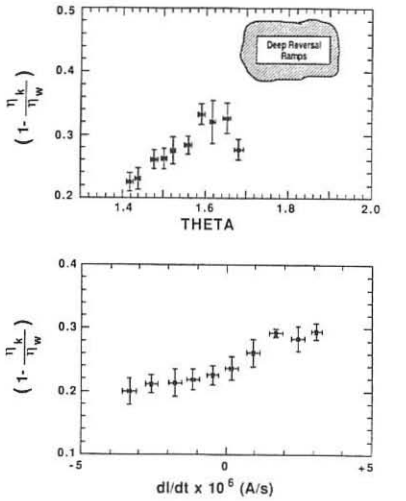

Figure 4: (a). $(1-\eta_k/\eta_w)$, the fraction of ohmic heating power absorbed by fluctuations in the discharge vs. Θ for dI/dt $<$ 500 A/ms, and (b), plotted vs dI/dt at constant $\Theta \simeq 1.4$, both for nominal 120 kA currents.

COMPARISON OF THE THEORY OF FLUCTUATION-DRIVEN DIFFUSION WITH EXPERIMENTAL OBSERVATIONS FROM HBTX

D E Evans and H Y W Tsui
Culham Laboratory, Abingdon, Oxon, OX14 3DB, UK
(UKAEA/Euratom Fusion Association)

INTRODUCTION Modified moment equations describing a steady state plasma in a reversed field pinch in which an outflow of plasma is balanced by an influx of neutrals subsequently ionized to become new plasma deep within the discharge have been derived [1]. Among the consequences of this analysis are that the outflow of plasma is driven by fluctuations in the fluid velocity and density. There is a drag force exerted on the fluid by the new particles, and the work done in overcoming this drag is directly associated with the mechanism whereby the dynamo provides non-Spitzer heating. Whereas the electrons continue to acquire energy Ohmically as well, ions have no source of heating apart from this if collisions are ignored. The particle recycling also causes loss of kinetic and thermal energy.

RADIAL PROFILES The equations of thermal energy balance that relate dynamo activity to ion temperature T_i, electron temperature T_e, plasma density n and the plasma source S for ions and electrons have the form,

$$n(\partial/\partial t + \underline{u}\cdot\nabla)\tfrac{3}{2}T = Q - p\,\nabla\cdot\underline{u} + \tfrac{1}{2}mu^2S - \tfrac{3}{2}TS \qquad \ldots.(1)$$

where Q, representing the gain in energy by collisions with members of the opposite particle species, is taken as zero for ions and ηj^2 for electrons. The quantity S is the number of new plasma particles $m^{-3}s^{-1}$, and the other symbols have their usual meanings.

Manipulation of this equation, recalling the axisymmetry of the mean variables and setting $\Gamma \equiv \underline{\Gamma}\cdot\nabla r$, produces an expression for the ions:

$$T_i\Gamma\left[\frac{3}{2}\frac{1}{T_i}\frac{\partial T_i}{\partial r} - \frac{1}{n_o}\frac{\partial n_o}{\partial r}\right] = \left(\tfrac{1}{2}m_i\langle\tilde{u}_i^2\rangle - \tfrac{3}{2}T_i\right)S \qquad \ldots.(2a)$$

and the for the electrons:

$$T_e\Gamma\left[\frac{3}{2}\frac{1}{T_e}\frac{\partial T_e}{\partial r} - \frac{1}{n_o}\frac{\partial n_o}{\partial r}\right] = \left(\eta + \tfrac{1}{2}\eta_t\right)j^2 - \tfrac{3}{2}T_eS \qquad \ldots.(2b)$$

from which temperature profiles could be deduced relative to that of the density $n_o(r)$. The quantity $\eta_t \equiv m_eS/(en)^2$ is an effective resistivity due to the requirement of replenishing the momentum constantly being lost by particle recycling.

Instead of calculating detailed profiles, we note that terms like $(1/T)\ (\partial T/\partial r) = -1/\Lambda_T(r)$ where $\Lambda_T(r)$ is an indication of the width of the T profile. The negative sign convention is adopted because in general T_e, T_i, and n have $\partial/\partial r < 0$. Accordingly, the foregoing equation can be rewritten, for ions:

$$\frac{\Lambda_{T_i} - \frac{3}{2}\Lambda_n}{\Lambda_{T_i}\Lambda_n} = \frac{3}{2}\frac{S}{\Gamma}\left[\frac{2}{3}\tilde{\epsilon}_i^2 - 1\right] \qquad \ldots(3a)$$

and for electrons

$$\frac{\Lambda_{T_e} - \frac{3}{2}\Lambda_n}{\Lambda_{T_e}\Lambda_n} = \frac{3}{2}\frac{S}{\Gamma}\left[\frac{2}{3}\left(1 + 2\eta/\eta_t\right)\epsilon_e^2 - 1\right] \qquad \ldots(3b)$$

where $\epsilon_e = u_{eo}/v_{e,th}$, the usual streaming parameter for electrons, and $\tilde{\epsilon}_i = |\tilde{u}_i|/v_{i,th}$ is the ion fluctuation streaming parameter, $|\tilde{u}_i|$ being the rms value of the fluctuation. In both cases, the denominators are the relevant thermal velocity.

In equations 3a and 3b, the term Γ is positive definite for positive S so the relative widths given by the terms on the left hand side are determined by the signs of the expression in square brackets on the right. For example, eq 3a indicates that, provided the level of fluid velocity fluctuations exceeds that of the ion thermal speed, the ion temperature profile is broader than that of the density. Since this is opposite to what is found in HBTX plasma [2], we may conclude that $|\tilde{u}_i| < \sqrt{(2T_i/m_i)}$ except near the axis.

NUMERICAL ESTIMATES On axis, symmetry considerations demand that the radial flux should vanish, i.e. $\Gamma = 0$, and eqs 3a and 3b thus provide an opportunity to deduce some numerical consequences of the model in a rather simple way. Thus on axis, eq 3a indicates that $2\,\tilde{\epsilon}_i^2/3 = 1$ or $|\tilde{u}_i| = \sqrt{(3/2)}\ v_{i,th}$. In HBTX, a typical axial value for T_i might be 200 eV [3], so on axis, $|\tilde{u}_i| \sim 1.7 \times 10^5\ ms^{-1}$. Armed with this number, and the knowledge from experiment of the amplitude of magnetic field fluctuations, at least at the plasma edge, namely $\sim 4 \times 10^{-3}$ tesla [4], and the strength of the dynamo on axis, $\sim 5\ Vm^{-1}$, one can compute a value for the degree of correlation $g = |\underline{\tilde{u}}\times\underline{\tilde{B}}|/|\tilde{u}||\tilde{B}|$ one might expect to measure between velocity and magnetic field fluctuations on axis. The result is only about 1%. This degree of correlation is readily achievable and may account for the apparent insensitivity to initial conditions observed when an RFP is set up. Since the axial dynamo activity increases with the loop voltage V_ϕ and $T_i(0) = m_i\langle\tilde{u}_i^2\rangle/3$, the ion temperature on axis increases with V_ϕ. This is consistent with the observations in the tile insertion experiment in HBTX [5].

One may likewise deduce the degree of correlation needed between the velocity fluctuations and those of density to account for the observed diffusion rate. Suppose $|\tilde{n}| = f\, n_o$ where $f \leq 1$ and g is the correlation coefficient. Then $\Gamma \sim n_o D/a \sim g|\tilde{n}||\tilde{u}|$ or $gfn_o|\tilde{u}|$. So $(gf) \sim D/(a|\tilde{u}|)$. Taking 0.25m for the plasma radius and the experimental value of $D \sim 100$ m^2s^{-1} [6] gives $(gf) \sim 2 \times 10^{-3}$. Thus, if density fluctuations are 10%, the coefficient of correlation between $\tilde{n}$ and $\tilde{u}$ has to be only 2%.

From the on-axis result of eq 3b together with quantities known from measurement in HBTX, estimates of η_t/η, S and the diffusion coefficient D may be constructed. On axis equation 3b reduces to

$$\frac{2}{3}\,(1 + 2\eta/\eta_t)\epsilon_e^2 = 1 \qquad \ldots(4)$$

Assuming the current density on axis, $j_\phi(0) \sim 4\bar{j}_\phi \sim 4 \times 10^6$ Am^{-2} for 200 kA toroidal current, and using $T_e(0) \sim 200$ eV, we find $\eta_t/\eta \sim 0.03$. Hence, in these normal conditions, η_t is negligible compared to η.

The new resistivity η_t does become important in low density discharges. In HBTX1B, the characteristic low density discharge had $I_\phi = 80$ kA and $T_e(0) = 800$ eV, which produced a high electron energy confinement time. The significance of η_t in this regime is revealed using eq 4 in the following table in which $j_\phi(0)/\bar{j}_\phi \sim 4$ as estimated from F and Θ values.

TABLE

n (m^{-3})	1×10^{19}	1×10^{18}	8×10^{17}	6×10^{17}	5×10^{17}
ϵ_e	0.06	0.59	0.74	0.98	1.18
η_t/η	0.004	0.6	1.2	2.6	25

It can be seen that when $n \leq 1\times10^{18}$ m^{-3}, η_t becomes more prominent than the conventional Spitzer resistivity. Moreover, it is seen to increase steeply with the streaming parameter, ϵ_e, and so may be expected to discourage runaways. In fact, the particle recycling imposes a limiting value of $\sqrt{(3/2)}$ upon the electron streaming parameter.

Knowing the experimentally determined value for resistivity on the axis, $\eta(0) = 0.28 \times 10^{-6}$ Ωm for $T_e(0) = 200$ eV under normal conditions, allows us to calculate the source strength S through the definition of η_t. We find for these rather typical HBTX conditions $S \sim 10^{23}$ $m^{-3}s^{-1}$. This produces the numerical estimate $D = 155$ m^2s^{-1} which compares very favourably with the measured value quoted above.

CONCLUSIONS Predictions from moment equations modified to take account of fluctuation-induced outward-directed plasma flux and a compensating plasma source deep within the discharge have been compared with experimental observations from HBTX plasmas. Under typical HBTX conditions, the ratio of the source-induced resistivity to the Spitzer one is, $\eta_t/\eta < 0.03$, but an achievable reduction in density might increase η_t so as to dominate the resistivity and influence the plasma behaviour, in particular, in such a way as to discourage runaways, and impose a limiting value on the electron streaming parameter.

The relative widths of the radial profiles of $T_e(r)$, $T_i(r)$ and $n_o(r)$ are determined by the source S. Using the known profile ordering in HBTX the rms value of the fluid velocity fluctuations is shown to be less than the ion thermal speed everywhere but near the axis, where $|\tilde{u}_i| = \sqrt{(3/2)}$ $v_{i,th} \sim 1.7 \times 10^5$ ms^{-1} for $T_i(0) = 200$ eV. This number together with the known $|\tilde{B}|$ allows the degree of correlation between the $\tilde{u}$ and $\tilde{B}$ in the axial dynamo to be computed. The result is that only 1% correlation is required. The degree of correlation between $\tilde{n}$ and $\tilde{u}$ needed for the particle flux is found to be 2% for 10% density fluctuations.

Under typical HBTX condition, the value of the source strength $S \sim 10^{23}$ m^{-3}s^{-1} corresponding to a diffusion coefficient $D \sim 155$ m^{2}s^{-1} is in favourable agreement with spectroscopic measurement.

REFERENCES

[1] H Y W Tsui and D E Evans: this conference
[2] P G Carolan, A R Field, A Lazaros, M G Rusbridge, H Y W Tsui, M K Bevir: in Contr. Fus. and Plasma Physics (Proc. 14th Eur. Conf., Madrid, Spain, 1987) Vol 11D Pt.II 469
[3] B Alper et al: in Plasma Physics and Contr. Nuc. Fus. Research (Proc. 11th IAEA, Kyoto, Japan, 1986) Vol II 399 (1987)
[4] H Y W Tsui, J Cunnane, and D E Evans: in Contr. Fus. and Plasma Physics (Proc. 14th Eur. Conf, Madrid, Spain 1987) Vol 11D Pt.II 511
[5] H A B Bodin and the HBTX team: Int. School of Plasma Physics, Varenna (1987) Vol I 307
[6] P G Carolan, C A Bunting, A M Manley, A Patel: in Contr. Fus. and Plasma Physics (Proc. of the 14th Eur. Conf., Madrid, Spain, 1987) Vol 11D Pt.II 515

ANALYSIS OF LINER CURRENT DISTRIBUTION AND INDUCED ERROR FIELD IN RFP DEVICE

Shunjiro Shinohara

Department of Physics, Faculty of Science, University of Tokyo, 7-3-1 Hongo, Bunkyo-ku, Tokyo 113, Japan

INTRODUCTION

Recently, Reversed Field Pinch (RFP) devices have produced experimental results indicating a favorable increase in plasma parameters with an increase in the plasma current. However, the field errors degrade the plasma and must be minimized in order to get the better plasma performance. Here, we calculate the liner current in the port section analytically and discuss it from a view point of the error fields.

ANALYTICAL SOLUTION

For simplicity, we assume a plane geometry of the liner with the circular or elliptical ports. From the fluid mechanics with two dimensional geometry without the vorticity and compressibility, the outer solution of the uniform flow in the presence of a circular cylinder is $f=U(Z+R^2/Z)$, where $f=\Phi+i\Psi$ (Φ: velocity potential, Ψ: stream function) is a complex velocity potential, U is a constant flow velocity, $Z=x+iy$ is a two dimensional position and R is a radius. Here, Ψ, Φ, $\nabla\Phi$ and U correspond to the electric flux function, electrostatic potential ϕ, electric field $-\vec{E}$ and constant applied electric field $-E_0$ (x direction), respectively. The current density $\vec{j}$ is expressed as $\vec{E}/\eta$ (η: resistivity) on the liner. In the hole (vacuum) region ($\vec{E}\neq\vec{0}$ and $\vec{j}=\vec{0}$), $f=2UZ$ is derived from $\Delta f=0$ and a continuity condition of the tangential electric field at the boundary (liner-vacuum interface).

Utilizing the Joukowski transformation of $Z=\zeta+a^2/\zeta$, ($a=$constant$<R$) and flow angle α with respect to the horizontal axis of x, we have the following equations on the liner and in the vacuum region, respectively, for an elliptical port.

$$f = U\left(e^{-i\alpha}\,\zeta + R^2\, e^{i\alpha} / \zeta \right), \tag{1}$$

$$f = 2\,U\, e^{-i\alpha}\,\frac{Z - i\,(a/R)^2\,\bar{Z}}{1-(a/R)^4}\,. \tag{2}$$

Here, $\bar{Z}$ is a complex conjugate of Z, and an elongation of the ellipse κ is $(R^2+a^2)/(R^2-a^2)$ (≥ 1). Note that values of Ψ and E_n (normal component) are not continuous across the boundary, although Φ value is continuous.

LINER CURRENT AND ELECTRIC FIELD DISTRIBUTIONS

First, a circular port is considered. Figure 1(a) shows the contours of Ψ, which shows the electric field and current flowing (on the liner) directions, when the constant E_0 (x direction) is applied. In Fig.1(b), the contours of Φ are shown. The electric field $\vec{E}=-\nabla\phi$ becomes smaller near the circular surface of $y=0$, and is constant of $E_{in}=2E_0$ in the vacuum region. Figure 1(c) shows the contours of $|j/j_0|$, where j_0 is a constant value at the infinite distance away

from the port. The distortion of the current density distribution near the port is evident; the value of $|j/j_0|$ has the maximum value of 2 at the top and bottom tips of the port and zero at the port surface on the midplane.

Next, an elliptical port with $\kappa=2.7$ is considered, as this shape is similar to the side port, 19cm high and 7cm wide, in the REPUTE-1 device [1]. Figure 2(a), (b) and (c) show the contours of Ψ, Φ and $|j/j_0|$, respectively, in the presence of E_0 (x direction), which is parallel to the minor axis of the ellipse. At the top and bottom tips of the port, $|j/j_0|$ has the maximum of $1+\kappa=3.7$, and E_{in} is constant of $(1+\kappa)E_0=3.7E_0$.

Contrary to the Fig.2 case, the current disturbance and the maximum current density are smaller when the electric field is along the major axis of the ellipse; both the maximum value of $|j/j_0|$ and E_{in}/E_0 are $1+(1/\kappa)=1.37$. In summary, $|j_{max}/j_0|$ and $|E_{in}/E_0|$ increase rapidly as $1+\kappa$ and decrease slowly as $1+(1/\kappa)$ in the presence of electric fields, which are parallel to the minor and major semi axes, respectively.

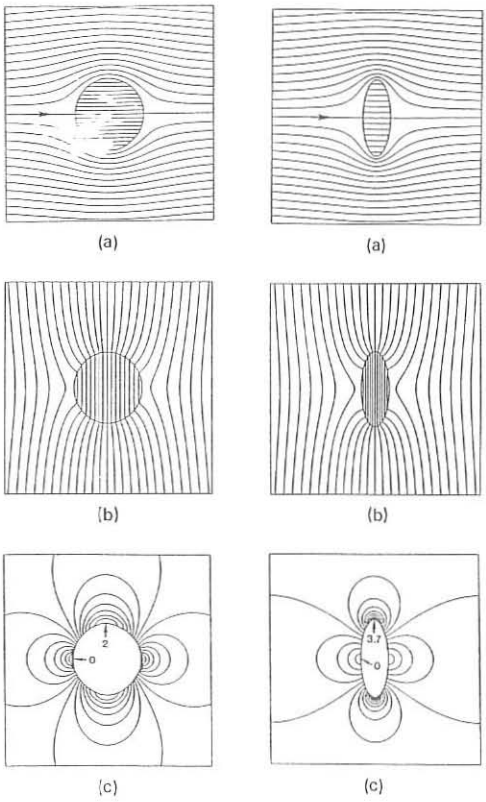

Fig. 1 Contours of Ψ(a), Φ(b) and $|j/j_0|$(c) for a circular port.

Fig. 2 Contours of Ψ(a), Φ(b) and $|j/j_0|$(c) for an elliptical port.

The disturbed region of the current density extends to an order of one port size ($|j/j_0|$ is ~ 1 at the outer region). In the REPUTE-1, the liner current distribution in the port section is not affected by the presence of the neighboured port, because the toroidal distance between the port sections is 36cm.

ERROR MAGNETIC FIELD DISTRIBUTION

Using the analytical liner current, the induced error magnetic fields are computed from the Biot Savart's formula. Figure 3 shows the contours of the magnetic fields on the $z=1$ plane for a circular port ($z=0$, $R=1$). Here, the z axis is taken perpendicular to the (x, y) plane. From this figure, $|B_x|$ has the maximum near the port edge on $y=\pm x$, B_y has the maximum on $(0,\approx 3)$ and the minimum on (0,0), and $|B_z|$ has the maximum near the port edge on $x=0$.

With the increase in the z direction, the value of y to have the maximum B_y increases rapidly, whereas the positions to have the maximum $|B_x|$ and $|B_z|$ depart from the port edge to the outer side slightly. Figure 4 shows the contours of the magnetic fields on the $z=1$ plane for an elliptical port ($z=0$). Here, κ is 2.7 (minor and major semi axis lengths are 0.4 and 1.08, respectively). The similar results with the circular port are found.

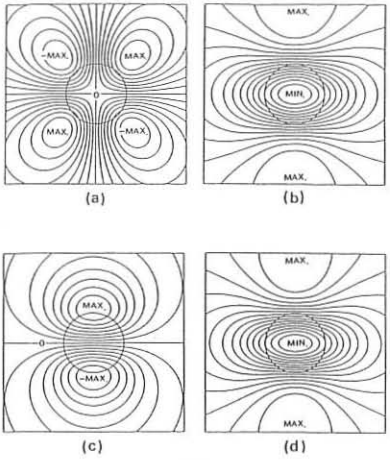

Fig. 3 Contours of B_x(a), B_y(b), B_z(c) and $|B|$(d) on $z=1$ plane for a circular port.

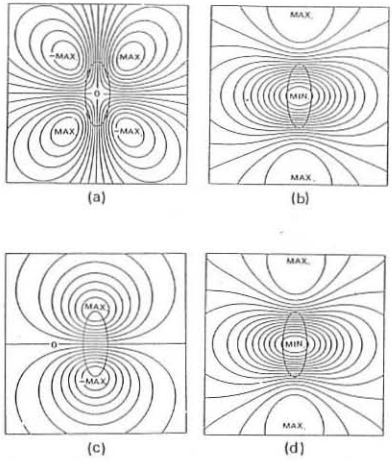

Fig. 4 Contours of B_x(a), B_y(b), B_z(c) and $|B|$(d) on $z=1$ plane for an elliptical port.

The e-folding length of the magnetic fields in the z direction is considered. Figure 5 shows the relation between the magnetic fields and the position Z^* (normalized by a port radius) in the z direction for a circular port ($j_0=1$A/m). The important error field considered experimentally is the B_z field, which is equivalent to the radial field for the cylindrical geometry. Near the port $|B_z|$ has the maximum of about 10^{-2} Gauss and the e-folding length is about 0.3. Without a port hole, $|B_y|$ has a constant value of $B_{y0}=\mu_0 j_0/2$ for the plane case regardless of the position, while, for the cylindrical case without a hole, B_y (poloidal field) is zero within the cylinder when the surface current flows along the central axis. Therefore, $\delta B_y=B_y-B_{y0}$ is equivalent to the inner poloidal field for the case of the cylinder with a port hole. From Fig.5, we can see δB_y has the maximum near the port (about a half of the maximum $|B_z|$ value) and B_y approaches to $\mu_0 j_0/2$ as z increases.

In Fig.6, the relation between the magnetic fields and the position Z^* (normalized by a major semi axis length) is shown for an elliptical port ($j_0=1$A/m). The same trend with the circular port is found; the absolute value of B_z near the port and the e-folding length of B_z are larger and smaller by about 20%, respectively, than those with the circular port. When the current flows along the major axis for an elliptical port, the induced error fields are smaller; the B_z value is reduced to about half of it for the elliptical port with

the current flowing along the minor axis, and the e-folding length normalized by the major semi axis length is ≈ 0.25.

Now we apply the numerical results to the REPUTE-1 device. For the case that the plasma current $I_p = 200$kA and loop voltage $V_l = 150$V, j_0 becomes 17kA/m as the toroidal resistance of the liner (minor radius is 22cm) is 6.5mΩ. Then, B_z, *i.e.*, the radial field B_r, is estimated to be 180 Gauss near the port, which is 10% of the poloidal field generated by the plasma current. In order to reduce the error field, an increase in the liner resistance and a decrease in the plasma resistance are necessary. Reducing the port size does not decrease the maximum error field near the port as long as j_0 is not changed, although the region of having the large error field diminishes.

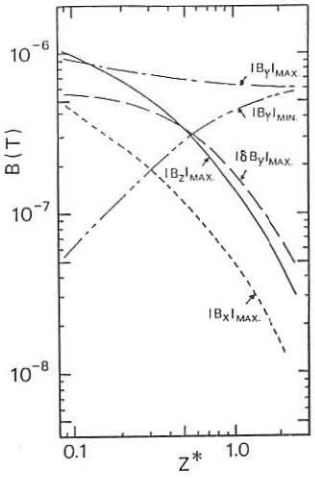

Fig. 5 Dependence of magnetic fields on Z^* for a circular port.

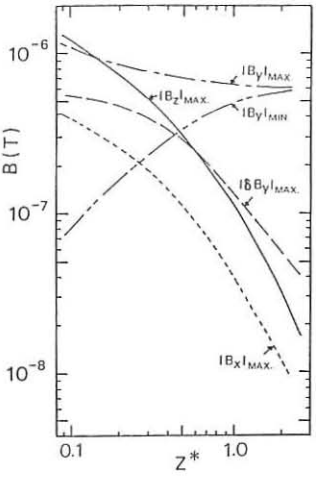

Fig. 6 Dependence of magnetic fields on Z^* for an elliptical port.

CONCLUSION

The liner current and electric field distributions near the port for the circular and elliptical cross sections are solved analytically in the plane geometry. The $|j/j_0|$ values become the maxima of $1+\kappa$ and $1+(1/\kappa)$ near the tips of the major and minor semi axes, respectively, which are perpendicular to the E_0 direction, and zero at the tips of the other semi axes. The disturbance in the current density distribution extends to about one port size.

The dominant error field is a B_z one, which has the maximum value near the point of the maximum current density (port edge). The e-folding length (z direction) of B_z is about 0.25-0.3 normalized by a characteristic radius of the port. However, the maximum value does not change with the port size as long as j_0 is not changed.

REFERENCE

[1] N. Asakura *et al.*, *Proc. 11th Int. Conf. on Plasma Phys. and Contr. Nucl. Fus. Res.* (Kyoto, 1986) **2** (1987) 433.

FLUCTUATION MEASUREMENTS IN EDGE PLASMA OF THE REPUTE-1 REVERSED FIELD PINCH

H. Ji, S. Matsuzuka, A. Fujisawa, S. Shinohara,
K. Yamagishi, H. Toyama and K.Miyamoto

Department of Physics, Faculty of Science, University of Tokyo,
7-3-1 Hongo, Bunkyo-ku, Tokyo 113, Japan

Introduction

Recently edge plasma phenomena have been a great interest in the toroidal plasmas, as it is thought to play an important role in the confinement of the main plasma. Plasma fluctuations and turbulence are considered as a possible mechanism for anomalous transport in the tokamaks. RFP configuration has a reversal surface of the toroidal magnetic field near the edge region. A lot of the rational surfaces exist near the reversal surface, consequently fluctuations or turbulence are expected to have a high level compared to tokamaks in the edge region. In this paper we describe the results of fluctuation measurements using Langmuir probes and magnetic probes in the edge plasma of the REPUTE-1 RFP, which has a major radius of 82 cm and a minor radius of 22 cm [1].

Measuring system

A square array of four single Langmuir probes (5 mm separation between adjacent probes) is used to measure the plasma density and the floating potential at the edge plasma. The ion saturation current is measured with the bias voltage of typically 50 V between two single probes, and floating potential of the plasma is measured using the unbiasing single probe which is connected to the vacuum chamber with an 1MΩ resister. The magnetic fluctuations are measured by a pair of magnetic probes (8 mm separation), each of which can pick up three components of the fields and their fluctuations with a good frequency response up to 250 kHz.

Properties of Edge Plasma

Parameters of typical discharge in our experiments are as follows: the plasma current $I_p \sim 150$ kA, the loop voltage $V_l \sim 200$ V, the pinch parameter $\Theta \sim 2.0$, the reversal ratio $F \sim -0.4$, and the chord-averaged electron density $\bar{n}_e \sim 3 \times 10^{13} \mathrm{cm}^{-3}$. The time derivative of the toroidal fields B_t , the poloidal fields B_p, the radial fields B_r, and the ion saturation current I_{sat} measured at the edge region ($r \sim$ 19cm), are shown in Fig.1. Magnetic fluctuations are 3−4% of the total field amplitude, and the toroidal component fluctuations predominate by 2−3 times over those of the poloidal or radial component: $|\tilde{B}_t/B|_{rms} = 2-4\%$, $|\tilde{B}_p/B|_{rms} \sim |\tilde{B}_r/B|_{rms} = 1-2\%$ Density fluctuations are found to be typically 10%−30%, estimated from I_{sat} assuming the fluctuations of electron temperature are negligible.

Radial profiles of I_{sat} , floating potential V_f, B_t , B_p and their fluctuations measured with a shot-to-shot radial scan of the probes, are shown in Fig.2. In the reversal region of the toroidal field ($r \sim$ 17cm), (1) I_{sat} has a steep gradient, (2) V_f has the minimum value, (3) fluctuation levels of B_t, B_p, I_{sat}, and V_f are higher than those in the other regions.

Fluctuation Spectra

Power spectra of frequency are obtained for $\tilde{n}$, $\tilde{\phi}$, $\tilde{B}_t$, $\tilde{B}_p$ and $\tilde{B}_r$ near the reversal region ($r\sim18$ cm), shown in Fig.3. No coherent modes are observed in either spectrum, showing broad spectral properties, and spectral indexes for frequency $p=1.4-3.7$ are obtained.

Wavenumber spectra of fluctuations are obtained using a technique introduced by Beall et al. [2]. The results are shown in Fig.4(a) for k_x (toroidal direction) and in Fig.4(b) for k_y (poloidal direction). Asymmetry of spectra in plus and minus direction of k_x or k_y is not observed. As in the case of frequency spectra, no coherent modes are observed in the wavenumber spectra. Spectral indexes for wavenumber q are in the range of $1.7-3.6$ for k_x and $2.3-4.6$ for k_y. In each case of the density, potential and magnetic fluctuations, the wavenumber spectra in toroidal direction are broader than those in poloidal direction, which mean that the fluctuations have longer correlation length along the field line than across the field line. Calculations from the wavenumber spectra show typical correlation length along the field line are about 2 times of that acorss the field line. This result is similar to that in the tokamak measurements [3].

Confinement and Fluctuations

Fluctuations are classified to electrostatic and electromagnetic ones. Heat flux caused by electrostatic fluctuations is proportional to $<\tilde{p}\tilde{E}>/B$ or $T<\tilde{n}\tilde{E}>/B$ if the temperature fluctuations $\tilde{T}$ are negligible. Phase difference and coherence between $\tilde{n}$ and $\tilde{\phi}$ are measured at the edge plasma of REPUTE-1, which are shown in Fig.5. Phase difference between $\tilde{n}$ and $\tilde{\phi}$ is found about π throughout the frequency range. Consequently, almost no heat flux is induced by the electrostatic fluctuations, which is contrast to results in tokamaks [3].

A collisionless model proposed by Rechester et al. [4] , which gives an estimation of heat transport caused by electromagnetic fluctuations, is considered to be appropriate for RFPs. Heat and particle transport are considered to be induced by stochastic magnetic fields, which are produced by overlappings of different islands resulting from several helical modes as in the reversal region of RFPs. This model gives an effective perpendicular energy diffusivity $\chi_e\sim\pi R v_e|\tilde{B}_r/B|^2$ [4], where v_e is the electron thermal speed. Taking $T_e\sim100$ eV, $|\tilde{B}_r/B|\sim2\%$ in our case, the energy confinement time τ_E is estimated to be $\sim85\mu$s, assuming that the whole of the plasma experiences this stochastic diffusion. This value is consistent with the estimation of $\tau_E\sim60\mu$s from the energy balance, assuming $T_i=T_e\sim100$ eV and the radiation loss power is 70% of ohmic input.

Conclusion

Radial profiles, frequency and wavenumber spectra of $\tilde{B}_t$, $\tilde{B}_p$, $\tilde{B}_r$, $\tilde{n}$ and $\tilde{\phi}$ are measured by Langmuir probes and magnetic probes in the edge plasma of the REPUTE-1 RFP. Fluctuations have relative levels of 1-4% for the magnetic fields and 10-30% for the density. In the reversal region of B_t, it is found that fluctuation levels are higher than those in other regions, corresponding to localized existence of the rational surfaces. No coherent modes are observed in either frequency spectra or wavenumber spectra, spectra indexes $p\sim1.4-3.7$, $q\sim1.4-3.7$ for k_x and $q\sim2.3-4.6$ for k_y are obtained. The typical correlation length of fluctuations along the field line is about 2 times of that acorss the field

line. Almost no heat flux due to electrostatic fluctuations is observed, and energy confinement time estimated from energy diffusion induced by stochastic fields are found to be consistent with experimental parameters, which suggests that confinement of RFPs is determined by a high level of magnetic fluctuations.

Reference

[1] N. Asakura et al., Plasma Phys. **28** (1985) 805.
[2] J.M. Beall et al., J. Appl. Phys. **53** (1982) 3933.
[3] S.J. Levinson et al., Nucl. Fusion **24** (1984) 527.
[4] A.B. Rechester et al., Phys. Rev. Lett. **40** (1978) 38.

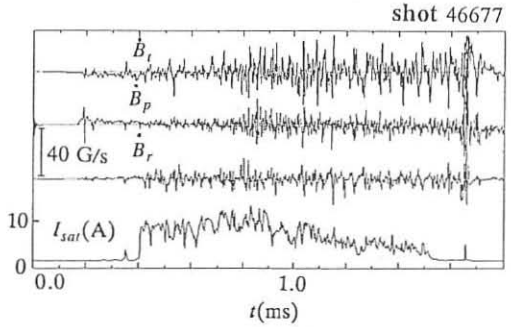

Fig. 1 Waveforms of $\dot{B}_t$, $\dot{B}_p$, $\dot{B}_r$ and I_{sat} at edge.

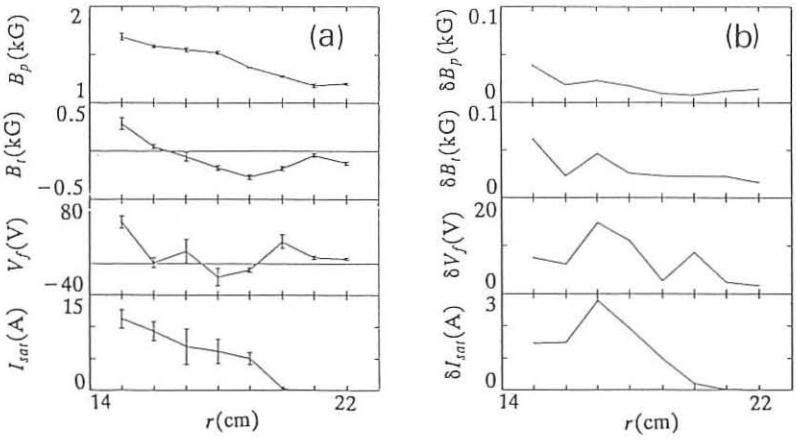

Fig. 2 Radial profiles of B_p, B_t, V_f and I_{sat} (a) and their fluctuations (b) in edge region. Here error bar indicate the fluctuation level.

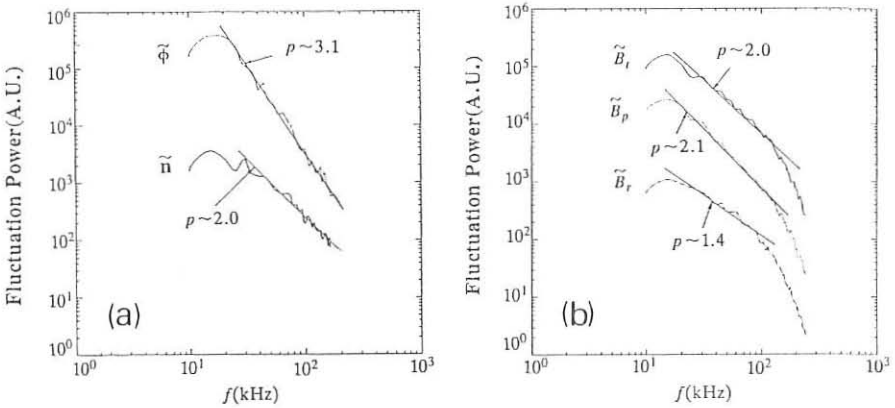

Fig. 3 Power spectra of frequency for $\tilde{n}$, $\tilde{\phi}$ (a) and for $\tilde{B}_t$, $\tilde{B}_p$ and $\tilde{B}_r$ (b).

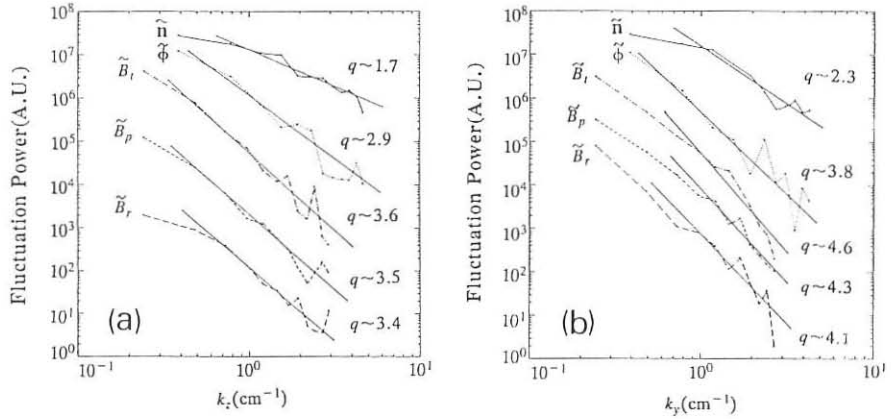

Fig. 4 Power spectra of wavenumber for $\tilde{n}$, $\tilde{\phi}$, $\tilde{B}_t$, $\tilde{B}_p$ and $\tilde{B}_r$ in the toroidal direction (a) and in the poloidal direction (b).

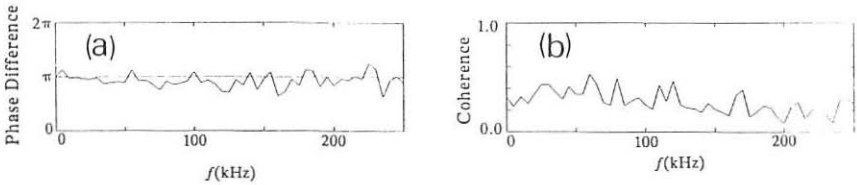

Fig. 5 Phase difference (a) and coherence (b) between $\tilde{n}$ and $\tilde{\phi}$.

ION TEMPERATURE MEASUREMENTS OF REPUTE-1 RFP

A. Fujisawa, Y. Nagayama, K. Yamagishi,
H. Toyama and K. Miyamoto

Department of Physics, Faculty of Science, University of Tokyo
Hongo 7-3-1, Bunkyo-ku, Tokyo 113, Japan

Introduction

REPUTE-1 is one of RFP device, which has a major radius of 82cm, and a minor radius of 22cm[1]. Various improvements have been performed with carbonization, matching the vertical coil waveform with the plasma current. It is observed that the ion temperature is extremely high in the discharges after "thorough wall conditioning", which implies the wall condition after a few hundred normal discharges with several times carbonization. In this paper we report the experimental results about both ion temperatures after and before "the thorough wall conditioning", which we call "the wall conditioning".

Spectroscopic Systems

An 1m visible spectrometer is used for Doppler broadening measurements. The observable wavelength of this spectrometer is from 200nm to 300nm. The cylindrical lens is set at the exit focal plane, and magnifies the entrance slit image on the surface of 8-ch photomultipliers.The instrumental width of each channel and the separation between channels are both 0.015nm in the range of 200nm to 300nm, when the second diffraction is used. The optical system has an movable mirror which allows the observed position of the plasma to be changed. The impurity lines observed with this spectrometer are mostly those of light impurities, such as oxygen and carbon. The ion temperatures are measured using impurity lines, mainly CIII(229.6nm), CV(227.1nm), and OV(278.1nm). Figure 2 shows time evolutions of carbon and oxygen lines in the typical discharges, where the plasma parameters are as follows; the plasma current is 250kA at the flat top, the loop voltage is 180V, and F, Θ are -0.4, 2.0, respectively(Fig. 1).

Ion Temperatures Before and After "the Wall Conditioning"

Before "the wall conditioning", the ion temperature T_i was measured mainly from Doppler broadening of OV(278.1nm). This is because CV(227.1nm) had weak intensity at the current flat top. In fig. 3, the ion temperature at the current flat top is indicated as a function of the line-averaged electron density $\bar{n}_e$, which is measured by CO_2 interferometer. It is apparent from this figure that the ion temperature increases with the decrease of the electron density.

Statistical analysis gives the following scaling of ion temperature;

$$T_i = 2.0 \frac{\sqrt{I_p}}{\bar{n}_e},$$

where T_i is in eV units, I_p in kA, and $\bar{n}_e$ in $10^{20}\mathrm{m}^{-3}$, and the above parameter ranges are following; I_p, n_e are from 100kA to 250kA, from $0.1\times10^{20}\mathrm{m}^{-3}$ to $2.7\times10^{20}\mathrm{m}^{-3}$[1]. In this analysis the partial correlation coefficient between T_i and $\bar{n}_e$ is absolutely larger than that between T_i and I_p. Therefore, the ion temperature has the essential dependence on the electron density.

After "the wall conditioning", CV(227.1nm) has been observed with the strong intensity, and "pump-out" phenomena have been reduced in lower density discharges; the line-averaged electron density are often maintained to about $1.0\times10^{20}\mathrm{m}^{-3}$ when the peak electron density is $1.2\times10^{20}\mathrm{m}^{-3}$. The dependence of the ion temperature at the current flat top on the electron density is shown in fig. 4. The plasma currents of these data are about 250kA. In this figure open circles and closed circles correspond to the ion temperature from CV and OV, respectively. This figure also shows the increase of the ion temperature with the decrease of the electron density. In low density discharges about $0.2\times10^{20}\mathrm{m}^{-3}$, the ion temperature from CV is above 700eV. The ion temperature from CV is a few times higher than that from OV in lower density discharges ($<1.0\times10^{20}\mathrm{m}^{-3}$), while in higher density discharges ($>1.0\times10^{20}\mathrm{m}^{-3}$) both temperatures are nearly same. Figure 5 shows both time evolutions of ion temperature from CV(227.1nm), and OV(278.1nm) in lower density discharges. In lower density discharge the ion temperature from CIII(229.6nm) is about 90eV, which almost agrees with that from OV. Therefore, the position of OV is more close to the plasma edge in lower density discharge, and the ion temperature from CV reflects at the plasma center.

Comparison with Condutivity Electron Temperature

In this section we compare the ion temperature with the conductivity electron temperature. The electron temperature has been estimated from the plasma resistance through the Spitzer's formula. Assuming that Z_{eff}, and the geometrical factor are 2 and 8, respectively, the conductivity temperature at the current flat top is written as

$$T_{e0}^{\sigma}(eV) = 70\left(\frac{I_p}{V_l}\right)^{2/3},$$

where I_p is in kA units. From this formula the electron temperature in REPUTE-1 RFP is about 100eV in the optimum discharges both before and after "the wall conditioning". After "the wall conditioning" the ion temperature is higher than the conductivity temperature in electron density below $1.0\times10^{20}\mathrm{m}^{-3}$, while this phenomena are found in the electron density below $0.5\times10^{20}\mathrm{m}^{-3}$ before "the wall conditioning".

The ion temperatures are plotted versus the drift parameter in Fig. 6. Here, the drift parameter is defined as

$$\xi = \frac{v_{dr}}{v_{th}} = \frac{I_p}{\pi a^2 \bar{n}_e e}\left(\frac{m_e}{3k_B T_{e0}^{\sigma}}\right)^{0.5}.$$

Note that according to this definition the drift parameter is not local, but global. The fig. 6 shows that the ion temperature is higher than the conductivity temperature when the drift parameter is larger than 0.025. The relation between MHD activity and this extremely high ion temperature is being studied in REPUTE-1 RFP.

Conclusion

The ion temperature of REPUTE-1 RFP from the Doppler broadening of CV(227.1nm) is above 700 eV. This results from "thorough wall conditioning". In REPUTE-1 RFP the ion temperature is higher than the conductivity temperature when the drift parameter ξ is larger than 0.025, or in lower density discharges($<1.0\times10^{20}\mathrm{m}^{-3}$) before "thorough wall conditioning".

REFERENCE

[1] N. Asakura *et al.,Proc. 11th Int. Conf. on plasma Phys. and Contr. Nucl. Fus. Res.* (Kyoto, 1986)**2**(1987)433.

[2] R.B. Howell and Y.Nagayama, Phys. Fluids **19**(1985)743

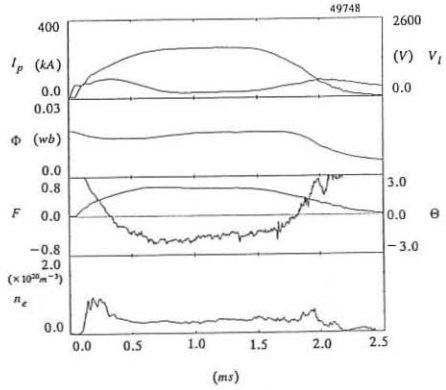

Fig.1. The time evolution of typical discharge in REPUTE-1 RFP.

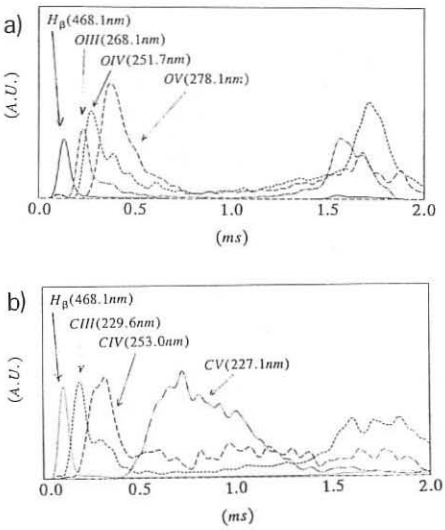

Fig.2. The time evolutions of oxygen lines(a), and carbon lines(b) in typical discharges.

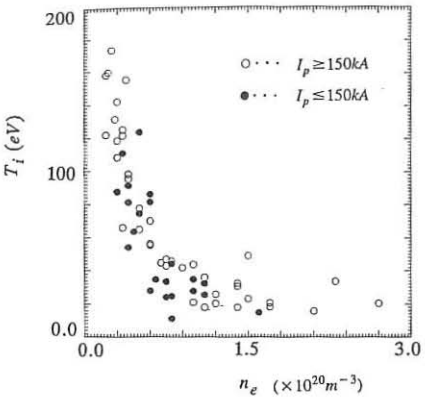

Fig.3. The dependence of the ion temperature on the electron density before "thorough wall conditioning".

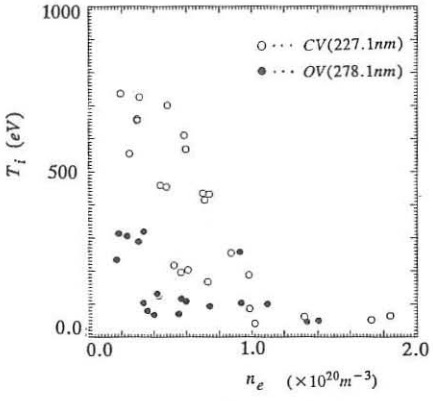

Fig.4. The dependence of the ion temperature on the electron density after "thorough wall conditioning".

Fig.5. Time evolution of ion temperature measured from Doppler broadening of OV, and CV.

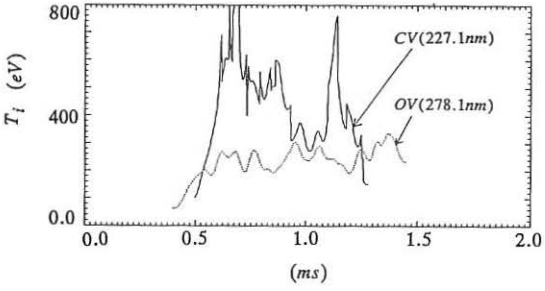

FIg.6. The ratio of the ion temperature to the conductivity electron temperature as a function of the drift parameter.

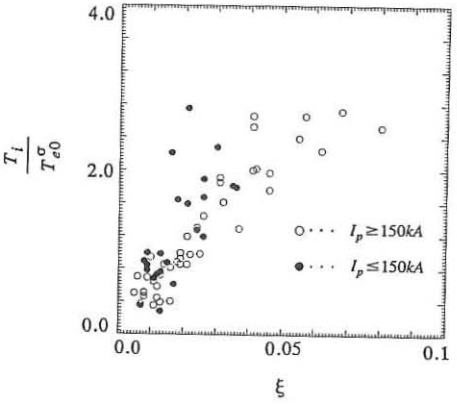

RECENT RESULTS FROM THE ETA-BETA II RFP EXPERIMENT

Antoni V., Bagatin M., Baseggio E., Bassan M., Buffa A., Carraro L., Costa S., Flor G., Giudicotti L., Innocente P., Martin P., Martini S., Noonan P.G.**, Ortolani S., Paccagnella R., Puiatti M.E., Sass B.*, Scarin P., Sorensen H.*, Valisa M., Villoresi P.,Weisberg K.*, Zago S.

Istituto Gas Ionizzati del C.N.R.
ENEA-EURATOM-CNR Association
Padova, Italy

The injection of pellets with mass of $\approx 10^{20}$ deuterium atoms and velocities of $\approx$ 100 m/s results in high density ($\approx 10^{20}$ m^{-3}) sustained discharges. Three examples of the line average density time behaviour are shown in fig. 1. In this type of discharges the values of β are sustained in time at about $\beta_{\theta e} \geq 6\%$ and the resistivity remains low and close to classical throughout the pulse. This is in contrast to the generally lower β and higher resistivity values associated with the lower density discharges [1].

Multichord interferometry and multipoint Thomson scattering have been used to gain insight in the density and temperature profiles time evolution during pellet injection. Figures 2 and 3 show respectively examples of the density profiles obtained by Abel inverting the interferometer data, and of the temperature profiles averaged over many discharges. In most of the discharges, at later stages the density profile is hollow. However discharges with pellet performed after low density shots show flat or peaked density profiles suggesting that in addition to the pellet ablation, gas influx and recycling under different gas wall loading conditions may play an important role in determining the density profiles. To illustrate this point, in Fig. 4a and b are drawn the profiles for two subsequent shots performed after low density discharges.

* Riso National Laboratory, Denmark
** Culham Laboratory, U.K.

In order to discriminate among the various phenomena determining the time behaviour of the average density a simple O-D model has been used to simulate the plasma density and power balance. First, discharges without pellet injection have been considered and, with particle confinement times of about 50 μs, a recycling coefficient $R \equiv 0.9$ is necessary to simulate the measured time behaviour. Assuming the same particle confinement times and wall recycling, the measured time dependance of the density for discharges with pellet injection corresponds to pellet ablation times of typically 0.5 ms. This simulation should be appropiate to describe discharges where gas wall loading effects due to previous high density shots can be neglected.

In Fig. 5 are compared the density measurements by the multichord interferometer and the single chord interferometer, located respectively 120° and 60° apart in toroidal angle from the pellet injection port. Density disturbances are seen to propagate with a velocity $\gtrsim 5\ 10^3$ m/s ; the lower values are too slow compared with the ion sound speed unless an effective length accounting for particle flow along field lines is considered.

The low and high density discharges also differ in terms of magnetic fluctuation amplitudes, and of impurity line emission as illustrated in figures 6 and 7 respectively. In particular the lower temperatures corresponding to the higher densities discharges [1] are probably associated with the relatively larger fluctuation amplitudes (fig. 6) and the lower ion impurity sputtering from the wall (see fig. 7). In particular from fig. 7 it is seen that the FeI lines are one order of magnitude less intense in the high density discharges with pellet compared to those measured without pellet injection. This difference can be due to both an higher edge electron temperature and an increased sputtering in the lower density regimes.

REFERENCES

[1] Antoni, V., et al., in Controlled Fusion an Plasma Physics (Proc. 14th Europ. Conf. Madrid 1987), Vol. 11D, Part II, p. 532

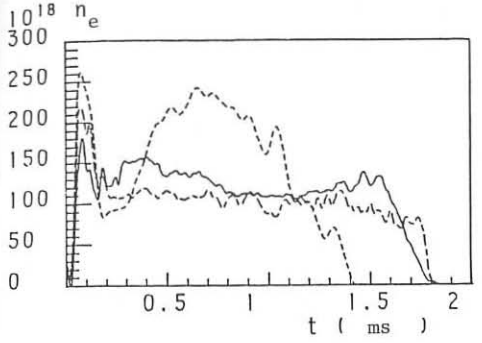

Fig. 1

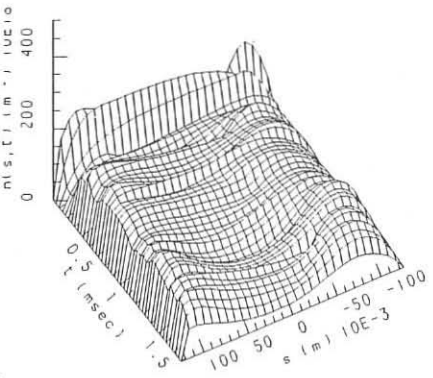

Fig. 2

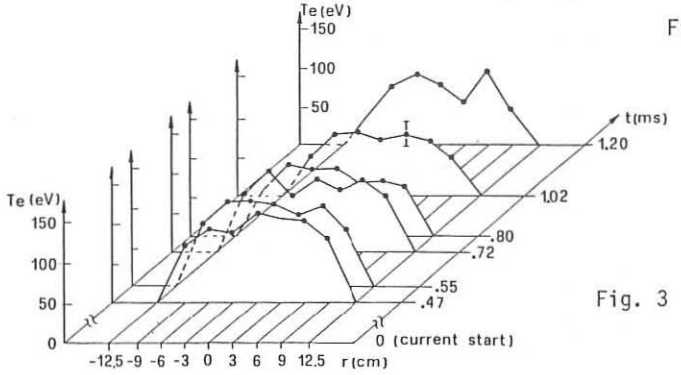

Fig. 3

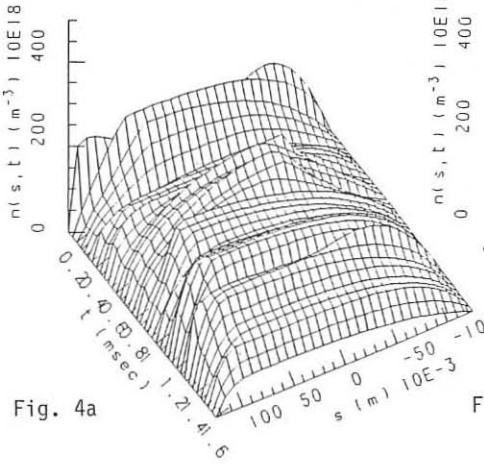

Fig. 4a

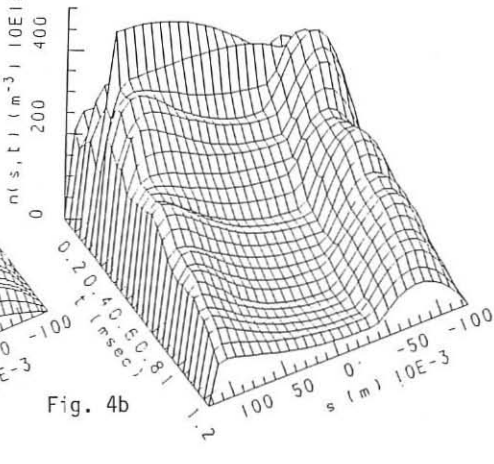

Fig. 4b

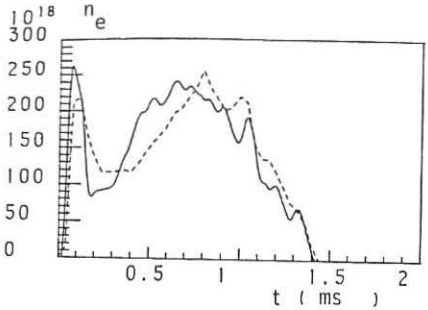

Fig. 5

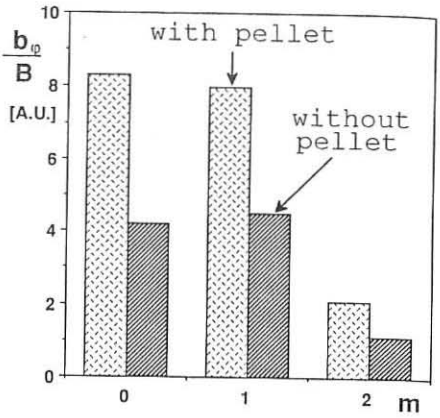

Fig. 6

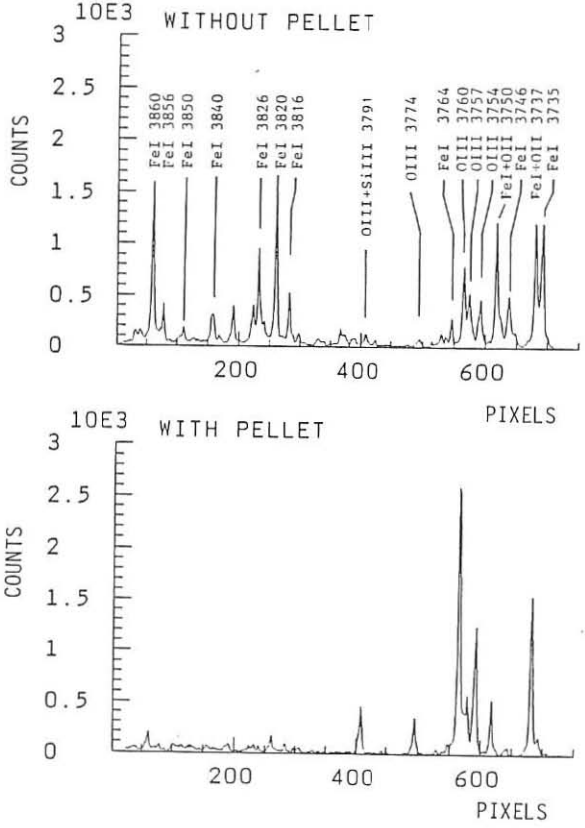

Fig. 7

LINEAR MHD STABILITY PROPERTIES OF RFP CONFIGURATIONS

D. Merlin, S. Ortolani, R. Paccagnella, M. Scapin
Istituto Gas Ionizzati del C.N.R.
EURATOM-ENEA- C.N.R. Association
Padova, Italy

In this paper the linear resistive MHD stability properties of Reversed Field Pinch (RFP) configurations, are analysed for a plasma in contact with a perfectly conducting wall and in cylindrical geometry. In particular we extend previous work [1,2] regarding the fixed boundary and the free boundary force free cases, by studying the effects on stability of an hollow $\mu=\mu_0\, \mathbf{J}\cdot\mathbf{B}/B^2$ profile and of finite pressure. The pressure equilibrium profile is introduced using a parameter which specifies the deviation from the Suydam's stability criterion.

HOLLOW μ PROFILE

A stability analysis of RFP configurations with equilibrium fields characterized by an hollow μ profile finds its motivation on an experimental basis. Magnetic probes have been inserted in the Eta-Beta II experiment [3] and in some cases the reconstruction of the μ radial profile from the magnetic field data has shown evidence of a μ hollowness. By using the Δ' tecnique, a marginal stability analysis of hollow μ configurations described by the analytic expression

$$\mu(r)=\frac{2\theta_0}{a}\left(\mu_M - c'[1-\exp(-c(r-r_M)^2)]\right)$$

has been performed. In the radial interval $[0,\ r_M]$ c' is defined as

$$c'=\frac{\mu_M-1}{1-\exp(-cr_M^2)}$$

and we have chosen $c=10$. In the radial interval $[\ r_M,\ a]$ c' is defined as

$$c'=\frac{\mu_M}{1-\exp(-c(1-r_M^2))}$$

and c has been set to 1. Hollowness is present if $\mu_M > 1$.

The new feature introduced by the hollowness, i.e. the existence of an inner region with a positive $d\mu/dr$, results in the appearance of a new kind of

internal m=1 modes: these modes are resonant between the axis and the radius where μ is maximum and are well distinguishable from the usual m=1 internal modes also from their typical eigenfunctions (see fig. 1). For example in the case $\theta_0=1.4$ and $\mu_M=1.2$ it is possible to observe that if r_M equals 0.6 or 0.5 the corresponding configurations are stable, but if r_M is decreased to 0.4 the configuration is destabilized by m=1 internal resonant modes excited by the too high $d\mu/dr$ close to the axis.

The results of an extensive parametric analysis of m=1 modes for the cases r_M=0.5 and 0.6 are reported in fig. 2. The marginal stability curves are drawn on a θ_0 vs μ_M plane: the region of interest is limited by the curves F=0 ($F=B_\phi(a)/<B_\phi>$) and $\Phi_T=0$ (Φ_T is the total toroidal flux). For each case (with r_M fixed) two curves are shown, corresponding to the excitation of internal and external current driven modes. The behaviour of external modes does not differ qualitatively from the results obtained in previous analysis [1], since they are related to the negative μ gradient beyond the reversal surface. In the present case the configurations with r_M=0.6 are of course more unstable for the m=1 external modes, since they are characterized by greater $|d\mu/dr|$ values in the external region.

Moreover Fig. 2 shows that internal modes are largely affected by a variation of r_M and μ_M. As expected, smaller values of r_M and greater μ_M, resulting in larger values of $d\mu/dr$ in the internal region, correspond to more unstable configurations. The case r_M=0.5 is particularly interesting, in fact in this situation, varying μ_M up to μ_M=1.15 does not influence the stability. Since μ_M gives a measure of the hollowness of the profiles, we conclude that there is in correspondence to each value of r_M (above r_M=0.4) a critical ratio $\mu_M/\mu(0)$, $\mu(0)$ being the on axis μ, beyond which the internal modes are destabilized. In particular for the case r_M=0.5 if μ_M exceeds the on axis μ by 15%, the stability is significantly influenced by the hollowness.

FINITE β MHD STABILITY

The equilibrium state is obtained solving the equations

$$\nabla \times \mathbf{B} = \mu\mathbf{B} + \mu_0 \frac{\mathbf{B}\times\nabla p}{B^2} \qquad 2\mu_0 \frac{dp}{dr} + r\chi(r)\left\{\frac{1}{2}\mu\frac{B^2}{B_\theta} - \frac{B_z}{r}\right\}^2 = 0$$

which with $\chi(r)<1$ corresponds to satisfying the Suydam's condition. Varying the value of χ (which here is assumed constant along the radius) between 0 and 1, imposing the constraint of vanishing pressure at the wall and choosing a μ radial profile of the form $\mu(r)=2\theta_0/a[1-(r/a)^\alpha]$, it is possible to obtain equilibrium RFP configurations which reproduce well the experimental magnetic field profiles. The linearized resistive MHD equations are solved in this case as an eigenvalue problem assuming constant resistivity and density, and an incompressible plasma. The study as been restricted to modes with poloidal periodicities m=0,1 , in a wide range of normalized toroidal wavenumbers $\tilde{k}$=ka.

In Fig. 3a, b (θ_0=1.95, α=4, $S=10^3$ (S is the magnetic Reynold's number), χ=0,1) the spectrum of external m=1 and m=0 modes is shown, while Fig. 3c (θ_0=2, α=2, $S=10^3$, χ=0,1) refers to m=1 internal modes. The values of θ_0 and α are chosen to correspond to a force-free unstable configuration in the θ_0-α, just beyhond the ideal syability limit [1] . From Fig.3 it is clear that finite pressure modifies the current driven (ideal and tearing) part of the spectrum (at low $\tilde{k}$) and also

extends the spectrum at high $\tilde{k}$ values. If $\chi \neq 0$ the long wavelength part of the m=1 spectrum is due to ideal pressure driven modes.

For m=0 (Fig. 3b) at this values of θ_0 and α only pressure driven modes are found. A stabilizing effect is observed for m=1 external and m=0 modes by decreasing θ_0 at a fixed α value. In particular the growth rates of the ideal interchange m=1 modes vary rapidly both with θ_0 and β. For example for $\theta_0 = 1.85$ and $\alpha=4$, they are not present if $<\beta><10\%$. By decreasing further θ_0 (at a fixed α and χ) only the resistive pressure driven part of the m=0,1 spectrum survives, but the growth rates, of these g-modes become smaller and smaller. For example, for $\alpha=4(S=10^3, \chi=1)$, if $\theta_0 = 1.68$ than $\tilde{\gamma} \approx S^{-1}$, i.e. the growth rate is comparable with the resistive diffusion time of the configurations.

A similar decrease of the growth rates has been observed for m=1 internal modes if θ_0 and χ are fixed and α increased. Fixing $\theta_0=2$ $(S=10^3, \chi=1)$ at $\alpha = 2.28$, the maximum value of the growth rate is around S^{-1}. Moreover the position of the maximum of the spectrum varies largerly with θ_0 for m=0 and m=1 external modes (Fig. 4a, b) while does not depend very much on θ_0 and α for m=1 internal modes (Fig. 4c).

Finally in Fig. 5 "β limits" for m=0, 1 modes (m=1 external and internal) are given in the case $\alpha=4$ and $S=10^3$. In the figure is also reported the boundary due to ideal m=1 pressure driven modes al low $\tilde{k}$ (dashed curve), which is strongly dependent on θ_0. The β limits for resistive pressure driven modes are deduced fixing a lower bound for the growth rates at $\tilde{\gamma}=S^{-1}$. This gives values of $<\beta>$ around 8% for m=1 external, between 4% and 10% for m=1 internal and 4% for m=0 modes, in typical region of operation of RFP, $1.7 \leq \theta_0 \leq 1.9$. Although these β limits seem to be not too unrealistic [4] for actual RFP experiments (at low S values), it is clear that the criterium used here to determine these "β limits" is quite inappropriate at larger values of plasma conductivity. In fact, since the pressure driven modes scale like $S^{-1/3}$ for large S, it is obvious that the β limit becomes neglegible at large S.

In conclusion, while in previous work [1,2] the importance of current driven m=1 modes in the relaxation of RFP toward the minimum energy state, has been pointend out, in this paper the effect of finite pressure has been considered. With finite β many resistive g-modes are originated, well below the Suydam's condition, and in correspondence to resonant high toroidal wavenumbers. For these modes the associated islands can easily overlap [5], leading to magnetic stochasticity in the external region of the plasma and determining the characteristics of the transport. Thus only nonlinear simulations of plasma dynamics, including self consistent calculations of transport coefficient, can give an estimate of true β limits, while the present linear analysis can only suggest the way to optimize RFP profiles against ideal and resistive interchange modes.

[1] Antoni, V., Merlin, D., Ortolani, S., Paccagnella, R., Nuclear Fusion **26** (1986) 1711

[2] Merlin, D., Ortolani, S., Paccagnella, R., in Controlled Fusion and Plasma Physics (Proc. 14th Europ.Conf. Madrid 1987), Vol. 11/D, Part II, p.442

[3] Antoni, V., et al., in Mirror-Based and Field-Reversed Approaches to Magnetic Fusion, Varenna (1983), Vol. II, p. 107

[4] Antoni, V., et al., in Controlled Fusion and Plasma Physics (Proc. 14th Europ. Conf. Madrid 1987), Vol. 11/D, Part II, p. 532

[5] Rechester, A.B., Rosenbluth, M.N., Phys. Rev. Lett. **40** (1978) 38

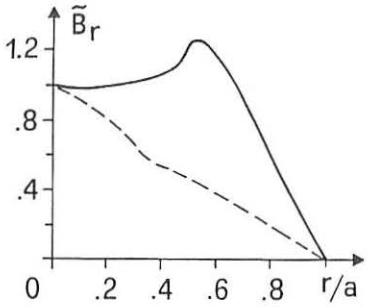

Fig.1

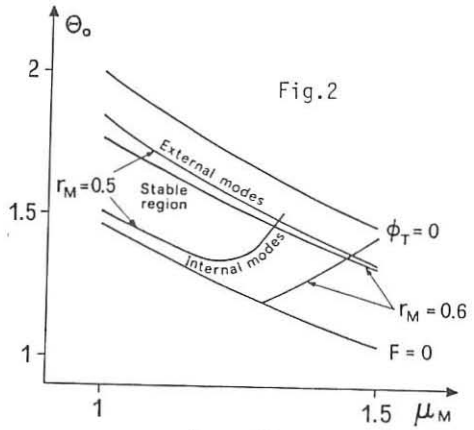

Fig.2

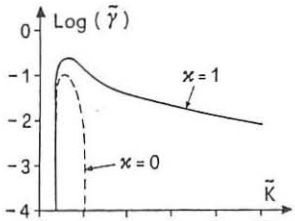

Fig.3a

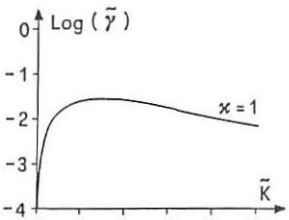

Fig.3b

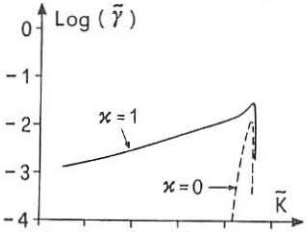

Fig.3c

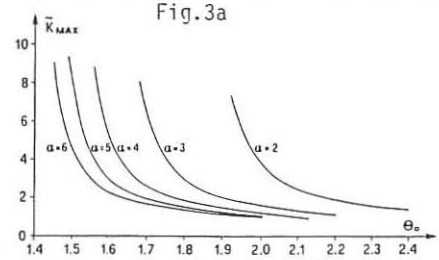

Fig.4a

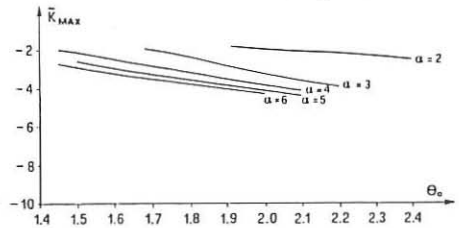

Fig.4c

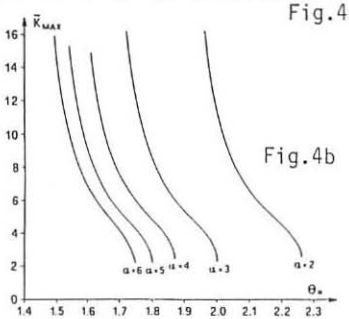

Fig.4b

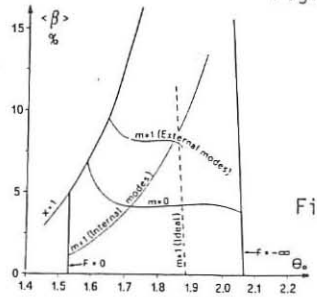

Fig.5

IMPURITY DIFFUSION IN RFP PLASMAS

L. Carraro, S. Ortolani, M.E. Puiatti
Istituto Gas Ionizzati del C.N.R.
ENEA-EURATOM-CNR Association
Padova, Italy

A one-dimensional diffusion code has been implemented to simulate the impurity diffusion in various RFP plasma conditions. The basic equations are parabolic with non linear coefficients and source terms; to solve this initial value problem a Cranck Nicholson scheme with an adjustable degree of implicitness is used. Time centering of the transport coefficients is accomplished using a predictor-corrector scheme. In cylindrical geometry, assuming the coronal atomic model to evaluate the source terms, the diffusion equations may be written as:

$$\frac{\partial n_i}{\partial t} = -\frac{1}{r}\frac{\partial}{\partial r}(r\ \Gamma_i) + n_e\ (n_{i+1}\ \alpha_{i+1} + n_{i-1}\ S_{i-1} - n_i\ S_i - n_i \alpha_i)$$

where Z is the atomic number of the considered species, S_i and α_i are, respectively, the ionization and recombination coefficient for the ionic species i and Γ_i is the corresponding diffusion flux.

To derive the expression of the ion flux Γ_i a classical transport model has been assumed; however, to account for the high diffusion regimes typical of a RFP plasma, the classical fluxes are enhanced by a space-dependent coefficient K(r). Properly setting the function K(r) it is possible to simulate the transport conditions characterizing the plasma.

The assumed boundary conditions are:

$$\left(\frac{\partial n_i}{\partial r}\right)_{r=0} = 0 \qquad i=1,2,\ldots Z+1$$

$$\left(\frac{\partial n_i}{\partial r}\right)_{r=a} = 0 \quad \text{or} \quad n_i(a)=b_i \qquad i=2,\ldots Z+1 \quad \text{and} \quad \Gamma_1(a) = -R \sum_{i\neq 1} \Gamma_i(a) + \Gamma_0$$

where R is the recycling rate at the wall and Γ_0 is a neutral impurity influx from the wall. The condition with R=1, $\Gamma_0 = 0$ corresponds to a constant total impurity number.

The model is suitable for studying the diffusion of light impurities and up to now it has been implemented for oxygen, which is the principal impurity in ETA-BETA II, and carbon, whose effect may be important in machines with a carbon tile covered liner.

To solve the diffusion system typical ETA-BETA II temporal behaviours of T_e and n_e have been considered as measured for discharges with and without pellet injection (see Fig. 1 where the data with pellet injection correspond to symbols in full). The profiles of the components of the magnetic field have been evaluated solving the equation $\nabla \times \mathbf{B} = \mu\ \mathbf{B}$ with $\mu(r)=\mu\ (0)\ (1-(r/a)^4)$ and

neglecting the pressure effects.

The examples of the oxygen ion population obtained in the two different discharge conditions (with and without pellet injection) are shown in Fig. 2 and 3. Two different times for each condition are shown, corresponding to the ionization phase of the impurities (200 μs) and to the flat-top phase of the plasma current (1 ms). The assumed T_e and n_e profiles are: $T_e(r)=T_e(0)(1-(r/a)^4)$ and $n_e(r) = n_e(0)(1-(r/a)^4)$ and the total oxygen concentration has been taken to be 10^{18} m^{-3}, corresponding to about 1% of the electron density. To simulate the transport in ETA-BETA II, the classical expression of the fluxes has been multiplied by a factor K(r) according with [1].

The Z_{eff} profiles obtained for t=1 ms are similar to that derived from spectroscopic experimental results on ETA-BETA II [2], showing a value close to 1-1.5 in a large region near the plasma centre, with a pronounced peak near the plasma border. The ion distributions obtained in these two plasma conditions are very similar at the early time and show some difference only at the later time, according to the fact that the T_e and n_e temporal behaviours related to the two conditions differ mainly during the flat-top phase of the plasma current (Fig. 1). From the ion populations obtained in the case without pellet injection some line emissivities have been calculated, to compare them with the lines measured by a multichord spectrometer [3]. In particular the OIV λ=3411 Å and OV λ=5606 Å during the flat-top phase and the OVI λ=3434 Å during the early phase have been considered; the results are reported in Fig. 4, showing a similar radial distribution. The emissivity absolute values agree within a factor of two; however, to obtain more reliable values more complex atomic models than the coronal would be necessary, to take into account the population distributions among ground, metastable and excited states.

The results obtained for carbon impurities are substantially similar. In particular, an analogous Z_{eff} profile is obtained, as shown in Fig. 5 for example without pellet injection and with a carbon concentration of 10^{18} m^{-3}.

However, the effective charge profile is largely affected by the T_e and n_e profiles. To illustrate this point, various Z_{eff} radial profiles obtained with different T_e and n_e profiles are drawn in Fig. 6 and 7. Fig. 6 shows that peaked T_e profiles lead to an effective charge profile decreasing with radius, while a hollow Z_{eff} profile is obtained with a flatter T_e. Moreover a lower maximum value for Z_{eff} is obtained if a flatter n_e profile is considered as shown in Fig. 7.

In conclusion, the oxygen line emission and the Z_{eff} profiles measured in ETA-BETA II have been simulated by an impurity diffusion model. The effects of various T_e and n_e profiles on the diffusion have been studied, showing that different T_e and n_e profiles, more than the particular impurity species and the T_e and n_e temporal behaviours, may justify different effective charge profiles measured in various RFP devices [2,4].

REFERENCES

[1] Ortolani, S. in Twenty Years in Plasma Physics, p. 75 (1985)
[2] Gabellieri, L. et al., Nucl. Fusion 27, (1987), p. 863
[3] Gabellieri, L. et al., in Plasma Physics (Proc. 7th Int. Conf. Kiev 1987) Vol.III p.259
[4] Carolan, P.G., et al., in Controlled Fusion and Plasma Physics (Proc. 14th Europ. Conf. Madrid 1987) Vol. 11 D, part II, p. 515

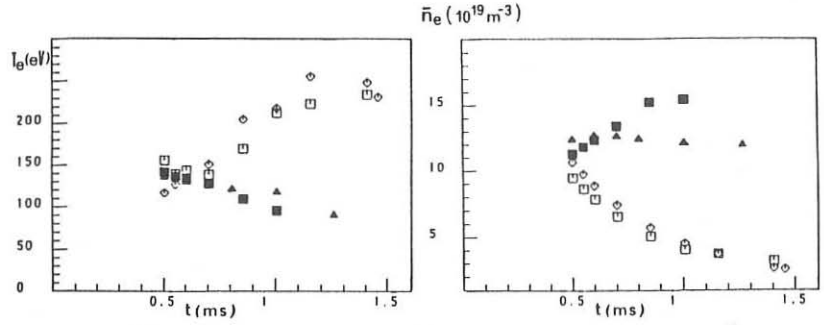

Fig.1

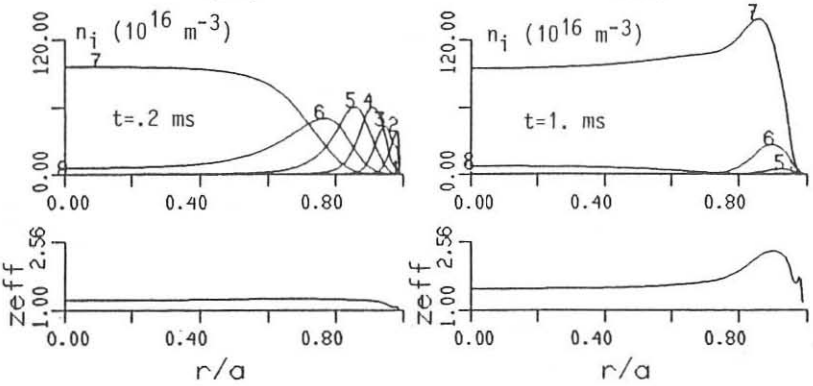

Fig.2 Oxygen ion populations and Z_{eff} obtained in the simulation of discharges without pellet injection

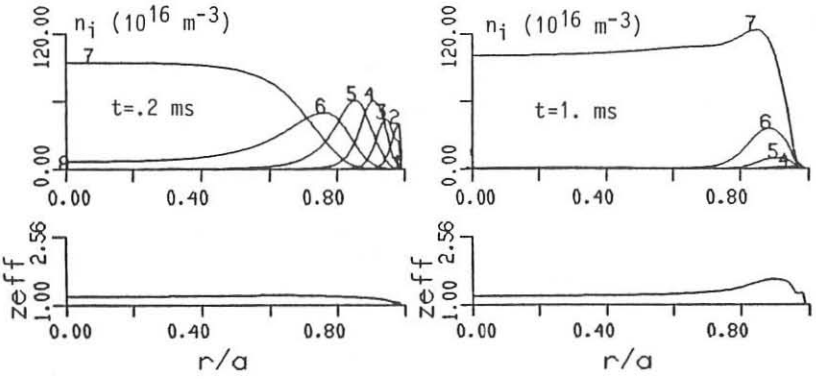

Fig.3 Oxygen ion populations and Z_{eff} obtained in the simulation of discharges with pellet injection

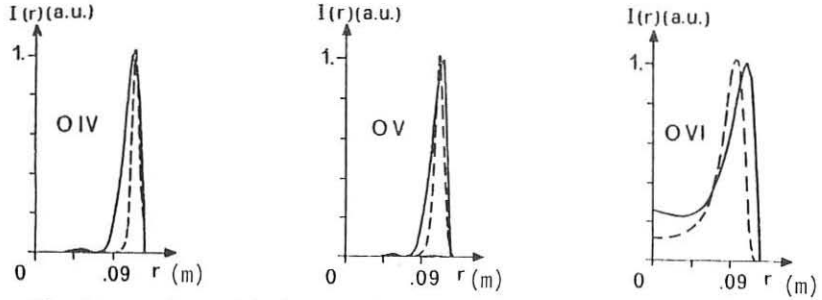

Fig.4 Experimental(—) and simulated (- -) radial emissivities of OIV,OV,OVI lines.

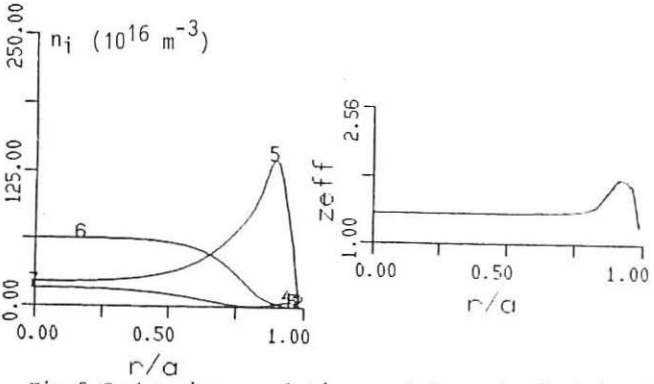

Fig.5 Carbon ion populations and Z_{eff} obtained in the simulation of discharges without pellet injection.

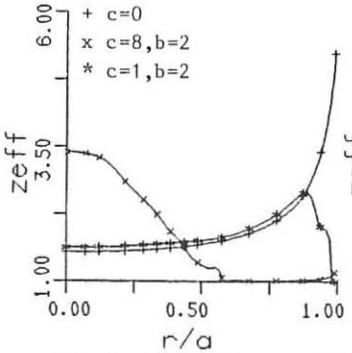

Fig.6 Various Z_{eff} profiles obtained with $n_e(r)=n_e(0)(1-(r/a)^2)$ and $T_e(r)=T_e(0)(1-(r/a)^b)^c$

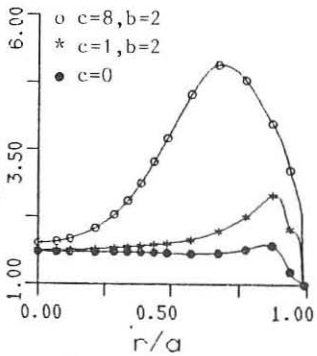

Fig.7 Various Z_{eff} profiles obtained with $T_e(r)=T_e(0)(1-(r/a)^2)$ and $n_e(r)=n_e(0)(1-(r/a)^b)^c$

INVESTIGATIONS OF BREAKDOWN BETWEEN PLASMA-FOCUS ELECTRODES

Sz.Brandt, A.Jerzykiewicz, K.Kociecka, W.Nawrot

Institute for Nuclear Studies, 05-400 Swierk, Poland

The experimental studies of breakdown processes between plasma-focus electrodes have been undertaken within a program of the neutron emission optimization from the PF-360 facility (1). For this aim an auxiliary stand has been completed. Thus it has been possible to perform certain tests of different electrodes and insulators dimensions and shapes at various experimental conditions. The electrodes have been supplied from a low energy HV-pulse generator that enabled an initial voltage-rise steepness adjustment by charging voltage changes. The breakdown voltage and current have been measured by means of a resistive voltage divider and a shunt, respectively, connected with a fast oscilloscope. The response time of the measurement system was lower than 2 ns. The breakdown characteristics have been estimated for the hydrogen pressure range from 1 up to 30 Torr, at the voltage-rise steepness 490 +-120 kV/μs, for an electrode set shown in Fig.1. The breakdown voltage on the surface of the insulator has been measured in the case of quartz tubes being put on the outer electrode rods and the complex breakdown voltage - in the case of the tubes being taken off. There have been used two kinds of alumina insulators (Fig.2). The inner and the front surface of the insulator "A" were covered with a thin silver layer in order to shield the space between the insulator and the outer electrode from the magnetic field induced by the current in the inner electrode. The insulator "B" corresponded to that used in the PF-360 device. The measurements have been performed at both voltage polarities, when charging a 0.25 or 0.8 μF capacitor (C in Fig.1) to 30 and 50 kV.

A typical shape of measured voltage has been shown in Fig.3 in which the analized values have been also pointed. The investigations results have been shown in Fig.4 (insulator "A") and Fig.5 (insulator "B") and can be summarized as follows:

- the breakdown voltage (V2) measured with the insulator "A" actually was not dependent neither on the pressure , nor on CE polarity, nor on charging voltage and capacitance in the ranges given above.
- the comparison of the breakdown voltage on the insulator surface with the complex one has indicated that at the

insulator "A", the breakdown has occured on the surface only.
- in the case of the insulator "B" being used and the polarity being negative the breakdown voltage (V2) has increased even 2 - 3 times, compared with that measured at the positive polarity. In such conditions some breakdown events at the front of the electrodes have been observed.
- the breakdown voltages V1 and V2 at the positive polarity were much lower than those measured previously with the PF-360 facility.

In order to explain the last result the measurements with the PF-360 device have been started. They have been performed at an electrode set shown in Fig.1. There has been applied the positive voltage polarity only. It has been found out that the breakdown voltage depended mainly on the capacitance of the storage bank (Fig.6). The results were comparable to those measured with the auxiliary stand only at the low capacitance. The breakdown voltage and the voltage-rise steepness (Fig.7) were increasing with the bank capacitance. It should be stressed that for the whole range of experimental conditions the voltage-rise steepness measured in the PF-360 device was not higher than that measured in the auxiliary stand. So, the differences in the voltage-rise steepness have not been the cause of the breakdown voltage increasement. It seems that the influence of the magnetic field is the only cause which could explain this phenomenon.

Considering that the breakdown voltage depends on the storage bank capacitance it is necessary to take into account the fact that the circuit inductance diminishes with the increase of the capacitance. It involves the increasement of the V_0/L value which is equal to the initial current-rise steepness in the circuit. This parameter connected with the magnetic field magnitude has been mentioned as one of the most important in the considerations of the neutron emission limitations (2,3).

The conclusions that result from the investigations presented above are the following:
- the magnetic field influences strongly the breakdown voltage, especially at the negative voltage polarity.
- as the result of the voltage increase on the insulator surface there can occur a breakdown at the front of the insulator or of the electrodes, which involves the diminution of the neutron yield from Mather type plasma-focus devices.

(1) JERZYKIEWICZ,A.,et al.,Proc.11th European Conf. on Contr. Fusion and Plasma Phys. /Aachen, 1983/, Part I, pp 485-488
(2) PATTERSON,E.L., Sandia Laboratories Research Rep. SC-RR-69 -233
(3) JERZYKIEWICZ,A., KOCIECKA,K., KOCINSKI,L., Proc.4th Int. Workshop on PF and Z-pinch Research. /Warsaw 1985/ pp 71-73

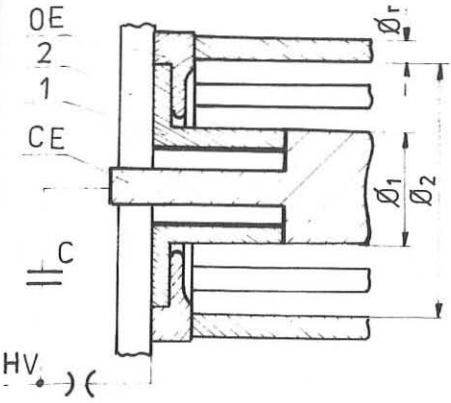

	$Ø_1$	$Ø_2$	$Ø_r$	n_r
aux.st.	100	150	10	12
PF-360	120	170	12	16

Fig.1 Electrode set with an insulator
1. Insulator
2. Insulating material

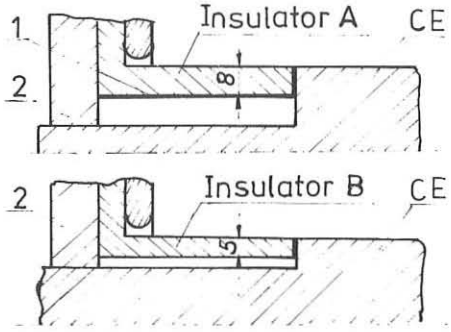

Fig.2 Insulator configuration
1. Silver layer
2. Insulator material

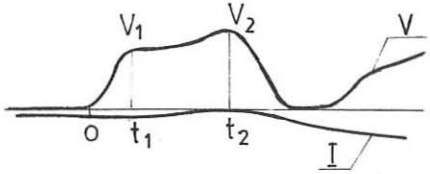

Fig.3 Voltage and current shapes

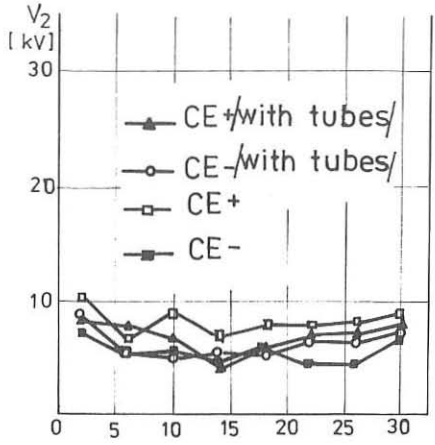

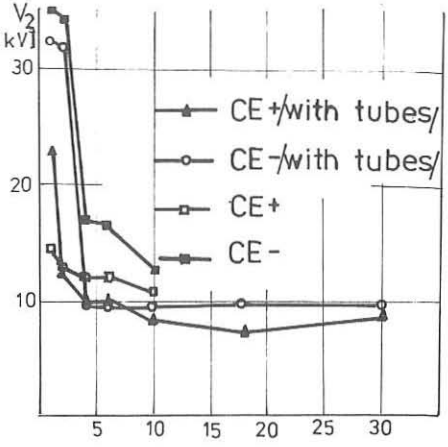

Breakdown voltage characteristics

Fig.4 Insulator A

Fig.5 Insulator B

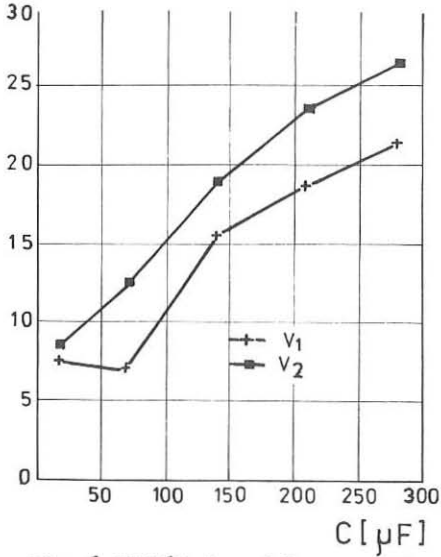

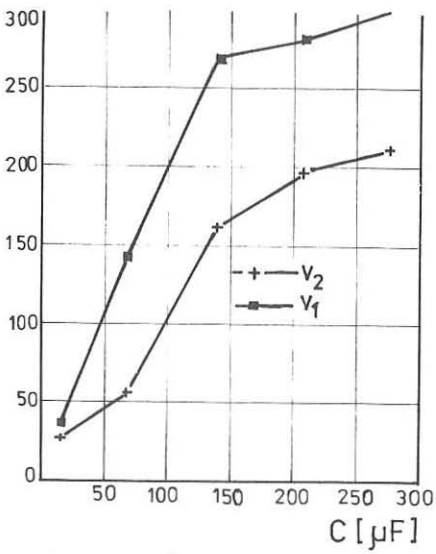

Fig.6 PF360 breakdown voltage characteristics
V_o= 30 kV, p_o= 5 Torr

Fig.7 PF360 voltage-rise steepness characteristics
V_o= 30 kV, p_o= 5 Torr

THREE DIMENSIONAL RESISTIVE MHD MODELING OF THE RFX REVERSED FIELD PINCH EXPERIMENT

S. Ortolani
Istituto Gas Ionizzati del CNR
EURATOM-ENEA-CNR Association
Padova, Italy

D.D. Schnack, D.S. Harned, and Y.L. Ho*
Science Applications International Corp.
San Diego, CA, USA

I. INTRODUCTION

The RFX device, currently under construction at Padova, will take a major step in pushing the parameters of Reversed Field Pinch experiments into a new regime. RFX is designed for currents of up to 2MA and pulse lengths of 250 ms. In order to achieve the most effective operation in this new regime, it is important to attain a better theoretical understanding of the plasma dynamics and transport. Pulse lengths in the present RFX design will be comparable to the resistive decay time of the shell. However, in order to optimize active plasma position control and minimize magnetic field errors, a thinner (more resistive) shell may be required in the future and is presently under design. It is critical, therefore, to understand RFP dynamics in the presence of a resistive shell in order to preserve the dynamo effect and ensure the maintenance of reversal. A better understanding of RFP dynamics and transport in the specific RFX parameter range will also be necessary to make reliable predictions of beta values and loop voltages for the RFX experiment. A new numerical model has been developed to address these RFX design issues. The model, a three dimensional, nonlinear, resistive MHD simulation code, is used to make estimates of the optimum shell thickness for the RFX resistive wall and the change in loop voltage expected when RFX is operated with a resistive shell.

II. NUMERICAL MODEL

The numerical model used here [1] to study RFX dynamics solves the full nonlinear resistive MHD equations in three dimensions. Cylindrical geometry is used with a pseudospectral spatial representation. The equations are advanced in time using the semi-implicit method [2,3], which allows much larger time steps than would be possible with an explicit method. The code is bounded at $r=r_W$ by a shell, which may be chosen to be either a perfect conductor or a resistive shell with a specified time constant. When a resistive shell is chosen, a second conductor may be placed at a radius outside of the resistive shell. This second conductor is used to represent the position of the toroidal field coils, which can act as a conducting wall on the time scales of reversed field pinch experiments. The formulation of the resistive wall boundary conditions has been obtained previously by Ho [4].

* Permanent address: University of Wisconsin, Madison, WI, USA.

III. RESISTIVE SHELL COMPUTATIONS FOR RFX

The primary purpose of the resistive shell computations is to assist in determining the optimum shell thickness for RFX. The relevant experimental parameters are minor radius r_W=50 cm, aspect ratio R/r_W=4, Lundquist number $S=4.2\times10^7$, Alfven time τ_A=0.27 μsec, and the toroidal field coils are located at radius r_C=62 cm. The toroidal field coils are considered to be a perfect conductor since their time constant, 190 ms, is comparable to the pulse length of 250 ms. Our computations indicate that a reversed equilibrium state can be maintained in RFX with a resistive shell having a time constant longer than the plasma relaxation time, which is much shorter than the pulse length. This state, however, will be characterized by a larger loop voltage than would be found in shots with a perfectly conducting shell. These results are consistent with those of Ho [4], who found for different parameters that the final relaxed state with a resistive shell is independent of the shell resistivity and that for cases with $r_C/r_W<1.4$ the loop voltage is larger by approximately two percent for every one percent increase in the radius of the outer conductor.

In order to simulate RFX operation with a resistive shell, we use the following procedure. The initial conditions are chosen to be a modified Bessel function model (MBFM) and a low level of fluctuations is introduced. As an example we fix Θ=1.8 and choose $S=3\times10^3$. The other parameters are the same as the RFX parameters described above. The reason for choosing the lower value of S is that realistic experimental values are too large to be practical for use in three dimensional computations. It is important that the resistive diffusion time be longer than the nonlinear plasma relaxation time. We have found the relaxation time to be approximately 200 τ_A for this case, so that $S=3\times10^3$ is a sufficiently large value. For this example we also make the assumption of zero beta. The equilibrium is initialized with a perfectly conducting shell at r_W. The plasma then evolves until it reaches a relaxed steady state. The plasma relaxation occurs as resistive diffusion destroys the initial reversed equilibrium, but a new reversed helical equilibrium state is eventually established due to the nonlinear interaction of the dynamo modes. The dominant unstable modes have m=1 and n=-7 to -10. After this new steady state is reached, the conducting wall is replaced with a resistive shell having a time constant of $\tau_{shell}=360\ \tau_A$. The plasma is again allowed to relax until it reaches a new steady state (about 4 shell times). The structure of the plasma may be seen in Fig. 1., which shows surfaces of constant current. Figure 1a shows the initial cylindrical equilibrium. Figure 1b shows the new helical steady state after relaxation in the presence of a perfectly conducting shell. Finally, Fig. 1c shows the plasma after relaxation with a resistive shell. This new multi-helical state is much more complicated that the state existing in the presence of a conducting shell and the amplitude of the distortions is considerably larger. These large amplitude distortions are associated with a higher toroidal loop voltage. Figure 2 shows the evolution of the loop voltage from the time the conducting wall was replaced with a resistive shell until the final relaxed state is reached. In the final state the voltage is 33 percent larger than in the state with a conducting shell. This increase is comparable to the 40 percent increase that would follow from Ho's results. In RFX, this 33 percent increase is what the simulations would predict with a shell having a very short time constant, e.g. 10 ms. The voltage increase in the final relaxed state is independent of the shell time constant. Therefore, in order to significantly reduce volt-second consumption, the shell time must be a substantial fraction of the pulse length.

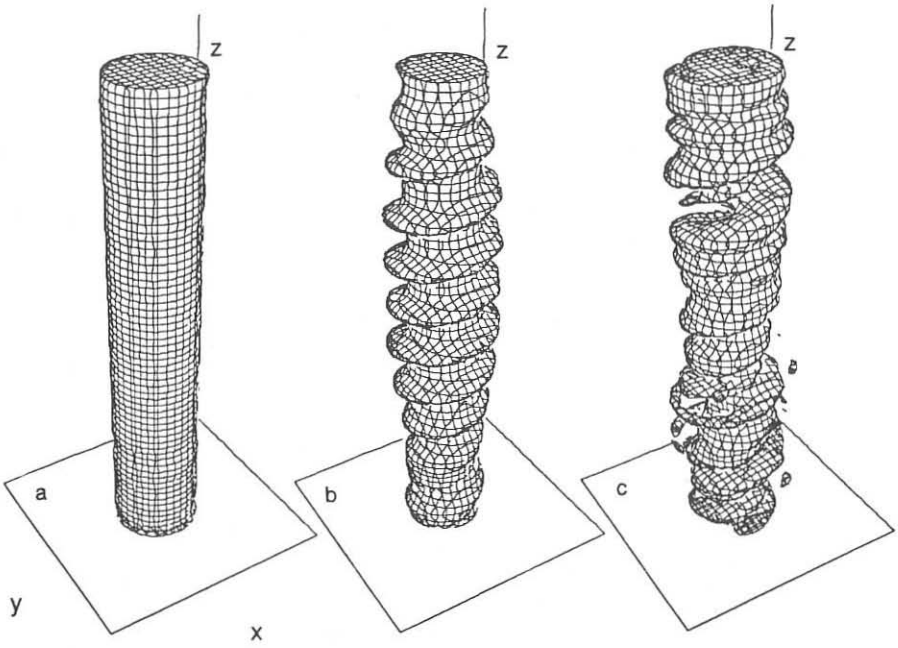

Fig. 1. Surfaces of constant current, showing the initial equilibrium (a), the relaxed state in the presence of a perfectly conducting shell (b), and the relaxed state with a resistive shell (c).

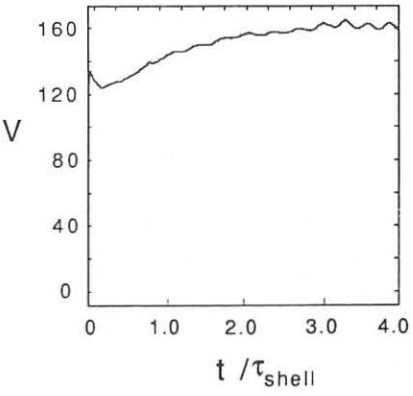

Fig. 2. Toroidal loop voltage as a function of time from the introduction of the resistive shell (t=0) to the final relaxed state (t=4) in units of the shell time.

IV. SIMULATION OF START-UP

We have also performed three dimensional simulations of start-up processes beginning with a cold uniform plasma in a uniform toroidal magnetic field. A toroidal current is driven through the plasma, leading to compression, Ohmic heating and relaxation to a reversed state. The transport model used here includes, in addition to Ohmic heating, thermal conduction, Bremsstrahlung radiation, and temperature dependent resistivity. The current is increased linearly from zero for 500 Alfven times until Θ=1.8, after which Θ is clamped at this value. The evolution of the field reversal parameter, F, as a function of time is shown in Fig. 3. Note that reversal is achieved by a sequence of two sudden relaxation events, corresponding to the destabilization of the m=1 dynamo modes. The final state has F=-0.15, Θ=1.8, and β_p=0.12.

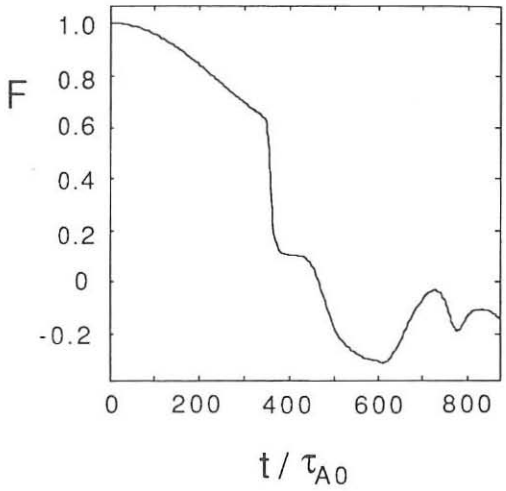

Fig. 3. The reversal parameter, F, as a function of time for a cold start-up case. τ_{A0} is the Alfven time at t=0.

REFERENCES

1. D. D. Schnack, D. C. Barnes, Z. Mikic, D. S. Harned, E. J. Caramana, and R.A. Nebel, Comput. Phys. Commun. 43, 17 (1986).
2. D. S. Harned and D. D. Schnack, J. Comput. Phys. 65, 57 (1986).
3. D. D. Schnack, D. C. Barnes, Z. Mikic, D. S. Harned, and E. J. Caramana, J. Comput Phys. 70, 330 (1987).
4. Y. L. Ho, S. C. Prager, and D. D. Schnack, Bull. Am. Phys. Soc. 32, 1832 (1987).

SUSTAINMENT OF REVERSED FIELD PINCH PLASMAS IN OHTE

P. Taylor, C. Greenfield, R. La Haye, S. Ortolani*, M. Schaffer, and T. Tamano.

General Atomics, San Diego, USA
Istituto Gas Ionizzati del C.N.R., EURATOM-ENEA-CNR Association, Padova, Italy*

Sustainment of reversed field pinch (RFP) plasmas in OHTE for times much longer than the resistive shell time was previously reported [1-3]. Recently, the OHTE power supply was upgraded and the resistive shell experiment has continued. The purpose of the upgrade is to extend the sustainment time and to significantly increase the plasma current beyond the previous level of up to 200 kA. This paper reports the results of the experiments.

The OHTE device ($R = 1.24$ m, $a = 0.18$ m) has a thin resistive shell with vertical field time constant of 1.5 ms. After setting up an RFP plasma within 2 ms, the plasma is sustained by firing sustaining capacitor banks in sequence. The recent power supply upgrade added another sustaining bank (120 mF, 5 kV), increasing the total bank energy from 1.8 MJ to 3.3 MJ. A chopper power system was also installed for more precise control of vertical fields.

With the upgraded system, reproducibility of discharges sustained over 10 ms has been greatly improved. Thus, we are able to examine more detailed characteristics of sustained RFP discharges. Sustained RFPs are relatively insensitive to equilibrium position changes of a few mm from optimum. However, most discharges show an increase in the toroidal one-turn voltage at some time during the discharges. The amount of the increase is tens of percent, and it occurs in less than 1 ms; the plasma current starts decaying afterwards. This current decay frequently leads to termination of the discharge. An example is shown in Fig. 1. Figures (a), (b), (c) and (d) are plasma current I, toroidal field at the plasma edge, one-turn voltage V, and toroidal flux inside the vacuum liner. The voltage starts increasing at 5 ms. Increased MHD activity is suspected as a cause of the resistance increase. Analyses are made on the low-pass-filtered signals obtained from the 128 pick-up loops, 32 toroidally by 4 poloidally, covering the entire torus. The total energies of $m = |2|$, $m = 1$, $m = 0$ and $m = -1$ are examined as a function of discharge time. It is found that the energies of both $m = 0$ and $m = 1$ (internal mode) sharply increase preceding the resistance increase. The energies of $m = -1$ (external mode) and $|2|$ also often increase at the same time. These are non-rotating (locked) modes. An example of the mode energies is shown in (e), (f), (g) and (h) of Fig. 1. Each m mode consists of several n modes. The raw

pick-up loop signals indicate that the locked modes are toroidally localized, typically within one quadrant of the entire torus. However, the location of the modes varies from shot to shot. The locked modes sometimes continue for a few ms, but sometimes cease within one ms. However, the one-turn voltage tends to remain high. A possible explanation for this is that the locked modes connect the inside and outside field lines. As a result, the plasma temperature drops and the plasma resistance increases.

The plasma current has been increased to 328 kA. The minimum attained plasma resistance R is consistent with the scaling law obtained in the OHTE conducting shell system

$$R(m\Omega) = [\frac{I(A)}{10^5}]^{-3/2},$$

as seen in Fig. 2. High current discharges often exhibit a sudden, fast termination (hard termination), particularly when the plasma density is very high. Figure 3 shows the attained reversal time vs. the ratio of plasma density to plasma current n/I. The attainable reversal time decreases as n/I increases. The inner wall of the OHTE vacuum vessel is entirely covered by graphite tiles. When the plasma current increases, n/I tends to increase more than linearly. In particular, if the density keeps increasing, the discharges terminate hard. This problem has been overcome by implementing helium glow cleaning in order to reduce the hydrogen wall loading.

Even when the discharge does not terminate, the minimum plasma resistance at the current peak (i.e., V/I) tends to be high for high density shots. Figure 4 shows the plasma resistance normalized by the current dependence, $VI^{1/2}$ vs. n/I. This indicates that n/I for good discharges is lower than $5 \times 10^{14} m^{-3} \cdot A^{-1}$, which is consistent with the typical RFP density limit. The measured electron temperature is proportional to plasma current, and the coefficient is approximately 1 eV/kA. Therefore, this density limit corresponds to the poloidal beta value β_p of about 20%, assuming a uniform pressure profile.

Plasma stability is examined by use of a Freidberg-Hewett resistive code. The analysis shows that both $m = 0$ and $m = 1$ modes can be unstable for a Lundquist number $S \gtrsim 10^4$. The growth rate normalized to Alfvén time $\gamma\tau_A$ increases approximately from 10^{-4} to 10^{-3} as β_p varies from 0 to 20%, but has a weak dependence on S. The calculations also show increased growth rate for a steeper edge current density gradient, in particular at low β_p. This general trend matches the experimental observations.

In conclusion, the plasma sustainment was limited because of the sudden increase in one-turn voltage preceded by both the $m = 0$ and $m = 1$ locked modes. The plasma characteristics are strongly tied to high plasma density, suggesting that this is the result of the β_p limit.

[1] R.R. Goforth et al., *Nuclear Fusion* 26, 4(1986) 515.
[2] S. Ortolani et al., *Europhysics Conference Abstracts*, Vol. 11D, Part II (1987) 477.
[3] T. Tamano et al., *Phys. Rev. Lett.* 59, 13 (1987) 1444.

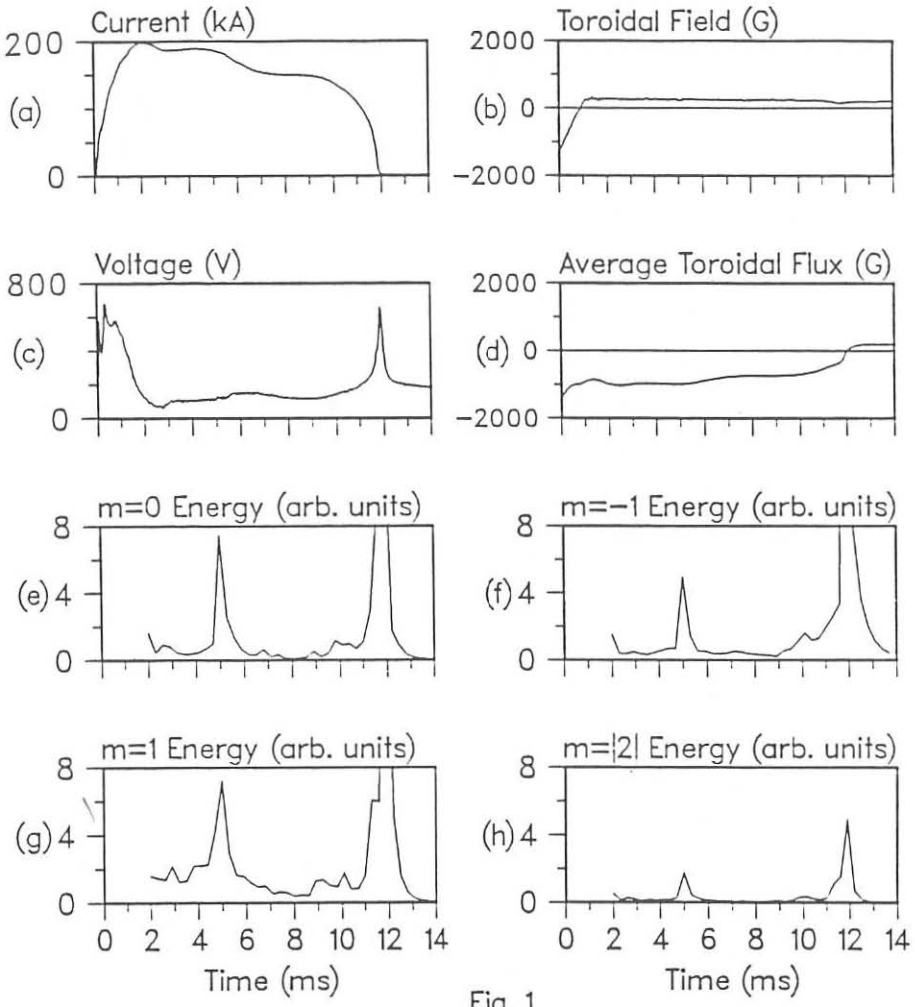

Fig. 1

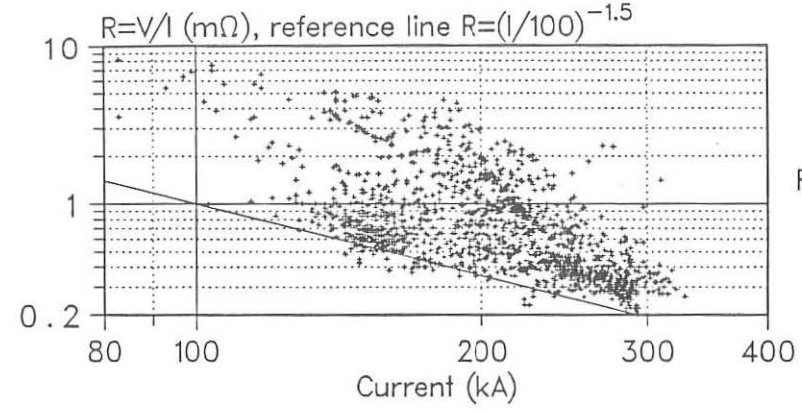

Fig. 2

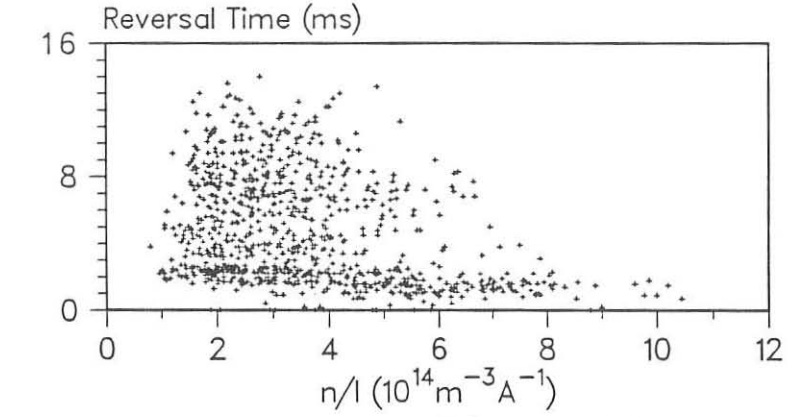

Fig. 3

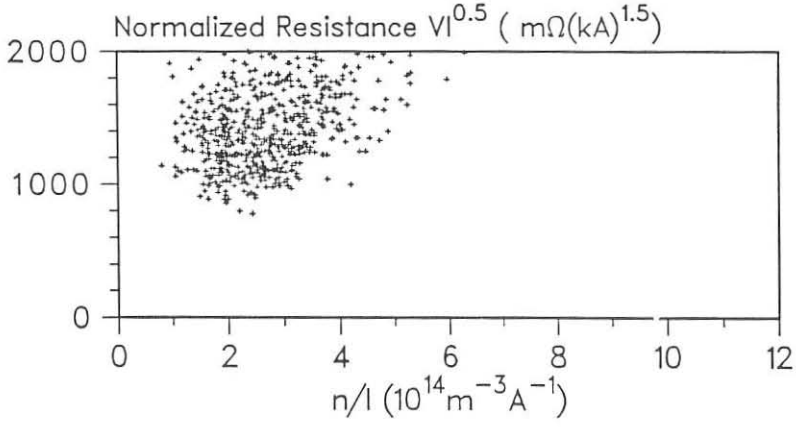

Fig. 4

ION POWER BALANCE MODEL FOR REVERSED FIELD PINCH PLASMAS

P G Carolan, A Lazaros+, J W Long*, M G Rusbridge+,
Culham Laboratory, Abingdon, Oxon, OX14 3DB, UK
(UKAEA/Euratom Fusion Association)
+ UMIST Manchester, * Oxford Polytechnic

Introduction It is a general finding in RFP's that ions are heated by non-collisional processes. This is clearly the case when T_i exceeds T_e[1,2], but preceeding these results, when more typically $T_i \sim T_e$[3], collisional heating was also ruled out because the electron-ion equipartition time greatly exceeded the energy confinement time. The observation, first noted in HBTX1A[4] and then more clearly shown in HBTX1B[5], that Z_{eff} was too low to account for the plasma resistance, even at relatively low values of I/N (5×10^{-14} A.m), led to considerations of edge losses of magnetic helicity[6,7]. The scaling of loop voltage with current on HBTX1B[8] also reveals an anomalous voltage, ΔV_ϕ, which decreased with removal of the carbon tiles. Helicity balance considerations revealed that only a small fraction of the power $I_\phi \Delta V_\phi$ would ohmically heat the electrons[6]. In an ion power balance model[1] ΔV_ϕ is assumed to augment the ion heating and calculations of T_{io}/T_{eo} agree with many of the observations in HBTX1B[1]. The model also gives the T_i profile ($T_i(r) \sim T_{io}\{1-(\frac{r}{a})^2\}^2$) which agrees with the NPA measurements in HBTX1B[1] and ZT-40M[2], and the fluorescence scattering results from HBTX1B[9]. In this paper we include finite β_θ effects, consider the electron power balance, derive scaling laws of T_{io}/T_{eo} and further examine and analyse some of the assumptions used in the original model[1]. These mainly consisted of assuming (i) a constant μ profile over a wide current range, although the F/Θ relationship changes, and (ii) the electron power loss on axis is dominated by convection, which enabled us to obtain the diffusion coefficient for the ion power loss.

Finite β_θ effects Inclusion of pressure gradients, in the so-called Modified Bessel Function Model[10], alters the μ profile required to maintain the same F/Θ values. The MBFM, modified to include pressure gradients, is used to calculate $\underline{B}$ and $\underline{j}$ distributions from which F and Θ are obtained. We find that it is β_θ, rather than the relative pressure profile, which dominates the F/Θ relationship. Results of the calculations are shown in Fig 1 for $\Theta = 1.4$ and 1.7 where it is assumed $\mu(r) = \mu(0)\{1 - (\frac{r}{a})^\gamma\}$ and γ is varied from 2 to 12. In HBTX1B, in common with other RFP's, decreasing I_ϕ is generally accompanied by an increase in β_θ, |F| and Θ. Consequently, the μ profile often remains fairly constant. For example, in HBTX1B $I_\phi \sim 80$ kA had $\beta_\theta \sim 25\%$, $\Theta = 1.7$, F = -0.2 and $I_\phi \sim 220$ kA had $\beta_\theta \sim 9\%$, $\Theta = 1.4$ and F = -0.06, both conditions requiring $\gamma \sim 10$ as used in the original ion power balance model[1]. This justifies the implicit assumption of a constant μ profile in the method

used in extracting the anomalous voltage, ΔV_ϕ, from a current scan[8]. Since $I_\phi \Delta V_\phi$ is found to dominate the ion heating[1] the inclusion of β_θ effects is crucial to the assumption of constant μ profile.

Electron Power Balance The relative profile of the diffusion coefficient, D(r), calculated from the particle balance[1] can be fitted by: $D(r) \sim D(0)\ \{1 + 7\ (\frac{r}{a})^5\}$ and where D(0) ($\sim 50 m^2 s^{-1}$) was obtained after assuming the electron conduction losses to be negligible on axis. These estimates compare well with those derived from spectroscopic measurements[5] and from turbulent convection calculations for HBTX1B[11]. The corresponding equation for the electron power balance is: $-\frac{1}{r}\frac{d}{dr}(rD\frac{d}{dr}U_e) = \eta j^2$ where $U_e = \frac{3}{2} n_e k T_e$. The resultant T_e profile, shown in Fig 2, and using a parabolic density distribution, is typical of RFP's. The profile is similar to that given by Robinson[12] using turbulent convection. The solution satisfying the boundary conditions $dT_e/dr = 0$ at $r = 0$ and $T_e = 0$ at $r = a$ can be shown to lead to: $T_{eo}^{5/2} = 6.5 \times 10^{-5}\ (I_\phi^2 Z_{eff})/(a^2 n_{eo} D(0))$. The scaling of T_{eo} with I_ϕ and n_e is similar to that found experimentally[3] (i.e. $T_{eo} \propto I_\phi^{0.8} n_e^{-0.5}$). Using HBTX1B values of $a = 0.25m$, $I_\phi = 220$ kA, $n_{eo} = 3 \times 10^{19} m^{-3}$, $D(0) = 50 m^2\ sec^{-1}$, $Z_{eff} = 2$ we obtain $T_{eo} = 215$ ev which agrees well with the measured value of 250 ± 40 eV. It therefore seems reasonable that diffusion losses dominate the electron power balance, at least on axis, as assumed in our earlier ion power balance model to obtain D(0).

Normalised Calculations of T_{io}/T_{eo} First we derive the D(0) from the electron power balance on axis. It can be shown that $D(0) = C_1 \eta(0) I_\phi^2/(6\pi^2 a^2 n_{eo} k T_{eo})$ where η is the Spitzer resistivity and C_1 is a profile constant ($C_1 = j_\phi^2(0)/[j_\phi]^2$). The diffusive power loss of the ions on axis is given by: $W_i(0) = -(\frac{1}{r})\frac{d}{dr}\{r D \frac{d}{dr} U_i\}$ (for $r \to 0$) where $U_i = \frac{3}{2} n_i k T_i$. Equating $W_i(0)$ with the non-ohmic input power, $\underline{E}.\underline{j}(0) - \eta j^2(0)$, it can be shown that:

$$T_{io}/T_{eo} = (1+\alpha)^{-1}\{C_2^{-1} V_\phi/V_p - 1\}$$

where α determines the near-axial ion temperature profile ($T_i(r) = T_{io}\ \{1 - \alpha(\frac{r}{a})^2\}$), V_ϕ is the loop voltage and $V_p = (1/\Phi)\int \eta \underline{j}.\underline{B}\ d^3x$ for the bulk plasma[6] and $C_2 = [B_\phi] j_\phi(0)/[\tilde{\eta}\underline{j}.\underline{B}]$ where $\tilde{\eta}(r) = \eta(r)/\eta(0)$. Calculations[1] yield a value of $\alpha \sim 2.5$ which is close to the $\alpha \sim 2$ as estimated from NPA measurements on HBTX1B[1] and ZT-40M[2]. Plots of β_θ, C_1 and C_2 as functions of θ are shown in Figs 3a and 3b for a selection of axial total beta's ($\beta_o = 0$, 3% and 8%) and assuming $\mu(r) = \mu(0)\{1-(\frac{r}{a})^{10}\}$, $T_o(r) \propto T_e(r) = T_{eo}\ \{1 - (\frac{r}{a})^6\}$ and $n_e(r) = n_{eo}\{1 - (\frac{r}{a})^2\}$. We note that C_2 is fairly insensitive to β_θ as it depends mostly on the μ and η profiles, in contrast to C_1 which decreases substantially with increasing β_o. Since $D(0) \propto C_1\ \beta_\theta^{-1}$ these results are in accord with the increased τ_E generally found at low I_ϕ in RFP's which also record the highest β_θ's.

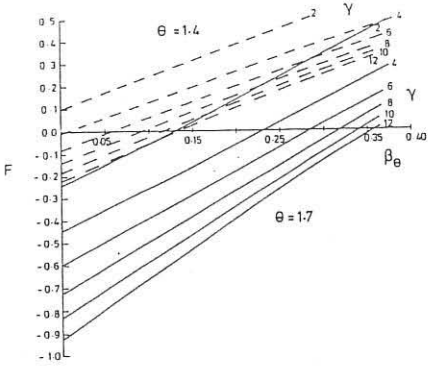

FIG. 1 Dependence of F on β_θ, for θ = 1.4 and 1.7 and selected values of γ where $\mu(r) = \mu(0)\{1-(r/a)^\gamma\}$.

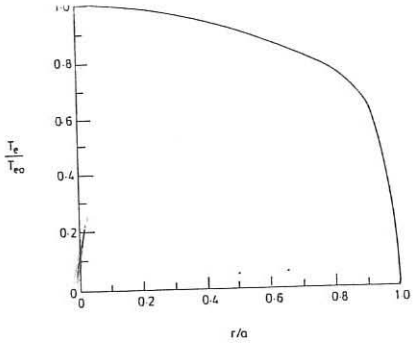

FIG. 2 Relative T_e profile where convection losses are assumed to be dominant.

FIG. 3(a) Variation of β_θ with θ for β_0 = 3% and 8%.

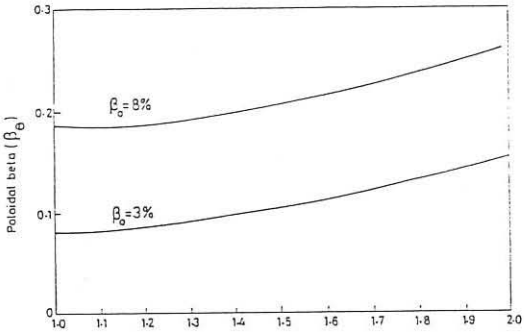

FIG. 3(b) Profile averaged constants $C_1 (=\langle j^2_\phi / [j^2_\phi] \rangle)$ and $C_2 (=[B_\phi] j_\phi(0)/[\hat{n}\underline{j}.\underline{B}])$ for β_0 = 0, 3% and 8%. These constants are used to determine D(0) and T_{io}/T_{eo}, respectively.

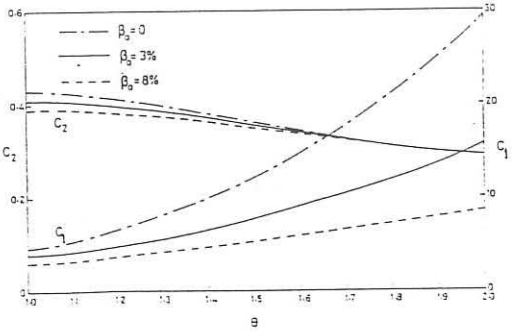

High θ Conditions The foregoing calculations of profile averaged quantities assume axisymmetry. However, at elevated θ's ($\theta \gtrsim 1.7$) helical plasmas can be observed[13] and are often accompanied by sawteeth-like behaviour in soft X-rays and T_i and a large increase in magnetic fluctuations, $\tilde{B}$. The increase in loop voltage is higher than expected from calculations assuming axisymmetry with a consequent reduction in τ_E. For example, in HBTX1B (220 kA and edge limiter tiles in position), increasing θ from 1.35 to 1.75 resulted in V_ϕ increasing from $\sim$ 30V to $\sim$ 100V[13] much greater than the $\sim$ 40V expected for axisymmetric plasmas. The results suggest that it is the greatly increased $\tilde{B}$ rather than increased velocity fluctuations which sustains the RFP configuration in these conditions, with the consequence of greater field line stochasticity and reduced confinement and a smaller increase in ion heating from viscous damping of the fluid velocity fluctuations.

Conclusions The basis of an earlier ion power balance model have been further analysed and some of the assumptions justified. Profile averaged quantities have been derived allowing generalised expressions for T_{io}/T_{eo} and D(0) to be used on all RFP's. Results from HBTX1B and ZT-40M support the model. Different physics apply at elevated θ's; in particular the resulting helical configurations, enhanced loop voltage, reduced τ_E and increased $\tilde{B}$.

References

(1) P G Carolan, A R Field, A Lazaros et al, Proc Int Sch of Plasma Physics, Varenna, III 1071 (1987).
(2) G A Wurden et al this conference.
(3) B Alper et al (Proc of 11th Int Conf on Plasma Physics and Contr. Nucl. Fusion Res. (IAEA, Vienna), Vol 2, 339 (1987).
(4) P G Carolan et al (Proc of 10th Int Conf on Plasma Physics and Contr. Nucl. Fusion Res. (IAEA, Vienna), Vol 2, 449 (1985).
(5) P G Carolan et al Proc 14th EPS Conf (Madrid) II, 515 (1987).
(6) T R Jarboe and B Alper Physics of Fluids 30, 1177 (1987).
(7) H Y W Tsui Proc 14th EPS Conf (Madrid) II, 473 (1987).
(8) B Alper et al, Plasma Physics and Contr. Fusion (to be publ).
(9) M J Forrest et al Rev Sci Instrum (to be publ).
(10) S Ortolani Proc Int Sch of Plasma Physics, Varenna, II, 513 (1983).
(11) H Y W Tsui et al Culham Laboratory Memorandum CLM-M110 (1985).
(12) D C Robinson Proc 3rd Top. Conf. Pulsed High Beta Plasmas, 273 (1976).
(13) H Y W Tsui and J A Cunnane Plasma Physics and Contr. Fusion (to be publ)

COHERENT OSCILLATIONS IN HBTX1B REVERSED FIELD PINCH PLASMAS

R J Hayden* and B Alper

Culham Laboratory, Abingdon, Oxon, OX14 3DB, UK
(UKAEA/Euratom Fusion Association)

* University College, Cork, Ireland

ABSTRACT

Large amplitude low frequency oscillations which are in phase across the minor radius have been observed in soft X-ray emission since the removal of limiters from HBTX1B Reversed Field Pinch for plasmas with small field reversal. These oscillations, due to variations in electron temperature, are in phase with edge magnetic field measurements and in antiphase with oscillations in plasma resistivity and ion temperature. They occur near the lowest measured values of plasma resistance and therefore do not appear to degrade plasma confinement.

1. SOFT X-RAY OSCILLATIONS

On HBTX1B since the removal of limiters large amplitude coherent oscillations in the frequency range 750 Hz to 2 kHz have been observed in soft X-ray (SXR) emission, see example in figure 1, for plasmas at all toroidal currents, I_ϕ , from 70 kA to 512 kA, and low values of F ($=B_\phi(\text{wall})/\bar{B}_\phi$). They occur when the measured plasma resistance is close to its lowest values. The oscillations are observed using a twenty chord surface barrier diode (SBD) array at one toroidal location. The diodes are fitted with 5000 Å copper foils and so, for the range of electron density (n_e), impurity mix, electron temperature (T_e) and confinement time in HBTX1B, are predominantly sensitive to line radiation from oxygen VII (1s2-1s2p) at 574 eV. The fractional abundance of this species is almost constant under HBTX1B conditions, hence the SBD signal intensity (I_{SBD}) depends only on the excitation rate coefficient at constant n_e. For the electron temperature range considered here, $I_{SBD} \propto n_e^2 T_e^2$ [1].

The oscillations with typical peak-to-peak amplitude of ~30% of the signal are clearly visible on all chords of the SBD array and are in phase across the plasma minor radius. Chord integrated radial profiles and their corresponding Abel inversions have been calculated at the peak and the trough of oscillations and show no change in shape.The data show no evidence of contraction of the plasma column during these large oscillations, nor the existence of an inversion radius in the SXR emission. The ratio of rise to to fall time of the oscillations is typically 3:1 but on some discharges this ratio is as large as 10:1. The line averaged electron density measured by a three chord interferometer remains constant and the relative impurity density, inferred from a polychromator, does not change, suggesting that the oscillations in SXR emission are due to variations in T_e. This interpretation is supported by oscillations in antiphase at the same frequency in the plasma resistivity, calculated using helicity balance and the Modified Bessel Function Model (MBFM).

2. COMPARISON WITH OSCILLATIONS IN OTHER PARAMETERS

The large scale modulation on the SXR flux is accompanied by oscillations at the same frequency on discrete magnetic field pick-up edge coils. These data show oscillations with mainly m=1, |n|=5 and non-rotating behaviour. Some m=0 structure is present but is much weaker, [2]. In figure 2, in a discharge at 310 kA, the SXR emission (top trace) is compared with data from an m=1 cosine wound Rogowski coil (bottom trace). We observe a phase where the m=1 mode amplitude and SXR signal increase, which we interpret as an increase in T_e, followed by a more rapid collapse phase on both traces perhaps due to some magnetic reconnection process where T_e falls.

No measureable fluctuations in the poloidal magnetic field at the wall, $B_\theta(a)$, occur. The toroidal field at the wall, $B_\phi(a)$, exhibits coherent oscillations of about 30% around a mean value of 10 mTesla. During the fall phase of SXR oscillations increases in toroidal flux of 6% are observed. Quasi-linear calculations [3] of the flux generated by fluctuations with the m and n numbers quoted above indicate that the oscillations increase the reversed toroidal flux at the wall by 1 mTesla, or 10% of the mean value. The corresponding decrease in poloidal flux at the wall is only 0.6 mTesla, or 0.3% of the mean value.

Coherent oscillations have also been observed on HBTX1B with limiters and other experiments, but only for deeply reversed, turbulent and resistive plasmas, eg [4] and references therein. These oscillations are also accompanied by closed F-θ trajectories, see figure 3, which are similar on all experiments. The experiments operate to the right of the locus of Taylor minimum energy Bessel Function Model (BFM) states due to both finite β_θ and non-flat μ-profiles, where $\mu=j.B/B^2$. During the oscillations in SXR emission the discharges describe closed trajectories in the F-θ plane suggesting that the oscillations are caused by the recovery of an initial state from which the plasma departs periodically. An expanded trajectory (see inset) shows,using the MBFM, that as the SXR emission falls the current profile is broadening and is peaked when the SXR emission is a maximum. From the finite width of the trajectory we infer a phase difference between the oscillations in $\langle B_\phi \rangle$ and $B_\phi(a)$.

If the SXR oscillations are due to changes in T_e in phase across the plasma minor radius, it raises the question of where the electron energy goes during a fall in SXR emission since it does not appear at outer radii, ie. there is no inversion radius. Impurity lines representative of edge T_e viewed by a polychromator confirm that T_e does not increase near the edge. Measurement of ion temperature (T_i) versus time using a Neutral Particle Analyser (NPA), see figure 2, shows that the peak ion temperature oscillates in antiphase to the SXR emission. Thus the observed variations in T_i could maintain the energy density constant locally and thus not require the outward transport of energy or an inversion radius during the fall phase of an oscillation.

To explain the F-θ trajectory by a change in β_θ would require, in the example shown, an increase in β_θ from about 6% at the trough to 8% at the peak of the SXR emission. After allowing for the oscillations in T_i, this would require excursions in T_e of ±150 eV around a mean of 430 eV, as there is no evidence for a change in either n_e or B_θ. Since the SXR emission is proportional to T_e^2, the amplitude of the SXR oscillations indicate

excursions in T_e corresponding to <50 eV. This suggests, when the measured excursions in T_i are included, that β_θ remains constant during an oscillation period and consequently that the F-θ trajectory is predominately due to changes in the current profile which are not detected using the SBD array. If the μ-profile is described by $\mu(r)=\mu(0)[1-(r/a)^\nu]$ changes in ν from 6 to 7 would explain the change in F and θ.

A remarkable feature of the SXR signals is the rapid fall in signal intensity across the plasma radius when the applied loop voltage is removed even though I_ϕ takes several milliseconds to decay and n_e remains constant. This reduction in SXR flux coincides with a sharp fall in the photon count rate observed using a Si(Li) detector filtered to detect bremsstrahlung radiation above 1 keV in photon energy, suggesting a rapid fall in T_e when ohmic input power to the plasma is stopped, even though the power input to the plasma remains approximately constant at 7 MW via a decrease in the magnetic energy. The width of the radial SXR emission profile does not change during the run-down period. A calculation of the MBFM Cut-off Radius indicates no change in the μ-profile either. This fall in T_e coincides with an increase in T_i, see figure 2, again indicating that some mechanism may be trying to maintain a constant kinetic energy density during a discharge even when V_ϕ is turned off.

The time taken for the rapid changes in T_i seen in these two phenomena indicates that the ions are not heated classically via collisions with the electrons [5]. If the indicated fall in T_e is due to some turbulent reconnection process then the ions may be heated by an increase in MHD activity during this period.

Simulations [2] show that many aspects of the coherent magnetic oscillations (m=1, n=5, wall locking, 1ms timescale) seen on HBTX1B at low F can be explained by a resistive wall mode resonant on axis. The growth rate of this mode is very sensitive to both wall position and plasma profiles and could have been triggered by the removal of limiters, bringing the marginal point for the mode inside the shell where it can grow on the liner timescale. As the mode amplitude increases the marginal point may move outside the shell where the mode is stabilised, producing the observed cyclic behaviour.

3. CONCLUSIONS

Large amplitude oscillations in soft X-ray emission, in the frequency range 0.8 to 2.0 kHz, have been observed since the removal of limiters from HBTX1B for plasmas with low F. The emission oscillates in antiphase with T_i and the plasma resistivity suggesting that the SXR oscillations are due to fluctuations in T_e. The SXR emission falls rapidly when the applied electric field is removed while T_i increases during this period. The inverse behaviour of ion and electron temperature seen in these two phenomena suggest a trend towards constant β_θ during a discharge. The large scale coherent oscillations observed on a range of plasma parameters occur when the measured plasma resistance was near its lowest values. The oscillations are interpreted as a resistive wall mode whose marginal point has been brought inside the shell by a small change in plasma profiles caused by the removal of limiters.

REFERENCES
[1] W Lotz, Z. Phys. 216, (1986), 241.
[2] J A Cunnane et al., Physics of Mirrors, Reversed Field Pinches and Compact Tori, Varenna 1987, Vol 3, p1017.
[3] C G Gimblett, Culham Laboratory, Private Communication, Feb. 1988.
[4] V Antoni, Physics of Mirrors, Reversed Field Pinches and Compact Tori, Varenna 1987, Vol 1, p 431.
[5] P G Carolan et al, Proc 14th EPS, Madrid 1987, Part II, p 469.

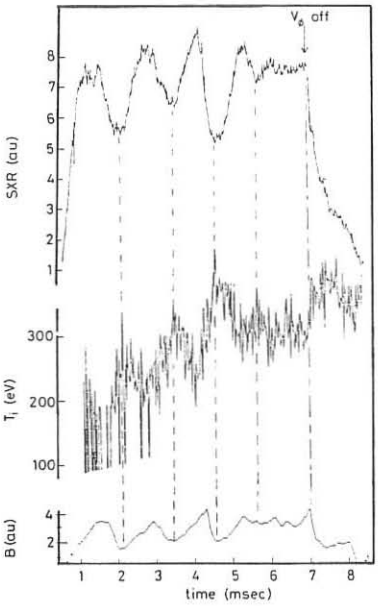

Fig. 2 SXR emission, ion temperature and m=1 cosine wound Rogowski coil signal versus time at 310 kA.

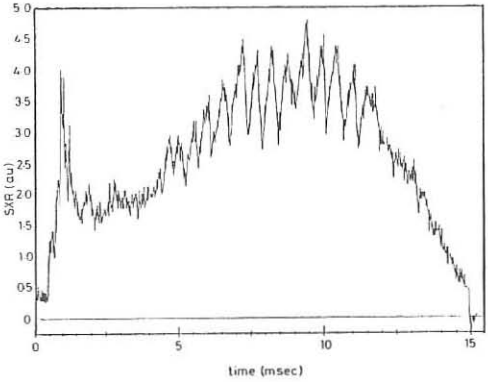

Fig. 1 Oscillations in SXR emission at 80 kA and shallow reversal without limiters.

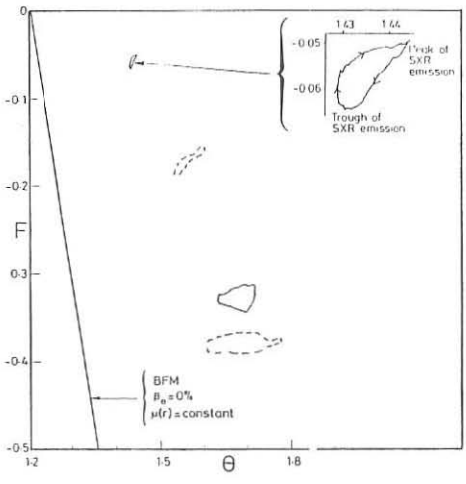

Fig. 3 Closed F-θ trajectories on HBTX —— and on ETA BETA II---. Insert shows HBTX trajectory in relation to SXR emissions.

FLUCTUATION-DRIVEN DIFFUSION AND HEATING IN THE REVERSED FIELD PINCH

H Y W Tsui and D E Evans
Culham Laboratory, Abingdon, Oxon, OX14 3DB, UK
(UKAEA/Euratom Fusion Association)

INTRODUCTION This paper explores the possibility that fluctuations can provide a mechanism to account for the anomalous diffusion, ion heating and loop voltage observed in reversed field pinch plasma. There is spectroscopic evidence for outward diffusion of plasma in the Culham reversed field pinch experiment HBTX. The diffusion coefficient $D \simeq 100$ $m^2 s^{-1}$ is significantly greater than can be explained by collisions alone [1]. Fluorescent scattering [2] reveals a population of neutral deuterium extending far into the discharge, and this could provide a source of new plasma to balance the outward flow implied by the radial diffusion [3]. A process of this kind, that is, inflow of neutrals balancing outflow of plasma, is consistent with a steady radial plasma-fluid velocity. However, in the RFP, fluctuations in the magnetic field and in the fluid velocity have been invoked with some success to explain the dynamo [4] that sustains the reversed field configuration. It has been shown [5] that the departure from the fully relaxed Taylor state is associated with non-Ohmic energy loss from the dynamo activity which may provide ion heating. An imperfect boundary with $\underline{B}.\underline{n} \neq 0$, which can enhance dynamo activity through leakage of helicity, increases this non-Ohmic energy throughout [6]. This has been observed in experiments as increases in the loop voltage [7] and ion temperature [8]. Here, the equations governing the processes of diffusion and heating by fluctuations are established. A companion paper [9] compares some predictions of the theory with experiment.

As in previous work, the influence of fluctuating quantities in standard equations under steady state conditions is investigated. We introduce into the Boltzmann equation a source term $S(\underline{x},t)\delta(\underline{v})$, which means particles are born with no velocity. The fact that in HBTX the neutral population actually has temperature close to that of ions is ignored. It is expected that the finite neutral temperature has no global effect but may influence the ion temperature profile. By integration over velocity in the usual way (see for example, [10]) we obtain the 2-fluid moment equations for continuity, momentum balance, and thermal energy balance. Then variables are separated into mean and fluctuating parts and averages are formed. Our attention is restricted to plasma confined within a torus in which mean variables are axisymmetric so that they vary only in the radial direction.

CONTINUITY EQUATION With $\langle \ldots \rangle$ denoting the average over time and a flux surface, the continuity equation is separated into mean and fluctuating components by treating particle density and fluid velocity as sums of mean and fluctuating parts: $n = n_o + \tilde{n}$, $\underline{u} = \underline{u}_o + \tilde{\underline{u}}$, and letting

the radial mean fluid velocity $\underline{u}_o.\nabla r = 0$: $\partial n_o/\partial t + \nabla.\langle \tilde{n}\underline{\tilde{u}}\rangle = S$; $\partial \tilde{n}/\partial t + \nabla.(n_o\underline{\tilde{u}}) = 0$. Recognizing that $\underline{\Gamma} = \langle \tilde{n}\underline{\tilde{u}}\rangle$ is a non-vanishing particle flux, and setting $\partial n_o/\partial t = \partial\langle\tilde{n}^2\rangle/\partial t = 0$ to describe a steady state, allows us to write the foregoing equations as

$$\nabla.\underline{\Gamma} = S; \qquad n_o\langle\tilde{n}\nabla.\underline{\tilde{u}}\rangle = \underline{\Gamma}.\nabla n_o \quad . \qquad ...(1)$$

MOMENTUM EQUATIONS We now aim to write equations for kinetic and thermal energy balance for ions and electrons separately. Without loss of generality, the mean fluid velocity of the ions will be deemed to vanish so that the net electric current density = $-en_o\underline{u}_{eo}$. Ions are assumed to be singly charged, viscosity and radiation are ignored, and pressure is treated as a scalar.

The momentum balance equation for the ion and electron fluids are:

$$nm_i(\partial\underline{u}_i/\partial t + \underline{u}_i.\nabla\underline{u}_i) = en(\underline{E} + \underline{u}_i x\underline{B}) - \nabla p_i - \underline{R}_{ie} - m_i\underline{u}_i S \qquad ...(2a)$$

$$nm_e(\partial\underline{u}_e/\partial t + \underline{u}_e.\nabla\underline{u}_e) = -en(\underline{E} + \underline{u}_e x\underline{B}) - \nabla p_e - \underline{R}_{ei} - m_e\underline{u}_e S \qquad ...(2b)$$

The only new terms in these equations involve S and represent the rate of change of momentum due to birth of new plasma with zero mean velocity. The negative sign implys that ions lose momentum to newly born plasma to accelerate it to the average velocity. In other words, since the rate of appearance of new plasma exactly balances the loss of old plasma, which is accompanied by a loss of momentum, work must be done in compensation. This says that the appearance of newly ionized material gives rise to an effective resistivity, η_t, additional to the Spitzer quantity. More explicitly, by converting eq 2b into Ohm's law form, $-\underline{R}_{ei}/en$ can be identified with $\eta\underline{j}$, involving Spitzer resistivity, while the other term involving S becomes $(m_eS/e^2n^2)\underline{j} = \eta_t\underline{j}$.

PLASMA HEATING BY DYNAMO ACTION We next form the dot product of $\underline{u}_i$ and $\underline{u}_e$ with eq 2a and 2b respectively, and add, setting $\partial/\partial t = 0$ for steady state, to get

$$(\underline{E}.\underline{j} - \eta j^2) = \underline{u}_i.\nabla p_i + \underline{u}_e.\nabla p_e + (m_iu_i^2 + m_eu_e^2)S + n[\underline{u}_i.\nabla(\tfrac{1}{2}m_iu_i^2) + \underline{u}_e.\nabla(\tfrac{1}{2}m_eu_e^2)] \quad . \qquad ...(3)$$

The term $(m_iu_i^2 + m_eu_e^2)S = 2n(\tfrac{1}{2}m_iu_i^2 + \tfrac{1}{2}m_eu_e^2)(S/n)$ which is the rate of change of fluid kinetic energy due to S, consists of two halves. The first replenishes the loss of fluid kinetic energy to the particle recycling at a rate S/n. The second which appears as heating (see eq 6) is the work done to overcome the drag force exerted by the newly born zero momentum particles on the fluid.

Once again separating variables into their mean and fluctuating parts, we average to obtain an expression for the dynamo power available for non-Spitzer heating when fluctuations in resistivity and temperature are neglected, namely

$$\langle \underline{E}\cdot\underline{j} - \eta j^2\rangle = \nabla\cdot[\langle \tilde{p}_i\tilde{\underline{u}}_i\rangle + \langle \tilde{p}_e\tilde{\underline{u}}_e\rangle + (\tfrac{1}{2}m_i\tilde{u}_i^2 + \tfrac{1}{2}m_e\tilde{u}_e^2)\langle \tilde{n}\tilde{\underline{u}}\rangle]$$
$$+ \nabla\cdot\tfrac{1}{2}m_e u_{eo}^2\langle \tilde{n}\tilde{\underline{u}}\rangle - \langle \tilde{p}_i\nabla\cdot\tilde{\underline{u}}_i\rangle - \langle \tilde{p}_e\nabla\cdot\tilde{\underline{u}}_e\rangle$$
$$+ (\tfrac{1}{2}m_i\tilde{u}_i^2 + \tfrac{1}{2}m_e\tilde{u}_e^2)S + (\tfrac{1}{2}m_e u_{eo}^2)S \quad . \qquad ...(4)$$

We note by virtue of quasi-neutrality $\langle \tilde{n}\tilde{\underline{u}}_i\rangle$ and $\langle \tilde{n}\tilde{\underline{u}}_e\rangle$ are equal. So the particle flux $\underline{\Gamma} = \langle \tilde{n}\tilde{\underline{u}}\rangle = \langle \tilde{n}\tilde{\underline{u}}_i\rangle = \langle \tilde{n}\tilde{\underline{u}}_e\rangle$.

The power given by eq 4 constitutes only a part of the total dynamo power, which, using Poynting's theorem, can be shown to be the sum of a part deposited locally and available for heating, and an energy flux [6]:

$$-\langle \tilde{\underline{u}}\times\tilde{\underline{B}}\rangle\cdot\underline{j}_o = \langle \underline{E}\cdot\underline{j} - \eta j^2\rangle + \nabla\cdot\langle \tilde{\underline{E}}\times\tilde{\underline{B}}\rangle \qquad ...(5)$$

The lhs of the equation above will be recognized as the total dynamo power, while the first term on the right hand side is the non-Spitzer heating and the second is the transport of the dynamo power.

The right hand side of eq 4 sums all the processes by which the dynamo changes energy locally. The divergence terms account for influx and outflow of energy; those explicitly involving S are the 'drag' force heating discussed above, and it can be shown using eq 1 that

$$-\langle \tilde{p}_i\nabla\cdot\tilde{\underline{u}}_i + \tilde{p}_e\nabla\cdot\tilde{\underline{u}}_e\rangle = (T_i + T_e)\,\underline{\Gamma}\cdot\nabla n_o/n_o$$

corresponding to a thermal expansion/compression of outflowing plasma. This exchange of energy between heat and fluid is a new condition to the dynamo.

The dynamo generates non-Spitzer heating of electrons and ions alike. Although the electrons continue to acquire energy ohmically as well, ions have almost no other source of heating but the dynamo. But scrutiny of eq 4 reveals that heating is a function of S such that when S vanishes so does every term on the rhs of the equation, implying that particle recycling is necessary for this ion heating mechanism. It is dynamo heating of ions that prevents the plasma from reaching the fully relaxed state and determines the $\mu = \underline{j}_o\cdot\underline{B}_o/B^2$ profile.

THERMAL ENERGY BALANCE Turning next to the equations of thermal energy balance we have, for either ions or electrons, neglecting the heat conduction term,

$$n(\partial/\partial t + \underline{u}\cdot\nabla)3T/2 = Q - p\,\nabla\cdot\underline{u} + \tfrac{1}{2}mu^2S - (3T/2)S \quad . \qquad ...(6)$$

As is customary, Q represents the gain in energy by collisions with the opposite species, where $Q_i + Q_e = \eta j^2$. The first of the two terms associated with the plasma source $\frac{1}{2}mu^2S$, is the rate of conversion of kinetic energy into thermal energy, due to appearance of new particles. The second, $-(3T/2)S$, accounts for the fact that the plasma is obliged to heat the newly born particles, and in doing so, is cooled by the heat they take up.

CONCLUSION A mechanism by which fluctuations in fluid velocity and density could account for particle diffusion and heating has been identified.

A mathematical model for a steady state plasma like HBTX, whose radially-outward particle flux arising from and driven by fluctuations is balanced by a source of new plasma internal to the discharge has been constructed by taking moments of the Boltzmann equation with the source term $S(\underline{x},t)\delta(\underline{v})$. The particle source within the plasma gives rise to a new resistivity $\eta_t \equiv m_e S/(en)^2$ which adds only a few percent to the Spitzer quantity in normal HBTX plasma [9]. It is different from the resistivity attributed to edge helicity loss. The work done in overcoming the drag force exerted on the fluid by the new zero-momentum particles provides non-Ohmic ion heating, and though it originates in the dynamo, this heating does not consume the whole dynamo power, which, through a Poynting vector term, also sustains the field reversal.

The throughput to ion heating prevents the plasma from reaching the fully relaxed state, determines the μ-profile, and provides an explanation for the experimental observation that the increase in loop voltage by increased helicity loss at the boundary results in ion heating. It is shown that the expansion or compression of the out-flowing plasma contributes to the dynamo by exchanging energy between heat and fluid motion, and according to this theory the fully relaxed Taylor state is only achievable when there is no particle recycling.

REFERENCES

[1] P G Carolan, C A Bunting, A M Manley, A Patel: in Contr. Fus. and Plasma Physics (Proc. of the 14th Eur. Conf., Madrid, Spain, 1987) Vol IID Pt. II 515

[2] D E Evans, M J Forrest, M G Nicholson, D D Burgess, P G Carolan and P Gohill: Rev Sci Instrum 56 (1985) 1012

[3] P G Carolan, A Lazaros, J W Long, M G Rusbridge: this conference

[4] H R Strauss: Phys. Fluids 28 (1985) 2786

[5] H Y W Tsui, A A Newton, M G Rusbridge: in Contr. Fus. and Plasma Heating (Proc. 13th Euro Conf, Schliersee, FRG, 1986) Vol 10C Part 1, 345

[6] H Y W Tsui: in Contr. Fus. and Plasma Phys. (Proc. 14th Euro Conf, Madrid, Spain, 1987) Vol IID Pt. II 473

[7] B Alper et al: to be pub. in Plasma Physics and Contr. Fusion

[8] P G Carolan, A R Field, A Lazaros, M G Rusbridge, H Y W Tsui, M K Bevir: in Contr. Fus and Plasma Physics (Proc. 14th Euro Conf, Madrid, Spain, 1987) Vol IID Pt.II 469

[9] D E Evans, H Y W Tsui: this conference

[10] J Wesson: 'Tokamaks' 1987 Clarendon Press, Oxford pp 50

CALCULATING THE MHD EQUILIBRIUM AND STABILITY OF A PLASMA WITH ANISOTROPIC PRESSURE IN AXISYMMETRIC OPEN TRAPS

Drozdov V.V., and Martynov A.A.
Keldysh Institute of Applied Mathematics
USSR Academy of Sciences,
Moscow

I. Equilibrium. In the axisymmetric shearless system of magnetic confinement with field $\bar{B} = \nabla\Psi \times \nabla\varphi$ and anisotropic pressure $p_{\perp,\parallel} = p_{\perp,\parallel}(\Psi, B)$ the MHD plasma equilibrium is described by the equation [1]

$$(1) \qquad \nabla\cdot\left(\frac{\sigma}{r^2}\nabla\Psi\right) = -\frac{\partial p_\parallel}{\partial\Psi}, \quad \sigma = 1 - \frac{1}{B}\frac{\partial p_\parallel}{\partial B}.$$

The equilibrium is calculated by basing on the numerical solution of equation (1) in the domain bounded by the fixed (not varying with growing pressure) magnetic surfaces: separatrix Γ_s and ideally conducting wall Γ_w, on which $\Psi = 0$ and $\Psi = \Psi_w$ (Fig. 1). In the vacuum domain between Γ_w and the actual plasma boundary Γ_p, where $\Psi = \Psi_p$, the homogeneous equation (1) with $p_\perp = p_\parallel = 0$ is satisfied. It is assumed that the system is symmetric with respect to the plane Γ_m and the energy flow through the butt-end Γ_T is absent: $\bar{B} \times \bar{n}_T = 0$.

The form of the functions $p_{\perp,\parallel}(\Psi, B)$ used in the calculations was determined by a choice of the distribution function $f(\mathcal{E}, \mu, \Psi)$ from the class of functions of the form $f = G(\mathcal{E}, \Psi)\cdot F(\nu, \Psi)$, $\nu = \mu/\mathcal{E}$, $F = 0$ for $\nu < \nu_0 = 1/B_{max}(\Psi)$. Three choices of the function $F(\nu, \Psi)$ were considered:

$$(2) \quad F_1 = const, \quad \nu_0 < \nu < 1/B,$$

(3) $F_2 = (\nu - \nu_0)/\nu$,

(4) $F_3 = \nu - \nu_0$.

In the general expression

$$p_{\perp,\parallel}(\Psi, B) = \sum_i \left(p_{\perp max}(\Psi) \cdot p^{B}_{\perp,\parallel}(B/B_{min}, B_{max}/B_{min}) \right)_i$$

for each kind of particles i , that differ by location in the system, the $p_{\perp max}(\Psi)$ describes the "radial" function of pressure while the functions $p^{B}_{\perp,\parallel}$ are determined by the choice of $F(\nu, \Psi)$.

For solving the equilibrium problem we used a modification of the numerical method [2] based on the computational grids adaptable to the magnetic field lines $\Psi(r, z) = const$.

2. Stability conditions. We use the sufficient and necessary conditions for stability of axisymmetric equilibria, that are based on estimates of the kinetic term in the Kruscal-Oberman functional from above and below [3]. The stability problem is reduced to determining the property of positivity of respective quadratic forms: the two-dimensional forms for finite values of wave number m and a series of one-dimensional forms (on each magnetic surface) for small-scale modes $m \to \infty$ [4, 5].

The properties of distribution functions (2)-(4) were compared with respect to the mirror instability following from a negative value of $\tau = 1 + B^{-1} \partial p_\perp / \partial B$. In the zone of small field strength in a cusp the requirement $\tau > 0$ restricts the pressure from above while the requirement of the flute mode stability - from below. As a result, for distribution functions with a sufficiently high degree of anisotropy (in particular, for function (4)) there are no stable profiles $p_{\perp max}(\Psi)$ near $B = 0$. The function (2) is not physical and exibits a nonregular behaviour of

pressure near magnetic mirrors where also $\tau<0$. In the computations considered here the distribution function (3), free from the above faults, was used in a cusp, and the function (4) was used in a main trap. A portion of general particles was assumed small.

3. Computational results. The "radial" pressure profiles $p_{\perp max}^{t}(\Psi)$ in an external part of the main trap $(\Psi>\Psi_*)$ and $p_{\perp max}^{c}(\Psi)$ in an internal part of a cusp $(\Psi<\Psi_*)$ were optimized [5]. As a result the maximal small-scale mode limits β_t^{∞} with respect to stability were determined, and the minimal pressure $p_{\perp max}^{c}(\Psi_{ad})$ near zero field in a cusp was obtained for different β_c. Here $\beta_i = 2p_{\perp max}^{i}(\Psi_*)/B_i^2$, B_i is the minimum of the vacuum magnetic field strength at the plasma-vacuum boundary, $i=t,c$; Ψ_* describes the location of pressure maximum; Ψ_{ad} describes size of cusp domain where the adiabatic law is violated. In the computations under consideration $\Psi_p = 0.5\Psi_w$, $\Psi_* = 0.5\Psi_p$, $\Psi_{ad} = 0.001\Psi_p$.

Figures 2 and 3 show the stability deterioration for the tandem mirror-cusp system with growing β : a stabilizing role of the cusp decreases (β_t^{∞}/β_c drops), the plasma losses near zero field increase ($p_{\perp max}^{c}(\Psi_{ad})/p_{\perp max}^{c}(\Psi_*)$ grows). For the modes with finite m the stability limits β_t^{m} are determined by increasing proportionally the pressure in the tandem mirror. For sufficiently large $\beta_c \gtrsim 0.05$, when unstable displacements become essentially unflute, the pressure limits appreciably differ at finite m from $m\to\infty$. For example, at $\beta_c = 0.19$ we have $0.64<\beta_t^5<0.7<\beta_t^3<0.75<\beta_t^1<0.8$, $\beta_t^{\infty}=0.4$.

REFERENCES

1. Zakharov L.E., Shafranov V.D. - In: Problems of the Plasma Theory. M.: Energoatomizdat, 1982, vyp. 11, p.118.
2. Degtyarev L.M., Drozdov V.V. Comp. Phys. Reports, 1985, v.2, p.343.

3. Hall L.S., McNamara B. Phys. Fluids, 1975, v.18, p.552.
4. Drozdov V.V., Martynov A.A. Plasma Physics, 1986, v.12, vyp.12, p.1429.
5. Drozdov V.V., Martynov A.A. Preprint, Keldysh Inst. Appl. Math., Ac.Sci.USSR, 1987, N 16.

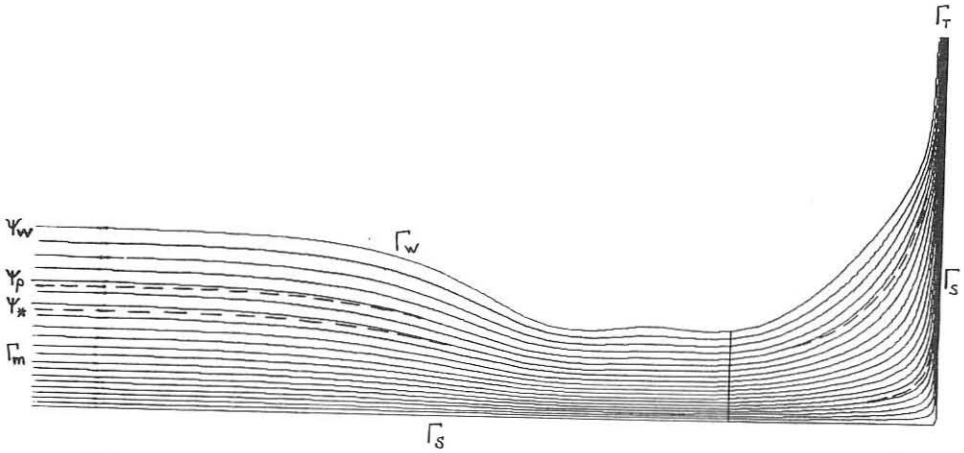

Fig. 1. Magnetic field lines for MHD equilibrium with $\beta_c \approx \beta_t^{\infty} \approx 0.5$ in tandem mirror-cusp system. Dotted lines - vacuum field lines.

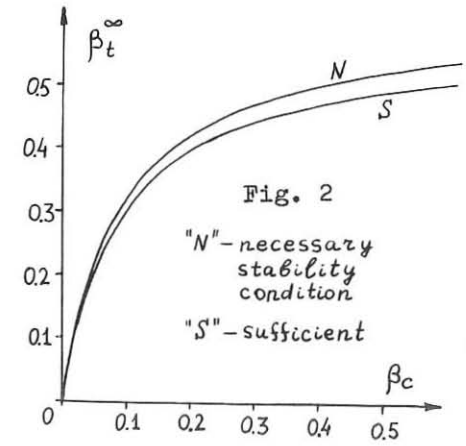

Fig. 2

"N" - necessary stability condition

"S" - sufficient

Fig. 3

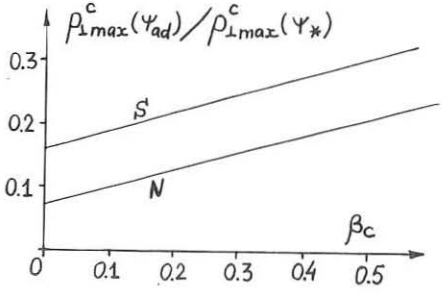

PARTICLE BALANCE STUDIES BY SPECTROSCOPIC METHOD ON THE TANDEM MIRROR GAMMA 10

N. Yamaguchi, S. Adachi, T. Cho, M. Hirata, H. Hojo, M. Ichimura, Y. Imai, M. Inutake, K. Ishii, A. Itakura, J. Jeong, T. Kariya, I. Katanuma, Y. Kiwamoto, T. Kondoh, A. Mase, S. Miyoshi, Y. Nakashima, T. Saito, K. Sawada, F. Tsuboi, D. Tsubouchi K. Yatsu, K. Okazaki† and Y. Sakamoto†

Plasma Research Center, University of Tsukuba, Tsukuba, Ibaraki 305, Japan
†The Institute of Physical and Chemical Research, Wako, Saitama 351-01, Japan

INTRODUCTION

Particle confinement in a tandem mirror device involves the suppression of both axial and radial losses. Long axial confinement has been achieved in thermal barrier experiments on TMX-U[1] and GAMMA10[2]. For the next step after the establishment of long axial confinement the radial transport becomes important. The nonambipolar particle flux can be measured in terms of a net current flowing into end plates. The scaling of nonambipolar radial confinement time, $\tau_{\perp}^{NA}$, has been investigated with respect to potentials[2,3]. The behavior of $\tau_{\perp}^{NA}$ is explained by the neoclassical theory and the nonambipolar radial transport can be suppressed by floating the end-plates in GAMMA 10[4]. The residual particle losses are ambipolar losses which cannot be measured by the particle current measurement directly because it consists of equal ion and electron fluxes in the ambipolar transport. We have investigated ambipolar losses by combining the ionization source measurement and the total particle balance. The spectroscopic studies on impurities in GAMMA 10 plasmas will also be described briefly.

PARTICLE BALANCE IN UNPLUGGED CASE

The ion particle balance equation is written neglecting the contributions of impurities, i.e., Z_{eff} is nearly equal to unity, as

$$e \frac{dN}{dt} = I_S - I_{\parallel} - I_{\perp}^{NA} - I^{A} \quad \cdots \quad (1)$$

where N is the total number of plasma particles in confinement region, I_S is the ionization source current, $I_{\parallel}$ is the axial ion-loss current, $I_{\perp}^{NA}$ is the radial nonambipolar-loss current and I^{A} is the ambipolar-loss current. The term I^{A} is determined as the residual loss current required to balance the equation. The ionization source I_S can be estimated from $H\alpha$ emissivity and the consideration of atomic processes including collisional-radiative model[5]. $H\alpha$ detectors, consisted of a collection lens, an interferometric filter and a photodiode are placed

at the central cell and other part of the machine to view a plasma radially. The axial observation of Hα emission from the machine end occasionally. Each Hα detection system is absolutely calibrated by using a standard lamp. The cross-calibration with laser fluorescence spectroscopy has been carried out recently.

At first the particle balance has been investigated in the case where the particle source and the power source are localized only in the central cell and there is no axial-plugging. The plasma is started up by injecting a short pulse gun-produced plasma from both ends of GAMMA 10 and is sustained by applying an ICRF pulse of 9.6 MHz frequency together with gas puffing. Though the ICRF antennas are located at both ends of the central cell, only the east antenna is excited in this case. The central cell line density, the central chord Hα brightness at the central cell and both end-loss ion fluxes are shown in Fig. 1. The net current due to nonambipolar radial transport is negligible in this case, because the end plates are floated. The radial profile of Hα emissivity has been obtained through Abel-inversion of measured radial Hα brightness profile. The radial end-loss flux profile has been measured by using movable end-loss-analyzers. In the steady state the axial loss current nearly equal to the source current in the core region of which the radius is smaller than one half of the central cell limiter radius (R_L=18cm), for example I_s=7.3A and $I_{\parallel}$=7.5A at 12ms. It is confirmed that ambipolar losses are small in the unplugged case.

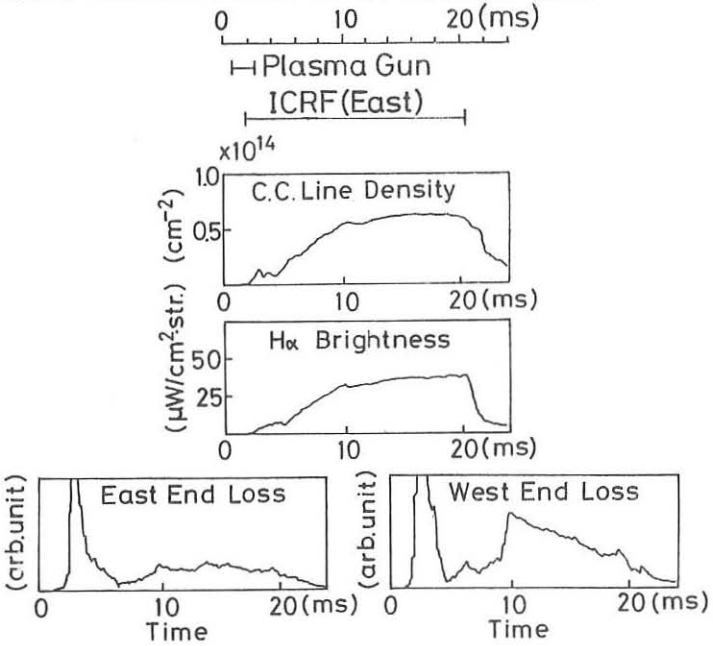

Fig.1 Line density, Hα brightness and end losses for unplugged case.

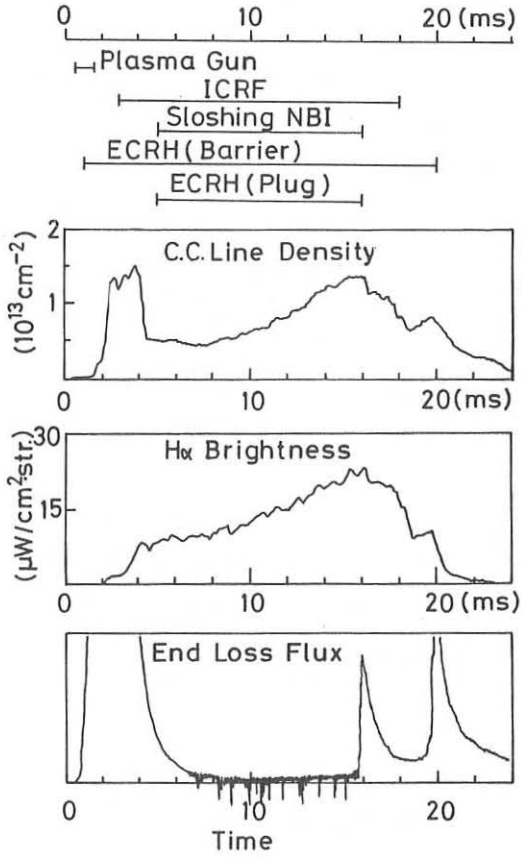

Fig.2
Central cell line density, Hα brightness and end loss flux together with the time sequence. The reduction of axial ion loss can be seen during the ECRH (plug) pulse.

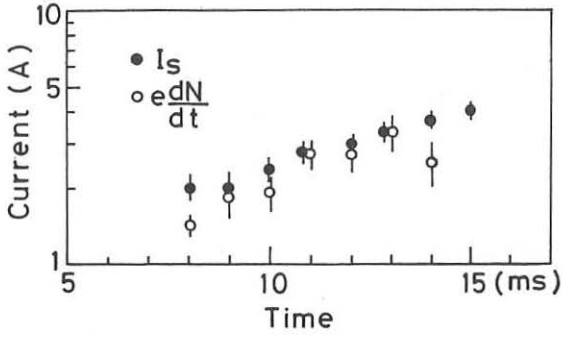

Fig.3
Ionization source current and particle buildup rate in the core region for the case that strong end plugging occures.

PARTICLE BALANCE IN PLUGGED CASE

End plugging experiments are carried out with a combination of sloshing neutral beam injection (NBI) and electron cyclotron resonant heating (ECRH). The electrostatic potential formed at the fundamental ECRH resonance region is for end plugging, and that at the second harmonic resonance is for the thermal barrier which is a deep potential well to reduce electron thermal conduction across the barrier. The central-cell plasma is heated with ICRF power. The typical data are shown in Fig. 2 together with the time sequence of the heating systems. Strong suppression of both end loss fluxes are observed during the time when the ECRH power for plug is applied. In this period both the ion confining potential and the potential dip at the barrier are observed. In this case $I_{\parallel}$ and $I_{\perp}{}^{NA}$ is negligible in Eq. (1), then I_S should be balanced with the particle buildup rate if I^A is also small. The core ionization source current determined from the same procedure mentioned above and the particle buildup rate is shown as a function of time in Fig. 3. During strong end plugging (from 8 to 13ms) the ionization source current is balanced with the particle buildup term well. Therefore ambipolar losses are small in a plasma confined by axial potentials.

IMPURITIES IN GAMMA 10

Impurities in the GAMMA 10 have also been investigated by using an UV-visible spectrometer. Dominant impurities are C and O, and no metal impurities are observed clearly. The intensity level of line radiations is reduced by a factor of 5~10 after the extensive wall conditioning by pulsed plasmas, though it takes about 1000 shots. Recently ECR discharge cleaning (ECR-DC) has been carried out to shorten the time required for wall conditioning. Light impurities have been observed to be strongly reduced after the ECR-DC.

SUMMARY

To account the total particle balance including the ambipolar radial transport, $H\alpha$ emissivity measurement has been performed by means of absolutely calibrated $H\alpha$ detection systems. The particle balance has been investigated for the two cases of the confinement configuration, one is without axial plugging and another is the normal operation of GAMMA 10 with strong plugging. In both cases the ambipolar loss current is determined to be small.

REFERENCES

[1] D.P. Grubb, S.L. Allen, T.A. Casper, J.F. Clauser, et al., Phys. Rev. Lett. **53** (1984) 783
[2] M. Inutake, T. Cho, M. Ichimura, K. Ishii, et al., Phys. Rev. Lett. **55** (1985) 939
[3] E.B. Hooper, R.H. Cohen, D.L. Correll, J.M. Gilmore, D.P. Grubb, Phys. Fluids **28** (1985) 3609
[4] T. Cho, M. Ichimura, M. Inutake, K. Ishii, et al., Proc. 11th Int. Conf. Plasma Physics and Controlled Nuclear Fusion Research 1986, Nucl. Fusion, Suppl. Vol.2 (1987) 243
[5] L.C. Johnson and E. Hinnov, J. Quant. Spectrosc. Radiat. Transfer **13** (1973) 333

AVERAGE MINIMUM-B IN AN AXISYMMETRIC STEEPLY-CURVED MIRROR

V.V.Arsenin

I.V.Kurchatov Institute of Atomic Energy, Moscow,USSR

A compact mirror of simple geometry is described,where the MHD stability is produced by large sign-inverted curvature.

The mirror is shown in Figure. The magnetic field as a function of the coordinate along the field line has two minima and the field line curvatures near them have opposite signs. The whole mirror is filled with plasma so that a perturbation in the electrical potential in a flute-like motion is constant along the field line, $\varphi=\varphi(\psi)\exp(im\theta)$. Here ψ is the flux coordinate, θ is the asimuthal angle. For simplicity (in order it would be possible to use analytical expressions) let us assume that a hot component determining stability is anisotropic, $p_\perp \gg p_{||}$, and concentrated in the vicinity of longitudinal field minima. Let us designate these regions with indices 1,2 . The potential energy of a flute-like perturbation in a low pressure plasma ($\beta \ll 1$) has the form [1,2]

$$W=-\alpha\int|\varphi(\psi)|^2\frac{\partial B}{\partial\psi}\frac{\partial}{\partial\psi}\left(\frac{p_\perp}{B^3}\right)d\chi\,d\psi. \qquad (1)$$

Here α is the positive constant, χ is the longitudinal coordinate, $\nabla\chi=\vec{B}$. Let the plasma occupy a layer, $\Delta\psi$ thick, which is much less than a distance to the axis and a field line curvature radius. Let us choose a magnetic surface within the layer and assume $\psi=0$ there. Let us designate the field on this surface as $B_0(\chi)$, a current distance to the axis $r_0(\chi)$,

its curvature $K_0(\vartheta)$. Here ϑ is the length counted off along the field line, $ds = d\chi/B_0$. The quantity B within the layer $\Delta\psi$ is represented by the following expansion

$$B = B_0(\vartheta) - \frac{K_0}{r_0}\psi + \frac{1}{2}\left(\frac{d''}{d} + \frac{K_0}{r_0}\cos\gamma + K_0^2\right)\frac{\psi^2}{B_0 r_0^2} + \ldots, \quad (2)$$

where γ is the angle between a normal to the surface $\psi = 0$ and a radial direction, $d = \Delta\psi/r_0 B_0$ is the thickness of a magnetic tube, prime means differentiation with respect to ϑ. Let us assume that the quantity $P_\perp/B^3$ has a maximum, as a function of ψ, at $\psi = 0$ and monotonously decays from this surface to the boundaries of the layer $\Delta\psi$ for both (1,2) hot populations. Then for stability is sufficient to satysfy two conditions:

$$\int \frac{K_0}{r_0}\,\frac{P_\perp}{B^3}\,d\chi = 0 \quad (3)$$

with an accuracy not worse than $K_0 d$ (absence or compensation of the curvature effect described by the main order ψ-term in $\partial B/\partial\psi$) and

$$\frac{d''}{d} + \frac{K_0}{r_0}\cos\gamma + K_0^2 > 0 \quad (4)$$

in the regions 1,2, where $P_\perp \neq 0$.

The case $K_0 = 0$, $d'' > 0$ (concave tube of force) corresponds to Andreoletti's mirror [3,4]; stabilization due to $d'' > 0$ at $K_0 \neq 0$ (effect of a concavity in the magnetic tube "hidden" upon the general curving background) has been discussed in [5]; the systems with average $\min B$, where $K_0\cos\gamma > 0$ is of importance at least in one part of the trap, are described in [6]. The stability of the trap considered in this paper is due to an effect of large curvature related with the third item in Eq.(4). In difference from a term with $K_0\cos\gamma$, this item does not vanish with a distance from the axis. Therefore it is convenient to single it out in a "pure" form, considering the case $K_0 r_0 \gg 1$, that corresponds to the transition to

a plane layer geometry. To satisfy (4) in this limit it is sufficient to have

$$B_o\left(\frac{1}{B_o}\right)'' + \kappa_o^2 > 0. \qquad (5)$$

References

1 Arsenin V.V. Pis'ma J.Ehksp. Teor. Fiz., 1986, 43, 270.
2 Ryutov D.D., Stupakov G.V. Fisika Plasmy, 1986, 12, 1411.
3 Andreoletti J. Comptes rendus, 1963, 256, 1469.
4 Furth H.P. Phys. Rev. Lett., 1963, 11, 308.
5 Arsenin V.V. Intern. Conf. on Plasma Phys., Losanne, 1984. Contrib. papers, v. 1, p. 206.
6 Arsenin V.V. Pis'ma J.Ehksp. Teor. Fis., 1983, 37, 534; Mirror-Based and Field-Reversed Approaches to Magnetic Fusion. Proc. of the course held at Varenna (Como), Italy, 7-17 Sept., 1983, v. 2, p. 419.

Figure captions

Mirror diagram: a - configuration of field lines, b - field and pressure distributions along a field line, c - pressure distribution across field lines.

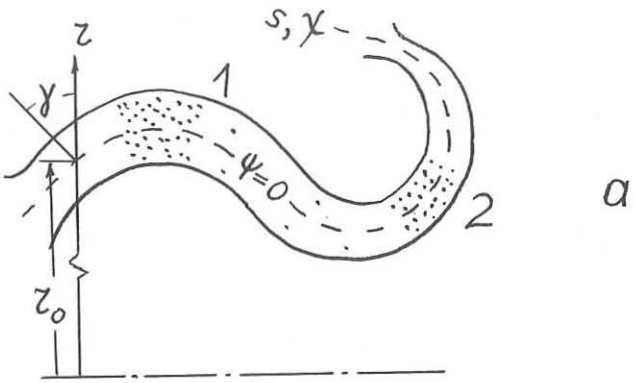

b

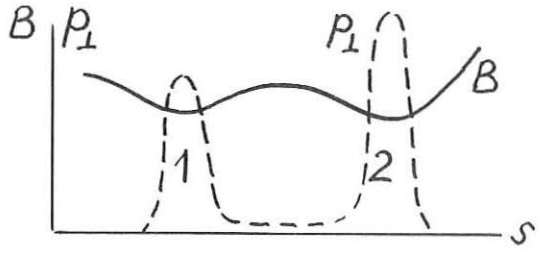

c

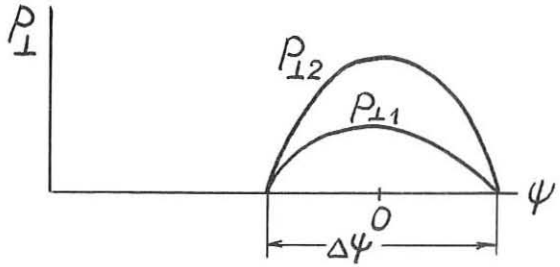

ECRH TRAPPING OF HIGH ENERGY GYRATED ELECTRON BEAM IN A MAGNETIC MIRROR

Zhao Hua, Yang Si-ze*

Institute of Physics, Chinese Academy of Science
P. O. Box 603, Beijing, P. R. China

* Center of Theoretic Physics, CCAST (World Laboratory)

There are various ways[1] of heating a magnetic mirror plasma. Among those are electron cyclotron wave resonance heating(ECRH)[2,3], neutral beam injection(NBI)[4,5], the electron beam heating(REB)[6], etc. In this letter one of the authors (Yang) proposed to use the ECRH trapping of a high energy gyrated electron beam which is generated from a gyrotron tube and incident directly into the magnetic mirror axially to heat the plamma. The advantage of using this method is that only a small ECRH power for trapping of electrons is required. Trapping rate is high. Thus high efficient use of electric power is obtained without the costly magnetic field system which is used to convert the gyrotron electron beam energy into electron cyclotron wave energy.

The high energy gyrated electron beam is axially injected into the mirror from one end and right-hand circularly polarized wave is incidented from the other as shown in Fig-1:

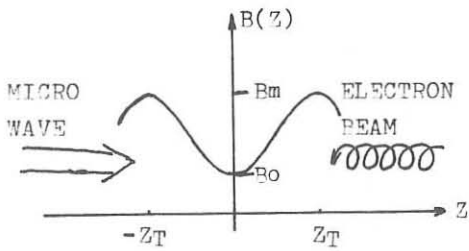

Fig-1. The diagram shows the location of the injected high energy gyrated electron beam and the incident direction of microwave in a mirror magnetic field.

A magnetic field of the form:

$$B(z) = Bo(1+(R+1)z^2/Z_T^2) \qquad (1)$$

is used. Where Bo is the field strength at the midplane, R the mirror ratio, z the axial distance from the midplane and Z_T the distance at the mirror throat from the midplane. If the ECRH resonance surface for injected beam is set at the midplane, then the Doppler shifted resonance condition fulfills:

$$\omega + k_z * v_{\parallel}(z=0) = \omega co \qquad (2)$$

where ω and k_z are the wave frequency and wave number, $v_{\parallel}(z=0)$ the parallel velocity of gyrated beam at the midplane and ωco the electron cyclotron frequency at the midplane. Since the beam and the wave are incidented from opposite ends, so the frequency of the incident wave ω is always smaller than the electron cyclotron frequency at the midplane. Therefore the incident wave inside the mirror region satisfies the propagation of a whistler wave and there is no resonance interaction of microwave with the background plasma because of $\omega < \omega co$.

The parallel and perpendicular velocity of the electron beam at every location is assumed to be a single value. Also we assume that the motion of electrons of injected beam along the magnetic field inside the mirror is adiabatic except at the resonance region where a jump in perpendicular energy $\Delta W_\perp$ can occur. Hence the magnetic moment of the beam electrons before reaching the resonance at midplane is: $\mu_o = m * v_{\perp T}^2/2Bm$. Where Bm is the field strength at mirror throat, $v_{\perp T}$ ($v_{\parallel T}$) is perpendicular(parallel) velocity at the throat. There is a jump in magnetic moment at resonance: $\Delta\mu = \Delta W_\perp / Bo$. After crossing the resonance at midplane the magnetic moment of the beam electron along the field line maintains a constant: $\mu = \mu_o + \Delta\mu$. Then the parallel velocity $v_{\parallel}(z)$ after crossing the resonance is:

$$\begin{aligned} v_{\parallel}^2(z) &= v_{\parallel T}^2 + v_{\perp T}^2 + 2\Delta W_\perp/m - 2\mu B(z)/m \\ &= v_{\parallel T}^2 + v_{\perp T}^2\left(1 - B(z)/Bm\right) + 2\Delta W_\perp\left(1 - B(z)/Bo\right)/m \end{aligned} \qquad (3)$$

From equation (3), if $v_{\parallel}^2(z) \leq 0$ for certain z, where $|z| \leq Z_T$ then the injected electron will be trapped in the mirror. For critical condition $z = -Z_T$, the perpendicular energy gain requi-

red to trap the injected electrons is: $\Delta W_\perp \geq m V_{\parallel T}^2/(R-1)$. (3′)

To obtain $\Delta W_\perp$ for an injected electron crossing the resonance zone, we consider only the non-adiabatic equation of motion. The field of the right-hand circularly polarized is:

$$Ex=\frac{1}{2}Eo^*\exp[i(k_z^*z-\omega_1^*t)],\ Ey=\frac{1}{2}Eo^*\exp[i(k_z^*z-\omega^*t)],\ Ez=0 \quad (4)$$

where we have assumed k_z to be a constant, which coresponds to a low density of background plasma. To be pricise, the dispersion relation of whistler wave has to be used to obtain k_z. The solution of interaction equation between electron and microwave is: $V_\perp(t)=\sqrt{B(t)/Bm}\left[V_{\perp T}\exp(i\psi_1)-eE_0W(t)/m\right]\exp\left[-i\int_0^t \omega_c(t')\,dt'\right]$ (5)

where W(t) can be considered as the effective time that an electron interacts with microwave while crossing the resonance.

The energy gain $\Delta W_\perp$ in one transit from t=0 to $t=t_b$, the time particle bounce back at the mirror throat at the other end, is that:

$$\Delta W_\perp = \frac{1}{2}m\left[|V_\perp(t=t_b)|^2-|V_\perp(t=o)|^2\right]$$
$$=\frac{1}{2}m\left|eE_oW(t_b)/m\right|^2+\left|eE_oW(t_b)\right|V_{\perp T}\cos\psi \quad (6)$$

where ψ is considered as the phase angle between the electric field and particle. Substituting (6) into (3′) yields:

$$\frac{1}{2}m\left|eE_oW(t_b)/m\right|^2+eE_o|W(t_b)|V_{\perp T}\cos\psi \geq \frac{1}{2}mV_{\perp T}^2/(R-1) \quad (7)$$

The phase angle between the incident electrons and electric field is purely random. Those particles for which angle ψ satisfies: $|\psi|\leq\psi_0=\cos^{-1}[(V_{\parallel T}^2/(R-1)-|eE_oW(t_b)/m|^2)/2V_{\perp T}|eE_oW(t_b)/m]$ (8)

will be trapped in the mirror. With the trapping of high gyrated electrons in the magnetic mirror, the electric potential of mirror plasma will be droped due to the extra negative charges appear in. And more low energy electrons which confined in the mirror will run out mirror faster than the trapped high energy ones. During the potential dropping, the trapped high energy electrons will convert a part of parallel energy into potential energy of electrons and the trapped electrons bounceback at the midplane and other place of the mirror, the resonance condition (2) will not be satisfied due to the electrons parallel velocity decrease. Hence the trapped particles will stay in mirror for a comparatively long time. So we roughly consider the heating efficiency of this method is:

$$\eta = \frac{1}{\pi}\cos^{-1}\left[\left(v_{\perp T}^2/(R-1) - |eE_0W(t_b)/m|^2\right)/2v_{\perp T}|eE_0W(t_b)/m|\right] \qquad (9)$$

if $v_{\perp T}^2/(R-1) < |eE_0W(t_b)/m|^2$, then $\eta \geq 50\%$.

The advantage of shooting the electron beam and microwave from different ends can be seen from (2) that the wave frequency is always smaller than the electron cyclotron frequency at the midplane of magnetic mirror, therefore it gets rid of the problem of using very high frequency gyrotron. Besides of this, the microwave can propagate to the midplane even in a dense plasma, because it is a whistler wave.

In a dense plasma the k_z is then modified according to the dispersion relation of a whistler wave:

$$k_z^2 c^2 = \omega^2\left[1 + \omega_{pe}^2/\omega(\omega_{ce} - \omega)\right] \qquad (10)$$

where ω_{pe} is the plasma frequency . we can see that the required wave frequency is reduced even further for a high dense plasma.

The trapping of the electron beam can produce a negative potential inside the mirror which can be used as a thermal barrier in a tandem mirror. The negative potential does not effect the trapping efficiency, but slows down the electron parallel velocity which cause a shift of frequency to satisfy the resonance condition.

Likewise a high energy gyrated ion beam can be trapped in a magnetic mirror with ICRH.

We wish to thank Ms. Y.P. Chen for her valuable help. This research was supported by National Natural Science Foundation of China under Grant No. 1860196.

The authors like to give their thanks to the Association for Plasma Studies.

REFERENCE:

(1) B.I. COhen(Editor), Status of Mirror Fusion Research UCAR 10049-80-Rev. 1.(1980)

(2) R.A. Dandl, et al. Nuclaar Fusion vol.4 344(1964)

(3) Y. Kiwamoto, et al. Phys. Fluids vol.29 2781(1986)

(4) F.H. Coensgen, et al. Phys. Rev. Lett. vol.35 1505(1975)

(5) F. Bibe, Phys. Rev. vol.83 1217(1951)

LOWER AND UPPER LIMITS OF THE PINCH RADIUS IN EXTRAP

B. Lehnert

The Royal Institute of Technology, S-10044 Stockholm, Sweden

Abstract A simple hybrid MHD-kinetic model is presented for Extrap which is a Z-pinch immersed in a magnetic octupole field. The model results in a lower and an upper stability and equilibrium limit for the pinch radius, being consistent with so far performed experiments.

Introduction An example of a linear Extrap configuration [1] is given in Fig.1 where a Z-pinch with the total current J_p and average pinch radius $\bar{a}$ is immersed in an octupole field generated by currents J_v in four external rod conductors at the distance a_v from the pinch axis. A magnetic separatrix is formed with four x-points at the axial distance a_x. In addition to the resulting transverse (poloidal) magnetic field $\underline{B}$, a rather weak axial (toroidal) field $\underline{B}_t$ can be superimposed. Extrap theory is still at an early stage, and several attempts have so far been made to explain the experimentally observed macroscopic stability [2-5]. In this paper one such attempt is presented which is based on a collisionless

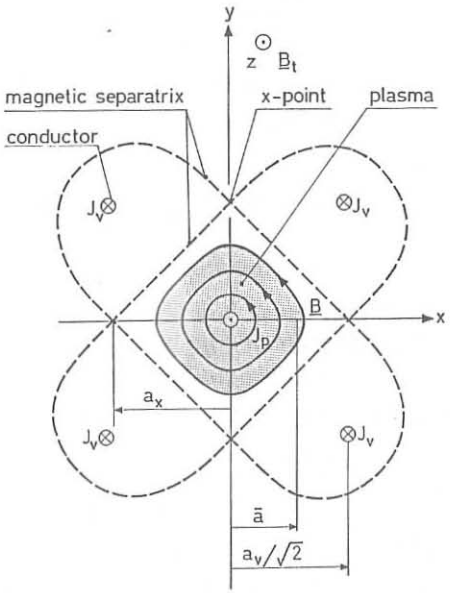

Fig.1. A linear Extrap system.

hybrid MHD-large Larmor radius (LLR) model.

Kinetic Effects Extrap is a high-beta system in which the number

$$\theta_i = \int_0^{\bar{a}} (dr/a_i)$$

of ion Larmor radii a_i within the pinch radius is limited. In present experiments $4 \lesssim \theta_i \lesssim 8$. The corresponding kinetic phase-mixing and damping effects are expected to become substantial for all perturbation wave lengths $\lambda = 2\pi/k$ when $ka_i \gtrsim 0.5$ [6,7]. This implies that all wave lengths $\lambda \lesssim \lambda_c = (4\pi/\theta_i)\bar{a}$ which form an integrating part of a perturbation will be "smeared out" and damped by LLR effects. In the experiments $\lambda_c \simeq 2\bar{a}$. Therefore the entire fine-structure of any perturbation should become damped, and only the nearly rigid displacements of the plasma cross section become unaffected.

Additional phase-mixing and dispersion effects arise in a high-beta system with large magnetic field inhomogeneities, due to thermal dispersion and differential ion-electron motion of the guiding centre drifts [8]. In this model it is thus assumed that the spectrum of all axial wave lengths $\lambda_z \ll \lambda_{zc}$ in Fig.1 is damped by such effects. Here $\lambda_{zc} \simeq (32\pi/\theta_i)\bar{a}$ is defined by the condition that the time for differential drift motion along the axis by a distance $\lambda/4$ becomes comparable to the time for an Alfvén wave to propagate around the pinch cross section.

Lower Pinch Radius Limit In this first attempt to combine MHD and kinetic theory, the perturbation fine-structure is sorted out, and only rigid displacements and axial wave lengths $\lambda_z \gtrsim \lambda_{zc}$ are considered. This residual class of perturbations can then be treated by conventional MHD theory. We first turn to the case where $\bar{a} < a_x$ and limit ourselves to plane or spiral-shaped kink-like perturbations which are one of the most important instability modes of the pinch. The energy principle with included surface (image) currents due to the octupole field inhomogeneity [1] then yields the stability condition

$$L \equiv n_o^2 a_v^4 (J_p/J_v) \lesssim (\mu_o F_k Q/4\pi^2 K)^2 [M_c \pm (J_p/4J_v)] \qquad (1)$$

where $F_k \simeq 7/5$ for a current density profile $j/j_o = 1 - (r/\bar{a})^4$ and a slightly non-circular cross section, a plasma density n_o and temperature T_o at the axis, $Q = J_p^2/T_o$, K standing for Boltzmann's constant, and

$$M_c = -a + [b + (cf_t^2/Q)]^{1/2} \qquad (2)$$

where $a \simeq 1.74$, $b \simeq 3.81$, $c \simeq 2.53 \times 10^5$ and $f_t = [1 + (B_t/B_{pa})^2]^{-1/2}$ with B_{pa} denoting the transverse field strength at the pinch surface. The plus and minus signs in eq.(1) refer to coparallel and antiparallel pinch and conductor currents. Condition (1) applies to a range $M_c \gtrsim 2$ where $\theta_i \lesssim 18$ and $0 \lesssim B_t < B_{pa}/2$. Since $Q \propto \bar{a}^2$ at fixed values of n_o, the result (1) implies that there is a limit of $\bar{a}/a_x$ below which the pinch becomes unstable. This is due to the fact that the plasma is in a region where the octupole field is weak, i.e. when the pinch radius is small.

Upper Pinch Radius Limit Provided that $n_o T_o$ increases more slowly with J_p than J_p^2, the pinch radius will increase with J_p. Since a_x is a slow function of J_p/J_v, $\bar{a}/a_x$ will then approach and even tend to exceed unity. In such a case the plasma pressure gradient ∇p will increase near the pinch boundary, as seen from the Bennett relation. When $\bar{a}/a_x$ approaches unity the plasma will then either become ballooning unstable, or there will be a lack of equilibrium. The driving force of the ballooning mode is proportional to $|\nabla p|/|\underline{B} + \underline{B}_t|^2$ and has a maximum in the planes through the axis which pass through the x-points of Fig.1. It reaches the stability limit when $\bar{a}$ approaches a_x. Also an equilibrium of the Bennett type becomes limited to a maximum value of $n_o T_o/J_p^2$ as $\bar{a}$ approaches a_x. Both cases thus result in an upper limit of $\bar{a}$ given by

$$U \equiv n_o^2 a_v^4 (J_p/J_v)\{1/[1 \pm (J_p/4J_v)]\} \gtrsim (\mu_o Q/4\pi^2 K)^2/2 \qquad (3)$$

Comparison with Experiments The present results are illustrated by Fig.2 in which the regions to the left and right of the lines represent instability or lack of equilibrium. In the domain between the lines there could exist unstable modes not being treated in this context. A superimposed axial field $B_t = B_{pa}/2$ slightly modifies the lower limit. The rectangular areas represent the parameter ranges of so far performed experiments [2-5], where LO and TO denote earlier linear and toroidal sector devices, and L1 and T1 present linear and fully toroidal devices. For LO and TO a lower stability limit has been observed at $J_p/J_v \simeq (0.25, 0.36)$ and $\bar{a}/a_x \simeq (0.57, 0.62)$, respectively, in agreement with condition (1). For L1

and T1 the values of $\bar{a}/a_x$ are somewhat below unity and $J_p/J_v \simeq 2$ and somewhat above 2, so far without any sign of macroscopic instability.

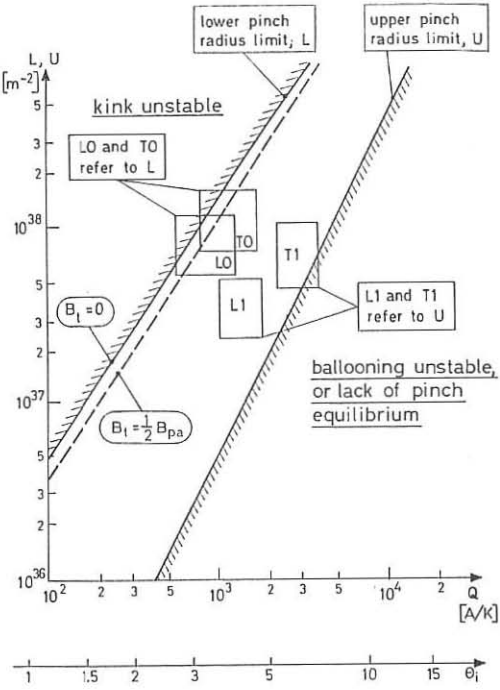

Fig.2. The pinch radius limits.

References

[1] B. Lehnert, in Unconventional Approaches to Fusion, Ed. by B. Brunelli and G.G. Leotta, Plenum Press, New York 1982, p. 135.

[2] J.R. Drake et al., Nuclear Fusion, Suppl. II(1981)717.

[3] B. Bonnevier et al., Nuclear Fusion, Suppl. II(1983)135.

[4] J.R. Drake et al., Royal Inst. of Tech., Stockholm 1987(unpublished).

[5] J.R. Drake et al., Royal Inst. of Tech., Stockholm, TRITA-PFU-87-12(1987).

[6] B. Lehnert, Plasma Phys. Contr.Fusion 29(1987)341.

[7] B. Lehnert, Royal Inst. of Tech., Stockholm, TRITA-PFU-87-02(1987).

[8] B. Lehnert, Royal Inst. of Tech., Stockholm, TRITA-PFU-87-08(1987).

Breakdown in the Toroidal Extrap Experiment

Jin Li
Dept. of Plasma Physics and Fusion Research
Royal Institute of Technology
100 44 Stockholm, SWEDEN

In the present paper we study a kind of breakdown in which the energy balance plays an important role. In gas discharge research the concept of the Townsend first coefficient is usually used to describe the ionization process and the ionization rate depends only on the local parameter E/p, i.e., $\alpha/p = f(E/p)$; here E is the externally applied electric field, p the filling pressure of the background neutral gas, α the Townsend first coefficient, and the function f is an empirical relation. This geometry-independent formula actually requires a special energy balance structure where the energy flow can be omitted. Fortunately it works well for most types of gas discharges, including some fusion plasma breakdowns[1,2]. However, this mechanism still fails sometimes and here an example is given. So special care should be taken when using the Townsend first coefficient in cases where the energy flow is serious.

Let's first describe the magnetic field configuration, the Extrap[3] pinch, in which the discharge is carried. Extrap, in its original form, is a fusion confinement concept which is basically a z-pinch immersed in an octupole field produced by four external conductors. It can be a linear or a toroidal device, but only the electrodeless toroidal Extrap is considered here. At the beginning of the discharge all the magnetic field is supplied by the external source. A poloidal field, which is produced by four rings and is supposed to stabilize the pinch later on, is inhomogenous across the discharge cross section and generally has three nulls ($B_R = B_z = 0$), as shown in Fig. 1. A toroidal field of typically 500~1000 Gauss, which did not appear in the prototype of

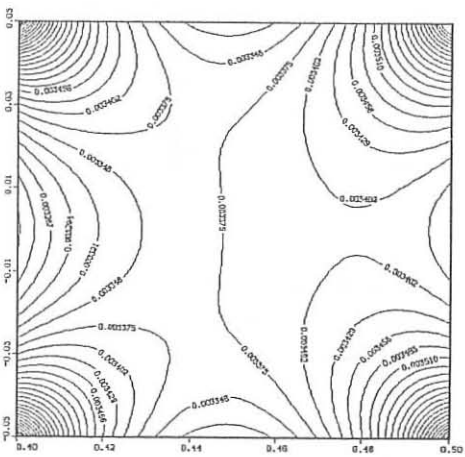

Fig.1 A flux plot of the poloidal magnetic field typically for the Extrap configuration, three x-points or nulls can be seen.

Extrap, is applied for achieving breakdown in experiments. The existence of the octupole field and the weak toroidal field (compared with the tokamak) leads the field lines directly to the surrounding walls. The charged particles are thus driven to the walls along the field lines by electric fields in such a way that they can only be hindered by elastic collisions with the neutrals. So the confinement is almost absent before the plasma current is built up and the plasma behaves like an open system. The energy flow due to the particle losses is therefore serious: the particles are heated at the central region and lost to the wall with their high energy before giving enough ionizations. This energy loss mechanism leads to a substantial change to the ignition condition of the Extrap discharge at low filling pressure range and can explain the unusually high lower-threshold of the filling pressure observed in the experiments.

To formulate the breakdown problem a fluid model is used to describe the electron motion in a weakly ionized gas. Ions are considered as either decoupled from the electron motion (free motion) or moving with the electrons (ambipolar motion), depending on whether the Debye length is much larger or smaller than the characteristic length. The particle loss can be described by an eigenvalue problem:

$$\lambda_E n = \nabla\cdot(\Omega\cdot(\nabla n + nE/T)). \qquad (1)$$

$\lambda_E^{-1/2}$ is equivalent to the discharge radius in the magnetic field-free case. The tensor Ω reflects an anisotropic influence of the magnetic field. For the free motion case it has the form

$$\Omega = \frac{1}{\omega^2}\begin{bmatrix} \nu_{el}^2+\omega_R^2 & -\nu_{el}\omega_z+\omega_R\omega_\phi & \nu_{el}\omega_\phi+\omega_R\omega_z \\ \nu_{el}\omega_z+\omega_\phi\omega_R & \nu_{el}^2+\omega_\phi^2 & -\nu_{el}\omega_R+\omega_\phi\omega_z \\ -\nu_{el}\omega_\phi+\omega_z\omega_R & \nu_{el}\omega_R+\omega_z\omega_\phi & \nu_{el}^2+\omega_z^2 \end{bmatrix} \qquad (2)$$

Here ν_{el} is the electron-neutral elastic collision frequency, and $(\omega_R, \omega_\varphi, \omega_z) = eB/m$ the vectorial electron gyro-frequency. Cylindrical coordinates (R,φ,z) in a toroidal geometry is used. The particle balance can then be written approximately in the form

$$\lambda = \nu_{ioni} - D_0\lambda_E \qquad (3)$$

λ is the growth rate of the electron density, ν_{ioni} the ionization frequency, and D_0 the diffusion coefficient of electrons. The ignition condition for the breakdown can be expressed as $\lambda > 0$.

The energy balance is coupled to the problem by the fact that the electron temperature is needed in order to evaluate ν_{ioni}, D_0 and λ_E in Eq.(3). The estimation of the particle losses from

Eq.(1) allows the energy balance to be written in an algebraic form:

$$3.6\times10^{4}E^{2}/p = 6.3\times10^{4}\lambda_{E}T^{2.2}/p + 4.0\times10^{3}Tp + 1.5\lambda T + 3.3\times10^{19}p\sum_{in}\varepsilon_{in}<c\sigma_{in}> \quad (4)$$

The filling pressure p is in mTorr, electron temperature T in eV and others in SI. The L.H. side of Eq.(4) is the joule heating, the first term of the R.H. side corresponds to the energy outflow, the second is the elastic collision loss, the third is the time-dependent energy increase, and the fourth is the inelastic collision losses. At low filling pressure p (~10 mTorr) the major energy loss is the energy outflow which is inversely proportional to p, and at high p(>20 mTorr) the inelastic collision losses (which are proportional to p) seem to dominate. Heavy energy outflow at low p leads to a fairly high (compared with tokamak) filling pressure threshold (~5mtorr) below which no breakdown is possible. From Eq.(4) it can be seen that only at high p, where the first and the third terms of the R.H. side of Eq.(4) can be omitted, does the temperature T scale with E/p, which is actually the implicit condition for which the Townsend formula $\alpha/p = f(E/p)$ applies. Generally the concept of the Townsend first coefficient seems not to be applicable when energy flow cannot be omitted.

The solution of the eigenvalue problem (1) becomes nontrivial when an inhomogeneous poloidal magnetic field is considered. At the nulls of the poloidal field Eq.(1) becomes singular in a sense that the coefficients of the 2nd-order derivatives are much smaller than those of the 1st-order derivatives. This means that the eigenfunction (electron density) concentrates near the magnetic nulls and decreases rapidly in the strong field region, as shown in Fig. 2. Physically this corresponds to the fact that the discharge will develop first at the central nulls, because there particles can be confined for a longer time. However an overall estimate of the particle loss rate needs a 2-dimensional solution of Eq.(1) because of the inhomogeneity of the poloidal field.

The space-charge effect is considered in an ambipolar form. The ambipolar motion influences the results mainly through its effects on the eigenvalue λ_E. The effects of the ambipolar motion on confinement in an inhomogeneous magnetic field, where the electrons are magnetized but the ions are not, is found to be interesting. With a strong electric field the particle confinement is slightly improved. But the particle confinement can be even worse for the case with ambipolar motion if no electric field is applied.

The curves of breakdown voltage versus filling pressure for different parameters are calculated numerically and are compared with the experimental results, as shown in Fig.3.

References

[1] Andrianov, A.I. and Osovets, S.M., 1959, in *Plasma Physics and the Problem of Controlled Thermonuclear Reactions Vol.1* (translated from Russian), Pergamon, London, p.112.

[2] Papoular, R., 1976, Nucl. Fusion **16**(1), 37.

[3] Lehnert, B., 1974, *Physica Scripta* **10**, 139; 1977, *Physica Scripta* **16**, 147.

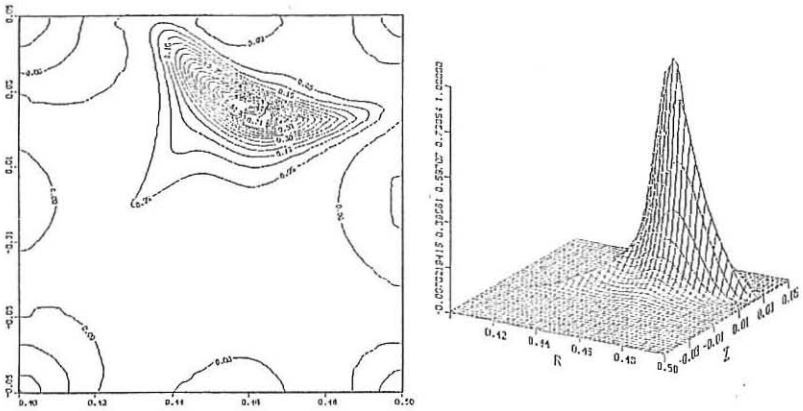

Fig.2 The density distribution $n(R,z)$ (eigenfunction) over the discharge cross section. Correlation with the poloidal field (Fig.1) and strong 2-dimensionality can be seen.

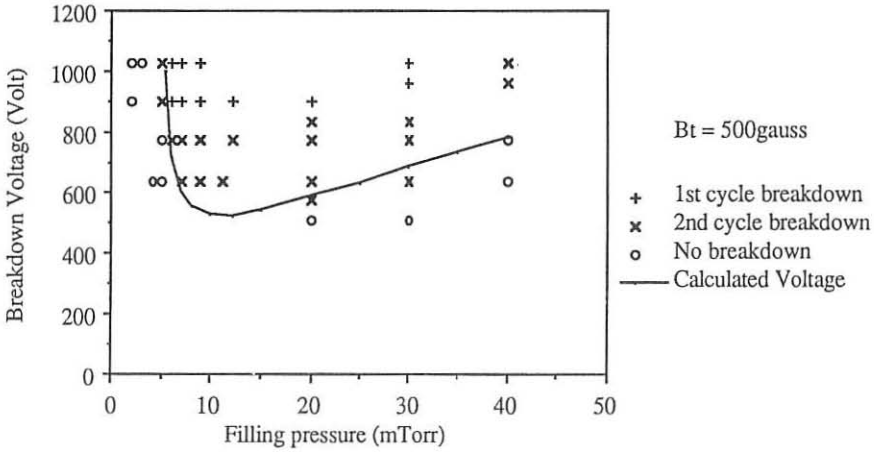

Fig.3 The comparison of the theoretical results with the experimental data.

HEAVY ION FUSION IN A DENSE PINCH WITH ENHANCED COMPRESSION, ION ACCELERATION AND TRAPPING*

A. Bortolotti, J. S. Brzosko, F. Mezzetti, V. Nardi, C. Powell, D. Zeng

Stevens Institute of Technology, Hoboken, New Jersey 07030 (U.S.A.)
Universita di Ferrara, Ferrara 44100 (Italia)
Cooperative Research Program

High space resolution imaging with a pinhole camera of the plasma focus pinch (from X-ray and particle emission) indicates the existence of localized hot spots which are the source of the hard component of the pinch emission (> 3 MeV D^+ ions and > 10 keV X-rays)[1-4]. These hot spots (with typical linear dimensions of 10-200 μm) are embedded in an extended, diffuse source of softer radiation (X-rays, ion and ion clusters) which form the profile of the plasma focus pinch. The hot spots are clearly linked to the filamentary fine structure of the pinch from X-ray pinhole images which show space correlation and overlapping of those elements of the pinch fine structure.

We present here independent data which supports the ubiquitous nature of these elements of the pinch fine-structure.

Important information about plasma hot spots which are the site of high nuclear reactivity and of the acceleration, confinement and/or emission of high energy ion beams (HEB, say) has been obtained from (d,n) nuclear reactions involving heavy nuclei ($A \gtrsim 15$)[5]. During our experiments the discharge chamber of the advanced plasma focus (APF, say) fed with a 7 kJ (at 17 kV) capacitor bank was filled with a suitable mixture (e.g., D_2 and N_2 or D_2 and C_3D_8) with an atomic ratio, r, of heavy nuclei as large as r = 0.15/1. The β^+ radioactivity of the reaction products in the gas was measured after each APF shot and, at the same time, we have observed the β^+ radioactivity from (d,n) reactions in solid external targets of ^{10}B, ^{12}C, ^{14}N, ^{16}O (axial, 0°, and side-on, 90°, directions).

The "effective" D^+ energy, E_e, fitting the observed amount of each of those reactions is $E_e > 2$ MeV if we take the D^+ energy spectrum of the form $\partial\phi/\partial E = \phi_o E^{-m}$ with m = 2.5 ± 0.5 and ϕ_o as determined from the observed D-D neutron spectrum and other data[5]. Special precautions were taken for a correct identification of the reaction products in the gas and in the solid targets. From the observed β^+ radioactivity of each species in the plasma and in the external targets (in the same shot) we determine the (d,n) reaction yield, Y, of each reaction; the measured neutron yield, Y_n, provides the yield of the $D(d,n)^3He$ reactions. Our data from many shots indicate: (i) a linear correlation among all measured yields Y's of the heavy ion reactions; (ii) functional dependence $Y \sim Y_n^2$ on the neutron yield. For a specific reaction the measured ratio of the yield in the plasma, Y_p, and the yield in the external target, Y_{ET}, in the same shot can be equated to the analytic expression, i.e.,

$$(Y_p/Y_{ET})_{exp} = n\tau \cdot r/r+1 \cdot A \cdot \int(\partial\phi/\partial E)\sigma E^{0.5}dE/\int(\partial\phi/\partial E)y a dE \qquad (1)$$

In this equation the only unknown quantity is $n\tau$, n-is the total density of nuclei in - and τ is time of the HEB transit through- the plasma target. A - is a unit dependent constant, a-accounts for the β^+ selfabsorbtion in the external target, $y(E) = \int \sigma(dE/dx)^{-1}dE$ is the experimental thick target yield of a monoenergetic beam , σ-is the (d,n) reaction cross-section. In the integrals the lower limit is the reaction threshold energy and the upper limit is the highest observed energy of the ejected D^+ HEB, i.e., = 10 MeV.

From Eq. (1) we find $3\cdot10^{12}cm^{-3}s \leq n\tau \leq 1.2\cdot10^{13}cm^{-3}s$ from shots with $Y_n \cong 10^9$, independently on r, for all reactions with ^{12}C, ^{14}N in the plasma, and ^{10}B, ^{12}C, ^{14}N, ^{16}O in the solid external targets. The uncertainty in the determination of $n\tau$ depends on the detector geometry, the accuracy of the cross-sections and the relative fluctuations of the β^+ activity for a specific value of Y_n. By taking an "effective" life-time of HEB (inside the reacting plasma region, possibly a multiplicity of hot spots) equal to $\tau \approx 25$ ns (where τ is the FWHM of our neutron emission signal from an NE-102 scintillation detector) we find $1.2\cdot10^{20}$ $cm^{-3} < n < 4.8\cdot10^{20}$ cm^{-3}. This value of n (a minimum value estimate) contradicts the value from usual density measurements ($n_{exp} = 5\cdot10^{18}$ cm^{-3}) with a 2mm spatial resolution [6]. Alternative attempts of explaining the observed high value of Y_p/Y_{ET} (specifically $Y_p/Y_{ET} = 0.03$ for $^{12}C(d,n)\,^{13}N$ with r = 0.15 in the filling mixture) fail as: (a) the assumption of an anomalous concentration of the heavy nuclei with an increase of r in the hot spots, above the initial value of r in the filling gas, decreases the reaction-fitting value of n by factor = 4 for the heavy ions but simultaneously decreases Y_n by a factor ~ 3 in contradiction with the observations, (b) the assumption of a significant slowing down-over extended plasma regions-of accelerated D^+ ions from the hot spots changes Y_p/Y_{ET} but it requires (for an estimate of Y_n consistent with the measurement) an HEB population of such a magnitude (via ϕ_o) that it would exceed the capacitor bank energy (the D^+ slowing-down time would also be too long, i.e., about 3 times longer than neutron signal FWHM).

Since no valid alternative is found to the picture of high-density hot spots where the bulk of the nuclear reactions takes place we conclude that the heavy-ion reaction yield is an excellent supporting argument in favour of the hot-spot existence and leading role. The validity of the concept of high-density hot spots requires that the hot-spot dimensions are small enough for not significantly contributing to the direct measurements of n with space resolution of = 2 mm. By assuming that a multiplicity of hot spots can change n not more than 10% (the experimental uncertainty in a direct measurement of n) we estimate a hot spot diameter of about 100 μm, in agreement with our direct experimental observation.

The pinhole image of the pinch from particle emission is recorded on a CR-39 target (with suitable ion filters) where the nonuniform distribution of etched tracks of ions and ion clusters indicates that some of the localized sources of D^+ ions with energy 2-4 MeV have dimensions smaller than the pinhole diameter = 100 μm. The small dimensions of the localized sources and the extreme collimation of the ejected HEB's of microscopic diameter are consistent with an accelerating - field intensity of = 1 GV/cm. A compression in the HEB time of emission which is similar to the space compression of a localized HEB source is revealed from time

resolved Thomson spectrometer data (the duration of the ion pulse is shorter the higher is the ion energy; e.g., slow ions, 100 keV D^+, are ejected 50 - 100 ns earlier than 1 MeV ions)[5,7]. An increase in the quantity of these hot spots (with a consistent increase of the neutron yield Y_n and of the heavy-ion reactions in the pinch) was obtained in our experiments with the insertion of suitable field distortion elements in the interelectrode gap. This establish the possibility of controlling and increasing the amount of hot-spot activity for a variety of practical applications.

*Work supported in part by AFOSR, ONR (USA), CNR, MPI (Italy).

REFERENCES

1. W. H. Bostick, V. Nardi, W. Prior, J. Plasma Phys. 8, 7 (1972).
2. V. Nardi, C. Powell, A.I.P. Conf. Proc. 111, p. 463 (1983).
3. V. Nardi, "Megagauss Technology and Pulsed Power Application" Ed. C. M. Fowler, Plenum Publ. Corp. 1987, p. 269.
4. M. Sadowski, et al., Phys. Letters 113A, 25 (1985).
5. V. Nardi, et al., IEEE Trans. on Plasma Science (to be publ. June 1986).
6. H. Herold, et al., IAEA-CN-44/D-III-6-3 p. 579 (1985).
7. V. Nardi, et al., European Conf. Abstracts 11D part II, p. 548 (1987).

Fig. 1. Pinhole image of the pinch from the nonuniform distribution of etched ion tracks on a CR-39 target (pinhole diameter 150 μm; 45°). The V-shaped image of the pinch is caused by a 5 kG permanent magnet inserted behind the pinhole, between the pinhole and the target; the electrodes are at the left. The magnet induces the splitting of the pinch image by deflecting the D^+ ions but it is not affecting the trajectory of the heavy clusters with $e/m \cong 0$. The clusters at the right disintegrate later than the cluster at the left. Note diffuse image of hot plasma emitting a relatively small fraction of neutrons (≈ 30% of total) - low side of image. The lower part of the V-shaped image along the horizontal electrode axis is formed from the heavy clusters. The focalization of the current reaches a maximum at the right side - this pinch region with a maximum of current density ejects clusters with a longer life time.

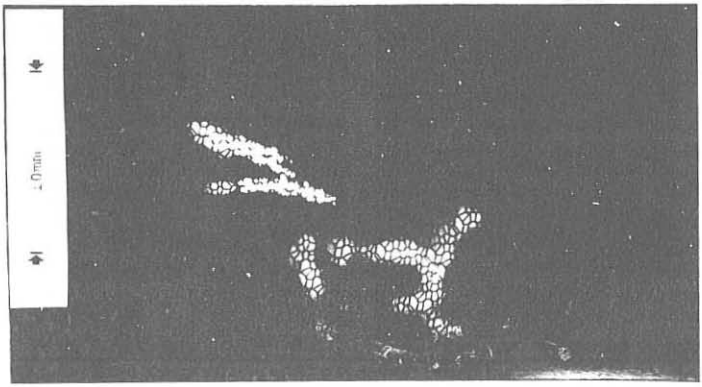

Fig. 2. Zero degree pinhole image of the plasma focus pinch. The central figure shows the typical diameter of the HEB (= 1.5 MeV of D^+) ejected at 0^o . Some magnification for 1,2,3,4,5,6 reporting details of center photograph; #1 reports ion tracks of central spots behind 25μm mylar screen.

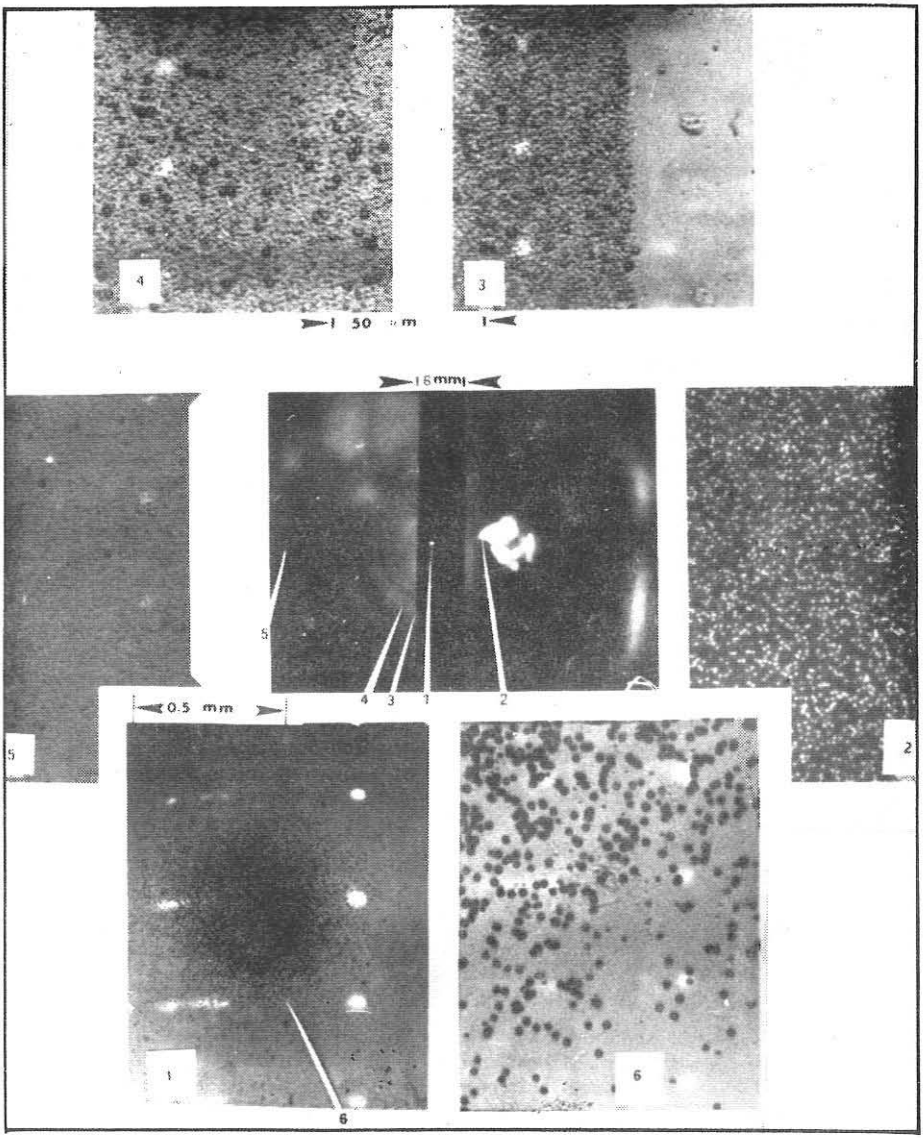

INITIAL RESULTS FROM DRIFT WAVE SCHEME IN A COMPACT TOROID

S.Sinman and A.Sinman *

Plasma Engineering Laboratory, Electrical and Electronic Engineering Department, Middle East Technical University

* Nuclear Fusion Laboratory, Nuclear Research and Training Centre, Turkish Atomic Energy Authority

Ankara, Turkey

INTRODUCTION

Investigation on compact toroid (CT) /1,2/ is complementary to tokamak research and will improve the understanding of plasma physics in toroidal devices, with CTs permitting an overall optimization of the toroidal experimental arrengements.

In 1985, we presented a conceptual system design for the realization of a CT, using four magnetized T-tubes, and discussed the results to be expected /3/. Further, we constructed a small-scale device with single magnetized T-tube and presented the preliminary experimental results /4/. Subsequently, modifying the conventional T-tube, we developed a C-gun. In our previous study, it has been domonstrated experimentally that by means of the C-gun in flux conserver a CT may be formed in two different behaviours /5,6/. In the latest study /7/ the findings were evaluated in the light of minimum energy state /8/ and helicity injection concepts. In this work, the initial results related to the generation of a CT different particularly from the classical spheromaks are given.

GENERATION OF DRIFT WAVE

The C-gun is a noval and alternative version of conventional magnetically driven plasma gun. Its electrical characteristics conform with the Critical Damping and Under Damping Modes (CDM and UDM) of operation depending upon the back ground gas pressure /5,6/.

When the distance between the vertical electrodes is not changed according to the back ground gas pressure in the critical range of 40 - 70 mTorr, the discharge through the vertical electrodes of the C-gun occurs with the aid of the inner walls of the flux conserver. This result is very natural, since the distance between the vertical electrodes is larger than the distance from these electrodes to the wall. In this condition, the currents passing through the inner wall and the back strap are in opposite directions. Because of the mutual inductance between the wall and back strap, the serial leakage inductance of the capacitor bank circuit becomes smaller. Thus the discharge

ends as can be expected in the CDM.

In the CDM, the shock heated electrons in the plasma belt with energies around 20-50 eV, interacting with the toroidal magnetic field produced by the current through the closed loop of the plasma belt and back strap, a helical plasma current channel is formed. Thus without a poloidal, toroidal flux translation, a toroidal field together with a current channel (E-layer produced by the energetic helical electrons) at the flux conserver may be generated. This procedure fits to the principle of helicity injection. On the other hand, by means of the self toroidal magnetic field of the C-gun directly, it has been generated the ion cyclotron wave in CDM scheme. So, due to the effects of the ion cyclotron wave and the density profile of E-layer at the beginning, in the reasonable back ground gas pressure between 40 and 70 mTorr, drift wave instabilities in the frequency range of 4-25 kHz have been distinguished.

DIAGNOSTICS USED

Taking into account the specifications of the problem to be investigated, the main diagnostic techniques such as Langmuir and electrical surface probes, magnetic loops and charge-exchange cell have been used. In order to measure the plasma resistivity for a unit length and then to determine the flow in the current channel, a high impedance, floating electrical surface probe has been employed.This probe is very similar to a simple double probe and its operating point is at the space potential of the plasma. Besides, to reduce the surface impedance, the terminals of the probe have shunted with 6.5 mOhms. The primary winding of a low impedance transformer to the probe and the secondary to the data proceesing channel after an operational integrator have been connected.

The charge-exchange cell without any magnetic analyzer is a simple ionization cell and it essentially behaves like a cylinderical Langmuir probe with a radius of 5.4 cm and 18 cm in length. In this cylinder the back ground gas at the pressures of 40-70 mTorr is ionized by the run-away electrons. The cell takes part on the way of vacuum connection of the flux conserver and by means of some interface units, it has been electrically isolated from either flux conserver or vacuum system. Its place is at the angular distances of 45 and 180 degrees from the C-gun and the electrical surface probe respectively.

When the Langmuir and the electrical surface probe signals are correlated by the plasma space potantial variations of the charge-exchange cell with respect to time, it has been seen that the drift wave alternances and the density fluctuations are at the same phases. Thus during the on-set and after the off-set of the C-gun, it has been possible to determine the fluctuation phases of the C-gun.

EXPERIMENTAL OBSERVATIONS

By means of a passive conducting rod, located near the centre of the flux conserver and parallel to the vertical wall of the C-gun, the upper and the lower walls of flux conserver are short circuited; also the currrent passing through the wall is transformed to a closed-loop current, the discharge on capacitor bank circuit is suddenly cut-off, a potential difference between the electrodes of the C-gun up to 70 kV occurs. This voltage decays exponentially in 1.5 us to 6-8 kV, which is the minimum threshold voltage of the capacitors, according to a time constant of the external discharge circuit of 250 ms, this value continues for the lifetime of the CT.

While the drift wave is going on, the floating potentials of the charge-exchange cell are 350-400 V. The respective Langmuir probe potentials are 100-150 V, the cell currents are 350-400 uA and the probe currents are 100-150 uA.

The variations on the plasma space potential of the charge exchange cell generated probably by means of the transverse shock front of the density fluctuations are changed between 10 kHz and 25 kHz. On the other hand, the drift wave frequencies on the electrical surface probe are in the frequency range of 4-6 kHz.

Calculating the experimental data on Spitzer's resistivity formula, the avarage electron temperatures in the range of 30-45 eV have been found. The maximum electron density is about 5X10^14 cm-3. While the C-gun on-set, the volume averaged beta is about 0.12. The lifetimes of the CT have been lasted 5 ms or even up to 20 ms depending on the back ground gas pressure between 40 and 70 70 mTorr.

CONCLUSIONS

This compact toroid is not an unstable state of a toroid in MHD property having the microinstabilities, but it is a closed wave-electron ring which is the current channel modulated by the drift wave itself. Taking into cosideration the guiding centre approximation, for the electrons in this character, one can mention from the closed loop formation in the flux conserver. The mutual inductance between E-layer and the flux conserver can confine this system. Due to the current channel of the CT modulated, the azimuthal and toroidal field distributions may not be in clasical meanings. Nevertheless in the period of 5-20 ms passing up to the diffusion depending on the back ground gas pressure, it is a hot and dense plasma ring conserving its properties. Here, it has been seen that a CT which is not a conventional spheromak can be realized. The density profile of E-layer and its variations versus time are now investigating.

Consequently, a CT model is expected which is occured as a closed loop in the E-layers consisting of temperature and density fluctuations and serial plasma spheres like a string beads.

REFERENCES

/1/ BARNES, C.W., et al., Nuclear Fusion 24 (1984) 267.

/2/ UYAMA, T., et al., Nuclear Fusion 27 (1987) 799.

/3/ SINMAN, S., SINMAN, A., in Controlled Fusion and Plasma Physics (Proc. 12th Europ. Conf. Budapest, 1985), Vol. 9 F, Part I, European Physical Society (1985) 642.

/4/ SINMAN, A., SINMAN, S., in Controlled Fusion and Plasma Heating (Proc. 13th Europ. Conf. Schliersee, 1986), Vol. 10 C, Part I, European Physical Society (1986) 377.

/5/ SINMAN, S., SINMAN, A., ibid., p. 381.

/6/ SINMAN, S., SINMAN, A., in Plasma Physics and Controlled Nuclear Fusion Research 1986 (Proc. 11th Int. Conf. Kyoto, 1986), Vol. 2, IAEA, Vienna (1987) 731.

/7/ SINMAN, S., SINMAN, A., in Controlled Fusion and Plasma Physics (Proc. 14th Europ. Conf. Madrid, 1987), Vol. II D, Part II, European Physical Society (1987) 465.

/8/ TAYLOR, J.B., Phys. Rev. Lett. 33 (1974) 1139.

ACKNOWLEDGEMENT

This work was performed under a co-operative agreement between the Turkish Atomic Energy Authority and the International Atomic Energy Agency, Vienna, Contract No. 3823/R3/RB.

HEATING AND CONFINEMENT IN SK/CG-1 SPHEROMAK

A.Sinman and S.Sinman *

Nuclear Fusion Laboratory, Nuclear Research and Training Centre, Turkish Atomic Energy Authority

* Plasma Engineering Laboratory, Electrical and Electronic Engineering Department, Middle East Technical University

Ankara, Turkey

ABSTRACT

It has been understood that a spheromak (SK/CG-1, "World Survey of Activities in Controlled Fusion Research" 1986 Edition, IAEA Vienna, p. 197) can be formed using a C-gun, when the back ground gas pressure in the floating flux conserver is selected in the range of 70-250 mTorr. As a result of evaluation of signals taken from the magnetic and electric probes and the total flux loop, it has been seen that this procedure is in a very close agreement with the minimum energy state (k = uoJ/B = constant) and magnetic helicity injection concepts. Measurements have been done in either poloidal or toroidal planes on a cross section at the angular distance of 135 degree from the gun. At the beginning, the ion cyclotron waves at the frequency range of 10-15 MHz which are generated by the field of C-gun directly and which are damping in the first half period of 5 us, rethermalize the shock heated electrons by the C-gun, having average energies between 15 and 35 eV. All of these phases are come together on the ohmic heating consept. Thus, a portion of 8-10 % of the bank energy is interchanged into the plasma volume of 1381 cm3. The spheromak plasma parameters obtained are as follows: the electron densities and temperatures are in the ranges of 10^14-5X10^15 cm-3 and 20-30 eV, the toroidal-poloidal flux densities at 7 cm distant from the wall of flux conserver are about 600-800 G. and the volume averaged beta calculated are between 0.006 and 0.085.

INTRODUCTION

The spheromak configuration has been succesfully formed by three different type of production schemes of: i) the magnetized co-axial injector; ii) the field reversed theta pinch with the center column Z discharge and iii) electrodless quasi-static scheme /1-3/.

In order to produce a compact toroid (CT) by means of four magnetized T-tubes; a conceptual design and its expected results had been presented /4/.

In our previous study, it has been experimentally demonstrated that in the flux conserver, using a C-gun, the CT particularly in two different behaviours may be formed /5/.

Especially in spheromaks, as in the Los Alamos (CTX) and the Osaka (CTCC) devices /6,7/, the toroidal fields at the flux conserver are produced by the poloidal field injection (magnetized co-axial plasma gun) through the flux conserver. This is a toroidal poloidal flux translation mechnism and it can be explained by the magnetic helicity consept /8/.

Although, the spheromak formation schemes are different from each other, in practice, to arrive to needed Lawson's fusion energy product, it will be necessary some additional heating systems together with the confinement techniques.

In this study, bearing in mind this approachment, agreeable heating and confinement mechanisms in the spheromak plasma generated by the C-gun have been investigated and from the view point of conceptial design, some additional heating alternatives have been proposed.

THE DEVICE

The experimental arrangement has a 40 L octagonal floating flux conserver which is also the vacuum chamber either. The back pressure in the flux conserver is 5X10^-6 Torr. Four C-guns in 90 degrees aparts are arrenged around the flux conserver.

The C-gun is noval and alternative version of the conventional magnetically driven plasma gun. The vertical two electrodes at the toroidal plane in the flux conserver and the back strap outside the conserver are the main structure of the C-gun. Its electrical characteristics conform with the Critical Damping and Under Damping Modes (CDM and UDM) depending upon the back ground gas pressures.

The system consists of 2 kJ capacitor bank for each C-gun, and the spark-gap switches controlled by self generated UV ring.

The main diagnostic techniques used are: the Langmuir probes, paramagnetic and total flux loops, the magnetic probes, the Rogowski coil,the L-R fast operational integrator and visible light spectrum analyzer.

RESULTS

By the present status of the SK/CG-1 machine driven by the C-gun, which is presented here, have not the additional heating and confinement techniques yet on it.

The operating period of the C-gun is about 50-60 us. The maximum toroidal magnetic flux density generated by the poloidal loop current of 150 kA of the C-gun is approximately 15-20 kG. and the internal electric field is 900 V/cm. The optimum Helium gas pressure is 200-250 mTorr.

It has been determined that, in the initial phase of the discharge lasting 2-4 us and at the frequency region of 10-15 MHz the intense ion cyclotron waves are generated and as being in the magnetic beach, the plasma electrons are rethermalized by the damping of these waves in a few microseconds. The ion cyclotron

waves have been detected directly by a magnetic pick-up coil at an angular distance of 135 degrees from the C-gun. It has been understood that the mentioned ion cyclotron waves have a propagation vector and according to the guiding center approximation principle, it is conserving the characteristics of a closed wave motion in the flux conserver.

On the total flux measurements, it has been observed that the diamagnetism is begining again at the initial phase of the discharge. After the off-set state of the C-gun, the diamagnetism is translated into paramagnetism. Depending on the total flux decay time, the paramagnetism duration is about 2.5-3.5 ms.

On the other hand, the shock heated hot electrons in the plasma belt by the energies of 45-60 eV, either ionizes the back ground gas at the pressures of 200-250 mTorr, or thermalize this plasma collectively.

According to the measurements carried out by the Langmuir probe and paramagnetic loop, after reconnection, in 0.5-1.5 us the electron temperatures of the spheromak plasma have been found around 15-35 eV.

CONCLUSIONS

The main results obtained in this work are:

-In the initial phase of the discharge, the shock heated electrons of the plasma belt, either ionize the back ground gas (He, 200-250 mTorr) or thermalize the electrons in this plasma medium.

-By the influence of the toroidal field (15-20 kG) produced by plasma belt inside the flux conserver and the back strap, a closed helical current channel in the flux conserver is coming into existance.

-The energetic helical electrons in the current channel are formed the E-layer and as in the beam-plasma interactions, under the influence of toroidal field, the ion cyclotron waves (10-15 MHz) are generated. Damping this waves in 3-4 us, the electrons in the plasma channel are rethermalized.

-The paramagnetism at CT is probably the event of the self toroidal magnetic field of the helical current channel.

-In the heating mechanism, there exist the phases of; shock heating, rethermalization by ion cyclotron wave damping and the ohmic heating by paramagnetism.

-For the confinement of CT, the mutual inductance between the flux conserver and the E-layer is fairly effective. In addition, it is supposed that, the electrons with closed helical orbits behave as the toroidal electron field coils.

-Due to the mutual inductance between the back strap and the wall of flux conserver, The energy transfer from capacitor bank to the conserver is possible. Thus, because of the eddy currents, the flux conserver contains the self poloidal fields.

-The C-gun is a new magnetically driven high efficiency plasma gun. By means of the C-gun, either a CT is formed, or the pre-heating of the CT is realized.

Consequently, these initial experimental results and their original constructional properties of SK/CG-1 have shown that, the effective additional heating methods can extensively used on it. In this content; i) by means of the external poloidal fields, some additions to the ohmic heating and confinemant, ii) using the floating flux conserver as a cavity, the high frequency heating and iii) applying the modulated poloidal magnetic field, the current drive processes can successfully be realized.

REFERENCES

/1/ Jarboe, T., et al., Phys. Rev. Lett. 45 (1980) 1264.

/2/ Goldenbaum, G., et al., Phys. Rev. Lett. 44 (1980) 393.

/3/ Yamada, M., et al., Phys. Rev. Lett. 46 (1981) 188.

/4/ Sinman, S., Sinman, A., in Controlled Fusion and Plasma Physics (Proc. 12th Europ. Conf. Budapest, 1985), Vol. 9F, Part I, European Physical Society (1985) 642.

/5/ Sinman, S., Sinman, A., in Controlled Fusion and Plasma Physics (proc. 14th Europe. Conf. Madrid, 1987), Vol II D, Part II, European Physical Society (1987) 465.

/6/ Barnes, C.W., et al., Nuclear Fusion 24 (1984) 267.

/7/ Uyama, T., et al., Nuclear Fusion 27 (1987) 799.

/8/ Taylor, J.B., Phys. Rev. Lett. 33 (1974) 1139.

ACKNOWLEDGEMENT

This work was performed under a co-operative agreement between the Turkish Atomic Energy Authority and the international Atomic Energy Agency, Vienna, Contract No. 3823/R3/RB.

TOROIDAL Z PINCH EXPERIMENT

K. SUGISAKI

Electrotechnical Laboratory
1-1-4 Umezono, Tsukuba, Ibaraki, Japan

Equilibrium (θ = constant) field configuration of toroidal Z pinch ZP-2 is examined for discharges of a plasma current below 22 kA. Field and current profiles agree with a modified Bessel function model. Pressure distribution is deduced from magnetic field profiles and gives β_p of 10 to 15%.

Field fluctuations, observed during setting-up and equilibrium stages, are investigated by means of magnetic probes inserted in a plasma. Evolution of local toroidal fields of m=1 mode leads to spontaneous generation of toroidal field flux during setting-up stage. It is also shown that m=0 and m=1 field fluctuations during equilibrium stage are correlated with regeneration of the field flux.

For a discharges of plasma current as high as 40 kA, the plasma of electron temperature of 90 eV and average electron density of 5×10^{13} cm^{-3} is obtained.

1. Introduction

In a toroidal Z pinch, the plasma current is produced by induction of OH coils, while toroidal magnetic fields are spontaneously generated from relaxation of field configurations. Then, the toroidal Z pinch provides a class of toroidal plasma confinement schemes which does not have toroidal coils and may show promise for plasma confinement systems in fusion use[1]. In the previous report[2], we have shown that a nearly force free field configuration, similar to that of spheromak, is established in ZP-2 plasmas. Typical parameter traces of a discharge are shown in Fig. 1 for loop voltage V_{loop}, OH coil current I_{OH}, toroidal plasma current I_p, toroidal flux loop signals ϕ_{1-4} and pinch parameter θ. The discharge is initiated at t=100 μs. Pinch parameter θ of 1.3 to 1.4 is obtained and is held constant during the discharge (constant θ stage). However, field fluctuations of m=1 mode persist during equilibrium stage.

In the present report, we examine details of equilibrium of the plasma with the aid of numerical calculations. Physical mechanism of spontaneous generation of the field flux is discussed in relation to m=1 kink mode in a linear Z pinch. Relation with field fluctuations observed during equilibrium stage and flux regeneration are also investigated.

2. ZP-2 device

Details of ZP-2 device are described elsewhere[2] and we describe briefly its outline. Figure 2 shows a cross sectional view of ZP-2 device. The vacuum vessel is a 1.5 mm thick stainless steel liner with insulating brakes and consists of four sectors. Each sector has 18 mm thick connection flange and is connected to each other with 15 mm thick Teflon flanges, of which the plasma side is covered with a 5 mm thick ceramic limiter. The plasma current is produced from induction of OH coil current.

3. Equilibrium field configuration

We calculate field and current density distribution from magnetic field measurements, as seen in Fig. 3. Using pseudo-toroidal coordinates (ρ, θ, ζ) and arbitrary functions F and G of the radius ρ, we express field and current profiles as

$$B_\rho = 0,\ B_\theta = \frac{F}{(1+\rho/R\cos\theta)},\ B_\zeta = \frac{G}{(1+\rho/R\cos\theta)},$$

$$j_\rho = 0,\ j_\theta = -\frac{1}{(1+\rho/R\cos\theta)}\frac{\partial G}{\partial \rho},\ j_\zeta = \frac{1}{\rho}\frac{\partial}{\partial \rho}\left(\frac{\rho F}{1+\rho/R\cos\theta}\right).$$

Field profiles are obtained from expansion of F and G in powers of ρ as

$$F = C_0+C_1\rho+C_2\rho^2+C_3\rho^3+C_4\rho^4+\cdots\cdots,$$

$$G = D_0+D_1\rho+D_2\rho^2+D_3\rho^3+D_4\rho^4+\cdots\cdots,$$

where ρ is measured from the magnetic axis. Coefficient C's and D's are calculated from best fitting to magnetic field profiles. We define two parameters $\mu_{//}$ and $\mu_\perp$ as

$$\mu_{//} = \frac{jB}{B^2},\quad \mu_\perp = \frac{j\times B}{B^2}$$

which represent the parallel and perpendicular current densities. Figure 4 shows profiles of $\mu_{//}$, $\mu_\perp$, safety factor $q(\rho) = \rho B_\zeta / RB_\theta$ and plasma pressure P normalized by magnetic pressure $1/2(B_\zeta^2 + B_\theta^2)$. The different type of β are defined as

$$\beta_0 = \frac{P(0)}{B_\zeta^2(0)},\quad \beta_p = \frac{\langle P\rangle}{B_{\theta,\ wall}^2}.$$

We obtain β_0 of 12.9% and β_p of 13.2% for the field configuration shown in Fig. 3.

4. Field Fluctuations

Figure 5 shows time evolution of toroidal and poloidal field profiles immediately after a discharge. Local toroidal fields with positive and negative directions appear during 6 to 10 μs after appearance of the poloidal field. The points where the troidal field is maximum agree fairly with the points where the poloidal field is null. Then, the points are regarded to represent the center of the plasma. The inside toroidal field, which includes plasma center, persists whereas the outside field disappears, and net toroidal flux is generated. It is shown theoretically that m=1 helical deformation in Z pinch produces positive and negative toroidal field inside and outside the plasma center. Then, we conclude that the local field inside the plasma contributes to the spontaneous generation of the field flux. As the plasma current rises, the toroidal field increases and a quasi-equilibrium (θ=constant) is established. However, field fluctuations persist during equilibrium stage. Figure 6 shows time evoluation of average field flux Φ_{avg}, time derivatives of flux loop signals $d\Phi_{1-4}/dt$, radial shift δ_p of toroidal current channel, the ratio ε of the edge toroidal field to peak toroidal field, and width of toroidal and poloidal current channels d_p, d_t. Shift δ_p represents m=1 mode and width d_p, d_t m=0 mode. Apparently, regeneration of the field flux is correlated with m=0 and m=1 field fluctuations.

5. High current operation

Soft x-ray emission is observed after burning of CIII impurity line. The electron temperature T_e is evaluated from relative absorption of soft x-rays through aluminium foil, using two silicon-barrier diodes equipped side and down ports at the same toroidal location. The electron temperature of 90 eV is obtained for a discharge of the plasma current of 40 kA. Spectroscopic measurements indicate appearance of CV line late in the discharge and support soft x-ray measurements. The electron density is determined from a CO_2 laster Michelson interferometer and gives the average line electron density of 3 to 5 $\times 10^{13}$ cm^{-3}. The electron density is nearly constant during discharges. Poloidal beta β_p is calculated from plasma parameters and is about 10%.

References

1) K. Sugisaki and K. Hirano: Bull. Electrotechnical Laboratory **49** (1985) 50.
2) K. Sugisaki: J. Phys. Soc. Japan **56** (1987) 3176.

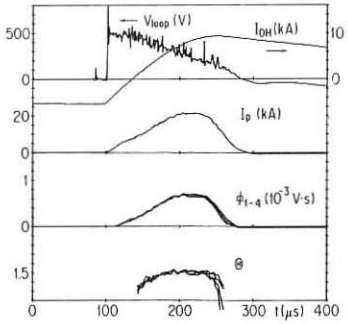

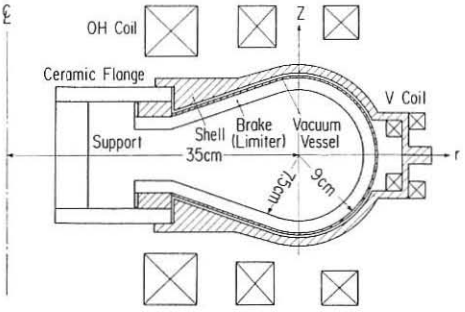

Fig. 1 (left): Typical parameter traces. Fig. 2 (right): Cross sectional view of ZP-2.

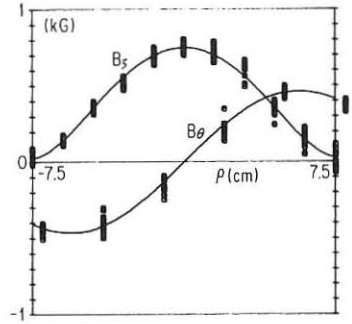

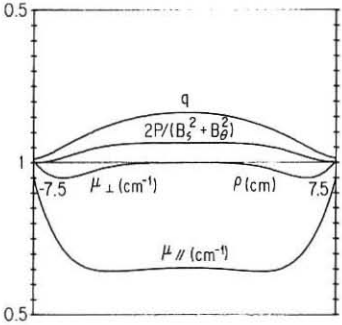

Fig. 3 (left): Profiles of magnetic fields. Fig. 4 (right): Profiles of calculated equilibrium plasma parameters.

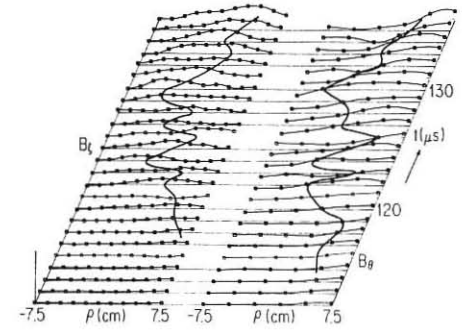

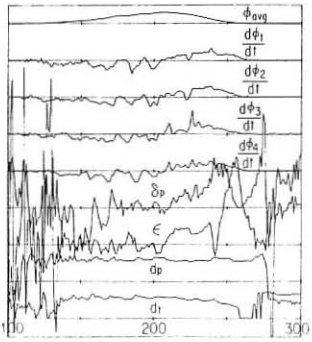

Fig. 5 (left): Time evoluation of magnetic field profiles. Bold curves indicate the points where B_θ=0 and B_ζ=max.

Fig. 6 (right): Time evoluation of field flux and fluctuations.

RECENT RESULTS OF THE TOROIDAL SCREW PINCH SPICA II

H. S. Lassing, J. Lok, A. F. G. van der Meer, G. A. Navratil*, D. Oepts, A. A. M. Oomens and M. Verreck
Association Euratom-FOM, FOM-Instituut voor Plasmafysica, Rijnhuizen,
P. O. Box 1207, 3430 BE Nieuwegein, The Netherlands

1. Introduction.

SPICA II is a toroidal screw-pinch device with an elongated minor cross-section (R= 0.45 m, b/a= 0.7 m /0.3 m). The physics objective is to study the production and evolution of plasmas with high (local) values of ß [1]. Dense plasma columns are obtained by shock heating and they should be stabilized by force-free currents flowing in the dilute plasma occupying the region between column and conducting wall. Earlier reports on the experimental results can be found in Refs.[2] and [3]. The experiments in SPICA II were terminated in October 1987. In the preceeding months more than 1000 discharges were made, the majority in the normal, fast, screw-pinch mode, a number in the "slow" screw-pinch mode (without shock heating) and a few in the reversed-field-pinch mode. The results from this latter mode will be discussed elsewhere. With the discharges in the "slow" screw-pinch mode we have tried to reproduce the high-ß plasmas obtained in the Japanese TPE-2 device [4]. In this mode the power crowbar banks are switched on when the predischarge current and the bias field have reached their maximum value. It turned out that at these low plasma currents ($\leq$ 70 kA) the stabilization by the conducting wall could not prevent disastrous plasma-wall contact. It is concluded that for this mode of operation a pulsed vertical field, like in TPE-2, is essential. After a few remarks about the diagnostics, the remainder of this paper will be restricted to a discussion on the results obtained in the normal screw pinch mode.

2. Diagnostics.

As reported before, the aluminium shell of SPICA II contains a large number of viewing holes. Twenty-two of these holes in one poloidal cross-section are used to observe the emission of plasma light in the near-infrared [3].The viewing angle of the fibres is shown in Fig.1, together with the viewing chords of the interferometers. The signals from the separate channels are digitally recorded and processed after the shot. In the infrared region the contribution by recombination and line radiation is small, and since $E/kT_e \ll 1$ the emission intensity can be written as $dP(E)/dE \approx n_e^2 T_e^{-1/2}$. The weak dependence on T_e is of little importance in SPICA II where the temperature profile is rather flat. The emission profile in the near-infrared can therefore be identified with the profile of n_e^2. A reconstruction of the emission profile is made by a maximum entropy method, without making additional assumptions on the structure of the source. The software has been developed by Holland and Navratil to determine density profiles in the Columbia University High Beta Tokamak experiment [5]. There has also been an increase in the number of pick-up coils. The poloidal magnetic field at the wall has been measured at 20 positions in one cross-section and 12 at a different toroidal angle. A software package, to calculate from the magnetic measurements global parameters like the radial and vertical shift of the current centre, $ß_p$, the internal inductance etc., has been developed.

---

* Permanent address: Plasma Physics Laboratory, Columbia University, New York, N. Y., U. S. A.

3.**Plasma operation.**

The predischarge phase. A series of predischarges, without main discharge, was made,while scanning the input parameters to investigate the role of the predischarge conditions. It is concluded that a low temperature plasma could be produced with a degree of ionization between 10% and 80% in the filling pressure range from .5 to 2 Pa. The ionization could be achieved with a unidirectional plasma current (in contrast to the ringing discharges used before), resulting in a strongly reduced interaction with the quartz wall. The toroidal magnetic field in this plasma has been varied between 1 and 10% of the value in the main discharge. The variation in density is about 10% from shot to shot, the spatial distribution is unknown.

The formation phase. During the formation the safety factor at the wall, q_I, is kept almost constant. Slight changes are inevitable, since the plasma inductance is strongly related to the shape of the plasma column, hence influenced by the difference in horizontal and vertical contraction. Most of the discharges were done with q_I around 2 ($I_p \approx 0.4$ MA) and a filling pressure of 1 Pa. The highest temperature that could be obtained reliably was 100 eV, measured with the multi-point Thomson scattering at 10 μs, and the maximum value of the local ß was around 27% (Fig.2). A scan in q_I from 0.75 to 3.4 did not show a significant difference in T_e- and n_e-profiles nor in the density traces from the interferometers. Varying q over this range was only possible by varying B_T, so one would expect a change in T_e, as was observed in the earlier (circular) devices. It should be remarked that also the observed ß-values are not in accordance with the modified snow-plow model [1] which predicts ß-values in the range from 40 to 70%. An attempt was made to reach higher temperatures by operating at low filling pressures ($0.2 \text{ Pa} < p_0 < 1.0 \text{ Pa}$). These discharges appeared to be very unstable. The formation can be described by a horizontal implosion on a short timescale (2 μs) and a vertical compression on a longer timescale (≤10 μs). During the first few μs the plasma column shows an extreme elongation. This observation, made earlier from streak pictures, is confirmed by the pick-up coils and by tomographic reconstruction as illustrated in Fig.3.

The decay phase. In spite of all the attempts, no discharges were found with a compression lasting longer than 200 μs. In fact in the majority of the discharges the density was suddenly lost within 50 μs. The observed, irreproducible, lifetimes do not seem to be correlated to any external parameter, except for the filling pressure. The lifetime tends to decrease with a decreasing p_0. From the limited number of measurements with Thomson scattering data at times later than 10 μs, but before the sudden loss of compression, we conclude that the central values of T_e and n_e remain constant, but that the width and the position of the column change in the horizontal plane. From the magnetic field measurements we conclude that the current distribution is very broad and elongated (1:2) during the whole discharge. Most often this toroidal current distribution is maintained much longer (up to 500 μs) than the density distribution. There is no experimental evidence that impurities play an important role in the discharges. In Fig. 4 some parameters of a shot with a relatively long lifetime are shown.

Conclusion. The method of shock heating is not suitable to produce high-ß plasmas with strongly elongated minor cross-section if one relies completely on wall stabilization via force-free currents.

Acknowledgements. The authors wish to thank Mrs. B. J. J. Grobben, W. Kooijman, W. J. Mastop, B. J. H. Meddens and P. H. M. Smeets for operation of the machine and for their assistance in diagnostics and data-handling.
This work was performed under the Euratom-FOM association agreement with financial support from NWO and Euratom.

References

[1] SPICA II Team, Nucl. Instrum. Methods **207** (1983) 49.

[2] SPICA II Team : C. Bobeldijk et al., Proc. 12th Eur. Conf. on Contr. Fusion and Plasma Phys., Budapest (1985) Vol. 9F-I, p. 594.

[3] A. A. M. Oomens, H. S. Lassing et al., Proc. 14th Eur. Conf. on Contr. Fusion and Plasma Phys., Madrid (1987) Vol. 11D-II, p. 458.

[4] A. A. M. Oomens, S. Kiyama et al., Proc. 14th Eur. Conf. on Contr. Fusion and Plasma Phys., Madrid (1987) Vol. 11D-II, p. 494.

[5] A. Holland, G. Navratil, Columbia University Rep. no. 99, DOE/ET/53016-88 UC-20d (1985).

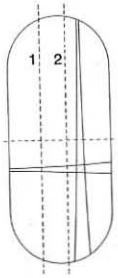

Fig. 1. Examples of the viewing ← angle of the fibres used in the tomography diagnostic. In total there are 11 channels in vertical and 11 in horizontal direction. The viewing chords of the interferometers, located at a different toroidal angle, are indicated by dashed lines.

Fig. 2. T_e- and n_e-profile in the → equatorial plane at 10 μs in a discharge with p_o= 1 Pa, B_o= 0.01 T and B_T = 0.8 T

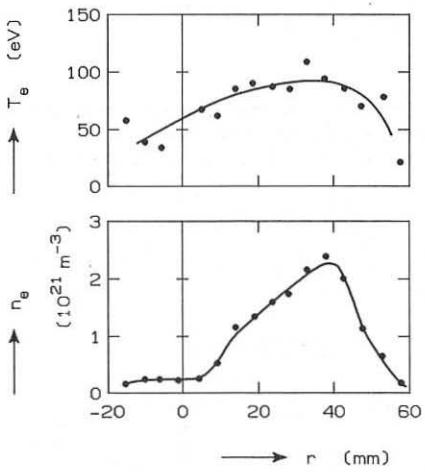

Fig. 3. a. A digital streak picture of a discharge ↓ with relatively long compressed phase. (top : top view; bottom : side view)

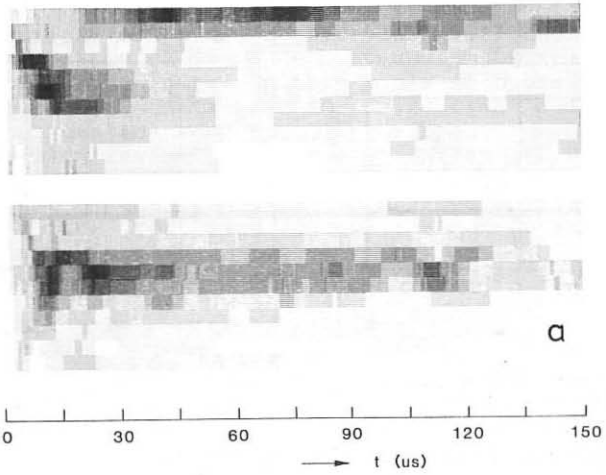

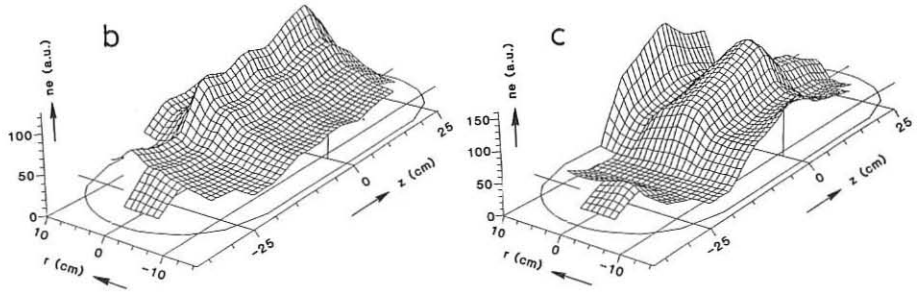

Fig.3b. Reconstructed emission profile in a poloidal cross-section at t = 4 μs, showing an extremely elongated column,
c. profile at t = 12 μs after vertical compression.

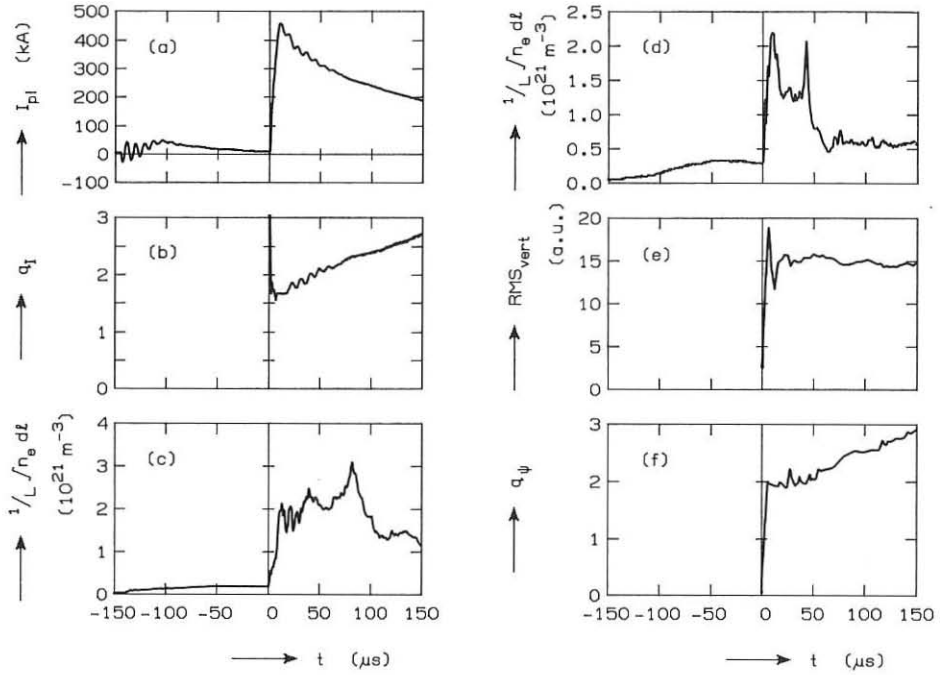

Fig. 4. Some parameters of the discharge of Fig. 3. From top to bottom : a. The plasma current. b. q_I at the wall. c. $1/L \int n_e dl$ along a horizontal chord. d. $1/L \int n_e dl$ along a vertical chord at r = 0.025 m (nr 2 in Fig 1.). e. RMS-vert, a parameter representative for the vertical elongation from B_p-analysis.f. q_ψ at the wall from B_p -analysis.

INVESTIGATION OF CONVERGENT DEUTERON BEAMS WITHIN A PENETRABLE ELECTRODE SYSTEM

E.Skladnik-Sadowska, J.Baranowski, and M.Sadowski

Soltan Institute for Nuclear Studies,
05-400 Swierk,Poland

INTRODUCTION

The paper reports on studies of a penetrable electrode set designed for the generation of convergent deuteron beams required for the cylindrical ion implosion /1-2/. Experimental studies have been performed mainly with the MAJA-60 facility equipped with multi-rod cylindrical electrodes or quasi-conical ones with different inter-electrode gaps.

EXPERIMENTAL RESULTS

The mass and energy analysis of the ion beams emitted along z-axis, as well as time-resolved measurements of the deuteron pulses, have been performed /3-4/ especially for the quasi-conical electrodes supplied by a 48 μF condenser bank charged up to 40 kV. In order to study a spatial structure, several series of stereoscopic observations with a ion-pinhole camera which were equipped with CN track detectors, have been carried out. On the basis of those measurements, it was possible to determine the location and approximate dimensions of ion sources. It has been found that for the so-called slow regime of the operation /at τ=210 μs/ in the system of the cylindrical electrodes /see Fig.1/ as well as in that of the quasi-conical ones /see Fig.2/, there is formed an ion focussing region of about 40 mm in dia. and about 80 mm in length.

Using the CN films with and without additional Al-foil filters, it has been shown that the ion foci in question are formed usually by deuterons with energy >30 keV. The sharp (contrast) ion pinhole pictures taken under the conditions discribed above suggest a balistic character of the ion motion. Analogous measurements performed for other modes of the operation, i.e., for a medium regime at τ=160 μs and for a fast regime at τ= 120 μs, have shown that the ion pinhole picture taken at the distance of 40 cm are blurred and they have a background of some 10^7 ions/cm^2. These effects suggest

lower efectivity of the focussing of ion beams in the other operational regimes.

Simultaneously with the ion measurements in the MAJA facility, there have also been performed observations of a plasma by means of X-ray pinhole cameras /equipped with 10 μm-thick Be-filters/. In all the cases, when a marked ion focus was formed, there was also observed a distinct region of the X-ray emission /see Fig.1, Fig.2/. The plasma focus region, as observed in the X-rays, has been about 10 mm in diameter and about 60 mm in length, i.e., considerably smaller than the ion focus region. It should also be noted that in such cases the neutron yield has reached the maximum value of the order of 10^9 neutrons/shot.

CONCLUSIONS

These observations show some interdependence between processes of ion/electron acceleration and the yield of the fusion reactions in the multi-rod electrode systems.

It may be concluded that the MAJA-60 kJ facility, based on the high-current, low-pressure discharge between particle-transparent, multirod electrodes, is the efficient source of convergent ion beams.

REFERENCES

1. Gryzinski, M. et al..: Proc.7th Intern.Conf.PPCNFR /Innsbruck 1978/, Vol.III, p.225.
2. Skladnik-Sadowska, E., Baranowski, J., Gryzinski, M., Langner, J. and Sadowski, M.: J.Physique 43/1982/715.
3. Skladnik-Sadowska, E. et al.: Proc.18th Intern.Conf.PIG /Swansea 1987/,p.420.
4. Gryzinski, M. et al.: Proc. 14th Europ. Conf. CFPP /Madrid 1987/, Vol.II, p.645.

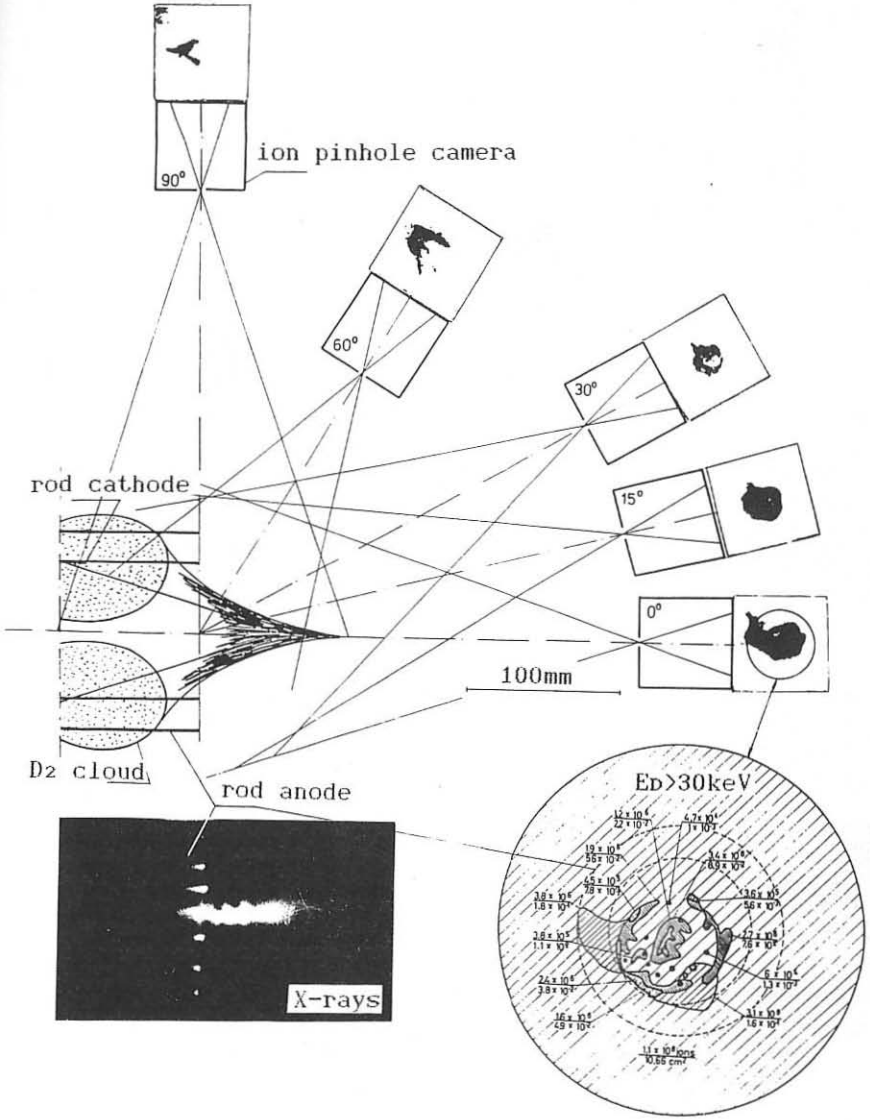

Fig.1. *Ion pinhole pictures taken at different angles in the* **MAJA-60** *facility equipped with the cylindrical penetrable electrodes and operated in a "slow regime" with a time delay* τ= 210μs. *Below-an X-ray pinhole picture taken side-on, and an enlarged ion density map corresponding to the end-on ion picture.*

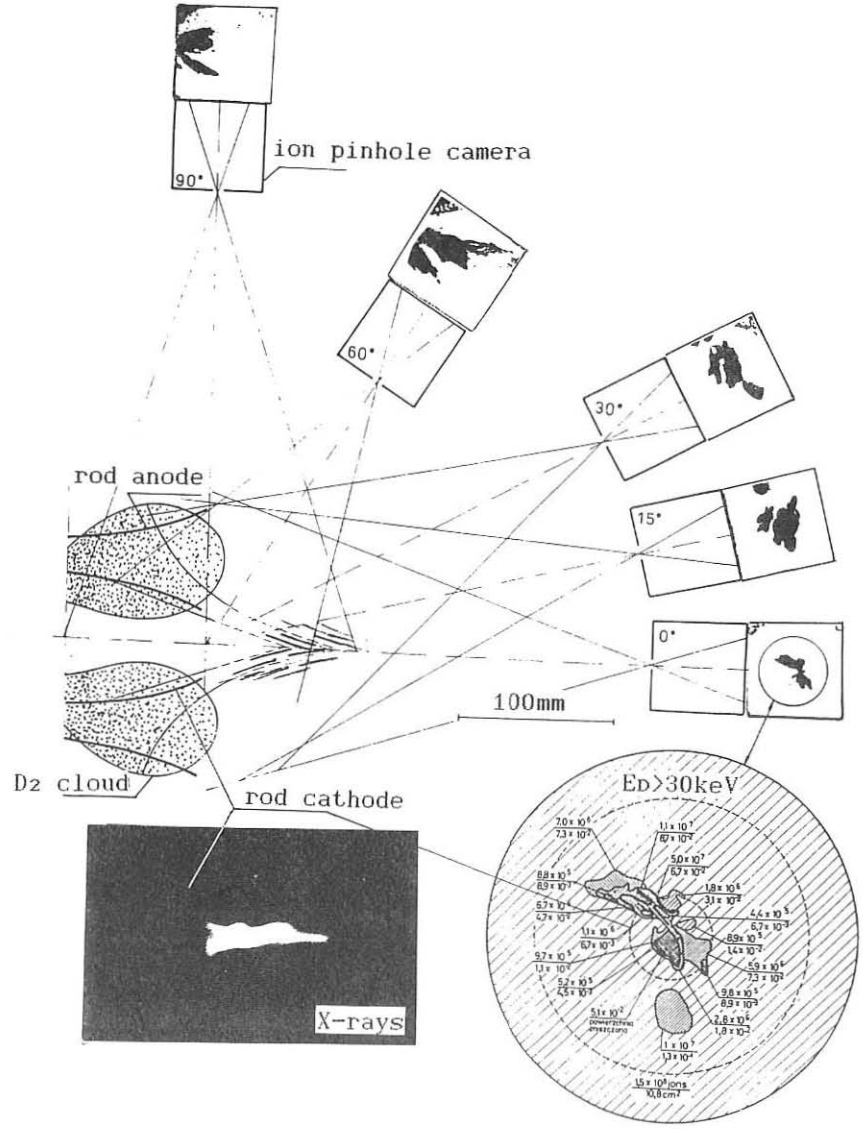

Fig. 2. *Ion pinhole pictures in the* **MAJA** *facility for the quasi-conical electrodes and a slow operation mode (τ=210 μs). Below - an X-ray pinhole picture taken side-on, and enlarged ion-density map corresponding to the end-on ion picture.*

STABILITY OF EXTENDED TAYLOR STATES IN A WEAKLY RESISTIVE, CYLINDRICAL, FINITE β PLASMA TO HELICAL PERTURBATIONS

J.B.M.M. Eggen, Eindhoven University of Technology,
P.B. 513, 5600 MB, Eindhoven, The Netherlands.
W.Schuurman, FOM-Institute for Plasma Physics,
P.B. 7, 3430 AA, Nieuwegein, The Netherlands.

Abstract: The stability of cylindrical symmetrical equilibria as predicted by a minimum magnetic energy principle for a weakly resistive, cylindrical, finite-β plasma, to helical perturbations with dependence exp (imθ + ikz) on the cylindrical coordinates θ,z is investigated. A Rayleigh ratio method is applied to obtain the sign of the second order generalised energy functional of the describing energy principle for various perturbations. An equilibrium is stable if this sign is positive. The resulting stability condition is first given in terms of equilibrium parameters and then transformed to a condition on the total longitudinal plasmaflux Ψ. This condition is $\Psi/2\pi aB_0 > 0.1$.

The model and its resulting equilibria.

An extended version of Taylor's minimum magnetic energy principle [1] for the relaxation of a weakly resistive,cylindrical,finite-β plasma enclosed by a perfectly conducting metal wall minimises the magnetic energy Wb of the plasma for fixed magnetic helicity $K = \int A\cdot B\, d\tau$ and total longitudinal flux Ψ with the total potential energy $E = \int \{B\cdot B/2\mu_0 + p/(\gamma-1)\}\, d\tau$ and force- balance $P = \nabla p - j \times B = 0$ as additional constraints. The mathematical formulation to determine the extrema is then:

$$\delta W = \delta \{ Wb - \alpha E - \lambda K - \Psi \Psi - \int \mu\cdot P\, d\tau \} = 0 \qquad (1)$$

where α,λ,Ψ are constant Lagrange multipliers and $\mu(r)$ is a space dependent one. For a cylindrical,infinitely long plasma of radius a with rotational and translational symmetry the extremal profiles are derived in [2]. If we restrict ourselves here to equilibria describing reversed field pinch (RFP) experiments with peaked pressure profiles, characterised by $0 \leq \alpha < 1$, the profiles are:

$$B_z(r) = B_0 J_0(\sigma r)\ ; \qquad B_\theta(r) = B_0 f J_1(\sigma r) \qquad (2a,2b)$$

$$p(r) = p_0[\alpha(J_0^2(\sigma r) - 1)/\{1-\alpha)(\gamma-1)\beta_0\} + 1]\ ;\ \mu(r) = \alpha r/2 \qquad (3a,3b)$$

with J_n the ordinary Besselfunction of the first kind, $f^2 = \{(1+\kappa\alpha)/(1-\alpha)\}$, $\kappa = (2-\gamma)/(\gamma-1)$, $\beta_0 = 2\mu_0 p_0/B_0^2$, $\gamma = 5/3$ and $\sigma^2 = \lambda^2/\{1+\kappa\alpha)(1-\alpha)\}$.

Stability of the equilibria.

To determine whether an extremum of the form (2,3) is an unstable equilibrium (maximum) or a stable equilibrium (minimum, or true equilibrium) the second variation of the generalised energy functional has to be calculated. For the used model this second variation can formally be expressed as:

$$\delta^2 W = \delta^2 Wb - \lambda\delta^2 K - \alpha\delta^2 E - \Psi\delta^2\Psi - \int \mu\cdot\delta^2 P d\tau \qquad (4)$$

and this functional can explicitly be written as ($\nabla\times\delta A = \delta B$)

$$\delta^2 W(\delta B) = (1-\alpha)\int \delta B\cdot\delta B d\tau - \lambda\int \delta B\cdot\delta A d\tau + \int \mu\cdot(\nabla\times\delta B)\times\delta B d\tau \qquad (5)$$

If $\delta^2W > 0$ for all allowed perturbations the extremum is a minimum and the equilibrium is stable. The idea is to determine the perturbation that extremises δ^2W and to calculate δ^2W for this perturbation. This is however not straightforward since it has to be determined whether this extremising perturbation itself is a minimum or maximum. To avoid this complication we will calculate (5) by means of a Rayleigh ratio technique [3]. We will consider two classes of perturbations: 'free' perturbations that satisfy only regularity and boundary constraints imposed by the surrounding perfectly conducting metal wall, and 'restricted' perturbations that have to satisfy also global constraints. In both cases purely symmetrical (m=k=0) perturbations have to be treated differently from helical perturbations.

1. Free perturbations

To calculate δ^2W with a Rayleigh ratio method we rewrite (4,5) as

$$\delta^2F = (1-\alpha)c^2(1 - \lambda R) \qquad (6)$$

where $c^2 = \int \delta B \cdot \delta B \, d\tau$; $R = c^{-2}(\delta^2K + \int \mu \cdot \delta^2P \, d\tau)/\{\lambda(1-\alpha)\}$.

Now suppose the maximum of R equals M^{-1}: $\max\{R\} \equiv M^{-1}$. Then for $0 \leq \alpha < 1$ a necessary and sufficient condition for stability is: $M > \lambda$. After straightforward calculus it follows that the perturbations that maximise R have to satisfy the equation:

$$(1-\alpha)M^{-1}\nabla x\delta B - \delta B + 1/\{(\gamma-1)\lambda\} \nabla x\{\nabla x(\delta B x\mu) + \mu x(\nabla x\delta B)\} = 0 \qquad (7)$$

For perturbations of the form $\delta B = (\delta B_r(r), \delta B_\theta(r), \delta B_z(r))\exp(im\theta+ikz)$ this equation can be written out in components, that can be combined into one solvable ordinary differential equation. The solution has to satisfy $\delta A_\theta(a)=0$ for the m=k=0 mode and $\delta B_r(a)=0$ for the other modes (due to the perfectly conducting metal wall). This condition yields M in terms of α and λ. For both symmetrical and helical perturbations M can be given in terms of the equilibrium parameters and the mode numbers m,k by the transcendental equation:

$$(1-b)\, mJ_m(\chi) + b\chi\, J_{m-1}(\chi) = 0 \qquad (8)$$

with $\chi^2 = (1-b^2)/\sigma_1$, $b=k(1-\alpha)/M$ and $\sigma_1^2 = [(1-\alpha)/M + \alpha/\{(\gamma-1)\lambda\}](1-\alpha)/M$. Using this result the stability of the equilibrium is given in fig.1. in terms of the equilibrium parameters λ and α.

2. Restricted perturbations.

In our model we took helicity, potential energy, flux and force-balance as constraints for the extremalisation of the magnetic energy. If we require that these constraints also hold in first order the perturbations δB and δp must satisfy:

$$\delta K = 2\int \delta B \cdot A_0 \, d\tau = 0 \quad ; \quad \delta P = \nabla\delta p - \{(\nabla x\delta B)xB_0 + (\nabla xB_0)x\delta B\} = 0 \qquad (9a,b)$$

$$\delta E = \int(\delta B \cdot B_0 + \delta p)\, d\tau = 0 \quad ; \quad \delta A_\theta(a) = 0 \quad ; \quad \delta A_z(a) = 0 \qquad (10a,b,c)$$

Eqs.(9a,10a) are the first order constraints, B_0 and A_0 are the equilibrium profiles (denoted by subscripts zero). Eq.(10b) expresses conservation of total toroidal flux and eq.(10c) corresponds to the flux through the hole of the 'torus' being zero. In addition the first order boundary condition used to derive the profiles (2,3) has to be satisfied:

$$\delta p(a) + B_0(a)\cdot\delta B(a) = 0 \qquad (11)$$

This approach has been performed in [4] for the helical and symmetrical modes. The result for the symmetrical mode was that the equilibrium is stable if

$$\lambda^2/\{(1+\kappa\alpha)(1-\alpha)\} < (5.324..)^2 \qquad (12)$$

For the helical modes only some special cases were investigated and we will now comment further on the analysis for the helical modes.

For helical modes eq.(9b) together with $\nabla\cdot\delta B = 0$ determine the perturbations completely. These equations can be reduced to the familiar infinite conductivity equation or the marginal Hain-Lust equation with $ir\delta B_r(r)$ replacing ξ as the dependent variable. This equation should hold throughout the plasma region. But for certain values of the mode numbers m,k the plasma region includes points for which $m/r_S B_{\theta 0}(r_S) + kB_{z0}(r_S) = 0$. These are singular points r_S for the describing differential equation In the case of finite resistivity this equation should be replaced by a more exact fourth order equation in the vicinity of the singular points [5]. It seems therefore too restrictive to require $\delta P = 0$ to hold (a velocity term will be needed to obtain balance in first order in the momentum equation). If we nevertheless solve the describing equation it follows that only for certain m,k values non-trivial perturbations exist. As a result of this it is possible that some of the most dangerous free perturbations are not allowed anymore and that the stability region will become greater.

Stability in terms of experimental quantities.

Up till now the equilibria were described by the Lagrangian multipliers λ and α. These parameters are determined by the value of K and E. They can also be related to experimental quantities. Often the longitudinal flux and current are measured in an experiment. Using the equilibrium profiles eq.(2,3) these quantities can be expressed as:

$$\mu_0 I = 2\pi B_0 f J_1(\sigma r) \quad ; \quad \Psi = 2\pi B_0 a^2 J_1(\sigma r)/\sigma r \qquad (12a,b)$$

These relations can be inverted to yield λ and α in terms of total flux and current. The boundary of the stability region in fig.1 can approximately be expressed as $\sigma a < 3.11$. If we use eq.(11b) we can transform this condition into a condition on the flux :

$$\Psi/\ 2\pi a^2 B_0 > 0.1 \qquad (13)$$

The criterion $\sigma a < 3.11$ also implies that a RFP will be stable according to this model if it has no more then 30% reversal at the wall in the longitudinal magnetic field:

$$\text{abs}\ (B_z(a)/B_0) < 0.3 \qquad (14)$$

Discussion.
From the previous sections and fig.1. we can conclude that an equilibrium as determined by (1) is certainly stable if it is stable to the 'free' perturbations. The condition to be met then is that $\sigma a < 3.11$, or that (13) or (14) hold. The difference in results between the obtained stability criterion for free and restricted perturbations demonstrates that more constraints on the perturbations yield a larger stable region for the equilibria since the most dangerous perturbations may thus be eliminated. The lower bound on the flux is in agreement with intuition: larger F means a lower value of σa, which corresponds with lesser peaked profiles for the magnetic field components and an equilibrium should become more stable if its profiles get flatter (more constant). Since the model used here is an extension to Taylor's principle it is worth to note that Taylor's stability results are recovered if the parameter α is set to zero.

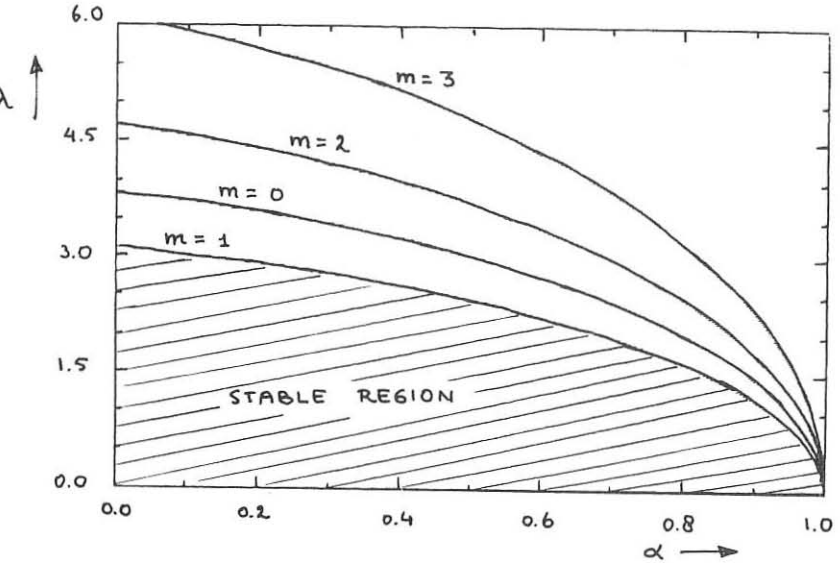

Fig.1. Stability of the equilibria as function of the parameters λ and α.

Acknowledgement:
This work was partly performed under the Euratom-FOM association agreement with financial support from ZWO and Euratom.

References:
[1] J.B. Taylor, Rev. Mod. Physics 56 (1986) p. 741.
[2] J.B.M.M. Eggen and W. Schuurman, Proc. 13th Conf. on. Contr. Fusion and Plasma Heating, Schliersee, 14-18 April (1986) Vol 10 C,Part I, p. 356.
[3] J.W. Edenstrasser and W. Schuurman, Proc. 1984 Int. Conf. on Plasma Physics, 27 June - 3 July, Lausanne.
[4] J.B.M.M. Eggen and W. Schuurman, Proc. 14th Conf. on. Contr. Fusion and Plasma Physics, Madrid, 22-26 June 1987, Vol 11 D,Part III, p. 1115.
[5] H.P.Furth, J.Killeen, M.N.Rosenbluth, Phys. of Fluids 6 (1963), p. 459.

MAGNETIC PROPERTIES OF THE SPHERICAL TORUS

H. Bruhns+, G. Raupp, J. Steiger, R. Brendel

Institut für Angewandte Physik II, Universität Heidelberg
Albert-Überle-Str. 3-5, D-6900 Heidelberg, FRG
+ Max-Planck-Institut für Plasmaphysik, EURATOM-Association
D-8046 Garching bei München, FRG

The Heidelberg Spheromak Experiment (HSE) uses the theta-z-pinch formation method to create compact field reversed plasmas (Spheromaks) with both poloidal and toroidal plasma currents. These plasmas are about spherical and have a full diameter of 24 - 30 cm. For two axially aligned toroids (doubly toroidal configurations) a length of up to 80 cm is possible. Spheromaks with plasma currents up to 300 kA have been created. With internal multiprobe arrays the magnetic structure of the toroids has been investigated during formation and decay.

While previously the standard operation of the experiment aimed at the production of spheromaks and doubly toroidal configurations of the spheromak-type /1,2/, we have modified the device and thus have been able to achieve for the first time the generation of spherical tori with aspect ratio 1.1 /3/. These configurations have been named and studied theoretically by Peng and Strickler /4/. The spherical torus differs from the spheromak (where there is no linkage of material along the center axis of the toroid) by the existence of a current carrying central conductor which adds a vacuum toroidal field to the magnetic configuration. Hence a spherical torus is a tokamak with a very low aspect ratio. While the q-value of a spheromak is everywhere below unity (ideally it is around 0.82 near the magnetic axis and decreases to 0.72 towards the separatrix), a spherical torus has a tokamak-like q(axis) >1 and q increases towards the separatrix. We have also investigated two axially aligned spherical tori.

For the purpose to generate a sperical torus the experimental device was equipped with an axial conductor. Two methods of operation are possible /3/: (1) if the conductor is unshielded against the plasma, part of the poloidal plasma current can commute onto it, (2) with the axial conductor being insulated against the plasma discharge we can drive an externally generated current through the conductor. Thus, (1) the current along the axial conductor will be appropriate to the self-relaxation of the plasma while (2) we can apply any desired external current (and hence any vacuum toroidal field) onto the toroid up to the technical limit of about 30% of the usual maximum plasma poloidal current.

Spheromaks are unstable to n=1 tilt and shift modes. In presence of an axial (currentless) conductor stabilization is achieved only if the diameter of the conductor becomes appreciable compared to the minor radius of the plasma /5/. This is not the case in HSE, where the axial conductor has a diameter of 15 mm. However, if a current of sufficient amplitude (in HSE more than 15% of the poloidal plasma current) is driven along the central conductor, the tilt- and shift modes are suppressed and the plasma decays stably on a resistive time scale.

We have investigated the magnetic topology by internal magnetic probe arrays which allow the simultaneous measurement of all three components of the magnetic field at ten radial positions in the range of r= +- 12 cm. In order to obtain a two-dimensional picture of the plasma, a shot-to-shot scan was performed for different axial probe positions.

Fig. 1 shows the measured poloidal flux pattern in the r-z half plane of a spherical torus for two different times, the intervals being $\Delta\Psi$ = 1 mWb. At t = 25 μs the separatrix length is 28 cm, the diameter 26 cm. We have already presented magnetic field profiles both in radial and axial direction for the spherical torus which demonstrate the close accordance between experimental and theoretical equilibrium /3/. For the analytical solution of the equilibrium differential equation we used a streamfunction which varies linearly with the poloidal flux. Such a dependence is to be expected if a complete relaxation into a Taylor-state takes place /6/. Experimentally we find a nonlinear relation between the stream function (i.e. the poloidal current) and the poloidal flux only during the early formation, when the z-pinch dominates and flux amplification takes place. During the whole equilibrium decay phase a linear dependence is present. This is demonstrated in fig. 2 which presents the poloidal current versus poloidal flux at t= 25 μs where the flux at the magnetic axis is 4 mWb. Note that the individual measurements shown scan the whole r,z plane of the confined plasma. The figure shows that a current of about 35 kA flows in the axial conductor at the investigated time point.

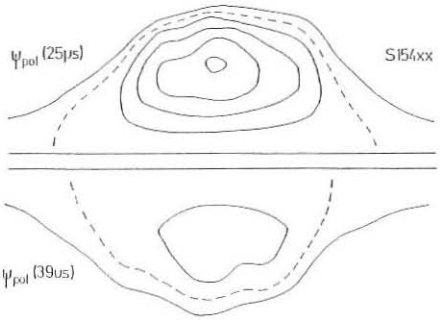

Fig. 1

For the plasma pressure, we find that during the early formation phase an inverted pressure profile is most consistent with the magnetic measurements. Lateron the maximum pressure clearly is seen on the magnetic

axis. The relation of plasma pressure to poloidal flux can be assumed best to be linear, however, from the measurements any exponent between 1/2 and 2 might fit into the scatter of the data. This is because the determination of the radial and axial plasma pressure profiles from magnetic measurements is inaccurate since it results from the difference of large quantities.

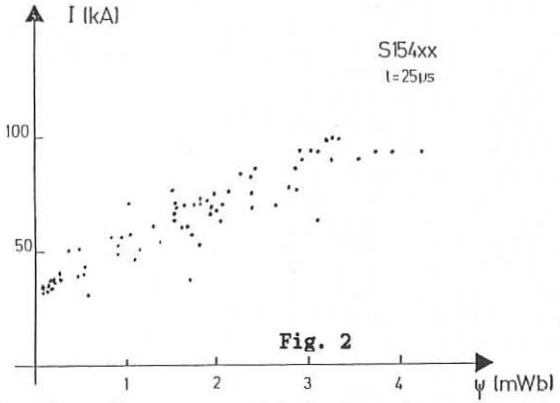

Fig. 2

We can, however, infer the volume averaged beta from the magnetics. Such a study was performed for two axially aligned spherical tori. The details will be reported elswhere /7/. Here we refer to the measurement in one of the two toroids where we find β-values between 11 and 13 %, lower than estimated in our preliminary investigations /3/. The present value results consistently both from (1) a consideration of the measured magnetic energy i.e. the relative contributions from the poloidal, the plasma toroidal, and the vacuum toroidal field energy as compared to the corresponding contributions which are anticipated theoretically as well as (2) from profile fits. Fig. 3 shows a fit of the experimental radial magnetic profiles in the symmetry plane of one of the aligned tori with (a) a force free numerical calculation (Fig. 3a) and (b) another one assuming an average beta of 12% (Fig. 3b), both at t = 32 µs. From our present investigations we anticipate that these results are valid also in the case of a single (standard) spherical torus. We note that the approximative analytical solution of the equilibrium differential equation in the symmetry plane /3/ cannot be used for a determination of the pressure.

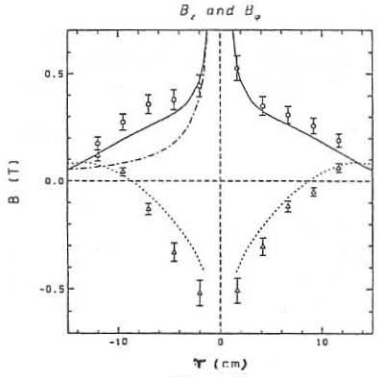

Fig. 3a

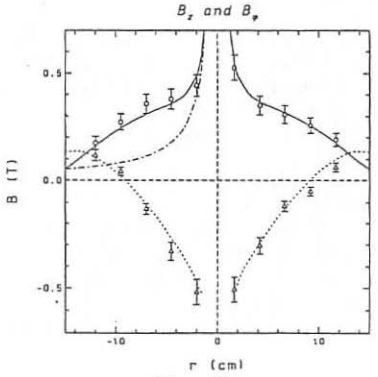

Fig. 3b

Considerable effort has been spent on the determination of the q-profile for various experimental conditions. Fig. 4 shows the q-profile for various time slices for the same scan which was used for the evaluations of figs. 1 and 2. Since the current through the conductor can be considered as a free parameter at least in the case when the current is driven externally, intuitively one might expect that the q-profile would vary with the applied current. Experimentally, with a unshielded conductor, we almost always find a linear stream function and a q-profile as shown. It seems that there is no stable smooth transition to the spheromak case where q is below unity and decreases towards the separatrix. Decreasing the applied axial current, the plasma becomes unstable.

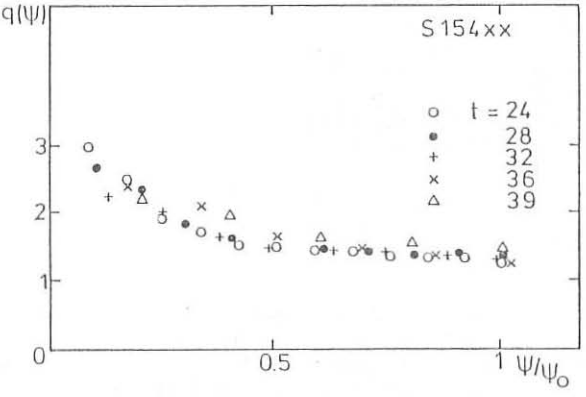

Fig. 4

In conclusion we find that in the modified HSE device spherical tori (both single ones and two axially aligned one) are very well described by a Taylor-like relaxed equilibrium with a stream function $I(\Psi) = I_0 + I_1\Psi$ where I_0 ist the conductor current and I_1/Ψ the eigenvalue of the configuration which is independent over the crossection. The q-profile, as is the whole equilibrium, corresponds well to the one anticipated for the spherical torus /4/.

This work was supported by the Deutsche Forschungsgemeinschaft

References

/1/ Bruhns, H., Allgeier, C., Böckle, G., Raupp, G., Steiger, J., Weichelt, A., Wintermeyer, G., in Controlled Fusion and Plasma Physics (Proc. 12th Europ. Conf. Budapest, 1985) Vol. 9F, Part I, European Physical Society (1985) 659.
/2/ Bruhns, H., Allgeier, C., Raupp, G., Steiger, J., Weichelt, A., ibid., p. 655
/3/ Bruhns, H., Brendel, R., Raupp, G., Steiger, J., Nucl. Fusion 27 (1987), 2178
/4/ Peng, Y.-K.M., Strickler, D.J. Nucl. Fusion 26 (1986) 769
/5/ Taguchi, K., Miyazaki, T. Kaneko, S. J. Phys. Soc. Jap. 54 (1985), 2162
/6/ Taylor, J. B., Plasma Phys. and cont. Fusion Research. Proc. 5th IAEA Conf. Tokyo, Vol. 1, p. 161 (1974); Rev. Mod. Phys. 58 (1986) 741
/7/ Bruhns, H., Steiger, J., Raupp, G. to be published

STUDIES OF THE SMALL TIGHT ASPECT RATIO TORUS CONCEPT

J Hugill, P C Carolan, M F A Harrison, P Haynes, T Hender, J Hicks, B Lloyd, A Sykes and T N Todd

Culham Laboratory, Abingdon, OX14 3DB, UK
(UKAEA/Euratom Fusion Association)

Introduction

Small aspect ratio devices have received considerable attention in recent years, especially from Peng and co workers [1]. They have a number of potential advantages over tokamaks of conventional aspect ratio. The most stable equilibria are naturally elongated and D-shaped allowing a substantial reduction of the currents in poloidal and, particularly, toroidal field windings required to sustain a given plasma current. Theoretically the volume averaged β is high, though β_I is small and the paramagnetic enhancement of the toroidal field can be substantial. The toroidal field gradient in the discharge centre is reduced and $|B|$ tends to remain constant on the outside of the flux surfaces, reducing the width of banana orbits. At small aspect ratios current profiles can be found which are stable to tearing modes with q_o well below unity [2].

We have studied a number of these issues and also considered some of the problems associated with reactor designs based on this concept.

Equilibrium and stability

A series of equilibria have been studied with uniform external vertical field and bell-shaped current distributions at aspect ratios down to 1.02. Fig.1 shows their elongation, K as a function of R/a for low β. The flux surfaces for a case with volume average toroidal β, $\langle\beta_T\rangle$=30% at R/a=1.08 are shown in Fig.2. Even at these high β levels, the paramagnetic enhancement of the toroidal field is substantial, amounting to a factor $\sim$ 3 for this case as illustrated in Fig. 3. The q-profiles are typically flat near the centre, with $q_o<1$ and strong shear close to the boundary. At low β, q_o approaches the value appropriate for a spheromak (0.825) as B_T is reduced towards zero.

The stability of these equilibria has not yet been tested but, from previous work [2], we anticipate that only slight modifications to the current profiles will ensure stability for m=1 tearing modes. Profiles of this type stable to m$\geq$2 tearing modes can also be found [3]. At more modest aspect ratio, R/a=1.78 equilibria stable to high-n ballooning modes at $\langle\beta\rangle \sim$ 13% have been found with $q_o \sim 1$. It should be noted that these could still be unstable to low-n ideal modes (infernal modes) near the centre, where there is an extended region of low shear.

Reactor Prospects

Reactor studies, such as the Ignition Spherical Torus at FEDC and the Advanced Tokamak Reactor at LASL have identified some of the major problems of the tight aspect ratio, in particular the difficult design of the central column and the need to generate and sustain a plasma current, $I_p \sim 20$ MA by non-inductive means.

To minimise the recirculating power required for continuous operation, the plasma density, n should be maximised, because the thermonuclear power, $P_{TN} \sim n^2$ whereas the power required to sustain the current, $P_{CD} \sim n$. A 0-D power balance analysis indicates the optimum burn temperature is ~ 25 keV and that the condition $P_{CD} < P_{TN}/20$ leads to

$$\eta_{CD} = \frac{0.1\ n(10^{20}m^{-3})j(MA\ m^{-2})}{P_{CD}(MA\ m^{-3})} > \frac{8.3}{\beta_I\ I_p(MA)} = \frac{0.52\ j(MA\ m^{-2})}{n(10^{20}m^{-3})} \qquad (1)$$

where η_{CD} is an arbitrarily defined current drive efficiency and (at T = 25 keV) β_I is defined as $16\ n(10^{20}m^{-3})/I(MA)\ j(MA\ m^{-2})$.

Equation (1) brings out the importance of η_{CD} and β_I in determining the plasma current and hence the reactor size. A current drive efficiency, $\eta_{CD} \sim 0.8$, is needed to keep $I_p < 20$ MA with $\beta_I = 0.5$. This is close to the theoretical maximum for coupling to relativistic electrons by fast waves. In any case, $\eta_{CD} > 0.52$ is required to avoid the conventional tokamak density limit at $j/n < 1$ (units as above).

We may note that continuously operating tokamaks with more conventional aspect ratio would generally have higher critical values of β_I (~ 2 say), allowing a reduction in either η_{CD} or I_p. However, the scaling of energy confinement time may independently set a lower bound on I_p of order 10-20 MA in order to achieve a sufficiently high value of τ_E.

Experimental Requirements

Devices which can confirm the properties of tight aspect ratio equilibria are urgently required to make an impact on the design of next-generation experimental reactors. Some information on mhd stability may be obtained by adding a central, current carrying rod to spheromaks, as reported recently from the Heidelburg spheromak experiment [4]. Another option is to compress a conventional tokamak discharge by a factor ~ 3 in major radius while simultaneously reducing the toroidal field. Such discharges cannot be sustained by conventional transformer action but should be capable of exploring very low aspect ratios, $R/a > 1.1$.

At $R/a \sim 0.5$ m/0.3 m, a steady-state device seems feasible with $B_T(vac) \sim 0.5$-1.0T, increased by a factor of 2 due to paramagnetism, using water-cooled copper conductors and $I_p \sim 1$-2MA driven by a few MW of LH and/or ECR waves. This should be capable of studying start-up and current ramp at $n_e \lesssim 10^{19}$ m^{-3} and low β. It would also contribute to the technology for continuous operation and provide new information on long time scale

plasma-wall interactions and wall chemistry. Injection of high speed pellets should allow transient, high-β, joule-heated discharges to be studied.

Conclusions

In principle, the low aspect ratio tokamak offers the prospect of a compact, high-β, continuously operating reactor design which could have substantial benefits in cost and size compared with the conventional approach. Such potential justifies a vigorous theoretical and experimental programme to study the unique properties of this configuration.

References

[1] Y-K. M. Peng and D. J. Strickler Nucl. Fusion 26 (1986) 769.

[2] T. C. Hender in Plasma Physics and Controlled Nuclear Fusion Research (Proc. 12th Inter. Conf. Kyoto, 1986) I.A.E.A. Vol. I (1987) 291.

[3] C. Z. Cheng, H. P. Furth, A. H. Boozer, Plasma Phys. and Contr. Fusion 29 (1987) 351.

[4] H. Bruhns, R. Brendel, G. Raupp, J. Steiger to be published in Nucl. Fusion (1988).

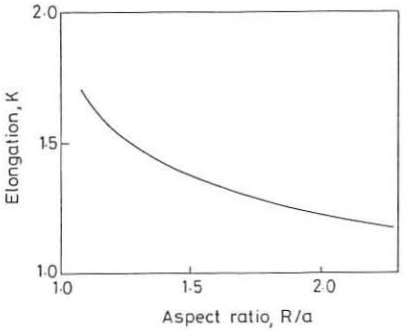

Figure. 1. Elongation versus aspect ratio for a series of low-β equilibria with uniform external vertical field.

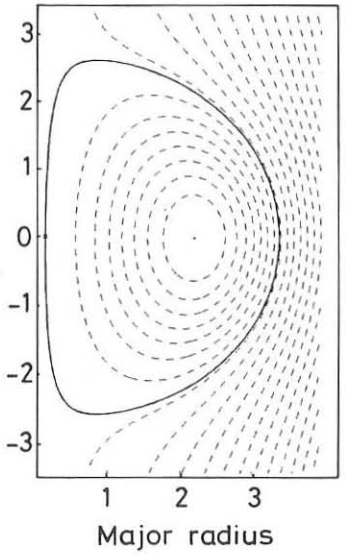

Figure. 2. Flux surfaces for equilibrium with R/a=1.08, $\langle\beta\rangle$=0.3.

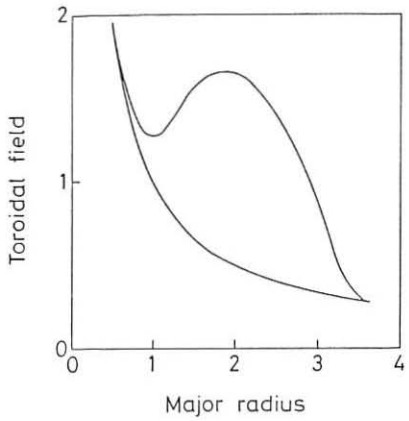

Figure. 3. Toroidal field profile for equilibrium of Fig. 2 showing paramagnetic increase (upper curve) compared to vacuum field (lower curve).

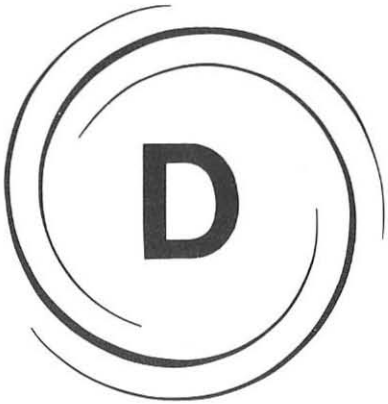

Plasma Edge Physics

EDGE FLUCTUATION MEASUREMENTS DURING X-POINT PLASMAS IN JET

A Hubbard, D Bartlett, P Cripwell+, R Gill, P J Harbour, M Malacarne, P D Morgan, N Salmon and J Snipes

JET Joint Undertaking, Abingdon, Oxfordshire, OX14 3EA, UK
+ Imperial College of Science and Technology, London SW7, UK

1. INTRODUCTION

Strong edge fluctuations are a characteristic feature which distinguish the L-mode phase of JET X-point plasmas from the relatively quiescent, high confinement (H) phase. Periodic spikes, seen by several diagnostics viewing the outer region of the plasma, usually appear with the application of ICRH or NBI, initially at a repetition frequency of $\sim$ 1-2 kHz. If sufficient power is applied, the spikes slow to a frequency of $\sim$ 100 Hz before disappearing at the L-H transition. Under some conditions, the H-phase is followed by a further period of similar spikes, during which a reduction in the global particle and energy content occurs. This sequence of L and H phases can be repeated several times during a discharge (see Figure 1).

Previous studies of the coherent edge spikes have relied mainly on data from magnetic pick-up coils and soft X-ray diodes /1,2/. Detailed measurements, described below, have recently been made with a number of new diagnostics. These include Langmuir probes and pick-up coils near the X-point position, a poloidal D_α array and a multichannel reflectometer and an ECE heterodyne radiometer viewing near the midplane. Comparison of the observed local perturbations with global changes, presented in Section 3, leads us to conclude that convection of particles from the outer region of the plasma during the spikes could be responsible for much of the observed reduction in plasma energy.

2. LOCAL MEASUREMENTS OF EDGE FLUCTUATIONS

A typical series of spikes leading up to an L $\rightarrow$ H transition is shown in Figure 2. The magnetic coil nearest to the X-point shows a field change of up to 9 T/S. The rise time of the initial spike is 50 μs, while the burst of activity lasts for $\sim$ 300 μs. A simultaneous spike of similar shape occurs on the current of all of the Langmuir probes in the X-point tiles. Previous analysis using a poloidal array of coils has shown simultaneous changes in $\tilde{B}$ at all locations, with a magnitude largest at the top and bottom of the plasma and weakest at the outer midplane. The field perturbation which would be produced by a current flowing in the scrape-off layer has been calculated using Langmuir probe data for a similar discharge (Figure 3), and is consistent with these measurements.

Reflectometry and D_α measurements show well correlated but slightly slower changes. The coherent detector signal of the 18.6 GHz channel of the reflectometer, which corresponds to a critical density of 4.3 x 10^{18} m^{-3} (r_c/a = 0.92), shows a phase change of $\sim \pi$. Taking the density gradient from FIR interferometer measurements, a local density change of $\sim$ 1.1 x 10^{18} m^{-3} (25%) is calculated. The effect on a second channel with n_c= 1.9 x 10^{19} m^{-3} (r_c/a = 0.83) is much smaller, indicating a perturbation localized outside this radius. More complete analysis of $\delta n_e(r)$ should be possible when the full 12 channel system is operational /3/. During the same period, a 75% increase in D_α emission is seen along the chord viewing the X-point, indicating substantial recycling of particles at the divertor.

On a discharge with a lower field of 1.7 T, the electron temperature at r_c/a = 0.93 was measured using a heterodyne radiometer. Sharp dips of 20-30 eV are seen, correlated with the fluctuations on other diagnostics. At the end of the L-phase the edge T_e is 450 eV, 200 eV above the ohmic level. During the L → H transition it increases by 100 eV in $\sim$ 10 ms, apparently due to a sawtooth heat pulse. This jump does not occur on all discharges.

Soft X-ray measurements made on 2 MA X-point discharges in 1986 give further information on the topology of the perturbations. The outermost channels of the vertical poloidal array show an increase in $\sim$ 80 μs, while the effect on inner channels is reversed and on a slower time scale of $\sim$ 800 μs. This indicates a disruptive-like instability originating near the edge, with an inversion radius of r/a ≥ 0.9. The relative amplitude of the perturbation on different chords shows a strong localization to r/a ≥ 0.7 (Figure 4). The inversion radius is no longer visible with this diagnostic due to the loss of its outer channels.

3. EFFECT ON GLOBAL PARTICLE AND ENERGY CONTENT

Near the start of NBI, the plasma density and energy are rapidly increasing and there is often no abrupt change in $\hat{N}$ or $\hat{W}$ at the initial L → H transition. The global effect of the edge spikes is more clearly seen during the short L-phases later in the discharge. For example, during the first such phase of Pulse 13806 (Figure 1), the volume integrated particle content N_{tot}, obtained from the FIR interferometer, shows a mean net loss of 1.5 x 10^{19} particles (0.4%) for each of 17 spikes. For comparison, this would correspond to a local decrease of 10^{18} m^{-3} extending over $\sim$ 8 cm and is consistent with reflectometer and soft X-ray measurements. Calculations based on the typical enhancement of I_{sat} ($\sim$ 85%) give 4 x 10^{19} additional particles reaching the X-point tiles during a spike /4/. D_α measurements show that in this L-phase an average of ≥ 5 x 10^{18} particles/spike are recycled from the divertor region. While these values have absolute uncertainties of $\sim$ 50%, they indicate that a rapid outward convection of particles associated with edge spikes could cause the observed global loss.

The plasma energy W, as measured by the diamagnetic loop, shows similar time behaviour to N_{tot} but has a smaller relative change during the L-phase. In the above case, there is a mean decrease of 7.6 kJ (0.2%) per D_α spike, which could be accounted for by convective losses if the

particles ejected have a mean energy of ≤ 1.56 keV. This is only half the average plasma energy and is equal to the electron temperature at r/a = 0.8, inside the inversion radius for the edge instability inferred from soft X-ray data. The conclusion that increased losses during the L-phase are associated mainly with convection from the outer region is supported by specroscopic observations of Ni radiation, which continues to increase steadily in the centre while decreasing near the edge /5/.

While the initial transition from L to H-mode is necessary to attain improved confinement, the subsequent appearance of short L-phases may have operational advantages. Since the fluctuations appear to eject relatively cool particles, high plasma energies are achievable at lower densities than would be present in a continuous H-mode. This may be a useful means of controlling plasma density and avoiding disruptions, which will be increasingly important at higher currents and heating powers. The regime at which L-phases reappear has not yet been fully explored. They tend to occur earlier, and be of shorter duration, in discharges with a small separation from the outer limiter.

4. DISCUSSION AND CONCLUSIONS

Experimental data on JET indicate that fluctuations localized in the outer region of the plasma (r/a ∿ 0.9) are important to the physics of the L → H transition and to corresponding changes in N_{tot} and W. The gradual decrease in their frequency and the fact that parameters between spikes (eg. D_α, I_{sat}) are very close to those in the H-mode suggest that the plasma passes through a region of marginal stability before reaching a quiescent H-mode. Understanding the nature of the instability should help to assess the conditions necessary for the improved confinement.

Recent measurements and analysis of pressure and shear profiles in the outer region of the JET plasma /6,7/, show that conditions are stable to ballooning modes during the L-phase. They only marginally approach the second stability region at the L-H transition, although the measured T_e of 450 eV should be sufficiently high to attain this /8/. There is also evidence of currents flowing in the scrape off layer during the disruptive spikes /9/, though it is not clear whether they are a cause or effect of magnetic perturbations. Parameters in the divertor region are being assessed to see whether they support the presence of a thermal barrier.

REFERENCES

[1] M. Malacarne et al, Plasma Physics and Controlled Fusion 29 (12) (1987) 1675-1686.
[2] A. Tanga et al, Nuclear Fusion 27 (1987) 1877.
[3] R. Prentice et al, this conference.
[4] L de Kock et al, this conference.
[5] K. Behringer, B. Denne et al, this conference.
[6] E. Lazzaro et al, this conference.
[7] C. Gowers et al, this conference.
[8] C. Bishop, Nuclear Fusion 27 (1987) 1765.
[9] P.J. Harbour, Int. Workshop on Plasma Edge Theory in Fusion Devices, Augustusburg, DDR (April 1988).

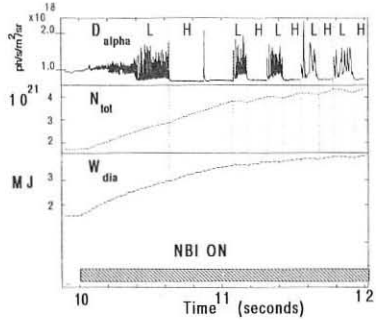

Fig. 1 Series of 5 L and H phases, showing effect on particle and energy content, (Pulse 13806, I_p = 3 MA, B_T = 2.1 T, P_{NBI} = 5.5 MW).

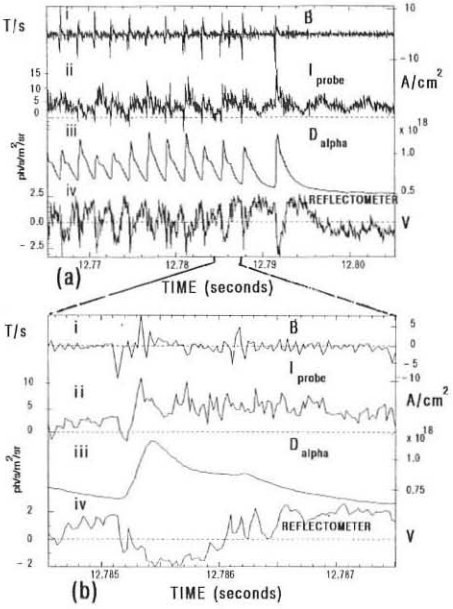

Fig. 2a) Edge fluctuations prior to an L → H transition, Pulse 14384 (I_p = 3.0 MA, B_T = 2.1 T, P_{NBI} = 7.5 MW), on
i) magnetic coil XPO4,
ii) Langmuir probe (200 Hz oscillation is due to changing voltage),
iii) D_α channel viewing X-point
iv) Reflectometer channel with $n_c = 4.3 \times 10^{18}$ m^{-3}.

b) Expansion of a single spike.

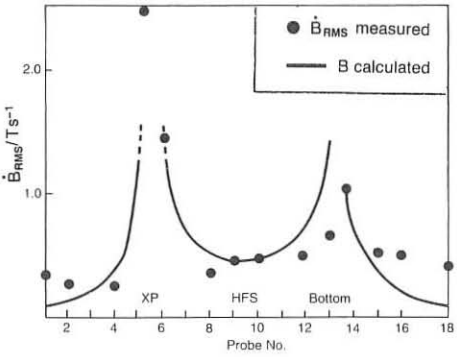

Fig. 3 Comparison of measured poloidal variation of $\dot{B}$ (Pulse with the field calculated from current typically measured in s.o.l. (normalized units). Absolute levels of B agree to within the scatter of present

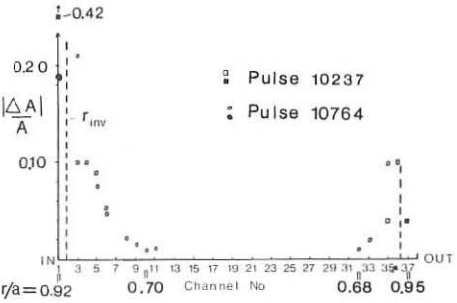

Fig. 4 Relative change in the soft X-ray emission during edge fluctuations (I_p = 2 MA, B_T = 2.2 T). Open and closed symbols indicate negative and positive changes. Minor radii of the outer flux surfaces crossed by the chords are shown.

THE ROLE OF THE SCRAPE-OFF LAYER IN X-POINT DISCHARGES IN JET

P J Harbour, L de Kock, S Clement, S K Erents, N Gottardi,
A E Hubbard, M Keilhacker, E Lazzaro, P D Morgan, D Stork,
D D R Summers, J A Tagle and A Tanga

JET Joint Undertaking, Abingdon, Oxfordshire, OX14 3EA, UK

INTRODUCTION

The plasma parameters in the X-point divertor in JET have been measured using an array of Langmuir probes in the divertor target tiles and supported by measurements of D_α radiation (2D with CCD camera viewing the target tiles; 1D using a poloidal array of telescopes) and bolometry. The Langmuir probe measurements show that the saturated flux of ions, I_{SAT}, parallel to the magnetic field is about 10 A cm^{-2} at the divertor separatrix in ohmic discharges. In L-mode with NBI it increases by a factor < 2, depending on power level (P_{NBI} < 7.5 MW) and then decreases when H-mode is established. The scrape-off thickness, λ_{ISAT}, is the same in ohmic and L-mode but decreases when H-mode is established. The corresponding values of electron temperature at the divertor target are $T_{e,t}$ ∿ 30 eV (OH) and ∿ 50-60 eV (H-mode). L-mode temperatures are not reported here because of rapid fluctuations in parameters. During ICRH the values of I_{SAT} increase by a factor ≤ 5 and T_e also appears to increase.

There are 40 poloidal bands of graphite tiles in JET (1987/8), shaped to collect the diverted plasma. The plasma impinges on two separate patches on each poloidal band (figure 1a). Eight Langmuir probes are flush-mounted in the target tiles, being designed to receive the inner

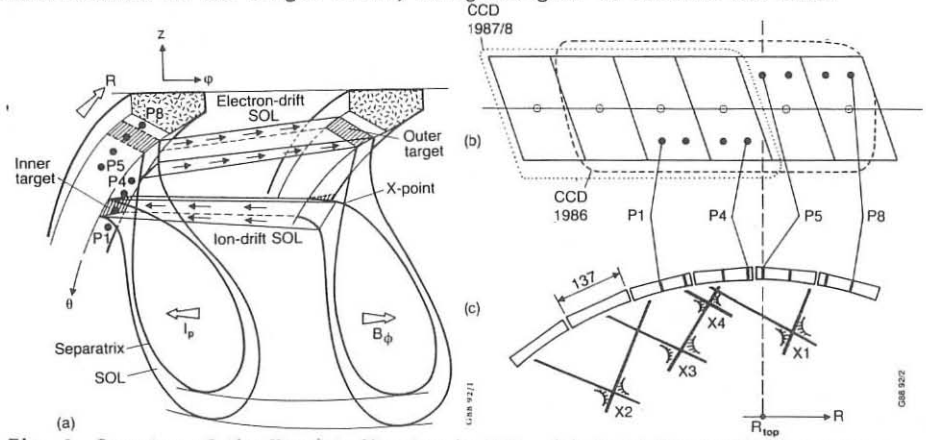

Fig. 1 Geometry of the X-point divertor in JET. (a) Shows two bands of graphite target tiles with scrape-off layer impinging on Langmuir probes P1-4 and P5-8. (b) Shows the tiles and probes and the view of the CCD camera. (c) Is a poloidal section through the tiles with X-point positions, estimated from our data, X1 (# 10722), X2 (# 14083), X3 (# 14820-34) and X4 (# 14883). (R_{top} = 2.630 m).

(high field side) and outer (low field side) diverted scrape-off layers. Fig. 1(b), (c) shows more detail of the experimental arrangement, including the view of the CCD camera, which actually covers 3 bands of tiles, whereas the D_α telescope array views a sector midway between two bands of tiles. The position of the X-point and hence of the inner and outer separatrices in the divertor may be varied: examples for several discharges are shown in Fig. 1(c). The Langmuir probes and D_α telescope are in Octant 8 and the CCD camera is in Octant 6, viewing tiles in Octant 5 and Octant joint 5/6.

EXPERIMENTAL RESULTS

Figure 2 shows the variation of parameters in a typical beam-heated discharge. The flux of ions towards the target measured by one of the probes, I_{SAT}, varies in a very similar way to the D_α (CCD) intensity at the same location on the tiles, but there are some differences between these signals and the intensity of D_α measured between the tiles, D_α (POL). During the ohmic phase of the discharge ($t \leq 12$ s), D_α and I_{SAT} are fairly constant but with small inverse sawteeth. With NBI they increase and fluctuate rapidly. The fluctuations (ELMs) [1] are best shown by the I_{SAT} trace because its sampling rate was faster for $12.1 \text{ s} < t < 13.1$ s. The fluctuation rate decreases in the late L mode and at 12.5 s the H mode is established with much more quiescent signals, again with inverse sawteeth, more prominent than before. There is an H → L transition at 14 s and a series of L-H-L transitions thereafter. Each group of ELMs, especially the first group, shows maximum and minimum values of I_{SAT} which are typical of L and H modes respectively. The power radiated from the X-point region (not shown) varies in a similar way to I_{SAT} and D_α, increasing from ∿ 0.9 MW (OH) to ∿ 1.2 MW (L), then decreasing to 0.8 MW (H1) and rising slowly during the H-phase to ∿ 1.2 MW (H2) with bursts of up to 1.8 MW in later L phases. The total electron content, N, is also shown in figure 2 and increases rapidly during L and H mode, decreasing at each subsequent L phase.

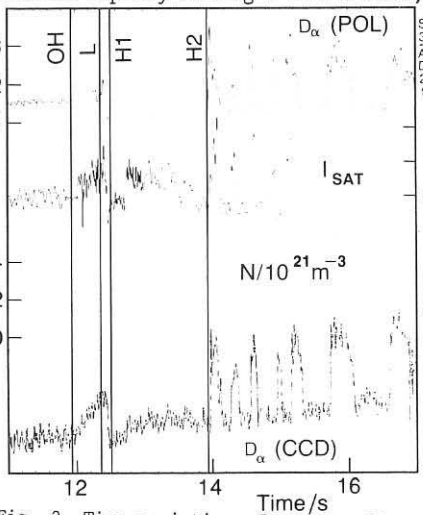

Fig. 2 Time variation of scrape-off parameters in a 2.0 MA, 2.1 T pulse.

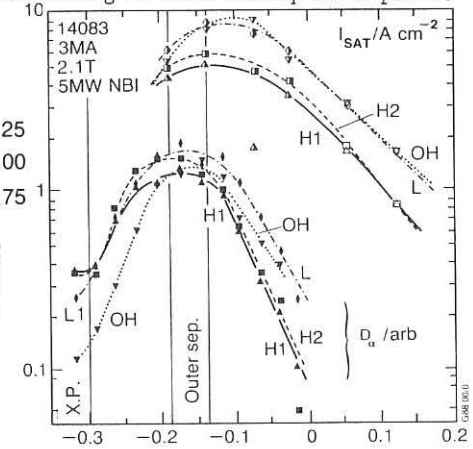

Fig. 3 Poloidal profile of D_α and I_{SAT} on the divertor tiles for the pulse shown in Fig. 2. Distance s is measured along the tiles from R_{top} (Fig. 1c).

Poloidal profiles of D_α and I_{SAT}, taken at the times indicated in figure 2, are shown in figure 3. The profiles are measured in terms of the poloidal distance, s, from the target tiles at the top of the torus, R_{top} = 2.630 m (figure 1 b,c). As is evident from figure 1 (c), only the X-point (X2) and outer scrape-off layer are visible for this discharge (# 14083). Probes 1-4 are not facing the plasma directly but are shadowed by the apex of the tile and corrected as described elsewhere [2]. The profiles of both D_α and I_{SAT} agree in showing a well defined maximum at the outer separatrix which appears to move to smaller radius during the H-phase. The profiles of I_{SAT} are flatter than for D_α, but both show no change between ohmic and L mode. Outside the separatrix the profiles are exponential with λ_{ISAT} = 133 mm (OH), 122 mm (L). Profiles in H-mode are steeper with λ_{ISAT} = 102 mm (H1), 92 mm (H2). The values of λ_{ISAT} quoted here are measured in the s-direction and will be modified later to equivalent midplane values. The similarity between scrape-off thickness in OH and L phases suggests, that, as with limiter discharges, there is no change in $D_\perp$ with NBI. The decrease in λ_{ISAT} by $\sim$ 25% in H mode suggests a strong decrease in $D_\perp$ to $D_\perp(H) \sim 60\% D_\perp(L)$ and even larger decreases have been observed.

The H-mode was studied in detail in a series of 3 MA, 2.1 T discharges with 7.5 MW NBI (# 14820-34). Figure 4 shows the average values during the H-phase of T_e, I_{SAT} and D_α. The profile of D_α on the electron drift side shows a maximum at s = -8 cm and that for I_{SAT} shows a maximum at s = -6 cm. Taking the outer separatrix at s = -7 ± 1 cm the data suggest that the maximum in T_e is not on the separatrix but further out into the scrape-off layer. The reduction in T_e at the separatrix is believed to be related to local recycling and finite thermal conductivity. The D_α profile on the ion drift side of the target tile shows the location of the inner separatrix. Extrapolating the I_{SAT} and T_e profiles to the inner separatrix suggests that I_{SAT} is larger and T_e smaller than at the outer separatrix and this is supported by other data (eg. # 14338 ohmic phase). The different T_e values at opposite ends of the same flux tube in the scrape-off layer lead to differing sheath potentials, causing electric current to flow around the scrape-off layer [3]. Currents of up to 10 A cm^{-2} have been measured, especially during the ELM phase [1].

The measured parameters from figure 4 have been used to calculate the density in the divertor ($n_d = 2\, I_{SAT}\, c_s/e$) and the heat flux parallel to the field at the target ($P_{\parallel,t} = 8\, I_{SAT}\, T_e$) and these are shown in figure 5(a) which also shows values of parameters at the midplane (n_m, $T_{e,m}$) derived using Spitzer conductivity and the sheath convection as described in [4]. The power flux to the target in these 7.5 MW discharges can be compared to that in a 9 MW discharge, # 10755 in 1986 [5] in which P_t^{outer} was determined by infrared thermography to be 10 MW m^{-2} onto the target tiles . The maximum H-mode value of $P_{\parallel,t}$ for this discharge was 60 MW m^{-2}, agreeing well with the 57 MW m^{-2} deduced here with Langmuir probes, even allowing for the difference in power. The profile of $T_{e,m}$ is monotonic despite the dip in the separatrix values of T_e in the divertor. Both $T_{e,m}$ and n_m are consistent with LIDAR and ECE profiles [1].

Figure 5(b) shows profiles of mean free paths in the outer divertor. The Coulomb mean free path (1 m < $\lambda_{ee,d}$ < 8 m) is always smaller than the connection-length, hence allowing a temperature difference to develop between midplane and divertor as is shown in figure 4 and 5a. The mean free path for deuterium atoms, $\lambda_D^{(0)}$ is also shown. This has been

evaluated using $\lambda_D^{(0)} = v^{(0)}/[n_d\langle\sigma v\rangle]$ with $\langle\sigma v\rangle = \langle\sigma v\rangle(T_e)$ and with $v^{(0)}$ taken at 1 eV or at T_e. The mean free path for D atoms with energy ≤ 1 eV is always smaller than λ_n in the divertor (= 110 mm, see figure 5a) and so slow D atoms (and D_2 molecules) are almost always ionised in the divertor in their first transit of the scrape-off layer. Faster charge exchange atoms have $\lambda^{(0)} > \lambda_n$ except at the outer separatrix. This may be critical and will be studied in more detail.

CONCLUSIONS

The plasma parameters measured in the divertor suggest that $D_\parallel(H) \leq 0.6\ D_\parallel(L)$. The power flow deduced agrees with that from 1986 discharges. The power and particle flow will be discussed in [2]. All atoms and molecules recycling from the divertor near the separatrix may be ionised locally but further out in the divertor scrape-off layer (larger s) the fast recycling atoms will escape from the divertor.

REFERENCES

[1] A. Hubbard et al, Edge Fluct. Measts. During X-Pt. Plasmas in JET. This Conf.
[2] P.J. Harbour et al, 8th Int PSI Conference, Jülich, May 1988.
[3] P.J. Harbour, paper presented at Int. Workshop on Plasma Edge Theory in Fusion Devices, Augustusburg, DDR, April 1988.
[4] P.J. Harbour, Nuclear Fusion 24 No 9 (1984) 1211.
[5] H.J. Jaeckel, P.J. Harbour, N. Gottardi et al, (EPS, Madrid), 1987.

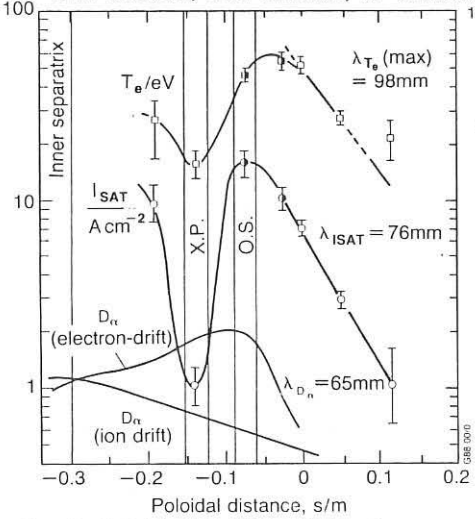

Fig. 4 Poloidal profiles of D_α, I_{SAT} and T_e in the divertor in a 3 MA H mode discharge (# 14820-34) (above).

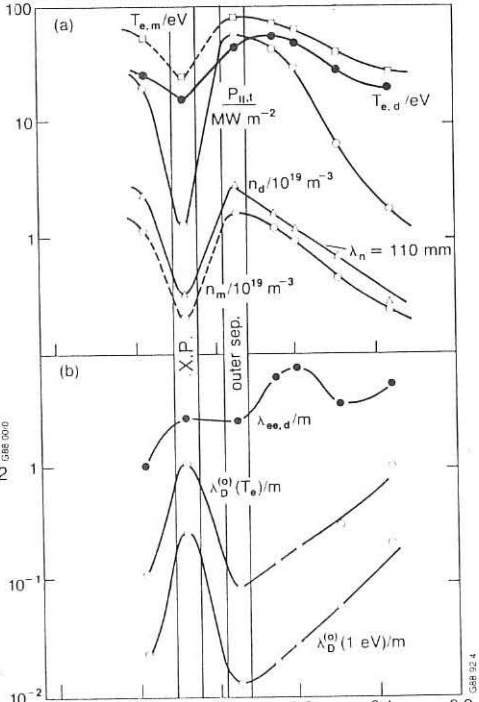

Fig. 5 Poloidal profiles of (a) power flux, $P_{\parallel,t}$, and density and temperature in the divertor, n_d, $T_{e,d}$ with equivalent midplane parameters n_m, $T_{e,m}$, (b) profiles of mean free path in the divertor (right).

PLASMA EDGE EFFECTS DURING ADDITIONAL HEATING IN JET WITH BELT LIMITER CONFIGURATION

H Brinkschulte, S Clement+, J P Coad, L de Kock, S K Erents*, G Neill, J Partridge*, J C B Simpson° and J A Tagle

JET Joint Undertaking, Abingdon, Oxfordshire, OX14 3EA, England
* Culham Laboratory, Abingdon, Oxfordshire, OX14 3EA, England
+ Association CLEMAT/EURATOM, Madrid, Spain
° Surface Analysis Technology PLC, Ascot, Berkshire, SL5 7PW, England

Introduction

The efficiency of ICRH heating and current drive with Lower Hybrid waves is influenced by the properties of the plasma boundary. In addition, ICRH heating has a strong effect on the edge plasma: the plasma parameters density, temperature and particle flux increase. A knowledge of all these effects is essential in understanding the influence of the edge plasma on the behaviour of the confined main plasma during additional heating (impurity generation and transport, transition from L-regime to H-regime in discharges with magnetic separatrix, particle confinement during neutral beam fuelled discharges, etc).

Since the summer of 1987, the original arrangement of 8 discrete limiters in JET has been replaced by belt limiters (to allow heating powers up to 50 MW). Two toroidal rings of narrowly spaced carbon tiles were mounted close to the outer wall of the vacuum vessel, both rings separated by ≈ 1 m above and below the equatorial plane. Although the plasma boundary showed generally the same behaviour as for the discrete limiter configuration [1 - 3], new features were found with the new full toroidal belt limiter configuration with a total input power up to 22 MW.

Experiment

During the last upgrading of JET a large number of diagnostics for the scrape-off layer (SOL) were installed as shown in Fig 1.

- 20 fixed Langmuir probes in the belt limiter tiles at 4 different toroidal and poloidal positions.
- 2 fixed Langmuir probes in each of the ICRH antennae side protection tiles in octants 1D and 5D, at different radial positions.
- An array of 6 Langmuir probes (3 facing the electron drift direction and 3 the ion drift direction). These can be positioned at any radial position from the wall through the intermediate top vertical port in octant 5D.
- A fast transfer system (FTS) containing a collector probe (rotatable during the pulse or between pulses) and fixed Langmuir probes, entering the torus ≈ 40 cm above the equatorial plane in octant 7D.

Toroidal and Poloidal Symmetries and SOL Thickness

Measurements with the 20 belt limiter probes biased at -100V

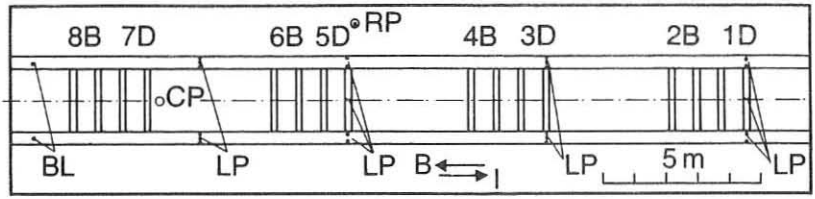

Fig 1: Unfolded view of the torus wall as seen from inside with 2 belt limiters (BL), 8 ICRH antennae (1D to 8B), 24 Langmuir probes (LP), reciprocating probe (RP) and collector probes (CP) on FTS.

revealed all particle fluxes to be identical to within ± 10 % indicating that the plasma is toroidally symmetric to be better than 2 mm and consequently that the power is deposited uniformly on the 2 belt limiter rings. This simplifies the investigation of the plasma properties in the poloidal direction which can be done at any convenient toroidal location.

The 2 belt limiters define 2 different areas for the SOL: an inside or high field area (< 1 m above and below outer mid plane) and an outside or low field area (> ± 1 m away from the outer mid plane). Both areas - which are analysed by the corresponding probes - are separated by the plasma tangent lines on the belt limiters, (last closed flux surface LCFS) the exact location of which is unfortunately not known in JET with a precision better than 1 - 2 cm from the magnetic flux surface calculations.

Fig 2 gives the particle flux e-folding length as a function of total ICRH heating power for 3 different cases: a) and b) the 1986 discrete limiter configuration, b) after conditioning of the machine by heavy carbonisation, and c)-d) the 1987-88 belt limiter configuration for the inside area. For all plasma currents, the flattening of the profiles due to RF heating is always less pronounced for the belt limiter discharges than for the discrete limiter configuration. The boundary behaves differently when the plasma is heated by neutral beams (NB) where the SOL thickness does not change with total input power. Fig 3 shows almost constant particle flux (λ_I) and deposited power (λ_p) e-folding lengths for 5 MW NB heated discharges whereas λ_I and λ_p increase by a factor of 2 for the same RF power.

The latter has been attributed to direct deposition of RF power in the boundary causing an increase in the diffusion in the edge ($D_\perp$) or an ionisation in the boundary layer [3]. However, machine conditions and density behaviour (Figs 2 and 3) clearly show that flattening is associated with these effects as well as different phasing of the ICRH antenna [4].

The behaviour of the SOL inside and outside the belt limiters is presented in Fig 4, and was investigated for discharges with ohmic heating up to 3.5 MW and RF heated discharges up to 10 MW. For all cases, the SOL thickness is less outside ($\lambda_{ne} \approx 6$ mm, after correction by a factor of two for field line compression factor for 4 MA discharges) than inside ($\lambda_{ne} \approx 10$ mm). During RF heating profiles flatten outside ($\lambda_{ne} \approx 13$ to 24 mm for 4 MA discharges) but do not change inside. The

edge parameters also increase during additional heating outside the belt limiters ($n_e(o) \approx 0.8 \times 10^{18}$ to 1.3×10^{18}, Fig 4) remaining almost constant inside the belt limiters.

Particle and Impurity Fluxes during Additional Heating

The total particle fluxes to the belt limiter from the outside and inside areas were determined from the appropriate probes in the belt limiters. During ICRF on JET the main species neutral influxes always increase with a magnitude which is proportional to the ICRH power, as is shown in Fig 5 for the fluxes measured by a probe located 24 mm from the LCFS in the area between the belt limiters. These fluxes are generally higher in Helium discharges than in Deuterium discharges for the same amount of total input power.

The impurity influxes also increase during RF heating in JET. The behaviour of Ni and C impurities in the SOL during high power combined heating discharges (ICRH and NBI) was investigated with the collector probe mounted in the fast transfer system. The probe was rotated from pulse to pulse yielding the radial distribution of the integrated deposition from each pulse. Ten consecutive high power discharges were recorded with up to 20 MW total input power. Fig 6 shows the Ni deposition increasing as a function of total RF input power. The impurity production is less when the power is applied in stages and/or the RF antennae are powered in dipole configuration. This Ni deposition is found to depend linearly with the total integrated He flux measured with the Langmuir probes located at the same position of the collector probes, on the FTS. This correlation is shown in Fig 7 and is remarkably good for the data gathered with these two independent diagnostics [5].

Conclusions

- For the belt limiter configuration, the general behaviour of the plasma boundary upon application of different types of heating does not change significantly compared with discrete limiter operation.
- The generally observed flattening of SOL profiles during RF heated discharges is dependent not only on RF power level but also on the density rise during heating and machine configuration and wall conditioning.
- It is found that SOL profiles outside the belt limiters are steeper than inside, when field line compression is taken into account. This is surprising in view of the shorter connection lengths between belts.
- A very good correlation has been obtained for helium fluxes and impurity fluxes measured by collector probes and Langmuir probes. Ni fluxs increases with additional input power, and is less during RF heated discharges with the antennae in dipole phasing than in monopole phasing.

References

[1] H Brinkschulte, et al... Proc. 13th EPS, Schlierse, April 1986 p.403
[2] J A Tagle, et al... Proc. 14th EPS, Madrid, June 1987, p. 662
[3] S K Erents, et al... J Nucl.Materials
[4] M Bures, et al... to appear in Plasma Physics and Controlled Fusion
[5] J P Coad, et al... 8th Internation. Conference Plasma Surface Interactions, Julich, May 1988

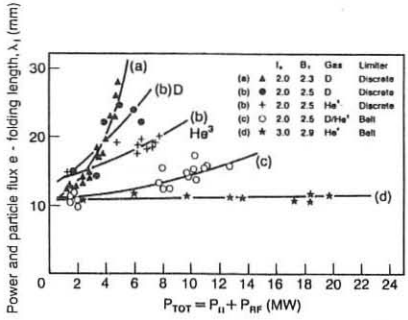

Fig 2: λ vs total RF power. For (b) carbonisation of wall.

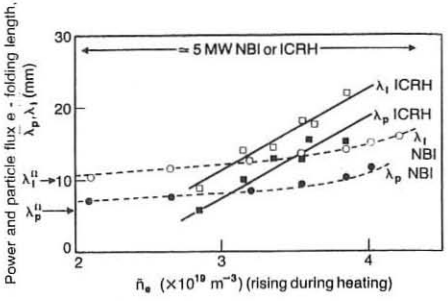

Fig 3: Effect of density rise on particle flux and deposited power for ICRH and NB heated discharges.

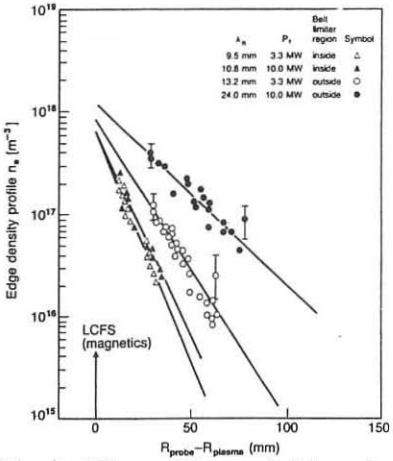

Fig 4: SOL profiles outside and inside belt limiters for ohmic and RF discharges.

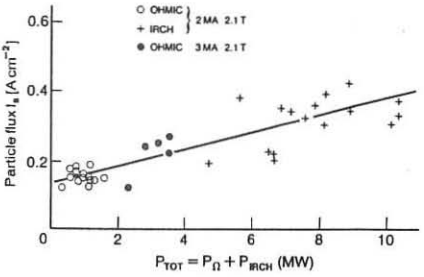

Fig 5: Particle fluxes 24 mm from separatrix vs RF power.

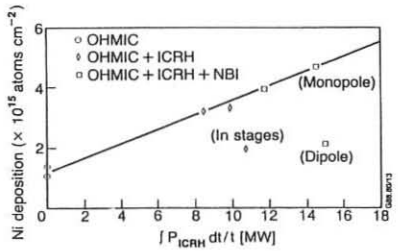

Fig 6: Ni deposition vs integral RF input power.

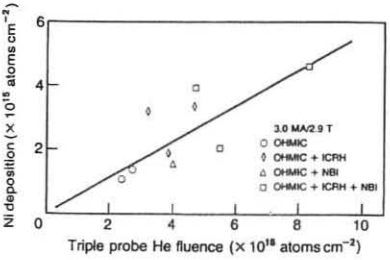

Fig 7: Ni deposition vs total He fluence.

ANALYSIS OF THERMOGRAPHIC MEASUREMENTS ON THE TOROIDAL PUMP-LIMITER ALT-II

K.H. Finken[1], J.C. Watkins[2], W.J. Corbett[3], K.H. Dippel[1], D.M. Goebel[3], R.T. McGrath[2]
[1] Institut für Plasmaphysik, Kernforschungsanlage Jülich GmbH, Association Euratom-KFA Jülich, Fed. Rep. Germany
[2] Sandia National Laboratories, Albuquerque, NM, USA
[3] University of California, Los Angeles, CA, USA

Abstract
The temperature rise of the ALT-II pump limiter surface during a TEXTOR-discharge is observed by an IR-camera. The complex temperature pattern is explained by geometric effects, toroidal field ripple and plasma flow asymmetries. A twodimensional heat transport code calculates the heat flux density impinging on the surface from the temperature rise. Results from "test" and "real" discharges with and without additional heating are presented.

1. Introduction

Thermographic observations of a limiter surface have several benefits: The surface temperature by itself is an important quantity for questions like melting, evaporation or thermal stress. The temperature distribution over the surface can indicate non-uniformities in plasma heat flux. Additionally, by including the heat conduction into the bulk of the limiter, the heat flux density to the limiter can be derived quantitatively. In this paper the IR image of the ALT-II pump limiter surface is described and reasons are given for the observed complex pattern. For the further analysis of these data the two dimensional code package TWODEPEP is applied and several proposals for its use are given. This program package allows one to prescribe either the heat flux or the temperature rise as boundary conditions. Results of this analysis for both kinds of boundary conditions are presented. The heat transport code also connects the surface with the bulk temperature and thus allows a direct comparison between IR and thermocouple data.

2. The ALT-II Configuration

Textor/1/ is a medium size tokamak with a major radius of 175 cm, a minor radius of up to 48 cm and a current of up to 0.5 MA. The discharge length for Ohmic or ICRH heated discharges is up to 4 s. Recently the large surface area Alt-II pump limiter/2,3,4,5/ has been installed. ALT-II surrounds the torus like a belt located 45° below the outboard midplane. The belt is subdivided into eight blades of about 140 cm length, 28 cm width and a thickness of 1.7 cm. The blades which are individually movable in the radial direction consist of an Inconel base plate covered with graphite tiles. The tiles have a size of approximately 110 * 140 * 6 mm^3. The surface facing the plasma is designed to be tangent to the plasma edge over the center 2/3 of the area. It is contoured in the poloidal direction such that a constant heat flux will be incident on the outer 1/3 of the surface if the plasma has a radius of 44.5 cm and a power e-folding length of 1 cm.
The temperature pattern is registered with two IR scanners positioned in the equatorial plane looking nearly tangentially into the torus. To avoid disturbances by the magnetic field a NaCl relay lens system is installed between a TEXTOR window and the camera. By changing the positions of the field lens and the camera, different views of a blade can be achieved.

3. Temperature Distribution on ALT-II Blades

The temperature rise pattern gives an overview of the heat flux distribution on the blades. The heating depends on plasma parameters like plasma current, line averaged

density,impurity content and others. It is found that the heating is not uniform over the whole blade toroidally or poloidally; typical structures of different scale lengths appear during the discharge. The ripple of the toroidal magnetic field causes a modulation with a wavelength of half a blade length. The modulation amplitude is inversely proportional to the power e-folding length and it is found to be more distinct at low electron densities than at high ones. Additionally, a top - bottom asymmetry is found. This asymmetry is attributed to different plasma fluxes in the ion and electron drift directions. At low electron densities ($n_e \approx 1*10^{19}$ m^{-3}), a three times higher heat flux is found on the ion drift side as compared to the electron side. At high densities ($n_e > 3*10^{19}$ m^{-3}), the heat flux is lower and nearly symmetric. Finally there is a third distinct effect seen on each tile: On the upper part of the blades, the left edges of the tiles are preferentially heated while on the lower half the right edge is more strongly heated. The heat flux asymmetry over this distance of only 10 cm is quite substantial and varies by a factor of about two. The effect can be explained by the fact that each graphite tile is toroidally flat; this leads to an asymmetry between the surface normal vector and the B-field.

4. Analysis of Thermographic Measurements

a. The TWODEPEP Code

To derive quantitatively the heat flux from the surface temperature rise observed on the tiles, a heat transport calculation is performed. The simple approximations such as the semi-infinite or the very thin heat conductor are not valid because the experimental time of three seconds allows the heat front to penetrate the 6 mm thick graphite tile. However, a radial temperature gradient is expected to persist during the experimental time. Also, the tiles are not uniformly thick so that a 1 dimensional model is not applicable. Therefore a two-dimensional heat conduction code is applied to the tile geometry. The TWODEPEP program package /6/ solves up to two coupled partial differential equations which are first order in time and up to second order in two space coordinates. After defining the partial differential equation in a preprocessor language including the temperature dependent graphite material properties /7/, the contour of the tiles must be prescribed. This can be done in the given case with a set of different arcs such as straight lines, circles and a spline fit approximation of the plasma facing arc. For each arc a different type of boundary condition such as heat flux or surface temperature can be prescribed. For testing the thermal response of a tile it is convenient to prescribe the incoming heat flux; this is here done with step functions along the surface to see the heat wave expansion or with a time dependence to simulate changing heat fluxes. For the analysis of actual discharges the temperature value observed at the surface is prescribed in the form of a two dimensional matrix (surface parameter M and time) which yields the heat flux as a function of time.

The finite element code TWODEPEP allows to solve the differential equations by different mathematical methods which can be preselected depending on their stability. Initially a triangulation has to be defined and these triangles are automatically subdivided by the program to a level which is selected beforehand. Fig. 1 shows the cross-section of a tile and its final triangulation. The tile is oriented in space as it is in TEXTOR. This set up is chosen in order to later fit the magnetic field structure to the tile geometry.

The program provides different output options. One of the most informative graphs is the temperature or heat flux along a given curve. The plasma facing surface is one of these curves. In figure 2, the ordinate number represents points along this curve from the left corner point (0) of fig. 1 to the tip of the tile (50). Other convenient curves are cuts perpendicular to the surface in order to see the temperature distribution inside a tile during a run. In fig.3, the ordinate numbers $1 < M < 20$ represent a radial cut at A, $21 < M < 40$ a cut at B and $41 < M < 60$ a cut at C. Finally, it is also possible to plot the temperature or flux of a given point as a function of time.

b. Results of the Analysis

The curves in fig. 2 represent the thermal history of the surface. In this run, the power flux to the tiles is constant in time during the first two seconds (10 W/cm^2) and decreased linearly to zero in the third second. The order of magnitude of the heat flux in an actual TEXTOR discharge is presently comparable to this "test-discharge". Spatially, the heat flow is a step function where only the outer 2/3 of the tile has a uniform non-zero heat flux. This boundary condition demonstrates the heat transport through the tile section of constant thickness. Curve number 1 gives the temperature distribution 0.1 s after the beginning of the heat pulse. It also represents the heat pulse pattern. The temperature at 2.5 s is shown in curve 2 and at 6 s in curve number 3. From the picture, it is deduced that the heat propagates about 14 mm (i.e 5 points in fig. 2b) during a typical TEXTOR discharge. This is somewhat larger than the spatial resolution of the IR - camera. After about 6 seconds the heat front has smeared out to 28 mm.

In fig. 3, for the same boundary conditions, the heat distribution in the tile is plotted for three different cuts at a time t=2.5 s. The start temperature in this run is 150^0 C. It is obvious that the heat penetrates more easily through a thin carbon piece (curve B) than through a thick one (curve C). But even in the thickest spot, the heat wave has penetrated through the tile. The nearly constant temperature gradient in the tile persists as long as the incoming heat flux is constant. About 1 s after the end of the discharge the radial temperature gradient in the tile becomes fairly flat. This heat equalization after the pulse is also seen in the surface temperature: It peaks at the end of a "test discharge" and converges at the given flux condition to 85% of the maximum value. The analysis of the radial heat profile connects the surface temperature reading to those of the thermocouples embedded half way into selected tiles. It is found that the temperature rise given by the thermocouples amounts to 50% - 75% of the surface value during most of the discharge. According to the code calculations both values should agree after about one second. This allows the calibration of one system against the other.

Finally, the curves in fig. 4 show the time dependence of the heat flux at one surface point derived from actual discharges. The lower curve represents an Ohmic discharge and the upper one a discharge with ICRH - heating. The ICRH - pulse starts at t=0.8 s and lasts up to t=1.5 s. The ICRH power level of 300 kW is comparable with the Ohmic power (350 kW). The additional heat flux to the tiles is here roughly in agreement with the power ratio. The absolute value of the heat flux density (here about 7 W/cm^2 and up to 20 W/cm^2 at low densities) is still very low. It is more than one order of magnitude smaller than the design value for the ALT-II blades. This leaves enough safety margin for successful operation with NI + ICRH heating of TEXTOR at a full auxiliary heating power of 6 MW for 3 s.

5. Conclusions

The program TWODEPEP is a powerful tool to analyze the heating of the limiter surface obtained by IR measurements. The code has been applied to the ALT-II limiter blades in order to simulate and evaluate plasma discharges (Ohmically and ICR heated). Heat flux densities at the limiter surface and temperature distributions in the limiter bulk have been obtained from the observed temperature pattern on the limiter tiles.

References

1. H.Soltwisch et al, Plasma Phys. Contr. Fus., 23, **26**, 1984
2. D.M. Goebel et al, 8th Intern. Conf Plasma Surface Interact., paper 66, 1988
3. K.H. Finken et al, 8th Intern. Conf Plasma Surface Interact., paper 58, 1988
4. W.J. Corbett et al, 8th Intern. Conf Plasma Surface Interact., paper 42, 1988
5. D.M. Goebel et al, this conference
6. J.-Fr. Hake, W. Homberg, Angew. Informatik, 185, **5**, 1987
7. B. Brandt, Int. Symp. Fus. Nucl. Techn., Paper 68-09

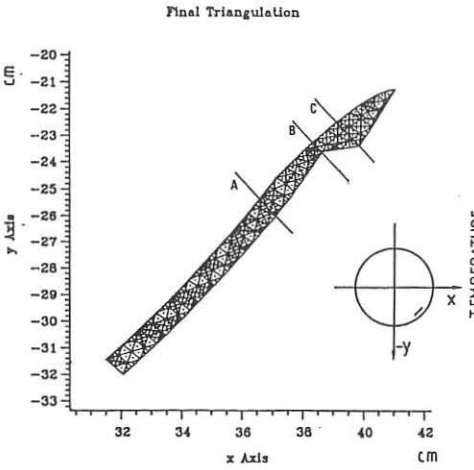

Fig. 1: Cross-section through a tile, orientation like in Textor. The three curves in fig. 3 are along cuts A, B and C. The circle at the right represents a poloidal cross section of TEXTOR with ALT-II.

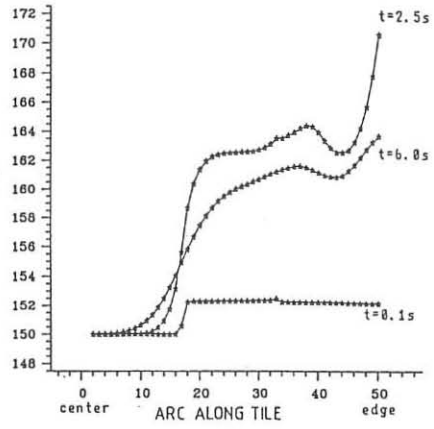

Fig. 2: Temperature along the tile surface for three different times. Heat flux = 0 for points less than 17; rest 10 W/cm^2.

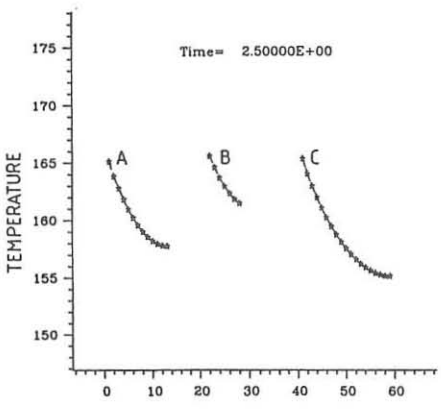

Fig. 3: Temperature distribution inside the tiles for cuts A, B and C (see fig.1).

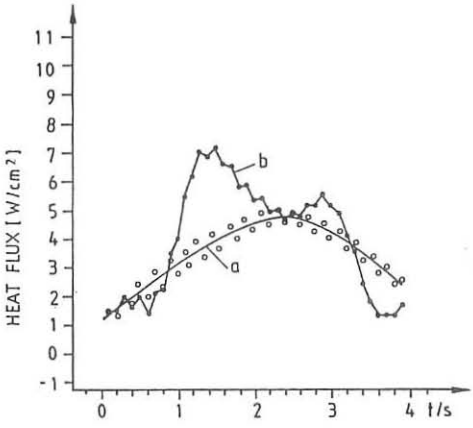

Fig. 4: Heat flux derived from Ohmic and ICRH discharges.

EDGE PLASMA CHARACTERISTICS IN TEXTOR WITH THE ALT-II TOROIDAL BELT PUMP LIMITER

D.M. Goebel, W. J. Corbett, R.W. Conn, K.H. Dippel*, K.H. Finken*

Institute of Plasma and Fusion Research and Dept. of Mechanical, Aerospace and Nuclear Engineering, University of California, Los Angeles, California 90024 USA
* Kernforschungsanlage Jülich GmbH, FRG, Association Euratom-KFA

Introduction

The ALT-II pump limiter is an axisymmetric toroidal belt installed in the TEXTOR tokamak. The toroidal geometry of this limiter has resulted in significant modifications in the boundary plasma compared to operation with the TEXTOR poloidal limiters. Since the particle exhaust capabilities of the pump limiter are ultimately determined by the the core plasma efflux and the plasma conditions in the scrape-off layer (SOL) leading to the particle collection and pumping ducts under the belt, a study of the boundary plasma characteristics has been made as part of the ALT-II program. The SOL density, flux, and electron temperature profiles are measured by a scanning double probe located on the horizontal midplane, two Li-beam diagnostics located on the top and bottom of the machine, and an array of 21 Langmuir probes mounted under the limiter blades. Measurements of the SOL plasma parameters and characteristic profiles by these diagnostics are used to determine the core efflux and global particle confinement time, characterize the edge plasma during belt limiter operation with ohmic and ICRH heating, and explain the particle collection and removal efficiency of the pumping system.

Experimental Arrangement

The ALT-II pump limiter[1,2] in TEXTOR[3] consists of eight radially moveable Inconel blade segments which form a full toroidal belt located 45° below the outside horizontal midplane. Each blade is covered by shaped graphite tiles and equipped with particle collection scoops and vacuum ducting under the blade. Standard conditions in the tokamak during ALT-II operation are: n_e = 1 to $5x10^{13}cm^{-3}$, B_T = 2.0T, I_p = 340kA, R = 1.75m, a = 44cm. During ICRH heating, the two pairs of antenna located 180° toroidally apart and on the outside-top of the torus are normally positioned at a=47cm such that a 1.3cm gap exists between the bottom of the blade and the antenna for particles to flow into the collection scoops.

The scanning probe diagnostic is a pneumatically driven double probe which scans a distance of 15 cm, moving from behind the TEXTOR liner to near the limiter tangency point in a time of about 0.1sec. The two Mo probe electrodes are insulated by a ceramic tube, which is protected on the outside from plasma bombardment by a floating graphite tube with an outside diameter of 0.5cm at the probe tip. The probe has a remotely adjustable insertion depth so that changes in the limiter position can be followed, and has been inserted into the limiter tangency point without damage. The probe voltage is periodically swept ±70V by a 2 msec ramp such that a double probe current-voltage characteristic is acquired at every 0.4 cm of motion into and out of the SOL. The probe moves approximately 1.2mm during the time of each voltage sweep. After each shot the probe characteristics are automatically fitted and

analyzed by the data acquisition system, and profiles of the plasma flux, density, and electron temperature plotted.

The standard direction of the toroidal field and plasma current in TEXTOR is such that the plasma flowing in the ion drift direction in the boundary passes along the bottom of the torus and strikes the lower side of the toroidal belt. Likewise, the plasma flow in the electron drift direction crosses the outside (large major radius) of the torus and strikes the top of the belt. The toroidal belt and plasma neutralization plates effectively bifurcates the torus, and the particle collection is accomplished by separate scoops on the ion and electron drift sides of the belt leading to common vacuum ducting. The scanning probe is normally located on the electron drift side of ALT-II. The Li-beam diagnostics on the top and bottom of TEXTOR are then used to determine the poloidal symmetry of the density and electron temperature, and their respective scrape-off lengths. One thermal Li-beam[4] from a heated oven is located on the bottom of the torus and 45° toroidally from the scanning probe. The second Li-beam diagnostic utilizes laser ablation[5] to propel Li and C into the edge plasma, and is located on the top of the machine, 180° toroidally from the scanning probe. The thermal Li-beam provides density profiles, and the laser ablation diagnostic produces both density and electron temperature profiles.

SOL Measurements

Typical density and electron temperature scrape-off lengths, measured by the scanning probe on the outside horizontal midplane during operation with ALT-II for two shots at low and high density, are shown in Fig.1. The limiter is positioned at a=44 cm for these ohmic deuterium shots. Increasing the line averaged density results in an increase in the edge plasma density n_e near the tangency point, and a decrease in the density e-folding length. The combination of a higher tangency point density and shorter scrape-off length results in an almost constant collection of ions by the electron drift side scoops, which collect from 45.7 to 48.2 cm for this limiter position, as the core density is increased.

The electron temperature profiles shown in Fig.1 illustrate the tendency of the edge T_e to decrease rapidly and the profile to flatten as the core density increases. The electron temperature is found to vary strongly only within 1 to 2 cm of the limiter tangency point, with λ_{Te} in this region ranging between 0.5 and 2 cm. Beyond 2 cm from the tangency point, the T_e profile is always very flat during ohmic heating with $\lambda_{Te} > 4$ cm, and the temperature varies only between 5 and 12eV as the core density changes.

The SOL structure with ALT-II is markedly different than operation with the poloidal TEXTOR limiters[7] or a modular limiter such as ALT-I. Modular limiter systems, especially with near integer q values at the boundary, can have flux tubes with extremely long connection lengths to the limiters and therefore regions with very long e-folding lengths. With a toroidal belt limiter, the average connection length to the limiter is the same at any toroidal or poloidal angle in the torus, and the longest connection length is approximately q times around the torus. The effect of this difference is shown in Fig.2, where the density and T_e profiles are plotted for the case of one ALT-II blade at a=44cm (a modular limiter) and the remaining 7 blades forming an effective belt at 47.5 cm. In the region of the single blade, the n_e and T_e e-folding lengths are both greater than 4 cm because the probe flux tube is not directly connected to the limiter. Starting at the position of the belt limiter, the n_e and T_e characteristic lengths decrease to the standard values associated with ALT-II.

The SOL n_e and T_e are found to be toroidally symmetric with ALT-II from an evaluation of the Langmuir probe data from the 21 probes in the scoops. The values of n_e and T_e in the scoop region are an order of magnitude lower for n_e and a reduced by factor of 2 to 3 for T_e with ALT-II compared to data from the entrance region of ALT-I[6]. The tenuous edge plasma in the shadow of ALT-II results in the majority of the convective losses going to the belt limiter, with a reduced amount of particles going to the liner walls. It is estimated from

the probe and H_α data that less than 15% of the core efflux reaches the liner during normal operation with ALT-II, compared to 30 to 50% found with the poloidal limiters and ALT-I.

Poloidal Asymmetries

The toroidal belt acts to separate the flows to the limiter from the inside and outside of the torus. The e-folding length from the scanning probe on the outside midplane always exceeds the e-folding length on the bottom/inside of the torus from the thermal Li-beam by a factor of 1.5 to 2 for non-detached plasma operation, independent of the ion and electron drift directions. The poloidal λ_{ne} asymmetry is shown in Fig.3, where the SOL density profiles are plotted for the three diagnostics during ohmic operation with ALT-II. While the outside midplane n_e e-folding length is found to always be longer than the bottom Li beam, the laser ablation n_e e-folding length from the top of the machine is typically close to the value from the scanning probe. The data from the Langmuir probes in the scoops of ALT-II also supports the inside/outside e-folding length differences found by the three edge profile diagnostics. In addition, the electron temperatures measured by the laser ablation system, the scanning probe, and the ALT-II Langmuir probes agree very closely. The observation of a longer density e-folding length on the outside of the torus may be explained by a major radius scaling for the perpendicular diffusion rate. The profiles on the outside and top of the torus are similar because there is no belt limiter between these regions to separate the plasma flows.

The values of n_e at a given radius from the three diagnostics are usually within a factor of 3 for normal tokamak operation. It is not known if this difference is due to a true poloidal density asymmetry, or if it is due to diagnostic position mis-alignment and differences in the data sampling times. However, the plasma n_e, T_e and e-folding lengths measured by the three diagnostics are within about 20% for detached plasmas, indicating that a strong poloidal symmetrization occurs. The SOL for a detached plasma with ALT-II is characterized by a very low T_e (~5eV), but the flux to the limiter is not greatly modified by detachment.

ICRH Modifications to the SOL

Operation with ICRH auxiliary heating modifies the boundary plasma parameters and profiles. Figure 4 shows typical n_e and T_e profiles from the scanning probe during 1.33 MW ICRH heating. The ICRH is found to shorten λ_{ne} near the tangency point to 1cm or less, and broaden the n_e profile deeper in the SOL. The electron temperature is seen to increase by at least a factor of two everywhere in the SOL with ICRH, and the value of λ_{Te} also decreases near the tangency point. The n_e and T_e profiles tend to develop bumps deep in the SOL, with the size of the perturbation depending on the ICRH power. The non-uniform profiles with ICRH are also observed with the laser ablation diagnostic. Reports of both increasing and decreasing SOL n_e and T_e profiles found in the literature for ICRH heating may be due to the details of where the measurement is made. The profile modification appears to be caused by direct coupling of the rf power into the SOL plasma. The increase in both flux and temperature deep in the SOL may be responsible for the hydrogen and impurity release often observed during ICRH heating.

References

1. R.W.Conn, et.al, J.Nucl.Mat. 121 (1984) 350.
2. D.M.Goebel, et.al., Proc. 8th Int.Conf. on PSI, Jülich, FRG, May 2-6, 1988.
3. K.H.Dippel, et.al, J.Nucl.Mat. 145-147 (1987) 3.
4. E.Hintz and P.Bogen, J.Nucl.Mat. 128&129 (1984) 229.
5. A.Pospieszczyk, Proc.14th EPS, Vol. III-1280, Madrid Spain, June 22-26, 1987.
6. D.M.Goebel, et.al, Plasma Physics and Controlled Fusion, 29 (1987) 473.
7. U.Samm, et.al., Proc. 8th Int.Conf. on PSI, Jülich, FRG, May 2-6, 1988.

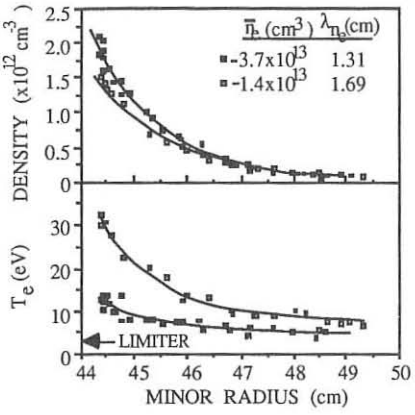

Fig.1 Density and electron temperature profiles at two values of the line averaged density. Increasing core density raises edge density and decreases the SOL electron temperature.

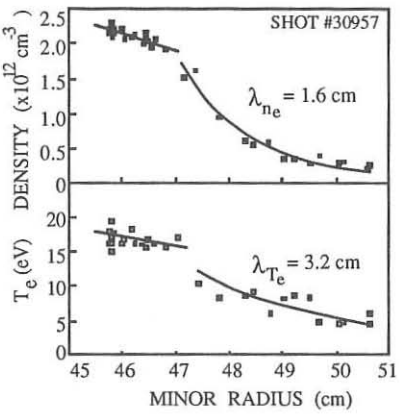

Fig.2 Density and electron temperature profiles for one blade at 44cm and the remaining 7 blades at 47.5cm. SOL profiles are considerably shorter for the belt limiter.

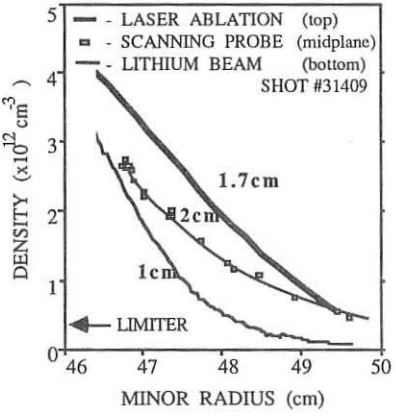

Fig. 3 SOL density profiles from diagnostics on the top, midplane and bottom of the torus. Poloidal differences are observed for the e-folding lengths.

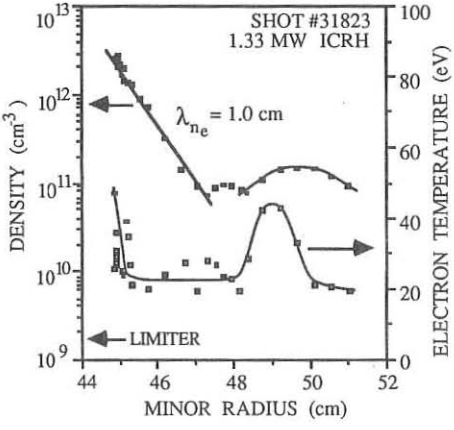

Fig. 4 Density and electron temperature profiles during 1.33MW ICRH heating. Profile modification increases with the level of ICRH power.

PLASMA BOUNDARY STUDIES IN DITE WITH ECRH AND A PUMP-LIMITER

P. C. Johnson, S. J. Fielding, G. F. Matthews,
R. A. Pitts*, J. Pritchard and G. Vayakis•

Culham Laboratory, Abingdon, Oxon, OX14 3DB, UK
(UKAEA/Euratom Fusion Association)

*Royal Holloway College, University of London
•University of Oxford

Introduction

Studies of the boundary plasma have been carried out in the DITE tokamak both with inside-launch electron cyclotron heating at the fundamental resonance (1) and with a new large pump-limiter (2). In this paper we present firstly a preliminary assessment of the response of the edge plasma to ECRH, and secondly an assessment of the particle handling characteristics of the pump-limiter in ohmic discharges.

Before October 1987 the limiter configuration on DITE comprised a full poloidal ring of 0.26 m minor radius centred on 1.17 m and adjustable top and bottom rails, all of carbon. In order to accommodate the ECRH antennae near the inside wall, the plasma major radius was increased to 1.19 m and the rail limiters were used at a minor radius of 0.21 m. In October, the poloidal limiter was replaced (see Fig.1), on the inside wall, by a 160° arc, and on the outside mid-plane, by a pump-limiter. Both are in carbon and have radii of curvature of 0.24 m centred on 1.19 m. A more detailed description of the pump-limiter is given below.

The main diagnostics of the edge plasma on DITE are Langmuir probes on reciprocating and incremental drives. The new limiters also have arrays of built-in probes, 11 in the inner-wall limiter and 8 in the pump-limiter. This arrangement gives good poloidal and radial cover in the boundary plasma.

Response of the Boundary Plasma to ECRH

The ECRH installation on DITE comprises three 60 GHz, 200 kW Varian gyrotrons delivering power to three antennae on the high field side of the torus (3). Each antenna assembly has a rotatable grooved mirror which for this work was used at an angle of 45° to the major radius.

The response of the boundary plasma to 240 kW of ECRH is illustrated in Fig. 2 for a 2T, 100 kA helium discharge on the rail limiters at a density of 2.7×10^{19} m $^{-3}$. The probe data was obtained at a distance of 24 mm behind the last closed flux surface using a retarding-field deposition probe (1). The increase in J_{sat} with ECRH is a consequence of increases in both T_e and n_e in the scrape-off plasma. When looked at on a finer time-scale, close to the limiter radius, the increase in J_{sat} occurs in $\sim$ 3 ms after an initial delay of $\sim$ 1 ms. This behaviour is probably due to increased

particle transport out of the main plasma in the presence of ECRH. Close to the wall, J_{sat} increases in less than 500 μs; such a short time-scale could be explained by thermal desorption of atoms/molecules due to the residual ECRH power at the wall. Changes in T_e in the scrape-off plasma occur in less than 10 ms, which is however the limit of resolution of the present equipment. The retarding-field deposition probe also allows T_i to be estimated; results obtained so far show no evidence for an increase in edge T_i with ECRH. Although the absolute level of density fluctuations increases with ECRH, there is little change in the value when normalized to the increased density.

Fig. 3 shows the relative change in electron density at various distances behind the last closed flux surface as a function of the major-radial position of the cyclotron resonance. Helium, 100 kA, rail-limiter discharges were used at $n_e \sim 1.3 \times 10^{19}$ m^{-3}, and with 315 kW of ECRH. Also shown in this figure is the increase in the poloidal β, which is a measure of the heating efficiency. At higher densities, the heating is optimised when the power is deposited near the magnetic axis, but at the value of density used in the figure, effective heating occurs with the resonance displaced outwards, consistent with Doppler-shifted resonance absorption (4). The relative change in edge density is lowest when heating is optimised, and is highest when the resonance is placed well to the inside of the magnetic axis.

Data from the probes closest to the main plasma confirm that there is little change in the scale-length of the density gradient in that region. Close to the wall there is evidence for a larger increase in density when there is poor heating. An H_α monitor looking at a patch of the wall shows a similar trend. This is consistent with increased thermal desorption from the wall either of hydrogen or helium (the H_α monitor is sensitive to a HeII line); a sniffer probe tuned to the gyrotron frequency shows that the residual power at the wall increases as the heating efficiency reduces.

For these experiments two of the antennae gave a mixture of 'O' and 'X' modes with a broad (12° half-width) antenna pattern. More recent experiments with a pure mode launched from one of these antennae show broadly similar results, suggesting that the broad desposition profile associated with the mixed modes and wider antenna pattern had little effect on the edge data.

Particle Control with the Pump-Limiter

The pump-limiter (Fig.1) was designed for particle control, with only a minimal allowance for energy handling on the front face. It comprises a single piece of carbon, 430 mm high and 180 mm wide. The front face is a section of a cylinder, with a radius of curvature of 0.24 m. Although the tip radius is 2 mm, when allowance is made for the toroidal shape of the plasma, the 30° angle neutralizer faces are set some 7 mm back from the last closed flux-surface. A moveable surround with carbon side plates

allows the throat aperture to be varied from 0 mm to 25 mm. The surround is crudely sealed into a 0.1 m^3 rectangular tank by means of a PTFE skirt. Two 500 $l.s^{-1}$ (nominal) turbo-molecular pumps provide the main pumping on the tank which is also equipped with a titanium getter.

Langmuir probes are built into the limiter on both faces, at 7.5 mm and 17.5 mm from the last closed surface (inner limiter probes are at 3 mm and 15 mm). In the throat (at 7.5 mm) local n_e and T_e values up to 0.6×10^{19} m^{-3} and 60eV have been measured. Parameters extrapolated to the last closed surface from observations in 2.2T, 100 kA deuterium and helium discharges vary with line-average density as shown in Fig. 4. There is little difference between observations made on the electron and ion sides of the pump-limiter. The probe data allows estimates to be made of the total particle flux incident on the limiter and of the flux entering the pump-limiter throat, which here was set at 20 mm. The result is shown in Fig. 5. for the helium discharges.

The exhausted particle flux is estimated from the pressure rise in the tank measured with a Baratron gauge. Allowance is made for backflow through the throat (blocking is ignored), and the incoming particles are assumed to be He^{++} ions. Fig. 5 shows the result; about 18% of the incident flux in the throat is captured, which represents an encouraging 6% of the total leaving the plasma. Without pumping in the tank, pressures of about 2×10^{-3} torr are observed both in deuterium and helium. Use of the turbo-pumps reduces the pressure by a factor of about 2, and in deuterium a further two-fold reduction is achieved by gettering in the tank. When the width of the throat is varied, there is little increase in the tank pressure for openings greater than 8 mm. A wider throat was used in the experiments in order to take advantage of the full set of Langmuir probes. Further experiments are planned to explore the performance of the pump-limiter for a wider range of conditions. It is in routine use in the current experiments with ECRH, and with it, reproducible operation at low density has been possible, which had proved difficult with the previous conventional limiters in the absence of gettering in the torus.

(1) R. A. Pitts et al., presented at 8th PSI conf. (Julich 1988).
(2) P. C. Johnson et al., presented at 8th PSI conf. (Julich 1988).
(3) M. W. Alcock et al., 14th Europ. Conf. Contr. Fusion and Plasma Physics (Madrid, 1987) 813.
(4) A. C. Riviere et al., these proceedings.

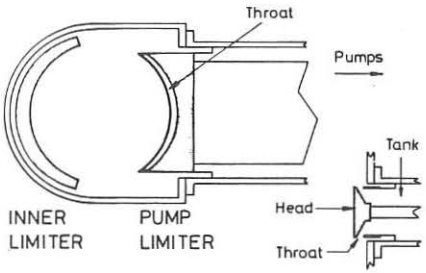

Figure. 1. Schematic view of limiters (toroidal separation is 67.5°) and section through mid-plane of pump limiter.

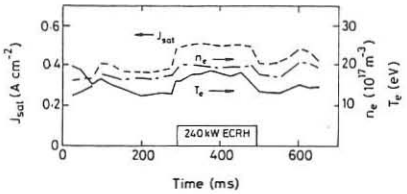

Figure. 2. Langmuir probe data at 24 mm behind the last closed surface. Helium, I_p = 100 kA, B_ϕ=2T, $\bar{n}_e$ = 2.7x10^{19} m^{-3}.

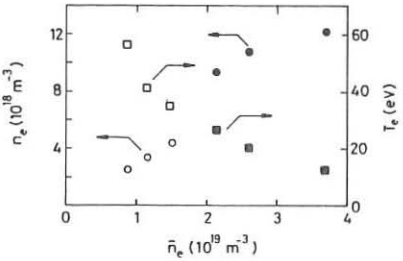

Figure. 4. Variation with $\bar{n}_e$ of n_e (○,●) and T_e (□,■) at the limiter radius for 100 kA discharges in helium (●,■) and deuterium (○,□).

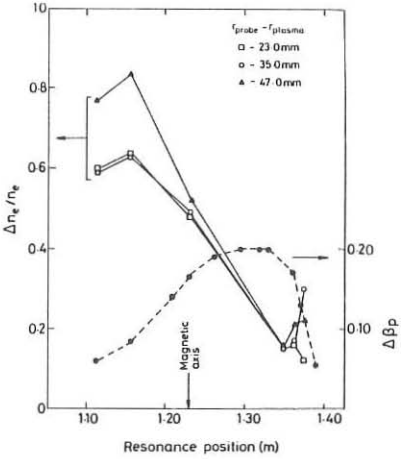

Figure. 3. Variation with resonance position of relative changes in density in the scrape-off layer and in poliodal beta. Helium, I_p = 100 kA, $\bar{n}_e$ = 1.3x10^{19}m^{-3}, P_{ECRH} = 315 kW.

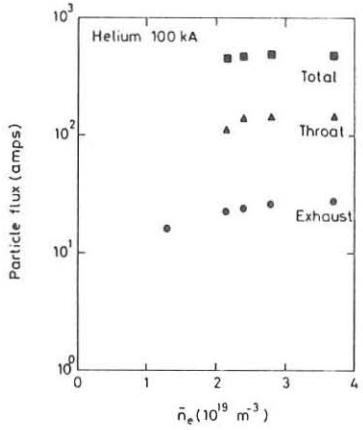

Figure. 5. Variation of particle fluxes with n_e in 100 kA, helium discharges. ■ - total leaving plasma, ▲- flux to pump-limiter throat, ●- flux captured by pump-limiter. Throat = 20 mm.

TOKAMAK EDGE PLASMA TRANSITION TO THE STATE WITH DETACHMENT FROM LIMITER

Tokar' M.Z.

Institute for High Temperatures of the USSR
Academy of Sciences, Moscow, USSR

I. As it has been observed in the experiments on a number of tokamaks /1-4/ the edge plasma is detached from a limiter when some parameters are changed. In the state with "detached plasma" (DP) the power put into a discharge is transfered to the wall in a form of the neutral and light impurity radiation. The transition to the DP state has a sharp character and may be induced by the growth of the mean plasma density $\bar{n}$ during a gas puffing /1/, the decrease of the current in the discharge /2,3/ or the power of an auxiliary heating /1/. The formation of a "virtual limiter" /4/ is seemingly analogous to DP. The study of the transition to the DP state is of great interest since it's realization in a reactor may be one of the perspective ways for the solution of the plasma surface interaction and impurity control problems.

In the present paper we consider the mechanism of the discharge transition to the DP state based on the edge plasma cooling instability due to the charge-exchange of the light impyrities on the hydrogen atoms arising as a result of the plasma recombination on the liner surface. The density of these atoms n_a^w, is sufficently homogeneous on a magnetic surface in contrast to the neutrals born on the limiter. n_a^w grows with $\bar{n}$ increase as a result of the growth of the plasma flows into the scrape-off layer (SOL), j_s, and on the liner, j_w. Due to the charge-exchange the impurity ionization equilibrium is displaced to the state with higher concentration of the ions of small charges and the radiative losses of energy grows sharply. The cooling instability mechanism under consideration differs from that discussed earlier by the nature of the impurity recombination process. It's more effective when the distance from the limiter edge to the liner, Δ, is sufficiently small and results in the poloidal symmetric transition to the DP state.

2. Let's consider the case when the charge-exchange on hydrogen atom outweighs of other impurity recombination processes. The densities of the impurity ions with different charges, n_z, can be determined from the following system of the particle balance equations (we don't take into account the impurity transport across the magnetic field):

$$-k_i^1 n n_1 + k_c^2 n_a^w n_2 = 0$$

$$(1 < z < z_c)\quad k_i^{z-1} n n_{z-1} - k_c^z n_a^w n_z - k_i^z n n_z + k_c^{z+1} n_a^w n_{z+1} = 0 \qquad (1)$$

$$K_i^{z_c-1} n n_{z_c-1} - k_c^{z_c} n_a^W n_{z_c} = 0$$

where $k_{i,c}^{z}$ are the constants of the impurity ionization and charge-exchange; the ions with charges no more than that in a coronal equilibrium, z_c, are taken into account because the density of the ions with $z > z_c$ is small.

If the total concentration of the impurity, $\mathcal{F}_I = \Sigma n_z/n$, is given the solution of Eq-s (1) has a form:

$$n_z = n\, \mathcal{F}_I \cdot \alpha_z / \Sigma \alpha_z \qquad (2)$$

where $\alpha_{z_c} = 1$, $\alpha_{z-1} = \alpha_z \cdot n_a^W k_c^z / n k_i^z$

The quantity n_a^W can be obtained from the following considerations. According to Ref./6/ the neutrals appearing during the plasma recombination on the material surfaces in a tokamak localize in the wall-near-region with the width of the order of $l = 1/n_o\sigma_*$. Here n_o is the plasma mean density in the region, $\sigma_* = \sqrt{k_i^H (k_i^H + k_c^H) m_i / T}$, $k_{i,c}^H$ are the ionization and charge-exchange of the hydrogen atoms. n_o depends on $\bar{n}$ and as a rule $n_o \simeq 0.5 \div 0.8\bar{n}$ in the discharges with gas puffing. The value of n_o determines the plasma flux into the SOL - j_s. The plasma density gradient in the wall-near-region is of the order of n_o/l and $j_s \approx D_\perp \cdot n_o/l \simeq D_\perp \cdot n_o^2 \sigma_*$. For Alcator like scaling of diffusivity - $D_\perp = A/n$ - one has:

$$j_s \simeq A n_o \sigma_* \qquad (3)$$

The plasma flux on the liner surface is $j_w = j_s \cdot \exp(-\Delta/\delta)$, where $\delta = \sqrt{D_s L / V_s}$ is the density fall length across the magnetic field in the SOL, L is the line of force length; D_s is the diffusivity in the SOL, assuming constant; $V_s = \sqrt{2T/m_i}$. During the charge-exchange the neutrals acquire the plasma temperature and the ion heat velocity $v_i = \sqrt{T/m_i}$. Hence

$$n_a^W = j_w / v_i \simeq A n_o \sigma_* / v_i \cdot \exp(-\Delta/\delta) \qquad (4)$$

The value of δ depends on the plasma temperature in the SOL, T_s, which can be determined from the heat balance. Neglecting the volumetric losses and sources of the energy in the SOL we equate the heat flux from the wall-near-region, q_s, to the flux transfered to the liner and limiter by the charged particles:

$$q_s = \gamma j_s T_s \qquad (5)$$

where $\gamma = 5 \div 10$ /7/.

As it follows from Eq-s (3),(5) an increase of n_o results in T_s decrease and hence the growth of δ. According to Eq.(4) this brings to the nonlinear increase of n_a^W.

The energy losses from the wall-near-region, Q_I, due to the impurity excitation depend on the electron and impurity ion densities and intensity of line radiation:

$$Q_I = n \sum_{z \le z_c} n_z L_z \qquad (6)$$

where $L_z = \sum_{i,j} k_{i,j}^z E_{i,j}^z$, $k_{i,j}^z$ are constants of the excitation from the state j, $E_{i,j}^z$ is the transition energy.

The radiation cooling rates of the light impurities, L_z, have the sharp maxima for the lithium like ions. In the carbon case $L_1 = 5 \cdot 10^{-10}$ eV·cm^3 · s^{-1}; $L_2 = 10^{-8}$ eV·cm^3 · s^{-1}; $L_3 = 5 \cdot 10^{-8}$ eV·cm^3 · s^{-1}; $L_4 = 10^{-9}$ eV.cm^3 · s^{-1}.

As a first approximation we assume the plasma parameters are constant over the wall-near-region and put them equal their mean values in the region n_o, T_o. In this case the heat balance in the wall-near-region has a form

$$q_o = q_s + Q_I \cdot 1$$

where q_o is the heat flux from the central part of the discharge. Using the Ex-s (3),(5),(6) one can obtaine the equation for T_o:

$$f(T_o) = \frac{\xi_I}{\sigma_*} \cdot \frac{\sum L_z \alpha_z}{\sum d_z} + \gamma\, \theta_o T_o A \sigma_* = \frac{q_o}{n_o} \qquad (7)$$

where $\theta_o = T_s/T_o \simeq 0.5$.

Fig. 1 shows the dependence $f(T_o)$ calculated with the typical values of parameters: $A = 2 \cdot 10^{17}$ cm^{-1}s^{-1}; $\gamma = 7{,}5$; $\sigma_* = 5 \cdot 10^{-15}$cm^2; deuterium is the discharge gas, the concentration of carbon impurity, ξ_{I_z}, equals 1%; the impurity charge-exchange cross-section σ_c^z have been taken from Ref./8/ and in the hydrogen atom energy range of 10÷100eV $\sigma_c^2 \simeq 2 \cdot 10^{-15}$ cm^2, $\sigma_c^3 \simeq 10^{-15}$cm^2, $\sigma_c^4 \simeq 3 \cdot 10^{15}$cm^2; $k_c^z = \sigma_c^z \sqrt{8T_o/\pi m}$; the ionization constants k_i^z were calculated by formulas of Ref./9/; the geometric characteristics correspond to the TEXTOR device /1/.

The dependence $f(T_o)$ has a nonmonotonous character since the first term corresponded to the energy radiative losses has a sharp maximum with T_o when the lithium like ion concentration is maximum. The plasma temperature in the wall-near-region is determined by the intersections of the curve $f(T_o)$ with the line $y = p$, where $p = q_o/n_o$. If the initial p value, p_o, exceeds the maximum f value, f_1, than with p decrease the discharge evolves in accordance with AB section of the curve $f(T_o)$. The decrease of p may be stipulated by the increase of n_o or the diminution of q_o. In the point B corresponded to the minimal f value, f_2, the wall-near-region plasma passes into the state C where the energy balance is defined by the impurity radiation, i.e. "DP" state.

The theoretical dependence of the heat flux onto the

limiter Q_L on n_o is represented on Fig. 2a. The calculations have been done for $q_o = 0.8$ W/cm^2, corresponded to the experiments of Ref. /1/. There is also the experimental dependence of Q_L on $\bar{n}$ taking from Ref. /1/ on the Fig. 2a. The calculated data are in a good agreement with experimental those with $n_o = 0{,}75\ \bar{n}$. According to the Ref. /1/ the slump of Q_L is attended with the sharp growth of the ratiation intensity D_{wall} of the deuterium neutrals coming from the liner. This may be explained by the nonlinear growth of dw with n_o.

The particle and energy losses from a tokamak discharge have a balloning character i.e. q_o and j_s depend on the poloidal angle θ. As it follows from Ex-s (2),(3) the lithium like ion density and the radiative losses of energy are proportional to n_a^W which depends on θ analogously j_s. Due to identical dependences of all terms in Eq.(7) on θ the transition to the DP state consided here is a poloidal-symmetric one. This result agrees with TEXTOR data /1/.

1. Pospieszczyk A. e.a., J.Nucl.Mater. 1987, V.145-147, p.181; Castracane J. e.a. Nucl.Fusion, 1987, V.27, p.1921
2. Strachan J.D. e.a. Rep. PPPL-2379, Princeton, 1986
3. McGracken G.M. e.a. J.Nucl.Mater. 1987, V.145-147, p.181
4. Vertiporoch A.N. e.a. Plasma Physics, 1982, V.8, p.437 (in Russian)
5. Ohyabu N. Nucl.Fusion, 1979, V.19, p.1491.
6. Vasiliev N.N. e.a. Plasma Physics, 1982, V.8, p.37 (in Russian)
7. Sengoku S. e.a. J.Nucl.Mater. 1980, V.93-94, p.75
8. Phanenf R.A. e.a. Rep. ORNL-6090, Oak-Ridge, 1987
9. Lotz W.Z. Phys., 1969, V.220, p.466.

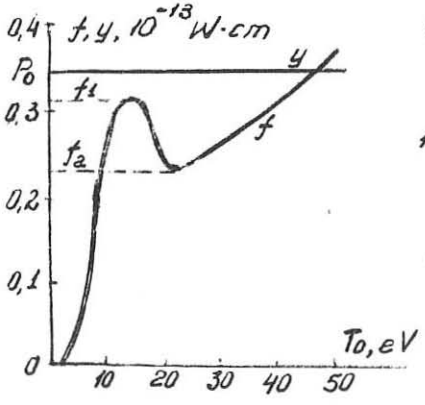

Fig. I

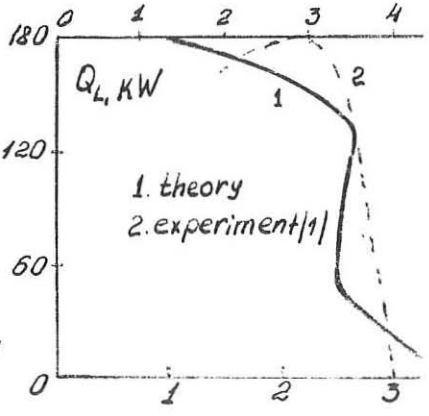

Fig. 2

STUDY OF EDGE PLASMA PARAMETERS UNDER OHMIC HEATING AND ECRH ON T-10 TOKAMAK

Berezovskij E.L., Vasin N.L.,Vershkov V.A.,Grashin S.A. Maksimov Yu.S., Medvedev A.A., Pimenov A.B., Sushkov A.V., Titishov K.B., Chankin A.V., Ziegenhagen G.*

I.V.Kurchatov Institute of Atomic Energy,Moscow,USSR

*Academy of Sciences of GDR,Central Institute of Electron Physics, 1086, Berlin, GDR.

The properties of the edge plasma in T-10 with Ohmic and EC-heating up to 2.1 MW of plasma-deposited power have been measured with $I_p \approx 200$ kA, $B \approx 3$T, $n_e = 1.5\text{-}4 \times 10^{13} cm^{-3}$, $q(a_L)=4.8$. The limiter system consisted of the main rail ($a_L=32$ cm) and poloidal ring ($a_L=34.5$ cm) graphite limiters. The chamber walls ($a_W=38.7$ cm) were also shielded with the stainless steel limiters at $a_L=36.7$ cm.

Several carbonizations of the chamber [1] during the experimental campaign were carried out at low walls temperature, using CH_4. As a result, sharp enhancement of the working gas flux from the walls in successive shots have been observed, leading to the reduction of electron and ion temperatures in the plasma bulk. The life-time of injected potassium turned out to be short and typical for the S-regime [2]. Some characteristics of one carbonization, nine days long, are given in Fig.1. A number of discharge is counted off along the abscissa.Spectral line intensities H_β/D_β, CIII, CV, CrI and OV were measured

180° toroidally apart from the main limiter cross-section in a steady state of the discharge. J_r is determined by the brightness of H_β/D_β line, using the coefficients from [3]. Effective plasma charge, Z_{eff}, was obtained from the measurements of visible continuum.

The electron temperature and half-sum of the ion saturated currents of Langmuir probes are also shown. The probes have area $S=0.12$ cm^2 and were mounted on the ion and electron sides of the rail limiter near the limiter tip, 0.45 cm outside the last closed flux surface.

The main impurity in the discharge was the carbon, whereas the contribution of metallic impurities and oxigen to Z_{eff} and integral radiation losses was neglig ble. Just after the carbonization carbon and working gas fluxes from the limiters and walls were maximal, as well as the $Z_{eff}=2$. Degassing of the chamber during the discharges led to the sharp reduction of C and H/D influxes with gradual replacement of hydrogen by deuterium. The influx reduction corresponds to a drop in Z_{eff} down to 1.3. However, at the same time the amount of integral radiation loss from the discharge was unchanged, P_{rad}

$\approx$75 kW. Also unchanged was the T_e measured by limiter tip probes. The rise in edge n_e just after the carbonization correlate with the interferometrically obtained broadening of the $n_e(r)$ - profile. Up to now we are not able to explain the difference in the behaviour of P_{rad} and carbon influx.

Working discharge cleaning of the chamber surface reduce the gas influx to plasma column. To sustain a given $\overline{n_e}$ addition gas puffing is necessary. Fig.2 exhibits the behaviour of some plasma parameters during the $\overline{n_e}$ rising phase of the discharge and after switching the valve off. The Electron temperature, T_e , was measured by Langmuir probe at r= = 36.2 cm, the probe n_e value dosn't change significantly during the discharge. One can see that during the density rise T_e remains at low level of 5 eV. The density rise is accompanied by a rise in the MHD-activity of the m=2 mode and integral radiation losses. After switching the valve off at 280-th ms a drop in U_{loop} , P_{rad} starts; however, T_e 2-fold rise occures only 120-140 ms later, that is close to the plasma column skin-time.

Thus, one can see that the neutral influx from the valve results in cooling of the plasma periphery; meanwhile influx from the walls does not induce the plasma column contraction. The measurements of D_α Doppler-broadenings on the wall and at a place of the valve location reveal a very similar energy of neutrals about 7-9 eV. Different influence of influxes from walls and the valve on plasma parameters may be due to the locality of particle source unduced by the valve, as in the experiments on JFT-2M [4] . The similar behaviour of the plasma column edge was also observed in TEXTOR, where the plasma remained in the "attached" state with fresh carbonized walls up to critical values of $\overline{n_e}$ [5] .

The temperature and density dependencies on $\overline{n_e}$ for ion and electron sides of the rail limiter tip, measured by probes, are shown in Fig.3. T_e and n_e values in the case of the fresh carbonization are significantly larger than before the carbonization. As the data were taken during, or just after the end of density build up phase, T_e -rise with carbonized walls is obviously due to the reduction in gas puffing. In both cases $T_e \sim \overline{n_e}^{-2}$. Attention should be paid to the difference in n_e on i and e-sides of the limiter with $\overline{n_e}$-growth. This confirms a recently-proposed hypothesis of preferential plasma transport through an external circumference of the torus at high $\overline{n_e}$ [6], as the magnetic field lines transit from e-side of the limiter to an external part of the torus in these discharges. Results from the limiter tip show that this asymmetry probably is peculiar to the plasma column, but not a limiter effect.

ECRH

Two gyrotron sets at λ_1= 3.7 mm and λ_2=4.0 mm, which allowed us to change the input power radial profile [7] were used on T-10. The edge parameters, as in the plasma bulk, have a weak dependence on resonance zone position. In the case of a periphery heating (r = 15-16 cm), maximal parameters were obtained for a shorter time than those under central heating. The ECRH-power dependence of the sum of ion saturated currents to i-and e-limiterprobes is shown in Fig.4. As a reply of the ECRH-power, fluxes are about 3 times enhanced; they are slighty large on carbonized walls. An electron temperature has a 1.5-2 - times rise on average, although there are some discharges with a 3-times rise. The plasma edge T_e and n_e dependences on the heating power measured with Langmuir probe at radius r=34.5 cm are shown in Fig.5. T_e does not change with the ECRH-power increase. Relative increase of n_e during ECRH for three radial positions of the probe is presented on Fig.6. Maximal increment in n_e occurs near the wall, that corresponds to an increase in the e-folding decay length from 1.0 cm to 2-3 cm.

Astimated total flux onto the rail and circular limiters rises from 1.5×10^{21} under Ohmic heating to 3×10^{22} particles/s under ECRH, that, apart from the reionization sourse of neutrals in scrape-off layer, should be equal to outflux from the plasma column. Astimation of convective power flux to SOL $Q_\perp = 5 \Gamma_\perp T_e$, using the probe data, is close to the input power of ECRH. Sharp rise of a particle flux from the limiters under ECRH does not allow the edge T_e to increase. As the $T_e(0)$ rise under ECRH, this means, that the $T_e(r)$ - profile relatively shrinks. This may be the reason of the confinement degradation with increased heating power.

Also should be noted a difference in the behaviour of $n_e(r)$ - profile under heating before and after carbonization. In the case of carbonized walls a large influx of hydrogen atoms to the plasma from the walls and the peaked $n_e(r)$ - profile are observed. Before the carbonization, the $n_e(r)$ - profile becomes more flat. The difference may be related, as in the Ohmic regime, with different influence of the fluxes from the wall and the valve.

References

1. S.A.Grashin et al. 14-th Europ. Conf. on Contr.Fus. and Plasma Phys. Madrid,1987,v.11D, part III, p. 798.
2. A.A.Bagdasarov et al. 12-th Europ. Conf. on Contr.Fus. and Plasma Phys. Budapest,1985,v. 9F, part I, p. 207.
3. L.C.Johnson, E.Hinnov, JQSRT, 1973, v. 13, p. 333.
4. S.Sengoku and JET-2M team,J.Nucl.Mater.145-147(1987)556.
5. U.Samm et al.Plasma Phys. and Contr.Fus.29,N10a(1987)1321.
6. V.A.Vershkov et al. J.Nucl.Mater., 145-147 (1987) 611.
7. V.V.Alikaev et al. Plasma Phys., 29 (1987) 140.

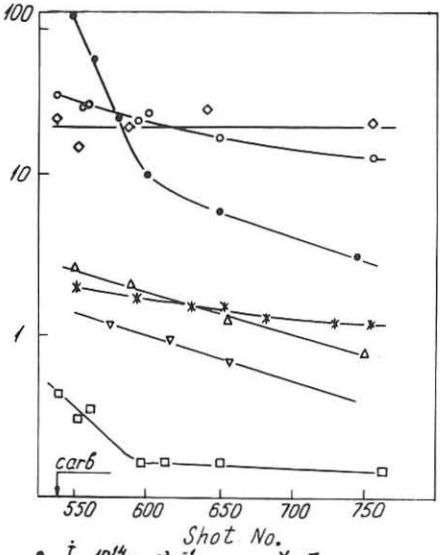

● $\dot{J}_r$, $10^{14}\,cm^{-2}s^{-1}$ ✱ Z_{eff}
○ H_α/D_α limiter, a.u. □ $(I_{Si}+I_{Se})/2$, A
▽ C III, $10^{-4}\,W\,cm^{-3}$ ◇ T_e, eV
△ C V, $10^{-4}\,W\,cm^{-3}$

Fig. 1

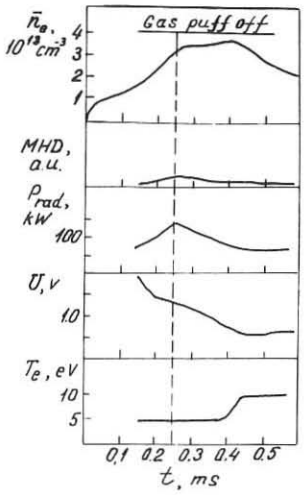

Fig. 2

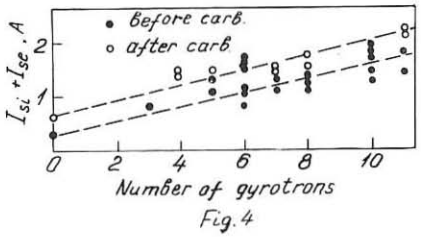

Fig. 4

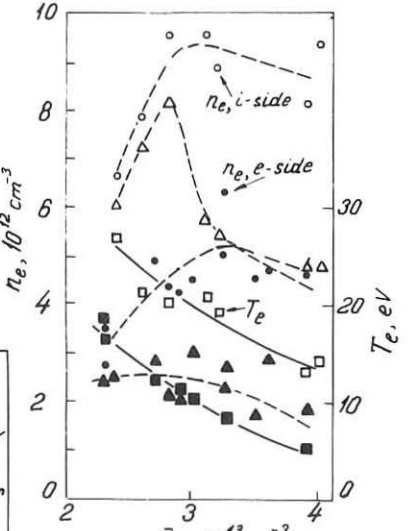

open symbols - fresh carb.
black symbols - before carb.

Fig. 3

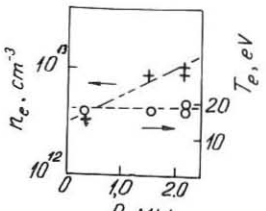

Fig. 5

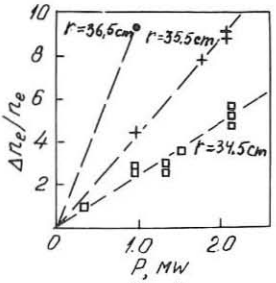

Fig. 6

THE INFLUENCE OF LIMITER CONFIGURATION ON THE IMPURITY FLUXES IN THE SCRAPE-OFF LAYER IN TEXTOR

M. Rubel[1*], H. Bergsåker[1], B. Emmoth[1], F.Waelbroeck[2], P. Wienhold[2], and J. Winter[2]

[1]Research Institute of Physics, S-104 05 Stockholm, Sweden

[2]Institut für Plasmaphysik, KFA, POB 1913, D-5170 Jülich, FRG

1. INTRODUCTION

Passive collector probes are often applied for the diagnostic of impurity and hydrogen isotopes fluxes in the scrape-off layer (SOL) of tokamaks' plasma/1,2/. This paper concerns analytical results of the measurements of angular and radial distribution of atoms deposited onto the surface of cylindrical probe during its time-resolved exposure to the plasma discharges in carbonized TEXTOR with graphite limiters. The main point of the investigation was to compare the influence of different limiters in TEXTOR upon the fluxes of oxygen, metals ($Ni + Cr + Fe$) and deuterium in the plasma edge. Moreover, it was also important to determine the correlation between the oxygen concentration and the concentration of metals and deuterium collected on exposed surfaces.

The investigation was carried out with two cylindrical graphite probes (A and B) which were rotated during the exposure. The probes were shielded by titanium hausing with a slit open to the "ion drift" side. The information concerning the probe system and experimental details is given elsewhere /3/. During the exposures of Probe A and B the configuration of limiters was different but the basic plasma parameters were very similar: maximum current 340 kA, density about $3 \cdot 10^{13}$ cm^{-3}, magnetic field 1.6 or 2 T and shot duration about 3 s. Probe A was exposed in the presence of the main poloidal limiter (ML) at the position 46 cm and ALT I pump limiter at 50 cm whereas in the case of Probe B, additionally, the toroidal pump limiter ALT II (not actively pumped) was at the position 46 cm. The probes were always placed 25 mm from the plasma egde.

The analysis of metals and oxygen deposited on the surface was performed by means of Rutherford backscattering spectroscopy whereas nuclear reaction analysis, $^3He(d,p)^4He$, was applied in order to determine the concentration of deuterium.

2. RESULTS

Figure 1 a-c illustrates the results for the time-resolved measurements of areal concentrations of metals, oxygen and deuterium deposited on the surface of Probe A exposed to one plasma discharge. In the case of the plots for oxygen the background level ($0.8 \cdot 10^{15}$ cm^{-2}) of this element was substracted. The shape of the time-resolved plots for all the analysed atoms is similar. In the beginning of the discharge the concentration increases to the maximum value followed by certain steady-state level and next decreases steply in the final period of the shot. However, areal concentrations of respective species differ distinctly. The values characteristic for the steady-state level which is approximately related to the "flat top" stage of the plasma discharge are equal to $5 \cdot 10^{14}$ cm^{-2} for metallic atoms, $8 \cdot 10^{15}$ cm^{-2} for oxygen and 6 - $8 \cdot 10^{16}$ cm^{-2} for deuterium.

More precise comparison of the results obtained is available by the determination of oxygen to deuterium (C_O/C_D) and oxygen to metals (C_O/C_{Me}) concentration ratios. For corresponding analysed points one obtaines 0.12 ± 0.02 and 15 ± 2 for C_O/C_D and C_O/C_{Me}, respectively. Similar results have also been observed for other probes exposed in carbonized TEXTOR in the presence of ALT I and the main poloidal limiter /4/.

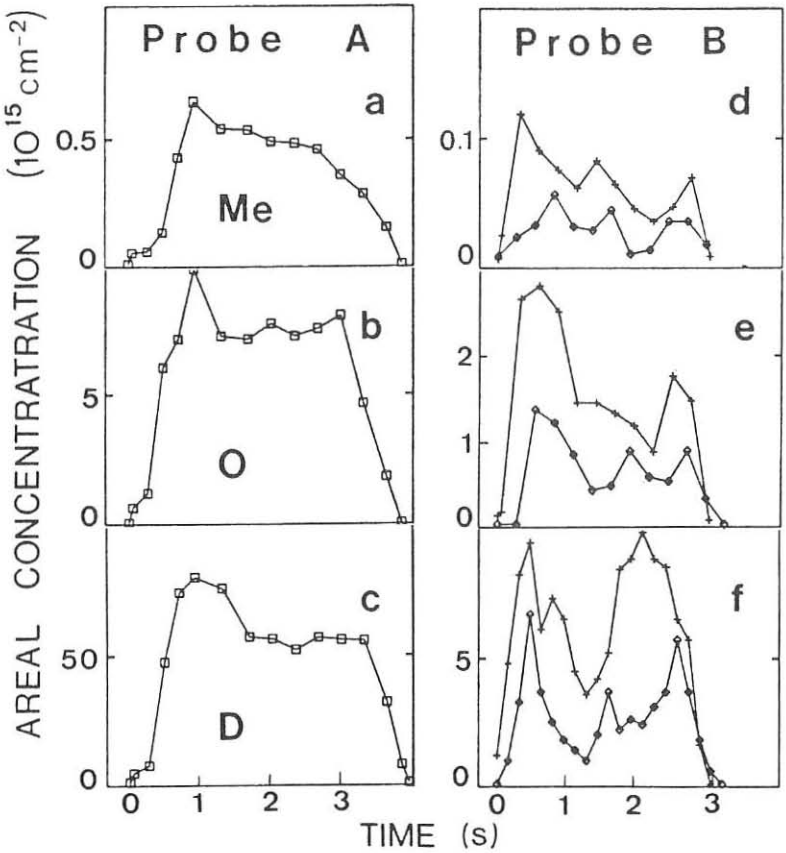

Fig. 1. Areal concentrations of metals, oxygen and deuterium deposited on Probe A and Probe B as a function of the discharge time.

Analogous set of data obtained for Probe B is shown in Figure 1 d-f. The results for single (diamont points) and double (crosses) exposure of the probe surface to the plasma discharges are collected. The amount of atoms deposited during one discharge is roughly twice lower than this detected after two subsequent overlaid discharges. Single and double exposure leads to the similar distribution of deposits but these time-resolved spectra are more complex than those recorded for Probe A. The accumulation of impurities and deuterium atoms is noticeable mainly at the begining and the end of the exposure. This feature will be discussed below.

Other distinct differences between the results for Probe A and B are connected to the total concentration and to the concentration ratios of species deposited on the probes. First of all, the areal concentrations determined on Probe B are several times lower than those characteristic for Probe A. The exposure of the second probe to one discharge yield following concentrations: 0.2 - 0.5 $\cdot 10^{14}$ cm^{-2} for metallic atoms, 0.5 - 1.5 $\cdot 10^{15}$ cm^{-2} for oxygen and 2 - 5 $\cdot 10^{15}$ cm^{-2} for deuterium. This very low amount of deposited species strongly influences on accuracy of the determination of the concentration ratios for corresponding analysed points on the probe surface. The values of C_O/C_D and C_O/C_{Me} are in the range 0.2 - 0.3 and 40 - 60. However, even this rough estimation indicates that the deposition rate of metals has been distinctly reduced in comparison to the situation observed for Probe A. Simultaneously, relatively higher concentration of oxygen is noticeable.

The plots in Figure 2 a and c present radial distributions of oxygen and other atoms on two probes. One observes characteristic /2,4/exponential decay of the areal concentration of deposits. High decay rate is especially pronounced for Probe B. However, for a given probe the slope of the plots is approximately the same which indicates similar decay rates for all the species. This suggestion is partly confirmed by the determination of concentration ratios for respective points. The values of C_O/C_D and C_O/C_{Me} are in the range: 0.10 $^+$ 0.02; 14 $^+$ 2 for Probe A and 0.24 $^+$ 0.04; 50 $^+$ 10 for Probe B. The results for the oxygen to deuterium ratio are shown in Figure 2 b and d.

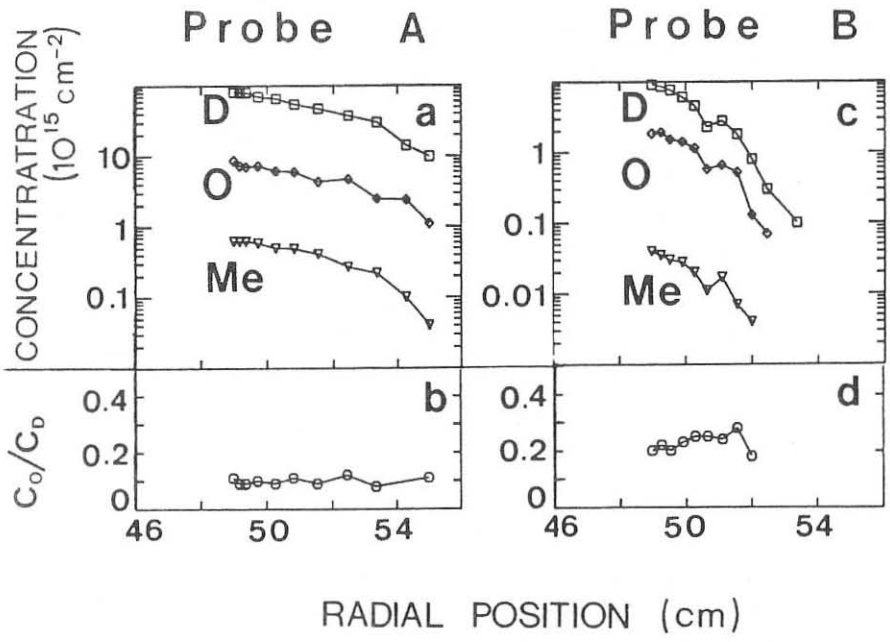

Fig. 2. Radial distributions of impurity and deuterium atoms and radial dependence of oxygen to deuterium ratio on Probe A and Probe B.

3. DISCUSSION AND CONCLUSIONS

The results obtained for two analysed probes can be discussed in terms of limiter configuration and processes responsible for deposition of plasma species onto surfaces exposed to the tokamak's discharges.

The concentration of deposited atoms is very low on the surface of Probe B which was exposed to the plasma in the presence of the toroidal ALT II limiter.Taking into account that other experimental conditions for both the probes were almost the same (see Introduction) one concludes that ALT II, even not actively pumped, very effectively reduces particle fluxes in the scrape-off layer of TEXTOR. Reduced fluxes are observed for all kinds of species but especially for metallic impurities. This result can lead to the suggestion that the limiter in use can be rather excluded as the main source of impurities in the machine.

In principle, probe technique allows to collect mainly ionized particles from the SOL. However, the results reported above stimulate to consider the contribution of neutrals to the deposition processes. The time-resolved plots for Probe B (Fig. 1 d-f) show the increase of the deposition rate of species in the final period of the discharge when plasma current is decaying. Moreover, such effects have been detected on other probes exposed under similar configuration of limiters. The increased deposition rate is noticed not only for impurities but also for deuterium atoms. This feature may indicate that the result observed is not caused by pre- or post-experimental artifacts (i.e. contamination) but is connected to the deposition of particles originating from the plasma. Our proposal is that the effect described is attributed to the deposition of excited neutrals onto the probe surface. Probably, neutrals always influence, to certain extent, the deposition phenomena investigated by means of collector probes. However, the contribution of neutral fluxes is small and can be noticed only on the probes which collected, due to the exposure conditions, relatively low amount of deposits.

The last problem to be considered here is connected to the values of C_O/C_D and C_O/C_{Me}. Oxygen concentrations are 5 or 10 times lower and 15 or 50 times higher (dependently on the probe) than the concentration of deuterium and metals, respectively. Such results cannot be simply explained by the formation of heavy water or metallic oxide molecules due to the reaction of atmospherical oxygen with deposits when the probe is exposed to air after the experiment. For a given probe concentration ratios are relatively stable indicating that the correlation between the amounts of respective species is not accidental but is influenced by processes responsible for the deposition of particle fluxes (containing also considerable amount of carbon) onto the collecting surface. These problems are dissused carefully elsewhere /4/.

The measurements performed prove the strong relation between conditions in the machine and deposition rate of particles onto the probe surface. Thus, the collector probes can be considered as an useful tool which sensitively reflects the behaviour of impurity and hydrogen isotope fluxes in the SOL.

4. REFERENCES

1. G. Staudenmaier, J. Vac. Sci. Technol. A3 (1985) 1091.
2. B. Emmoth, M. Braun, H.E. Sätherblom, P. Wienhold, J. Winter and F. Waelbroeck, J. Nucl. Mater. 128 & 129 (1984) 195.
3. H.E Sätherblom, M. Braun, B. Emmoth, T. Fried, J. Hilke, P.A.Holmström, F. Waelbroeck, P. Wienhold and J. Winter, Nucl. Instr. and Meth. A240 (1985) 171.
4. M. Rubel, B. Emmoth, H. Bergsåker, P. Wienhold, F. Waelbroeck and J. Winter, to be published.

---

*Permanent address: *Space Research Centre of the Polish Academy of Sciences, Ordona 21, Pl-01 237 Warszawa, Poland.*

INFLUENCE OF THE ALFVEN WAVE SPECTRUM ON THE SCRAPE-OFF LAYER OF THE TCA TOKAMAK.

Y. Martin, Ch. Hollenstein.

Centre de Recherches en Physique des Plasmas
Association Euratom - Confédération Suisse
Ecole Polytechnique Fédérale de Lausanne
CH-1007 Lausanne / Switzerland

Abstract The study of the Scrape-Off Layer (SOL) during Alfvén wave heating may lead to a better understanding of the antenna - plasma interaction. The SOL of the TCA tokamak has been widely investigated by means of Langmuir probes [1,2]. The aim of the present work is to present in detail the influence of the Alfvén wave spectrum on the SOL. The experiments have shown that the plasma boundary layer is strongly affected by the RF, in particular the ion density, the electron temperature and the floating potential. In TCA, as the spectrum evolves due to a density rise, the passage of the Alfvén continua and their associated eigenmodes (DAW) induces a strong depletion in the edge density of up to 70 % during the continuum part and a density increase during the crossing of an eigenmode. The floating potential becomes negative during the continua and even more negative crossing the eigenmodes. This behaviour changes as a function of the power transmitted to the plasma through the antennae, especially we have found with MHD modes a change around 100 kW. The profiles of the basic parameters are modified, depending on the wave spectrum. MHD mode activity which can occur during the RF phase considerably alters the behaviour mentioned above. Finally, the modulation of the RF power allows us to characterize the difference in coupling, for the continua and the eigenmodes, between the Alfvén wave field and the scrape-off layer.

INTRODUCTION The antennae for additional heating are always placed in the scrape-off layer of tokamaks. Thus, the plasma boundary strongly interacts with the wave field and, moreover, the behaviour of this boundary plasma could be connected with the efficiency of the wave heating. Therefore a good knowledge of the plasma boundary can help the understanding of the coupling between the wave and the core plasma. To analyse the scrape-off layer we used Langmuir probes which give information on its principal characteristics such as ion density, plasma potential and electron temperature. One aim of the TCA Tokamak being the study of the Alfvén Wave Heating (AWH), we present here the influence of the RF wave field on the scrape-off parameters.

EXPERIMENT The TCA is a medium sized tokamak with the following parameters: R = 0.61 m, a = 0.18 m, $B_\varphi \leq 1.5$ T. The working gas was H_2 or D_2 with currents of up to 130 kA, which gave a safety factor at the edge greater than 3.

The RF wave field is produced by eight groups of antennae regularly spaced around the torus, four on the top and four on the bottom, three centimeters away from the plasma.

The Langmuir probes are located in the outer equatorial midplane toroidally opposite to the limiter. The four probes can be moved radially in the plasma boundary. They are made of Molybdenum wire and measure 5 mm long and 0.5 mm diameter with 5 mm between them to form a square. Two of these serve to measure the ion density (absolute and

fluctuations) by the means of a current probe with a frequency bandwidth from DC to 50 MHz. Another gives the floating potential in a frequency range of DC to 20 MHz, and with the last one, swept from -130 V to 80 V in 1 ms, we can have a rapid calculation of the electron temperature.

RESULTS Using periodic cylindrical geometry to describe the toroidal plasma, the Alfvén wave can be excited with the following dispersion relation where ω is a function of the radius via the mass density and the safety factor:

$$\omega^2(r) = \left(\frac{1}{R_0}\right)^2 \left(n + m/q(r)\right)^2 \frac{B_0^2}{\mu_0\, \rho(r)} \left(1 - \frac{\omega^2}{\omega_{ci}^2}\right)$$

with n and m the toroidal and poloidal mode numbers. When a density rise occurs, according to the MHD theory, shear Alfvén waves (continua) are generated in the centre and move towards the edge. Besides that, we observe global eigenmodes (DAW) which are the low frequency counterpart of the ion cyclotron wave. These modes are superimposed on the continua and give the spectrum as shown in the previous papers on Alfvén waves in TCA [3]. In the scrape-off layer, the Alfvén wave field yields a strong perturbation in the ion density and in the floating potential. Firstly, when a shear Alfvén wave appears, the ion density decreases very rapidly and stays at this low level (down to 30 % of the Ohmic value) during all the presence of this mode (fig. 1). During this time, the floating potential decreases regularly and becomes very negative (-30 Volts). As a global mode enters the plasma, the density increases and reaches a value often higher than that of the Ohmic value. The floating potential becomes still more negative (up to -60 Volts).

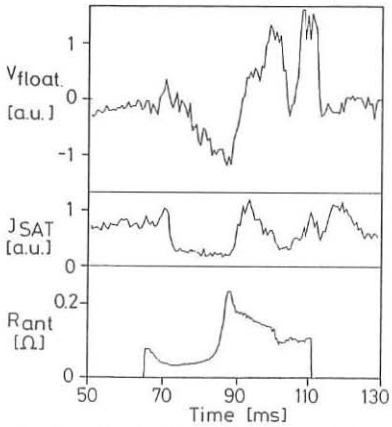

Fig. 1.

This behaviour is clearly seen in front of the antennae where the influence of the wave field is the strongest (fig 2). During the continua, in case of mode activity, the edge density rises. This explain the two curves on fig 2. Behind the antennae, which are also limiters in a way, the density is very low and the plasma interacts only slightly with the wave.

Looking more precisely on the loading curve, we can observe, just after the passage of a global mode, some small oscillations [4], which are also revealed with high sensitivity in our data.

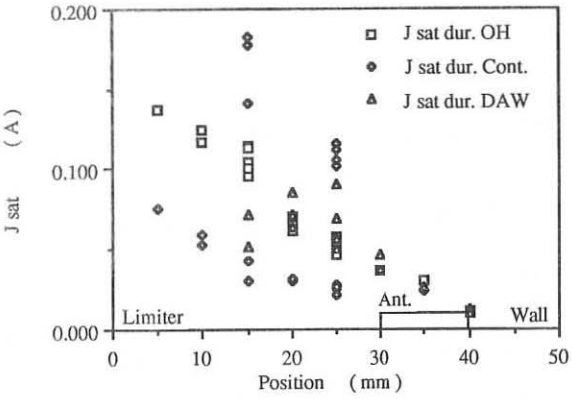

Fig. 2.

It is known that the presence of MHD mode activity usually increases the density in the scrape-off layer. In TCA we observe this phenomenon in Ohmic conditions. When Alfvén waves are injected, we find that, for an RF power greater than 100 kW, the mode activity is too strongly established so the decrease of the density does not occur, but the density goes up continuously. For smaller powers ($\leq$ 100 kW), the density decreases and the mode activity stops. In figure 3 we show the difference of the density taken at two times in the RF pulse as a function of the power delivered to the antennae.

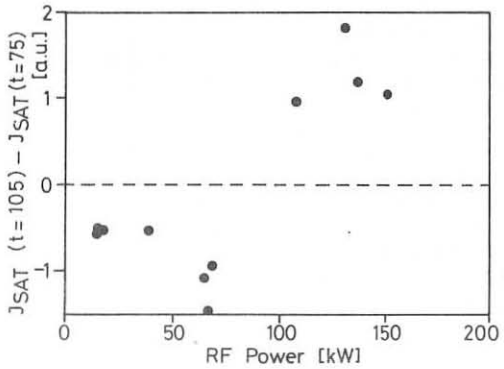

Fig. 3.

For the shots without any modes, we have shown the density and the floating potential as a function of the power delivered to the antennae (fig 4). The aim of this measurement was to verify a model which would explain the dependence of the loading on the RF power.

According to this model, the scrape-off layer, interacting with the local wave field of the antennae provides a sink for the direct dissipation of the antenna current [5]. When the RF power increases, the scrape-off layer is swept away and changes the antenna loading. The behaviour of the density agrees with this model. Our experiment however needs a more complete set of data on a wider range of power.

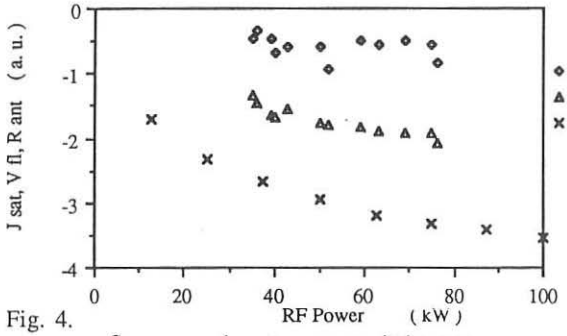

Fig. 4.

Some experiments were carried out on the tokamak to study the dynamic response of the plasma [6]. The RF power can be modulated. In this case, the modulation was fixed at 500 Hz and the peak to peak amplitude was almost twice the usual mean value. A calculation provides the gain and the phase of the transfer function from the input trace (RF power) to the output trace (J sat) as shown in the figure 5. We can see the difference of the gain between the continua and the discrete mode. This means that there is a strong interaction between the wave field and the scrape-off layer during the continua so we can say that a non-negligible part of the energy is deposited in the plasma boundary. When a global mode enters the plasma the coupling is more efficient with the bulk plasma and the energy is better deposited in the plasma core.

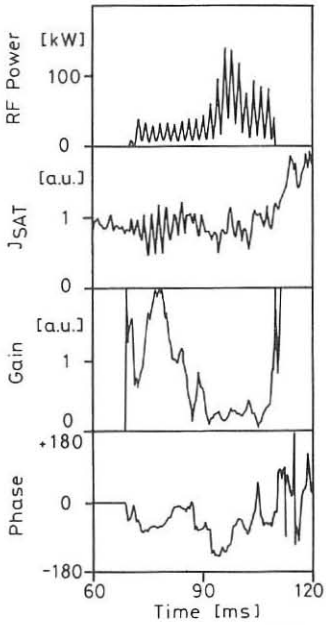

Fig. 5.

CONCLUSION All the measurements reveal a strong interaction between the wave field and the scrape-off layer. We show the difference of the behaviour of the plasma boundary especially when the spectrum of the wave field evolves. We find an important decrease of the edge density due to RF power deposited which could lead to a decrease of the impurity transport. The RF power seems to be more deposited in the plasma boundary during the continua. The boundary plasma density can be very strongly modified by the RF power, the modulation of the RF power and the mode activity.

ACKNOWLEDGEMENTS We wish to thank the whole TCA team for its excellent support. The present work was partially supported by the Fond National Suisse de la Recherche Scientifique.

REFERENCES [1] A. de Chambrier et al. J. Nucl. Mater. 128 & 129 (1984) 310.
[2] Ch. Hollenstein et al.: Proc XII EPS Conf. Contr. Fus. Plasma Phys. (Budapest 1985) vol. II p. 601.
[3] G. Besson et al. in: Plasma Phys.and Contr. Fus. (1986) Vol 28 no 9A p. 1291.
[4] K. Appert et al. in: Int. Conf. Plasma Phys. (Kiev 1987).
[5] G.A. Collins et al. Phys. Fluids 29 (7) July 1986 p. 2260.
[6] B. Joye et al. Dynamical plasma response to additionnal heating. Accepted for publication in Plasma Phys. and Contr. Fus. 1988.

THE FORMATION OF METHANE BY THE INTERACTION OF VERY LOW ENERGY HYDROGEN IONS WITH GRAPHITE

C.H.Wu*
J.W. Davis and A.A. Haasz**

*The NET Team, c/o Max-Planck Institut für Plasmaphysik
Boltzmannstraße 2, D-8046 Garching bei München

**Fusion Research Group, University of Toronto,
Institute of Aerospace Studies, Canada

ABSTRACT

The formation of hydrocarbon species by interactions of graphite with hydrogen leads to chemical erosion where the erosion yields are target temperature, flux density and particle energy dependent. Methane is one of the major volatile species in the H-C system. Therefore, the principal objective of the present study is the methane formation, particularly at H^+ energies lower than 100 eV, which will give useful information to assess the lifetime of graphite components in a fusion reactor.

The measurements were performed for graphite temperatures of 450 - 1000K, H^+ energies of 20 - 300 eV, and H^+ flux densities of $3x10^{13}$ to $3x10^{14}$ H^+/cm^2s. In general, the magnitude of peak methane yields decreases with decreasing particle energy at constant flux density. The temperature-dependent methane yield profiles are very pronounced for particle energies of >100 eV/H^+ at temperatures between 500 - 900K, whilst those for particle energies <100 eV/H^+ are much less sensitive to temperature. It is interesting to note that the temperatures of peak methane yields shift from 625K to 725K, when the particle energy varies from 20 to 100 eV. At particle energies of >100 eV, the temperature of peak methane yields remains almost constant.

INTRODUCTION

Graphite has been proposed as a first wall protection and divertor armour material for NET, because of its low Z and excellent mechanical and thermal properties. In addition, it has a low neutron absorption cross-section and retains its strength at high temperatures, which are particularly relevant to long pulse and high heat flux tokamaks, e.g. NET.

It has been recognized that erosion of graphite due to plasma contact will be one of the major limitations for using graphite as a plasma-facing material. The mechanisms responsible for this erosion include: physical sputtering, chemical erosion, radiation-enhanced sublimation and thermal sublimation. Each of these mechanisms dominates over a particular temperature range: (i) physical sputtering: T < 500 K; (ii) chemical

erosion: by hydrogen, 500 < T < 1200 K, and by oxygen, T ≥ 500 K, (iii) radiation-enhanced sublimation: T > 1300 K; (iv) thermal sublimation: T > 2300 K.

The formation of volatile species by interaction of hydrogen and oxygen with graphite leads to chemical erosion. The erosion yields have a strong dependence on target temperature, flux density and particle energy. Methane is the major volatile species in teh H-C system; therefore, the principal objective of the present work is to study the formation of methane due to H^+ interaction with graphite as a function of target temperature and particle energy, particularly in the very low ion energy regime.

EXPERIMENT

All experiments were performed in the University of Toronto UHV-accelerator facility, which is described elsewhere [1]. H^+_3 ions were produced by a high-flux, low-energy, mass-analyzed ion accelerator, and impacted on the sample at an angle of ~30°. The resulting beam spot was estimated to be ~0.2 cm^2. The beam intensity was measured on the sample, with the sample biased (to reduce secondary electron emission) to +5V for H^+_3 energies <300 eV, and +20V for H^+_3 energies ≥300 eV.

The sample was made of pyrolytic graphite, supplied by Union Carbide, in a strip of dimensions 50 mm x 6 mm x 0.2 mm. The sample was clamped at both ends by stainless steel jaws, and was heated resistively. Before and in between experiments, the sample was annealed by heating to ≥ 1500 K for several hours. The sample temperture was measured by optical pyrometry.

The methane produced by chemical sputtering was monitored in the residual gas, via the mass 16 signal, by a differentially pumped quadrupole mass spectrometer. The quadrupole was calibrated in situ using a know leak of CH_4, and was operated at a constant total pressure (mainly H_2) in order to maintain a constant conditioning of the ionizer region, and therefore a constant sensitivity to CH_4.

RESULTS AND DISCUSSION

The methane yields, Ch_4/H^+, as a function of graphite temperature are given in Fig. 1, for H^+ energies of 20 to 300 eV. In general, the magnitude of the peak methane yields, Y_m, decreases quite strongly with decreasing H^+ energy, and this trend is clearly shown in Fig. 2. (The two 100 eV cases in Figs. 1 and 2 correspond to different H^+ flux densities). The temperature-dependent methane yield profiles are quite pronounced for particle energies of > 100 eV/H^+ at temperatures between 500 and 900 K. For lower ion energies, the yield is less sensitive to the target temperatures. This broadening of temperature profiles has also been observed by other researchers, e.g. Ref.2.

It is interesting to note that the temperature of the peak methane yield, T_m, shifts from ~625 to 725 K when the ion energy varies from 20 to 300 eV/H^+, see Fig. 3. Also shown on this figure is the T_m value for CH_4 production due to sub-eV H^0 interaction with graphite [3,4]. The T_m values for the very low energy ions appear to be tending toward the value of T_m in the sub-eV H^0 bombardment case. The largest shift in the T_m value occurs for H^+ energies between 50 and 100 eV/H^+. It is found from Fig. 2 that this is also a region of strongly shifting Y_m values, and it is

noted from Fig. 1 that the activation energies (slopes of the temperature profiles) are changing as well. Previously, it has been shown (see Fig. 4 in Ref. 3) that the composition of hydrocarbon species produced, as shown by the ratio of CH_4 production to total hydrocarbon production, also changes in this energy regime.

It is expected that the observed changes result from a strong reduction in the nuclear energy deposited in the near-surface region of the graphite. For H^+ energies $\leq$ 100 eV, [5] there is a drop in the energy available for the breaking of C-C bonds in the graphite lattice, which is a requirement for the H^+-C chemical sputtering process [4].

CONCLUSIONS

While there is no clear threshold for chemical sputtering as a function of H^+ ion energy, it appears that there are changes in the dominating raction mechanisms for energies near and below ~100 eV/H^+. Four observable features all suggest this conclusion: (i) decreasing peak CH_4 yield, (ii) decreasing T_m value, (iii) decreasing activation energies, (iv) increasing importance of hydrocarbons other than methane [3].

ACKNOWLEDGEMENTS

This work was supported by the Natural Sciences and Engineering Research Council of Canada, and the Canadian Fusion Fuels Technology project.

REFERENCES

[1] J.W. Davis; Ph.D. Thesis, University of Toronto (1987).
[2] J. Roth; J. Nucl. Mater. 145-147 (1981), 87.
[3] J.W. Davis, A.A. Haasz and P.C. Stangeby; J. Nucl. Mater. 154-156 (1988) in press.
[4] A.A. Haasz and J.W. Davis; J. Chem. Phys. 85 (1986), 3293.
[5] J. Roth; in "Sputtering by Particle Bombardment II", Ed. R. Behrisch (Springer, Berlin, 1983).

Figure 1: Methane yield as a function of graphite temperature

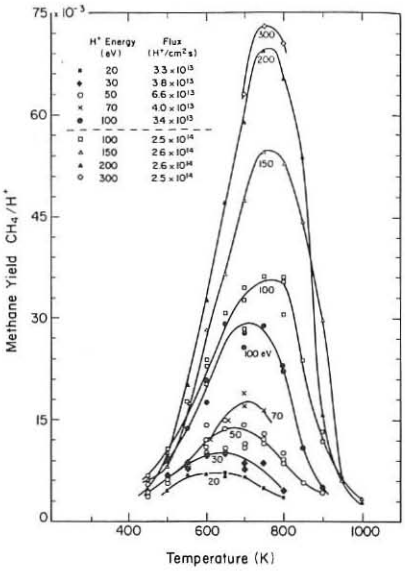

Figure 2: Methane yield at T_m as a function of H^+ ion energy.

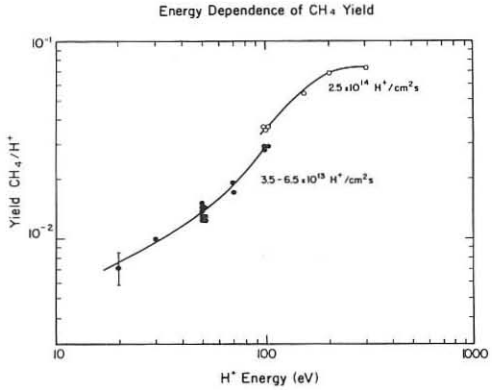

Figure 3: The change in the temperature for the maximum erosion yield, T_m, as a function of H^+ bombarding energy. The point at ~0.15 eV is for thermal H^0 bombardment of pyrolytic graphite [4].

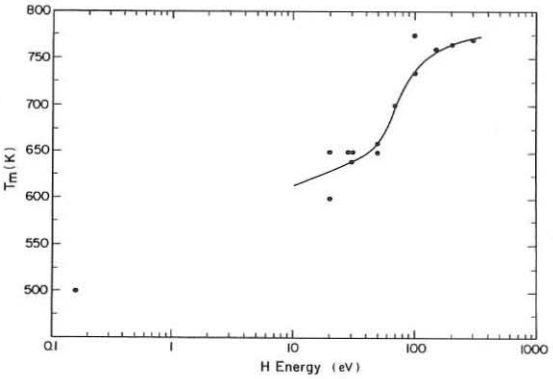

IMPURITY FLUX ONTO THE DIVERTOR PLATES OF ASDEX

A. P. Martinelli, E. Taglauer, and ASDEX Team

Max–Planck–Institut für Plasmaphysik, EURATOM Association,
D–8046 Garching, Federal Republic of Germany.

ABSTRACT

Fluxes of metallic impurities onto the divertor plates of ASDEX with different plasma parameters were collected and resolved in space and time by means of five carbon strips wound parallel on a cylindrical core rotating during the discharge.

Ion beam accelerator analysis (Rutheford Backscattering Spectroscopy (RBS), Proton Induced X-Ray Emission (PIXE)) of five carbon strips exposed to the plasma show a different distribution of the Fe and Cu atoms across the scrape-off layer (SOL). The Fe fluxes collected in the centre of the SOL are related to the Fe content in the central plasma; the Cu deposition has a maximum value close to the Cu divertor plates, indicating evaporation or sputtering from the plates.

INTRODUCTION

In earlier measurements prior to the "hardening" process, the Fe fluxes in the ASDEX divertor obtained by means of a collector probe were correlated with the Fe densities measured in the main discharge chamber by using a transport model [**1**]. First measurements with the collector probe differently positioned in the divertor of ASDEX after "hardening" are now reported and discussed, as a basis for establishing again a correlation between probe results in the divertor and plasma parameters in the main chamber, for the new ASDEX configuration after "hardening".

MEASUREMENT LAYOUT AND METHOD

The cross-section of ASDEX after "hardening", with the time-resolved collector probe positioned in the divertor chamber, is shown in Fig. 1. The collector probe is connected to the NNW window and consists essentially of a cylindrical head, which can be rotated by a stepping motor, and of a manipulator to insert the cylindrical head into the divertor chamber, and extract it.

The collector head consists of a set of five graphite (PAPYEX) strips wound parallel on a cylinder. During the plasma discharge the cylinder is rotated behind the fixed shield, which has five apertures, 4 mm in diameter, 14 mm apart, so that particle fluxes from the plasma can be collected. As a rule, the apertures are perpendicular to the toroidal magnetic field, so that only ionised particles are collected. The aperture diameter defines the local resolution and, together with the rotation speed, the time resolution (a few hundred ms).

After plasma exposure, the cylinder is withdrawn from the divertor chamber and the five strips are taken off and analysed for metallic impurities by PIXE and RBS

using a 2.5 MeV van de Graaf accelerator.

The measurement results show coverages (atoms/cm^2) on the strips between 1/10 of a monolayer (roughly the detection limit) and a few monolayers.

EXPERIMENTAL RESULTS

Figure 2 shows the Cu and Fe fluxes calculated from the measured coverages on strip 1 (1 cm from the Cu divertor plate), on strip 2 (2.4 cm from the Cu divertor plate), and so on, as a function of time during discharge no. 21007 (NI discharge).

The Cu flux attains a maximum value of $6 \cdot 10^{16}$ atoms/cm^2 s, a factor of 10 higher than the correspondent maximum Fe flux.

It is seen in Fig. 2 that after about 1.2 s both the Cu and Fe signals strongly drop. At the corresponding spot on the graphite strip one observes a surface-structure change. This change is a consequence of high-energy deposition during neutral beam injection; the deposited metallic impurities cannot be further observed.

Figure 3 shows the Cu and Fe deposits collected on strip 1, strip 2, and strip 3 (3.8 cm from the plate), as a function of the time during discharge no. 21861.

It is again seen that the Cu coverage (flux) is a factor of 10 larger than the Fe coverage (flux) on strip 1.

It is also observed that the coverage (flux) on strip 2 during NI is strongly reduced. Again, surface examination of the strip shows a substantial structure change. This indicates that strip 2 has reached a high temperature during the NI, higher than strip 1, which shows no surface alteration though closer to the divertor plate than strip 2.

This is explained by the position of strip 2 on the separatrix, where the energy deposition is maximal.

DISCUSSION

Further experimental results support the trend shown by the above reported results obtained with the collector probe in the ASDEX divertor after the "hardening" process. By way of discussion and preliminary conclusion the following can be stated:

- collected Cu and Fe fluxes are very different in value and show different radial dependences.
- collected Fe fluxes correlate with the Fe fluxes measured in the main plasma chamber and do not appear to be directly generated in the divertor chamber. The overall Fe outflux from the plasma can be determined by taking the values of the Fe fluxes over the width of the SOL in the divertor and integrating them over the circumference of the divertor and the four divertor sections (upper, lower, inner, outer). Overall Fe fluxes up to $5 \cdot 10^{18}\ s^{-1}$ are obtained.
- measured Cu fluxes close to the Cu divertor plates are a factor of up to 10 higher than the Fe fluxes; this indicates erosion of the divertor plates.

REFERENCES

[1] Taglauer, E., Nucl. Instr. and Meth. in Phys. Research B13 (1986)218-224

FIGURE CAPTIONS

Fig. 1. Schematic cross-section of the ASDEX Tokamak after "hardening" showing the position of the collector probe in the upper divertor chamber.

Fig. 2. Cu and Fe fluxes on strip 1 (1 cm from the divertor plate), strip 2 (2.4 cm), strip 3 (3.8 cm), strip 4 (5.2 cm) as function of the time in discharge no. 21007.

Fig. 3. Cu and Fe deposits (and fluxes) on strips 1, 2, 3 as functions of the time in discharge no. 21861. The upper part shows the discharge parameters I_p (plasma current), n_e (electron density), and NI (neutral beam injection).

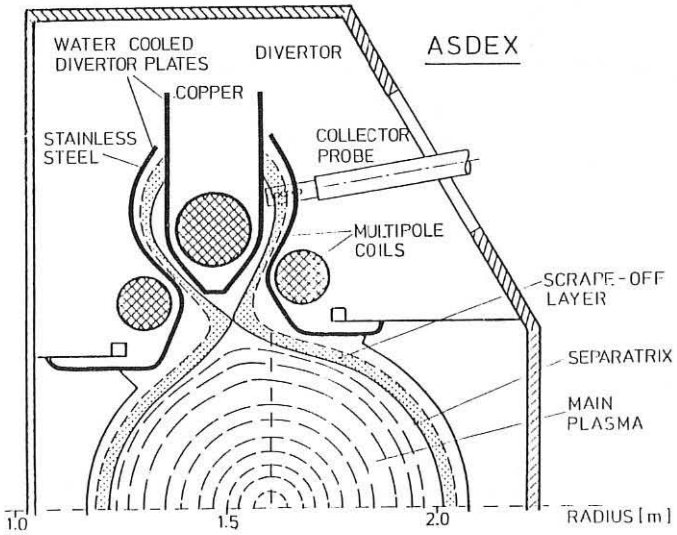

Fig. 1. Schematic cross-section of the ASDEX Tokamak after "hardening" showing the position of the collector probe in the upper divertor chamber.

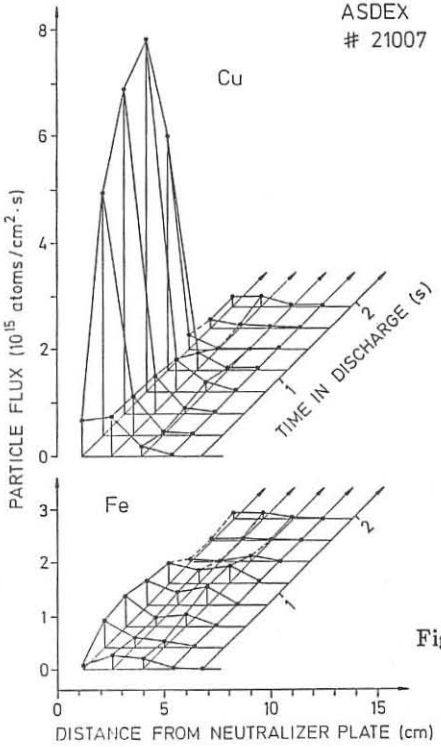

Fig. 2.

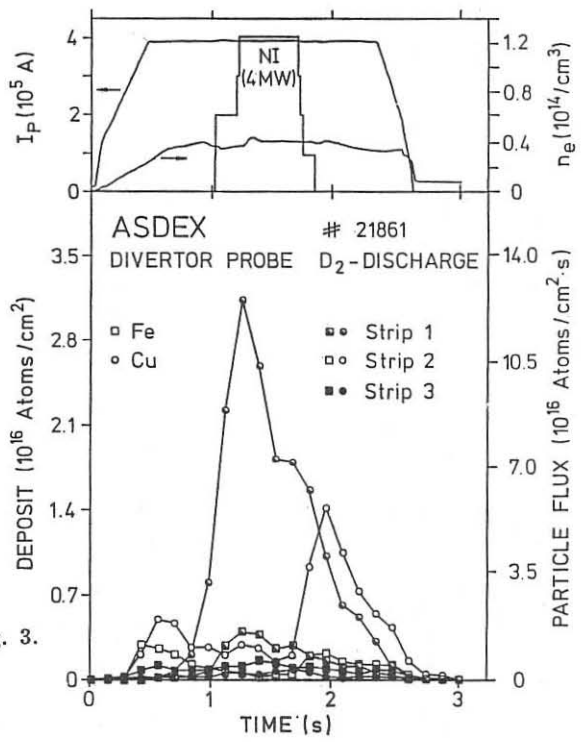

Fig. 3.

Fig. 2. Cu and Fe fluxes on strip 1 (1 cm from the divertor plate), strip 2 (2.4 cm), strip 3 (3.8 cm), strip 4 (5.2 cm) as function of the time in discharge no. 21007.

Fig. 3. Cu and Fe deposits (and fluxes) on strips 1, 2, 3 as functions of the time in discharge no. 21861. The upper part shows the discharge parameters I_p (plasma current), n_e (electron density), and NI (neutral beam injection).

STUDY OF EDGE ION THERMAL ASYMMETRIES IN THE TJ-I TOKAMAK

B. Zurro and TJ-I Group
Asociación EURATOM/CIEMAT. 28040 Madrid. Spain

INTRODUCTION

Some tokamak data suggest that particle and energy transport in tokamaks could be somehow poloidally asymmetric (1). In this paper, a new method which sheds some light on this problem, is being explored in the TJ-I tokamak. We contemplate the plasma edge as a place through which incoming and outcoming particles have to pass. By probing the edge ions using a method sensitive to their energy, it seems plausible to observe the preferential poloidal angles, if they exist, for particle outflux. The existence of boundary regions richer in hot ions should be revealed by studying the linewidth of some emission lines along different plasma chords.

It has been experimentally observed in tokamaks that highly ionized particles can reach the plasma edge (2), where they are accelerated by the sheath potencial producing surface sputtering. Line emissions of CVI and CV ions have been detected at the TJ-I plasma boundary and must be assigned to charge exchange recombination (CXR), because the low edge electron temperatures are insufficient to excite them. But with line integrated diagnostics, using spatially resolved measurements, it is not easy to separate this radiation from that due to electron excitation at the plasma core. For this reason, although the CXR radiation could provide direct information about the outflux asymmetries of central hot ions, it is not the most appropiated in the case of TJ-I.

On the other hand, states of ions with much lower charge can be populated by single or multiple charge exchange cascades. The width of lines from these intrinsic edge ions could reflect also these poloidal asymmetries. These processes have been recognized recently to play an important role on the radiated power balance at the plasma periphery (3).

EXPERIMENTAL

The measurents presented here have been performed in ohmically heated discharges of the TJ-I tokamak (R= 30 cm, a= 9.5 cm), operated with plasma currents of around 40 kA, toroidal field from 1 to 1.2 T and line average density of around 2 E 13 cm^{-3}. The hydrogen and impurity temperatures have been measured by scanning the lineshape of a selected line at a preprogrammed time of the discharge, using a 1 m monochromator provided with a rotating refractor plate. An optical system, using a set of three mirrors, forms a 90° rotated image of the input slit close to the tokamak window. One of them can be rotated, on a shot to shot basis, to perform the measurement along any selected plasma chord. In addition, it can be rotated at high velocity to obtain repetitive emission profiles during the 10 - 20 ms of the plasma life.

RESULTS

We have studied the Doppler linewidth of the following spectral features: H_β 4861 Å, CIII 2296 Å, 4647 Å and OII 4416 Å along different plasma chords using a set of good reproducible discharges. Results of these measurements are plotted in Figs. 1 to 4. The main feature common to all these scans is that the temperature reachs a maximun for chords passing around the magnetic axis, being smaller (by at least a factor 2) for chords going by the top and bottom plasma edges. The lower edge ion temperature deduced from all these lines is around 40 eV. For a fixed position the temperature increases almost linearly with the puffing level. The hydrogen temperatures were deduced from the H_β line wings; the maximum proton temperatures (80 - 90 eV) for this discharge is in good agreement with the that deduced from the charge exchange neutral spectrometer. Besides the edge thermal asymmetry already mentioned, the most remarkable feature observed is the different temperature found for CIII ions using two distinct spectral lines, unambigously assigned in the literature to this ion. This could be an experimental fact supporting the population of edge ions via CXR of outflux of central energetic ions. However, a more detailed study of the population of states in which these lines are originated must be carried out in the future to assess this interpretation.

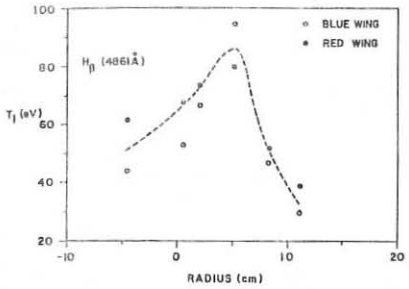

Fig. 1. Proton temperature profile deduced from the H_β line wings.

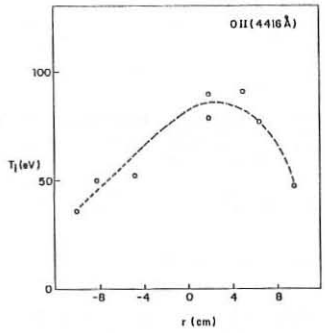

Fig. 2. Spatial variation of OII ion temperature measured by the 4416 Å line.

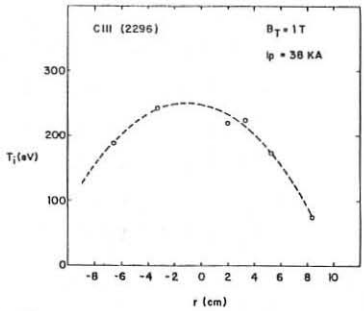

Fig. 3. Spatial variation of CIII ion temperature measured by the 2296 Å line.

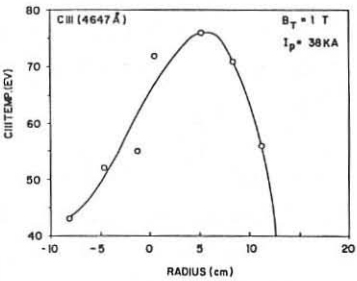

Fig. 4. Spatial variation of CIII ion temperature measured by the 4647 Å line.

In summary, edge ion thermal asymmetries have been observed in ohmically heated TJ-I plasmas, which could be due to asymmetric poloidal transport of particles. This transport must be more important for poloidal angles closer to the equatorial plane in order to account for these experimental results.

REFERENCES

(1) Terry J. L., Marmar E. S., Chen K. I. and Moos H. W., Phys. Rev. Lett. **39**, 1615 (1977).

(2) Voitsenya V. S., Solodovchenko S. I. and Tereshin V. I., Karkov Physico Technical Institute Report KhFTI **81 - 24** (1981).

(3) Abramov V. A. and Krotova G. I., Sov. J. Plasma Phys. **13**, 133 (1987).

BEHAVIOUR OF EDGE PLASMA UNDER ICRH IN TO-2 TOKAMAK

Artemenkov L.I., Vukolov K.Yu., Gott Yu.V., Gurov A.A.
Kovan I.A., Monakhov I.A., Mukhin P.A., Papkov L.N.,
Schwindt N.N., Yusupov K.Kh.
I.V.Kurchatov Institute of Atomic Energy, Moscow, USSR

SUMMARY

The behaviour of edge plasma under ICRH at a fundamental harmonic of hydrogen ions in operation with and without divertor was experimentally studied on the TO-2 tokamar.Radial and temporal plasma density, n_i, and electron temperature,T_e, dependences in a scrape-off-layer were registered with a five-lamella probe.The RF-power launch in both regimes was accompanied by a rise in n_i and by a weak reduction in T_e. A correlation between the behaviour of edge plasma density and fast ion fluxes emerging under ICRH was noticed. A phenomenon of edge plasma pumping-out was observed under weak recycling after switching the RF-generator "on".

A strong damping of fast magnetosonic waves and an effective plasma heating at a fundamental cyclotron frequency of hydrogen ions was registered in the ICRH experiments on the TO-2 tokamak.The heating was observed in pure hydrogen plasma [1] P_{RF}=100 kW, $\Delta T_i = \Delta T_e \simeq 100$ eV, $n_e = 2.10^{13} cm^{-3}$, and in a 50% D-H mixture [2] : P_{RF} = 150 kW, $\Delta T_i = \Delta T_e$ = 200 eV, $\tilde{n}_e = 2.10^{13}$ cm^{-3}. A set of obtained data, however, does not allow one to explain the mechanism of heating. In this connection, the study of the edge effects accompanying the heating and,in particular, an estimate of the role of Alfven resonance, localization of which under given conditions is at the plasma column periphery, are of a great interest.

The studies were done in a purely-hydrogen plasma in both regimes: with a magnetic divertor configuration (separatrix radius, a_s = 13.5-14.0 cm) and with a limiter, its role was performed by the ICRH - antenna (a =14.5 cm). The typical pa-

rameters of an Ohmic stage of the discharge are: I_p=30 kA, $V_p \simeq$2V, B_o=1.2T, n_e=1.5 $10^{13}cm^{-3}$, T_{io}=100 eV, T_{eo}=200 eV. The power launched into the plasma was P_{RF}=150 kW at f=18.3 MHz in the regime with a divertor and P_{RF}=100 kW in the divertor - free regime. A rectangular RF-pulse, 5-10 ms long, was used. An antenna with double elutrostatic screen and with protective graphite covering was located at a low toroidal field side. The antenna included a number of elements preventing a direct excitation of surface waves.

The edge plasma parameters were registered with a movable five-lamella probe. A constant bias at the lamellas (from zero up to - 48 V) provided the probe signals corresponding to five points on a volt-ampere dependence and an opportunity to measure the electron temperature, T_e, and the proton density during the discharge [3] . The probe was located in a cross-section shifted respective to the antenna in a toroidal direction at an angle 120° , and it could be translated along the major radius of the torus.

A spatial (Figs. 1,2) and temporal (Fig.3) behaviour of the edge plasma parameters is shown. One can see that an increment in the plasma density and some decrease in the electron temperature take place after switching the RF-generator "on". Both processes are more pronounced in the regime with a limiter. The power deposition into the plasma had a multimode nature dependent on density at a low plasma quality factor, $Q \simeq$30-50. A correlation among the behaviour of an RF-field of fast magnetosonic waves, the flux of fast atoms escaping from the plasma column and the plasma edge density was observed.A characteristic length of n_i-decay under ICRH was increased in both regimes. The divertor magnetic configuration was characterized, as a whole, by lower densities and by higher T_e under Ohmic heating and under ICRH as well. The dependence of T_e on the radius was rather weakly pronounced. It is interesting to note that differences in n_i and in T_e, obtained under OH and under ICRH, are reduced with the motion of the probe into the pla-

sma interiour.

As it has been noted, the RF-power input is accompanied by some reduction in the T_e that is probably related with a cooling of the plasma periphery due to an entry of impurities, the content of which under ICRH is increased by sputtering of the chamber walls and by that of the antenna with fast particles. A reduction in T_e also confirm the absence of periphery power deposition under ICRH in TO-2.

A phenomenon of "pumping-out" the edge plasma after switching the RF-generator "on" in the regimes with low recycling (Fig.4) was registered. This effect discussed previously (see, e.g. [4]) is probably related with the edge plasma polarization by an electrostatic potential of the RF-antenna. It can play an important negative role under ICRH, increasing an opaque zone for a fast magnetosonic wave and deteriorating the antenna - plasma coupling. A given phenomenon of "pumping out", as a rule, is masked by enhanced recycling under ICRH. Therefore it was clearly observed under the conditions when the chamber walls were carefully degassed and the fluxes of fast particles, emerging in the process of exciting fast magnetosonic modes in the plasma, were absent (compare Fig.3, with Fig.4).

REFERENCES

[1] Artemenkov L.I. et al. Proc. X-th Conf. on Pl.Sci. and Contr.Nucl.Fus.Research, London, vol. I, p. 615.

[2] Artemenkoc L.I. et al. Fizika Plasmy, v.14, No. 5, 1988.

[3] Artemenkov L.I. et al. USSR Contribution on 10-th sess. of Phase II-A (part 2) of the INTOR workshop, Vienna, October 1984, p. 116.

[4] Gugorieva L.I. et al. Preprint Kharkov Phys. Tech. Institute, N 13, 1986.

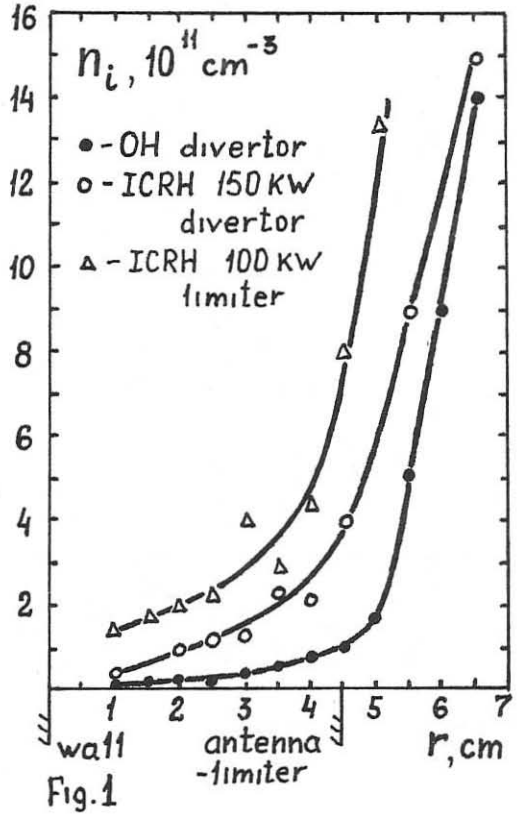
n_i, 10^{11} cm^{-3}
● - OH divertor
○ - ICRH 150 KW divertor
△ - ICRH 100 KW limiter
16
14
12
10
8
6
4
2
1 2 3 4 5 6 7
wall
antenna -limiter
r, cm

Fig.1

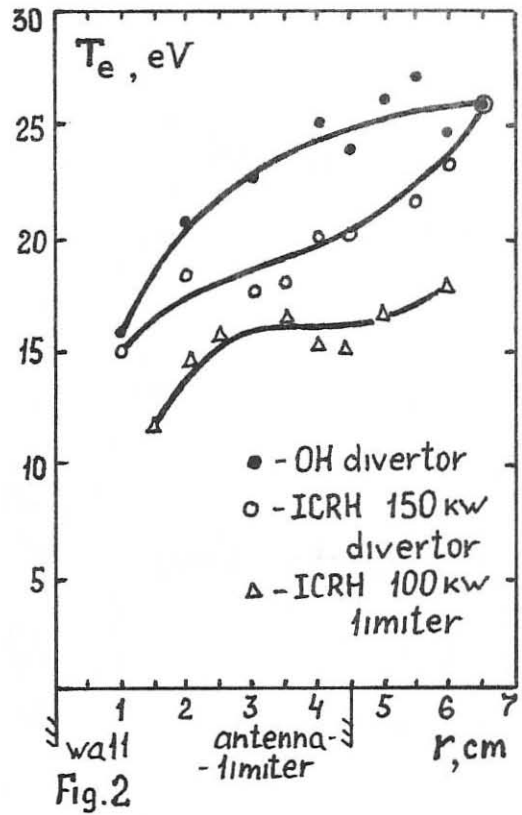
T_e, eV
30
25
20
15
10
5
● - OH divertor
○ - ICRH 150 KW divertor
△ - ICRH 100 KW limiter
1 2 3 4 5 6 7
wall
antenna - limiter
r, cm

Fig.2

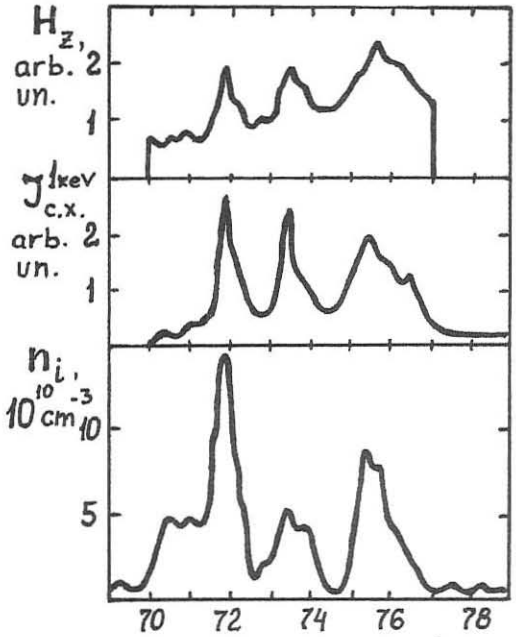
H_z, arb. un.
2
1
$J^{1keV}_{c.x.}$ arb. un.
2
1
n_i, 10^{10} cm^{-3}
10
5
70
72
74
76
78
t, ms

Fig.3

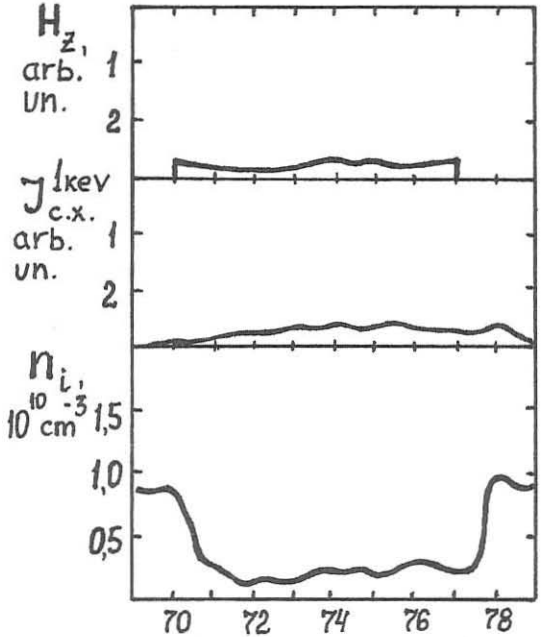
H_z, arb. un.
1
2
$J^{1keV}_{c.x.}$ arb. un.
1
2
n_i, 10^{10} cm^{-3}
1,5
1,0
0,5
70
72
74
76
78
t, ms

Fig.4

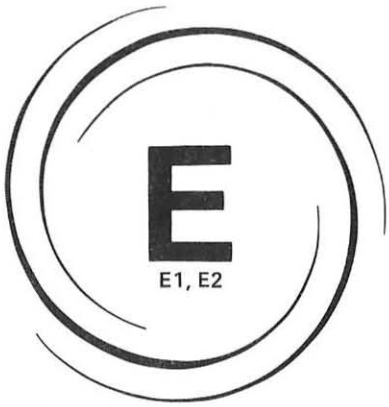

RF Heating

PREDICTIONS FOR ICRF POWER DEPOSITION IN JET AND MODULATION EXPERIMENTS DURING SAWTOOTH-FREE PERIODS

F. Tibone, M.P. Evrard[1], V. Bhatnagar, D.J. Campbell, J.G. Cordey, W. Core, L-G. Eriksson[2], J.C.M. de Haas[3], H. Hamnén[2], T. Hellsten, J. Jacquinot, S. Knowlton, R. Koch[1], H. Lean[4], F. Rimini, D. Roberts[5], D.F.H. Start, P.R. Thomas, K. Thomsen, D. Van Eester[1]

JET Joint Undertaking, Abingdon, Oxon., OX14 3EA, UK.
[1]LPP-ERM/KMS, Brussels, Belgium.
[2]Chalmers University of Technology, Göteborg, Sweden.
[3]FOM, "Rijnhuizen", Netherlands.
[4]Culham Laboratory, Abingdon, Oxon. OX14 3DB, UK.
[5]Princeton Plasma Physics Laboratory, New Jersey, USA.

Theoretical Predictions. Various computational tools are available at JET for prediction of ICRF power deposition profiles: these include the global wave codes LION and ALCYON [1,2], a ray-tracing code [3] and a simplified model [4] based on a parametrization of full wave code results. These codes can properly describe fundamental minority and 2nd harmonic majority heating, and direct electron heating due to transit time damping; the redistribution of power from the minority energetic ions to the background plasma is computed by solving the relevant Fokker-Planck equation. No satisfactory model is available for local electron heating due to mode conversion (experimentally observed in some of JET scenarios, see below).

Fig.1 shows a representative example of comparison between results from full wave and ray-tracing codes. They refer to on-axis minority heating of H in a D plasma, with strong single pass absorption. There is good agreement on the fractional power absorbed by the various species, and both codes predict strongly peaked deposition profiles. The local power density in the center is typically twice as high for the ray-tracing as for the global wave code; however, this figure is sensitive to the local geometry assumptions (volume effects) and to small uncertainties in the exact cyclotron resonance location related to magnetic field corrections. While this implies that we cannot rely on predictions in the vicinity of the magnetic axis, the integrated power absorbed within $r \sim (0.3\text{-}0.4)a$, i.e. the sawtooth region, is nearly the same for the two codes and is consistent with the experiment. The power deposition for cyclotron absorption predicted by the two codes differs more for heating scenarios with weak absorption, for which full wave calculations yield less peaked profiles.

Narrow deposition profiles are also predicted by all codes for JET off-axis heating, with the resonance position as far out as $r \sim 0.6a$.

The assumption on the minority spatial distribution in the plasma is a major source of uncertainty for all predictions. Only sparse evidence is available on the total number of minority ions in each experiment, and it

is even difficult to assess the uncertainty of this datum. The minority radial density profile is arbitrarily assumed to be either uniform, or of the same shape as the measured electron density profile. 50% variations in the assumed minority concentration near the cyclotron resonance can yield changes of the same order in the computed local deposition. A similar variation in the overall minority concentration can also affect significantly (20-30%) the power distribution to the different species.

Modulation Experiments During Monster Sawteeth. Since the upgrade of the JET ICRF power system to 8 generators/24MW, it has been possible to launch into the plasma very highly modulated RF pulses with ΔP up to $\pm$ 2.5MW, superimposed on an average power in the range 5-10MW. The simultaneous disappearance of sawteeth at these levels of RF power has allowed us to obtain much clearer experimental data than in previous experiments [5].

Figure 2 refers to one of the most recent results: a square wave modulated RF power of 7.2±1.6MW at 4Hz was launched into a deuterium plasma with ^{3}He minority, yielding a ΔT_{eo} of more than ±200eV, in phase with the RF power.

A fast-Fourier-transform-based analysis [5] shows that the T_e-response is still visible at 12Hz, the first harmonic present in a square wave. This supports the idea that direct electron heating is the largest contributor to the observed T_e modulation. Indeed, the transmission of power through the minority acts as a supplementary integrator, decreasing the amplitude of the response by a factor $\omega\tau_s \sim 4.5$ in the 4Hz case (ω = modulation frequency, τ_s = fast ion slowing-down time). Thus, even if only 30% of the total power was directly absorbed by electrons, this effect would dominate the picture.

Information on the ratio between direct and indirect bulk plasma heating can be obtained by analyzing the effect of modulation on the plasma energy content W. This effect is clearly visible on both magnetic measurements available at JET, W_{dia} from diamagnetic loop (W_{dia}= 3/2 $W_\perp$, including the non-thermal component) and W_{mhd} from mhd equilibrium calculations (W_{mhd}= 3/2 $W_\parallel$+3/4 $W_\perp$). Fourier analysis yields for this case ΔW_{mhd}= 42kJ and ΔW_{dia}= 56kJ, corresponding to $\Delta W_\perp$ = 38kJ, $\Delta W_\parallel$ = 9kJ and ΔW(anisotropic) = 20kJ. Thus we estimate that only 40% of the RF power results in the creation of an anisotropy in the velocity distribution of the minority. However, it should be stressed that this deduction is particularly sensitive to uncertainties in W_{dia} and W_{mhd}, and requires further confirmation.

In order to compare the modulation experiments with theory, we turn now to a case of H minority heating in ^{3}He, where the effect of direct electron heating is expected to be low. Fig.3 presents both amplitude and phase of $\Delta T_e(r)$ resulting from Fourier analysis, corrected for the modulation of the magnetic axis shift, responsible for up to 400eV in ΔT_e in the gradient zone.

Of the total modulated RF power (ΔP = 1.7MW), 80% is seen in the modulation of the energy content. Plasma energy modulation amounts to ΔW_{mhd}= 34kJ and ΔW_{dia} = 62kJ, corresponding to $\Delta W_\perp$ = 41kJ, $\Delta W_\parallel$ = 2kJ and ΔW (anisotropic) = 37kJ. This means that 85% of the power goes to produce an anisotropic minority population. Considering that part of the remaining power will be absorbed by bulk minority ions, we conclude that direct electron heating is indeed a minor effect in this experiment.

The T_e-response has been simulated using a diffusion equation for the electron energy in cylindrical geometry, with radially constant heat

diffusivity. The assumed power deposition profile on the minority (a Gaussian with width 20cm) closely resembles those predicted by the various codes. The modulated component of the Ohmic power input has been found to be negligible, and non diffusive energy losses have been neglected. The model also allows for a small component of direct heating to be taken into account. A good agreement is found (see Fig.3a and 3b) assuming $\chi_e(0)$ = 2-4m²/s and a small amount of direct electron heating (5-10%). This value of χ_e near the plasma center is consistent with the local power balance, and is as large as that previously measured in the outer plasma using the heat pulse propagation technique [6].

Conclusions. Predictive calculations of ICRF power deposition profiles in JET using various numerical tools yield a consistent picture, in qualitative agreement with experimental evidence. Quantitatively the agreement is satisfactory, but the codes tend to overestimate the power density near the plasma center, and cannot describe situations where direct electron heating via mode conversion is important. Poor knowledge of the minority distribution in the plasma can cause a significant uncertainty in the predicted deposition profiles.

RF power modulation experiments have been successfully attempted during "monster sawteeth", without destabilizing the sawtooth-free discharge. We have presented a D(^{3}He) case where significant direct electron heating has been observed, and the measured T_e-response profile is dominated by this effect. Such a scenario is outside the boundaries of applicability of our theoretical models.

We have also shown results for a ^{3}He(H) plasma, where minority heating is clearly dominant. Theoretical predictions for power deposition can reproduce the observed amplitude and phase of $\Delta T_e(r)$ if an electron thermal conductivity χ_e = (2-4)m²/s is assumed in the central plasma region.

References

[1] L. Villard et al., Comp. Phys. Reports 4 (1986) 95.
[2] D.J. Gambier, A. Samain, Nucl. Fus. 25 (1985) 283.
[3] V.P. Bhatnagar, R. Koch et al., Nucl. Fus. 24 91984) 955.
[4] T. Hellsten, L. Villard, Proc. 14th European Conf. on Contr. Fusion and Plasma Heating, Madrid (1987), Vol.11D, Part III, p.1000.
[5] V.P. Bhatnagar et al., Proc. 12th European Conf. on Contr. Fusion and Plasma Heating, Schliersee (1986), Vol.10C, Part II, P.193.
[6] B.J. Tubbing, N.J. Lopes Cardozo, M.J. Van der Wiel, Nucl. Fus. 27 (1987) 1843.

Fig.1 Predictions from ray-tracing (solid) and global wave code LION (dashed lines) for H minority heating in a deuterium JET plasma. Due to the high temperature and toroidal mode number, mode conversion is negligible for this scenario.

Fig.2 Electron temperature traces at different radii (from the ECE polychromator) for a modulation experiment in a deuterium plasma with ^{3}He minority. RF power modulation at 4Hz; $\langle P_{RF}\rangle$=7.2MW, ΔP=±1.6MW. I_p=2MA, B_T=3.4T, n_{e0}=4.3×10^{19}m^{-3}, T_{e0}=7keV. ρ is a normalized flux coordinate.

Fig.3 Amplitude (a) and phase (b) of the T_e response versus major radius, corrected for the modulation of the magnetic axis shift. ^{3}He(H) plasma with I_p=2MA, B_T=2.1T, modulation at 5Hz, $\langle P_{RF}\rangle$=5MW, ΔP=±1.7MW. The solid lines are the result of the model as defined in the text.

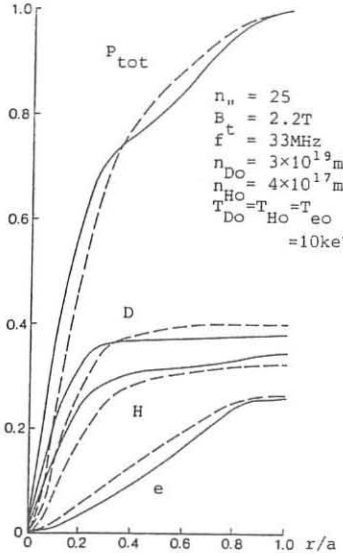

Fig. 1

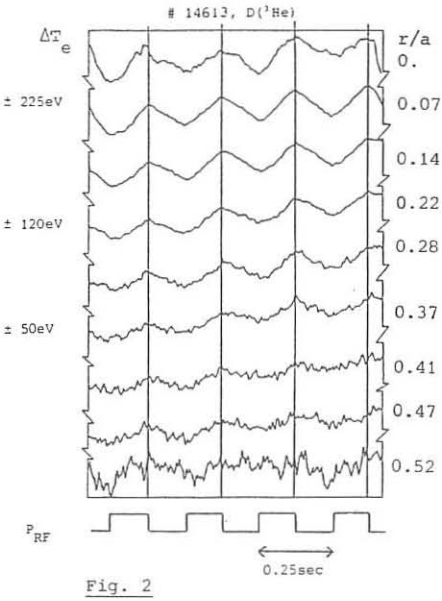

Fig. 2

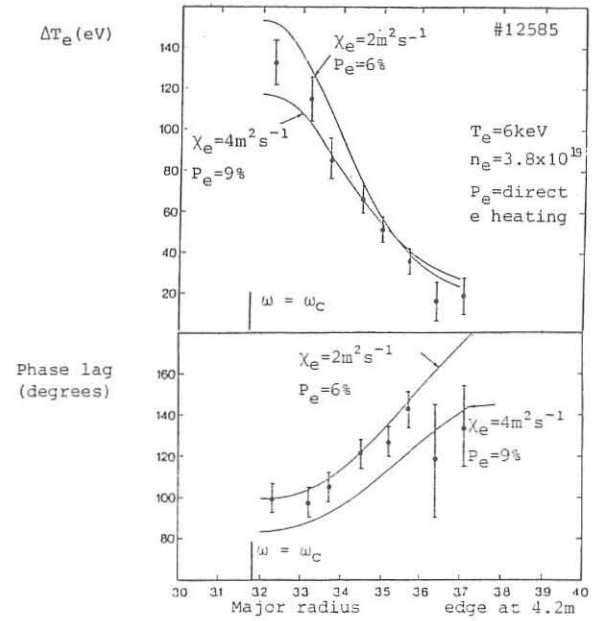

Fig. 3a

Fig. 3b

ROLE OF ANTENNA SCREEN ANGLE DURING ICRF HEATING EXPERIMENTS IN JET

M Bures, V Bhatnagar, S Corti, G Devillers[1], B Denne, M Forest[2], T Hellsten, J Jacquinot, D Start

JET Joint Undertaking, Abingdon, Oxfordshire, OX14 3EA, England

[1] Attached from University of Grenoble, France
[2] EURATOM/UKAEA Association, Culham Laboratory

Introduction

To eliminate the excitation of the $\tilde{E}_{\parallel}$ component of RF field, the screen elements of JET antennae were installed at an angle of 15° with respect to the toroidal field. This implies that the elements are aligned with the magnetic field during the discharges with B_ϕ = 3.4 T and I_p = 5 MA for which the design was optimised. To test the effects of the magnetic field line direction at the plasma edge with respect to the antenna screen elements, some RF heating experiments were carried out with a reversed direction of toroidal field. Experiments were performed with the same target plasma conditions B_ϕ = 2.1 T, I_p = 2 MA, ^{3}He(H) heating scenario and density $\langle n \rangle = 1.7 - 1.8 \times 10^{19}$ m^{-3}. The antennae were phased as monopoles with $K_{\parallel}$ spectrum peaked at $K_{\parallel} = 0$ m^{-1}. A few discharges in the reversed field condition were run at somewhat higher field B_ϕ = 2.25 T.

Coupling Resistance and the Plasma Edge Parameters

In the reversed field case the coupling resistance R_c is typically 30 % lower as plotted in Fig 1. Also the time evolution is different. In the normal case, the coupling resistance is strongly modulated by the radial eigenmodes of the magneto-acoustic (MA) wave. Eigenmodes result from the density increase caused by the RF enhanced neutral gas and impurity influx. In the reversed field case, the eigenmode activity is less evident, despite the density increase as a function of power being the same. The plasma edge density and temperature were measured by the Langmuir probes placed in the protection tile of the RF antenna. There is evidence that the average value (integrated over the RF pulse) of density in front of the antenna screen increases from 2 x 10^{18} m^{-3} to 4 x 10^{18} m-3 in both cases. Also temperature increases from 15 eV to 50 eV in the normal case. The measurements suggest that in the reversed field case, the temperature profile flattens and the increase of temperature in front of screen is lower.

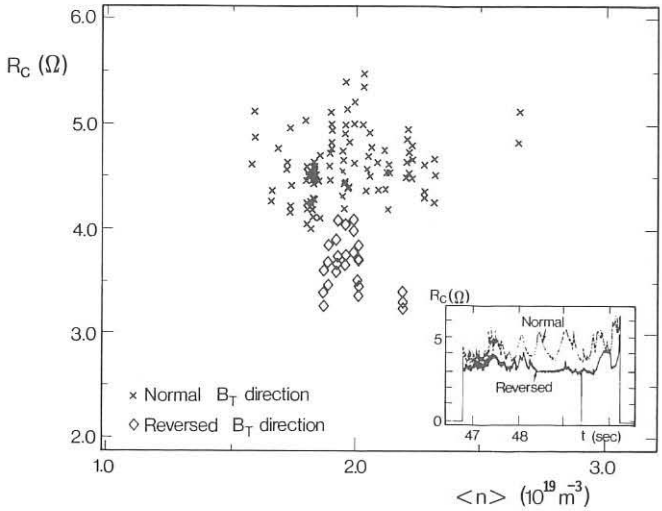

Fig 1: The coupling resistance as a function of average density. In the inset is plotted its time evolution.

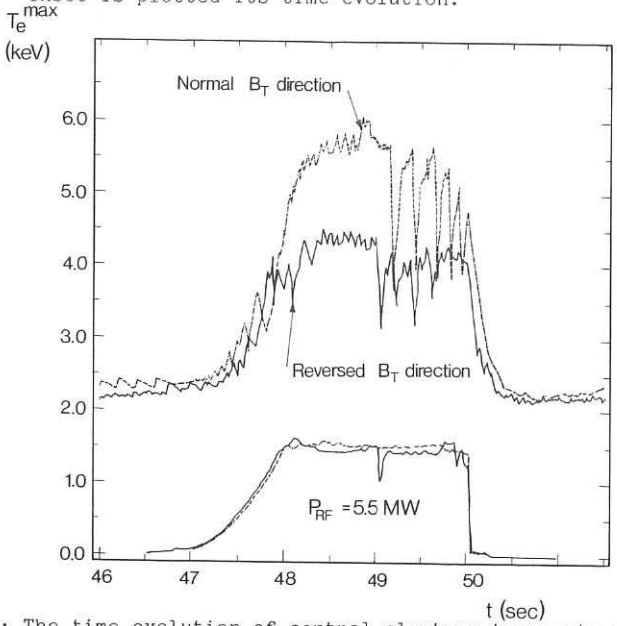

Fig 2: The time evolution of central electron temperature together with the trace of total RF power.

Heating Efficiency

In both cases the minority cyclotron layer was placed in the centre of the plasma. A number of significant differences in heating efficiency was observed. In the reversed field case:

a) The rate of increase of $T_e(0)$ and $< T_e >$ with $P_{RF}/< n >$ was 30 % lower. The example of $T_e(0)$ time evolution is plotted in Fig 2. "Monster" sawtooth phenomenon should be noticed.

b) The energy increase as a function of applied power can be characterised by the incremental confinement time $\tau_{INC} = \Delta W/(P_{RF} - \Delta P\Omega) = 0.16$ sec which is lower by 30 % than in the normal case (Fig 3). The plasma stored energy is derived from the electron temperature profile, ion temperature of plasma centre, density profile and Zeff. The same difference of 30 % is obtained from magnetic measurement.

c) The ion temperature increase measured by x-ray spectroscopy indicates no substantial difference in ion heating. Electron temperature profile does not show any particular feature in either case. Also the neutral hydrogen spectrum does not indicate any substantial difference in formation of an energetic hydrogen minority tail. The deuterium fast tail is starting to form due to the second harmonic minority heating in both cases.

Neutral and Impurtiy Influxes

When the RF power is applied, the density increases. The radiation power increases roughly linearly with density but somewhat faster in the reversed field case. The ratio P_{rad}/P_{TOT} versus P_{TOT} is plotted in Fig 4. The higher radiated fraction can be correlated to the enhanced

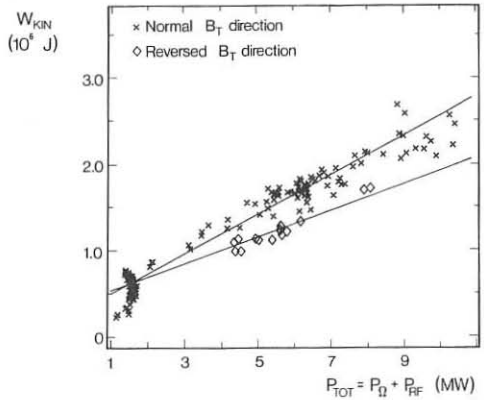

Fig 3: Plasma stored energy as a function of total power input

influx of metals, mainly the nickel. In Fig 5 the intensity of NiXXV line normalised to density is plotted versus the power input. It represents the number of nickel ions along the line of sight. Also the intensities of oxygen OV and carbon CIV lines differ in the 2 cases. Intensity of the oxygen line is higher roughly by factor 2 in the reversed field case, while the CIV intensity is lower. This might be correlated to lower deuterium influxes as measured by D_α emission recorded along the line of sight intercepting the limiters. No difference is observed monitoring the HeI line.

Conclusions

A clear difference in the impurity influxes as well as the heating efficiency was observed between the discharges with normal and reversed direction of the toroidal field. Also, the coupling resistance differs substantially. The results indicate that the coupling to MA wave respectively to slow wave is different in the 2 cases. The parallel component of the RF electric field is minimised when the screen elements are aligned along the magnetic field.

Acknowledgements

We wish to thank our colleagues in the JET team, especially the tokamak operating teams and those operating the diagnostics used in the experiments reported in this paper.

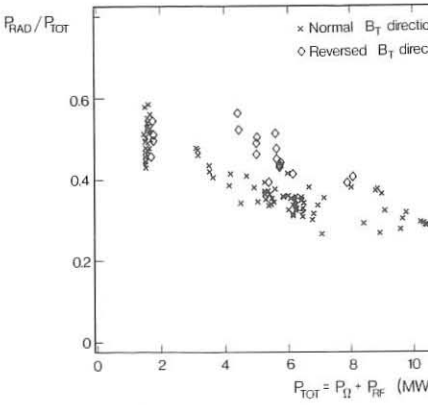

Fig 4: Fraction of radiated power as a function of total power input

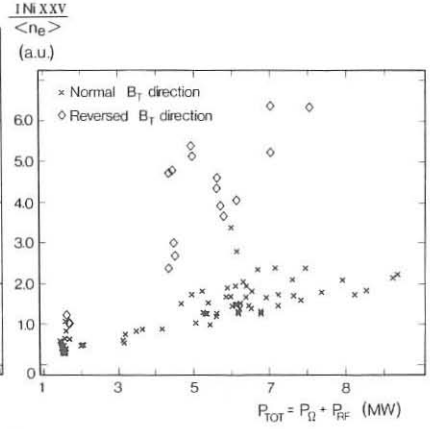

Fig 5: Measure of nickel ion density as a function of total power

IDENTIFICATION OF RADIAL AND TOROIDAL EIGENMODES IN THE COUPLING OF THE WELL DEFINED $k_{\parallel}$ SPECTRUM OF THE NEW JET ICRH ANTENNAS

A L McCarthy[1], V P Bhatnagar, M Bures, P L Colestock[2], M P Evrard[3], J M Gahl[4], T Hellsten, J Jacquinot, S Knowlton[5], D F H Start

JET Joint Undertaking, Abingdon, Oxfordshire, OX14 3EA, England

[1] Flinders University, Bedford Park 5042, South Australia
[2] Princeton Plasma Physics Laboratory, New Jersey, USA
[3] LPP-ERM/KMS; EUR-EB Association, 1040 Brussels, Belgium
[4] Texas Technical University, Lubbock, Texas 79409, USA
[5] Massachusetts Institute of Technology, Cambridge, Mass 02139, USA

Introduction

JET discharges heated with the new, wider antennas whose currents have a particularly well defined Fourier transform in $k_{\parallel}$, show a series of peaks in the coupling resistance when the monopole phasing is used. These peaks which we shall see to be characteristic of the excitation of eigenmodes [1,2] are particularly clearly seen in Fig 1a for which the magnetic field was ramped, and in Fig 2 in which the plasma density evolved linearly. In the monopole phasing the excited spectrum is peaked at $k_{\parallel} = 0\ m^{-1}$ and has half width $4\ m^{-1}$. For the dipole phasing, the maximum power is radiated at $k_{\parallel} = 7\ m^{-1}$ and the strength is zero at $k_{\parallel} = 0\ m^{-1}$. In the dipole configuration, variations of the coupling resistance are very much reduced, see Fig 1b.

By comparing predictions of a slab model with the analysis of the data for the spacings of the onset of these peaks, we make the first detailed and unambiguous identification of radial eigenmodes which are excited when low toroidal mode number fast waves are resonantly reflected between the ion-ion-hybrid cut-off layer and the antenna. We have developed an understanding of the asymmetry of the peaks in coupling resistance; we have modelled the peak-to-valley ratios for the coupling resistance; and we have shown why the variations of coupling resistance are very much reduced when the dipole phasing is used. Further, we have examined the data to gauge the effects of eigenmode excitation during high power ICRH heating.

The Slab Model

The plasma is treated as a slab between the antenna and the ion-ion-hybrid cut-off layer, having thickness d. In JET the poloidal length of the antenna is large compared to the width L_o, and we assume $k_y = 0$. All poloidal variations (y) are neglected.

The fast wave dispersion relation: $k_x^2 = k_o^2 S - k_z^2 - \dfrac{k_o^4 D^2}{k_o^2 S - k_z^2}$

applied to the slab can be considered in a manner analogous to that used by Stix [3] to identify and track the eigenmodes of the system; k_x, k_z and k_o refer to radial, toroidal and free space propagation. S and D are the usual sum and difference terms of the dielectric tensor.

The electric field at the antenna placed just outside the fast wave cut off layer is the sum of the incident wave E_y from the antenna, plus the multiply reflected waves, attenuated by α and phase shifted by β each transit around and across the toroidal slab to give:

$$E_{y\ \text{antenna}} = E_y \frac{1 + e^{-\alpha + i\beta}}{1 - e^{-\alpha + i\beta}}$$

In the full computation the attentuation α is determined by a mode conversion algorithm (Colestock and Kashuba [4]) dependent on the minority concentration and temperature.

The power P, delivered by the antenna may be written in terms of the antenna current I_o and this E field. Using ϕ, the antenna Fourier spectrum and $\bar{E}_y$ the Fourier transform of E_y, the coupling resistance R_c is then written:

$$R_c = \frac{2P}{I_o^2} = \frac{1}{I_o^2} R_e \left\{ \frac{I_o^*}{2\pi L_o} \int_{-\infty}^{\infty} dk_z\ \phi\ \bar{E}_y\ \frac{1 + e^{-\alpha + i\beta}}{1 - e^{-\alpha + i\beta}} \right\}$$

For $\alpha \ll 1$, as expected near $k_z = o$, and nearly radial propagation, $\beta = 2\ k_x d$. When $k_x d = n\pi$, the last factor of the integrand is $\frac{2}{\alpha}$ giving an enhanced real contribution. When $k_x d \neq n\pi$, the last factor is $i\cot \beta/2$ and the contribution is imaginary.

For α large, as expected for large k_z, the integral is unchanged from the single pass model.

These resonant contributions with $k_x d = n\pi$ will be referred to as "poles" and they define the radial eigenmodes.

Contributions occurring for values of k_x having corresponding values of k_z with large values of the Fourier transform of the antenna current can make dominating resonant contributions to the coupling resistance.

Because the k_z value associated with these strong resonant contributions changes as the plasma parameters evolve in time, the power absorption spectrum in k_z varies in time and does not have the same shape as the Fourier transform of the antenna current. For monopole phasing, as k_z approaches zero, the antenna output increases (because of the Fourier transform of the antenna current and reduced attenuation while tunnelling from the antenna to the plasma), and reflectivity increases. Thus, we get the highest contributions to R_c, ie eigenmode onsets when the density and magnetic field are set to values which access a radial eigenmode with toroidal mode number $n_\phi = 0$.

If now the plasma parameters are changed so that, eg the Alfvén velocity is reduced, the dispersion relation between k_x and k_z ensures that eigenmodes with successively higher toroidal mode numbers are accessed in order. Each of these higher k_z modes has decreasing reflectivity, and the antenna output in the monopole phasing decreases with n_ϕ so we obtain a decreasing coupling resistance giving the asymmetry typical of the peaks in the data presented in Figs 1a and 2a.

For the dipole phasing there is a zero antenna output with $n_\phi = 0$ so that poles at small n_ϕ cannot contribute significantly to the coupling resistance. For larger values of n_ϕ, changes of the antenna output are small and no variations of the the mean coupling resistance are expected. Only small variations of the coupling resistance are seen because of the stronger absorption.

Results and Discussion:

The Alfvén speed varies with both magnetic field B and density. When B changes the position of the ion-ion-hybrid, cut-off layer changes, effectively changing the slab thickness. In addition, in high power ICRH heating pulses, changes in Z-effective change the mass density. These points are all taken into account, where appropriate in calculating changes to the optical path length. The spacings of the onsets of the eigenmodes seen in the data of Figs 1a and 2a are then found to correspond very well to changes of the optical path length by λ. In Fig 2d the slope of $\frac{k_x d}{\pi}$ against radial mode number is close to one.

To fit the peak-to-valley ratios and shapes of the peaks in the coupling resistance data, the minority concentration is varied at known temperature in the mode conversion algorithm. For the data of Fig 1a, the best fit (Fig 1d) was obtained with 20 % hydrogen minority ion concentration, a value close to that measured via charge exchange.

In Fig 5 an individual eigenmode was tracked. The electron temperature was among the highest with the level of RF power used (10 MW), even though during the peak temperature, the high coupling resistance is evidence of a high reflection coefficient and thus low absorption of energy per pass. The electron temperature profile conformed to those normally observed both in the valley at 51.4 s and near the peak, eg at 51.83 s. Stored energy and C III impurity radiation intensity are not dependent on the excitation of eigenmodes.

In a pulse not shown, 12 MW of RF power produces T_e = 9.5 keV and T_i = 8.0 keV at times when there is eigenmode excitation. But the peak-to-valley ratio is very small at these high temperatures so throughout almost the whole range of k_z there must be high absorption per pass.

In dipole phasing the variations of coupling resistance are much reduced compared with monopole phasing particularly when using hydrogen minority species heating, even when dramatic changes of density and temperature occur, eg during pellet injection.

Sawtooth-free periods are achieved both with monopole phasing in which eigenmode excitation is observed and also with dipole phasing, so that no special effects are attributable to eigenmodes in this regard.

Conclusions

Though there are in some cases large excursions of the coupling resistance, the excellent ICRH heating results obtained with the new antennas installed in 1987 are important evidence that the existence of eigenmodes does not cause problems in the physics of ICRH heating at these high temperatures, and that technical problems which eigenmodes might cause through large variations of the coupling resistance are reduced at high temperatures. The data presented is all for hydrogen minority species heating; He^3 minority species heating gives a more complicated set of coupling resistance peaks which we have not modelled.

We acknowledge with pleasure the contributions of the JET RF Division technical teams and the JET operating teams.

References

[1] Lapierre, Y., J, Plasma Phys 29 223(1983)
[2] Hellsten, T., and Appert, K., 13th EPS Conf. Schliersee V2 129(1986)
[3] Stix, T.H., Nucl. Fusion 15 737 (1975)
[4] Colestock, P.L., and Kashuba, R.J., Nucl. Fusion 23 763(1983)

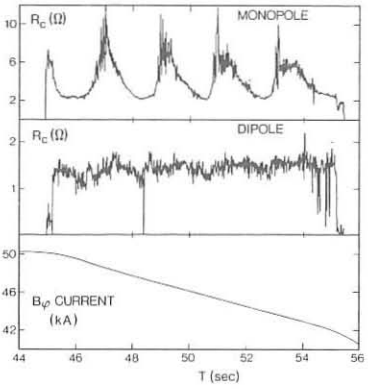

Fig 1: Eigenmodes: B_φ ramp
(a) Monopole, (b) Dipole
(c) B_φ Current
(d) Detailed Fitting

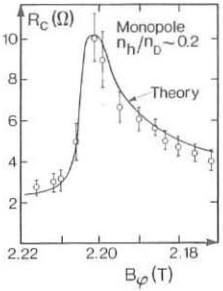

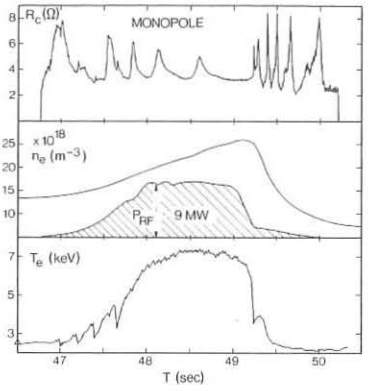

Fig 2: Eigenmodes: n_e ramp
(a) Monopole (b) n_e
(c) T_e
(d) Spacing of onsets

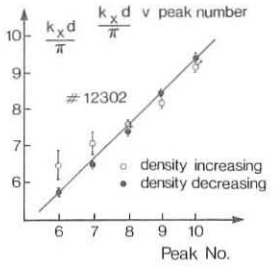

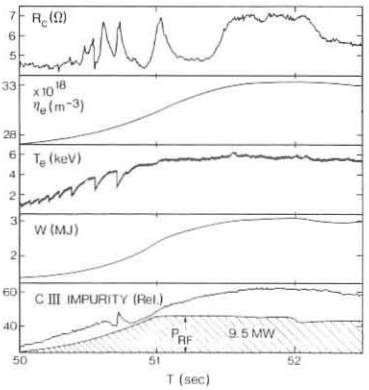

Fig 3: Eigenmodes during high power heating
T_e, Energy, Impurity, Profiles

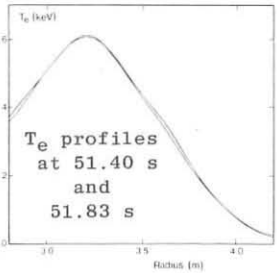

STUDY OF ICRF DRIVEN FUSION REACTIVITY

G.A.Cottrell, G.Sadler, P.van Belle, D.J.Campbell, J.G.Cordey, W.Core, T.Hellsten, J.Jacquinot, S.Kissel, D.F.H.Start, P.R.Thomas and J.Wesson
JET Joint Undertaking
Abingdon, Oxfordshire, OX14 3EA, England

1. INTRODUCTION AND EXPERIMENTS

A series of experiments is currently in progress on JET to study and optimise ICRF–driven fusion reactions between the highly energetic ^{3}He minority ions and the thermal deuterons during central high power RF heating at $\omega=\omega_c(^3\mathrm{He})$. The reaction rate in the tail was monitored by measuring the flux of 16.6 MeV γ–ray photons from the D[^{3}He,γ] ^{5}Li reaction[3,7]. With a coupled RF power to the plasma of 11.5 MW, the fusion yield so far achieved (in charged particle fusion products) is P_{fus}= 50 kW, giving a Q–value of $\simeq$ 0.5%, the highest achieved so far in a tokamak. Because of the strong non–linear variation of reactivity with RF power density, it has been possible to derive the effective RF power deposition radius in the plasma by data fitting. The value derived, r_d = 0.3 m, is close to that obtained from RF modulation experiments[1] as well as predictions by a full wave code.

Up to 11.5 MW of ICRH power was coupled to the plasma in the (^{3}He)D regime with plasma current: I_p= 2 MA–5 MA, toroidal field: B_φ=3.4 T, electron density: $\bar{n}_e=(2–4)\times 10^{19}\mathrm{m}^{-3}$, minority concentration: ($1.6\% \leq \eta \{\equiv n(^3\mathrm{He})/n_e\} \leq 8.0\%$), and f_{rf} = (32–35) MHz giving central heating with the resonance located within 0.1 m of the magnetic axis. The ^{3}He was injected into the target D discharge at t = 1 sec before the application of the 3–5 second RF heating pulse. In discharges with $P_{rf} \geq$ 5 MW, long duration sawtooth–free periods ($\tau_{st} \leq$ 3 s) were routinely obtained[2]. In other cases, normal sawtoothing behaviour was observed. The D[^{3}He,γ] ^{5}Li (16.6 MeV) reaction cross–section is $\simeq 10^{-5}$ of that of the charged particle fusion

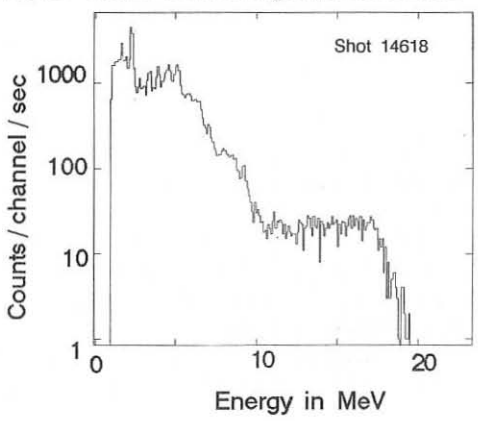

Figure 1.
Typical γ–ray energy spectrum observed during ICRH heating in the (^{3}He)D regime. Plasma parameters: I_p= 2 MA, B_φ = 3.4 T, $\bar{n}_e=2.5\times 10^{19}$ m^{-3}, P_{rf}=9.8 MW, η=2%, Z_{eff}=2. The 16.6 MeV γ–yield is equivalent to 30 kW of fusion power in this case.

cross–section in the range 0–1 MeV. The 16.6 MeV γ–flux was measured using calibrated NaI and BGO scintillation detectors[3]. A typical γ–ray energy spectrum with RF heating is shown in Figure 1. The shape of the spectrum at $E_\gamma \geq 10$ MeV is caused by the natural line width (1.5 MeV), the instrumental resolution, and the existence of a second line at $E_\gamma = 13.5$ MeV[3]. Below 10 MeV, the γ–ray emission originates from $^3He \rightarrow C$ reactions[7]. The variation of γ–ray count rate with RF power is shown in Figure 2 for a number of discharges. Within the present range of JET parameters, the γ–yield varies as $N_\gamma \propto P_{rf}^{5/3}$, implying that $Q_{rf} \propto P_{rf}^{2/3}$.

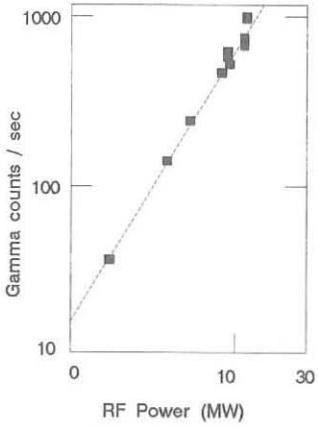

Figure 2.
Variation of γ–ray count rate from $D \rightarrow {}^3He$ reactions in the energy range (12–20) MeV with RF power for a number of discharges. Plasma parameters: $I_p = (2–4)$ MA, $B_\phi = (3.2–3.4)$ T, $\eta = (2–4)\%$. The highest count rate observed corresponds to 50 kW of fusion power.

2. THE MODEL AND METHOD OF ANALYSIS

The ICRH–driven minority tail was simulated using the steady–state, isotropic Stix formulation[4]. The minority velocity distribution function, $f(v)$, was calculated up to a maximum energy of 10 MeV ($\equiv mv_m^2/2$), beyond which orbit losses are expected to be important for the present range of plasma current in in JET and contributions to the reaction rate are in any case small. The local ^3He–D reaction rate was then calculated;

$$R(^3He–D) = 4\pi n_d \int_0^{v_m} v^2 dv\, f(v)\, \sigma(v)$$

where $\sigma(v)$ was taken as the Asher–Peres nuclear cross–section[5], and n_d is the deuterium density. The plasma model contained an admixture of three ionic species, D, ^3He, and an impurity assumed to be carbon with concentrations of the ion species adjusted initially to equate the model Z_{eff} with the experimental value (derived from measurements of the visible bremmstrahlung).

In applying the model to the experimental data, there were two main uncertainties. Firstly, there was no direct measurement of the absolute density of the minority ions. Therefore, in the present analysis, it was assumed that the the helium inventory (measured using the observed density increase at the time that helium was

injected into the discharge) was subsequently conserved and, moreover, was everywhere proportional to the plasma electron density. Secondly, there was no direct measurement of the RF power density. However it was possible to use the present γ–ray data to obtain an independent estimate of this quantity. The model was calibrated by assuming that a fraction, μ, of the total RF power coupled to the plasma was coupled to the minority ions within some plasma deposition volume, V_d. The remaining fraction $(1-\mu)$ was attributed to possible mode conversion, ion cyclotron and Landau damping and transit–time magnetic pumping. Analysis of the results of RF modulation[1], fast ion energy content with ICRF heating[6] as well as the results of full wave ICRF predictions, suggest that $\mu \cong 0.75$, a value which we use. The effective volume averaged electron temperature used in the model was 0.67 of the central value, a factor needed to bring measurements and predictions of the of the fast ion energy content in ICRF heated discharges into agreement[6].

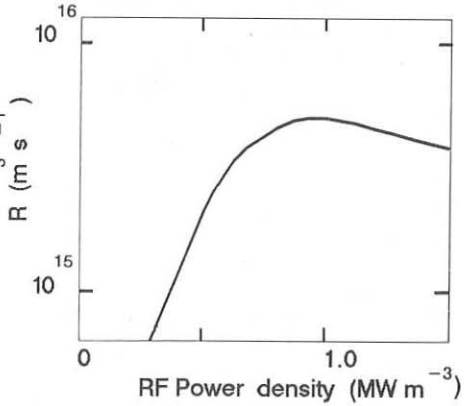

Figure 3.
Calculated ICRF–driven fusion reactivity shown as a function of RF power density for the typical JET parameters: $\overline{n}_e = 3 \times 10^{19} m^{-3}$, *volume–averaged temperatures* $\langle Te \rangle = \langle Ti \rangle = 4.5$ *keV*, $\eta = 4\%$ *and* $Z_{eff} = 2$.

A plot of the calculated local fusion reactivity as a function of RF power density is shown in Figure 3 for a typical set of JET parameters. The curve shows a characteristically steep rise in reactivity for RF power densities up to a threshold of approximately 1 MW m^{-3}, and thereafter a saturation. This behaviour is a consequence of the quasi–Maxwellian tail folded with the fusion cross–section which increases strongly with energy up to a maximum (at $E \cong 0.5$ MeV) and thereafter decreases. The integrated reactivity can also be seen to decrease at the highest RF power densities where too large a fraction of ^{3}He ions now appears in the far tail ($E \geq 0.5$ MeV). Because the JET γ–ray data spans a considerable range in RF power density, it was possible to calibrate the model (assuming V_d to be independent of RF power) using the measured relative fusion reactivities for a number of discharges with different RF powers. This makes use, in effect, of the strong variation and saturation shown in Figure 3. By minimising χ^2 with respect to the unknown deposition volume, a value $V_d = 6$ m^3 was obtained, equivalent to an effective deposition radius of $r_d = 0.3$ m.

This value is consistent with the <Te> taken in the fast ion energy analysis and is close to that obtained from analyses of RF modulation experiments. It was adopted in the model to compare measured and predicted values of the fusion power shown in Figure 4, where the code was run for the individual plasma parameters relevant to each discharge. It can be seen that reasonably good agreement was obtained between the experiments and the modelled fusion yields.

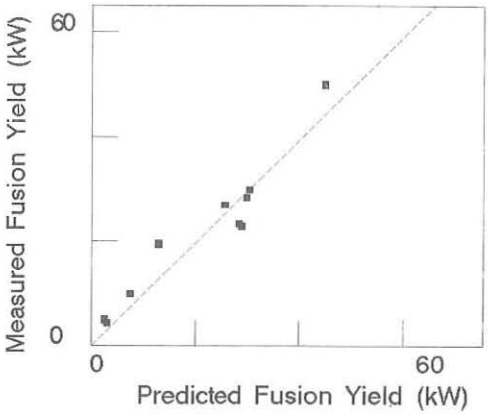

Figure 4.

Comparison of measured and calculated ICRF–driven fusion yields from (^3He)D nuclear reactions. The calculated yields are based on the isotropic Stix model as described in the text with plasma parameters relevant to each separate discharge in the diagram.

3. CONCLUSIONS

In experiments currently under way on JET to study the $^3He \rightarrow$ D ICRF–driven fusion reactivity, an effective $Q_{rf} \simeq 0.5\%$ has been achieved with the application of 11.5 MW of ICRH heating power to the plasma. The variation of Q_{rf} during systematic scans of plasma parameters has enabled the calibration of a simple Stix model and will be useful in the future to validate more comprehensive codes in the prediction of non–thermal fusion yields based, for example, on fundamental heating of deuterium in tritium.

REFERENCES

1. Evrard, M. et al (this conference)
2. Campbell, D. et al (this conference)
3. Sadler, G., Jarvis, O.N., van Belle, P. Proc. 14th EPS Conference on Controlled Fusion and Plasma Physics, Madrid, Spain. 11D(III), 1232–1235, (1987)
4. Stix, T.H., Nuclear Fusion, 15, 737–754, (1975)
5. Asher–Peres, J.Appl.Phys., 50(9), 5569–5571, (1979).
6. Cordey, J.G., (private communication)
7. Sadler, G.,Jarvis, O.N.,van Belle, P., Adams, M. (this conference)

RESONANT ION DIFFUSION IN ICRF HEATED TOKAMAK PLASMAS

T. Hellsten and W. Core

JET Joint Undertaking, Abingdon, Oxon. OX14 3EA, UK.

1. Introduction. Wave induced particle transport occurs during ICRH of the resonating ion species due to absorption of the waves toroidal angular momentum [1,2]. For an asymmetric toroidal wave spectrum in which there is a direct input of wave toroidal angular momentum to the plasma, the resonating ions will undergo a radial drift across the magnetic flux surfaces. The direction of the radial drift will depend on the toroidal direction of the wave. For a symmetric spectrum the drift vanishes and only a diffusion term remains.

The diffusion increases with energy. In large tokamak plasmas with intense ICRF heating ions are heated up to the MeV range for which RF-diffusion becomes important.

The simultaneous diffusion in real and velocity space caused by the RF-field can lead to a pump out of particles from regions with high power densities, flattening of the heating profile and reduction of the average energy of the resonating ions. Further, space charges set up by the radial diffusion leads to a toroidal rotation of the plasma.

The diffusion problem has been studied by reducing it to a 2-D, time dependent diffusion equation, 1-D in velocity and 1-D in real space, which is solved by a modified version of the BACCHUS code [3].

2. The Reduced Diffusion Equation. As an ion resonates with the wave at the cyclotron resonance it will change its perpendicular and parallel velocity. An increase in the perpendicular velocity can lead to a transition from a passing orbit to a trapped orbit. For trapped particles the orbit width is increased. When the parallel velocity is changed for a trapped particle this leads to a radial displacement of the turning point in a direction depending on the sign of the parallel wave number [2]. To measure the particle transport in real space we represent the trapped particles by the minor radius of their turning points and passing particles by the minor radius where their drift orbit intersects the cyclotron resonance. We assume the wave spectrum to be symmetric so that the drift term vanishes. A diffusion equation in real and velocity space can then be obtained by adding the corresponding diffusion term in the quasi-linear RF-diffusion equation [4] yielding

$$\frac{\partial f}{\partial t} = C(f) + Q(f) + D(f) \qquad (1)$$

$$D = \frac{1}{r}\frac{\partial}{\partial r}\left(D_{RF}\, r\, \frac{\partial f}{\partial r}\right)$$

$$D_{RF}=\begin{cases}\dfrac{v_\perp^2}{\omega\,\omega_{ci}}\left(\dfrac{n_\phi+\dfrac{m}{q}}{R_o}\right)^2\dfrac{\langle(\delta v_\perp)^2\rangle}{\tau_b} & \text{for trapped particles}\\ 0 & \text{for passing particles}\end{cases}$$

where C and Q are the quasilinear diffusion operators describing thermalisation due to Coulomb collisions and ion cyclotron heating, respectively. The perpendicular velocity at the cyclotron resonance is denoted by $v_\perp$, n_ϕ is the toroidal mode number, m the poloidal mode number, q the safety factor, R the major radius, r the minor radius, ω the wave frequency, ω_{ci} the cyclotron frequency, τ_b the bounce time for trapped particles and $\delta v_\perp$ the averaged increase in $v_\perp$ as the ion passes the cyclotron resonance. To obtain Eq.(1) we have assumed the cyclotron resonance to pass through the magnetic axis and that the poloidal cross-section of the magnetic surfaces are concentric circles. This time dependent, 3-D diffusion problem is rather difficult to solve. We wish therefore to reduce it further by integrating it over the pitch angle in the velocity space. To do so, we have to make an assumption of the anisotropy of the velocity distribution. By using various assumptions for the distribution function we can get upper and lower limits for the diffusion. A lower limit is obtained by assuming the distribution to be isotropic yielding a pitch angle averaged diffusion coefficient

$$D_1 = \left(\frac{\kappa m_i v}{B_o}\right)^2 \eta\,\frac{2P_M}{m_i n_i}\left[J_{n-1}^2\left(\frac{v\zeta k_\perp}{\omega_{ci}}\right)+\left|\frac{E_-}{E_+}\right|^2 J_{n+1}\left(\frac{v\zeta k_\perp}{\omega_{ci}}\right)\right]$$

$$\kappa = c(n_\phi + m/q)/Ze\omega R \qquad (2)$$

where η is the ratio of the trapped particle intersecting the cyclotron resonance to the total number of particles, ζ is a characteristic pitch angle for trapped particles intersecting the cyclotron resonance, $k_\perp$ the perpendicular wave number, P_M the local power density for a Maxwellian velocity distribution in the absence of higher order finite gyroradius correction.

For intense ICRH the particles tend to become more trapped and the isotropic model will underestimate the number of trapped particles. An upper estimate of the diffusion can be obtained by assuming all particles to be trapped having orbits intersecting the cyclotron resonance which yields

$$D_2 = \left(\frac{\kappa m_i v}{B_o}\right)^2 \frac{2P_M}{m_i n_i}\left[J_{n-1}^2\left(\frac{vk_\perp}{\omega_{ci}}\right)+\left|\frac{E_-}{E_+}\right|^2 J_{n+1}^2\left(\frac{vk_\perp}{\omega_{ci}}\right)\right] \qquad (3)$$

A third more realistic model can be obtained by assuming the low energy ions to be isotropic and the high energy ions to be trapped ions. We assume the transition between these models to take place at the velocity V_γ [4,5] above which the pitch angle scattering becomes negligible. The following model for the diffusion coefficient can then be constructed

$$D_3 = g(v)\,D_2 \qquad (4)$$

$$g(v) = (1 - 3\bar{v}^2)(1 - a) + a$$

$$\bar{v}^2 = \frac{1 + (v/v^*)^2}{3[1 + (v/v^*)^2 + (v/v^*)^4]}$$

$$v^{*2} = 0.25\ V_\gamma^2$$

The form of $\bar{v}^2$ has been chosen such that $\langle v_{//}^2 \rangle = \langle \bar{v}^2 v^2 \rangle$ where $\langle v_{//}^2 \rangle$ is the averaged parallel velocity squared calculated with the BAFIC code [6].

3. Numerical Results. The effect of RF-induced diffusion on the velocity distribution models were calculated for the following scenario with these models: minority heating of H in a D-plasma at the fundamental cyclotron resonance $n_H(0)=3.5\times10^{11}cm^{-3}$, $n_D=3.5\times10^{13}cm^{-3}$, $n_i(r)=n(0)\ \exp(-0.5\ r^2)$, $T(r)=T_o\ \exp(-1.75\ r)$, $T_o=10$ keV, f=33 MHz and $q(r)=const=1$. The wave field is determined such that a Maxwellian velocity distribution should have in the zero gyroradius limit given rise to a flux surface averaged power density profile $P(r) = P_o\ \exp(-20\ r^2)$. For a large central power density and a long slowing down time the ions will near the centre diffuse to high energies. The high energy ions will then diffuse away from the centre to regions with lower wave fields and cool down there. They will then diffuse back again but now with a lower rate since their energy is reduced. This leads to a pump out of resonating ions from the central region. Fig.1 shows the evolution of the resonating ions on the magnetic axis for the various models. Fig.2 shows how the density profile evolves in time as calculated with model 3. Fig.3 shows the density profile at t = 1.5s for the various models. In the absence of neoclassical diffusion the density profile does not reach a steady state. On the long time scale the neoclassic diffusion have to be included which will reduce the density depletion. However, the velocity distribution normalized locally in space reach a steady state after about a slowing down time (1s). Fig.4 shows the averaged velocity squared for the various models compared to that in the absence of spatial diffusion, normalized to the velocity at r=0 before heating.

Acknowledgement. The authors are grateful to Drs. K. Appert, S. Succi and J. Vaclavik for providing the BACCHUS code which has been modified to solve the diffusion equations.

References

[1] Riyopoulos, S., Tajima, T., Hatori, T. and Pfirsch, D. Nucl. Fusion 26 (1986) 627.
[2] Chen, L., Vaclavik, J. and Hammett, G. PPPL-2441, Princeton University.
[3] Appert, K. et al., J. Proc. 11th European Conf. on Contr. Fusion and Plasma Physics, Aachen (1983) paper B29.
[4] Stix, T.H. Nucl. Fusion 15 (1975) 737.
[5] Anderson, D., Eriksson, L-G. and Lisak, M. Plasma Physics and Controlled Fusion 29 (1987) 891.
[6] Hellsten, T. et al., Proc. of 12th European Conf. on Contr. Fusion and Plasma Physics, Budapest (1985) Vol.II, p.124.

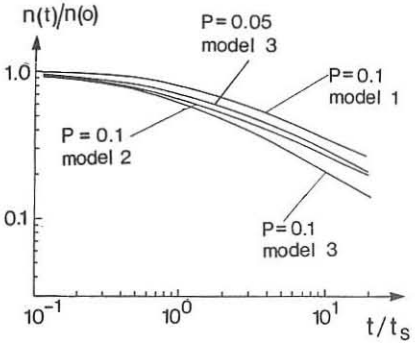

Fig. 1 Density on magnetic axis versus time. The slowing down time t_s = 1s.

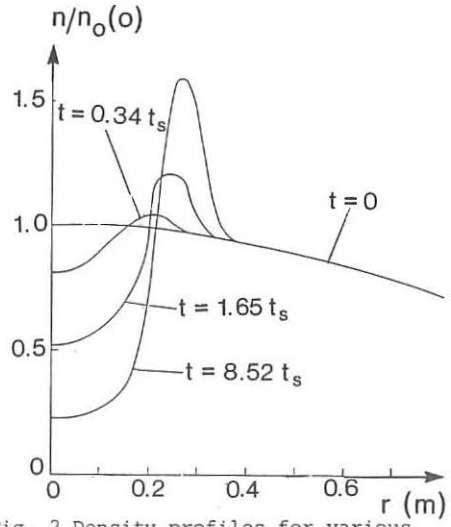

Fig. 2 Density profiles for various times as calculated with model 3 and p(0) = 0.1.

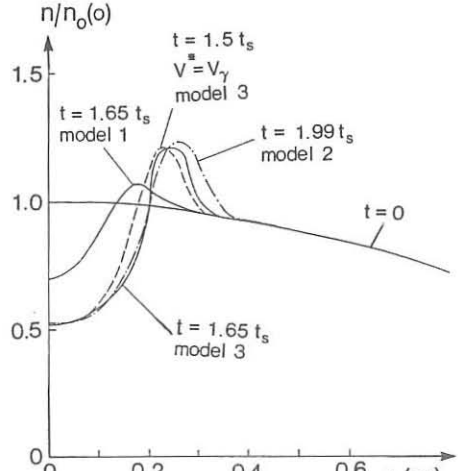

Fig. 3 Comparison of the density profiles with the different models at $t \approx 1.5 t_s$.

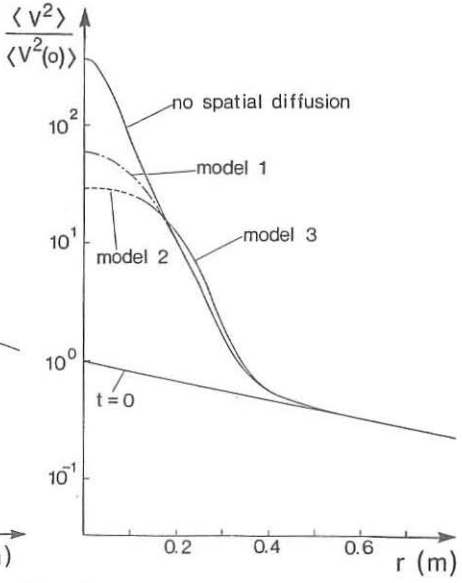

Fig. 4 Stationary profiles of the velocity squared for the various models.

ANALYTIC THEORY OF ABSORPTION, CONVERSION AND REFLECTION OF THE FAST MAGNETO-SONIC WAVE AT THE SECOND-HARMONIC LAYER

Allan N. Kaufman and Huanchun Ye
Lawrence Berkeley Laboratory and Physics Department
University of California, Berkeley CA 94720

One of the outstanding problems in ICRF heating of tokamaks is the mode-conversion process at the second harmonic gyro-resonance layer. The complexity of the problem is largely due to the presence of the several waves, i.e., incident and reflected magneto-sonic waves, ion-Bernstein wave, and particle modes (which are analogous to the ballistic modes in Landau damping). As a consequence, most of the work done on this problem has involved heavy numerical analysis. By considering the problem in wave phase space (x-k space), however, we can not only simplify it greatly, but also gain a better understanding of the physics of the process. In phase space, the mode-conversion occurs at two points, and by expanding the dispersion functions at those points, we can derive (using the WKB approximation) two sets of coupled linear first order equations:

$$[\omega \mp k_x c_A]\, b_\mp(x,t) = \alpha_\mp \int dv_\parallel\, p(x,t;v_\parallel)$$

$$[\omega - k_\parallel v_\parallel - 2\Omega_i(x)]\, p(x,t;v_\parallel) = \beta(v_\parallel)\, b_\mp(x,t)$$

where $\omega \to i\partial/\partial t$, $k_x \to -i\partial/\partial x$, $b_\mp(x,t)$ is the magnetic perturbation of the magneto-sonic wave ($\mp$ denotes incident/reflected branches), and $p(x,t;v_\parallel)$ is the $(v_x v_y)$ moment of the perturbed distribution function (it is thus termed *pressure-anisotropy wave*). $p(x,t;v_\parallel)$ contains both the ion-Bernstein wave and the particle modes, which can be reconstructed by van Kampen analysis. Solving these equations, we can then obtain the coefficients of transmission, reflection, conversion and absorption analytically. These results are compared with those obtained by other authors using different methods. Our model also gives rise to a new phenomenon which we call the *linear ion cyclotron echo*.

The merit of the present approach is its power and simplicity. It can be extended without much difficulty to more realistic geometries, such as magnetic field with rotational transform and general density profile of plasmas in tokamaks.

This research was supported by US DOE under contract number DE-AC0376SF00098.

PARAMETRIC INSTABILITIES OF AN INHOMOGENEOUS PLASMA NEAR ION-ION HYBRID RESONANCE UNDER ION CYCLOTRON HEATING.

T.A.Davydova, V.M.Lashkin

Institute for Nuclear Reseach of the Ukrainian Academy of Sciences, Kiev 28, USSR.

It is now an established fact that one of the most principal mechanism of RF power absorption under ion cyclotron range of frequency plasma heating of a Tokamak is the conversion of the fast magneto-acoustic wave into the strong damping plasma wave near the ion-ion hybrid resonance point $\omega_{ii}=\left(\frac{\omega_{p1}^2\omega_{c2}^2+\omega_{p2}^2\omega_{c1}^2}{\omega_{p1}^2+\omega_{p2}^2}\right)^{1/2}$ [1] .

Pump field amplitude increases considerably in the resonance domain [2] and therefore one could expect the rising of the different parametric instabilities which can be additional (turbulent) mechanism of RF power absorption. The parametric instabilities can lead also to formation of fast tails on the particle distribution function. This can influence both on the process of anomalous transport and the process of linear conversion.

Parametric instabilities of uniform pump field at $\omega_0 \approx \omega_{ii}$ (ω_0 -pump frequency) have been considered in [3-5]. The decay of the pump wave into another ion-hybrid wave and the drift mode was analysed in [3]. The basic dispersion equation is incorrect in [4,5].

In the present report the parametric instabilities are studied for the case of nonuniform pump field resulting from the linear conversion in the vicinity of the ω_{ii} resonance point at $\omega_0=\omega_{ii}$.

Let us consider the model of plane stratified plasma.

Uniform magnetic field is directed along the z-axis and plasma density monotonically decreases along the x-axis.
The field formed due to linear conversion near the ion-ion hybrid resonance point is almost electrostatic and directed along the x-axis. It's amplitude $E_0(x)$ has the following form

$$E_0(x)=\begin{cases} F_0\sqrt{\pi}\left(\frac{x}{\Delta}\right)^{-1/4} exp\left[i\frac{\pi}{2}+i\frac{2}{3}\left(\frac{x}{\Delta}\right)^{3/2}\right] & ,\text{for } x\gg\Delta \\ F_0\, G\left(\frac{x}{\Delta}\right) & ,\text{for } |x|<\Delta \end{cases} \qquad (1)$$

where $\Delta=\left(R^2L\right)^{1/3}$, L -the inhomogeneity scale,

$$R^2=\left|-\frac{2}{\omega_{ii}\varepsilon'(\omega_0)}\sum_i\frac{3v_{Ti}^2\,\omega_{pi}^2}{\left(\omega_{ii}^2-\omega_{ci}^2\right)\left(\omega_{ii}^2-4\omega_{ci}^2\right)}\right| \quad ,\varepsilon'(\omega_0)=2\omega_{ii}\sum_i\frac{\omega_{pi}^2}{\left(\omega_{ii}^2-\omega_{ci}^2\right)^2},$$

$G(\xi)$ is the Airy function, F_0 is the maximum field amplitude in the resonance domain, $i=1,2$ -denotes of ion species.

The development of the electrostatic perturbations of a plasma located in an uniform electric field $\vec{E}=\vec{E}_0\sin\omega_0 t$ (in the dipole approximation) for the case of presence of particles of many species can be described by the equation (for $\omega\ll\omega_c$) [3]

$$1+\sum_{\sigma,\eta}\sum_{\xi=+,-}\frac{|\mu_\sigma-\mu_\eta|^2}{\varepsilon\varepsilon_\xi}\left[\left(\varkappa_\sigma^\xi-\varkappa_\sigma\right)\left(\varkappa_\eta^\xi-\varkappa_\eta\right)+\varepsilon\,\varkappa_\sigma^\xi\,\varkappa_\eta^\xi\right]=0 \qquad (2)$$

where $\varkappa_\sigma=\varkappa_\sigma(\omega)$ -partial permittivity of particles of kind σ

$$\varkappa_\sigma^\pm=\varkappa_\sigma(\omega\pm\omega_0) \quad ,\ \varepsilon=1+\sum_\sigma\varkappa_\sigma \quad ,\ \varepsilon_\xi=1+\sum_\sigma\varkappa_\sigma^\xi \quad ,$$

$$\mu_\sigma=\left|\frac{e_\sigma}{m_\sigma}\right|\left[\left(\frac{K_z E_{0z}}{\omega_0^2}+\frac{\vec{K}_\perp\cdot\vec{E}_{01}}{\omega_0^2-\omega_{c\sigma}^2}\right)^2+\frac{\omega_{c\sigma}^2\left(\vec{B}_0\cdot[\vec{K}\vec{E}]\right)^2}{B_0^2\,\omega_0^2\left(\omega_0^2-\omega_{c\sigma}^2\right)^2}\right]^{1/2}\ll 1 \quad ,\vec{K} \text{ is the wave}$$

vector, $\vec{K}_\perp=\left(K_x,K_y\right)$ .The relative motion of the different species of ions plays the main role for the exiting of the instability at $\omega_c=\omega_{ii}$ .We consider the purely growing instability($\omega_c=\omega_{ii}$ and the decay is not possible) with $|\varepsilon|\gg 1$.

In that case the equation (2) may be presented in the form

$$1 - \frac{\mu^2}{2}\,\frac{\varkappa_1^2(\omega_0)}{\mathcal{E}'(\omega_0)}\,\frac{\delta}{\omega^2 - \delta^2} = 0 \qquad (3)$$

where $\mu = |\mu_1 - \mu_2|$, the frequency mismatch $\delta = -\frac{\omega_{ii}}{2} K^2 R^2 < 0$ (for D + H plasma). The equation (3) describes the purely growing instability with the growth rate

$$\gamma = \left(\frac{\mu^2}{2}\,\frac{\varkappa_1^2(\omega_0)}{\mathcal{E}'(\omega_0)}\,\delta - \delta^2\right)^{1/2}$$

The growth rate is at maximum at $\delta_{opt} = \frac{\mu^2 \varkappa_1^2(\omega_0)}{4\,\mathcal{E}'(\omega_0)}$ and $\gamma_{max} = \delta_{opt}$

In the case of the nonuniform pump field described by (1) one can obtain the differential equation of IV order

$$\left[1 - \alpha_0^2(1-\xi^2)\right]\Psi^{IV} - 2q_y^2\left[1 - \frac{\alpha_0^2}{2}(c+1)(1-\xi^2)\right]\Psi'' + q_y^4\left[1 - c\alpha_0^2(1-\xi^2)\right]\Psi + \frac{4\lambda^2}{\alpha^4}\Psi = 0 \qquad (4)$$

where $\alpha_0^2 = \frac{A\,\varkappa_1^2(\omega_0)\,E_0^2}{\mathcal{E}'(\omega_0)\,\omega_0 R^2}$, $\alpha = \frac{R}{\Delta}$, $\xi = \frac{x}{\Delta}$, $q_y = K_y \Delta$, $\lambda = \frac{i\omega}{\omega_0}$,

$A = \left[\frac{e_2}{m_2(\omega_0^2 - \omega_{c2}^2)} - \frac{e_1}{m_1(\omega_0^2 - \omega_{c1}^2)}\right]^2$, $C = \left[\frac{\omega_0(\omega_{c1} + \omega_{c2})}{\omega_0^2 + \omega_{c1}\omega_{c2}}\right]^2$, and $1 < c < 2$

The equation (4) has the singularity at $\alpha_0^2 \approx 1$ therefore it is incorrect near $\alpha_0^2 = 1$. This singularity may be removed by means of more exact calculation of dispersion in the expression for δ . The analysis shows that eq.(4) can be used at $\alpha_0^2 < 2/(c+1)$. Then we have $K_y \gg (\delta x)_{loc}^{-1}$ and n unstable modes are excited with the growth rates λ_n

$$\frac{4\lambda_n^2}{\alpha^4} = (K_y\Delta)^4(c\alpha_0^2 - 1)\left[1 - \frac{\sqrt{2 - \alpha_0^2(c+1)}\,\sqrt{c\alpha_0^2}}{(c\alpha_0^2 - 1)}\,\frac{(2n+1)}{K_y\Delta}\right] \qquad (5)$$

and width of the localization domain

$$(\delta x)_{loc} = \frac{[2 - \alpha_0^2(c+1)]^{1/4}}{\sqrt{c\alpha_0^2}}\,\frac{\sqrt{2(2n+1)}\,\Delta}{\sqrt{K_y\Delta}} < \Delta$$

The growth rate is at maximum for the mode $n = 0$. Taking the transformed wave into account make it possible to consider the modes located in the domain more than Δ . In this case the growth rates are less than ones given by (5).

The generalization of (1) for the case of nonuniform pump field make it possible to describe also the quasidecay-

-the instability caused by Landau damping on electrons. In this case $\mathrm{Re}\,\omega \sim \delta \gg \mathrm{Im}\,\omega$ .This instability for nondissipative case and uniform pump field has not the threshold unlike the purely growing instability considered above. In the nonuniform field on the weak exceeding of the threshold $a_0^2 \gtrsim 1/K_y^2\Delta^2$ this instability is absolute with the growth rate($\delta_0 = \omega_0 K_y^2 R^2/2$, $B = (\varkappa_1 - \varkappa_1^{(a)})(\varkappa_2 - \varkappa_2^{(a)}) / |\varepsilon|^2 \varkappa_1^2(\omega_0)$)

$$\frac{\gamma_n}{\omega_0} = \frac{c a_0^2 B \delta_0}{2\omega_0} \frac{\omega_{pe}^2}{K_y^2 v_{Te}^2} \sqrt{\frac{\pi}{2}} \cdot \frac{\delta_0}{K_z v_{Te}} \exp\left(-\frac{\delta_0^2}{2K_z^2 v_{Te}^2}\right)\left[1 - \frac{(2n+1)}{\sqrt{2c}\, a_0 K_y \Delta}\right]$$

and the width of the localization domain less than Δ . This instability can lead to electron heating since $\mathrm{Re}\,\omega \sim K_z v_{Te}$.

The thresholds calculated above can be easly exceeded in experiments on RF plasma heating in tokamaks.Under some conditions this thresholda can be entirely caused by the nonuniformity of the pump field in the resonance regions.

REFERENCES

1.D.Swanson. Phys.Fluids (1985),v.28, 2645.

2.D.Grekov,K.N.Stepanov. Ukr.fiz.zhurn. (1980),v.25,1281.

3.M.Ono,M.Porkolab,P.Chang. Phys.Fluids (1980),v.23,1654.

4.Y.Satya,A.Sen,P.Kaw. Nucl.Fusion (1975),v.15,195.

5.S.Bujarbarua,Y.Satya,A.Sen. Plasma Phys. (1977),v.19,N 5.

PLASMA HEATING AND QUASI-STEADY-STATE CURRENT DRIVE AT HALF-INTEGER ION CYCLOTRON FREQUENCY HARMONICS IN THE TOROIDAL OMEGA DEVICE

I.A.Dikij, S.S.Kalinichenko, A.B.Kitsenko, A.I.Lysojvan, S.V.Prikhod'ko, T.Yu.Ranyuk, K.N.Stepanov, O.M.Shvets

Institute of Physics and Technology, the Ukrainian Academy of Sciences, Kharkov 310108, USSR

Introduction. In connection with the ongoing search for effective methods of plasma RF heating and driving currents, much attention has been given recently to the properties of short wavelength waves ("slow" waves), in particular, ion Bernstein waves (IBW). Thus, it appeared possible to employ a nonlinear cyclotron wave absorption at half-integer ion cyclotron harmonics /1,2/, as it was first predicted in /3/ (see also refs. /4,5/).

In the present work we have investigated i) plasma heating by launching short wavelength ($k_\perp \rho_{Li} \sim 1$, $k_\perp \gg k_\parallel$) slow waves, and ii) quasi-steady-state current drive in a toroidal plasma at the ion cyclotron frequency ω_{ci} and its half-integer harmonics $(n/2)\omega_{ci}$, where n = 1, 3.

Results and discussion. Experiments have been performed in an upgraded toroidal device Omega with no rotational transform /6/ (major radius of the torus R = 44 cm, vessel radius r = 10 cm, plasma radius a = 6 cm) and with a smooth adjustment of longitudinal ($B_0 \lesssim 10$ kG) and transverse ($B_\perp \lesssim$ 0.1 kG) magnetic fields. RF power ($P_{RF} \lesssim 200$ kW, f = 3.2 MHz, $\tau_{RF} \lesssim 10$ ms) was delivered by the use of two antennas arranged in the torus and designed as current-carrying frames elongated along the magnetic field /6/. The controlled phase shift of RF currents in both antennas, $\pm\Delta\varphi$, ensured the formation of RF radiation spectra, differing in $k_\parallel$, with the RF field structure enabling the excitation of axially nonsymmetric ($m \neq 0$) electromagnetic (fast) and slow waves (fig. 1). The experiments were performed at a hydrogen pressure of $P_{H_2} \approx 5 \cdot 10^{-4}$Torr. The antenna-emitted RF power was used simultaneously for plasma creation and heating, and also for driving currents in a plasma. Owing to the $\tilde{E}_z$ component in the RF field structure of the antennas and the finite width of the $k_\parallel$ -spectrum, we could create the plasma with a density $n_e(0) \approx (1 - 8) \cdot 10^{12}$ cm^{-3} in a wide range of magnetic field values ($\Omega = \omega/\omega_{ci} = B_{ci}/B_0 = 0.4 - 6$). Toroidal currents of different values and duration were generated for the same magnetic field range. When the pumping wave frequency ω was in coincidence with half-integer harmonics of the ion cyclotron frequency $(n/2)\omega_{ci}$, (n = 1, 3), and also for $\omega = 0.8\omega_{ci}$,

there occurred a resonant enhancement of both the plasma energy content, $\overline{nT}$, and the current generated in the plasma, I_p (fig. 2). The plasma current magnitude, duration and direction depended in a complicated way on a variety of the parameters: $\pm B_0$, $\pm B_\perp$, $\pm \Delta\varphi$, P_{H_2}, $\overline{nT}$, n_e. The analysis of the oscilograms suggests different possible regimes for a current drive (CD), including the operation at a quasi-steady state of the tokamak-type plasma discharge with $q \gtrsim 4$ (fig. 3). The direction of the driven current changed to its reverse with the change in the sign of the phase difference of antenna RF currents (fig. 4). This CD due to the waves travelling along the torus showed up most clearly at $\Omega \lesssim 0.5$ and $\Omega \gtrsim 1.5$. Note that the value and even direction of the current changed as the magnetic field B_0 direction changed at a fixed phase difference $\Delta\varphi$. Besides, as seen from the analysis of the current density profile, at $\Omega < 1$ and $\Omega > 1$ (except the $\Omega \sim 1$ range), the currents flow in opposite directions on the external side of the torus (away from the axis)(see fig. 5).

As mentioned above, the antennas could excite both long wavelength electromagnetic waves (the Alfven wave at $\Omega < 1$, and fast magnetosonic waves at $\Omega > 1$ for a high-density plasma) and short wavelength ($k_\perp \rho_{ui} \lesssim 1$) "slow" waves (a short wavelength branch of the Alfven wave at $\Omega < 1$ and IBW at $\Omega > 1$). Even for the first toroidal modes l ($l = k_\parallel R$) the $Z_e = \omega/\sqrt{2} k_\parallel v_{Te}$ ratio is not large. This can cause the electron Cherenkov absorption of the waves, the heating of electrons and, hence, initiate the CD ($T_e \sim 40$ - 90 eV, $Z_e \sim 0.3$ - 2). According to the data given above, only a fraction of the currents observed depends on the wave directivity and may be associated with the CD. However, most of the current portion may probably be due to dipole equilibrium currents and a diffusion bootstrap current.

The $\overline{nT}$ peak at $\Omega \approx 0.8$ may be the result of a linear cyclotron absorption of the electromagnetic wave, and the current generation associated with this wave was observed previously /7/. The absorption is especially great after the wave conversion into a slow wave in the local Alfven resonance (AR) region $(k_\parallel c/\omega)^2 \approx \omega_{pi}^2/(\omega_{ci}^2 - \omega^2)$.

The $\overline{nT}$ and I_p peaks at $\Omega \approx 0.5$ may be due to a nonlinear cyclotron absorption of the wave by resonance ions with the velocity $v_\parallel = (\omega - (n/2)\omega_{ci})/k_\parallel$. This absorption predicted in /3/ is particularly great for short wavelength oscillations with $k_\perp \rho_{ui} \sim 1$ /3,4/:

$$\frac{\mathrm{Im}\, K_r}{K_r} \sim 0.1 \frac{u^2}{v_{Ti}^2} \frac{\omega}{k_\parallel v_{Ti}} \exp\left[-\left(\frac{2\omega - n\omega_{ci}}{\sqrt{8}\, k_\parallel v_{Ti}}\right)^2\right], \quad (n = 1, 3, \ldots)$$

where $u = c(\tilde{E}/B_0)$ is the amplitude of the ion oscillation rate in the wave field. At $\Omega \approx 0.5$, the antenna may launch a slow wave at the plasma periphery with $k_\perp^2 \approx (m_i/m_e)(1/\Omega^2 - 1)k_\parallel^2$.

This wave can also result from the electromagnetic wave conversion in the AR region. At $\Omega \approx 1.5$ the IBW can directly be launched by the antenna.

The nonlinear absorption of these waves can be very strong, the optical thickness being $\tau \sim I_m k_r \Delta R \sim 0.1(U/v_{Ti})^2 \cdot (R/\rho_{ci}) \gtrsim 1$, where $\Delta R = (k_\parallel v_{Ti}/\omega)R$ is the width of the absorption zone. As in the case of linear cyclotron resonances, $\omega \approx n\omega_{ci}$, the peaks of the currents generated at $\Omega \approx (n/2)$ may be due to a preferential absorption of slow waves by particles with $v_\parallel > 0$ (or $v_\parallel < 0$) /8,9/, which actually occurs at $\tau > 1$.

The peaks at $\Omega = (n/2)$ may also be related to a linear cyclotron absorption by molecular ions H^+_2 at $\omega = n\omega_{cH_2^+}$ ($n = 1, 3$). The density of these ions in the discharge may be sufficiently large at low T_e.

Summary. In the present experiments on plasma creation and heating in the toroidal device Omega by the use of the waves ($\omega \sim \omega$) running along the torus, we were able to realize CD discharges and attain a quasi-steady-state tokamak-type regime ($q \gtrsim 4$). The current generation may be attributed to the wave absorption by resonance electrons and ions, and also to equilibrium and bootstrap currents.

The resonant enhancement of plasma heating and CD at $\omega \approx (1/2)\omega_{ci}$, $\omega \approx (3/2)\omega_{ci}$ and $\omega \approx \omega_{ci}$ was observed. As shown by estimates, the peaks at half-integer harmonics may be due to a nonlinear cyclotron absorption of short wavelength modes ($k_\perp \rho_{ci} \sim 1$) by resonance ions.

REFERENCES

1. M. Ono, T. Watari, R. Ando et al., Phys. Rev. Lett. 54 (1985) 2339.
2. R. Wilson and PLT Group, in: Radiofrequency Plasma Heating. Proc. of the 6th Topical Conf., Callaway Gardens, N.-Y., (1985) 28.
3. A.B. Kitsenko, I.M. Pankratov, K.N. Stepanov, Zh. Ehksp. Teor. Fiz. 67 (1974) 1728.
4. M. Porcolab, Phys. Rev. Lett. 54 (1985) 434.
5. H. Abe et al., Phys. Rev. Lett. 53 (1984) 1153.
6. O.M. Shvets et al., Nucl. Fusion 26 (1986) 23.
7. S. Yoshikawa, H. Yamato, Phys. Fluids 9 (1966) 1814.
8. N.J. Fisch, Nucl. Fusion 21 (1981) 15.
9. A.V. Longinov, S.S. Pavlov, K.N. Stepanov, in: Controlled Fusion and Plasma Heating. Proc. of the 13th Europ. Conf., Schliersee (1986). Contrib. Papers, Part 2, p.105.

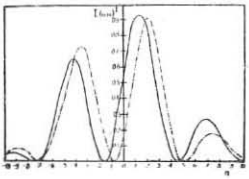

Fig. 1. Antenna spectrum. Solid curve: $\Delta\varphi = +90^{\circ}$; dash-dotted curve: $\Delta\varphi = +130^{\circ}$.

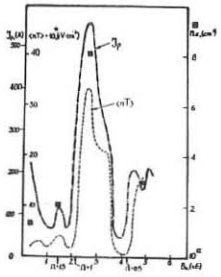

Fig. 2. $\overline{nT}$ and I_p versus B_o ($\Delta\varphi = +130^{\circ}$).

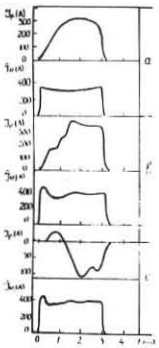

Fig. 3. Behaviour of the plasma (I_p) and antenna (I_{RF}) currents ($\Delta\varphi = +90^{\circ}$). a: B_o = 0.5 kG; b: B_o = 2.5 kG; c: B_o = 5.2 kG.

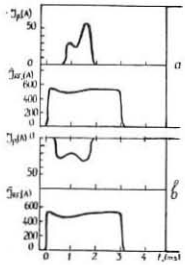

Fig. 4. I_p and I_{RF} versus the $\Delta\varphi$ sign. (B_o = 0.7kG). a: $\Delta\varphi = +130^{\circ}$; b: $\Delta\varphi = -130^{\circ}$.

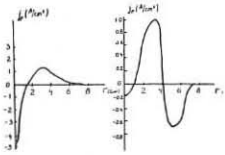

Fig. 5. Plasma current density profile j_p in B_o = 0.5 kG. a: $\Delta\varphi = -90^{\circ}$, b: $\Delta\varphi = +90^{\circ}$.

ION TRAPPING EFFECT ON CYCLOTRON FAST MAGNETOSONIC WAVE ABSORPTION IN A TOKAMAK

D.L.Grekov, A.I.Pyatak
Institute of Physics and Technology, the Ukrainian Academy of Sciences, Kharkov 310108, USSR

and

M.D.Carter
Oak Ridge National Laboratory, Oak Ridge, Tennessee, USA

Up to the present the theory of ion-cyclotron absorption of fast magnetosonic waves (FMSW) in tokamaks has been based on the interaction of the waves with passing ions /1,2/. As to the trapped particles, their amount was considered to be too small to contribute essentially to the FMSW absorption (e.g., the Maxwellian plasma with equal transverse $T_\perp$ and longitudinal $T_\parallel$ temperatures comprises trapped ions by a factor of $1/\sqrt{\varepsilon_t}$ less than passing ones, ε_t being the inverse aspect ratio). However, it appears unreasonable to neglect the role of trapped particles in cyclotron FMSW damping, because many of these particles, having a low velocity $v_\parallel$ along the field lines, stay in the resonance region for a longer time in contrast to passing ions, and this may result in the enhancement of their interaction with the wave.

It is therefore of interest to elucidate the role of trapped ions in the process of cyclotron absorption of FMSW. We solve this problem by considering an interaction between FMSW and resonance ions at a multiple cyclotron resonance ($\omega = n\omega_{ci}$, $n = 2, 3 \ldots$).

In the case of large-size tokamaks, the FMSW electric field can be written, just as other perturbed quantities, in the form of a single harmonic

$$\vec{E}(r,\vartheta,\zeta) = \vec{\mathcal{E}}(r,\vartheta)\exp\left[i\left(\int \kappa_r dr + m\vartheta - l\zeta - \omega t\right)\right] \qquad (1)$$

where ζ is the coordinate along the major azimuth of the tokamak, ϑ is the poloidal coordinate.

The expression for perturbed distribution functions of

α-species particles f_α is derived from the kinetic equation by the method of characteristics as

$$f_\alpha = -\frac{e_\alpha}{2m_\alpha} \int_{-\infty}^{t} dt' \left[\vec{v}'(t') \frac{\partial f_{0\alpha}}{\partial \mathcal{E}} + \frac{\vec{v}_\perp'}{B} \frac{\partial f_{0\alpha}}{\partial \mu} \right] \vec{E}(t') \qquad (2)$$

where $\mathcal{E} = v^2/2$ is the total energy of the particle related to its mass, $\mu = v_\perp^2/2B$ is the transverse adiabatic invariant, $B = \bar{B}(1 + \varepsilon_t \cos\vartheta)$ is the magnetic field of the tokamak, $\bar{B}$ is its value on the torus axis, and $f_{0\alpha}(\mathcal{E},\mu)$ is the Maxwellian distribution function with $T_\perp \neq T_\parallel$.

The integral in (2) is extended along the unperturbed particle trajectory that combines the Larmor rotation and the guiding centre motion along the field line.

The guiding centre motion in the poloidal direction is given by

$$\frac{d\vartheta}{dt} = \frac{v_\parallel(\vartheta)}{qR} = \pm \frac{1}{qR} \left[\frac{2\varepsilon_t \mathcal{E}(2\varkappa^2 - 1 - \cos\vartheta)}{1 + \varepsilon_t(2\varkappa^2 - 1)} \right]^{1/2}. \qquad (3)$$

Here $\varkappa^2 = [\mathcal{E} - \mu\bar{B}(1-\varepsilon_t)]/(2\mu\bar{B}\varepsilon_t)$ defines the ion trapping (for trapped particles $0 \leq \varkappa \leq 1$), q is the stability factor.

Inside the narrow resonance region, if it is located far away from the $\vartheta = 0, \pi$ points, eq.(3) leads to the relation between ϑ and the running value of the coordinate

$$\vartheta' - \vartheta = \sigma f_1 v_b (t'-t) + \sin\vartheta \cdot v_b^2 (t'-t)^2/4 \qquad (4)$$

where $\sigma = \pm 1$, $f_1 = (2\varkappa^2 - 1 - \cos\vartheta)^{1/2}$,

$$v_b = (2\varepsilon_t \mathcal{E})^{1/2} / \{ q^2 R^2 [1 + \varepsilon_t (2\varkappa^2 - 1)] \}^{1/2}. \qquad (5)$$

The second term in eq.(4) is essential for the ions which experience a strong deceleration ($f_1 \ll 1$).

Using eqs. (1), (2) and (4) for the left- and right-handed polarized components of the plasma current density $j^\pm = j_r \pm i j_\vartheta$, we obtain the following expressions

$$j_\alpha^+ = -\sum_{n=-\infty}^{\infty} \frac{\pi e^2}{m_\alpha} \int_0^\infty v_\perp^3 dv_\perp \int_{-\infty}^{\infty} dv_\parallel \left(\frac{\partial f_{0\alpha}}{\partial \mathcal{E}} + \frac{1}{B} \frac{\partial f_{0\alpha}}{\partial \mu} \right) \left(J_{n-1}^2 E^+ + J_{n-1} J_{n+1} E^- e^{2i\psi} \right) \int_{-\infty}^{t} e^{iS(t,t')} dt', \qquad (6)$$

$$j_\alpha^- = -\sum_{n=-\infty}^{\infty} \frac{\pi e^2}{m_\alpha} \int_0^\infty v_\perp^3 dv_\perp \int_{-\infty}^{\infty} dv_\parallel \left(\frac{\partial f_{0\alpha}}{\partial \varepsilon} + \frac{1}{B}\frac{\partial f_{0\alpha}}{\partial \mu}\right)\left(J_{n-1}J_{n+1}E^+ e^{2i\psi} + J_{n+1}^2 E^-\right) \int_{-\infty}^{t} e^{iS(t',t)} dt' \qquad (7)$$

where $S(t',t) = -\omega(t'-t) + \kappa_\parallel q R(\vartheta' - \vartheta) + n\int_t^{t'} \omega_{c\alpha}(t'')dt''$, $\kappa_\parallel = (m - lq)/qR$, $J_n(\kappa_\perp v_\perp/\omega_{c\alpha})$ is the Bessel function, $\kappa_\perp^2 = \kappa_r^2 + m^2/r^2$, $\psi = \operatorname{arctg}(m/r\kappa_r)$. In (6) and (7) we have neglected the longitudinal component of the electric field $E_\parallel$, which is justified for FMSW.

Substituting (6) and (7) in the Maxwell equations, assuming $\kappa_\perp v_\perp \ll \omega_{c\alpha}$ and using the "cold" approximation for electron currents, we obtain the following dispersion equation

$$1 - \frac{\omega^2}{\kappa_\perp^2 v_A^2} = \frac{i}{\sqrt{\pi}} \frac{(n+1)(\kappa_\perp \rho_i)^{2n-2}}{2^{n-2} n!(n-2)!\sqrt{\varepsilon_t}} \eta \xi_\perp \int_{-\infty}^{\infty} dz\, z^{2(n+1)} e^{-z^2} \int_{\cos^2\frac{\vartheta}{2}}^{\infty} \frac{d\varkappa^2}{f_1(\varkappa) f_2^{2n+3}(\varkappa)} I(\varkappa, \vartheta, z, \kappa_\perp) \qquad (8)$$

where

$$I(\varkappa,\vartheta,z,\kappa_\perp) = \int_{-\infty}^{0} d\vartheta' \left[1 - \frac{2\omega^2}{(n+1)\kappa_\perp^2 v_A^2}\right] \exp\left[-i\xi_\perp\left(\frac{\Delta\omega}{\varepsilon_t \bar{\omega}_{ci}} - n\cos\vartheta - \frac{\kappa_\parallel q R}{\xi_\perp}\sqrt{\varepsilon_t}\frac{f_1}{f_2}z\right)\vartheta' - \right.$$

$$\left. - \frac{i\sqrt{\varepsilon_t}}{2}\xi_\perp \sin\vartheta\left(n\frac{f_1}{f_2}z - \frac{\kappa_\parallel q R}{2\xi_\perp}\frac{\sqrt{\varepsilon_t}}{f_2^2}z^2\right)\vartheta'^2 - \frac{i\varepsilon_t \xi_\perp z^2 n}{4 f_2^2}\left(\sin^2\vartheta + 2f_1^2\cos^2\vartheta\right)\vartheta'^3\right]. \qquad (9)$$

Here

$\xi_\perp = \varepsilon_t qR/(\sqrt{2}\rho_i)$, $\rho_i = v_{T\perp}/\bar{\omega}_{ci}$, $v_A = \bar{B}/(4\pi n_0 m_i)^{1/2}$, $\Delta\omega = \omega - n\bar{\omega}_{ci}$,

$v_{T\perp} = (T_\perp/m_i)^{1/2}$, $\eta = v_{T\perp}/v_{T\parallel}$, $f_2 = (\eta^2\varepsilon_t f_1^2 + 1 + \varepsilon_t\cos\vartheta)^{1/2}$

Let us put $\kappa_\perp = \kappa_0 + \Delta\kappa$, $|\Delta\kappa| \ll \kappa_0$, where $\kappa_0 = \omega/v_A$. Then, for $\Delta\kappa$ we have

$$\frac{\Delta\kappa}{\kappa_0} = i\frac{(n-1)(\kappa_\perp\rho_i)^{2n-2}}{\sqrt{\pi}\,2^{n-1} n!(n-2)!\sqrt{\varepsilon_t}} \eta\xi_\perp \int_{-\infty}^{\infty} dz\, z^{2(n+1)} e^{-z^2} \int_{\cos^2\frac{\vartheta}{2}}^{\infty} \frac{d\varkappa^2}{f_1 f_2^{2n+3}} I(\varkappa,\vartheta,z,\kappa_0). \qquad (10)$$

We shall write the expression for the damping factor given by the imaginary part of $\Delta k/k_0$ in the long wavelength limit, where $\kappa_\parallel qR \ll \sqrt{\xi_\perp}$. The damping factor χ_t, averaged over the magnetic surface and determined by the contribution from trapped ions ($\cos\vartheta/2 < \varkappa < 1$), is

$$\chi_t = \frac{(n-1)^2(2n+1)!!(\kappa_\perp\rho_i)^{2n-2}}{2^{2n+1} n!\,\varepsilon_t \sin\vartheta_0} \sum_{\kappa=0}^{n} \frac{(-1)^\kappa}{(2\kappa+1)(n-\kappa)!\kappa!} \left[\frac{\eta^2\varepsilon_t(1-\cos\vartheta_0)}{\eta^2\varepsilon_t(1-\cos\vartheta_0)+1}\right]^{\kappa+\frac{1}{2}} \qquad (11)$$

where ϑ_0 is the point of the local resonance. Hence, for the damping factor χ_c contributed by passing ions we have

$$\chi_c = \frac{(n-1)^2(2n+1)!!(\kappa_\perp \rho_i)^{2n-2}}{2^{2n+1} n!\, \varepsilon_t \sin\vartheta_0} \sum_{\kappa=0}^{n} \frac{(-1)^\kappa}{(2\kappa+1)(n-\kappa)!\,\kappa!} \left\{1 - \left[\frac{\eta^2 \varepsilon_t (1-\cos\vartheta_0)}{\eta^2 \varepsilon_t (1-\cos\vartheta_0)+1}\right]^{\kappa+\frac{1}{2}}\right\}. \quad (12)$$

Equations (11) and (12) lead to the criterion of the predominant contribution from trapped ions to the wave absorption

$$r > R\left[\frac{\sqrt{\pi}}{4}\frac{T_\parallel}{T_\perp}\frac{(n!)^2}{(2n+1)^2\Gamma^2(n+\frac{1}{2})} + \frac{\Delta\omega}{n\bar{\omega}_{ci}}\right]. \quad (13)$$

Besides, the condition $r \gtrsim R\frac{\Delta\omega}{n\bar{\omega}_{ci}}$ $(|\cos\vartheta_0| \leqslant 1)$ must be fulfilled. The criterion (13) has the same form in the short wavelength region and is not very sensitive to the resonance number. For the second-harmonic resonance (n=2) we have

$r > R\frac{T_\parallel}{14\,T_\perp} \mp R\frac{|\Delta\omega|}{n\bar{\omega}_{ci}}$ (the minus sign corresponds to the case when the resonance line is on the low field side, $\Delta\omega < 0$)

$r > R\frac{\Delta\omega}{n\bar{\omega}_{ci}}$

It is evident that for the central position of the resonance zone, and especially, for its location on the low field side ($\Delta\omega < 0$), the RF power in the greater part of the plasma volume is absorbed predominantly by trapped ions even in the Maxwellian plasma with $T_\perp = T_\parallel$. The effect of the predominant FMSW damping due to trapped ions increases as the $T_\perp/T_\parallel$ ratio grows.

If the resonance zone is on the high field side ($\Delta\omega > 0$), then the contribution of trapped ions to the wave damping factor may exceed that from passing ions in the plasma periphery.

Thus, in spite of their relative minority in the tokamak, the trapped ions may absorb an essential RF power fraction of FMSW at a multiple cyclotron resonance.

References

1. Cattanei, A., Croci, K., Nucl. Fusion 17 (1977) 239.
2. Kaladze, T.D., Pyatak, A.I., Stepanov, K.N., Ukr. Fiz. Zh. 28 (1983) 995.

ICRF ANTENNA SYSTEM FOR EXCITING SLOW WAVES IN A PLASMA

A.V.Longinov, V.A.Lukinov

Institute of Physics and Technology, the Ukrainian Academy of Sciences, Kharkov 310108, USSR

The possibility that slow waves (SW) can directly be excited in a magnetoactive plasma in the frequency range $\omega \sim \omega_{Bi}$ was first indicated in /1-4/. First experiments on stellarators /5,6/ and tokamaks /7,8/ have demonstrated this method of RF power coupling to the plasma to be a viable alternative to a conventional method of fast-wave excitation.

Here we investigate the antenna for SW excitation, designed as a set of metal screens arranged near the plasma surface /2/ (see fig. 1). RF power sources were connected to the slots between adjacent screens by coaxial or waveguide transmission lines. The reactive component of the antenna impedance can be compensated by means of reactances Z_c. This antenna design was first used experimentally in /5/.

Our statement of the problem and the methods of its solution are similar to those in /2/, with the difference that we investigate the $\omega_{Bi} \lesssim \omega < \omega_{pi}$ case. In this range, together with nonpropagating slow electromagnetic waves (SEW) there exist propagating slow kinetic (ion Bernstein) waves (SKW) in a plasma. Hence, in contrast to /2/, the solution of the Maxwell equations for a plasma is sought as a superposition of SEW and SKW fields with an additional condition $E'_x = 0$ at the plasma-vacuum boundary. As demonstrated in /2/, and later in /9/ where the problem of the SKW coupling by the antenna as a current layer was first investigated, the excitation of a fast wave can be neglected. The dispersion equation for the waves considered can be written in this case as

$$\delta\varepsilon N_\perp^4 - (\varepsilon_1 + \delta\varepsilon\,\varepsilon_{33}) N_\perp^2 + \varepsilon_{33}(\varepsilon_1 - N_\parallel^2) = 0 \,, \tag{1}$$

where

$$\varepsilon_1 = 1 + \frac{\omega_{pe}^2}{\omega_{Be}^2} - \frac{\omega_{pi}^2}{\omega^2 - \omega_{Bi}^2} \,, \quad \delta\varepsilon = \frac{3}{2}\frac{v_{Ti}^2}{c^2}\frac{\omega_{pi}^2\,\omega^2}{(\omega^2-\omega_{Bi}^2)(\omega^2-4\omega_{Bi}^2)} \,,$$

$$\varepsilon_{33} = 1 + \frac{2\omega_{pe}^2}{k_\parallel^2 v_{Te}^2}\left(1 + i\sqrt{\pi}\, Z_e W(Z_e)\right), \quad Z_e = \frac{\omega}{k_\parallel v_{Te}}, \quad W(x) = e^{-x^2}\left(1 + \frac{2i}{\sqrt{\pi}}\int_0^x e^{t^2} dt\right).$$

An important role in the SKW excitation may belong to surface-wave eigenmodes (SWEM) /2/. In the finite plasma temperature case, the dispersion equation for these modes has the form

$$k_{\perp 1} k_{\perp 2}\left(k_{\perp 2}^2 - k_{\perp 1}^2\right) + i\sqrt{k_\parallel^2 - \frac{\omega^2}{c^2}\varepsilon_{33}}\left(k_{\perp 2}^3 - k_{\perp 1}^3 + \frac{\omega^2}{c^2}\varepsilon_{33}\left(k_{\perp 1} - k_{\perp 2}\right)\right) th\left(\sqrt{k_\parallel^2 - \frac{\omega^2}{c^2}}\, d\right) = 0 \tag{2}$$

Here $k_{\perp\,1,2} = (\omega/c) N_{\perp\,1,2}$, where $N_{\perp\,1,2}$ are the roots of eq. (1). For SWEM, $\mathrm{Im}\, k_\parallel$ is nonzero and is determined by the SKW coupling to the plasma, and the damping length $\ell' = 1/\mathrm{Im}\, k_\parallel$ for moderate distances between the plasma and the screens d

appears rather great ($\ell' \gg \lambda_v = 2\pi c/\omega$), with $R_e N_{||} = R_e c k_{||}/\omega \gtrsim 1$ and increasing as d decreases. Here we analyse: active ($R_e Z$) and reactive ($I_m Z$) components of the input impedance of the slot related to the unit length along the y axis, the quantity $Q = |I_m Z|/R_e Z$ responsible for resonance properties of the antenna, and the efficiency η defined as a ratio of the power coupled to the plasma to the ohmic losses in the screens. In our analysis we have employed the following plasma parameters: $n_i = n_e = 4 \cdot 10^{11}$ cm^{-3}, $T_i = T_e = 200$ eV, $\omega/\omega_{Bi} = 1.95$, $B_0 = 4$ T. The operating gas is deuterium, stainless steel is chosen as a screen material. The phase shift between voltages in adjacent slots is equal to π . Long ($\ell \gg \lambda_v$) and short ($\ell \ll \lambda_v$) antennas as two most typical cases were considered.

Figure 2 shows $R_e Z$, $I_m Z$, Q and η versus the gap d for a long antenna ($\ell = 3\lambda_v = 1500$ cm). It may be seen that the input impedance takes on purely active values at $d \approx 0.62$ cm, and $d \approx 1.05$ cm (which corresponds to the resonance excitation of single SWEMs with $R_e N_{||} = 1.8$ and $R_e N_{||} = 1.5$) and also at $d \approx 0.5$ cm and $d \approx 0.77$ cm (the multimode resonance condition /2/). Between these d values, the input impedance is a complex quantity, the Q value being relatively small. For small d, the SWEM damping length ℓ' becomes comparable with the screen length ℓ , and this accounts for the reduction of the oscillation amplitude $R_e Z$ as a function of d. The efficiency η is rather high for small d, however, ohmic losses may become essential with the gap growth.

In fig. 3 $R_e Z$, $I_m Z$, Q and η are plotted against d for a short antenna ($\ell = 0.2\ \lambda_v = 100$ cm). In contrast to the case of a long antenna, the d dependence of Z is monotonous, and $I_m Z$ shows a capacitance-like behaviour, except for the d values below 0.3 cm. Note that here Q reaches higher values, and the efficiency η is also essentially higher.

Figs. 4-6 show the field /E_x/ distribution in the edge plasma for long (figs. 4, 5) and short (fig. 6) antennas. In all the figures the field amplitude complies with the requirement that the averaged specific RF power flow to the plasma should be 10 W/cm^2. Fig. 4 illustrates the case of a relatively large gap d = 0.77 cm with $\ell' \gg \ell$. The field structure displays the interference of two SWEMs with $N_{||} = 5/3$ propagating in opposite directions. Figure 5 depicts the field distribution for small d values, when $\ell' \lesssim \ell$. Here the field amplitude of the SWEM propagating along the screen over the length ℓ falls off by a factor of 10 as a result of the SKW excitation. The important characteristic property of the long antenna is the predominant excitation of small-$N_{||}$ waves, irrespective of the slot size δ and the screen length ℓ . This determines an insignificant Cherenkov absorption in the plasma edge region. As seen from fig. 6, the field structure along the z axis is more uniform here (d = 0.77 cm) than in the long antenna case. However, here again the SWEM plays a crucial role in the SKW excitation.

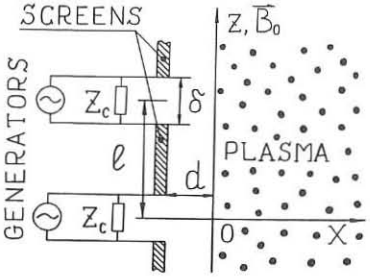

Fig.1

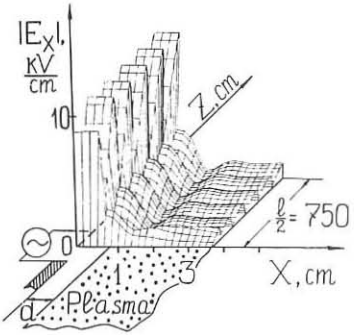

Fig.4

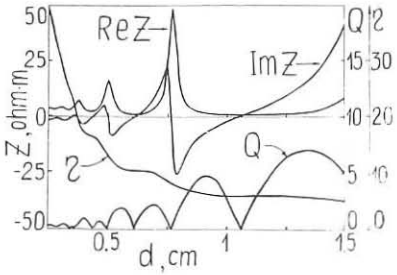

Fig.2

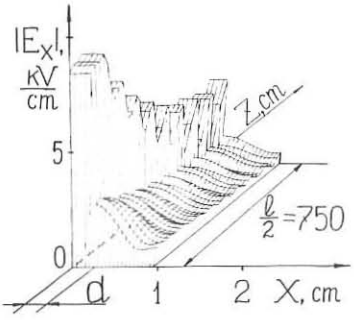

Fig.5

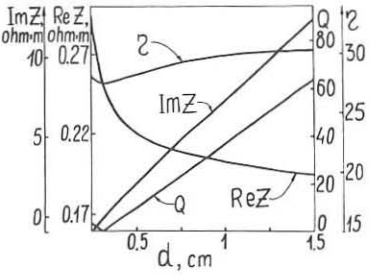

Fig.3

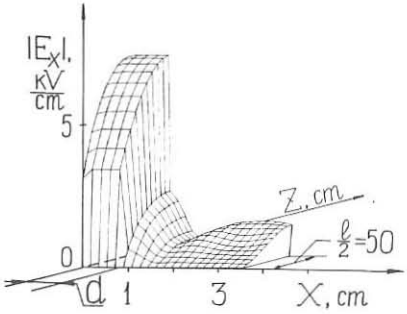

Fig.6

As is evident from figs. 4-6, the distinguishing feature of the SKW excitation in a sharp-boundary plasma is a great field E_x amplitude even at moderate RF power flows to the plasma. This situation , typical also of the loop antennas, can cause some undesirable effects (e.g., an enhanced impurity influx, arc discharges between plasma and screen surfaces, etc.) that would restrict the level of the power coupled to the plasma.

Further efforts are needed to improve the situation (e.g., the choice of optimum edge plasma parameters and profiles; the use of antennas with a well developed radiating surface, etc.), otherwise the possibility of a direct SKW excitation with high levels of RF power coupling may appear problematic.

References

1 Longinov, A.V., Stepanov, K.N., KhFTI Preprint 72-1, 2, Kharkov, 1972.

2 Longinov, A.V., Zh. Tekh. Fiz. 42 (1972) 1591.

3 Puri, S., Phys. Fluids 22 (1979) 1716.

4 Ono, M., et al., in Heating in Toroidal Plasmas (Proc. 2nd Varenna-Grenoble Int. Symp. Como, 1980), Vol.1 (1980) 593.

5 Burchenko, P.Ya. et al., Pis'ma Zh. Ehksp. Teor. Fiz. 16 (1972) 250.

6 Vojtsenya, V.S. et al., in Controlled Fusion and Plasma Physics (Proc. 5th Europ. Conf., Grenoble, 1972), Vol.1 (1972) 111.

7 Ono, M. et al., Phys. Rev. Lett. 54 (1985) 2339.

8 Ono, M. et al., in Plasma Physics and Contr. Nucl. Fus. Res. 1986 (Proc. 11th Int. Conf., Kyoto 1986), Vol. 1 (1987) 477.

9 Sy W.N.-C. et al., Nucl. Fusion 25 (1985) 795.

ICRF HEATING METHOD USING TWO-SPECIES ION ADMIXTURE

A.V.Longinov, S.S.Pavlov, K.N.Stepanov

Institute of Physics and Technology, the Ukrainian Academy of Sciences, Kharkov 310108, USSR

The plasma RF heating method, widely used in recent years, is based on the cyclotron absorption of the fast mode (FW) of the fast magnetosonic wave (FMSW) by minority ions (usually ^{3}He). This method, however, has considerable limitations in heating regimes with a high absorbed specific power due to the formation of high energy tails of the resonant particle (RP) distribution function (RP kinetic pressure rise, weakening of the Coulomb interaction between RP and bulk ions and RP bananas escape from the discharge, especially in relatively small traps). The report deals with the plasma heating method based on the cyclotron absorption of the slow mode (SW) of FMSW by ^{3}He ions.

Figure 1 shows the essence of the method, exhibiting the qualitative dependence of the transverse refractive index squared $N_\perp^2$ for FW and SW versus the major radius R in the tokamak equatorial plane. The (D+H) plasma (n_H/n_D = 0.5-0.8) with ^{3}He minority ions (n_{He}/n_D = 0.01-0.1) is used, the FW being excited from the HFS. The FW propagating into the plasma will pass, one by one, the FW-SW conversion layer (CL) in the vicinity of the D-H-^{3}He ion-ion hybrid resonance (1st CL), the fundamental ICR layer for ^{3}He ions located in the plasma column centre and, propagating to the plasma periphery, it will pass through the D-H ion-ion conversion layer (2nd CL).

For $T_{He} \gg T_d$, the FW-SW conversion effects in the 1st CL may be relatively weak. Besides, at higher ^{3}He concentrations, the FW absorption in the ICR layer for ^{3}He may also be relatively weak. Therefore, the decisive role in the RF power absorption will belong to the effects related to the FW-SW conversion in the 2nd CL and a subsequent SW absorption in the $\omega \approx \omega_c$ layer for ^{3}He ions. Since the SW is a small-scale one, its absorption by the minority ions will lead to the cut-off of high energy tails of the RP distribution function (cf. the method of heavy-ion minority heating /1/). As opposed to the method using cyclotron FW absorption, this cut-off will make it possible to increase essentially the portion of the power heating the bulk ions, to limit the RP kinetic pressure value and to diminish the energy losses due to fast RP leaving the trap. To realize high-power heating regimes, it is important that SW could reach the ICR layer even for relatively high ^{3}He minority concentrations /2/. This heating scenario can be realized in relatively small-size traps (see below).

The feasibility of the scenario suggested can be exemplified by the Tuman-3 tokamak /3/ with R_o =55 cm, a =20 cm, B_o = 0.9 T, $n_e(0) = 3 \cdot 10^{13}$cm^{-3}, n_H/n_D = 0.5 , $T_e = T_i$ = 200 eV, T_{He} = 1 keV. Figure 2 shows the results of calculations for

the FMSW excitation, propagation and absorption in the HFS regime for the toroidal number m=4. The calculations were carried out for the plasma cylinder model described in /2/. The figure shows the main field components E_z and E_r, the kinetic RF power flux (P_k) and the profiles of the energy absorbed by ions (D_i). Figure 2 exhibits practically a single-pass absorption of the excited wave due to the FW-SW conversion in the 2nd CL, R = 65 cm (no interference effects in the field E_z structure). The SW excitation effect displays itself in short wavelength field E_r oscillations and in the onset of P_k. The FW absorption due to the conversion in the 1st CL and damping in the $\omega \approx \omega_{CHe}$ layer are weak in this case (small bump in D_i). Figure 3 differs from Fig. 2 in that the FMSW is excited from the LFS. In this case, the conversion effects in the 2nd CL are also predominant and the energy deposition profile is close to that for the HFS excitation regime. Note that the energy deposition profile shows an essential asymmetry relative to the point where $\omega = \omega_{CHe}$, and this can be used, in principle, for current drive /4/.

Now compare two heating scenarios using the cyclotron absorption of FW and SW by ^{3}He minority ions at a high level of RF power deposited in the plasma. The solution of the one-dimensional kinetic equation for the RP distribution function $f(V_\perp)$ with the boundary condition $f'(V_\perp) = 0$ $(V_\perp > V_{LOS})$ takes into account the banana losses. The V_{LOS} is the maximum $V_\perp$ value of ^{3}He ions in the plasma core whose banana trajectories do not extend beyond the plasma column. Figure 4 presents the results obtained for the plasma with $n_H/n_D = 0.7$, $n_e = 3 \cdot 10^{13}$ cm^{-3} and $T_e = T_i = 500$ eV, the specific RF power, P_{RF}, absorbed by ^{3}He ions ($n_{He}/n_D = 0.05$) being 1.5 W$\cdot$cm^{-3}. In Fig. 4, P_D/P_{RF} and P_i versus V_{LOS} are presented for both cases (P_D is the RF power deposited in deuterons, protons and electrons, P_i is the specific RF power deposited in deuterons and protons; $K_\perp \varrho_D$ was assumed to be 0.37 in the absorption layer, where $\omega = \omega_{CHe}$).

As seen from Fig. 4, in the FW case, the portion of RF power carried away by RP from the discharge becomes appreciable even at rather high V_{LOS} values ($V_{LOS}/V_{TD} = 14$). At $V_{LOS} < 12\ V_{TD}$ this portion becomes predominant. By contrast, in the SW case, the RP losses become important at considerably lower V_{LOS}. Figure 4 exemplifies the V_{LOS} effect on the particles with $V_\parallel = 0$ being in the centre of the column at a plasma current I = 120 kA in the Tuman-3 tokamak. It may be seen that under these conditions and with FW heating in high-power regimes ($P_{RF} \sim 1$W$\cdot$cm^{-3}), the RF power losses due to RP escape become essential, whereas in the SW case, the losses are substantially lower. Even when the losses are negligible for the both cases, the P_i value is also higher in the SW absorption case. Thus, the employment of the proposed method of RF plasma heating may provide regimes with a relatively high

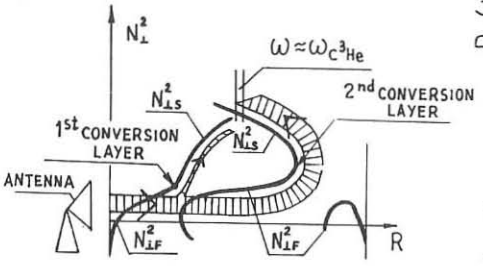

Fig. 1

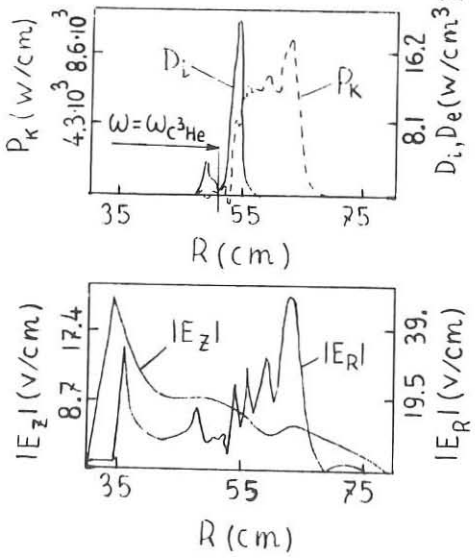

Fig. 2 $n_{He}/n_D = 0.15$

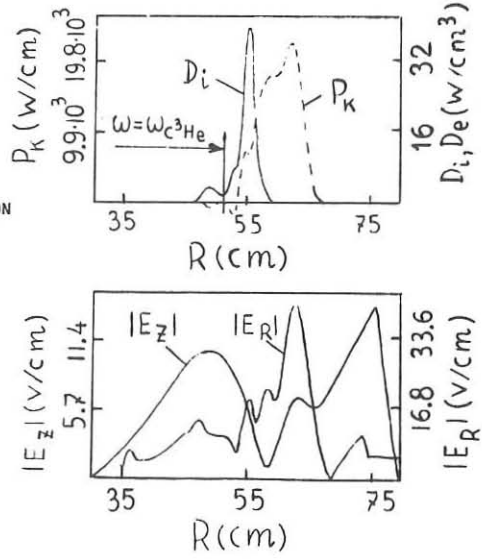

Fig. 3

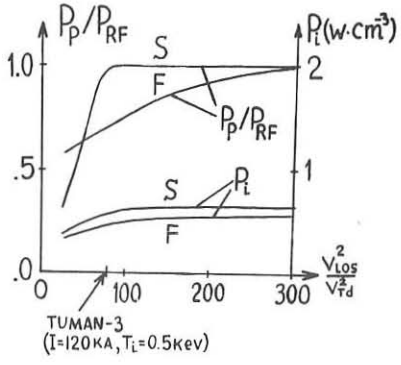

Fig. 4

specific power absorbed in the plasma and a predominant heating of the majority ions. This heating scenario may be especially efficient in small-size tokamaks and stellarators.

A similar scenario with the FW excitation and its subsequent conversion to SW may be realized in a D+H plasma with ^{3}He replaced by tritium (the power will be absorbed in this case at the second cyclotron harmonic for tritium ions). In this case, the method proposed seems particularly attractive for the realization of a two-component regime of a thermonuclear reactor /1/, where direct excitation of high-power SW presents serious problems.

References

1. Longinov, A.V. et al., in Controlled Fusion and Plasma Physics (Proc. 12th Europ. Conf., Budapest, 1985), Pt. 2, European Physical Society (1985) 132.

2. Longinov, A.V., Pavlov, S.S., Stepanov, K.N., Vopr. Atomn. Nauki i Tekhn., ser. Termoyad. sintez, Is.2 (1987) 3.

3. Askinasi, L.G. et al., in Plasma Phys. and Contr. Nucl. Fusion Research (Proc. 11th Int. Conf., Kyoto, 1986), vol. 1 (1987) 607.

4. Longinov, A.V. et al., in Contr. Fusion and Plasma Heating (Proc. 13th Europ. Conf., Schliersee, 1986), v. 10C, pt.2 (1986) 185.

APPLICATIONS OF THE 3-DIM ICRH GLOBAL WAVE CODE FISIC AND COMPARISON WITH OTHER MODELS.

T. Krücken, M. Brambilla

IPP Garching, EURATOM Association, Fed. Rep. of Germany

INTRODUCTION. The code FISIC solves the integro-differential wave equations for h.f. waves in the ion cyclotron frequency range in the finite Larmor radius approximation in tokamak geometry. The equations are discretised by a semispectral approach, using cubic Hermite finite elements in the radial direction, and an expansion in Fourier modes in the poloidal direction. The latter allows the analytic evaluation of the orbit integrals along magnetic field lines in the presence of a poloidal component of the static magnetic field. The code is thus able to describe mode conversion to ion Bernstein waves, ion cyclotron damping at the fundamental and at the first harmonic, and electron transit time and Landau damping, in full toroidal geometry. A detailed description of the model and the numerical method will be given elsewhere /1/. First results from FISIC were presented in /2/. Since then a few improvements have been made, particularly in the description of collisional and electron damping.

Here we present two simulations of ICH in ASDEX (R = 167 cm, a = 40 cm, B_0 = 2.24 and 2.265 T, I_p = 350 and 380 kA, $n_e(0) = 6 \cdot 10^{13}$; other parameters specified below), the first with low, the second with high single transit absorption according to simple estimates. For both cases we have run several toroidal modes, roughly scanning the spectrum excited by the antenna. We have used throughout between 80 and 100 radial elements, and 33 poloidal modes, ensuring good convergence within reasonable CPU time. The results are compared with those from two simpler codes, based on a slab model and on ray tracing, respectively. Agreement is good on the whole, but interesting purely toroidal effects are also identified, particularly on the efficiency of mode conversion and the propagation of ion Bernstein waves.

SECOND HARMONIC HEATING OF A D^+ PLASMA. The first example is a pure Deuterium plasma with T_D = 2 KeV heated at the second harmonic cyclotron resonance (f = 33.5 Mhz). In this case we expect weak single pass absorption, good efficiency of mode conversion to IBW, and excitation of global eigenmodes. These are indeed clearly seen as peeks in the power spectrum scanning the toroidal modes (Fig. 1). Comparison with the slab-model calculations shows qualitative agreement, although matching of the individual peaks cannot be expected due to the different geometry. Fig. 2 shows contour plots of the real part of E_x for one of the two resonant modes, n_φ = 14. The pattern is dominated by the poloidal modes $m = \pm 1$ (as

confirmed by examination of the poloidal spectrum). IBW are clearly visible to the high field side of the resonance, although for this mode their amplitude is small.

The total antenna resistance is found to be $R_A = 2.36$ Ohm, against $R_A = 7.6$ Ohm in the slab model. The latter value is closer to the experimental one. The discrepancy might be due to the fact that the model of the antenna is more idealised in the fully toroidal code. Of the total power, 81.3% is absorbed by the ions, 4.4% by electron TTMP, 0.1% by ELD and 15% by damping of the IBW, which is a direct measure of mode conversion. In slab geometry model conversion to IBW is considerably more efficient (62.2%), mainly due to modes with low n_φ ($|n_\varphi| \lesssim 5$). This illustrates one essential difference between slab and fully toroidal simulations: in the latter even $n_\varphi = 0$ corresponds to a quite broad spectrum of $k_\parallel$ values, a feature which considerably reduces the efficiency of mode conversion.

SECOND HARMONIC HEATING OF H^+ IN A D^+ PLASMA. The second example is a two component plasma consisting of 25% H and 75% D, preheated by neutral beam injection to central temperatures of 8.8 KeV and 4.4 KeV, respectively. ICRH is applied at $\omega \approx 2\Omega_{cH}$ ($f = 67$ Mhz). In this case the single pass absorption is large even for low toroidal modes, suppressing mode conversion; therefore excitation of cavity eigenmodes is not expected. This is confirmed by the n_φ power spectrum (Fig. 3), which shows almost no structure. Agreement with the slab simulation is even better than in the previous example, the major discrepancy occuring again for $n_\varphi = 0$. In slab geometry this mode with $k_\parallel = 0$ is very poorly damped (mainly by residual mode conversion); being non resonant, it is also poorly coupled. Broadening of the effective $k_\parallel$ spectrum in the real toroidal geometry leads to much better damping by IC harmonic heating, so that the minimum in the power spectrum at $n_\varphi = 0$ is nearly washed out. In the toroidal simulation therefore the radiated power is almost completely absorbed by harmonic ion cyclotron heating (98.3%); the rest is absorbed by electron TTMP (0.9%) and direct IBW damping (0.8%). For the total antenna resistance we obtain $R_A = 8.19$ Ohm, compared to $R_A = 10.2$ Ohm in the slab simulation.

Finally, Fig. 4 shows contour lines of the imaginary part of E_x for $n_\varphi = 16$. The large single transit absorption is evident here. Moreover, both the wave pattern and the power deposition profiles are in this case very similar to those obtained with ray tracing applying the code RAYIC /3/.

REFERENCES.

/1/ M. Brambilla, T. Krücken, submitted for publication.

/2/ M. Brambilla, T. Krücken, Proc. 14th Europ. Conf. on Controlled Fusion and Plasma Physics, Mardid 1987, Vol. 3, p. 996.

/3/ M. Brambilla, Comp. Phys. Reports 4 (1986) 1.

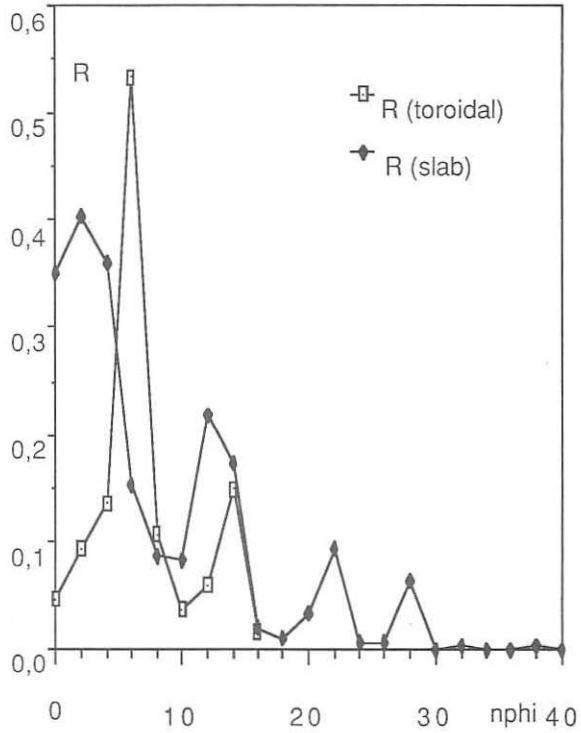

Fig. 1 Power spectrum. Harmonic heating of a Deuterium plasma, T(0)=2 keV.

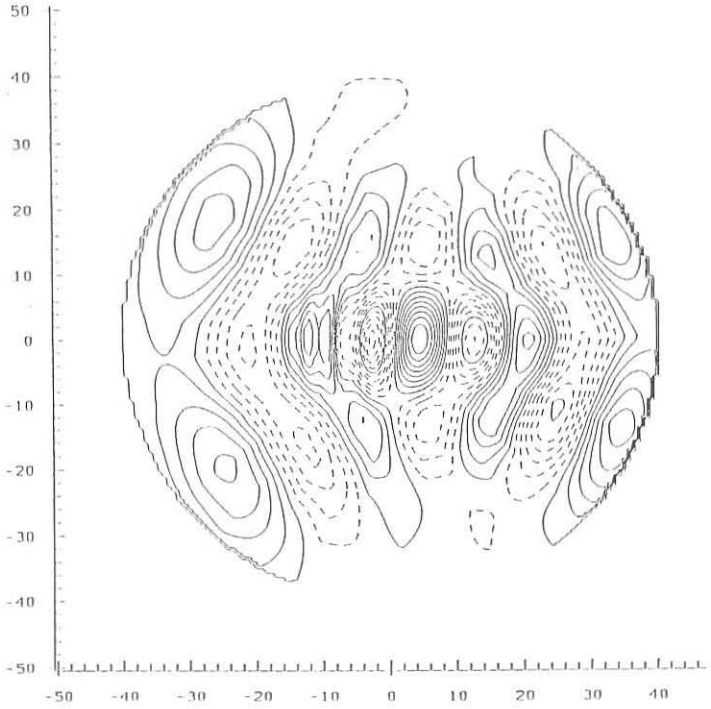

Fig. 2 - Re(E+) pattern in the poloidal cross-section for the resonant mode n = 14 .

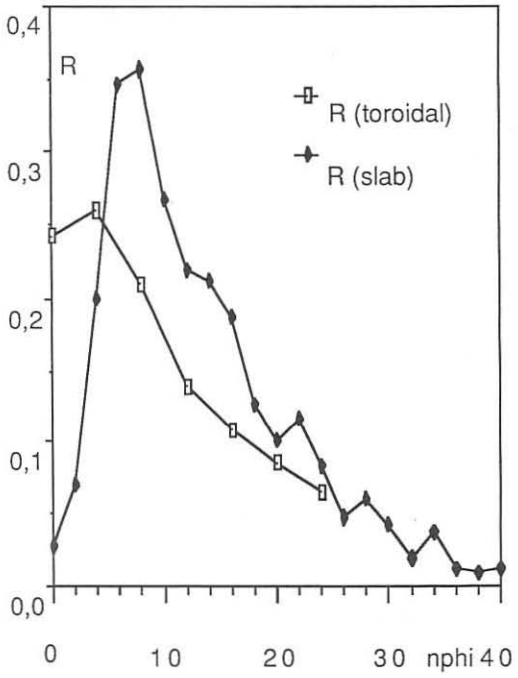

Fig. 3 - Power spectrum. Harmonic heating of H (25%, T(0)=8.8 keV) in D (75%, T(0)=4.4 keV)

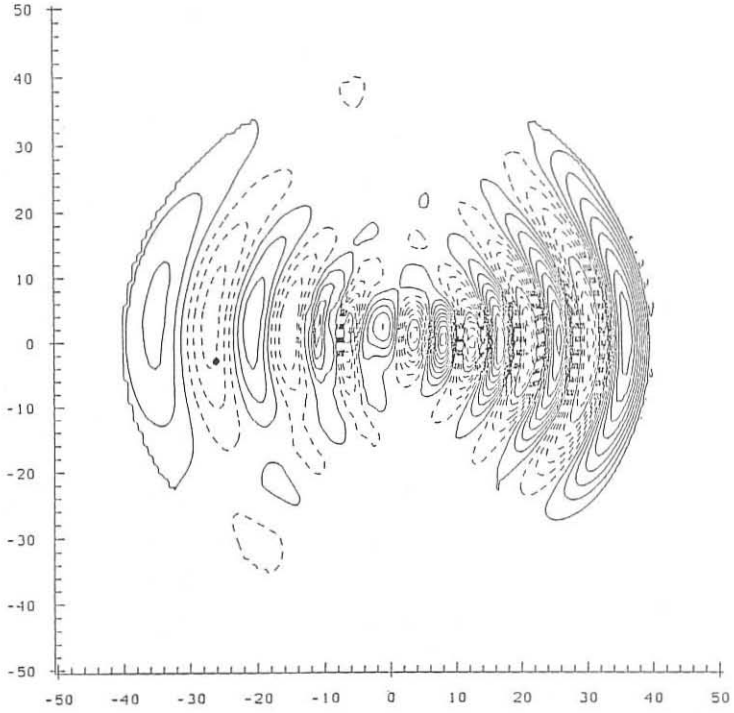

Fig. 4 - Re(E+) pattern in the poloidal cross-section, n = 16.

PARTICLE ACCELERATION NEAR THE FARADAY SHIELD VIA CYCLOTRON HARMONIC INTERACTION DURING ICRF PLASMA HEATING

Satish Puri
MPI für Plasmaphysik, EURATOM Association, Garching bei München

Energy absorption in the edge region via cyclotron-harmonic interaction during ICRF heating of thermonuclear plasmas is examined. It is shown that the electric field ripple caused by the closely spaced Faraday shield conductors gives rise to large effective perpendicular wavenumbers, resulting in strong cyclotron harmonic damping. Analytical expression for the particle acceleration rate, taking into account the radial evanescence of the perpendicular electric field, is derived. For the ASDEX fast wave ICRF heating parameters, it would be possible to accelerate the $Z = 3$ carbon impurities to energies in excess of $100\,eV$ in less than $10\,\mu S$. These observations have been confirmed through accurate numerical integration of the particle's equations of motion. The role of the plasma sheath is considered and a simple Faraday shield design capable of mitigating both the cyclotron-harmonic interaction and the sheath effects is suggested. Implications of direct impurity heating in the vicinity of the Faraday shield for the case of low-frequency heating schemes such as the Alfvén wave heating are examined.

1. CYCLOTRON HARMONIC INTERACTION

We consider the linearized motion of a particle in a uniform magnetic field B_0 and an electric field $E(\vec{r},t) = \int d\vec{k}\, E(\vec{k}) \exp\{i(\omega t - \vec{k}\cdot\vec{r})\}$, where $\vec{k} = k_x\,\hat{x} + k_y\,\hat{y} + k_z\,\hat{z}$ and the hats represent unit vectors. Let $E_{r,l} = E_x \pm iE_y$, $k_\perp^2 = k_x^2 + k_y^2 = k_0^2 - k_z^2$, $\tan\psi = k_y/k_x$, and $\vec{k}\cdot\vec{r} = k_\perp r_g \sin(\omega_c t + \psi) + k_z v_z t$, where r_g is the gyroradius, ω_c is the cyclotron frequency and v_z is the particle's velocity along B_0. Change in the perpendicular velocity $v_\perp = v_x + iv_y$ may be expressed in the form

$$\Delta v_\perp = \frac{1}{2}\eta \exp(-i\omega_c t) \int d\vec{k} \sum_n J_n(k_\perp r_g) \exp(-in\psi)$$

$$\times \int dt \left[E_r(\vec{k}) \exp\{i(\omega + \omega_c - n\omega_c - k_z v_z)t\} \right.$$

$$\left. + E_l(\vec{k}) \exp\{i(\omega - \omega_c - n\omega_c - k_z v_z)t\} \right] , \qquad (1)$$

where $\eta = Ze/MA$, is the charge to mass ratio and $J(k_\perp r_g)$ is the Bessel function of the first kind and order n.

The electric field spectrum $E(\vec{k})$ in Eq.(1) is weighted by the modulation factor $\mathcal{M} = J_n(k_\perp r_g)\exp(-in\psi)$. Since, in the case of the ICRF antenna near field, k_x is

imaginary while k_y is real by definition, ψ assumes imaginary values. One obtains $\exp(-2i\psi) = (k_x - ik_y)/(k_x + ik_y)$. Writing $k_x = i|k_x|$, and for the case $k_y < 0$, $\exp(-2i\psi) = (|k_x| + |k_y|)/(|k_x| - |k_y|)$. For $|k_y| \gg |k_x|$, $\exp(-2i\psi) = -4k_y^2/k_\perp^2$. Approximating the Bessel function as $J_n(k_\perp r_g) \approx (k_\perp^n r_g^n)/(2^n n!)$ gives $\mathcal{M} \approx (i|k_y|r_g)^n/n!$.

For fast wave ICRF antennas, large electric field gradients with correspondingly large $|k_y|$, occur directly in front of the Faraday shield. Assuming $n = 2$, $\omega = 3\omega_c$ and Δt the time available for acceleration, Eq.(1) yields

$$|\Delta v_\perp| \approx |.25\eta(k_y r_g)^2 E_l|\Delta t \ . \tag{2}$$

Upon integrating the differential equation obtained after replacing r_g by $v_\perp/\omega_c$ in Eq.(2), one obtains

$$t_{10} \approx 1.9\eta^{1/2} Z^{1/2} \frac{B_0^2}{k_y^2 E_l} T_i^{-1/2} \ , \tag{3}$$

where t_{10} is the time required for a tenfold increase in the kinetic temperaure T_i defined as $T_i = (1/2)MAv_\perp^2/e$, measured in electron volts.

For the ASDEX fast wave ICRF heating at the fundamental hydrogen cyclotron frequency $\omega = \omega_{cH}$, impurity harmonic resonances C_5^{3+}, C_3^{5+}, and O_4^{5+} (the subscripts denote the cyclotron harmonic number while the superscripts stand for the particle charge) occur at some location along the azimuthal arc spanned by the antenna. The dominant among these is the $Z = 5$, third harmonic carbon resonance C_3^{5+}. For the ASDEX parameters, $B_0 = 2.5\,T$, $|k_y| \approx 10\,cm^{-1}$, corresponding to a $3mm$ gap between the adjacent Faraday shield conductors and $E \approx 300\,V\,cm^{-1}$, it would take the carbon impurity atom approximately $5.0\,\mu S$ to be accelerated from $1\,eV$ to $10\,eV$. In further $2.9\,\mu S$ and $0.5\,\mu S$, respectively, the particle will attain energies corresponding to $100\,eV$ and $1\,keV$, respectively.

In the case of the second harmonic heating at $\omega = 2\omega_{cH}$, the deuterium resonance D_5^+ would be the dominant harmonic resonance. Starting with $100\,eV$ energy, the deuterium ion will require about $60\,\mu S$ to be accelerated to $1\,keV$. The initial $100\,eV$ will have to be supplied via the sheath acceleration process.

In the foregoing examples it was assumed that the particle orbit possesses the optimal phasing with respect to the electric field for maximum acceleration.

These results have been confirmed through accurate numerical integration of the particle's equations of motion in a steady, uniform magnetic field and an electric field produced by applying a voltage across two infinite cylindrical conductors (Fig. 1).

A simple solution to the problem presented by the cyclotron-harmonic interaction might consist in using a Faraday screen consisting of thin, inclined vanes in the form of a Venetian blind (Fig. 2). E_y in this case is substantially uniform, thereby effectively suppressing the cyclotron-harmonic acceleration.

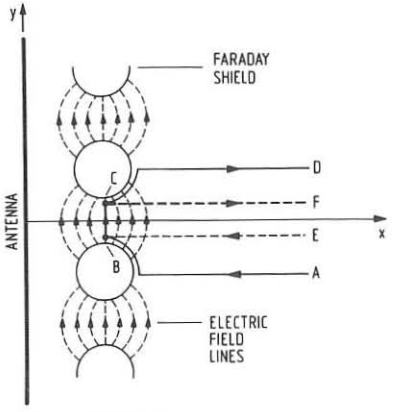

Fig.1 ASDEX antenna configuration

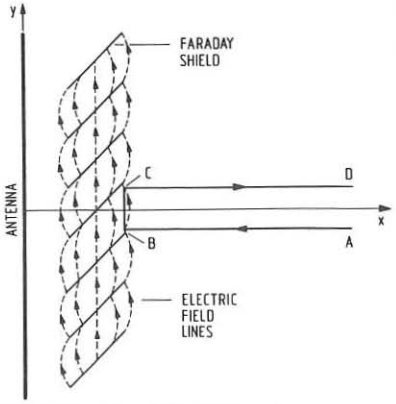

Fig.2 Venetian blind Faraday screen

2. PLASMA SHEATH EFFECTS

In the contour $ABCD$ (A, D, E and F extend to infinity) in Fig. 1, the electric field is primarily concentrated along BC and $\int E_{BC} \cdot dl \approx \int \mu_0 H \cdot da$, in the absence of a plasma sheath. If the contour $EBCF$ were to be used for estimating the electric field along BC, the diminished contribution of the magnetic induction is compensated for by the x-component of the electric field along EB and CF; which, of course, disappears in the presence of a plasma sheath, leaving only the magnetic induction component contributing to the field between BC, as was also the case in the absence of the Faraday shield. The missing electric field component along $ABCD$ reappears as the tangential electric field in the sheaths along the curved parts of the contour. Neglecting the small contribution to the magnetic induction from the induced Faraday shield currents [1], the following picture emerges in the presence of the sheaths:

(i) There is no material reduction in the electric field along BC in comparison with the field present in the absence of the Faraday shield.

(ii) The contributions from the contours ABE and FCD end up as sheath potentials (not necessarily symmetric). Together these potentials add up to the fields short-circuited by the Faraday shield conductors.

For the Venetian blind Faraday shield configuration of Fig. 2, since the short-circuited fields extend only over the thickness of the vanes, the sheath potentials would be correspondingly small. Thus the integration $\oint E \cdot dl$ along the contour $ABCD$ in Fig.2 is not materially affected by the introduction of the Faraday screen; the potential gradients making negligible contribution to the predominantly rotational electric fields.

3. IMPURITY ACCELERATION FOR LOW-FREQUENCY HEATING

For the low-frequency electric fields, the velocity gained by the particle in half a cyclotron period is given by $\Delta v_\perp \approx 2E_\perp/B_0$. This corresponds to an energy gain of

$$\Delta T_i \approx 2 \times 10^{-8} \, (E_\perp/B_0)^2 \, A \, . \tag{4}$$

The energy gained in this case is independent of the degree of ionization and increases with A. Thus the low Z iron impurities could be accelerated to potentially damaging energies, unless care is exercised in limiting the electric field to

$$E_\perp \leq 7.1 \, (T_{max}/A)^{1/2} \, B_0 \, kV/m \, , \tag{5}$$

where T_{max} is the maximum admissible impurity ion energy. Assuming $T_{max} = 50\,eV$ corresponding to a sputtering yield of $< 1\%$ for the iron impurity ions, $E_\perp \leq 17\,kV/m$ for the ASDEX parameters, allowing a coupling of over $3\,MW$ per antenna. The recycling problem may be further alleviated by coating the Faraday screen with a low atomic weight material such as carbon.

4. DISCUSSION

Indirect evidence of cyclotron-harmonic acceleration is indicated by the selective etching of the Faraday shield at two symmetric azimuthal locations possibly corresponding to the third harmonic deuterium resonances for the case of $\omega = 2\omega_{cH}$ ICRF heating in ASDEX [2]. High energy deuterons, presumably generated in the edge region, have also been observed in ASDEX.

The large sheath potentials could also lead to a uniform sputtering of the Faraday shield by direct ion acceleration [3]. Under appropriate conditions, the sheaths could eject high energy ions which, in turn, would undergo rapid cyclotron-harmonic interaction. A better understanding of the role played by the sheaths must await availability of precise experimental data.

ACKNOWLEDGMENT

I am pleased to acknowledge the helpful suggestions offered by Prof. R. Wilhelm and Dr. D. W. Faulconer during the course of this work.

REFERENCES

[1] FAULCONER, D. W., J. App. Phys. 54 (1983) 3810.
[2] BEHRISH, R. (private communication)
[3] NEUHAUSER, J. (private communication)

INTEGRO-DIFFERENTIAL EQUATION APPROACH TO ELECTROSTATIC WAVE PROBLEMS IN ICRF

O. Sauter and J. Vaclavik

Centre de Recherches en Physique des Plasmas
Association Euratom - Confédération Suisse
Ecole Polytechnique Fédérale de Lausanne
21, Av. des Bains, CH-1007 Lausanne, Switzerland

Abstract

We solve the linear electrostatic wave equation for an inhomogeneous bounded plasma in an inhomogeneous magnetic field using a hot model valid to all orders in Larmor radius. This leads us to solving a homogeneous second order integro-differential equation with two boundary conditions. Thus we are able to find wave solutions, for any given density and temperature profiles, having wavelengths even smaller than the Larmor radius.

1. Introduction

The linear wave equations in the Ion Cyclotron Range of Frequency (ICRF) have been thoroughly studied using first cold models and then hot models. We are now able to solve the full electromagnetic 1-D problem, i.e. three components for the fields, using the hot model with an expansion in Larmor radius up to second order [1]. This implies a very complicated form for the dielectric tensor [2] and it would not be reasonable to go to third or higher orders, even though we can find cases where the second order expansion breaks down. Moreover Bernstein waves, which may have wavelengths comparable to Larmor radius, are not only important in the well-known mode conversion mechanism, but may also be used to heat the plasma via direct launching [3]. Therefore, there is a need for a hot model valid to all orders in Larmor radius.

2. Physical Problem

We study the electrostatic wave problem of an inhomogeneous bounded plasma in a slab geometry. The magnetic field is parallel to the z-axis and the plasma is inhomogeneous along x and extends from $x=x_{pl}$ to $x=x_{pr}$. We first solve Vlasov and Poisson equations in Fourier space [4]. As the plasma is bounded we have to transform back to real space, which is done by using the following integral representation of the modified Bessel function $I_j(z)$:

$$I_j(z) = \frac{1}{\pi} \int_0^{\pi} e^{z \cos\theta} \cos(j\theta)\ d\theta$$

Assuming a Maxwellian equilibrium distribution function and neglecting the electron Larmor radius and k_y, we get:

$$-\left((1-\frac{\omega_{pe}^2\,\omega}{\omega_{ce}^2\,k_z v_{Te}}Z_{0e})\Phi'(x)\right)' + \left(k_z^2+\frac{(1+\frac{\omega}{k_z v_{Te}}Z_{0e})}{\lambda_{De}^2}\right)\Phi(x) \tag{1}$$

$$+\int_{x_{pl}}^{x_{pr}} K(x,x')\Phi(x')dx' = 0$$

with

$$K(x,x') = \frac{1}{2\pi^2}\sum_{\sigma}\sum_{j}\int_{x_{pl}}^{x_{pr}}dx'' \frac{(1+\frac{\omega}{k_z v_{T\sigma}}Z_{j\sigma})}{\lambda_{D\sigma}^2\rho_\sigma^2} \tag{2}$$

$$\cdot\int_0^\pi d\theta\,\frac{\cos(j\theta)}{\sin\theta}\exp\left(-\frac{(x-x')^2(1+\cos\theta)}{4\rho^2\sin^2\theta}\right)\exp\left(-\frac{(x''-\frac{x+x'}{2})^2(1-\cos\theta)}{\rho^2\sin^2\theta}\right)$$

and $Z_{j\sigma} = Z(\omega-j\omega_{c\sigma}/k_z v_{T\sigma})$, where the subscript e stands for electrons and σ for ions species. ω_p, ω_c, v_T, λ_D are the plasma and cyclotron frequencies, thermal velocity and Debye length respectively. Z is the plasma dispersion function corresponding to the NRL formula.

We see that the kernel is symmetric and rather complicated. The theta-integral is singular at $\theta=0$, $x=x'$ and at $\theta=\pi$, $x''=(x+x')/2$. These singularities give a global singularity of the kernel $K(x,x')$ proportional to $\ln|x-x'|$, which is a weak and integrable singularity. But if we integrate over theta directly, the θ-singularities are proportional to $1/\theta$, which are not integrable numerically. Therefore, we have to do at least two integrations analytically or use special changes of variables. As we use a finite element method (with linear basis functions) to solve (1) numerically, we can manage to perform the integrations over x" and x' analytically. Thus we take care of both singularities and end up with a well-posed numerical problem.

We have chosen the following boundary conditions:

$$\Phi'(x_{pl}) = 0$$
$$\Phi'(x_{pr}) = -1$$

which means that we specify some surface charges simulating an antenna on the right plasma boundary.

3. Results

We shall present the results of an argon plasma. The typical parameters used are: $x_{pr}=-x_{pl}=3cm$; density: $n=10^{17}m^{-3}$; $k_z=100m^{-1}$; $B_o=0.2T$; $T_e=14eV$; $T_i=0.1eV$. The dispersion relation is shown in Fig. 1. We consider the region between the third and fourth harmonics. We take the sum over j in Eq. (2) between -10 and +10. Note that this summation is not time-consuming at all, enabling us to solve (1) at any harmonics.

We have chosen these parameters because the two branches are decoupled and because both waves have comparable amplitudes, which is not always the case. We shall change the magnetic field and the electron and ion temperature profiles illustrating the effect of the boundary, cyclotron damping and the influence on the wavelengths of the ion-acoustic and the Bernstein waves.

Let us first look at the dependence of the waves, in particular of their wavelengths, on the electron and ion temperature profiles. The ion acoustic wave is mainly affected by the electrons, whereas the Bernstein wave depends on the ions. This is clearly shown in Fig. 2 where we have an electron temperature profile going up from 2eV on the right hand side of the plasma (i.e. at the antenna) to 30eV on the left, and for the ions from 0.05eV to 0.5eV. This gives us, from the dispersion relation, wavelengths for the ion acoustic wave from 0.9cm to 3.7cm and for the Bernstein wave from 2mm to 6mm respectively. The wavelengths calculated from the solution, Fig. 2, follow well these variations, i.e. follow well the temperature profiles.

Modifying the value of the magnetic field allows us to change the ratio $\omega/\omega_{ci}=3.95$ at one edge to 3.60 at the other edge of the plasma. In the region where $\omega/\omega_{ci}=3.95$ we expect the Bernstein wave to be strongly damped. This explains why only the acoustic wave is emitted in the Low Field Side (LFS) case, Fig. 3a, whereas both waves are excited at the antenna in the HFS case, Fig. 3b. On the left plasma boundary, both waves can be reemitted. But due to the cyclotron damping mentioned above, the Bernstein wave can reappear only in the region $\omega/\omega_{ci}=3.60$, Fig. 3a.

Conclusion

We are able to solve the electrostatic wave equation in a 1-D inhomogeneous bounded plasma with hot plasma model valid to all orders in Larmor radius. Therefore, we can resolve consistently wave solutions having wavelengths even smaller than the Larmor radius.

References:

[1] K. Appert et al., in Proc. 7th Int. Conf. on Plasma Phys., Kiev 1987, Invited Papers.
[2] Th. Martin , J. Vaclavik, Helv. Phys. Acta 60 (1987) 471.
[3] M. Ono et al., Phys. Rev. Lett. 60 (1988) 294.
[4] F. Yasseen, J. Vaclavik, Phys. Fluids 26 (1983) 468.

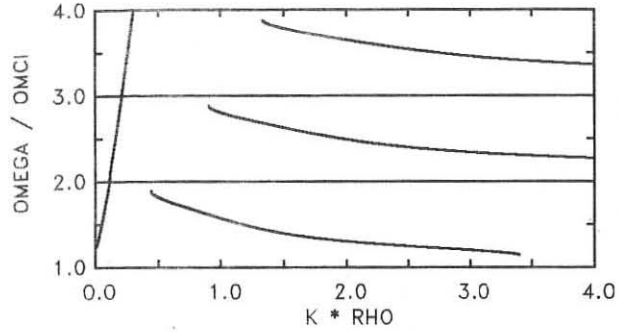

Fig. 1:
Dispersion relation, ω/ω_{ci} versus $k_x \cdot \rho_\sigma$, of the homogeneous argon plasma with ρ_σ=1mm.

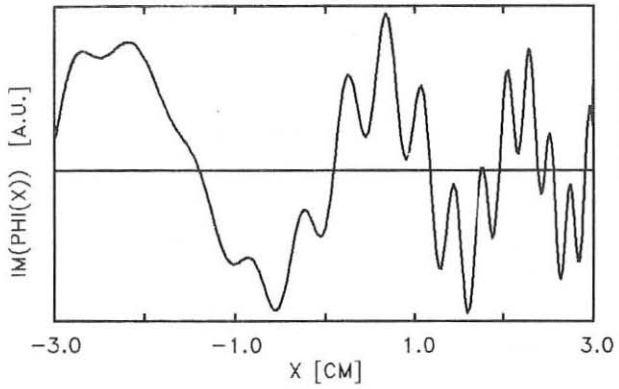

Fig. 2:
Imaginary part of solution $\Phi(x)$ versus x in the case of inhomogeneous electron and ion temperature profiles.

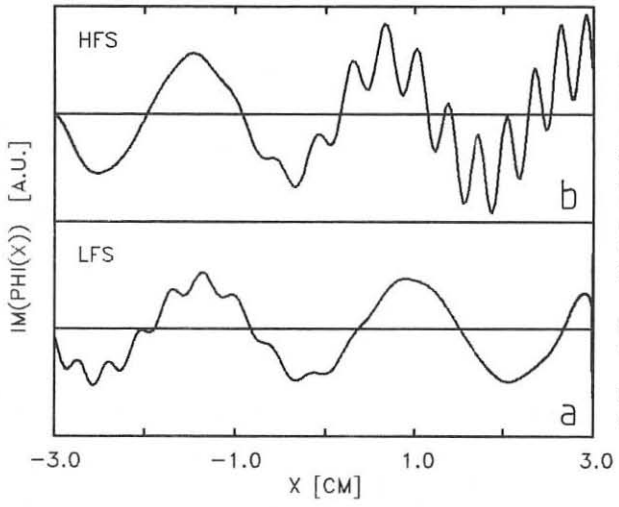

Fig. 3:
Imaginary part of $\Phi(x)$ versus x in the case of a inhomogeneous magnetic field, proportional to $1/(R_o \pm x)$, for LFS and HFS respectively. The same scale for both plots.

a) ω/ω_{ci}=3.60 at $x=x_{pl}$ and 3.95 at $x=x_{pr}$.

b) ω/ω_{ci}=3.95 at $x=x_{pl}$ and 3.60 at $x=x_{pr}$.

PARAMETRIC DECAY IN THE EDGE PLASMA OF ASDEX DURING FAST WAVE HEATING IN THE ION CYCLOTRON FREQUENCY RANGE

J.-M. Noterdaeme, M. Brambilla, J. Gernhardt

Max-Planck Institut für Plasmaphysik, Euratom Association
D-8046 Garching, Federal Republic of Germany

R. Van Nieuwenhove, G. Van Oost

Laboratoire de Physique des Plasmas-Laboratorium voor Plasmafysica
Association"Euratom-Etat Belge"-Associatie"Euratom-Belgische Staat"
Ecole Royale Militaire-B 1040 Brussels-Koninklijke Militaire School

M. Porkolab

Department of Physics and Plasma Fusion Center
Massachusetts Institute of Technology
Cambrigde, Massachusetts 02139, U.S.A.

Abstract: For the first time, in an ICRF heated tokamak, parametric decay instabilities were observed in the plasma edge. Two types of decay processes were found. Those instabilities provide a mechanism for the direct energy deposition, seen in many tokamaks, on the ions and electrons of the scrape off layer.

Introduction: During hydrogen second harmonic heating at 67 MHz /1/, frequency spectra were measured with an electrical probe. The measuring probe is 10^{o} toroidally away from one ICRH antenna, and 170^{o} from the other. The target plasma can be pure hydrogen or a hydrogen-deuterium mixture (n_H/n_e=25 to 100 %), ohmically heated (P_{OH}=450 kW) or preheated by neutral injection (P_{NI}=0.8-3.5 MW). Analysis of the frequency spectra, revealed the presence of parametric decay effects /2/. Parametric decay is a process by which a wave, called the pump wave (index 0), decays nonlinearly into two modes (index 1 and 2). These modes have to fulfill the selection rules : $\omega_0 = \omega_1 + \omega_2$ and $\overline{k_0} = \overline{k_1} + \overline{k_2}$. Theoretical studies /2,3/ indicate that several types of parametric decay processes can occur, two of which have been observed on ASDEX.

Parametric decay processes: In a first type, the pump decays into an ion Bernstein wave with frequency close to the pump wave (2e in Fig. 1) and a low frequency electron quasimode (obscured in the spectrum by the zero frequency peak of the spectrum analyser). Growth rate estimates /2/, predict that the convective threshold is easily exceeded.
In the second process, the pump decays into an ion cyclotron quasimode (with frequency near the ion cyclotron harmonic of an ion species in the edge, $\omega_1 = \omega_{ci}$) and an ion Bernstein wave (with, according to the selection rule $\omega_2 = \omega_0 - \omega_1$). The study of this process can benefit from

thorough analysis previously performed in a small research machine /4/. Because of the dependence of the frequency of the quasimode on the magnetic field, it is possible to identify this mode unequivocally. In Fig. 1 three spectra, at different toroidal magnetic field, and for a fixed pump frequency (67 MHz) show clearly how the frequency of the quasimode 1H depends linearly on B_T, and how the frequency of the corresponding ion Bernstein wave 2H then obeys the selection rule. In a multispecies plasma (i = H, D), we find that this proces can occur for both species. In a machine with carbonized walls, there are even indications that C at different ionisation stages can be the ion species supporting the quasimode. On first turn on of the RF in a shot, a more complicated spectrum (Fig. 2) can appear, with splitting of the peaks. This is thought to be due to the initial outgassing of the antenna, which can change the boundary temperature directly in front of the antenna, and the isotope concentration.

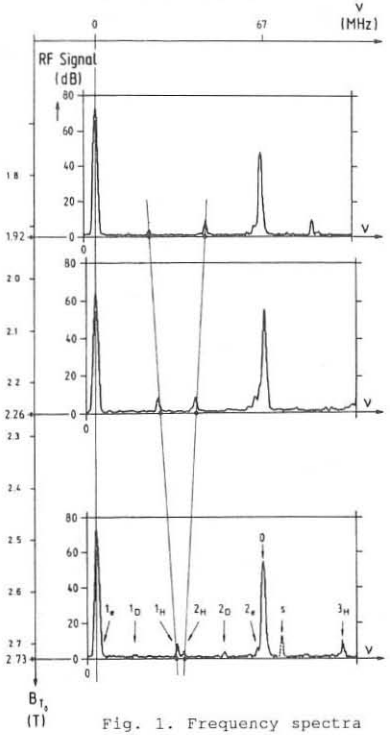

Fig. 1. Frequency spectra for three magnetic fields, showing the B dependence of the modes

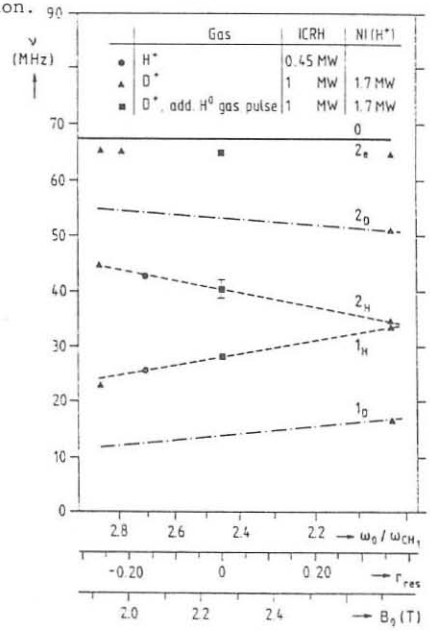

Fig. 3. Parameter region for the appearance of the decay instabilities

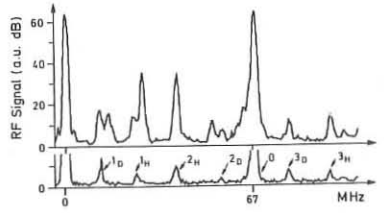

Fig. 2. Spectrum at the first turn on of the ICRH (top) compared to a spectrum (bottom), 800 ms later in the same pulse

Dependences: Whether or not the H and D decay processes were observed, depends strongly on the plasma composition and heating conditions. By varying the toroidal magnetic field, at constant pump frequency, the position of the second harmonic resonance layer was varied between r=-0.22m and r=+0.38m, with respect to the plasma centre at R=1.67m (with a=0.40m and the antenna protection limiters at r=0.45m). This also changes the ratio ω_0/ω_{ci} in the edge between 2.87 and 2.03. Fig. 3 show some of those conditions.

In a H plasma, with 0.45 MW of ICRH, on the antenna closest to the probe, the decay processes were observed only for positions of the resonance layer r<-0.13m ($\omega_0/\omega_{ci}>2.7$), with data available only up to r=+0.16m ($\omega_0/\omega_{ci}=2.3$). In a D and H mixture (30% H) with 1MW ICRH, on the antenna furthest from the probe, and 1.7 MW NI, they were observed only for r<-0.22m or r>0.38m (corresponding to $\omega_0/\omega_{ci}>2.9$ or <2.0).

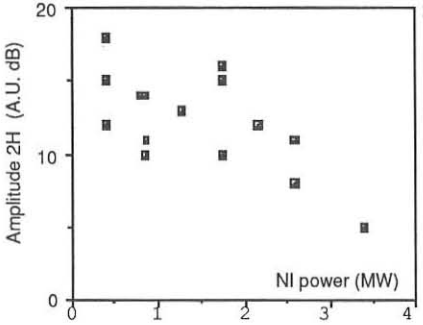

Fig. 4. Dependence of the 2H peak on NI power, for 1.2 MW of ICRH

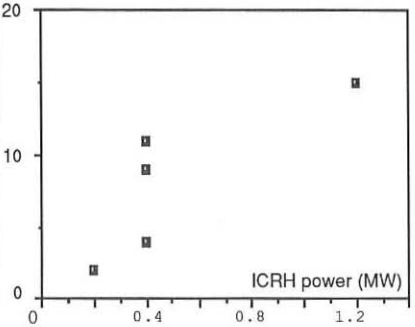

Fig. 5. Dependence of the 2H peak on ICRH power, no NI power

An additional H gas pulse made the instabilities appear, for a near central position of the resonance layer (r=0.03m), under all conditions (any antenna, down to 200 kW ICRH, any NI power). A clear anticorrelation, however, was then found between the amplitude of the 2H peak and the neutral injection power, as shown in Fig. 4. The amplitude of the 2H peak, measured under steady state conditions, increases with ICRH power (Fig. 5). This is in contrast to an experiment where, as the power was ramped up, the amplitude remained almost constant. Those effects can be understood in the following way: a better absorption of the fast wave, provided by the preheating with NI, will reduce the electric fields in the edge and thus the growth rate of the instabilities. The instabilities are also reduced by a higher NI power through the increased boundary temperature (theory predicts that the growth rate of the instabilities decreases for increasing boundary temperature). Higher RF powers result in higher RF electrical fields, and thus more instabilities. The heating of the boundary, due the instabities themselves, seems provide a type of feedback mechanism, so that, when the power is ramped up, the amplitude of the instabilities do not increase. We have also observed the instabilities, with a receiving probe located on the *inside* of the tokamak. Although fewer peaks were

present on the spectra, the 1H peak, with the frequency corresponding to the magnetic field at the *outside* egde of the plasma could, under some conditions, be identified.

Importance of those parametric decay instabilities: In many tokamaks direct energy deposition in the scrape off layer, was observed during ICRH. On Alcator, JET, Textor, among others, increases of electron temperatures in the edge were observed. On ASDEX, fast *deuterons* were observed in the edge, with second harmonic *hydrogen* heating /5/. To explain the Fe production at a target plate in Textor/6/, one has to postulate the presence of fast ions, accelerated in the perpendicular direction, in the plasma edge. The parametric decay instabilities, observed on ASDEX in the second harmonic regime, can provide the much sought after mechanism to explain the direct energy deposition in the scrape off layer. Measurements to find them in the minority regime were made on Textor, where now parametric decay instabilities have also been observed /7/.
Edge electron heating could be associated with electron Landau damping of the quasimode. Anomalous ion heating and the production of a suprathermal ion population could result from the damping of the ion quasimode. The ion Bernstein waves, excited in the edge, may be absorbed also on impurities in the boundary. The parametric decay processes may also partly explain why not all the RF power coupled to the plasma is found back in the bulk plasma. Since the probe was not calibrated, we can make no estimate of the total power transferred from the pump wave to the decay modes.

Summary: With the observation of those instabilities an important step was made in the understanding of the direct energy deposition on the ions and electrons of the scrape off layer. This direct energy deposition could be partly responsible for some of the impurity problems encountered with the ICRF heating method. Further investigation of the parametric decay instabilities may provide clues on how to avoid them and can thus contribute to an optimisation of the ICRF antennas and heating scenarios.

Aknowledgements: This work was carried out with the support of the Euratom Mobility of personnel scheme, and the support of the DOE/ASDEX,ASDEX-Upgrade collaboration contract. The authors also thank the ASDEX, ICRH and NI teams for their excellent support.

References:
/1/K.Steinmetz et al., Plasma Phys. and Contr. Nucl. Fus. Res., (Proc. 11th Int. Conf., Kyoto, 1986) Vol. 1, IAEA.Vienna(1987)461
/2/R.VanNieuwenhove,G.VanOost,J.-M.Noterdaeme,M.Brambilla,J.Gernhardt, M.Porkolab,subm.to Nucl.Fusion, and IPP Rep. III/129,Garching,Jan 88
/3/M.Porkolab, to be published
/4/F.N. Skiff, M.Ono, K.L.Wong, Phys. Fluids 27 (1984) 1051
/5/J.-M.Noterdaeme,F.Ryter et al.,Europhys.Conf.Abs,Vol11D,II(1987)678
/6/B.Schweer et al., Europhys.Conf. Abstracts, Vol 10C, I (1986) 399
/7/R.Van Nieuwenhove, G.Van Oost et al., this conference.

SECOND HARMONIC ICRF EXPERIMENT WITH OHMIC AND STRONG NBI-HEATED PLASMAS IN JT-60

T. Fujii, H. Kimura, M. Saigusa, N. Kobayashi*, K. Anno,
K. Hamamatsu, K. Kusama, S. Moriyama, K. Nagashima
M. Nemoto, K. Tobita, M. Yamagiwa and JT-60 Team

Japan Atomic Energy Research Institute
Naka Fusion Research Establishment
Naka-machi, Naka-gun, Ibaraki-ken 311-01, Japan
* Toshiba Corporation, Chiyoda-ku, Tokyo 100, Japan

1. Introduction

The second harmonic ion cyclotron range of frequencies (ICRF) heating experiments have been carried out at 120 MHz with hydrogen plasma in JT-60. A phased 2 x 2 loop antenna was developed for control of the radiated $k_{\parallel}$-spectrum [1], which has been confirmed to be very important to optimize the second harmonic ICRF heating [2]. The peak position of $k_{\parallel}$-spectrum can be changed from 0 to 15 m^{-1} with the phasing from (0,0) mode to (π,0) mode, where the former in the parentheses is the toroidal phase difference and the latter the poloidal one. After part of the TiC coated first wall and the antenna guard limiter were replaced with the graphite ones, increment of radiation loss during the ICRF heating has been substantially reduced. The combined heating of the second harmonic ICRF and strong neutral beam injection (NBI) has been intensively investigated. Injection power levels of the second harmonic ICRF and NBI are approximately 2 MW and 20 MW, respectively. The second harmonic ICRF heating with ohmic plasmas has been also studied. These experiments were performed in (π,0) and (0,0) modes with the diverted plasmas having the outside x-point.

In this paper, efficient increase in the plasma stored energy with beam acceleration and the antenna-plasma coupling at H-mode transition during the combined second harmonic ICRF and NBI heating are described. Comparison between on-axis (B_T = 4 T) and off-axis (B_T = 4.5 T) heating with ohmic plasmas is also presented.

2. Combined Second Harmonic ICRF and NBI Heating

(a) Efficient increase in the stored energy with beam acceleration [3]

During the combined heating, a remarkable beam acceleration was observed in the low electron density region, $\bar{n}_e$ = (2-3.5) x $10^{19}m^{-3}$. We also confirmed that the beam acceleration took place near the plasma center with on-axis ICRF heating [2]. Recently, a strong synergetic effect, namely, efficient increase in the stored energy has been observed during the combined heating of the intense NBI and the ICRF of (π,0) mode accompanied with the beam acceleration. Figure 1 shows the incremental energy confinement time τ_E^{inc} against $\bar{n}_e$ obtained for different auxiliary heating methods, where $\tau_E^{inc} \equiv \Delta W/\Delta P$ and ΔW is the incremental stored energy due to the additional heating power ΔP. In the lower density region, τ_E^{inc} of ICRF during the combined heating is greatly improved because the beam acceleration becomes dominant with decreasing electron density. The value of τ_E^{inc} of ICRF during the combined heating is more than 200 ms for B_T = 4 T and $\bar{n}_e$ = 2.2 x $10^{19}m^{-3}$. This value is about three times as large as that of NBI heating alone or

the second harmonic ICRF heating alone.

The scaling of τ_E^{inc} with the beam acceleration is given by

$$\tau_E^{inc} = \eta_b \cdot \tau_s + \tau_{E0}^{inc},$$

where η_b is the ratio of the ICRF power absorbed by the beam ions to the total ICRF power, τ_s the ion-electron relaxation time and τ_{E0}^{inc} the incremental energy confinement time of the bulk plasma [3]. The data of τ_E^{inc} for the combined heating shown in Fig. 1 are replotted as a function of $\eta_b \cdot \tau_s$ in Fig. 2. The evaluation of η_b is performed with the expression of the ICRF power density deposited on the ions whose velocity distribution has the non-Maxwellian beam-induced and rf-induced tail [4]. A good fit to the data is represented as

$$\tau_E^{inc} \ (\text{msec}) = \eta_b \cdot \tau_s + 53.$$

Since the constant term (53 msec) is consistent with the value of τ_{E0}^{inc} (50-60 msec) during strong NBI heating [5], τ_E^{inc} of ICRF during the combined heating is confirmed to follow the scaling mentioned above. Then, we can conclude that the stored energy of the fast ions increases classically.

The incremental stored energy of the fast ions is also analyzed with the self-consistent code which takes into account the global wave structure and the quasi-linear velocity space diffusion [6]. The experimental results are consistent with the calculation ones from the self-consistent code.

The fast ions enhanced by the ICRF consequently rises an effective ion temperature T_i^{eff} which is defined as the averaged ion energy over the whole velocity space. The value of T_i^{eff} evaluated for the best shot increases from 12 keV during NBI heating alone to 22 keV during the combined heating.

(b) Antenna-plasma coupling at H-mode transition

Short period H-mode phenomena were observed in both (0,0) and (π,0) modes during the combined heating. As shown in Fig. 3, the line-integrated electron density $\int n_e dl$ and the stored energy W^* gradually increase in both modes just after the intensity of H_α suddenly drops. At this transition from L-mode to H-mode, the density profile becomes flat and the density gradient near the plasma edge becomes steeper in both modes. The antenna coupling resistance also changes rapidly in both modes. The coupling resistance increases with the electron density in L-mode plasmas [7]. At the transition, the coupling resistance in (0,0) mode decreases from 5.9 to 5.5 Ω although the electron density increases. On the contrary, the coupling resistance in (π,0) mode increases from 1.5 to about 1.9 Ω. These coupling results at the transition qualitatively agree with the calculated ones with the three dimensional model of loop antenna where the change of the electron density profile is taken into account. In the calculations, the steeper density gradient and the decrease of the electron density near the separatrix generally reduce the coupling resistance. But the flattened density profile and the steeper density gradient shorten the length of evanescent layer for the excited fast wave with relatively large $k_\parallel$, which may increase the coupling resistance. Then, the wave excitation of such larger $k_\parallel$-spectrum as (π,0) mode can improve the coupling in H-mode plasmas. Therefore, it is possible to design an ICRF coupler whose coupling resistance scarcely changes even at the H-mode transition with the appropriate $k_\parallel$-spectrum [8].

3. Second Harmonic ICRF Heating with Ohmic Plasma

The second harmonic ICRF heating was carried out with ohmic plasmas of $\bar{n}_e$ = (2-3.5) x $10^{19} m^{-3}$, in which emphasis was placed on the comparison

between the on-axis and off-axis heating. In the off-axis case, the second harmonic resonance layer is at r ≃0.4 m. The ion temperature near the plasma center has been measured with the Rutherford scattering method. The ion temperature rose from 1.8 to 2.2 keV at $\bar{n}_e$ = 2.2 x $10^{19} m^{-3}$ during the ICRF injection of 0.9 MW. The difference of the ion temperature between the on-axis and off-axis cases was not observed clearly. On the other hand, the difference of the electron temperature was clear. The time behaviours of electron temperature T_e^{Fil} at five positions of r = 0, 0.2, 0.4, 0.6, 0.8 m during on-axis heating are shown in Fig. 4. The electron temperature is estimated from the soft x-ray absorption method. During the on-axis heating, the larger sawteeth appear in the central electron temperature. Their period becomes longer by a factor of about 2.5 than the one before the ICRF pulse. The central electron temperature rises from 2.0 to 2.6 keV at $\bar{n}_e$ = 3.2 x $10^{19} m^{-3}$ during the ICRF injection of 1.6 MW. Thus, the electrons near the plasma center are well heated in the on-axis heating. On the contrary, the electron temperature during the off-axis heating rises broadly. The sawteeth in the central electron temperature change slightly before and during the ICRF pulse. The data of the incremental energy confinement time for the second harmonic ICRF heating alone are plotted against $\bar{n}_e$ in Fig. 1. In the lower electron density, the incremental energy confinement time is enhanced in both on-axis and off-axis cases similar to that of the combined heating. It seems to be due to the beam component produced by the ICRF.

4. Conclusions

It is experimentally confirmed that the fast ions are efficiently produced and well confined in the plasma core during the combined second harmonic ICRF and NBI heating. The stored energy of the fast ions is found to increase classically.

Improvement of the coupling in $(\pi,0)$ mode at the H-mode transition was observed for the first time. It is shown that the wave excitation of such larger $k_{\parallel}$-spectrum as $(\pi,0)$ mode improves the coupling in H-mode plasmas.

The electron temperature profile with on-axis heating is more centrally-peaked than that of off-axis heating.

Acknowledgements

The authors would like to express their gratitude to Drs. S. Mori and K. Tomabechi for their continued encouragement.

References

[1] T. Nagashima, et al., Fusion Engineering and Design 5 (1987) 101.
[2] H. Kimura and JT-60 Team, Proc. of 14th Europ. Conf. on Cont. Fusion and Plasma Physics, Madrid (1987) Vol.11D, Pt.3, p.857.
[3] H. Kimura, et al., submitted to Phys. Rev. Lett..
[4] M. Yamagiwa et al., to be published in Plasma Physics and Cont. Fusion.
[5] M. Kikuchi, et al., Nuclear Fusion Vol.27 (1987) 1239.
[6] K. Hamamatsu, et al., Proc. of 14th Europ. Conf. on Cont. Fusion and Plasma Physics, Madrid (1987) Vol.11D, Pt.3, p.861.
[7] M. Saigusa, et al., Proc. of 7th Topical Conf. on Application of Radio-Frequency Power to Plasmas, Florida (1987).
[8] M. Saigusa, et al., paper in preparation.

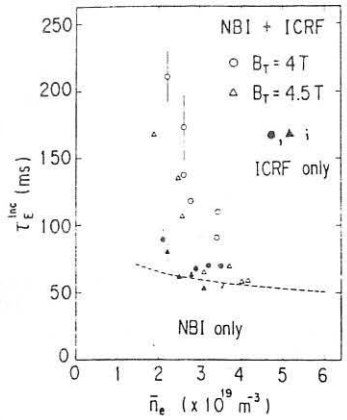

Fig. 1 τ_E^{inc} against $\bar{n}_e$ for different auxiliary heating methods. I_p = 1.5 MA, 2.0 MA, P_{NB} = 16-20 MW and P_{IC} = 0.7-1.8 MW.

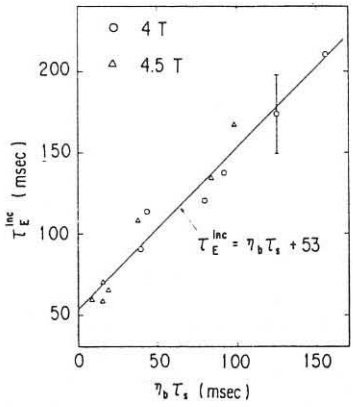

Fig. 2 τ_E^{inc} of ICRF during the combined heating versus $\eta_b \cdot \tau_s$. The solid line indicates the result of linear-regression analysis.

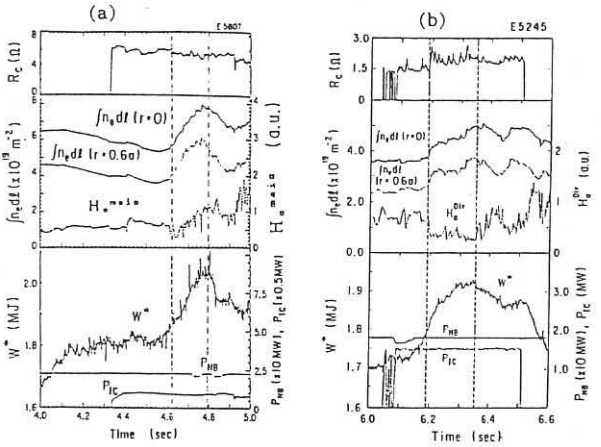

Fig. 3 Time behaviours of R_c, $\int n_e dl$, intensity of H_α and W^* during the combined heating of NBI and the second harmonic ICRF of (a) (0,0) mode and (b) (π,0) mode. The period between the two broken lines indicates H-mode.

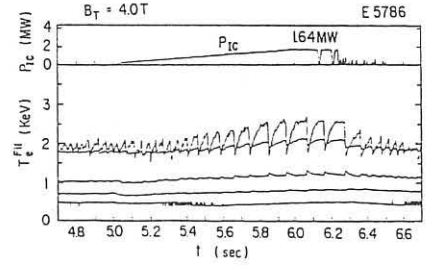

Fig. 4 Time behaviours of T_e^{Fil} at r = 0, 0.2, 0.4, 0.6, 0.8 m during the on-axis heating of the second harmonic ICRF alone.

THE ICRF ANTENNAS FOR TFTR*

D.J.Hoffman, P.L. Colestock,† W.L. Gardner, J.C. Hosea,† A. Nagy,† J. Stevens,† D.W. Swain, J.R. Wilson†

Oak Ridge National Laboratory, Oak Ridge, Tennessee 37831, U.S.A.

Two compact loop antennas have been designed to provide ion cyclotron resonant frequency (ICRF) heating for TFTR. The antennas can convey a total of 10 MW to accomplish core heating in either high-density or high-temperature plasmas. The near-term goal of heating TFTR plasmas and the longer-term goals of ease in handling (for remote maintenance) and high reliability (in an inaccessible tritium tokamak environment) were major considerations in the antenna designs. The compact loop configuration facilitates handling because the antennas fit completely through their ports. Conservative design and extensive testing were used to attain the reliability required for TFTR. This paper summarizes how these antennas will accomplish these goals.

The Antenna Designs

Two antennas have been designed, fabricated, tested, and installed on TFTR. One antenna, built by Princeton Plasma Physics Laboratory, is designed to couple 6 MW for 2 s at 47 MHz through the 74- by 90-cm Bay M port; the other, built by Oak Ridge National Laboratory, is designed to couple 4 MW through the 60- by 90-cm Bay L port. Figure 1 shows the layout of the Bay L antenna; Fig. 2, the layout of the Bay M antenna. Each antenna can be installed through its port and can move $\approx$10 cm relative to the plasma. Each one has a pair of current straps that can be independently phased to control the launched k spectrum. Both will operate at CIT-level power densities (on the Faraday shield) of $\approx$1.2 kW/cm^2.

Although the antennas were principally constructed for core heating of a hot, dense plasma, they were also intentionally designed with different features to provide experience in optimizing antenna design on future machines like CIT. One Faraday shield was built so that its TiC-coated elements would be relatively warm during operation; the other shield's graphite-covered elements will be actively cooled. Designs for CIT antennas call for matching by either stubs or capacitive structures. To help resolve this issue, one antenna is matched by variable capacitors at both ends of the current strap and is fed centrally. With properly chosen capacitance values, the antenna can be made to have a 50-Ω impedance at the feed point. This antenna is tunable from 35 to 68 MHz on the presently installed structure and can be modified without breaking vacuum for 60- to 80-MHz operation. The other antenna is end-fed, with all matching accomplished by external stubs. By phasing the feed lines, each strap can be made to operate as a magnetic dipole or quadrupole. The differences between the two configurations are summarized in Table I.

*Research sponsored by the Office of Fusion Energy, U.S. Department of Energy, under contract DE-AC05-84OR21400 with Martin Marietta Energy Systems, Incorporated.

†Princeton Plasma Physcis Laboratory, Princeton, New Jersey 08544, U.S.A.

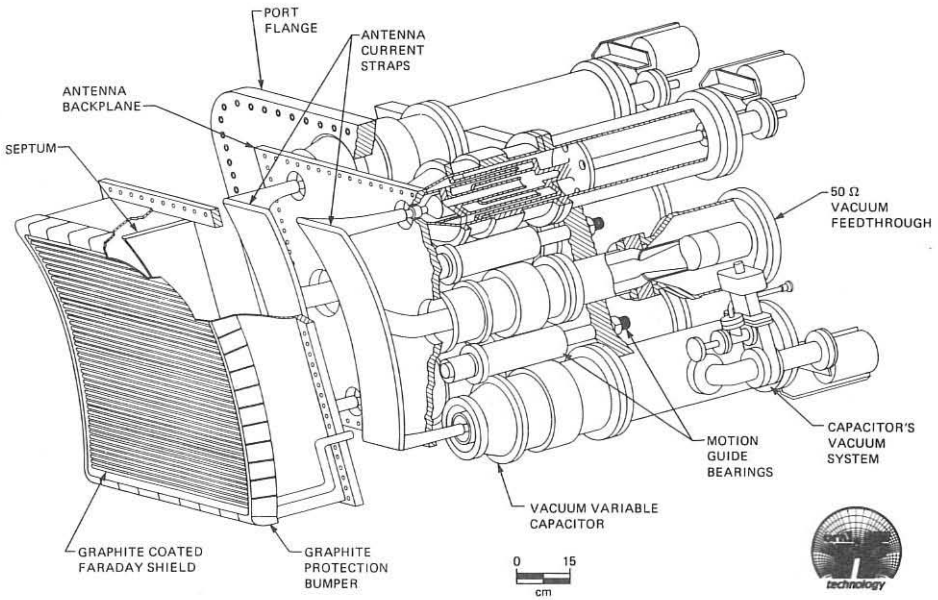

Fig. 1. The Bay L antenna.

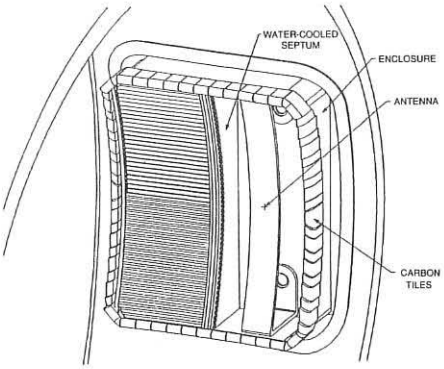

Fig. 2. The Bay M antenna.

Table I. Bay L and Bay M antenna characteristics

	Bay L	Bay M
Total power (MW)	4	6
Frequency (MHz)	40–60	47
Pulse length (s)	2	2
RF material	Copper	Silver
Matching		
Location	Internal	External
Method	Capacitors	Stubs
Current strap impedance (Ω)	62	40
Relative phase velocity (%)	81	43
Feed point	Central	End
Number of straps per port	2	2
Port size (cm × cm)	60 × 90	74 × 90
Shield power density (kW/cm²)	1.2	1.2
Antenna motion (cm)	11	11
Faraday shield		
Coating	Graphite	TiC
Material	Inconel 625	Inconel 625
Cooling	Active	Inertial
Side wall configuration	Closed	Slotted

Power Considerations

To couple all of the power, either relatively high-voltage, high-current capabilities or high loading is required. The compact loop configuration helps to increase loading by permitting the backplane to be almost totally recessed. Both antennas have this feature. To quantify the effect, the backplane is placed 20 cm (instead of 4 cm, as an internally mounted antenna might require) from the current strap in the Bay L coupler, which increases the plasma flux linkage a factor of 2. To further increase the coupling of the Bay M antenna, the antenna sidewalls are slotted, which improves coupling by a factor of 5 during in-phase operation. The Bay L antenna sidewalls are closed to prevent plasma penetration, but coupling modestly improves (1.2 times) during out-of-phase operation. Both antennas have high flux linkage and should have better coupling than antennas with close backplanes. The voltage and current requirements for full power, shown in Figs. 3 and 4 as functions of distributed plasma load, are similar for the two antennas. For the Bay L coupler, the slight electrical asymmetries in the circuitry and different strap impedance give curves different from those for Bay M. At the rated voltage of 50 kV peak, the efficiency of the antenna with the graphite Faraday shield is 96%; of the antenna with the TiC shield, 98%.

Testing

Both antennas were subjected to numerous tests to prove that they would operate reliably in TFTR: disruption thermal load tests of the Faraday shield elements, mechanical tests of the vacuum feedthroughs, bakeout tests, other miscellaneous tests, and high-voltage tests of the entire assembly. The last are the most important in

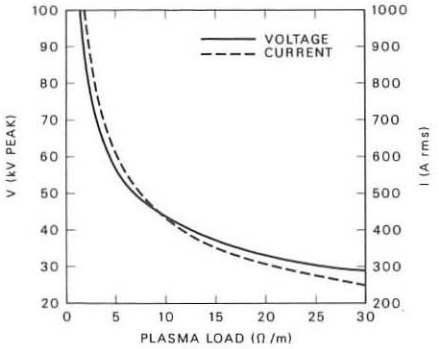

Fig. 3. Maximum capacitor voltage and current versus plasma load in the Bay L antenna, assuming 2 MW per strap at 47 MHz. The capacitors must vary as a function of plasma load and slightly change the site of current maximum. As a result, the curves do not follow a simple, distributed coaxial transformation.

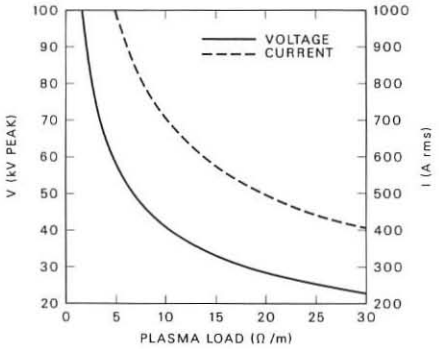

Fig. 4. Maximum strap voltage (at the feedthrough) and current (in the midplane) versus plasma load in the Bay M antenna, assuming 3 MW per strap at 47 MHz. This antenna follows the coaxial transformation.

qualifying the assemblies for high-power operation. Both structures were subjected to high-voltage, long-pulse tests in a variety of environments, including vacuum, gas, magnetic fields, and plasmas. Especially after the antennas were baked out, none of these items degraded the antennas' voltage capabilities. Both made reliable 2-s, 47-MHz pulses at 65 kV peak. This exceeds the 50-kV design value.

Spectral Considerations for Heating in TFTR

The spectral design of the antennas must accommodate good plasma heating and the constraints imposed by the ports. The larger port sets the lower limit of $k \approx 4\ \mathrm{m}^{-1}$. However, calculations for TFTR indicate that central ion heating is peaked around $k \approx 10\ \mathrm{m}^{-1}$. Figure 5 shows that the outgoing wave damps over 40% of the power on the ^{3}He minority in the core on the first pass. This case is for 47 MHz, $6 \times 10^{13}\ \mathrm{cm}^{-3}$, 5% minority in a high-$T_i$ deuterium plasma. Virtually no power is damped directly on the electrons. Thus, the antennas were designed with two current straps per port to generate $k \approx 10\ \mathrm{m}^{-1}$ in Bay M. The smaller port in Bay L restricts the out-of-phase spectrum to be centered on $15\ \mathrm{m}^{-1}$, well within the spectral peak of ion heating. Since TFTR runs under a variety of conditions, including dense hydrogen discharges, the achievable range of k is from $4\ \mathrm{m}^{-1}$ to $15\ \mathrm{m}^{-1}$. This, combined with the frequency range of the antennas, will ensure that ion heating is accomplished.

Conclusions

The antennas for TFTR have been optimized to heat the hot, dense plasma. Intentional differences have been designed into the two antennas to help selection of important features for future heating experiments on TFTR or CIT.

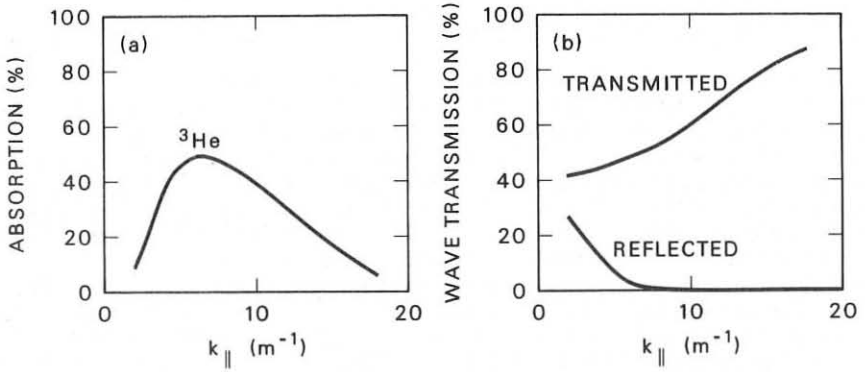

Fig. 5. (a) Wave damping on the ^{3}He minority as a function of $k_\parallel$. The absorption from the high-field side is virtually the same as that from the low-field side. (b) Propagation of the wave through TFTR. Little reflection is seen.

COMPARISON OF ICRH HEATING SCENARII AND ANTENNA CONFIGURATIONS IN TEXTOR

J-M. BEUKEN, L. DE KEYSER, T. DELVIGNE, P. DESCAMPS, F. DURODIE, M. GAIGNEAUX, M. JADOUL, R. KOCH, D. LEBEAU, A.M. MESSIAEN, J. ONGENA, X.M. SHEN, P.E. VANDENPLAS, R. VAN NIEUWENHOVE, G. VAN OOST, G. VAN WASSENHOVE, R.R. WEYNANTS

Laboratoire de Physique des Plasmas - Laboratorium voor Plasmafysica
Association "Euratom-Etat belge" - Associatie "Euratom-Belgische Staat"
Ecole Royale Militaire - B 1040 Brussels - Koninklijke Militaire School

and

TEXTOR and ALT-II TEAMS
Institut für Plasmaphysik, Kernforschungsanlage Jülich, GmbH
Association "Euratom-KFA", D-517O Julich, FRG
Institute of Plasma and Fusion Research, University of California, Los Angeles, USA
Sandia National Laboratory, Livermore, USA
IPP, Nagoya University, Japan

1. SUMMARY.

The predominantly high field side (HFS) antenna system (called OLD in this paper) of TEXTOR has been replaced by two low-field side (LFS) antenna pairs. Each pair can be fed in phase or out of phase (respectively O or Π configurations). The initial observations are the following : (i) in the Π configuration the interaction with the wall is reduced. Further improvement is possible with appropriate choice of wall condition (wall carbonization with liner at 400°C or, above all, boronization) (ii) the electron and ion heating efficiencies are roughly the same for the three antenna configurations (OLD, O, Π) in agreement with theory. For LFS excitation the anticipated influence of the presence of minority is observed.

2. TEXTOR ICRH SYSTEMS AND PROPERTIES OF THE NEW ANTENNAE.

The ICRH system hitherto used on TEXTOR has been described in various papers [see e.g. 1] and its performances discussed therein. Two independent heating lines are each fed by one 1.5 MW generator. Before 1987 each line was connected at the LFS to a $\lambda/4$ antenna. The two antennae were placed in the same polcidal plane so that they completely surrounded the plasma and provided mostly a HFS excitation. This antenna configuration allowed as main heating scenario mode conversion in a (H)-D plasma ; at sufficiently low minority concentration, minority or $\omega = 2\omega_{CD}$ heating was also possible [2,3,4].

In 1987 a new antenna system compatible with the toroidal pump limiter ALT-II requirements was installed in TEXTOR. It is constituted of four identical LFS antennae which are grouped in two pairs situated at diametrically opposite toroidal positions in the tokamak. A peculiarity of these antenna pairs (of electrical length $\lambda/7$) is that, due to the choice of their geometrical parameters, they can be fed in phase or out of phase without loss of plasma loading. This property is illustrated in Fig. 1 which shows the active power spectrum versus $k_{//}$ for the two phasing configurations (O and Π) computed by means of a 3-D code [5]. The power spectrum when only one antenna of the pair is fed is shown for comparison. The deduced plasma loading specific resistance R [5] of one antenna of a given

pair is respectively 2.2 and 2.4 Ω/m for the O and Π configurations and the parameters of Fig. 1. The approximate independence of R with respect to configuration, for the same antenna-plasma distance and plasma characteristics, has been experimentally confirmed. As shown in Fig. 2 R exhibits a linear increase when plotted versus the electron plasma density near the edge (at r = 40 cm). A corresponding data set for the OLD antenna, which has a lower loading due to its geometry, is also shown. For a power P_A = 1.4 MW applied to one antenna pair and R = 3 Ω/m the antenna input voltage amplitude is only 25 kV.

3. RESULTS AND DISCUSSION.

3.a. Theory. The subdivision of the deposited RF power in the (H)-D plasma into direct electron heating via mode conversion (DE), electron heating though the minority (ME) or ion heating though the minority (MI) is evaluated as a function of the minority concentration for the configurations O, Π and OLD. This is done from the dispersion seen by a ray propagating from the antenna in the equatorial plane [4] following the method explained in Ref. [6]. The absorptivity of the plasma is defined as being the fraction of radiated power F_G absorbed in a full transit (i.e. going one way and back over the plasma). The results are given in Table 1 for the best conditions of absorptivity (maximum F_G) and for a radiated power P_{RF} = 0.5 MW and a central chord density $\bar{n}_{eo} = 4 \times 10^{13}$ cm^{-3}. It appears that, although the absorptivity of OLD is greater, the ratio of power deposition in the ions and the electrons is approximately the same for the 3 configurations. For LFS excitation, the Π configuration has a better absorptivity and leads to relatively larger heating via the minority.

Configuration		OLD	0	Π
Maximum F_G		.85	.40	.60
Power repartition	DE	.77	.70	.45
	ME	.03	.13	.33
	MI	.20	.17	.22

Table 1

3.b. Wall interaction. The plasma-wall interaction is significantly altered by switching from O to Π phasing. Figure 3 shows the dependence on P_{RF} of a number of relevant signals : the RF induced rise in line density $\Delta \bar{n}_e$, the increments in brilliance of a CV and a OVI spectroscopic line (ΔB_{CV} and ΔB_{OVI} resp.) and the global bolometric radiation increase ΔP_{rad}. The data pertains to a base OH plasma with $2.0 < \bar{n}_{eo}$ (10^{13} cm^{-3}) < 2.5 with carbonized walls and a wall temperature T_L of 400°C. Two antenna pairs were fired in rapid sequence on the same plasma, one pair in O configuration and the other in Π. $\Delta \bar{n}_e$ scales roughly as $cP_{RF}^{0.8}/\bar{n}_{eo}^{0.7}$, and has almost no I_p dependence. For these conditions the factor c = 1.65 (units : MW, 10^{13} cm^{-3}) in the O configuration, increasing to 2.9 when T_L is lowered to 150°C ; for the Π one, c is reduced to 1.1 for T_L = 400°C. It is clear that for this last condition the inflow of wall-released neutrals is strongly reduced. Whereas the oxygen radiation is significantly lower with Π phasing, carbon shows an opposite, yet much weaker tendency, probably connected with the difference in spatial localization of the respective sources. As a result ΔP_{rad} is reduced by about 25 %. Detachment-free operation

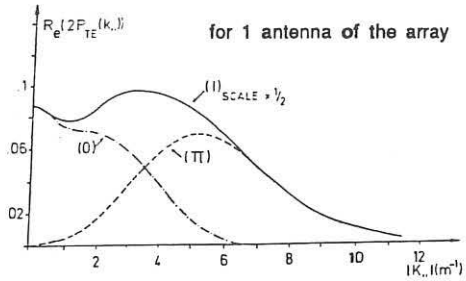

Fig. 1. Typical power spectra of the new antennae (distance antenna-plasma : 5.6 cm, parabolic density profile with $\hat{n}_{eo}$ = 3 x $10^{13}cm^{-3}$).

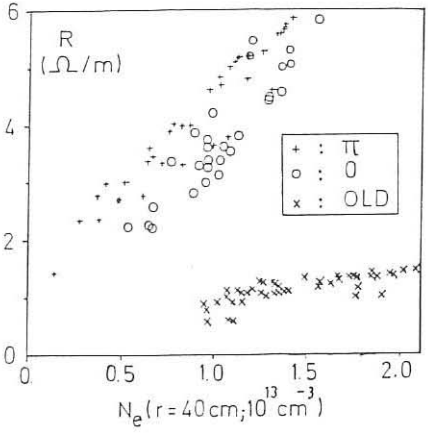

Fig. 2. Experimental plasma loading specific resistances versus density at r = 40 cm.

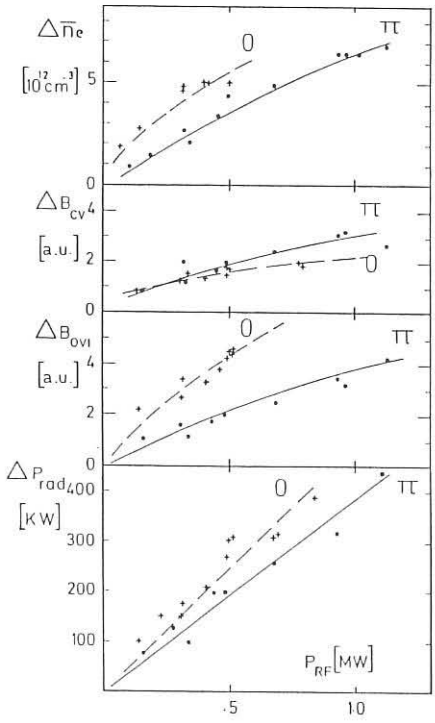

Fig. 3. Increases of density, impurity line brilliance and total radiated power due to ICRH (carbonized wall, T_L = 400°C).

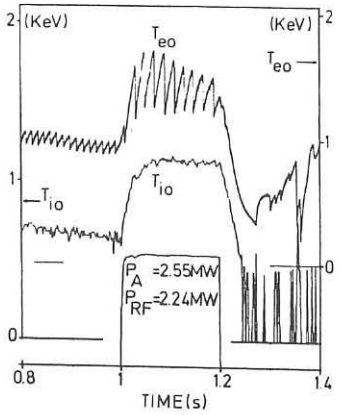

Fig. 4. T_{eo} (from ECE) and T_{io} (from neutron yield) versus time, together with antenna power P_A and radiated power P_{RF} (# 31837, carbonized wall, T_L = 400°C, Π).

with the Π-antenna is then possible for the given plasma condition, whereas the O-antenna causes the plasma to detach at about 900 kW of power input. The improvement seen with the Π configuration agrees with the thecretical larger absorptivity.

The factor c can be further reduced to 0.55 at T_L = 150°C for the Π configuration by the use of wall boronization (B-C wall coating [7]). The radiation level is also appreciably reduced. The data pertaining to the OLD case with carbonization have already been well documented in Refs [8,3,2].

3.c. Heating results. Fig. 4 shows the evolution of the central electron and ion temperatures, resp. T_{eo} and T_{io}, during an ICRH pulse exceeding 2 MW. The main trends seen from a first analysis of the results with carbonized wall are the following : (i) The global energy increases in the O and Π configurations with the same auxiliary confinement time as recorded previously for the OLD antenna [2,3]. (ii) In spite of smaller values of F_G for the O and Π cases, the radiated power P_{RF} is nearly completely retrieved in the bulk absorption as for the OLD case (see [4] for measurement method), so that the power fraction involved in the wall interaction is small. (iii) Electron and ion heating efficiencies $\eta_\alpha = \bar{n}_{eo}\,\Delta T_\alpha/P_{RF}$ seen with carbonized wall for the 3 cases are given in Table II ((H)-D, I_p = 0.35 MA, B_t = 2 T) together with the relevant density ranges. The precision on η is about ± 20 %. As theoretically expected η_e and η_i remain, within the errorbars, roughly the same for the 3 cases. (iv) The analysis of the central power deposition by the methods used in [2] indicates that the power deposition profiles for the O and Π cases are more peaked than in the OLD case but do not become as peaked as the OH power profile. The power density coupled to the electrons (DE) has also decreased as seen from the transient behaviour of the sawteeth, in agreement with Table 1. (v) For the Π configuration, the energy increase due to ICRH measured from diamagnetism is larger than that derived from MHD equilibrium ; it is also larger than for the other configurations. This is attributable to a larger minority energy tail for this configuration as expected from theory.

Configuration	η_e	η_i	$\bar{n}_{eo}(10^{13}cm^{-3})$
OLD	790	775	1.8-3.3
O	690	950	2.2-3.3
Π	900	770	2.9-3.5

Table II (η is expressed in eV 10^{13} cm^{-3}/MW)

REFERENCES.

[1] G. Van Oost et al., Fusion Technology, 12, 449 (1987).
[2] A.M. Messiaen et al., Plasma Phys. and Contr.Fusion, 28, 71 (1986).
[3] G.H. Wolf et al., ibid.,28, 1413 (1986).
[4] R. Koch et al., Europhysics Conf. Abstracts (Madrid 1987) Vol.11D, Part III, p.924.
[5] A.M. Messiaen et al., Heating in Toroidal Plasmas, Eur 7979 EN, Vol.I, 243 (1982).
[6] R.R. Weynants, Heating in Toroidal Plasmas, Int. School of Plasma Phys., Vol.I, 211 (1984).
[7] J. Winter et al., PSI Conference, Jülich, May 1988.
[8] U. Samm et al., Plasma Phys. and Contr. Fusion, 29, 1321 (1987).

OBSERVATIONS OF HARMONICS AND PARAMETRIC DECAY INSTABILITIES during ICRF heating on TEXTOR

R. Van Nieuwenhove, G. Van Oost, J.-M. Beuken, L. De Keyser, T. Delvigne, P. Descamps, F. Durodié, M. Gaigneaux, M. Jadoul, R. Koch, D. Lebau, A.M. Messiaen, J. Ongena, X.M. Shen, P.E. Vandenplas, G. Van Wassenhove, R.R. Weynants

Laboratoire de Physique des Plasmas - Laboratorium voor Plasmafysica
Association "Euratom-Etat belge" - Associatie "Euratom-Belgische Staat"
Ecole Royale Militaire - B 1040 Brussels - Koninklijke Militaire School

Abstract Measurements performed with electric and magnetic RF probes in the scrape-off layer of TEXTOR during ICRF operation reveal the presence of large-amplitude harmonics of the RF generator frequency, as well as three types of parametric decay instabilities. The large amplitude of the harmonics is not due to the RF generator, but could be due to the nonlinear sheath effect at the antenna. The first type of parametric decay instability is identified as decay into an ion Bernstein wave and an ion cyclotron quasimode, the second as decay into an ion Bernstein wave and a low frequency electron quasimode. Signals at the half-harmonics of the generator frequency are also seen and have been interpreted as parametric fast-wave pump decay into two ion Bernstein waves in the interior of the plasma. The presence of such nonlinear effects provide mechanisms which can modify the energy deposition profile.

1. Introduction There is growing evidence for a direct link between the unintended ICRF-induced changes in edge plasma parameters and bulk plasma properties. These changes are observed on several tokamaks (TFR, PLT, JFT-2M, Alcator-C, ASDEX, TEXTOR, JET, ...) and with different heating scenarios.

Several strong effects of ICRF on the edge parameters were seen on TEXTOR [1,2] : density rise, instantaneous electron heating, modification of scrape-off layer (SOL) profiles, influx of light and/or heavy impurities, increased heat flux to the limiters, and creation of energetic ions in the SOL. Furthermore, an important dc current was measured between ICRF-antenna and liner, roughly eight times higher than in the ohmic phase [3] .

The observed nonlinear RF phenomena on TEXTOR, namely harmonics generation and parametric decay instabilities, could be candidates to explain the direct ICRF energy deposition in the edge which can lead to impurity problems.

2. Experimental conditions The discharge- and ICRF-heating conditions are discussed elsewhere [4] . The RF probes are located at the low field side in the equatorial plane, about 1m away from one ICRF antenna pair and almost diametrically opposite to the other antenna pair. The RF electric and magnetic fields in the SOL can be simultaneously measured in two orthogonal directions (y and z) using two electric dipoles and two single-turn loop antennas, all mounted on a radially movable manipulator. The probes can be aligned with respect to the total magnetic field. A pneumatic fast-drive manipulator equiped with a double electric probe is also used. The probe signals are either fed to a spectrum ananlyzer or to linear RF detectors with selected filters, enabling to observe the fundamental and harmonic frequencies simultaneously.

3. Harmonics The RF spectrum of the different signals shows the presence of harmonics of the generator frequency (see Fig. 3) under all plasma- and heating conditions, even at very low ICRF power levels (order 10 kw): The amplitude of the second harmonic signal on the electric probes is usually of the same order of magnitude as that of the fundamental. The frequency spectrum measured by a magnetic pick-up coil located inside the ICRF antenna box does not reveal harmonics in the absence of plasma, implying that they cannot be due to the high power RF generator. Theoretical calculations show that the nonlinear sheath behaviour of the electric dipole probe (considering it as a double probe) cannot be responsible for the observed high amplitude harmonics. Furthermore, these harmonics are also detected when the probe is positioned in the vacuum region between liner and vessel where a probe sheath effect can be excluded.

The waves at the harmonic frequencies might be generated at the ICRF antenna by the nonlinear sheath effect. Effets due to the presence of a sheath and ensueing changes in the plasma edge are observed on TEXTOR [3] and strong nonlinear sheath effects were seen in another frequency domain [5].

The ratio R of the amplitude of the signal at frequency 2ω and that at the generator frequency ω for the poloidal electric field component E_y is found to be of the same order (typically 50 to 70 %) as for the toroidal electric field component (E_z). For the magnetic field components R is typically 10 % for By and 6 % for B_z. A typical time evolution of the fundamental and second harmonic E_y-components is shown in Fig. 1.

The nature of the waves at the harmonic frequencies has not yet been identified. However, from the high amplitude of the harmonics it is suspected that these waves can lead to a significant RF power deposition in the SOL, although part of the power is probably also launched towards the interior of the plasma. Experiments with modulated RF power show that R saturates rather quickly at a power level of about 200 kW, reaching a value of approximately 50 to 70 % for the electric field components.

The observed very significant E_z-component (E_z/E_y = 30 % for the fundamental as well as for the second harmonic signal) together with the small B_z (2ω) but large E_y (2ω) are not compatible with a magnetosonic wave, and point at the presence of an electrostatic type of wave.

The separate excitation of the antenna pair close to (A1) or far away (A2) from the probes gives some indications concerning the toroidal propagation of the harmonic waves in the SOL. The measurements show that R corresponding to A2 is usually 2 to 4 times lower than R corresponding to A1 (see Fig. 1) indicating an important toroidal decay (see Fig. 1).

Radial profiles of E_y, measured with the fast-drive probe located at about 1 m from A1 during a single discharge, reveal a strange structure (Fig. 2). The position of the peaks is found to be independent of plasma density, toroidal magnetic field and plasma current, thereby excluding surface waves [6] or global modes as possible explanations. Preliminary measurements indicate however that this structure is changed when the ICRF antenna position is slightly varied. The details of the structure show that the position of the peaks in the radial profile of the second harmonic E_y-signal correspond to dips inside the main peaks on the fundamental signal. More details will be give in an separate publication [7].

4. Parametric decay instabilities Three types of parametric decay instabilities (PDI) are detected in the SOL of TEXTOR during ICRF, in both single and two-ion species plasmas.

4a. PDI involving quasimodes For the first time in an ICRF-heated tokamak two types of parametric decay instabilities were observed in the SOL of ASDEX[8,9] during hydrogen second harmonic heating. The same two types of PDI are also found on TEXTOR for plasma- and heating conditions differing from those in ASDEX.

The first type, corresponding to the sideband 2_D and the low frequency decay mode 1_D in Fig. 3 was identified as decay into an ion Bernstein wave (IBW) and a deuterium ion cyclotron quasimode (IQM) excited near the deuterium ion cyclotron frequency in the SOL. The second type, corresponding to the sideband 2_e and the low frequency decay wave 1_e (here not clearly observable due to the zero frequency peak of the spectrum ananlyzer), was identified as decay into an IBW and a low frequency electron quasimode (EQM). The indices 0,1,2, and 3 refer to pump, low frequency decay mode, lower sideband wave, and upper sideband wave, respectively.

No conclusions can be drawn from the absolute amplitude of the different modes, since the sensitivity of the probe can be different for each mode, and since all the signals which do not correspond to decay modes are saturated.

Both types of PDI are observed in $2\omega_{CD}(o)$ heating (almost pure D) as well as in the minority heating scheme D (H). In contrast with previous experiments[8] where ICRF powers below 200 kW could not be applied, parametric decay is observed on TEXTOR for very low power levels (order 10 kW). It is not yet clear if this depends on particular wall conditioning procedures shuch as carbonization on boronization [10]. The PDI are not observed in H- and ^{3}He(H)-plasmas. Parametric decay phenomena are observed when A1 as well as when A2 is excited. The decay wave amplitudes are much weaker on the magnetic probes. As seen on Fig. 3, sideband modes (2_i) and low frequency modes (2_i), excited near a cyclotron or cyclotron harmonic of impurity ion species in the SOL, were observed. At lower densities, generally more peaks corresponding to impurities appear. Sidebands are also observed around the harmonics, demonstrating again that the harmonic signals correspond really to waves and are not due to a probe sheath effect. When the RF power is further increased above threshold, the decay mode amplitudes quickly saturate, but the peaks broaden and sometimes split up.

4b. PDI involving half-harmonics Signals at half-harmonics of the generator frequency were detected (Fig. 4) in the D(H) and ^{3}He(H) minority heating schemes, similarly as on TFR[11]. They have been interpreted[12] as parametric fast-wave pump decay into two Bernstein waves, occurring in the interior of the plasma and providing a mechanism for majority ion heating in an otherwise minority heating scheme.

5. Discussion The clear experimental evidence for the existence of harmonic waves in the SOL for all discharge- and ICRF conditions, as well as of parametric decay phenomena for a more limited variety of experimental conditions, provide possible mechanisms to explain the observed direct energy deposition to electrons and ions in the SOL, and ICRF-induced side-effects. Especially the occurrence of harmonics may also partly explain why not all the RF power which is coupled to the plasma is deposited in the central bulk plasma. A thorough understanding of these phenomena may be the way to improve antenna design as well as the heating scenarios so as to minimize the possible impact on the plasma heating performance.

Acknowledgements The authors are very grateful to Dr. D. Goebel and J. Corbett of the TEXTOR ALT-II team for the use of their fast-drive probe.

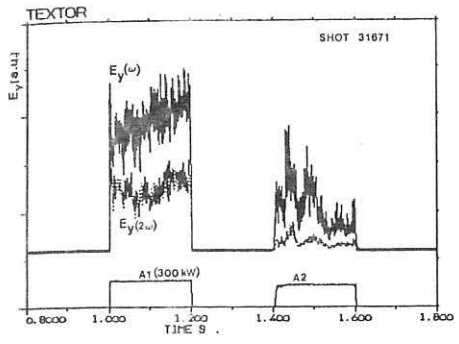

Fig.1 Time evolution of E_y for the fundamental (ω) and second harmonic (2ω) signal, with the antennas A1 and A2 excited separately; D(H) minority heating; $B_T = 2.0\ T, I_p = 340\ kA$, $\bar{n}_{e0} \simeq 1.3 \times 10^{13}\ cm^{-3}$

Note the different $E_y(2\omega)/E_y(\omega)$ ratio when the probe is close to the antenna (A1) or far from it (A2).

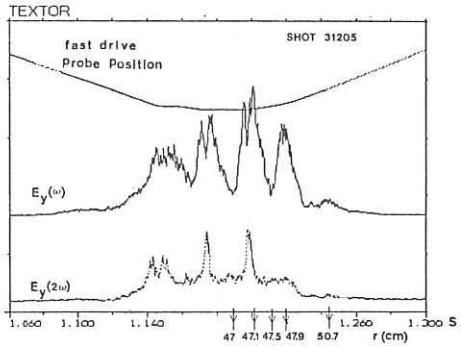

Fig.2 Radial, uncalibrated profiles of $E_y(2\omega)$ measured by the fast-drive probe in a $^3He(H)$ discharge, with 300 kW on A1 and 300 kW on A2; ALT-II limiter at r = 46 cm, antennas at r = 47 cm; $B_T = 2.1\ T,\ I_p = 340\ kA,\ \bar{n}_{e0} = 2.0 \times 10^{13}\ cm^{-3}$

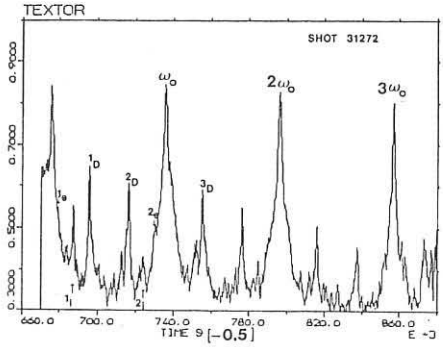

Fig.3 Parametric decay spectrum measured with the E_z -probe in a mixture of deuterium(92 %) and hydrogen(8 %), 900 kW on A1 and 680 kW on A2 at 29 MHz ($\omega_0/2\pi$), $B_T = 2.0T$, $I_p = 340\ kA,\ \bar{n}_{e0} = 1.5 \times 10^{13}\ cm^{-3}$

The signals at ω_0, $2\omega_0$, $3\omega_0$ are saturated.

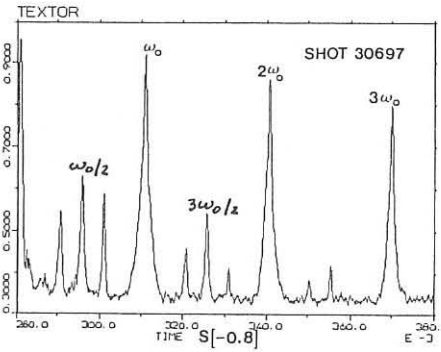

Fig.4 Parametric decay spectrum measured with the E_y-probe in a D(H) minority heating scheme (less than 2 % H) with a transmitted power of 770 kW on A2 at 29 MHz($\omega_0/2\pi$); $B_T = 2.0\ T$, $I_p = 480kA$, $\bar{n}_{e0} \simeq 3.5 \times 10^{13} cm^{-3}$. The signals at ω_0, $2\omega_0$, $3\omega_0$ are saturated.

References

1. B. Schweer et al; Europhys. Conf. Abstr.Vol. 10C, I, 399
2. U. Samm et al; Plasma Physics and Contr. Nucl. Fusion 29, 1321 (1987)
3. R. Van Nieuwenhove and G. Van Oost, 8th Int. Conf. on Plasma Surface Interactions, Jülich, May 1988
4. J.-M. Beuken et al; this conference
5. A.M. Messiaen, P.E. Vandenplas, G. Peter, Electronics Letters 4 (1968) 29
6. R. Van Nieuwenhove, R. Koch, G. Van Oost, J. Gernhardt, J.-M. Noterdaeme, Europhys. Conf. Abstr. Vol. 11D, III, 928
7. R. Van Nieuwenhove, G. Van Oost et al; to be published
8. R. Van Nieuwenhove, G. Van Oost, J.-M. Noterdaeme, M. Brambilla, J. Gernhardt, M. Porkolab, Nucl. Fusion, to be published, and IPP Report III, 129, Garching, Jan. 1988
9. J.-M. Noterdaeme et al; this conference
10. J. Winter et al., 8th Inf. Conf. on Plasma Surface Interactions, Jülich, May 1988
11. W.H.M. Clark, Proc. 4th Int. Symp. Heating in Toroidal Plasmas, Rome, March 1984, Vol. I, 385
12. V.K. Tripathi, C.S. Liu, Nucl. Fusion 26 (1986) 963.

ON A POSSIBILITY OF REALIZING A HIGH-POWER RF HEAVY MINORITY ION HEATING OF A PLASMA

A.V.Longinov, S.S.Pavlov, A.A.Chmyga

Institute of Physics and Technology, the Ukrainian Academy of Sciences, Kharkov 310108, USSR

Recent progress in coupling high levels of RF power to the plasma and the development of methods for first-wall conditioning of magnetic traps with an aim of reducing the impurity influx to the discharge encourage physicists to investigate RF heating regimes with the cyclotron absorption of fast magnetosonic waves by minority ions at high input powers. In this case, however, the limitations of the minority ion heating method such as a reduced heating of bulk ions and an enhanced kinetic pressure of resonant particles, become essential. The method of heavy minority ion heating is more free from these limitations, though its application at a high specific power ($P \gtrsim 1 W/cm^3$) requires relatively high concentrations of heavy minority ions. This would raise the effective charge in the plasma, $\Delta Z_{eff} \gtrsim 1$, which may lead to some negative effects.

This report deals with the feasibility of the method of heavy minority ion heating at a high specific RF power without involving an additional enhancement of Z_{eff}. The essence of our proposal lies in the employment of the elements with $Z/A < 1/2$, e.g., Be and ^{13}C isotope (Z, A are the charge and mass numbers, respectively) as first wall materials of the chamber, that might also be used as a heavy ion admixture /1/. Figure 1 shows the behaviour of $K_\perp \varrho_d$ versus ω/ω_{cd} in a deuterium plasma with a 1% hydrogen minority at $n_e = 3 \cdot 10^{13} cm^{-3}$, $T_i = T_e = 10$ keV, $N_\parallel = 3$. As is seen from the figure, the $\omega \approx 2\omega_{cBe}$ and $\omega \approx 2\omega_{c^{13}C}$ zones lie in the region, where the slow wave (SW) exists and the $K_\perp \varrho_d$ parameter is rather large ($K_\perp \varrho_d \sim 1$). The heating method using the ^{13}C isotope can be realized, for example, through carbonization /2/ using ^{13}C-base methane instead of a conventionally employed methane CH_4 based on ^{12}C. The carbonization of the chamber wall surface results in the formation of the coating consisting of ^{13}C isotope-enriched compounds. Hence, in the process of the plasma-wall interaction it is ^{13}C that will come to the plasma instead of ^{12}C. Since after the carbonization the carbon concentration in the plasma may be rather high ($Z_{eff} \approx 2$-3 /3/), it will ensure the attainment of the high concentration of heavy minority resonant ions (^{13}C isotope). Similarly, a high concentration of heavy minorities can be achieved by using ^7Li isotope or beryllium as first-wall component materials (e.g., a diaphragm, etc. /4/).

As an example, we shall consider the feasibility of the proposed method in the device having the JET parameters ($R_0 = 300$ cm, $a = 100$ cm, $B_0 = 3$ T) with a fast mode excitation of

fast magnetosonic waves from the high magnetic field side. The problems of excitation and absorption were investigated using a numerical code similar to that of /1/ for the following plasma parameters: $n_e = 3 \cdot 10^{13}$ cm^{-3}, $T_i = T_e = 10$ keV, H(3%) and Be(1%) being the minority species in a deuterium plasma. The $\omega = 2\omega_{cBe}$ zone lies in the plasma core. Computations were performed for the toroidal m=2 mode under the assumption that $T_{Be} = 50$ keV. Figure 2 illustrates the field components E_r and E_z, the kinetic flux P_k and the profiles of energy deposition in ions (D_i) and electrons (D_e). It is seen that in spite of a relatively low hydrogen concentration, the fast wave (FW) penetration through the opacity zone in the two-ion hybrid resonance region is negligible, and therefore, the absorption by deuterons and protons does not practically occur in the cyclotron resonance region (R = 337.5cm). The main part of the injected RF power goes to Be ions due to the absorption of the SW excited in the two-ion hybrid resonance region because of the fast-to-slow wave conversion (the region of the kinetic flux P_k onset in Fig. 2).

For certain plasma parameters, the efficient fast-to-slow wave conversion may also occur /1/ during the FW excitation from the low magnetic field side. Figure 3 exemplifies similar calculations for the T-10 tokamak ($R_0 = 150$ cm, $a = 35$ cm, $B_0 = 3$ T) with the plasma parameters: $n_e = 3 \cdot 10^{13}$ cm^{-3}, $T_i = T_e = 5$ keV, the working gas being deuterium with H(0.2%) and ^{13}C(1%) minorities, $T_C = 50$ keV and m=4. The $\omega = 2\omega_{c^{13}C}$ zone is in the centre of the column. As seen from Fig. 3, despite the excitation regime from the low magnetic field side, the power portion absorbed by deuterons and protons is relatively small ($\approx 20\%$), and most of the injected power is absorbed by ^{13}C ions due to SW generation.

To demonstrate the feasibility of the proposed method of plasma heating, we present the calculated results for plasma heating dynamics. The results were obtained from the solution of the 1-D kinetic equation similar to that used in /5/ with taking into account the Coulomb interaction of the heavy minority ions with deuterium and electrons of the bulk plasma. In the example considered, $n_d = n_e = 5 \cdot 10^{13}$ cm^{-3}, $T_i = 18$ keV, and the heavy minority ion concentration corresponds to $\Delta Z_{eff} = 1$ (^{13}C $\approx$ 3%, Be $\approx$ 6%). In the cyclotron absorption region the parameter $k_\perp \rho_d$ was chosen to be 0.7 and 0.9 for ^{13}C and Be, respectively. Figure 4 shows the portion of the RF power that goes to deuterium ions, P_i, versus the specific RF power absorbed by the minority ions for $T_e = T_i = 18$ keV and $T_e = 6$ keV, $T_i = 3T_e = 18$ keV. It may be seen that in spite of rather high P_{RF} values (2 - 3 W/cm^3), the main part of the RF power heats the deuterons even in the case of low electron temperature. The same figure depicts the dependence of the relative kinetic pressure of resonant particles $\beta^j = \frac{n^j m^j \langle V_\perp^2 \rangle}{2(n_i T_i + n_e T_e)}$

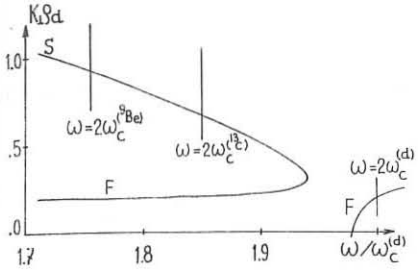

Fig.1

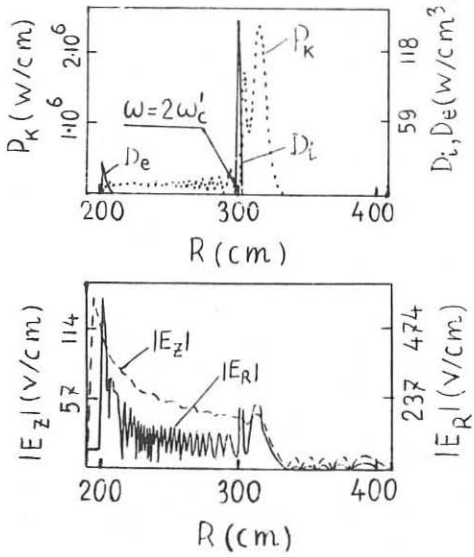

Fig.2

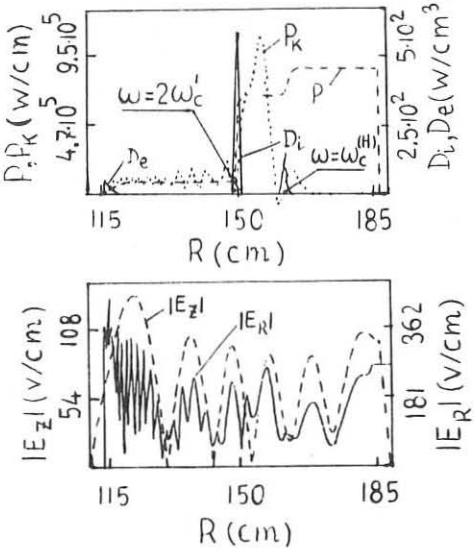

Fig.3

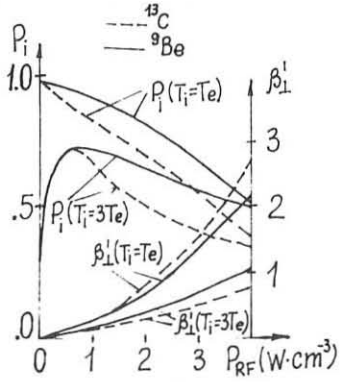

Fig.4

on P_{RF}. The kinetic pressure of the minority ions may be dominant ($\beta' > 1$) at $P_{RF} > 2.5$ W/cm^3 for $T_i = T_e = 18$ keV and $P_{RF} > 4$ W/cm^3 at $T_i = 3T_e = 18$ keV. Note that with the heating method based on the FW absorption by hydrogen ions with $n_i/n_i < 10\%$ and employed under similar conditions for power levels $P_{RF} \gtrsim 1$W/cm^3, the power going for ion heating is about 1%, $\beta' \gg 1$, and the $T_i \gg T_e$ regime is unattainable at all because of a low P_i value.

Thus, the employment of special materials (^{13}C, Be) in first wall coatings or components makes it possible to realize high-power plasma heating regimes with a predominant heating of the bulk ions without an additional Z_{eff} enhancement of the discharge.

References

1. Longinov, A.V., Pavlov, S.S., Stepanov, K.N., in Controlled Fusion and Plasma Physics (Proc. 12th Europ. Conf., Budapest, 1985), Pt.2, European Physical Society (1985) 132.

2. Winter, J. et al., J. Nucl. Mater. 128&129 (1984) 841.

3. Coad, J.P. et al., in Controlled Fusion and Plasma Physics (Proc. 12th Europ. Conf., Budapest, 1985), Pt.2, European Physical Society (1985) 571.

4. Rebut, P.H. et al., Preprint JET-R (85) 03, Culham (1985).

5. Longinov, A.V., Pavlov, S.S., Stepanov, K.N., Vopr. Atomn. Nauki i Tekhn., ser. Termoyad. sintez, Is. 2 (1987) 3.

ICRF FULL WAVE FIELD SOLUTIONS AND ABSORPTION FOR D-T AND D-^{3}He SCENARIOS

J. Scharer and R. Sund

Department of Electrical and Computer Engineering
University of Wisconsin, Madison
Madison, Wisconsin 53706 U.S.A.

ABSTRACT We consider full wave solutions [1] for fields and power absorption in moderate and high density tokamaks. These include D-T scenarios for JET and CIT and a D-^{3}He concept for NET. Optimum single pass absorption cases for D-T operation in JET and CIT are considered as a function of the $k_\parallel$ spectrum of the antenna with and without a minority He^3 component near either the fundamental deuterium or He^3 resonance. It is found that at elevated temperatures >4 keV, minority (10%) fundamental deuterium absorption is very efficient for either fast wave low or high field incidence or high field Bernstein wave incidence. In addition, scenarios with ICRF operation without attendant substantial tritium concentrations are found for second harmonic higher concentration helium (33%) heating in a deuterium plasma. The harmonic heating with substantial concentrations should provide enhanced Q operation for typical energy and particle confinement times with moderate fusion yields. This scenario is also found to be attractive for larger machines the size of NET. For the high field, high density operation of CIT, we find a higher part of the $k_\parallel$ spectrum yields good single pass absorption with a 5% helium concentration in D-T. For ^{3}He-D operation in JET we find the second harmonic ion Bernstein wave absorption by the helium from the high field side to be particularly good. We also consider the influence of fusion reaction products on the absorption process to determine optimum heating scenarios for future tokamaks.

I. INTRODUCTION We consider wave absorption in the ICRF for minority fundamental and second harmonic heating for D-T and D-^{3}He plasmas. Of primary concern is finding a single pass absorption of the ion species in the plasma core for $k_\parallel$ spectrum appropriate for a launching antenna. We also consider both startup ion concentrations and those for maximum fusion power operating conditions which provide strong single pass absorption for the ions for ion cyclotron frequency range waves.

To examine the efficiency of ICRF absorption we use a computer code corresponding to an appropriate definition power absorption and the associated conservation relation for inhomogeneous plasmas developed by McVey, Sund and Scharer [1]. The code correctly solves the propagation and coupling of incident fast magnetosonic waves from the low field side or fast or ion Bernstein waves incident from the high field side of the machine to ion Bernstein waves in the resonant core region.

II. D-T AND D-T-(^{3}He) ICRF ABSORPTION We first examined the absorption for second harmonic tritium for high field, high density CIT parameters (B_0 = 10 T, T = 10 keV and $n_e = 5 \times 10^{14}/cm^3$, and 50/50 D/T). The single pass absorption for tritium is quite low (<20%) for all of the $k_\parallel$ spectrum. As noted by Scharer et al. [2], the tritium absorptivity always lies below that of the deuterium at the second harmonic for this range of plasma parameters. This curve illustrates that it is difficult to rely on minority ^{3}He absorption for ohmic startup conditions and make a transition to second harmonic tritium absorption as the plasma reaches the 10 keV operating conditions of CIT. A minority hydrogen to second harmonic deuterium transition would be more productive for a CIT startup scenario if the hydrogen concentration could be substantially reduced during the startup.

The 5% minority ^{3}He case in a 45%-45% deuterium-tritium plasma as a function of the $k_\parallel$ spectrum for CIT parameters is illustrated in Fig. 1. One notes that the ^{3}He single pass absorption of 65% peaks at a high $k_\parallel$ of 18 m^{-1}. The associated electron absorption is 12% and the tritium absorbs 4% of the incident fast wave power from the low field side for a 20 cm absorption width near the core of the machine. At elevated temperatures one has to be sure that the electron absorption over the whole machine profile via Landau and transit-time damping is not stronger than the ion heating in the core. One also notes that a substantial fast wave reflection (>40%) from the helium cyclotron resonance occurs for lower (<10 m^{-1}) values of $k_\parallel$.

For JET operating conditions for B_0 = 3.45 T and $k_\parallel$ = 6 m^{-1} at an electron density of $5 \times 10^{13}/cm^3$ at 4 keV with 10% deuterium resonant at the fundamental at the core the fast wave provides 51% absorption to the deuterium and 3% absorption to the electrons. When the other parameters are held constant and the species temperatures are raised to 10 keV the fast wave provides 68% absorption to the deuterium and 4% to the electrons. We also find that the ion Bernstein wave incident from the high field side provides 92% absorption on the deuterium and 5% absorption to the electrons. These results yield good absorption and possibilities for breakeven for reasonable confinement times in JET.

III. SINGLE PASS FAST WAVE ABSORPTION FOR JET AND NET D-^{3}He PLASMAS We consider optimum absorption scenarios for cases in which a high concentration of ^{3}He is desired to provide a high fusion yield without the use of substantial tritium concentrations or neutron activation. This is an interesting case to study confinement and plasma heating by the 3.6 MeV alpha and 14.7 MeV protons produced by the reaction.

We first considered JET parameters at high helium concentrations. The best case is second harmonic ^{3}He heating. We assume machine parameters of B_0 = 3.45 T with an electron density of 5×10^{13} on the axis and a species concentration of 25% ^{3}He/50% D at 10 keV. Full wave solutions for $k_\parallel$ = 6 m^{-1} yield 43% helium absorption, 6% electron absorption and negligible reflection for fast wave incidence from the low field side, 27% helium and 6% electron absorption from the high field side for the fast wave and 75% helium and 3% electron absorption for the ion

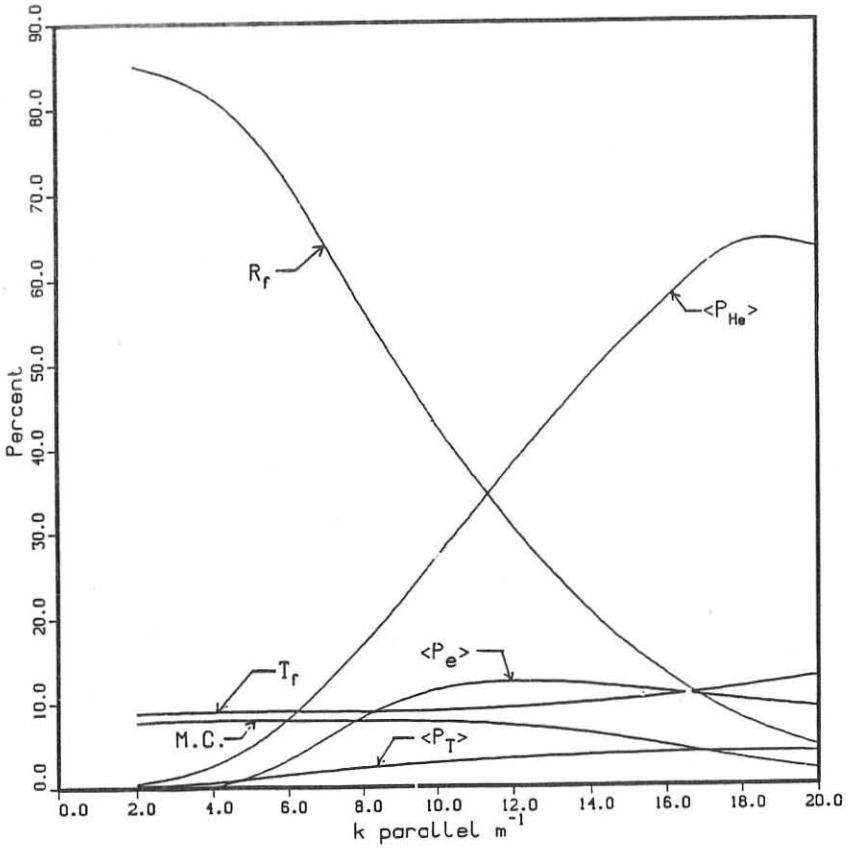

Fig. 1 ICRF Power Conservation for D-T-(^{3}He) CIT Plasma

Bernstein wave incidence from the high field side. Mode conversion for the fast wave from the low field side is negligible whereas 15% of the incident wave of both the fast and ion Bernstein modes are converted from the high field side.

When the parallel wavenumber component is changed to $k_\parallel = 10\ m^{-1}$, the fast wave absorption from the low and high field sides is 32% to the helium and 7% to the electrons. For the ion Bernstein wave incident from the high field side the helium absorption is 91% and the electrons are 4% for the central core 20 cm. One notes that the fast wave absorption for JET at the second harmonic is fairly good whereas the ion Bernstein wave absorption from the high field side is excellent.

We next consider NET at a 7 keV temperature for all species with an electron density of $1.78 \times 10^{14}/cm^3$, a toriodal field on axis of 5.6 T and a minor radius of 1.7 m. The helium fraction is taken to be 2% initially to achieve optimum single pass absorption at lower temperatures. The electron absorption is a small part of the heating (7%) with the majority of the 65% single pass total absorption done by the helium species. The production of ion tails should broaden this absorption curve and increase the single pass values.

Next, we consider NET operated as a D-^{3}He machine at high concentrations of helium to increase the fusion power output. The magnetic field is 5.0 T at a major radius of 5 m with a core electron density of $1.4 \times 10^{14}/cm^3$. At a frequency corresponding to the helium fundamental at the core, a helium temperature of 80 keV with a deuterium temperature of 40 keV and an electron temperature of 20 keV with a helium concentration of 14% and a $k_\parallel = 8\ m^{-1}$ yields 87% helium and 12% electron absorption in the 20 cm core region. At an ion temperature of 40 keV with 33% of the helium distribution having a tail temperature of 200 keV and all other parameters the same, 50% of the fast wave incident power goes to the bulk helium ions and 29% to the tails with 19% going to the electrons. This means that an ICRF amplifier and antenna designed for minority helium absorption in D-T could provide reasonable absorption at higher concentrations in a D-^{3}He plasma when the temperature is increased.

At higher concentrations of helium, the fundamental absorption degrades but the second harmonic fast wave absorption on the ^{3}He is quite efficient. At a helium concentration of 25% with 10 keV plasma temperatures and a $k_\parallel = 8\ m^{-1}$, the helium absorption is 85% with a 7% electron absorption. At more elevated ion temperatures of 50 keV with 40 keV electrons and 25% helium concentrations, a parallel wavelength of $k_\parallel = 4\ m^{-1}$ yields 75% absorption by the helium and 25% by the electrons in the 20 cm core.

IV. SUMMARY These results indicate that good ICRF ion absorption can be obtained in hotter, moderate to high density tokamaks in both D-T-(^{3}He) and D-^{3}He cases. However, particular attention to ICRF antenna design and coupling physics as well as core species concentration will have to be carried out to avoid substantial reflections and dominant electron heating for higher temperature tokamaks.

*This research was supported in part by DOE Grant DE-FG02-86ER52133.

REFERENCES

1. B. McVey, R. Sund and J. Scharer, Physical Review Letters 55, 507 (1985).

2. J. Scharer, J. Jacquinot, P. Lallia and F. Sand, Nucl. Fusion 22, 255 (1985).

ION CYCLOTRON MINORITY HEATING OF A TWO–ION COMPONENT TOROIDAL PLASMA

G. Cattanei and A. B. Murphy

Max–Planck–Institut für Plasmaphysik, EURATOM Association,
D–8046 Garching, Federal Republic of Germany.

Ion cyclotron heating by the magnetosonic wave is a widely used supplementary heating method in present day tokamaks. Good heating efficiency has been achieved, at least in larger devices [**1**, **2**], generally with most of the rf power deposited in the central region of the plasma. A common feature of the experiments has however been the production of a large amount of impurities. Although the precise mechanism of impurity production is not yet well understood, it must be related to the fraction of the rf power absorbed close to the wall, which may in turn be a consequence of the high rf fields close to the antenna. As the control of impurity production is crucial in all ICRF heating experiments, and the quantitative evaluation of the rf field profiles is an important tool in understanding the problem, the large number of numerical investigations that have been performed [3 – 6] is justified.

We consider here the case of minority heating of an axisymmetric toroidal plasma of circular cross–section. We neglect finite Larmor radius and electron inertia effects but take into account finite parallel temperature $v_{\|}^{th}$ of the minority ions. We approximate the toroidal plasma by a straight plasma cylinder and require all quantities to be periodic in z with period $2\pi R$ where z is the toroidal coordinate and R the major radius. We assume further:

$$
\begin{aligned}
&a) \quad \vec{B} = \vec{e}_z B_o(1 - r/R\cos\theta) + \vec{e}_\theta B_o r/qR \\
&b) \quad n_e(r) = n_e(0)[1 - (r/s)^2] \quad \text{for} \quad 0 \le r \le p \\
&\qquad\quad n_e(r) = n_e(p)e^{-(r-p)/\lambda} \quad \text{for} \quad p \le r \le s \\
&c) \quad \vec{E}(r,\theta,z) = \sum_m \vec{E}_m(r)\cdot\exp[i(m\theta + N\phi - \omega t)], \qquad \phi = z/R
\end{aligned}
\tag{1}
$$

We consider a deuterium plasma with a minority of hydrogen ions. We introduce rotating coordinates for the perpendicular components of the electric field: $E_m^{\pm} = E_r \pm iE_\xi$, where $E_\xi \approx E_\theta - (r/qR)E_z$, so that, neglecting terms of order r/R with respect to unity, we can write the plasma currents J_p in the form

$$
\begin{aligned}
&J_m^- = \sigma^-(r)\cdot E_m^-, \quad J_m^+ = \sum_n \sigma_{m,n}^+(r)\cdot E_n^+, \quad J_{\|} = \sigma_{\|}(r)\cdot E_{\|} \\
&\sigma^-(r) \approx \frac{\Pi_D^2}{c^2}\frac{\omega^2}{\Omega_D(\omega+\Omega_D)} + \frac{\Pi_H^2}{c^2}\frac{\omega^2}{\Omega_H(\omega+\Omega_H)}
\end{aligned}
\tag{2}
$$

where $\vec{J} = 4\pi i\omega \vec{J}_p/c^2$, $\Omega_j = q_j B_o/m_j c$ is the ion cyclotron frequency at $r = 0$ and $\Pi_j = \sqrt{4\pi q_j^2 n_j/m_j}$ is the ion plasma frequency. If electron inertia is neglected, it follows that $\sigma_{\|} \to \infty$, so that $E_{\|} \approx 0$, $E_z \approx -(r/qR)E_\theta$ and $E_\xi \approx E_\theta$.

An expression for $\sigma^+_{m,n}$ has been evaluated in [7, 8]. Note that the expression found in [7] is correct in spite of what is affirmed in [8]. It is indeed easy to see that both eq. (2.14) and eq. (2.15) of [8] have the same singularities associated with zeros of their denominator i.e., $[\Delta\omega/(\bar{\omega}_{ci}\epsilon_t)]\varsigma^o_{\|}/u + p_o = m + p$. We use here a simpler expression valid when collisions are sufficiently high, i.e. $\nu >> v^{th}_{\|}/qR$. From [9] we have for $\omega = \Omega_H$:

$$\sigma^+_{m,n} \approx \frac{\Pi_D^2}{c^2}\frac{\omega^2}{\Omega_D(\omega-\Omega_D)}\delta_{m,n} + i\frac{R}{r}\frac{\Pi_H^2}{c^2}\sqrt{\pi\mu}\, I_{\frac{|m-n|}{2}}\left(\frac{\mu}{2}\right)\exp\left(i|m-n|\frac{\pi}{2}-\frac{\mu}{2}\right) \tag{3}$$

where $\mu = (r/\rho_{\|})^2/[N + (m+n)/(2q)]^2$ and $\rho_{\|} = v^{th}_{\|}/\Omega_H$. From eq. (3) it is clear that, even in the case when $k_{\|} = (N + n/q)/R \to 0$, the plasma current J^+ remains limited: $|J^+| \lesssim (\Pi_H^2/c^2)[R/(|N\rho_{\|}| + \sqrt{r\rho_{\|}/q})]|E^+|$

We assume a perfectly conducting wall at a radius $r = w$, and an antenna at $r = s$ approximated by a sheet current distribution: $J^{ext} = J^{=}(\theta)\ \delta(r-s)\ \exp[i(N\phi - \omega t)]$ with $J^{=}(\theta) = J^{=}_o$ for $\theta_o - \Delta \le \theta \le \theta_o + \Delta$ and zero otherwise.

We have integrated Maxwell's equations numerically for several values of the toroidal mode number. To this purpose the plasma radius was divided into M subintervals and a Runge–Kutta method used to integrate Maxwell's equations in each subinterval. The M free constants which arise in this way were eliminated by using the boundary conditions at $r = s$. Note that this method tends towards equivalence with the finite element method as M becomes large. It has however the advantage that the integration step length adjusts itself independently of M, which can therefore be kept relatively small. The integration time increases as the cube of the number $\bar{m}$ of poloidal harmonics taken into account, which can be a major limitation of the method when applied to a large device. One can estimate roughly the number of poloidal harmonics required to correctly describe the fields in large devices. From eq. (3) we have for $\mu \gg |m-n|$,

$$\sigma^+_{m,n} \approx \frac{\Pi_D^2}{c^2}\frac{\omega^2}{\Omega_D(\omega-\Omega_D)}\delta_{m,n} + i\frac{R}{r}\frac{\Pi_H^2}{c^2}\exp\left[i|m-n|\frac{\pi}{2} - \left(\frac{m-n}{2}\right)^2\left(N+\frac{n}{q}+\frac{m-n}{2q}\right)^2\left(\frac{\rho_{\|}}{r}\right)^2\right] \tag{4}$$

so that $\bar{m}$ must be larger than $2/[\ |N\rho_{\|}|/r + \sqrt{\rho_{\|}/(qr)}\ ]$.

The following parameters, appropriate to ASDEX, have been chosen: $R = 165$ cm, $w = 50$ cm, $s = 45$ cm, $p = 35$ cm, $B_o = 2.5$ T, $q = 2$, $n_e(0) = 5 \times 10^{13}$ cm^{-3},

$n_H/n_D = 0.03$, $T_H = 2$ keV. The spatial distribution of the rf fields has been evaluated for several values of the toroidal modenumber N, and $\theta_o = 0$, $\Delta = \pi/4$ which corresponds to low field side coupling. To avoid too large field gradients close to the ion–ion hybrid resonance layer, a small collisional damping $\omega = \Omega_H + i\nu$ has been introduced, where $\nu = v_{\|}^{th}/\Omega_H$. Fig. (1a) for $N = 0$ and Fig. (1b) for $N = 20$ show the radial dependence of $\int_0^{2\pi} P(r,\theta)d\theta$ where $P(r,\theta)$ is: (i) the total rf power absorbed by the plasma per unit volume, (ii) the rf power absorbed by the minority ions via cyclotron damping, (iii) the rf power absorbed by the majority deuterium ions via second harmonic cyclotron damping. Note that we have assumed the deuterium ions to be cold so that the rf power absorbed by deuterium has been evaluated non self–consistently assuming *a posteriori* $T_D = T_H$. For this reason the total power absorption given in (i) consists only of fundamental cyclotron damping and collisional damping. The units are arbitrary but the value of $J_o^=$ was the same in both cases. The total rf power coupled to the plasma in the case $N = 0$ is approximately eight times greater than in the case $N = 20$ which is in qualitative agreement with experiment [10]. Note however that in the case $N = 0$ most of the rf power is absorbed via mode conversion (in our case simulated by collisional damping) while the rf power directly absorbed by the minority ions via cyclotron damping is in both cases of the same order of magnitude.

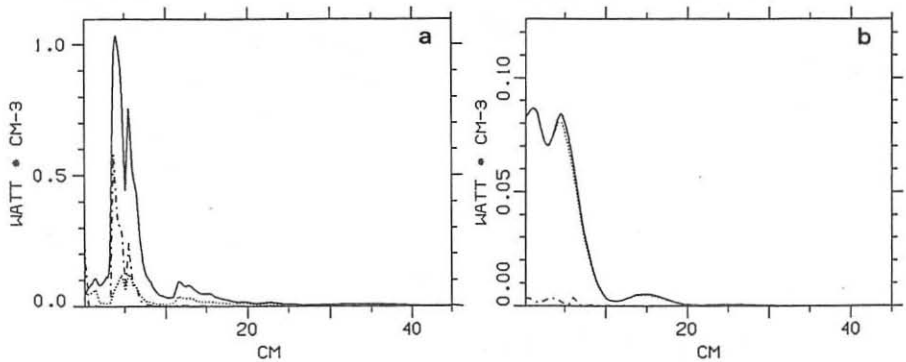

Fig. 1—Radial dependence of rf power absorbed per unit volume for (a) $N = 0$, (b) $N = 20$: total (solid line), ω_{cH} damping (dotted line), $2\omega_{cD}$ damping (dashed line).

Fig. (2a) for $N = 0$ and Fig. (2b) for $N = 20$ show the distribution of $|E^+(r,\theta)|$ over the minor cross–section. The units are again arbitrary but the total rf power absorbed is the same in both cases. It is clear that in the case $N = 20$ ($k_\phi = 0.12$ cm^{-1}) the electromagnetic fields are higher close to the antenna (this effect is even more accentuated for larger values of N). For this reason one would expect less impurity production close to the antenna in the $N = 0$ case which would be in disagreement with experimental evidence [10] if the majority of the impurities were produced close to the antenna.

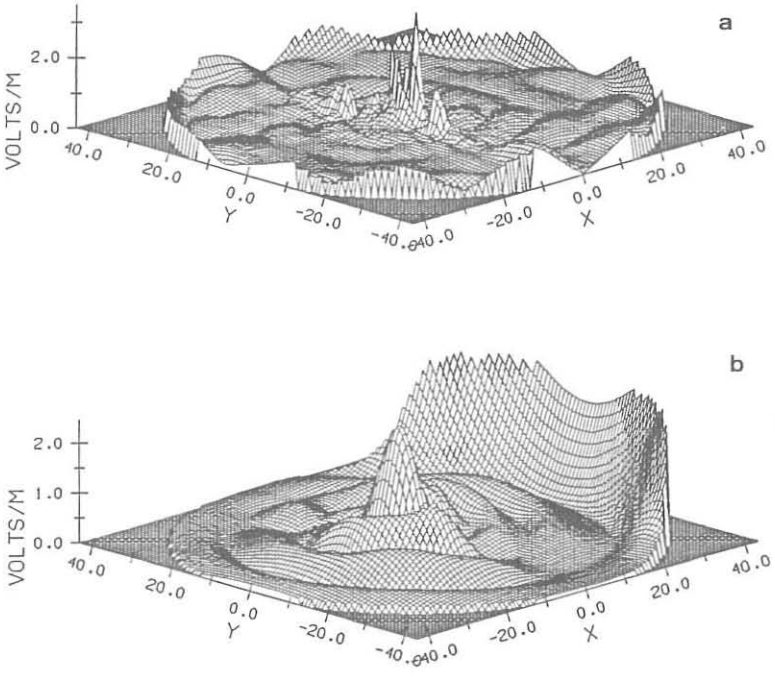

Fig. 2—Distribution of $|E^+(r,\theta)|$ *over a minor cross-section for (a)* $N = 0$, *(b)* $N = 20$.

REFERENCES

[1] The JET Team in *Plasma Physics and Controlled Nuclear Research, 1986* (Proc. 11th Int. Conf., Kyoto) (IAEA, Vienna, 1987) Vol. 1, p. 449.

[2] Adam J. *Plasma Phys. Contr. Fusion* **29** (1987), 443.

[3] Brambilla M. and Krücken T. in *Europhysics Conf. Abs. 11D* (Proc. 14th Eur. Conf. Contr. Fusion and Plasma Phys., Madrid, 1987) (EPS, 1987) Part 3, p. 996.

[4] Hellsten T. *et al.* Report JET-R(87)09 (JET, 1987).

[5] Edery D. *et al.* Report EURATOM CEA-FC 1334 (CEN Cadarache, 1987).

[6] Fukuyama A., Itoh K. and Itoh S.-I. *Comp. Phys. Rep.* **4** (1986), 137.

[7] Cattanei G. and Croci R. *Nucl. Fusion* **17** (1977), 239.

[8] Stepanov K. N., Kaladze T. D. and Pyatak A. I. in *Heating in Toroidal Plasmas* (Proc. 4th Int. Symp., Rome, 1984) (ISPP, Varenna, 1984) Vol. 1, p. 476.

[9] Cattanei G. IPP Report 2/272 (IPP Garching, 1984).

[10] Bureš M. *et al. Plasma Phys. Contr. Fusion* **30** (1988), 149.

ANALYSIS OF PLASMA COUPLING WITH THE PROTOTYPE DIII-D ICRF ANTENNA*

P.M. Ryan, D.J. Hoffman, T.S. Bigelow, F.W. Baity, W.L. Gardner, M.J. Mayberry,† K.E. Rothe

Oak Ridge National Laboratory, Oak Ridge, Tennessee 37831, U.S.A.

Coupling to plasma in the H-mode is essential to the success of future ignited machines such as CIT. To ascertain voltage and current requirements for high-power second harmonic heating (2 MW in a 35- by 50-cm port), coupling to the DIII-D tokamak with a prototype compact loop antenna has been measured [1,2]. The results show good loading for L-mode and limiter plasmas, but coupling 2 MW to an H-mode plasma demands voltages and currents near the limit of present technology. We report the technological analysis and progress that allow coupling of these power densities.

Introduction

Loading on the DIII-D prototype antenna at 30 MHz ranged from 1 to 3 Ω in diverted L-mode, beam-heated discharges and was approximately half that for H-mode [2]. Loading in limiter discharges was as high as 6 Ω over the 40-cm current strap length. In general, this range of loading is being used to assess antenna power capabilities. Our goal is to provide 2-MW capability for frequencies from 30 to 60 MHz, based on these measurements. If the prototype antenna is unchanged, the power capabilities scale as shown in Fig. 1. Plasma loading must be increased by a factor of 2 at the high power level to maintain a voltage maximum below 30 kV (the previous limit on commercial capacitors) and by a factor of 4 to keep currents below 650 A. The only ways to ensure operation with some margin of safety are to (1) improve the voltage capabilities of the high-voltage elements and (2) modify the antenna structure to link more flux to the plasma.

High-Voltage Tests and Improvements

To improve the voltage capabilities of the antenna, we have developed and tested two capacitance matching structures. These structures were tested to full voltage during long-pulse to cw operation in the ORNL RF Test Facility (RFTF). Constraints on the structures include range of capacitance required, room for housing the structure, and cooling requirements. The required capacitance ranges from a minimum of 10 pF to a maximum of 150 pF. The total space available for these structures is approximately 25 cm in diameter by 1 m long. Although it can be 1 m long, the active part must be less than ≈30 cm because of upper frequency (60–80 MHz) considerations. The available cooling techniques implicitly limit the pulse length or the current density in moving parts.

In RFTF, we first tested a Jennings CWV 250 capacitor, rated at 650 A rms and 30 kV peak. This commercial capacitor reached its maximum rated voltage at 25 MHz in a cw version of the prototype antenna after some slight modifications to a corona ring. The maximum voltage was limited by available transmitter power. An equivalent Comet capacitor was successfully run at 900 A cw, 30 kV. Both capacitors were tested under a variety of conditions, including good vacuum, high gas pressure, magnetic fields, fields plus high gas pressure, and plasma. The maximum current is limited by

*Research sponsored by the Office of Fusion Energy, U.S. Department of Energy, under contract DE-AC05-84OR21400 with Martin Marietta Energy Systems, Incorporated.

†GA Technologies, Inc., San Diego, California 92138, U.S.A.

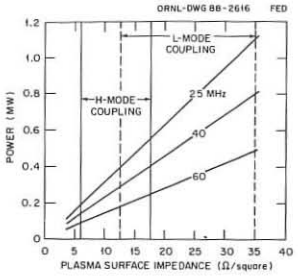

Fig. 1. Maximum power capability of the unmodified antenna vs plasma surface impedance (Z_p). The antenna loading (in ohms) is $0.0843 Z_p$.

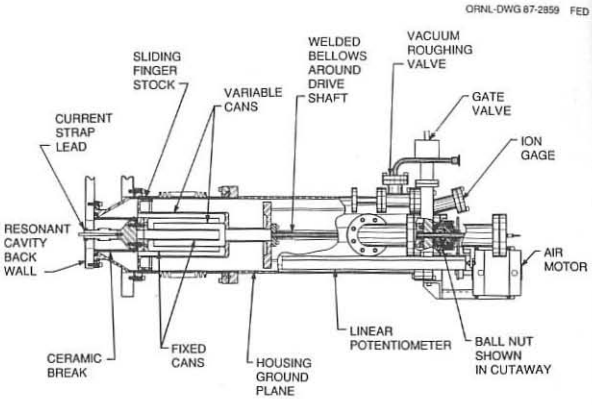

Fig. 2. The ORNL capacitor for the TFTR antenna.

internal cooling on the moving bellows. These voltage and current ratings had to be improved, so high-current, high-voltage capacitors were developed; one by Comet for use on Tore Supra and one by ORNL for use on TFTR.

The Comet Capacitor for Tore Supra

Specifications for the Comet capacitor included 750 A rms at 80 MHz, 50 kV peak, and 13 to 150 pF cw. Although the actual full voltage of 50 kV is as yet untested, the capacitor's internal electric fields at full voltage were the same as tested on RFTF, ≈100 kV/cm. This high field allows a 15:1 capacitance range in the allotted space. The only major principle that was untested was the current rating. This was tested to full cw current on a "capacitor killer" at ORNL.

The ORNL Capacitor for TFTR

The second approach was to design a capacitor specifically for fusion use. The ORNL design (Fig. 2) is the same as the commercial designs, except that motion is accommodated by finger stock and no cooling was permitted for the 2-s rf pulses. The range of capacitance (14 to 97 pF) was sacrificed to reduce the internal electric fields to 43 kV/cm at 50 kV. This capacitor was fully tested in an antenna structure and sustained 65 kV, 800 A at 47 MHz for a variety of test conditions. On the basis of the three capacitor tests in real antenna structures, it is believed that the DIII-D antenna voltage and current limits can be pushed to 50–60 kV and 1 kA for 2 s.

Antenna Improvements

The DIII-D antenna design was analyzed with a two-dimensional magnetostatic model similar to that of Mau [3] and Chen [4]. The analysis solves for the poloidal component of the vector potential, A_y, from which the magnetic field and strap inductance may be calculated; the plasma surface is assumed to be a conducting boundary. Two coupling factors are also calculated: the current coupling factor or specific radiation resistance R and the voltage coupling factor R/L^2. The specific radiation resistance is the ratio of the antenna loading resistance per unit length to the plasma surface resistance,

$$R = (R'_{\text{load}}/R_{\text{plasma}}) = (\mathbf{L}'/\mu_0)^2 \int_{-\infty}^{\infty} |B_z|^2 \, dz \quad ,$$

where L' is the inductance per unit length and the plasma resistance R_{plasma} has been integrated over the toroidal direction. This factor indicates how well the toroidal flux is coupled to the plasma surface; it depends only on the launcher geometry and plasma position and is independent of plasma properties.

The voltage coupling factor R/L^2 is proportional to the loading per strap volt and depends on the operating frequency as well as the antenna/plasma geometry,

$$R/L^2 = \int_{-\infty}^{\infty} |B_z|^2 \, dz = (s^2/h)(\omega\mu_0/V_0)^2(2P_{\text{plasma}}/R_{\text{plasma}}) \quad .$$

Here L is the normalized inductance per unit length ($L = \mathbf{L}'/\mu_0$), V_0 is the maximum allowable voltage excursion, s is the total strap length including leads, and h is the poloidal extent of the strap (radiating length).

The analysis has been validated by comparison with the electrical measurements performed on a bench-top model of the DIII-D antenna [5]. The experiments used a vector impedance meter to measure the antenna inductance and resistance, with sheets of dissipative material serving as a resistive "plasma" load. Four different current straps were studied:

Strap	Thickness (cm)	Width (cm)
Beanpole	2.54	2.54
Popsicle Stick	2.54	8.00
Fat Man	5.50	8.00
Surfboard	2.54	16.00

The cavity was 20 cm wide and the distance from first wall to "plasma" was 6.25 cm; the positions of the current strap and the back wall were adjustable. After accounting for the lead inductance, the electrical length, and the residual resistive losses, the model calculations and the experimental measurements for resistance and inductance agreed quite well. For example, Fig. 3 is a comparison of calculations and measurements for antenna loading, normalized to the resistance of the dissipative surface, as the cavity depth changes. The success of the calculations prompted us to reanalyze the DIII-D antenna geometry to estimate the improvement in coupling due to the proposed changes. The modifications included (1) removing the back tier of rods from the Faraday shield, (2) moving the current strap forward by a distance corresponding to the thickness of the back tier of tubes, and (3) retracting the back plane from the current strap, thus minimizing undesired return currents in the backplane.

Increasing the cavity depth from 15.24 cm to 17.78 cm with the strap position kept constant increased $\mathbf{L}'$ by 8%, R by 18%, and R/L^2 by less than 1%. Decreasing the distance between strap and first wall from 5.08 cm to 3.10 cm with the depth held constant decreased $\mathbf{L}'$ by 1%, increased R by 75%, and increased R/L^2 by 79%. Changing both strap position and cavity depth increased $\mathbf{L}'$ by 4%, R by 93%, and R/L^2 by 80%; the power coupling should increase by about 80% for short pulses, for which the antenna was previously voltage limited, and by about 93% for long pulses, for which the antenna was current limited.

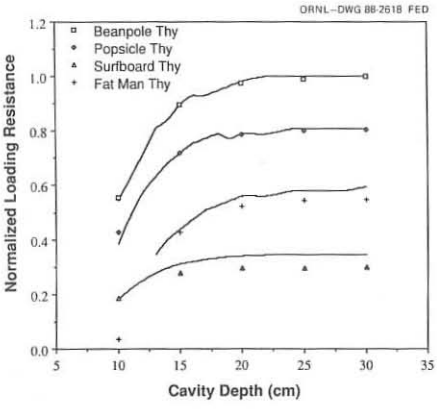

Fig. 3. Comparison of theoretical calculations with measured loading for four different current strap shapes.

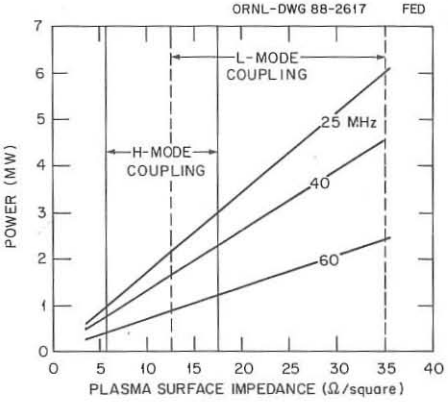

Fig. 4. Maximum power capability of modified antenna vs plasma surface impedance (Z_p). The antenna loading (in ohms) is $0.1626 Z_p$.

Conclusions

Ultimately, the goal of achieving high power density in the H-mode requires the pursuit of technology development and optimization of the antenna structure. The results of our efforts are illustrated by comparing the power limitations in Fig. 1 with those of Fig. 4. With 60-kV capability, a factor of 4 in power capability was gained. The antenna modification produced another factor of 1.8. This gain will be confirmed by more coupling measurements in the DIII-D tokamak this summer. These improvements should allow us to meet the high-power target for DIII-D.

References

[1] J. Luxon et al., in *Plasma Physics and Controlled Nuclear Fusion Research* (Proc. 11th Int. Conf. Kyoto, Japan, 1986), Vol. 1, p. 159 (1987).

[2] D.J. Hoffman, F.W. Baity, W.E. Bryan, E.F. Jaeger, T.L. Owens, D.B. Remsen, J. Luxon, and J.M. Rawls, "ICRH Coupling in DIII-D", in *Proc. 13th European Conf. on Controlled Fusion and Plasma Heating (Schliersee, 1986)*, Vol. 10C, Part II, pp. 141–144 (1986).

[3] T.K. Mau, S.C. Chiu, and D.A. Baker, GA Technologies Report GA-A17776 (1986).

[4] G.L. Chen, P.M. Ryan, D.J. Hoffman, F.W. Baity, D.W. Swain, J.H. Whealton, *AIP Conf. Proc.* **159** (7th Topical Conf. on Application of RF Power to Plasmas, Kissimmee, Florida, 1987), 382 (1987).

[5] C.L. Rettig, P.M. Ryan, and D. J. Hoffman, *Bull. Am. Phys. Soc.* **30**, 1589 (1985).

RF STABILIZATION OF EXTERNAL KINK MODES

J.P. Goedbloed* and D.A. D'Ippolito**

*FOM-Instituut voor Plasmafysica, Nieuwegein, The Netherlands
**Lodestar Research Corporation, Boulder, Colorado, USA

In tokamaks external m=1 kink modes are stabilized by the geometric constraint that the modes should fit into the torus. This condition, when expressed in terms of the current, is the well-known Kruskal-Shafranov limit. No such simple device is available to stabilize the higher-m modes. Since these modes depend on details of the current distribution, which cannot be controlled very well at present, it is a realistic starting point to expect instabilities with respect to $m \geq 2$ modes when the safety factor at the plasma surface $q_1 < 2$. This condition (i.e., its high-β generalization) also puts a limit to the maximum achievable β predicted by the Troyon scaling law since it restricts the plasma current and, hence, cuts through the monotonically increasing function $\beta\ (I_\phi)$ predicted by that law. Hence, it appears imperative for high-β tokamak operation to find a reliable method to externally control the $m \geq 2$ external kink modes.

In a completely different context the opposite problem arises, viz. the apparent absence of external kink modes in current-carrying solar coronal loops, as evidenced by their long life-time, spanning many orders of magnitude of the characteristic growth-time of these instabilities. Here, anchoring of the foot points of the field lines in the photoshere is generally considered to be the responsible agent for stabilization.

One possible way of stabilizing external MHD modes in a tokamak is the application of a strongly evanescent external ICRF surface field, such as the near field of an ion Bernstein wave antenna. This field produces a ponderomotive force at the plasma boundary which introduces an additional positive definite surface term in the ideal MHD energy principle. This term represents the work done by the MHD modes against the ponderomotive force [1]. Hence, the problem can be cast into a variational form:

$$\delta\Lambda = 0 \ , \quad \Lambda \equiv W/N \ , \quad W = W_{MHD} + W_{RF} \ , \tag{1}$$

where W_{MHD} is the usual form of the ideal MHD energy principle, W_{RF} is the additional energy due to the ponderomotive force, and N is a special normalization involving the displacement at the plasma boundary only.

We have computed the effect of the new term W_{RF} for the stability of external kink modes in a low-β plasma for two idealized cases: 1) a single coil toroidal antenna situated at $\theta=0$ and producing a field $A(\theta)$ at the plasma boundary which couples the poloidal harmonics $\exp(im\theta)$ [Fig.1]. 2) a poloidal antenna system at $\phi=0$ (which one could imagine to consist of a poloidal array of toroidally localized ion Bernstein wave antennas) producing a field $A(\phi)$ which couples the toroidal harmonics $\exp(in\phi)$ [Fig.2].

For the toroidal case, W_{RF} for a strongly evanescent RF field may be written as

$$W_{RF} = \frac{1}{2\pi}\left(\frac{aB_o}{q_1 R}\right)^2 \int\oint \alpha_{RF}\,\xi^2\,dr\,d\theta = \frac{1}{2\pi}\oint A(\theta)\chi^2(\theta)d\theta\ , \qquad (2)$$

where α_{RF} is the parameter introduced for the description of RF stabilization of ballooning modes [2], and $\chi(\theta)$ is the amplitude of $\xi(r,\theta)$ at the plasma edge. Exploiting the normalization

$$N = \frac{1}{2\pi}\oint \chi^2(\theta)d\theta\ , \qquad (3)$$

(which yields a reasonable estimate for the growth rates of external kink modes and evades the problem of the superposition of continuum modes), the discretized version of the variational principle (1) becomes

$$\Lambda = W/N = \left[\Sigma\lambda_m x_m^2 + \Sigma\Sigma a_{|m-m'|}\,x_m x_{m'}\right]/\Sigma x_m^2\ , \qquad (4)$$

where a_m and x_m are the Fourier harmonics of $A(\theta)$ and $\chi(\theta)$, respectively, and the λ_m's are the different eigenvalues of the system in the absence of an RF field. Notice that n is still a good quantum number for this case.

To fix the equilibrium, we have arbitrarily chosen a diffuse current profile $j_\phi \sim 1-\psi$, where ψ is the poloidal flux, which is unstable with respect to m=-1,-2,-3 for all n≠0. In a similar fashion, the antenna function $A(\theta)$ has been assumed to have the following shape:

$$A(\theta) = A_o \exp\left[-(2/\theta_w^2)\sin^2 \tfrac{1}{2}\theta\right]\ , \qquad (5)$$

where A_o measures the amplitude and θ_w the width of the RF field at the plasma boundary.

In Fig. 1 the lowest branches of the eigenvalues λ_m are indicated by the dashed curves labeled "without RF". These exhibit the instability of the m=-1,-2,-3 external kink modes for the unperturbed low-β plasma. The average influence of the RF field is easily found by adding the Fourier harmonic a_o to λ_m: This yields the dotted curves labeled "no coupling" in Fig. 1, which present an overestimate of the stability. The full effect of the coupling of all the poloidal modes through the RF field is obtained by solving the 2D problem expressed by Eq. (4). This yields the drawn curves.

In Fig. 1a the results are shown for a highly localized RF field. These results are very similar to the ones obtained in Ref. [3] for the problem of stabilization of external kink modes by a toroidal limiter. For that case it was shown that the stabilization is only apparent when a finite number of harmonics was taken into account. (The limit of infinitely many harmonics converged to the case without a limiter.) This stabilization now becomes genuine when an RF field of finite extent is considered (Fig. 1b).This is analogous to the stabilizing effect by toroidal limiters of finite extent [4]. Clearly, the m=-2 and -3 kink modes are easily stabilized, whereas even the Kruskal-Shafranov limit for the m=-1 mode is relaxed to q_1=0.7.

Figure 2 shows the analogous results for a poloidal antenna system as described above. Here, the results of Fig. 2a are again quite analogous to the ones obtained for poloidal limiters [3], whereas Fig. 2b shows that the m=-2 external kink modes are also easily stabilized by a poloidal RF field. The Kruskal-Shafranov limit for the m=-1 modes (not shown here) shifts to $q_1 \approx$ 0.77. Hence, it is possible in tokamaks with RF to mimic the effects of line-tying which is so effective in stabilizing solar coronal loops [5].

Finally, it should be noticed that the required antenna structures do not have to match the structure of the expected unstable modes, neither in space nor in time.

ACKNOWLEDGEMENTS. This work was performed under the Euratom-FOM association contract with financial support from NWO and Euratom. It was also supported by the US Department of Energy.

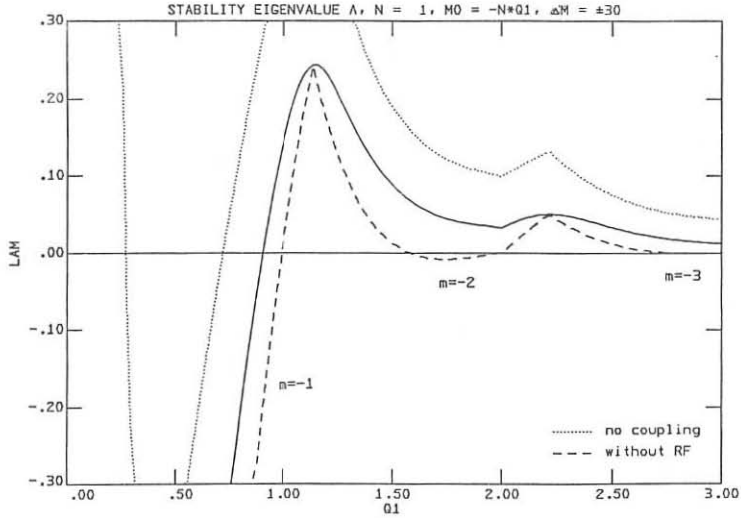

a. narrow antenna function (A_o=10, θ_w=0.1)

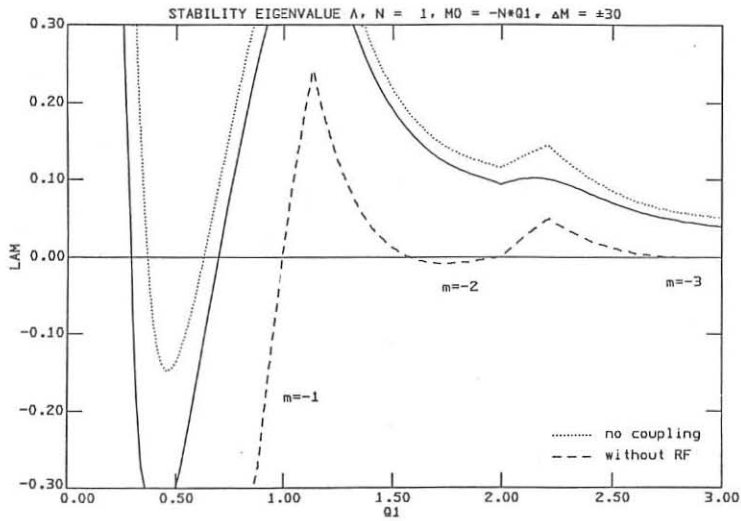

b. broad antenna function (A_o=1, θ_w=1)

Fig. 1. Stability diagram $\Lambda(q_1)$, toroidal antenna, n=1 mode

REFERENCES
[1] D.A. D'Ippolito, Phys. Fluids **31** (1988) 340.
[2] D.A. D'Ippolito, J.R. Myra, G.L. Francis, Phys. Rev. Lett. **58** (1987) 2216.
[3] J.P. Freidberg, J.P. Goedbloed, R. Rohatgi, Phys. Rev. Lett. **51** (1983) 2105.
[4] J.K. Lee and N. Ohyabu, Phys. Fluids **27** (1984) 2874.
[5] G. Einaudi and G. van Hoven, Solar Phys. **88** (1983) 163.

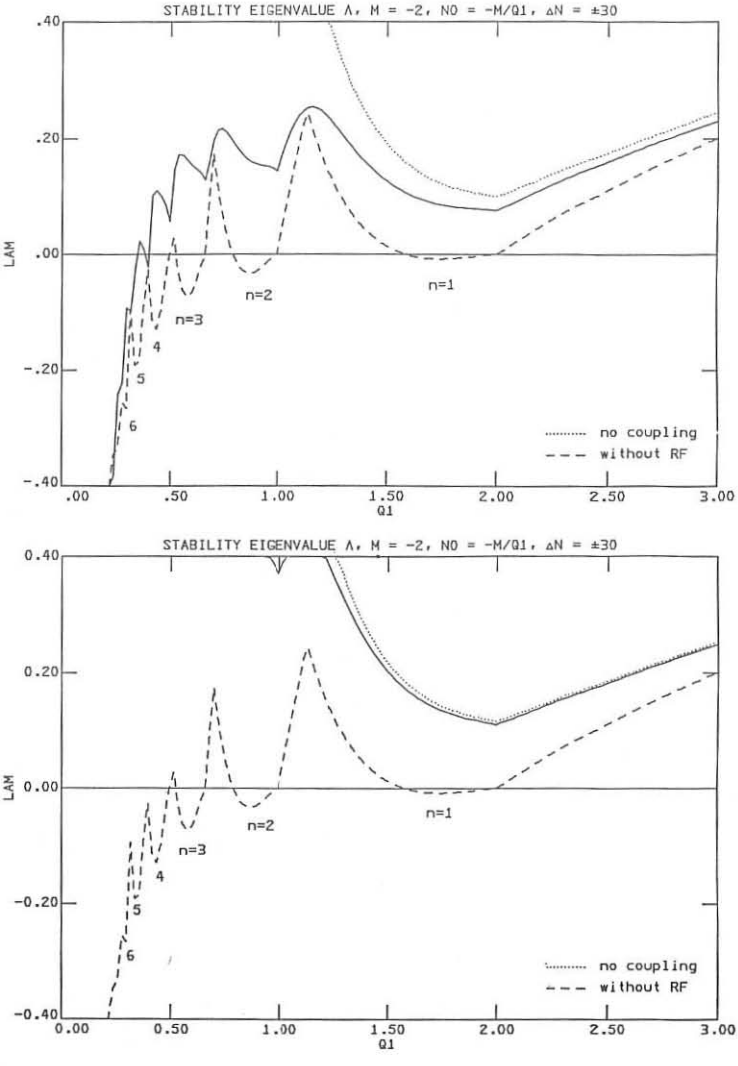

a. narrow antenna function (A_o=10, ϕ_w=0.1)

b. broad antenna function (A_o=1, ϕ_w=1)

Fig. 2. Stability diagram $\Lambda(q_1)$, poloidal antenna system, m=-1 mode

ANALYSIS AND SIMULATION MEASUREMENTS OF ICRF WAVEGUIDE COUPLING TO DIVERTOR TOKAMAKS*

N. T. LAM, J. L. LEE, J. SCHARER, B. JOST
Electrical and Computer Engineeering Department
University of Wisconsin, Madison
Madison, WI 53706 USA

ABSTRACT

Recent experiments have indicated the importance of the H-mode confinement in tokamaks with divertors. To simulate the H-mode, we take the edge plasma to consist of a pedestal of variable length followed by a region of variable gradient indicative of L to H-mode edge density transitions. A radiation condition is assumed from inside the plasma, with both slow and fast waves taken into account. We consider three different launcher geometries: dielectric-filled rectangular, air-filled double-ridged and folded waveguides. The eigenmodes and eigenvalues of the ridged and folded waveguides are obtained from Ritz's variational method. The advantages and disadvantages for each launcher are discussed for plasma parameters appropriate to CIT and NET. We find that the addition of the lower density edge region raises the launched fast wave reflection coefficient but that proper tailoring of the waveguide launcher aperture and n_z, n_y spectrum can optimize the coupling to H-mode profiles. We also present results for the coupling properties of a simulated plasma-loaded waveguide coupler. We performed reflection measurements by terminating the dielectric-filled waveguide coupler with an equivalent load which yields the same complex reflection coefficient at the guide-plasma interface as that calculated for realistic edge density profile plasmas. Inductive and resistive loads along with an impedance transformation were applied to realize the normalized plasma impedance at the waveguide aperture. Measurements for plasma impedances using the time-domain gating features of an HP 8510 network analyzer obtained an input reflection coefficient of the plasma-loaded waveguide coupler at 85 MHz, $\Gamma = P_{ref}/P_{inc}$, ($\Gamma \simeq 0.2$) and obtained good agreement between the measurements and our analytical model.

INTRODUCTION

For coupling ICRF power into tokamak plasmas, coil antennas have succeeded in producing up to 1.5 MW/antenna and fluxes of 7 kW/cm^2. In a fusion reactor environment, a waveguide launcher may be more advantageous because of its structural rigidity, compactness and power handling capability. We present analytical and experimental studies on a dielectric-filled rectangular waveguide suitable for near-term coupling tests of ICRF heating.

*Work supported by DOE grants DE-FG02-86ER52133 and DE-FG02-86ER53218.

PLASMA IMPEDANCE

Let x = radial direction; y = poloidal direction; z = toroidal direction. In the waveguide, the transverse fields can be written as linear combinations of TE and TM modes, i. e.

$$\vec{E}_T^w = \sum_\ell \vec{E}_\ell(y,z)\,[A_\ell \exp(i\beta_\ell x) + B_\ell \exp(-i\beta_\ell x)] \tag{1}$$

$$\vec{H}_T^w = \sum_\ell D_\ell^w \vec{H}_\ell(y,z)\,[A_\ell \exp(i\beta_\ell x) - B_\ell \exp(-i\beta_\ell x)] \tag{2}$$

where β_ℓ = axial propagation constant of the ℓ mode; $\vec{E}_\ell(y,z)$ and $\vec{H}_\ell(y,z)$ = mode transverse fields; D_ℓ^w = mode admittance. The TE_{10} mode corresponds to $\ell = 1$, and it is the only mode which can propagate for the waveguide dimensions of interest. Thus, $A_\ell = 0$ for $\ell > 1$.

In the slab model, the plasma fields are Fourier-analysed as, e. g.

$$\vec{E}_T^p = \frac{1}{4\pi^2} \int dk_y dk_z \vec{E}_T^p(k_y,k_z,x) \exp[i(k_y y + k_z z] \tag{3}$$

Continuities of $\vec{E}_T$ and $\vec{H}_T$ at the interface ($x = 0$) and mode orthogonality yield a formula for the reflection coefficient $\Gamma = B_1/A_1$ in terms of the surface admittance tensor $\vec{\vec{Y}}^p$ defined as

$$\vec{H}_T^p(k_y,k_z,0) = \vec{\vec{Y}}^p \cdot \vec{E}_T^p(k_y,k_z,0) \tag{4}$$

Assume a cold plasma. To estimate $\vec{\vec{Y}}^p$, we use the method of Bers and Theilhaber [1] specialized to the case $E_z = 0$ (this approximation is good for the plasma parameters we are considering, since the slow wave is strongly evanescent). Assuming a radiation condition from inside the plasma, the differential equations determining $\vec{\vec{Y}}^p$ have been solved numerically by a Runge-Kutta algorithm. Given the reflection coefficient Γ, one can define an equivalent surface plasma impedance by the formula $Z_p = Z_w(1+\Gamma)/(1-\Gamma)$ with Z_w = waveguide impedance for the TE_{10} mode.

We consider a CIT-like plasma with the following parameters : edge density/center density = 1% ; major (minor) radius = 170 (55) cm ; B_0 = 10.4 T; 1-1 D-T plasma with $n_0 = 2.0 \times 10^{14}$ cm^{-3} and 1% He^3. To simulate the H-mode, we take the plasma density to consist of a pedestal followed by a region of gaussian variation. The waveguide has a width of 30 cm and is filled with a dielectric of $\epsilon_r = 81$. The heating is at the second harmonic frequency of tritium f = 95 MHz ($Z_w = 51.7\Omega$). Table I lists the power reflection $|\Gamma|^2$ and plasma impedance for various waveguide heights and pedestal lengths. Up to 10 TE and 5 TM modes have been included in the calculation.

Table I $|\Gamma|^2$ and Z_p for various waveguide heigths

	H(cm)	Power reflection coefficient	Plasma impedance (Ω)
pedestal	30.0	0.41	$43.5 + j\,79.0$
length	20.0	0.52	$41.1 + j\,95.9$
=0.0 cm	10.0	0.69	$33.2 + j\,121.0$
pedestal	30.0	0.59	$32.4 + j\,96.8$
length	20.0	0.71	$26.6 + j\,112.5$
=5.0 cm	10.0	0.82	$19.8 + j\,135.3$
pedestal	30.0	0.67	$29.7 + j\,110.7$
length	20.0	0.79	$21.1 + j\,125.3$
=10.0 cm	10.0	0.88	$14.3 + j\,144.1$

Note the high reactance values. The power reflection coefficient increases as the waveguide height decreases and the pedestal length increases. This means that a L to H-mode transition would affect ICRF launcher coupling adversely. However, it should still be possible to design a waveguide array with proper phasing, so as to maximize coupling in the H-mode regime.

LABORATORY EXPERIMENTS

We use a 24 cm × 12 cm rectangular waveguide as a laboratory version of the launcher. Deionized water ($\epsilon_r = 78$ in the ICRF) is chosen as the dielectric filling the waveguide. We have adopted a shorted probe excitation scheme and analyzed it theoretically in reference [2]. For a matched waveguide ($Z_p = Z_w$), we vary ℓ_S = distance between probe and shorting plate and measure $|S_{11}|$ = magnitude of reflection coefficient at the probe for various probe radii, over a 60 - 130 MHz range. An HP8510 network analyser has been used in the measurements. Figure 1 shows the measured and theoretical $|S_{11}|$ vs. ℓ_S for the indicated waveguide and probe parameters. The two curves agree fairly well, especially near the optimally tuned region where the power coupling efficiency can reach 90%. A small interface offset has been included in the theoretical model. Our experiments also show that deionized water gives an average Q of 185 at 100 MHz and an attenuation coefficient of .13 dB/ft, which are considered acceptable for laboratory tests.

In Figure 2, we plot $|S'_{11}|$ = magnitude of reflection coefficient at the probe with respect to ℓ_S for a loaded waveguide, with a simulated $Z_p = 8.6 + j\,45\,\Omega$. The measurements are carried out at a frequency $f = 85$ MHz, with a copper probe of radius $r = 1.65$ cm. Note that the discrepancies between the measured and theoretical values are larger in the optimal region and smaller in the detuned region. Even for this case of relatively large mismatch, $|S'_{11}|$ can decrease to 0.4, corresponding to an optimal power coupling efficiency of nearly 84%. This suggests that it may be possible to design tuning schemes for the plasma loading range of interest for ICRF. Measurements on a folded waveguide coupler are in progress.

REFERENCES

1. A. Bers and K. Theilhaber., Nucl. Fusion 23, 41 (1983).

2. N. T. Lam, J. L. Lee, J. Scharer and R. J. Vernon, IEEE Trans. Plasma Science PS-14, 271 (1986).

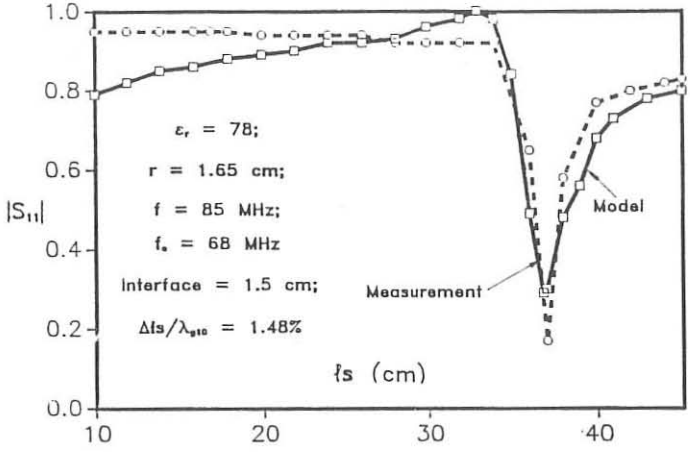

Figure 1: $\mid S_{11} \mid$ vs. ℓ_S for a matched waveguide

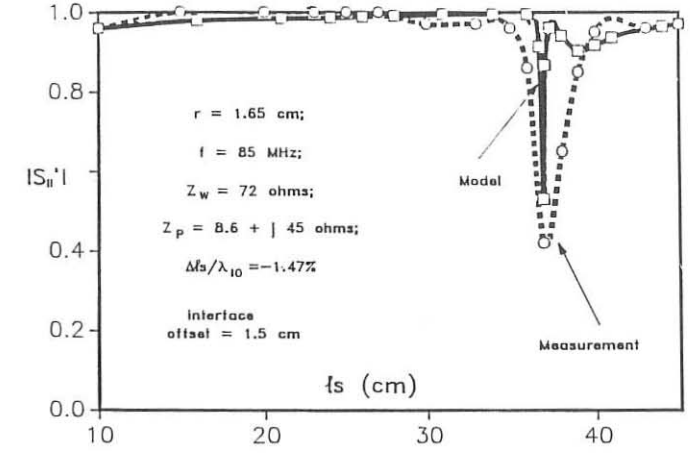

Figure 2: $\mid S'_{11} \mid$ vs. ℓ_S for a loaded waveguide

TRANSPORT STUDIES IN THE DITE TOKAMAK WITH MODULATED ECRH

J Hugill, M Ashraf, M Cox, N Deliyanakis*, H Lean, W Millar, A Simonetto•

Culham Laboratory, Abingdon, OX14 3DB, UK
(UKAEA/Euratom Fusion Association)

*University of Oxford
•Attached under a Euratom Fellowship

Introduction

Measurement of the plasma response to power input modulated at angular frequency ω, where $\omega\tau \sim 1$, τ being a characteristic thermal transport time, in principle allows the power deposition profile and energy transport coefficients to be estimated. Developing previous studies of this kind [1, 2, 3], we have applied modulated electron cyclotron resonance heating (ECRH) to tokamak discharges in DITE and measured the resulting fluctuations in plasma temperature, density and soft X-ray emissivity. The data are interpreted in terms of an effective coefficient of thermal diffusivity, χ_e^{EC}, which is compared with the corresponding values obtained from an analysis of sawtooth heat pulse propagation, χ_e^{HP} and the steady-state power balance, χ_e^{PB}.

Experimental Method

Discharge parameters used for these experiments were: major/limiter radius 1.20/0.21 m (He^{++} plasma) or 1.19/0.24 m (D^+ plasma), plasma current 100 kA, density $0.6\text{-}3\times10^{19}$ m^{-3}. The major radius of EC resonance was varied from 1.1-1.4 m. Power from a 60 GHz Varian gyrotron oscillator was launched from the high field side of the discharge in X-mode at an angle of 45° to the major radius vector. This was 100% modulated at frequencies of 143 or 333 Hz for pulse lengths up to 160 ms and peak power levels up to 200 kW.

The plasma response was measured using two soft X-ray diode arrays viewing from the top and side with a total of 40 channels, giving a resolution of 11 to 19 mm; a 4-channel 2 mm microwave interferometer; a 14-channel heterodyne receiver for EC emission at the fundamental frequency with a spatial resolution of 16 to 21 mm, and a similar receiver for 2nd harmonic emission. The typical modulation levels observed with these instruments were $\tilde{n}_e/n_e < 2\%$, $(\tilde{I}/I)_{SXR} \sim 10\%$ p/p and $(\tilde{T}_e/T_e)_{ECE} \sim 20\%$ p/p. Comparison of the latter two modulation levels suggests $I_{SXR} \propto T_e^{\alpha}$ with $\alpha \sim 0.6$. This is consistent with recombination radiation from fully ionised C and O impurities given the cut-off in diode sensitivity below 1 keV. Most of the data to be described was obtained with the soft X-ray arrays.

The n^{th} Fourier component of the quantity X is represented by the complex quantity ${}^nX$, where $\mathrm{Arg}({}^nX)$ is the phase with respect to the power input (i.e. $\mathrm{Arg}({}^nP_{rf}) = 0$) and $\mathrm{Arg}({}^nX) < 0$ corresponds to a phase delay.

These components were obtained by fast Fourier transform of the digitised data or by subtraction of the slowly-varying part of the signals followed by least squares fitting of a sinusoid, which gave essentially identical results. Boxcar analysis on the modulation period was used to check for the presence of sawtooth oscillations locked in phase with the modulated power. The effect of sawteeth on $^1I_{SXR}$ is usually negligible because their perturbations are smaller than those produced by modulated ECRH and/or they are not locked in phase. A case with fairly large, locked sawteeth is shown in Fig. 1. Even for this case, the effect on $Arg(^1I_{SXR})$ is estimated to be small because the sawtooth is almost a linear superposition on the underlying waveform. There is no large change in $Arg(^1I_{SXR})$ at the sawtooth inversion radius, as seen in other experiments [4]. In order to obtain the profile of local soft X-ray emissivity, this was represented by a sum of four or more Gaussians of different widths whose amplitudes could be adjusted to cover a wide range of shapes, including central hollows. $Re(^1I_{SXR})$ and $Im(^1I_{SXR})$ were fitted separately but using the same geometry as for the slowly varying part of the signal, averaged over the period of analysis (usually the major part of the modulated pulse train).

A simple 1-D model of the deposition and transport of heat [3] was used to estimate the radial position and width of the deposition profile (assumed Gaussian in shape) and χ_e^{EC}. These parameters are adjusted until a plot of $Arg(^1I_{SXR})$ versus r matches the experimental results, as shown in Fig. 2.

The heat pulse following sawtooth collapse was used to estimate χ_e^{HP} either from the slope of the graph of time-to-peak v $\Delta r^2/8$, or from the formula $\chi_e^{HP} \simeq \frac{3\pi}{2\tau_{st}} \left(\frac{d}{dr} Arg(^1I_{SXR})\right)^{-2}$ where τ_{st} is the sawtooth period [5].

At low density the calculation of χ_e^{PB} from the central, steady-state electron power balance in ohmic discharges is relatively straightforward because radiation and equipartition are small, so that most of the power input is lost by electron conduction. The electron temperature profile is fitted by Gaussian or parabolic forms and we take Z_{eff} = constant with Spitzer or neoclassical resistivity.

Results and Discussion

In comparing chord average values of $^1I_{SXR}$ from the top and side arrays, a difference in the radial variation is immediately observed. Assuming $^1I_{SXR}$ to be a function only of the slowly varying part of the emissivity, I_{SXR}, this difference can be explained by an oscillation of the major radial position of the discharge centre of order 1 mm. On the steep sides of the SXR emission profile this small movement is sufficient to produce oscillations in the top array signals comparable with those produced by direct heating. The ECE and microwave interferometer diagnostics will be affected in the same way but to a smaller extent. The phase of the radial

oscillations is not what would be expected for the Shafranov shift inside a rigid boundary in our case. The phase is modified by the radial position control system, which has a response time comparable with the ECRH modulation period. To make estimates of χ_e^{EC}, $^1I_{SXR}$ from the side array only has been used, for which the effects of the radial motion are an order of magnitude smaller.

The most complete data sets have been obtained for He discharges, with $a = 0.21$ m and n_e in the range $1.1\text{-}1.7 \times 10^{19}$ m^{-3}. At $r/a \sim 0.5$ we obtain $\chi_e^{EC} = 2.3\text{-}3.2$ m^{2}s^{-1} with estimated errors of ± 0.6 m^{2}s^{-1}, $\chi_e^{HP} = 2.0\text{-}2.8$ m^{2}s^{-1} and χ_e^{PB} = (OH) 1.5-2.0 m^{2}s^{-1}. It should be noted that there is no evidence that the global value of τ_E is degraded during ECRH at the low density and low power levels used in these experiments. Thus, as in other devices [5] there is a tendency for the estimates obtained from heat pulse propagation to be larger than the steady-state value. However, we are not yet completely confident of the ECRH modulation technique. Central values of phase delay are observed, particularly with off axis heating, which are either too small (<0.5 radians) or too large (>1.6 radians) to be explained by our simple model. Locked sawteeth are present in some of these cases but do not provide an obvious explanation. In some conditions we have seen a complex response on off-axis SXR chords to a step function increase in ECRH power. The signal increases on a short time scale and then decreases, as illustrated in Fig. 3. This would suggest two different processes are responsible for the SXR signal. Electron density variations seem to be ruled out by the μ-wave interferometer results but changes in impurity transport are a possibility. Finally, the modelling of the heat deposition and transport is oversimplified. For example, there is no independent confirmation of the Gaussian profiles used to represent heat deposition and there is no term to represent the variation of the ohmic input produced by temperature perturbations.

Conclusions

A promising start has been made in developing the measurement of electron heat transport by modulated ECRH. The values obtained are of the same order as those from sawtooth heat pulse analysis and ∿ 2x larger than from the steady state energy balance. Further refinements to the electron transport analysis and better measurements of $\tilde{T}_e$ and $\tilde{n}_e$ are needed to make further progress.

Acknowledgements:

We would like to thank the DITE technical team for tokamak operations, and the ECRH Group for making available the ECRH power. Estimates of the dependence of SXR intensity on T_e were provided by S. J. Fielding.

[1] G. L. Jahns et al. Nucl. Fusion 26 (1986) 226
[2] H. J. Hartfuss et al. ibid 678
[3] N. Deliyanakis et al. (Proc. EC-6 Conf. on ECE & ECRH, Oxford, 1987).
[4] B. Joye, J. B. Lister and J. M. Moret (Proc. 14th Europ. Conf. on Controlled Fus. & Plasma Phys., Madrid, 1987) Europhysics Conference Abstracts 11D (1987) 950.
[5] E. D. Frederickson et al. Nucl. Fusion 26 (1986) 849

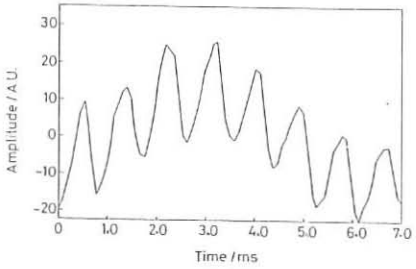

Figure. 1. Boxcar analysis of central SXR channel showing short period sawtooth oscillations locked in phase with ECRH modulation power.

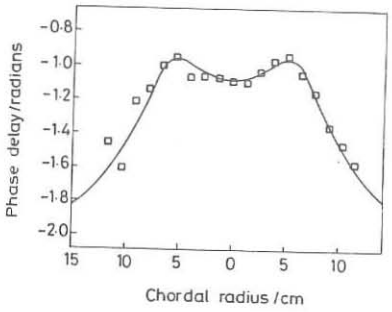

Figure. 2. Plot of SXR channel phase delay v tangent radius. Points are data from horizontal array. Solid line is from model with deposition profile at r=0.06 m, Gaussian width=0.02 m, χ_e^{EC}=2.5 $m^2 s^{-1}$ at r/a=0.5.

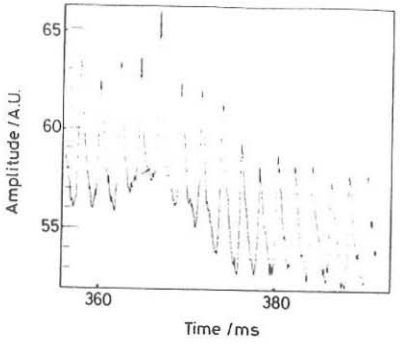

Figure. 3. Anomalous response of SXR channel to ECRH pulse showing initial increase followed by decrease on longer time scale.

DOWNSHIFTED ELECTRON CYCLOTRON HEATING EXPERIMENTS IN A NEAR THERMAL PLASMA

A C Riviere, R Barnsley*, T Edlington, S J Fielding, J Hugill,
P C Johnson, W Millar, M O'Brien and A Simonetto**

Culham Laboratory, Abingdon, Oxon OX14 3DB, UK
(Euratom/UKAEA Fusion Association)

* University of Leicester
** Attached under a Euratom Fellowship

INTRODUCTION

Electron cyclotron resonance heating experiments with high field side (HFS) launch at 60 GHz have been carried out on the DITE tokamak with emphasis on scaling with resonance location, electron density and launch-angle. At the fundamental resonance the X-mode can be strongly absorbed for $k_{||} \neq 0$ but the right hand cut-off prevents access to the plasma when the wave is launched from the low field side. When launched from the HFS this limit is avoided and the cut-off density can be up to twice the O-mode cut-off value, given by [1]

$$(\frac{\omega_p}{\omega})^2 = (1 - n_{||}^2)\ (1 + \frac{\omega_c}{\omega}) \qquad (1)$$

for a semi-infinite slab plasma. Here ω is the applied wave frequency, ω_p is the electron plasma frequency, $n_{||} = ck_{||}/\omega$ and $\omega_c = eB/m_o$. Earlier experiments on FT1 [2] and DIII [3] showed that significant heating can be achieved at line average densities ($\bar{n}_e$) up to more than double the value at which the X-mode left-hand cut-off is present on axis and it is of interest to study this effect further.

In addition, HFS launch requires $k_{||} \neq 0$ and this leads to damping of the rf wave on tail electrons and is of interest in the context of down-shifted resonance heating [4]. Absorption can only occur where the resonance condition is satisfied, that is,

$$\frac{\omega_c}{\omega} = \gamma(1 - n\beta_{||} \cos\theta) \qquad (2)$$

where $\gamma = (1 - v^2/c^2)^{-\frac{1}{2}}$, $n = ck/\omega$, $\beta_{||} = \frac{v_{||}}{c}$ and θ is the angle between k and B. With appropriate values of γ, $\beta_{||}$ and $\cos\theta$, (2) can be satisfied for $\omega_c/\omega \geq 1$, the down-shifted resonance condition. In previous down-shifted resonance experiments in JFT2M [5], WT2 [6], and PLT [7] power was absorbed under conditions where a substantial distortion of the electron distribution

was present, due either to lower hybrid heating or operation under slide-away conditions. In DITE the distribution is close to thermal.

EXPERIMENTAL ARRANGEMENT

The experiments were made in He plasmas with R = 1.2 m, a = 0.21 m and I_p = 100 kA, $3.4 \leq q_a \leq 4.6$. By operating in helium the discharges are well controlled and reproducible with a recycling coefficient close to unity. The rf power was launched from the HFS from three antennas using two designs [8, 9]. Each antenna was connected by a transmission line [10] to a 60 GHz Varian gyrotron capable of an output power in excess of 200 kW for several seconds but used for these experiments for pulse lengths up to 0.2s. The mirrors used to direct the rf power towards the magnetic axis could be rotated so that the launch angle θ with respect to the toroidal field could be varied between nominally parallel and anti-parallel values.

Electron temperatures are obtained from the SXR spectrum and from the ratio of helium and hydrogen-like lines of silicon observed with a Bragg spectrometer [11]. A Michelson interferometer provides T_e profiles. Density profile data is obtained from a movable 4 channel and a fixed single channel interferometers.

EXPERIMENTAL RESULTS

Values of I_p, V_{loop}, β_p (diamagnetic), β_p (equilibrium), 'H alpha' intensity, residual rf power and total radiated power are shown in Figure 1 as a function of time for $\bar{n}_e = 1.5 \times 10^{19}$ m^{-3} and P_{RF} = 315 kW. At this density little change in $\bar{n}_e$ is observed when ECRH is applied but a clear fall is observed at higher $\bar{n}_e$. The change in $\int n d\ell$ across the profile, $\Delta \int n d\ell$, from multi-chord interferometer measurements for $\bar{n}_e$ (central chord) = 3×10^{19} m^{-3} shows a flattening of the profile. At this density $T_e(o)$ increased from 750 $\pm$ 100 ev in the ohmic discharge to 1050 $\pm$ 100 ev during heating. A residual rf power detector located about 180° toroidally from the antennae, is used to assess the fraction of the rf power absorbed by the plasma. At n_e=1.5 and 3.0×10^{19} m^{-3} the absorption is >95% when the resonance is in the central region of the plasma.

Variation of resonance position

With the HFS launch of the X-mode with $k_{||} \neq 0$ strong absorption is expected before the wave reaches the cyclotron resonance zone. The extent of this depends on the electron temperature (T_e) since the absorption occurs where the Doppler shifted resonance condition is satisfied provided there are an adequate number of electrons present at that point with the required $v_{||}$. In addition the absorption coefficient is inversely proportional to n_e. Thus with a sufficiently high value of T_e and low $n_e$effective central heating can be expected when the cyclotron resonance zone is displaced towards the low field side - the downshifted resonance effect.

Results obtained at a power of 315 Kw using all three antennae (66% of the power in the X-mode) are shown in Figure 2(a) for two values of $\bar{n}_e$.

For $R_{res} \geq 1.4$ m there is an increase in V_ℓ, leading to increased ohmic heating which may be the reason for increased $\Delta\beta$ when the resonance lies in this region.) Corresponding single-pass absorption values for X-mode from ray tracing calculations are plotted in Figure 2(b). For these calculations a Maxwellian electron distribution was used. The absorption zone for the conditions corresponding to point A of Figure 2(b) lies close to the axis, not at the cyclotron resonance. The energy of the electrons in Doppler resonance with the wave is about 5 keV whereas $T_e(0)=1.5$ keV for these calculations. There is no evidence from the SXR or HXR diagnostics that a significant hot electron population is present. The ECE spectrum shows a down shifted peak consistent with a small hot electron population. Using the estimated temperature and density of this group ray tracing shows that it has very little effect on the results obtained with the thermal plasma assumption. The results therefore provide clear evidence for Doppler shifted resonance absorption (down-shifted resonance) in a near thermal plasma.

Variation with electron density

The earlier work with HFS launch on DIII [3] showed no fall off in $\Delta\beta_p$ as $\bar{n}_e$ was raised to nearly twice the value corresponding to cut-off on axis. At 60 GHz, $\omega_p^2/\omega^2=1$ at $n_e=4.46\times10^{19}m^{-3}$. Using equation (1), (with the relation $R.n_{||}$ = constant appropriate to toroidal geometry and the measured density profile) the cut-off density for a launch angle of 45° with respect to $\underline{R}$ and for the resonance zone at R=1.27m is $\bar{n}_e=3.8\times10^{19}m^{-3}$. As $\bar{n}_e$ is increased above this value the power will be absorbed increasingly nearer the plasma edge. The values of $\Delta\beta_p$ as a function of $\bar{n}_e$ observed in DITE are plotted in Figure 3 for two sets of conditions. These both show that the heating efficiency falls rapidly above $\bar{n}_e=3.8\times10^{19}m^{-3}$. The difference in behaviour compared with that observed in DIII is possibly because the present data is taken with the resonance off-axis or is taken in helium discharges for which the ohmic τ_E varies nearly linearly with $\bar{n}_e$ in this range. In contrast in the deuterium ohmic discharges of DIII [3] a very strong 'turnover' in the τ_E variation is seen. The edge heating produced by ECRH at high $\bar{n}_e$ may be recovering the 'degradation' in τ_E in the ohmic discharge in that case.

SUMMARY

The heating effect ($\Delta\beta_p$) for $\bar{n}_e=1.3\times10^{19}m^{-3}$ is maximum when the resonance zone lies at $R \simeq R_o + a/2$ which is consistent with Doppler shifted (down-shifted) resonance absorption in a thermal plasma.

The heating effect in helium discharges falls to zero as $\bar{n}_e$ increases above the value for which the cut-off appears on axis in contrast to similar experiments in FT1 and DIII in hydrogen or deuterium.

ACKNOWLEDGEMENT The authors wish to acknowledge the high quality work of the ECRH and DITE operating teams and of the COMPASS and DITE diagnostic teams in support of these experiments.

REFERENCES
[1] I FIDONE et al, Phys Fluids 21(1978) 645.
[2] Yu F BARANOV et al, Sov J Plasma Phys 8 (1982) 383.
[3] R PRATER et al, 11th IAEA Conf on Plasma Phys and Contr Nucl Fus Res, Nucl Fus Supplement 1987, Vol I, p587.
[4] I FIDONE et al, Phys Fluids 28 (1985) 1224.
[5] T YAMAMOTO et al, Phys Rev Lett 58 (1987) 2220.
[6] A ANDO et al, Nucl Fus 26 (1986) 107.
[7] E MAZZUCATO et al, Nucl Fus 26 (1986) 1165.
[8] A N DELLIS et al, 6th ECE and ECRH Workshop, Oxford, Sept 1987, Culham Report CLM-ECR(1988) to be published.
[9] C P MOELLER et al, 6th ECE and ECRH Workshop, Oxford, Sept 1987.
[10] A N DELLIS et al, Microwave Conference, PISA 1986.
[11] R BARNSLEY et al, Rev Sci Instr 57 (1986) 2159.

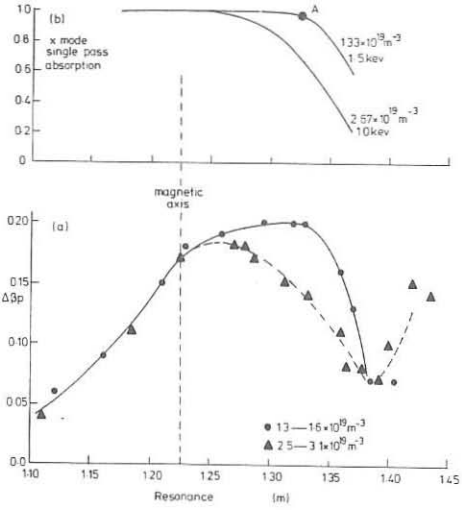

Figure 2
(a) Variation of $\Delta\beta_p$ as a function of resonance position for two densities. Three antennae are used giving a total launched power of 315 kW.
(b) Variation of single pass absorption from ray tracing calculations, for the two sets of conditions of (a), as a function of resonance position.

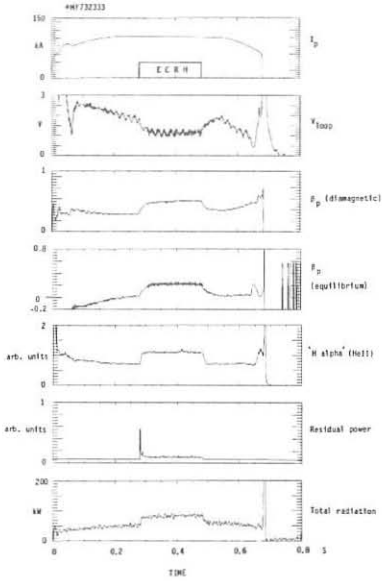

Figure 1
The variation of plasma parameters with time for R_{RES} = 1.33 m, P_{RF} = 315 kW and $\bar{n}_e = 1.5 \times 10^{19}$ m^{-3}.

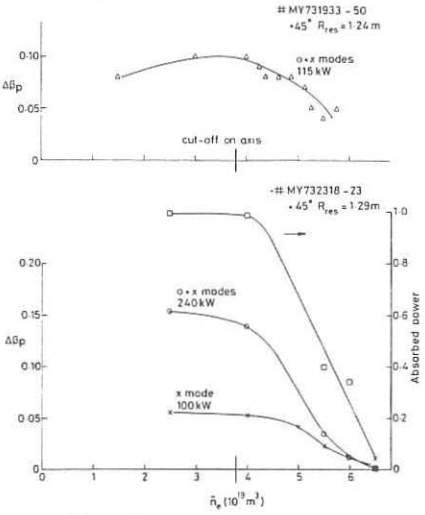

Figure 3
Variation of $\Delta\beta_p$ as a function of $\bar{n}_e$ for two sets of conditions

EXPERIMENTAL INVESTIGATION OF MAGNETIC FIELD OSCILLATIONS ON DITE TOKAMAK

P.Mantica, L.Argenti, S.Cirant
Istituto di Fisica del Plasma, ENEA-CNR/Euratom Fusion Assoc., Milano, Italy
J.Hugill, W.Millar
Culham Laboratory, UKAEA/Euratom Fusion Association, Abingdon, Oxon, U.K.

Fluctuations in the poloidal component of the magnetic field have been measured on DITE (a=24 cm; R0=120 cm) up to a frequency of 300 KHz, using 32 Mirnov coils arranged in two sets of 16, toroidally displaced by 90°.

Both the low frequency (f<50 KHz) region of the spectrum, corresponding to macroscopic MHD modes, and the high frequency one (f>50 KHz), where broad-band small-scale fluctuations are observed, have been investigated /1/. It has been recognized that the two classes of oscillations behave in time as independent phenomena (Figs.1a,b). However, the comparative study of their dependence on the main parameters of ohmic and EC heated plasmas can yield useful information on their relative roles in determining the measured anomalous transport, this question remaining so far unanswered /2,3/.

The ohmic data refer to target plasmas for ECRH (60 GHz, 400 KW for 200 ms, XM from high field side), with the main parameters varying in the following ranges: 30 kA < I_p < 150 kA; 1 T < $B\phi$ < 2.5 T; 3.4 < q_a < 8; 7×10^{12} cm^{-3} < $\bar{n}_e$ < 4×10^{13} cm^{-3}. The gas used was either hydrogen, deuterium or helium.

In these conditions, the low frequency MHD activity is rather quiet, its amplitude being in the order of $\tilde{B}\theta$ / B_p ~ 10^{-3}. Typical power spectra are shown in Figs.2a,b. Cross-correlation analysis allows the identification of the main peak as a m=3,n=1 mode, with a secondary m=4,n=2 component. The rms level is very dependent on the edge q value (see the step in Fig.1 due to the crossing of q=3.5 at the edge). Both the amplitude and the frequency of the two peaks are observed to increase when the density is lowered (Figs.1,2), the mode structure remaing the same.

This activity can be affected by the injection of EC power, depending on the resonance position. Fig.3a shows a case of stabilization of a m=5,n=1 mode for resonance at -6 cm, while when the resonance is progressively shifted towards the outside first no effect and eventually strong destabilization are observed (Fig.3b, a m=4,n=1 mode is destabilized for resonance at +15 cm).

The high frequency fluctuations, characterized by a broad-band spectrum (Fig.4), have amplitudes in the order of $\tilde{B}\theta$/ B_p ~10^{-6}- 10^{-5}, and show a strong inverse dependence on plasma density (Fig.5), a weaker direct dependence on the plasma current (Fig.6) and no measurable dependence on the toroidal field. Unlike the MHD activity, they are not affected by rational q values (Fig.1).

The coherence of these fluctuations is short in time, being in the order of one cycle. Cross-correlation analysis shows that, while for the low frequency modes the spatial coherence is ~ 1 all around the torus, the broad-band fluctuations show a finite correlation length, which is much shorter in the poloidal than in the toroidal direction/4,5/. The correlation within the same toroidal sector decreases to noise level for coils poloidally displaced by about $\Delta\theta$=45°, Δx=23 cm ~ a (Fig.7a). On the other hand, it can be very good (~0.8) between two coils located in different sectors, which are toroidally spaced by ~ 2m (Fig.7b), provided they are close to the same field line in the edge region. Fig.8 shows that, by varying the plasma current, the correlation between two coils achieves the maximum value for a rotational transform at r=a which

effectively corresponds to their angular displacement. A marginal correlation observed at the second pass of the field line after 4/4 and 5/4 of a toroidal turn, or at the pass after ¾ the other way round, indicates that the toroidal correlation length is in the order of the toroidal circumference (Δx=7.35 m).

The above-described experimental evidence suggests that the high frequency perturbations in the current density assume the form of long, narrow filaments lying on magnetic surfaces and extended along the field lines. The external coils are sensitive to the outermost ones, which lie at the plasma edge. Inner perturbations, elsewhere observed to increase towards the plasma centre /5/, give a contribution to the external field which is null on average because of their stochastic nature.

Assuming that the field measured by one coil is due to the closest filamentary perturbations, with contributions from the different filaments weighted by their distance from the probe, then a measurement of the radial decrease of the fluctuation level outside the plasma can provide information on the transverse size of the filamentary cells. This measurement has been performed by slightly (±1cm) displacing horizontally the plasma edge from one fixed coils, and will be improved in the near future by the use of a reciprocating magnetic probe. From the present measurements, it can be deduced on the basis of a simple model that the cell radius is smaller than the distance between two adjacent coils (Δx~10 cm), but not much smaller than the distance of the coil from the plasma edge (Δx~3.5 cm). The transverse size of the filaments is smaller at higher frequencies, and increases with increasing plasma current and decreasing density, consistently with a shrinkage of the poloidal correlation curve observed at high currents and low densities /1/.

Finally, during the injection of EC power, the whole high frequency spectrum is observed to increase (Fig.9) /6/. The enhancement is ≈ 30% for central resonance position and depends strongly on the resonance location. It is maximum when the resonance is at the high field side of the tokamak and gradually disappears when the resonance is shifted to the low field side (Fig.10).

The same behaviour is shown by the increase in the Hα emission measured both at the limiters and at the walls, which on DITE, where no gettering is applied, is the only visible effect that could be related to the deterioration of particle confinement during ECRH, usually seen as a drop in the electron density /7,8/. Both phenomena appear to be inversely correlated with the power absorption and heating efficiency of the EC waves /9/, either in the case of non-localized launch or well-localized wave beam.

Further investigation of magnetic fluctuations on DITE will therefore examine the question whether their enhancement during ECRH is due to edge interaction with the e.m. field or is an echo of internal processes, somehow correlated with particle and energy confinement.

/1/ P.Mantica, S.Cirant, J.Hugill, IFP report FP 88/3, Milano (1988)
/2/ P.C.Liewer, Nucl.Fus. Vol.25 No.5 (1985), p.543
/3/ C.Z.Cheng et al., Pl.Phys.and Contr.Fus., vol.29 No.3 (1987), p.351
/4/ Ch.P.Ritz et al., 29th APS meeting, Plasma Physics Division (1987)
/5/ S.J.Zweben et al., Phys. Rev. Lett. 42 (1979), p.1270
/6/ S.Cirant, P.Mantica, Proc. of EC-6 Workshop, Oxford (1987)
/7/ L.Argenti et al., Proc. 14th EPS Conf. on Contr.Fus.Plasma Phys., Madrid (1987), vol.III, p.819
/8/ B.Lloyd et al., Appl. RF Waves to Tok. Plasma, Varenna (1985), vol.II, p.804
/9/ A.C.Riviere et al., Proc. of EC-6 Workshop, Oxford (1987)

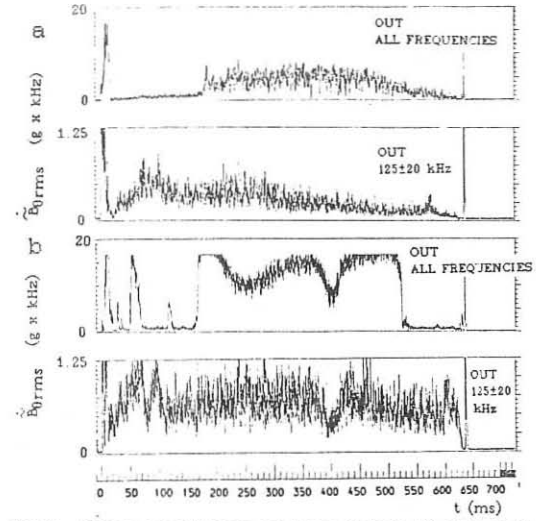

Fig.1: Time evolution of rms level of low and high frequency fluctuations for: a) shot 32815 (Ip=150 kA, B_T=2.1 T, $\bar{n}e$=3x10^{13} cm^{-3}); b) shot 32816 (Ip=150 kA, B_T=2.1 T, $\bar{n}e$=1.5x10^{13} cm^{-3}).

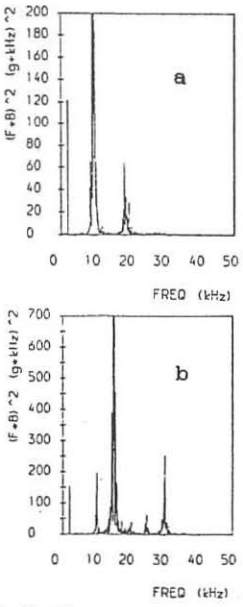

Fig.2: Power spectra of low frequency MHD activity for a)shot 32815; b)shot 32816.

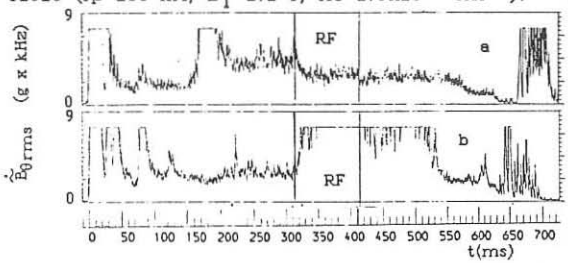

Fig.3: Time evolution of rms level of low frequency MHD activity during ECRH. a) m=5, n=1 is stabilized by resonance at +15.5 cm (qa=6); b) a m=4, n=1 is destabilized by resonance at -6 cm (qa=5).

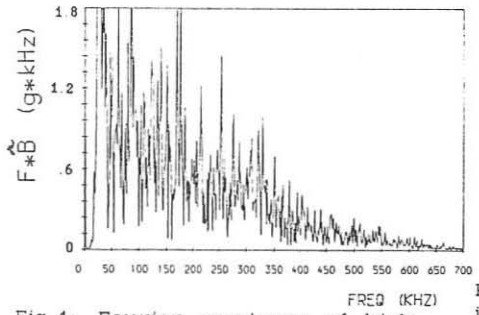

Fig.4: Fourier spectrum of high frequency fluctuations (Ip=100 kA, B_T=2.5 T, $\bar{n}e$=1.75x10^{13} cm^{-3}).

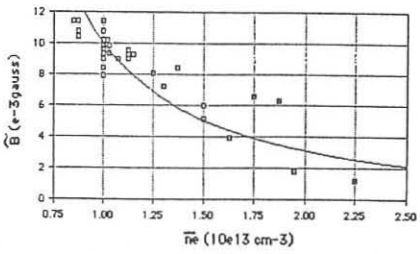

Fig.5: rms amplitude of fluctuations in the range 125±20 kHz as a function of plasma density (Ip=100 kA, B_T=2.25 T). The curve is a fit ∝ $1/\bar{n}e^{1.7}$.

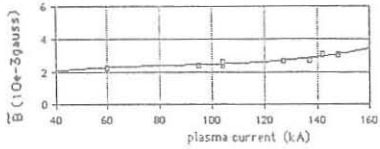

Fig.6: rms amplitude of fluctuations in the range 125±20 kHz as a function of plasma current ($\overline{ne}$=2.5x10^{13} cm^{-3}, B_T=2.1 T).

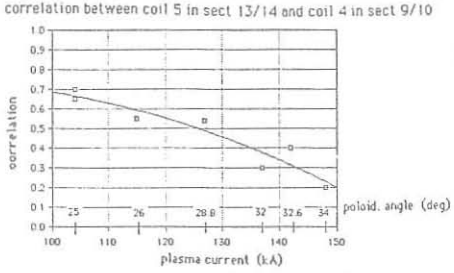

Fig.8: Correlation between two coils in different sectors as a function of the plasma current (or rotational transform at r=a); ($\overline{ne}$=2.5x10^{13} cm^{-3}, B_T=2.1 T).

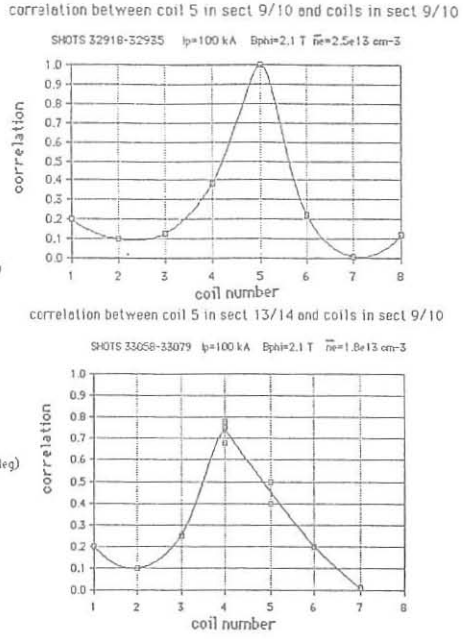

Fig.7: Measurement of correlation lengths for fluctuations in the range 125±20 kHz. a)within the same toroidal sector b)between two sectors spaced by 90°.

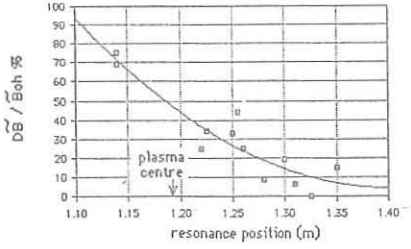

Fig.10: Percentage variation during ECRH of fluctuations in the range 125±20 kHz as a function of resonance position (Ip=100 kA, $\overline{ne}$=1.1x10^{13} cm^{-3}).

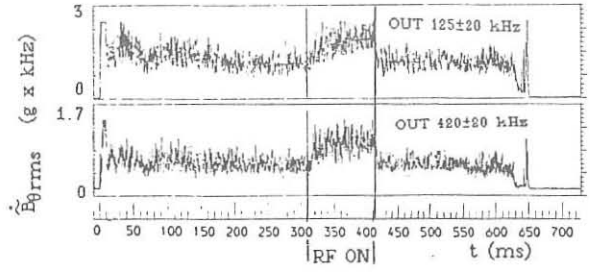

Fig.9: Time evolution of rms level of broadband fluctuations during ECRH (resonance at -6 cm).

ELECTRON CYCLOTRON RESONANCE HEATING ON CT-6B TOKAMAK

Luo Yao-quan, Wang Long, Yang Si-ze,
Qi Xiazhi, Li Zan-liang, Wang Wen-shu,
Li Wen-lai, Wu Xiao-wen, Zhao Hua

Institute of Physics,
Chinese Academy of Sciences,
Beijing

Abstract

An electon cyclotron resonace heating experiment has been performed by using a gyrotron system for the fundamental and second harmonic resonance heating on CT-6B tokamak. Obvious changes are observed in soft X ray radiations, electron cyclotron emission, displacement of plasma column, impurity line radiations, and bremsstrahlung radiation when the heating pulse is injected, indicating the increase of the plasma electron temperature.

The electron cyclotron resonance heating (ECRH) is one of the promising method of auxiliary heating in toroidal plasma and has received considerable attentions /1/. Recently, an ECRH experiment has been conducted with success on CT-6B tokamak in Institute of Physics, Chinese Academy of Sciences.

CT-6B tokamak is a small iron-core trasformer and conducting shellless research device/2/. The main device and plasma parameters in this experiment are as follows: main radius R=45cm; minor radius of plasma a=12cm; toroidal magnetic field B_t=5.8-13kGs; plasma current I_p=20-30kA; Ohmic heating power P_{Oh}=70-100kW; averaged electron temperature T_e=150-200eV; line averaged electron density $n_e=(1-2)*10^{13}$ cm^{-3} ; energy confinement time τ_E=0.7-1ms; particle confinement time τ_p=3-5ms.

The power source of ECRH is a D4032 type gyrotron manufactured by Institute of Electronics, Chinese Academy of Sciences, operating at 34.34GHz and in circular TE mode. The heating microwave is launched through a horn antenna installed on the outside of the vacuum vessel(weak field launch) with power output 50-100kW and pulse length 1-6ms.

Besides the common electromagnetic measurements, the

plasma density is measured by an HCN far infrared laser interferometer, the electron cyclotron emissions at 18.2 and 70GHz are detected by two receivers respectively, the soft X rays from different chords of plasma column are measured by a Au(Si) surface barrier detector array, the visible and ultraviolet radiations are detected by an optical fibre and monochrometer system, and the vacuum ultraviolet radiation is detected by an one meter VUV spectrometer.

A set of typical experimental oscillograms is shown in Fig.1. The main experimental results can be summarized as follows:

1, A substantial outward displacement of the plasma column is observed during the heating pulse. A typical change value is 1 cm for a 2 ms heating pulse. It indicates a rise of the poloidal β value due to the heating. The onset and termination of the displacement are delayed to that of the heating pulse by a short time about 0.7-1 ms, which is equal to the energy confinement time τ_E.

2, Enhancements of the cyclotron emissions at 18.2 and 70 GHz are observed during the heating pulse, which are higher than the background value by an order of magnitude, and show a very short delay to the heating pulse. These enhanced emissions should be electron cyclotron emissions due to the extra thermal electrons produced by heating microwave.

3, Obvious increases of emission intensities of the hydrogen atomic lines H_α, H_β, impurity lines OII 3973 Å and 4649 Å, OIII 3760 Å, OIV 3410 Å, OV 629 Å, OVI 1032 Å, CIII 4647 Å, CrI 4254 Å, as well as the bremsstrahlung in 4760 Å and 5360 Å are observed during the heating pulse with different delay times. The increases of intensities are the results of the extra thermal electron excitations or the rise of trmperature of the plasma, and could not be attibuted to the increase of impurities since the impurities would be accumulated in a tokamak plasma but the intensities of the impurity lines return their initial value after the heating pulse in the experiment.

4, Obvious increases of soft X ray radiations in the different channels are observed during the heating pulse, of which the rise and delay time are about 1 ms. The different channels show the different increase amounts and with different delay time between the channels due to the propagation of the heat pulse in radial direction in the plasma. It has became clear that a remarkable local heating is achieved during the heating pulse.

5, A detectable drop in loop voltage is observed during

the heating pulse for more powerful heating shots. In this case it is estimated that the conducting temperature of the plasma increases 10-20 eV due to the ECRH.

6, No obvious change in the line averaged electron density, hard X ray radiation, and the saturation ion current of a Langmuir probe installed in the limiter shadow region is observed.

In conclusion, the evidence of the bulk plasma heating due to the effect of an electron cyclotron wave has been observed in this experiment. The low heating effeciency is to be expected. This is an over-dense plasma heating experiment, since the density of the hot plasma center is higher than the cut-off density($1.5_{*}10^{13}$ cm^{-3}) for the O-mode propagation. X-mode cut-off region is reached before the O-mode cut-off. Therefore, in the fundamental frequency resonance heating, the heating effect seems due to the multi-reflection of wave in the vessel and tunnelling effect. X-mode heating has higher effeciency at high electron temperature for the second harmonic resonance heating. But the toroidal field is weak in this case, the plasma temperature is lower. Therefore, the experimental results in the two cases are similar to each other. However, some phenomena should be further studied in the dense plasma case.

The authors would like to express their thanks to the Association for Plasma Studies.

REFERENCES

1. For example
D.V.Alikaev et al, Technical Committee Meeting on RF Heating and Current Drive, Nov. 16-20, 1987, Moscow; R.W.Harvey et al, ibed.
2. Group 104, Institute of Physics, and Group 403, Institute of Electrical Engineering, Acta Physica Sinica 29 (1980) 577

FIGURE CAPTION

Fig.1. A set of typical discharge oscillograms on CT-6B tokamak including plasma current IP,OIII 3760 Å impurity line O-3760, horizontal displacement times plasma current DX*IP(positive shows inward), electron cyclotron emission at 70 GHz ECE, microwave heating pulse ECRH, soft X ray radiations SX-4#(r=5.8 cm chord), SX-5#(r=3 cm chord) and

SX-6#(central channel). The broken lines show the case without ECRH.

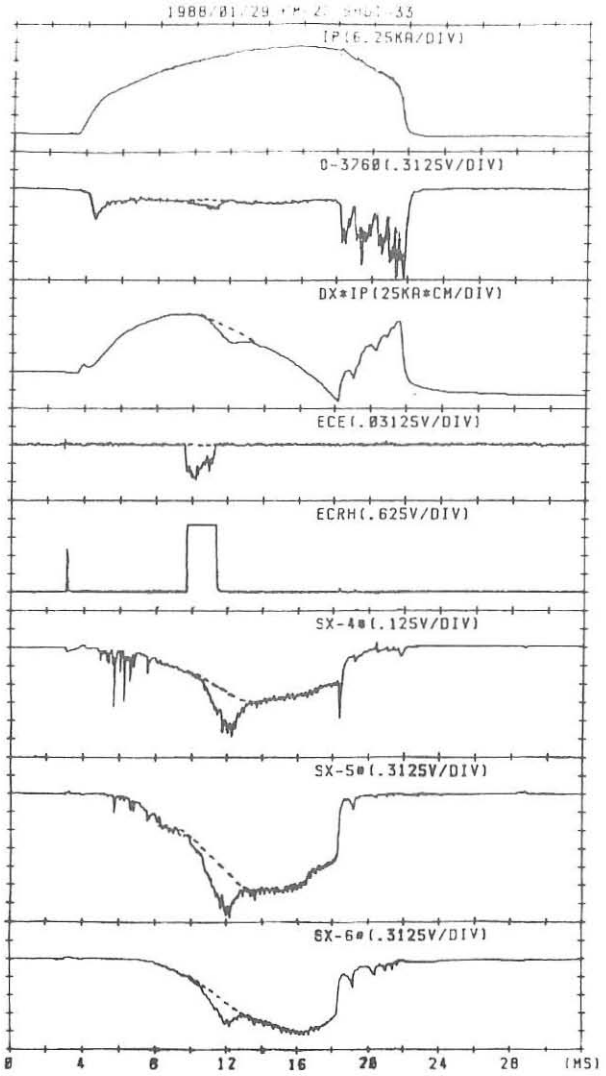

Fig.1

EFFICIENCY OF ELECTRON CYCLOTRON HEATING IN FT-1 TOKAMAK

D.G.Bulyginsky, S.G.Kalmykov, M.Yu.Kantor, M.M.Larionov, L.S.Levin, A.I.Tokunov, S.Yu.Tolstjakov, N.V.Shustova

A.F.Ioffe Physical-Technical Institute, Leningrad, USSR

Energy confinement degradation under electron cyclotron resonance heating (ECRH) was found in a number of tokamak experiments. The analysis of energy balance and its temporal evolution in FT-1 experiment /1/ has shown, that already in the initial stage of ECRH pulse the growth rate of a plasma energy dW/dt is smaller than the microwave power absorbed in a plasma. However, the time resolution was rather poor. In laser scattering measurements it was 0.3 ms, in diamagnetic ones it was limited to $\sim$ 0.2 ms due to the eddy currents in the discharge chamber walls. The investigation of a time dependence of dW/dt in the very beginning of ECRH pulse was the goal of a new set of measurements. It was believed that the radiation and transport losses were unchanged during this time. The improved version of diamagnetic measurements was used. The diamagnetic probe coil of N = 16 turns was uniformly distributed along the toroidal discharge chamber. Provided that the discharge current would be constant and the eddy currents could not arise in the chamber walls, the voltage of this coil V(t) and the total plasma energy W would be connected by the simple equation:

$$V(t) = \frac{N}{\alpha B_0} \frac{dW}{dt} \qquad (1)$$

B_0 - the toroidal magnetic field, α - the geometric factor of the experiment. In real conditions, the correction on eddy currents must be taken into account:

$$V(t) = \frac{N}{\alpha B_0 S} \cdot \int_0^t \frac{dW}{dt_1} \cdot \frac{dL(t-t_1)}{dt} dt_1 \qquad (2)$$

where L(t) - the skin function of the discharge chamber, or the response of a diamagnetic coil to the application at t=0 of a step-like voltage S to the discharge chamber in poloidal direction. Really, L(t) is measured by the application of a step-like voltage to the toroidal field winding of a tokamak. A true value of dW/dt in the beginning of ECRH can be obtained from (2).

Tokamak FT-1 (R = 62 cm, a = 15 cm, $B_0 \leq 1.2$ T) was operated at I = 30 kA, $\bar{n}_e = 0.6 \times 10^{13}$ cm^{-3}, P_{OH} = 65 kW. Two gyrotron generators (30.6 GHz, 2x100 kW) fed two microwave antennae of Vlasov type, having rather broad radiation patterns. One of them excited in a plasma mainly extraordinary (x) wave from the inner side of a torus, another one - mainly ordinary (O) wave from the external side. Fundamental resonance condi-

tions ($\omega = \omega_{ce}$) were used in experiment. As the initial stage of ECRH was studied, the pulse duration was limited to 0.5 ms. Some pick-up oscillations disturb the diamagnetic signals during first 40 μs of ECRH pulse, after this time interval the true data on dW/dt are available. Microwave power losses in waveguides and in discharge chamber walls were carefully measured. The waveguide attenuation was found to be 10%. To evaluate the wall losses, measurements of a quality factor of a discharge chamber were fulfilled. The attenuation of a microwave signal passing through the discharge chamber from gyrotron to the probe horn antenna was measured in a normal discharge and in vacuum conditions. The comparison of signal attenuation in both cases has shown that only 10% of a power is lost in the chamber walls under ECR conditions. So, 80% of a total power of gyrotrons, or about 160 kW is absorbed by a plasma during ECRH.

The results of diamagnetic measurements of a plasma energy evolution are presented in Fig.1,2. Fig.1 shows dW/dt (in kW) calculated using equations (1) and (2) in the case of a central position of ECR at B_o = 1.09 T, r_c = 0, when the most efficient heating is observed. The role of the correction on eddy currents introduced into equation (2) is clearly seen. In Fig.2 the same data calculated by equation (2) are presented at some positions of ECR in a plasma cross-section, from r_c =-9.4 cm to r_c = +4.7 cm. Data obtained lead to the following conclusions:

1. The maximal value of the power, spent for the increase of plasma energy at the moment of ECRH start, dW/dt(0), is not more than 60 kW, though the total microwave power absorbed by a plasma is about 160 kW.

2. The time constant describing the energy increase during ECRH, as well as its decrease after ECRH termination, is about 1 ms and is equal to the energy life time of an ohmic heated plasma before ECRH.

Fig.3 presents the data on dW/dt(0) (in kW), depending on the position of ECR, r_c. The cases of combined operation of both gyrotrons and separate ECRH by internal X wave and external O wave antennae are shown. In Fig.4 the energy increase of a plasma Q (in Joule) after 0.5 ms ECRH pulse is shown in the cases mentioned above. It follows from Fig.3 and 4, that dW/dt as well as Q under combined operation of both gyrotrons are equal to the sum of these values under their separate operation. So the linear dependence of the plasma heating rate on the applied ECRH power is observed up to $P_{ECRH} = 3\ P_{OH}$. The internal X wave heating is rather more efficient than the external O wave one, and in both cases the best results are found at the central position of ECR zone. At r_c = 0, dW/dt(0) and Q under ECRH by X wave are 1.4 times higher than by O wave.

The method of treatment of diamagnetic signals used here avoids the limitations of a skin and enables us to find the

true value of dW/dt(0) at the start of ECRH pulse (excluding first 40μs). It was found that rather slow processes of modification of T_e, n_e and plasma pressure radial profiles regarded in /2,3/ as a reason of increase of electron thermal conductivity and energy confinement degradation, in our experiment can not explain the fast increase of energy losses under ECRH. This increase is found to be just at the start of ECRH. Results obtained in this experiment and in /1/ can be explained as follows: some part of the microwave power radiated into the plasma is absorbed through the electron cyclotron mechanism in a plasma core and results in the electron heating. Analysis of the dynamics of this heating and cooling has shown that the electron thermal conductivity does not change essentially under ECRH. At the same time an essential part of ECRH power, exceeding 60%, also is absorbed in a plasma, but does not lead to the increase of a plasma energy. This power is lost during very short time, not exceeding 40 μs. The nature of this loss process is not clear yet. Some explanations are suggested:

1. Due to broad radiation patterns of antennae and refraction in a plasma a great deal of the ray trajectories are deflected to the periphery and are undergoing the reflections on the discharge chamber walls. The X waves may be absorbed there through a linear conversion in a Bernstein wave. This process may take place in a cold peripheric plasma, including the shadow of a limiter. The absorbtion in a limiter shadow was not taken into account in the ray tracing calculation of ECRH in FT-1 experiments /4/.

2. Basic processes of absorbtion in ECR frequency range lead to the increase of transversal energy of electrons. So the production of high energy electrons trapped in magnetic field ripples becomes possible. The confinement of these particles is poor, their drift time is about 20μs. Locally trapped electrons may absorb and carry out of a plasma a marked part of a microwave power.

REFERENCES

1. T.Yu.Akatova et al., Proc. XIV ECCFPF, Madrid, 1987, v.III p. 855.
2. V.V.Alikaev et al., Fizika Plazmy, 1987, v.13, No 1, p.3.
3. N.L.Vasin et al., Fizika Plazmy, 1987, v.13, No 1, p.109.
4. Yu.F.Baranov, V.I.Fedorov, Fizika Plazmy, 1983, v.9, No 4, p.677.

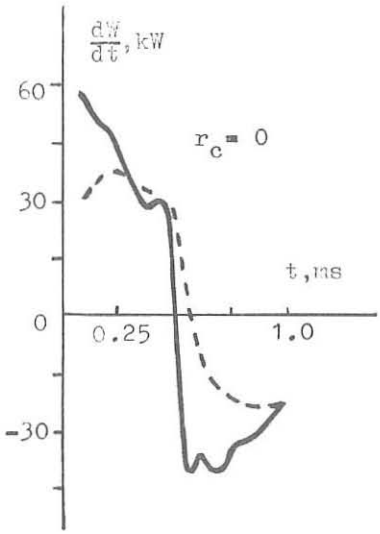

Fig.1
—— equation 2
– – equation 1

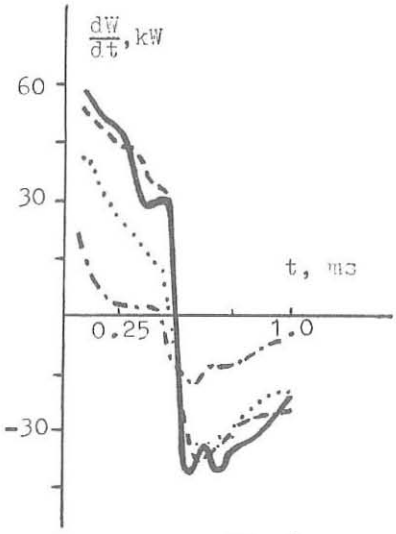

Fig.2
—— r_c = 0 cm
– – r_c = 4.7 cm
···· r_c = -4.7 cm
–·– r_c = -9.4 cm

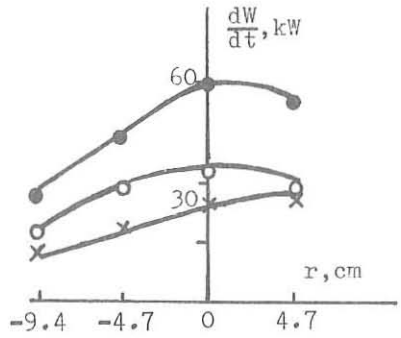

Fig.3

● - internal and external gyrotrons; o - internal gyrotron; × - external gyrotron.

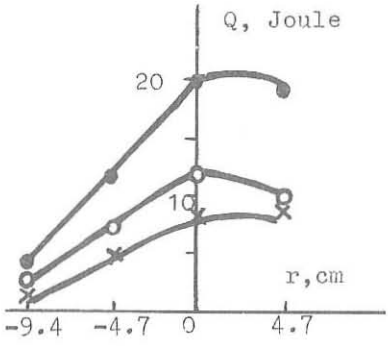

Fig.4

● - internal and external gyrotrons; o - internal gyrotron; × - external gyrotron.

LOW-POWER ECH RESULTS IN TEXT*

K. W. Gentle, B. Richards, D. C. Sing, M. E. Austin†††, Roger D. Bengtson, R. V. Bravenec, D. L. Brower†, G. Cima, P. H. Edmonds, R. Gandy†††, R. L. Hickok†††, S. K. Kim†, Y. J. Kim, N. C. Luhmann, Jr.†, S. C. McCool, D. M. Patterson, W. A. Peebles†, P. E. Phillips, Ch. P. Ritz, Terry L. Rhodes, William L. Rowan, P. M. Schoch††, and A. J. Wootton.

Fusion Research Center, The University of Texas at Austin 78712

Introduction

Initial results of electron cyclotron heating have been obtained in the TEXT device. A single 200kW gyrotron at 60GHz has been used to couple a maximum of 110 kW into the plasma in an ≈15 ms pulse using O-mode outside launch in the midplane. For these experiments, the target plasmas in this device of 1 m major radius and 0.26 m minor radius range in density from 1 to 4 x 10^{19} m^{-3} at a plasma current of 220 kA and a toroidal field for central resonance of 2.16T. The heating power was applied to these q(a) ≈3 discharges during a uniform plateau with sawteeth.

The heating efficiency and associated changes in density profile, particle confinement time, central and edge electrostatic fluctuations, and magnetic fluctuations have been examined over this range of densities for the ECH layer placed at R=1.00, 0.92, and 0.87 m, the latter corresponding to B=1.9 T. As in the early CLEO experiments[1], heating efficiency is found to drop sharply when the resonance moves outside q=1. A similar drop in efficiency occurs as the central density approaches the O-mode cutoff (4.4 x10^{19} m^{-3}). Strong effects on particle transport and fluctuations persist for conditions beyond those of optimum heating.

Heating Results

The ECH effects are illustrated in Fig. 1, which shows the time histories of the ECH pulse, the central electron temperature (from second-harmonic ECE), and the line-averaged density for the ECH resonance at the plasma center. The electron temperature nearly reaches equilibrium (τ_e≈7 ms), but the density does not. The fact that the heating pulse is too short to reestablish an equilibrium is a limitation, particularly with respect to inferring changes in particle transport.

The results for heating efficiency are summarized in Fig.2, which shows the various effects observed as a function of mean density and resonance position. Included are the increment in β_p (as inferred from the equilibrium, the times being too short for a change in internal inductance), the increment in central temperature from ECE, and the decrease in ohmic input power. The similarity in consequence of raising the density or moving the resonance off center can be simply understood from the ray tracing and absorption calculations. As the density is raised, refraction effects become significant, deflecting the principal absorption from the core toward the periphery. The effect is equivalent to moving the resonance position off axis. This explanation is confirmed by analysis of soft x-ray emission, which shows that the absorption occurs entirely within 7cm of the magnetic axis for low density central resonance. However, the signature of

[1] A.C. Riviere, Seventh APS Topical Conference on RF Heating, Kissimmee, Florida 1987.

central heating, the increase in the slope of the sawteeth, disappears as the mean density reaches $3x10^{19}$ m^{-3} or the resonance is moved off axis.

These effects also appear in Fig. 3, which shows electron temperature profiles from both Thomson scattering and ECE for low density central heating and from ECE for higher densities. The ECE is calibrated to Thomson scattering in the OH discharge; they agree within error bars for the ECH increment, although the Thomson value should be systematically lower because it was not taken at the end of the ECH pulse. Including the concomitant density decrease, the results are consistent with the increments in ß. An energy accounting which includes the drop in OH input is consistent with absorption of 70% to 80% of the incident ECH power and no degradation in confinement time for central heating at densities below $2x10^{19}$ m^{-3}.

Density Profiles and Particle Confinement

A set of typical density profiles taken during an ECH pulse is shown in Fig. 4. The profiles are based on 5 or 6 chord FIR interferometric data which spanned major radii from R=0.84 m to R=1.24 m (with R_0=1 m). During the pulse, we observe a local decrease in the electron density during the ECH pulse of up to 10%, with the maximum decrease at $\langle n_e \rangle \approx 2.5 \times 10^{19}$ m^{-3}. Usually, the density is still changing at the end of the pulse in spite of a particle confinement time, τ_p, of approximately 10 ms. As seen in Fig. 5, the spatial dependence of maximum local density drop is a function of plasma density. (For the low density central heating case, the apparent "increase" in density at the edges may be an artifact of the inversion technique used.) As the central density is varied from under-dense to over-dense, we see the position of maximum local change move from the inner to the outer regions of the plasma, presumably due to refraction by the plasma bending the rf away from the central axis and changing the absorption profile. As expected, changing the resonance position by changing the toroidal field also changes the spatial dependence of the local density decrease.

Figure 1 includes the change in the measured particle source taken from H_α measurements as a function of time. We note that, although we see a decrease in the electron density in the plasma, the particle source at the edge always increases. This implies that the particle transport itself must be changing during the application of ECH.

Fluctuations

Density and potential fluctuations during ECH have been measured in the interior with a Heavy Ion Beam Probe and at the edge with Langmuir probes. Small increases in the interior were observed, but they may be no more than would be occasioned by the density changes caused by ECH. The effects at the edge were more pronounced. Significant increases in the density fluctuations and large increases in potential fluctuations were found, although the edge density and temperature only changed modestly. Since the edge probes were at the major radius for resonance, this result may represent a specific local effect of ECH. There are other observations, for example the immediate increase in impurities at the edge, which suggest some direct edge effects of ECH.

Magnetic fluctuations were measured with probes within a few centimeters of the limiter radius. The spectrum above 50kHz, which has been identified in TEXT as arising from edge fluctuations for this arrangement, rises immediately by approximately 50% under all ECH conditions. Lower-frequency effects are more variable: a pronounced m=4

mode appears for central heating at low density; various modes with m=5 to 8 appear at other conditions, but amplitudes with ECH at most double.

Since there is no evidence of degradation of energy confinement and only modest changes in particle transport are implied by the changes in density, one would not expect gross changes in fluctuations to be driven by this mild heating.

Conclusions

The initial ECH experiments on TEXT reiterate the general conclusion that power at the electron cyclotron resonance is efficiently absorbed and provides an efficient method of heating. However, the heating efficiency in these experiments was high only for central deposition. If the deposition was moved away from the center, either by placing the resonance off axis or raising the density to refract the waves away from the core, heating efficiency dropped. Total absorption remained high, and peripheral heating and particle transport effects persisted.

The density drop often observed to accompany ECH is shown here to be a consequence of changes in particle transport coefficients, albeit modest ones, and not merely a consequence of changes in edge conditions or recycling. The largest changes in fluctuations are associated with changes at the edge.

*Operated by The University of Texas at Austin under DOE Grant No.DE-FG05-88ER53267.
†Institute of Plasma and Fusion Research, University of California, Los Angeles,
††Renssellaer Polytechnic Institute, Troy, New York 12180.
†††Auburn University, Auburn, Alabama 36849

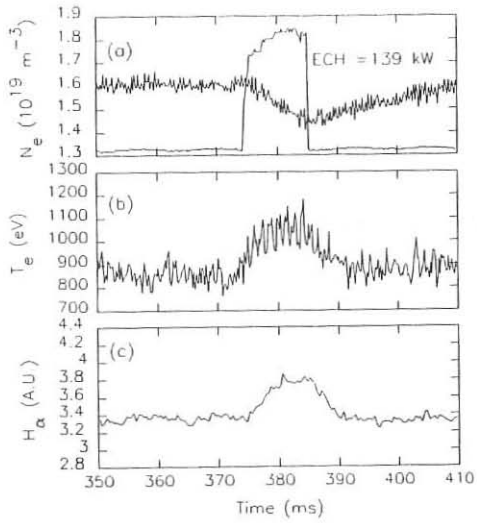

Fig. 1. Time evolution during ECH: (a) ECH power, mean density, (b) central electron temperature, and (c) particle source from H_α emission.

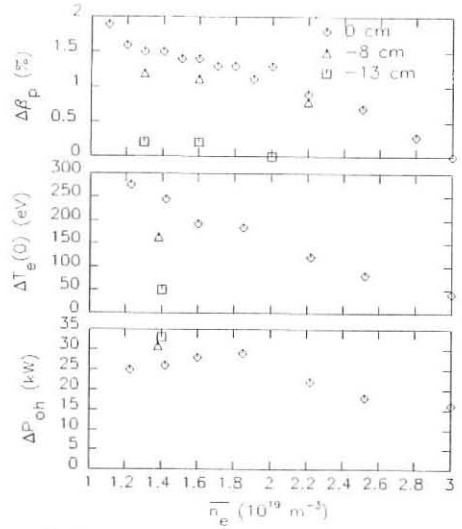

Fig. 2. Heating results: Increments in poloidal beta, central electron temperature, and ohmic power with ECH as a function of mean density for various resonance positions.

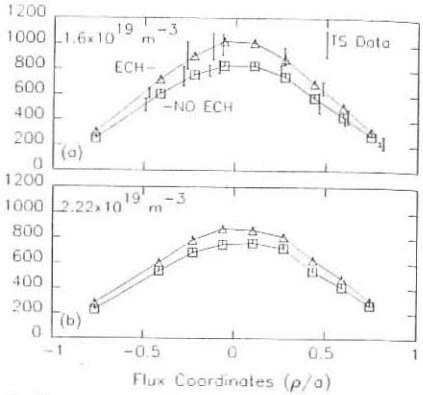

Fig. 3. Temperature profiles: (a) 1.6 x 10^{19} and (b) 2.2 x 10^{19} m^{-3} average density.

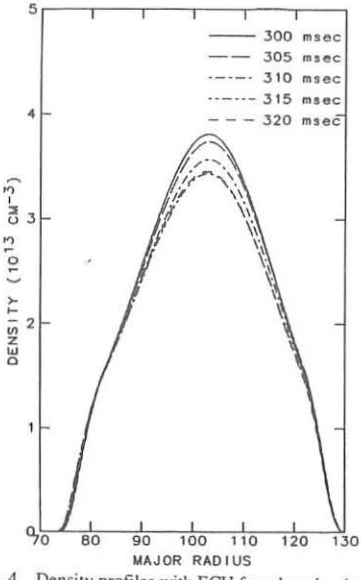

Fig. 4. Density profiles with ECH for a low density discharge, central resonance. The pulse started at t ≈ 302 ms and lasted ~ 12 ms.

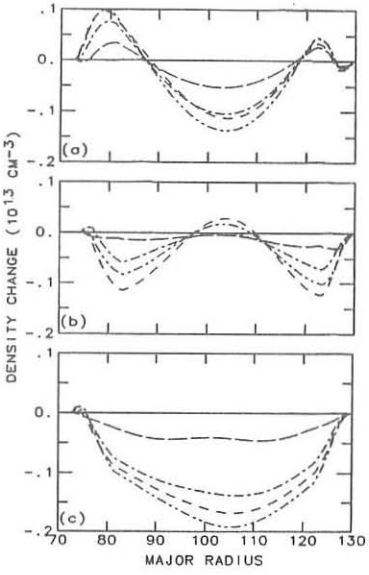

Fig. 5. Changes in the density profile for 3 different conditions: (a) 2 x 10^{19} m^{-3} peak density, central resonance, (b) 8 x 10^{19} m^{-3} peak density (c) 2 x 10^{19} m^{-3} peak density, resonance at R = 0.87 m. Note that the increase at the edge of case (a) may be an artifact of the inversion technique, but the central decrease is correct.

PREIONIZATION AND START-UP EXPERIMENTS WITH ECRH ON THOR TOKAMAK

S.Cirant, L.Argenti, G.Cima, P.Mantica
Istituto di Fisica del Plasma, EURATOM/ENEA-CNR Ass.
C.Maroli, V.Petrillo
Universita degli Studi di Milano

Experiments on plasma production and current start-up with EC waves have been performed on Thor tokamak by injecting up to 80 kW of microwave power at 28 GHz with a pulse length of 5 msec. The waves were launched from the low toroidal field side, perpendicularly to the magnetic field and polarized as an O-mode /1/. A corrugated mirror on the inner wall rotated the polarization of the reflected wave by 90deg, providing a perpendicular X-mode launch from the high field side.

Preionization

A four channel microwave interferometer and Thomson scattering have been used to diagnose the plasma production at different filling pressures, with only the toroidal field switched on and set at 1 Tesla in the centre during ECRH. In Figs. 1a, 1b, 1c it is shown that the plasma is being produced with a delay relatively to the start of the r.f. pulse, which is roughly inversely proportional to the working gas pressure. It is also seen that the line average density value slightly increases and the electron temperature decreases with the gas pressure. The time evolution of the line density measured by one horizontal and three vertical interferometric channels is shown in Fig.2, clearly demonstrating that the plasma fills most of the vacuum chamber since the early breakdown phase, contrarily to the expectations from the usual EC breakdown modelling /2/. Working gas pressures much lower than 10^{-6} torr were prevented by wall outgassing when ECW were injected. During these experiments an unexpected net toroidal current up to 900 A was observed (Fig.3), very sensitive to the filling pressure (Fig.4). Being its direction reversed by inverting the toroidal field, a classical current drive mechanism is excluded. Since the current could be cancelled by the addition of a vertical field of 17 gauss in a proper direction, its origin has been ascribed to the presence of a stray vertical magnetic field generated by the toroidal magnet, which in fact has been estimated by independent measurements to be between 15 and 20 gauss. Although not particularly relevant with respect to the main aspects of ECRH, this phenomenon is instructive since it well fits fairly simple models describing drifts in toroidal configurations and the predictions of high energy electron generation with EC waves in low density plasmas /3/. Furthermore, since the rotational transform so introduced can well explain the spreading of the discharge inside the vessel, useful indications can be drawn for the best use of EC preionization in larger devices. The toroidal field gradient induces a vertical drift which depends on the energy of the electrons, its direction being then the same for the particles flowing in opposite toroidal directions. On the contrary, the vertical drift due to the presence of a vertical magnetic field is opposite in the two toroidal directions, so that an asymmetric confinement, and hence a current, results. The electrons carrying the

current move with the parallel velocity $v=B_v Rq/m$ at which the vertical drifts cancel out. If the appropriate values are introduced, and taking into account the estimates of the stray field, an energy of a few tens of keV is obtained. Furthermore, the mean density of the carriers can be deduced from the measured current, since $I=n_e vSq$, where q is the electron charge and S the current channel cross section. If the proper values are introduced, n_e turns out to be less than 1% of the total volume averaged electron density. The presence of fast electrons is confirmed by the ECE radiative temperature above 1.5 keV. In Fig.5 the current measured at different values of the magnetic field is compared with the one calculated assuming that $I=\alpha n_{e,0} B_v$, where $n_{e,0}$ is the peak density obtained from the density profile. In Fig.6 three normalized density profiles are shown corresponding respectively to an almost zero total vertical field, to the stray field due to the toroidal winding alone and to an even grater one, obtained by adding an external vertical field. At zero field the current is negligible and the plasma is peaked around the resonance, with the tendency to fill the external part of the vessel, in agreement with the usual picture /4/. When no external fields are superimposed to the stray one the current is almost at maximum, and the plasma fills the chamber following the magnetic surfaces. By further increasing the magnetic field the losses cannot be balanced any more because a too high energy is required, so that the current drops and the density profile becomes hollow.
All these features can be reproduced by modelling the breakdown and plasma generation by ECRH with a zero dimensional computer code which takes into account the presence of a given toroidal current /6/. The steady state values of the mean electron density, temperature and the breakdown delay can be reproduced with good approximation. Also the time evolution of the density and the expansion caused by the current are satisfactorily described by the code.

Current start-up

The effect of EC preionization on a Thor tokamak discharge is described in Fig.7. The loop voltage at start-up is substantially reduced, with a flux saving of 40 mVsec over a total flux swing of 250 mVsec. The density build-up is much faster than in the purely ohmic discharge. The time derivative of the plasma current is unchanged, the main effect of preionization being the drastic shortening of an initial high resistivity transient phase. The plasma parameters at steady state were the same as for a normal discharge without preionization. In spite of the faster density build-up and the slightly higher steady-state loop voltage, also the suprathermal content typical of Thor plasmas /5/ was left substantially unchanged by EC preionization.

REFERENCES

/1/ S.Cirant, G.Falciasecca, 5th ECE and ECH Int. workshop, S.Diego, 1985
/2/ M.Fontanesi, C.Maroli, V.Petrillo, Plasma Phys.Contr.Fus., **27**, 1003(1985)
/3/ A.I.Anisimov et al., Sov.Phys.Tech. Phys., **20**, 629 (1976)
/4/ K.Ohkubo et al., Nucl. Fus. **21**, 1320 (1981)
/5/ A.Airoldi et al., 14th EPS Conference on Controlled Fusion and Plasma Physics, Madrid, 1987, III 823.
/6/ C.Maroli, V.Petrillo, NET rep.54, EUR-FU/XII-80/86/54, Marz 1986

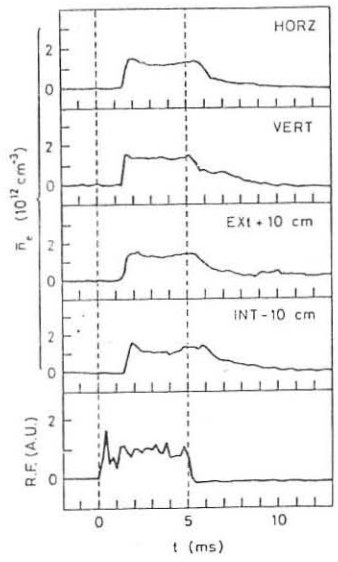

Fig.2-Time behaviour of the line density along different cords compared with the r f. pulse

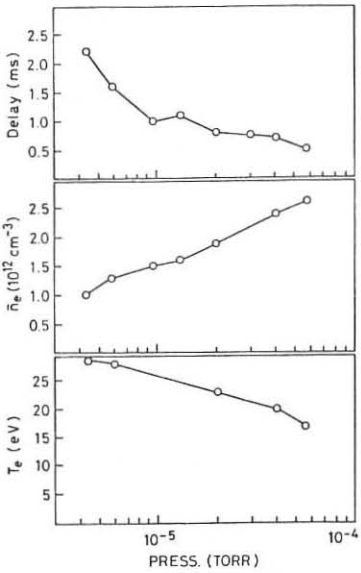

Fig.1-Delay, central mean line density and temperature during preionization at different deuterium filling pressures.

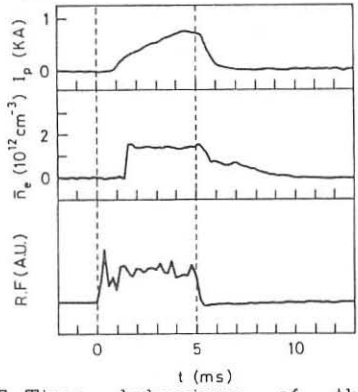

Fig.3-Time behaviour of the toroidal current observed during EC preionization in presence of a stray vertical field. The mean density and the r.f. signal are also shown.

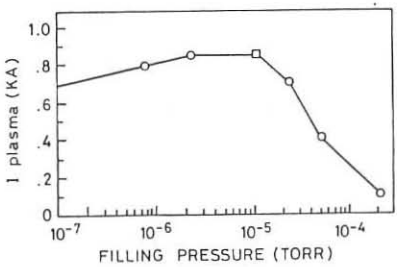

Fig4-Toroidal current measured at different hidrogen filling pressures. The stray field is 17 gauss and the r.f. power 80 kW.

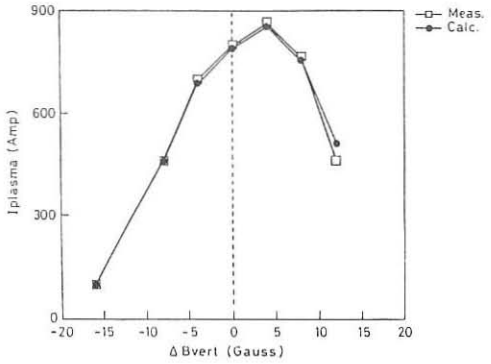

Fig.5-Toroidal current during EC preionization in function of a vertical field superimposed to the stray one. The points x have been calculated using the equilibrium velocity for the given field and a fraction (0.02%) of the central density.

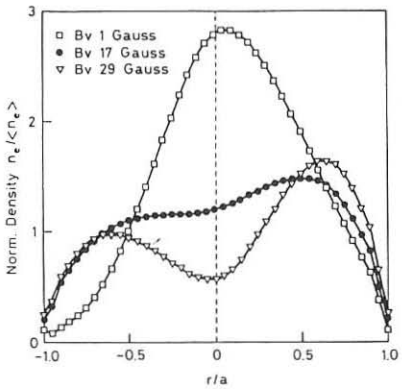

Fig.6-Density profiles for different values of the total vertical field. The profiles are normalized respect to the mean density averaged over the cross section.

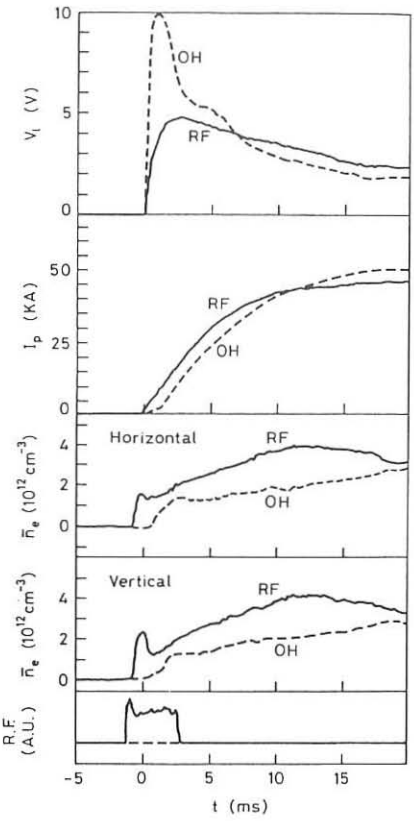

Fig.7-Time behaviour of the loop-voltage, plasma current, mean density along an horizontal and a vertical chord of a tokamak discharge with EC preionization.

HOT ELECTRON RING FORMATION IN ECR HEATED PLASMA

WANG Zhongtian JIAN Guangde E.Y.WANG
Southwestern Institute of Physics, Leshan, Sichuan P.R.China

INTRODUCTION

It is proposed by Rosenbluth et al[1] that introduction of a highly energetic trapped particles into a tokamak allows direct stable access to the second stable regime. The particles are like stoshing ions which are proposed to stabilize the plasma in a mirror machine. But the stoshing ions are difficult to produce in a tokamak. It is demonstrated by Hsu et al[2] that the energetic trapped electrons can be generated in a tokamak by ECRH. The energy of the electrons is limited by the relativistic detuning. In this paper, bounce frequency is taken into account. The resonant condition for large aspect ratio approximation is written as

$$2\Omega_0(1-\varepsilon)\cdot\gamma-\omega+\omega_b(J+6lP_\psi)\sqrt{2P_\psi}=0$$

where γ is the relativistic factor, ε the inverse aspect ratio, ω the wave frequency, Ω_0 the gyrofrequency of the electron, ω_b the bounce frequency, l the wave number associated with the bounce frequency, J the togitudinal invariant, P_ψ is a half of the magnetic moment. With l increasing, the relativistic detuning is avoided. The energy of the heated electrons is increased further, but limited by detaching of the adjacent overlapped islands. The energy estimated increases by factor of 1.2 compared with Hsu's[2]. The ring structure formed by the energetic electrons is presented.

The experiment to observe the transition from the passing electron to the trapped electron during ECRH has been performed by Wang et al[3] on MM-2 mirror machine. The trapping efficiency is about 70-80 percent. Negative potential is observed in the plasma. The same measurement in a tokamak will be performed in the near future.

THEORY

The typical ordering in tokamak is given as usual. There is a strong magnetic field in a tokamak, so the Larmor radius of an electron is much smaller than wave length of the electron cyclotron waves and the characteristic gradient length.

In an axisymmetric system, the magnetic fields have toroidal and potoidal

components

$$\vec{B}=B\hat{\phi}+\nabla\varphi\times\nabla\psi \qquad (1)$$

where $\psi=-RA_z$. A_z is the ϕ component of the magnetic vector potential. From the equation of the magnetic line, we get

$$V_{\parallel}=R\dot{\phi}\,B_z/B_\phi\approx R\dot{\phi} \qquad (2)$$

to the first order of ε. The unperturbed Hamiltonian of a charged particle can be written as

$$H_0=1/2[(P_z-eA_z)^2+P_r^2]+1/2R^2\dot{\phi}^2 \qquad (3)$$

where P_z and P_r are canonical momenta, $A_z=1/2\,R$, the R component of the magnetic vector potential, Gauss units are used with $m=c=1$, m the mass, c the speed of light. The gyration is so rapid that the parallel velocity almost does not change in a period. We transform R, Z coordinates into a guiding center system by using a generating function

$$F_1=\Omega_0[1/2(Z-\bar{Z})^2\mathrm{ctg}\Phi-R_0\bar{Z}\ln R] \qquad (4)$$

where Ω_0 is the gyrofrequency on the magnetic axis, $\bar{Z}=Z+\rho\sin\Phi$, Φ the gyroangle, ρ the Larmor radius, $\bar{Z}$ the guiding center position. Averaging over Φ, we get

$$H_0=\Omega_0P_\phi(1-\varepsilon\cos\theta)+P_r^2/2q^2R_0^2 \qquad (5)$$

to the first order of ε, where $P_\phi=1/2\Omega_0\rho^2$, $P_\theta=qR_0\bar{\theta}$, the conical momentum conjugate to θ, q the safety factor.

For the deeply trapped particles, θ is small. We can expand $\cos\theta$ into a series and only keep the first two terms. Eq.(5) is turned into

$$H_0=\Omega_0P_\phi(1-\varepsilon)+1/2F\theta^2+1/2GP_\theta^2 \qquad (6)$$

where $F=\varepsilon\,\Omega_0P_\phi$, $G=1/qR_0$.

A generating function is introduced

$$F_2=-p_\phi\beta-P_\theta\,\mathrm{tg}\,\alpha/2A \qquad (7)$$

where β and α are new coordinates, $A=(F/G)^{1/2}$, $P_\theta=A\theta_1\cos\alpha$, θ_1 is the poloidal angle at the banana tip. From Eq.(7), we have

$$H_0=\Omega_0P_\phi(1-\varepsilon)+\omega_bP_\alpha \qquad (8)$$

where $\omega_b=(FG)^{1/2}$

The perturbed Hamiltonian is given by

$$H_1=e\Phi_m\exp[i(\kappa z-\omega t)]+\mathrm{c.c.} \qquad (9)$$

where $k=m\,r$, $kz\approx m\theta_0 \sin\alpha - m_p \sin\Phi\, r$. If only second harmonic is considered, we have

$$H=\Omega_0 P_\theta\,(1-\varepsilon)+\omega_0 P_\omega+(e\Phi_0 k^2 P_\theta/2\Omega_0)\sum J_l\cos(2\beta-2l\alpha-\omega t) \quad (10)$$

where small θ_0 is neglected. Time variable can be eliminated by using a generating function

$$F_2=(2\beta-2l\alpha-\omega t)P_\psi+\alpha J \quad (11)$$

where P_ψ and J are the new momenta conjugate to Ψ and α respectively.

If only the lth resonance is taken into account, we have

$$H=2\Omega_0(1-\varepsilon)P_\psi-\omega P_\psi-\omega_0(J-2lP_\psi)+P\Omega_0 P\psi J_l(\chi)\cos\psi, \quad (12)$$

where $P=e\Phi_0 k^2/2m\omega^2$, $\chi=(4-2lp_\psi)/4P_\psi$, J is a constant of motion.

For the relativistic electrons, the resonance condition is

$$d\Psi/dt=\partial H/\partial P_\psi\approx 2\Omega_0(1-\varepsilon)/\gamma-\omega+\omega_0 J/2P_\psi-3l\omega_0=0 \quad (13)$$

where γ is the relativistic factor. For weak relativisticity,

$$\gamma=1-2\Omega_0(1-\varepsilon)P_\psi/C^2,$$

where we have returned to normal Gauss units.

We expand H about the fixed points P_{ψ_0} and Ψ_0 which satisfy

$$\partial H/\partial P_\psi=0, \qquad \partial H/\partial\Psi=0. \quad (14)$$

A pendulum type Hamiltonian is obtained

$$\Delta H=g/2(\Delta P_\psi)^2-f\cos\Psi, \quad (15)$$

where $g=\partial^2 H/\partial P_\psi^2=[4\Omega_0^2(1-\varepsilon)^2]/C^2-3l\omega_0/2p_\psi-\omega_0 J/4P_\psi^3$, $f=-P\Omega_0 P_\psi J_l(\chi)$.

The maximum excursion $\Delta P_{\psi m}$ occurs on the separatrix in the phase space and is given by half the separatrix width,

$$\Delta P_{\psi m}=2|f/g|^{1/2}. \quad (16)$$

From the resonance condition, the separation of adjacent resonances is given by

$$\delta P_\psi=|3\omega_0/g|. \quad (17)$$

Stochastic motion takes place whenever separatrices of neighboring islands overlap. Neglecting the difference of the maximum excursions in the adjacent islands, we can parametrize the overlap condition[6]

$$2\Delta P_\psi/\delta P_\psi>2/3 \quad (18)$$

that is, $P>P_c$, where

$$P_c=E_c\omega_B^2/8|J_L(X)|(1+E_s/4\mu^2)(1-\varepsilon)^2 \qquad (19)$$

where $\mu=v_\perp^2/2v_{t0}^2$, $E_s=2C^2/v_{t0}^2$, $X=(1-\varepsilon)^{1/2}/4\mu^{1/2}\omega_s-1/2$, v_{t0} is the initial parallel velocity at $\theta=0$ point.

HEATING PROCESS

In order to estimate the μ_{max}. We devise the method, if two islands overlap, the electron can jump from one island to the other. t changes all the time until $|t|$ reaches its maximum, for which the neighboring islands separate. The maximum increase of μ is $|J(X)|p\mu\Delta\tau$ for each step, where $\Delta\tau$ is the step length. For the parameters $\varepsilon=0.143$, $p=0.512*10^{-4}$, and $\phi_s=\pi/3$, we get $v_\perp^2\simeq 1.2*\sqrt{2}cv_{t0}$ where v_{t0} varies. The maximum perpendicular energy is greater than that presented by Hsu et al.

The distribution function is given by

$$f_{ef}=(1/\pi^{3/2}v_e)\exp(-v_\parallel^2/v_e^2)\,\delta(v_\perp^2-1.2*\sqrt{2}cv_\parallel). \qquad (20)$$

we can obtain the poloidal distribution of the density and the energy

$$n(\theta)=2/\sqrt{\pi}\int dy\sqrt{y}\exp(-y^2)/|y-\alpha|^{1/2}, \qquad (21)$$

where $\alpha=1.2(\sqrt{2}c\varepsilon/v_e)(1-\cos\theta)$. Numerical results are shown in Fig.1 in which the comparison between our results and the results given by Hsu et al[2] is given. The ring peak shifted towards $\theta=0$ point. The full width at half maximum becomes smaller.

References

[1] M.N.Rosenbluth et al, Phys.Rev.Lett., 31, 1967(1983).

[2] J.Y.Hsu et al, Phys.Fluids, 29, 507(1986).

[3] E.Y.Wang, et al, Private Communication.

[4] Wang Zhongtian, Commun. in Theor. Phys., 3(1984) 331.

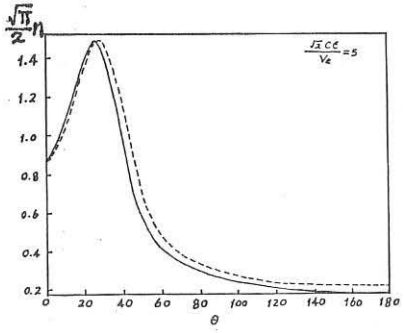

Fig.1 Comparison of the ring density between our result-solid curve and Hsu's -dashed curve.

METHOD OF DETERMINATION OF ECR EMISSION POLARIZATION CHARACTERISTICS IN TOKAMAK CONDITIONS.

Lazarev V.B.
I.V.Kurchatov Institute of Atomic Energy,Moskow,USSR.

The question about polarization measurements of elec - tron cyclotron emission (ECE) arose in connection with the problem of safety factor q(r) determination in tokamak plasma /1,2/. The first experiments performed by fast-scan Michelson interferometer /3,4/have shown that intensity of ordinary and extraordinary modes are comparable as a result of multyreflections and depolarization on the wall of a chamber. This fact does not allow to measure the rotation by a simple method. Recently /5/ it was shown theoreticaly that there is effect of limiting polarization, which essentialy restrict the possibility of safety factor determination through the ECE polarization in tokamak conditions. So there are two unsolved problems: strong depolarization due to walls and the effect of limiting polarization.

The objectiv of present paper is to show that at least the first of these problemes can be solved by measuring of correlation matrix elementes for componentes of stochas - tic field of ECR radiation

$$B_{ij}(\tau) = \langle E_i(t)\ E_j^*(t)\rangle = \begin{matrix} B_{xx}(\tau) & B_{xy}(\tau) \\ B_{yx}(\tau) & B_{yy}(\tau) \end{matrix} \qquad (1).$$

In terms B_{ij} one can determine a Stock's parameter which completely caracterize a partly palarizing radiation

$$S_o = B_{xx} + B_{yy} \qquad S_1 = B_{xx} - B_{yy}$$
$$S_2 = B_{xy} - B_{yx} \qquad S_3 = -i\,(B_{xy} - B_{yx}) \qquad (2).$$

where S_o and S_1 define a value and ratio of polarization ellipse exes; S_2 relates whith the rotation of axes ; S_3 is a defference of circular wave intensities whith opposite rotation. The polarization degree of ECR radiation in tokamak conditions according /3,4/ is $S_1/S_o \leq 0,2$. This prevents the measurments of small rotations ($\Theta \sim B_p / B_t \simeq 0,1$ rad) by a simple method.

However, if one can measure the elements $B_{ij}(\tau)$ (it is posible by polarization-type Michelson interferometer) the angle Θ may be definde through Fourier components B^{ω}_{ij} from condition $B'_{xy} + B'_{yx} = 0$, where B'_{ij} - correlation matrix in the coordinate system related whith polarization ellipse. In this way one obtain following relation

$$\Theta(\omega) = \frac{1}{2} \operatorname{arctg} \frac{B^{\omega}_{xy} + B^{\omega}_{yx}}{B^{\omega}_{xx} - B^{\omega}_{yy}} \qquad (3).$$

Let us consider the meaning of formula (3). B^{ω}_{xx} and B^{ω}_{yy} are spectral intensities of ordinary and extraordinary modes. Both this functions are real as a resalt of a parity of the autocorrelation functions $B^{\omega}_{ii}(\tau)$. B^{ω}_{xy}, B^{ω}_{yx} in general case are complex functions and are depended on the correlation $\langle E_x \cdot E_y^* \rangle$. But the sum $B^{\omega}_{xy} + B^{\omega}_{yx} = 2\mathrm{Re} \cdot B^{\omega}_{xy}$ at any case is real and defines the rotation angle of polarization plane. The imaginary part of function B^{ω}_{xy} is reletad with fase defference betwen the orthogonal compo - nents of E-field. Note that formula (3) is strietly valid only for radiation on the emission surface becouse it does not take into account a change of polarization state during propagation through the plasma to the receiver device. Let us consider this question in more detail.

The change of polarization mainly depends on the orien-

tation of wave vector and magnetic field as far as spectral range. At first let us consider the case when EC radiation propagates along major radius to low field side. In this case for tokamak configuration there is no radial component of magnetic fild, but as was shown in /5,6/ polarisation limiting takes place at the same conditions.

Due to this effect polarization "follows" to the rotation of the poloidal magnetic field up to external plasma region where electron density is small. In order to estimate the conditions in which this effect is significant one can use following relation /5/

$$(K_o - K_x) \cdot L \gg 1$$

where K_o, K_x - wave vectors for ordinary and extraordinary modes, L - the lenth of ray tracing. For modern tokamak conditions this criterion is met in the central and intermediate plasma regions for a frequency $\omega \simeq (2 \div 3)\omega_{ce}$ For that geometry according to the theory /5,6/ angle θ has not changed in $2\omega_{ce}$ range and must be over

$$\theta (\omega) - q (a)^{-1} \cdot a / R$$

(a-limiter radius, R-major toroid radius). Such experiment may be interesting from point of view examination of theoretical predictions in connection whith limiting polarazing effect.

But different experiment is possible. Let's assume that receiver antenna is shifted up or down and "observed" plasma in the major radius direction. In this case there is radial component of poloidal magnetic field along the ray tracing and for this reasone Faraday rotation must take place. So by means of measuring of function $\theta (\omega)$

it is posible to restore $q(r)$ in any region, if profile $n_e(r)$ is known.

However, one can try to determine density distribution along the ray with the imaginary part of B_{xx} function, which is related to the fase shift

$$\Psi(\omega) = \operatorname{arctg}\left[i(B^{\omega}_{xy} - B^{\omega}_{yx})/(B^{\omega}_{xy} + B^{\omega}_{yx})\right]$$

The function $\Psi(\omega)$ is caused by the defference between refraction index of the ordinary and extraordinary modes.

Note in conclusion that suggested method can be usefull not only for tokamak but for investigation of ECR radiation in other systemes.

REFERENCES

1. CanoR.,I.Fidone, and M.I.Schwarts, Phys.Rev.Letters v.27, p.783 (1971).
2. Engelmann F.,M.Curatolo, Nuclear Fusion v.13, p.497 (1973).
3. Costley A.E., Hastie R.S., Paul I.W.M., Chamberlain I., Phys.Rev.Lett., v.33, p.758 (1974).
4. Hutchinson I.H., Komm D.S., Nuclear Fusion v.17 (1977), p.1077.
5. Golant V.E., Physika plasmi, v.6, p.1396,1980.
6. Geleznykov V.V., Cocharovskiy V.V., Cochrovskiy Vl.V., UFN, v.141, p.257, (1983).

PERFORMANCE OF THE 70 GHz/ 1 MW LONG-PULSE E C R H SYSTEM ON THE ADVANCED STELLARATOR W VII-AS

W. Kasparek, G.A. Müller, P.G. Schüller, M. Thumm
Institut für Plasmaforschung, Universität Stuttgart
D-7000 Stuttgart 80, Fed. Rep. of Germany

V. Erckmann
Max-Planck-Institut für Plasmaphysik, EURATOM-Association
D-8046 Garching, Fed. Rep. of Germany

1. Introduction

Built-up and subsequent electron cyclotron resonance heating (ECRH) of net-current free plasmas (n_{e0}=1.8-5.3·10^{19} m^{-3}, T_{e0}=2.3-0.6 keV) using a single 70 GHz/200 kW/100 ms pulse gyrotron has been proven to be a powerful method to create a target plasma for neutral beam heating in the stellarator W VII-A [1]. For the new modular stellarator W VII-AS a 1 MW/70 GHz long-pulse microwave system is under construction which comprises five subsystems each designed to generate, transmit and radiate into the plasma 200 kW of millimetre-wave power with pulse length up to 3 s [2]. Low-loss power transmission from the gyrotrons to the W VII-AS device and mode transformation to achieve a linearly polarized, pencil-like microwave beam are basic requests for optimum ECRH applications. The high-power long-pulse performance of this W VII-AS ECRH system is described in the following paragraphs.

2. General Description

Each subsystem consists of a 200 kW/70 GHz gyrotron, a highly oversized circular waveguide transmission line and a quasi-optical wave launching antenna for plasma irradiation in the linearly polarized fundamental TEM00 wave mode. This Gaussian mode is ideal for the use with focusing mirrors and polarization twist reflectors. The conversion of the circular symmetric TE0n gyrotron output mode mixture (mainly TE02) to the HE11 hybrid mode, which couples with approx. 98% to the free-space Gaussian mode is performed by a sequence of highly efficient mode transducers (multi-step mode conversion: ΣTE0n → TE01 → TE11 → HE11) [3]. The intermediate TE01 wave is appropriate for weakly attenuated long-distance propagation through overmoded smooth wall circular waveguides (I.D. = 63.4 mm). The balanced HE11 hybrid mode is radiated from an open-ended, circumferentially corrugated, oversized circular waveguide (I.D. = 63.4 mm). The polarization plane can be changed by simply rotating the serpentine TE01-to-TE11 mode transformer around its axis [3]. The four transmission lines which are fed by the long-pulse gyrotrons (VARIAN VGE-8007) are mounted in two pairs at two adjacent tangential injection ports of W VII-AS and launch their microwave power from the low-field side (O-mode for fundamental or X-mode for 2nd harmonic heating). The fifth waveguide line is fed by the 100 ms pulse gyrotron (VARIAN VGE-8070) and radiates the millimetre-wave power from the high-field side (also from the outside of the torus, but with reversed magnetic field gradient, with a choice of X- or O-mode polarization) [2]. Arbitrary elliptical polarization of HE11, which is needed for current drive experiments by launching EC-waves

with the wavevector at oblique angles relative to the magnetic field, is achieved by polarization converters in the TE11 mode sections [4]. The mode purity in the transmission lines is conserved by using waveguide diameter tapers with optimized non-linear profile together with circumferentially corrugated, gradual waveguide bends with varying curvature distribution and matched corrugation. The overall efficiency in the desired mode of a complete transmission line was calculated and measured (at low power levels) to be approx. 90%. At high power levels the microwave power and the mode spectrum at the outputs of the gyrotrons as well as at various positions in the transmission lines have been measured by special calorimeters and wavenumber spectrometers, respectively.

3. Microwave Generator System

Each microwave-power module contains a commercial 70 GHz/200 kW gyrotron (with complex TE01/TE02 cavity), cooling systems for the tube and the microwave window, high precision electric power supplies for the magnets, the collector voltage (80 kV) (developed by IPP Garching) and the gun anode voltage (developed by IPF Stuttgart) and a tube protection circuit [5]. Programming of the gun anode voltage allows a fast modulation (0-50 kHz) of the gyrotron microwave power for heat wave experiments in order to analyze the thermal transport of the electrons [6]. Careful control of the various gyrotron parameters (accuracy $\leq 10^{-3}$) turned out to be the basic requirement for stable tube operation at the optimum parameter set for maximum output power and highest achievable mode purity.

The mode compositions of the four gyrotrons implemented in the system until now were analyzed in detail employing different wavenumber spectrometers [7]. The tubes exhibit a purity of the TE02 output mode between 80% and 95%. The main portion of the parasitic modes is due to the other TE0n modes (1-15% TE01, 3% TE0n ($n \geq 3$) and 1% asymmetric modes). The higher-order TE0n modes are probably excited by the TE02 working mode in the internal collector tapers of the gyrotrons. The high TE01 mode content may additionally directly originate from the complex cavity of the tube and depends sensitively on the different operational parameters. This high TE01 mode part cannot be tolerated since the first part of the waveguide system (see chapter 4) consists of a down-taper from 63.4 mm to 27.8 mm I.D. and a gradual 90°-bend, the curvature and wall corrugations of which are optimized for a pure TE02 mode. In this bend the TE01 part of the wave would suffer strong mode conversion into highly attenuated asymmetric modes increasing the risk of rf-breakdown in the waveguide. The TE01 content is therefore reconverted to the TE02 mode in front of the TE02-bend by properly designed, phase-matched mode transducer sections [3]. The phase adjustment was performed by varying the axial position of the converter within one beat wavelength of the two modes involved. The mode composition was determined with a k-spectrometer installed after the TE02-bend and a 100% TE02-to-TE01 mode transformer. Optimum phase matching is reached if the TE02-signal is minimum. The results for the tube VGE 8007/1 (transmission line no. 2) is shown in Fig.1. The initial mode mixture (15% TE01, 81% TE02 and 4% other modes) was converted to approx. 96% TE02 and 4% other modes.

In the case of the 100 ms-pulse gyrotron an amount of 6% TE13 was measured which results from an asymmetry within the tube. A serpentine-type mode converter which exactly handles the given TE02/TE13 mode mixture to produce a pure TE02 mode was designed and is being manufactured.

4. Transmission Line System

The following table gives an overview of the basic waveguide components of the transmission line between one of the long-pulse gyrotrons and W VII-AS. All components were developed, systematically improved and manufactured by the IPF Stuttgart. The indicated typical total losses (mode conversion and ohmic losses) were determined experimentally in specific low-power tests. All experimental values were found to be in very good agreement with the theoretical calculations.

component	w.g. modes	purpose/features	total losses
down-taper	TE02/TE01	reduction of gyrotron output w.g. diameter from 63.4 to 27.8 mm	< 0.1%
mode converter	TE02/TE01	mode purification TE02/TE01→TE02	< 0.1%
corrugated bend (90°)	TE02	sinusoidal curvature, corrug. depth $0.3\cdot(\lambda/4)$, arc length 1.74 m	≦ 1.5%
mode converter	TE02→TE01	periodic radius perturbations, 8 main periods, length 0.87 m	0.4%
up-taper	TE01	enlargement of w.g. diameter from 27.8 to 63.4 mm, length 0.71 m, for long-distance transmission (30 m)	< 0.1%
down-taper	TE01	reduction of w.g. diameter from 63.4 to 27.8 mm, length 0.71 m	< 0.1%
corrugated bend (90°)	TE01	triangular curvature, corrug. depth $0.2\cdot(\lambda/4)$, arc length 2.40 m	≦ 1.5%
k-spectrometer	TE01	power and reflection monitor	< 0.2%
corrugated mode filter	TE01	attenuation of spurious TEmn (m≠0)/ TMmn modes by 90-99%, length 1.2 m	≦ 1%
mode converter	TE01→TE11	periodic curvature perturbations, 8 main periods, length 2.53 m	2.7%
(polarizer	TE11	arbitrary elliptical polarization	3%)
corrugated mode converter	TE11→HE11	nonlinear variation of corrug. depth from $\lambda/2$ to $\lambda/4$, length 0.37 m	1%
corrugated bend (47°)	HE11	$\sin^2$-curvature, corrug. depth $\lambda/4$, arc length 1.50 m	≦ 1%
corrugated up-taper	HE11	enlargement of w.g. diameter from 27.8 to 63.5 mm, length 0.70 m	< 0.2%
barrier window	HE11	corrug. w.g., sapphire, FC75-cooled	≈ 1%

As result of the mode purification procedure described in chapter 3, the TE01 sections of the transmission lines (40–50 m long) including 3 tapers, 2 gradual bends and 2 mode transducers were routinely operated at full power and with a pulse length of 0.7 s without any mode filters (w.g. not pressurized). The measured mode purity at the input of the TE01-to-TE11 mode transducer is 97% (see Figs. 1 and 2) and the power losses are only 5% (10 kW). High-power long-pulse tests of the TE11/HE11 transmission line sections close to the torus are presently accomplished.

The pulse length limitation to 0.7 s is due to reflections from the compact, solid material absorbing load [2]. The low heat conductivity of the fire clay causes glowing of the material, which alters the absorption characteristics of the load. To improve the applicability to full gyrotron pulse length (3 s), modifications of the load are carried out: enlarging the volume of the absorbing material and increasing the cooling efficiency by directing the blower-driven air stream through numerous axial holes in the cylindrical fire-clay absorber.

References

[1] V. Erckmann et al., Plasma Phys. and Contr. Fusion 28 (1986) 1277.
[2] W. Kasparek et al., Proc. 14th SOFT, Avignon, 1986, Vol. 1, p. 829.
[3] M. Thumm, Int. J. Electronics 61 (1986) 1135.
[4] M. Thumm, H. Kumrić, Conf. Digest 12th Int. Conf. on Infrared and Millimeter Waves, Lake Buena Vista, 1987, p. 336.
[5] G. Müller et al., Proc. 13th SOFT, Varese, 1984, Vol. 2, p. 811.
[6] H.J. Hartfuß et al., Nucl. Fusion 26 (1986) 678.
[7] H.J. Barkley et al., Int. J. Electronics 64 (1988) 21.

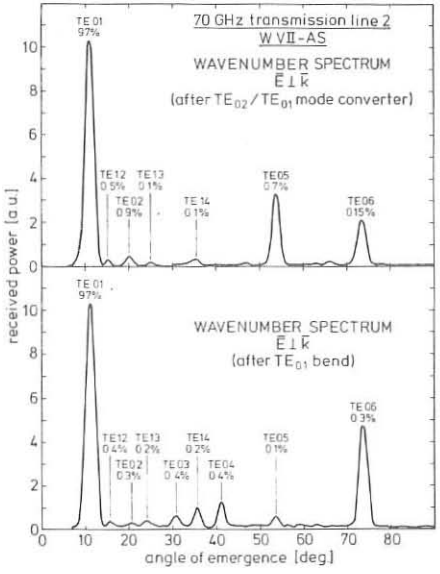

Fig. 1:
Mode spectra of TE modes measured in 70 GHz W VII-AS transmission line no. 2 at the output of the TE02-to-TE01 modes converter (upper part) and after the TE01 bend (lower part).

Fig. 2:
Thermographic burn pattern of the TE01 mode (97% mode purity) in 70 GHz W VII-AS transmission line no. 2 at the output of the TE01 bend.

MILLIMETER-WAVE GYROTRONS FOR ECRH*

H. Jory, K. Felch, H. Huey, and E. Jongewaard

Varian Associates, Inc.
611 Hansen Way
Palo Alto, CA 94303
U.S.A.

ABSTRACT

Gyrotrons are being developed to produce long-pulse or CW power output at frequencies of 106 GHz and 140 GHz. The goal of the 106 GHz gyrotron is 500 kW output with 200 ms pulse length. The goal of the 140 GHz gyrotron is 1 MW CW output.

An initial experimental version of the 140 GHz gyrotron has been constructed with the goal of demonstrating peak output powers of up to 1 MW for pulse lengths of a few ms and CW output powers of up to 400 kW. The design uses a $TE_{15,2,1}$ interaction cavity which results in a $TE_{15,2}$ output mode. Initial testing of the tube has been completed. Output powers of 300 kW have been obtained with pulse lengths of around 1 ms.

The 106 GHz gyrotron employs a similar type of configuration. Testing is currently scheduled for August 1988.

140 GHz, 1 MW EXPERIMENT

This experiment was conducted during 1987 to produce as much power as possible at 140 GHz and to obtain thermal design information for whispering gallery mode gyrotrons. The tube has the same basic configuration employed in earlier circular-electric-mode gyrotrons,[1,2] (as shown in Figure 1), except that a $TE_{15,2,1}$ cavity is used.[3] The power output in the $TE_{15,2}$ mode is brought out axially through the beam collector to an output window at the top of the tube. Table 1 summarizes the design parameters.

In initial testing, the gyrotron produced output power up to 300 kW peak with pulse lengths around 1 ms. Operation at longer pulse lengths or higher peak powers was prevented by spurious oscillations occurring in the beam tunnel between the gun and interaction cavity. At high peak power or long pulse length, the spurious oscillation activated protective circuitry and turned off the gyrotron.

Figure 2 shows power output versus gun-anode voltage for several values of beam current. Reasonably good dynamic range was observed with gun-anode voltage variation of 1 kV, producing power variation of order 2 to 1. The dynamic range at the high end was limited by spurious oscillation rather than gun-anode current. Output efficiencies were in the range of

* The 140 GHz gyrotron oscillator is being developed under contract with Lawrence Livermore National Laboratory, operated by the University of California for the U.S. Department of Energy under Prime Contract W-7405-eng-48.

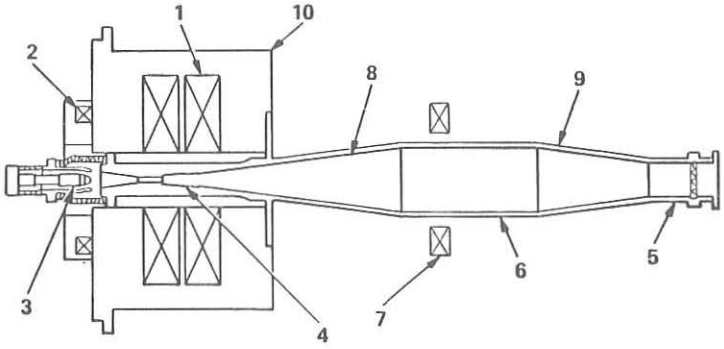

1. MAIN MAGNET COILS
2. GUN MAGNET COIL
3. ELECTRON GUN
4. CAVITY
5. OUTPUT WAVEGUIDE AND WINDOW
6. BEAM COLLECTOR AREA
7. COLLECTOR MAGNET COILS
8. OUTPUT GUIDE UP-TRANSITION
9. OUTPUT GUIDE DOWN-TRANSITION
10. DEWAR

D301
F942

FIGURE 1. GYROTRON OSCILLATOR

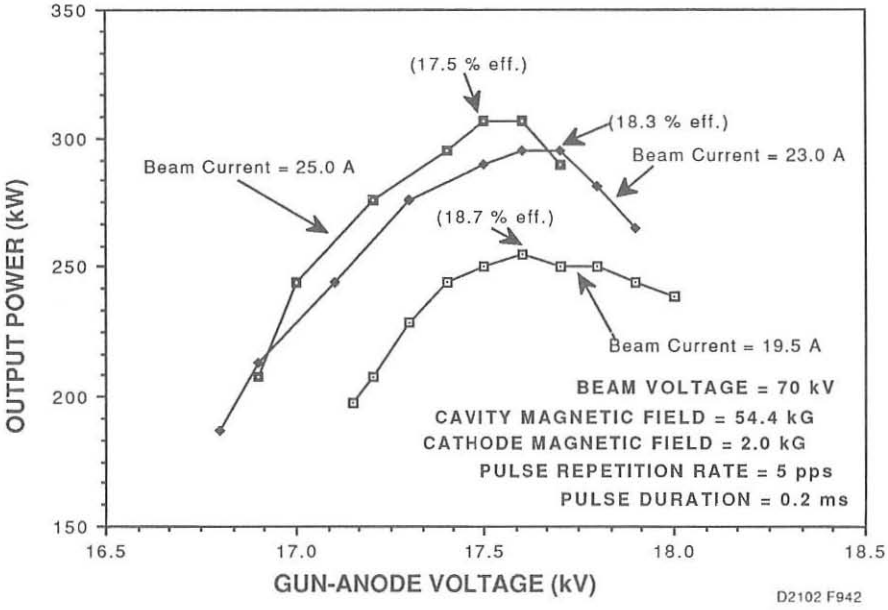

D2102 F942

FIGURE 2. OUTPUT POWER VS GUN - ANODE VOLTAGE

TABLE 1. BASIC DESIGN PARAMETERS

Beam Voltage	80 kV
Operating Current	35 A-50 A
Cavity Magnetic Field	5.55 T
Cavity Average Beam Radius	0.53 cm
Cavity $v_\perp/v_\parallel$	2
$\Delta v_\perp/v_\perp$	<0.04
Beam Thickness	0.59 mm
Magnetic Compression	30

17 to 19 percent, which nearly agreed with predicted values for that range of beam voltage and current. At the normal design values an efficiency of 25 to 30% is expected.

To allow thermal measurement of microwave power dissipated in various parts of the tube, tests were made with pulse repetition rates that produced 15 kW average output power. Power losses were measured in the beam tunnel, the interaction cavity, the tapered output guide, the collector insulator, and the output window. The results, except for the beam tunnel, agreed well with calculated values. For example, the output window losses as a percentage of output power were 3.8% compared with a predicted value of 3.1%.

The losses in the beam tunnel did not vary in proportion to output power and were higher than expected in many regions of parameter space. This behavior, together with the observation of occasional spurious frequencies in the output, led to the conclusion that spurious oscillations were occurring in the beam tunnel. This was later verified further by disassembling the tube and observing the damage pattern.

The distribution of the spent electron beam on the collector was also measured during the tests. The measurements were made at a level of 80 kV, 16 A The results indicate that the existing design should be capable of handling an 80 kV, 25-30 A beam.

FUTURE PLANS

The 140 GHz, 1 MW experimental gyrotron is being rebuilt with design changes in the beam tunnel to eliminate the spurious oscillations. Testing of the revised tube is scheduled for May-June 1988.

A 106 GHz gyrotron, that employs a configuration similar to the 140 GHz experimental gyrotron, is also under development at Varian. The goal of this tube is to generate output powers of 500 kW for 200 ms pulses. Tests on this tube are currently scheduled for August 1988.

REFERENCES

(1) H. Jory, "Status of Gyrotron Development at Varian Associates," Proc. 4th Int. Symp. on Heating in Toroidal Plasmas, 1984, Vol. 2 pp. 1424-1430.

(2) K. Felch, R. Bier, L.J. Craig, H. Huey, L. Ives, H. Jory, N. Lopez and S. Spang, "Achievements in the CW Operation of 140 GHz Gyrotrons," 11th Int. Conf. Infrared and Millimeter-Waves, *Conference Digest,* 1986, pp. 43-45.

(3) K. Felch, I. Ives, E. Jongewaard, H. Jory, and S. Spang, "Initial Operation of a High-Power, Whispering-Gallery-Mode Gyrotron," 12th Int. Conf. Infrared and Millimeter Waves, *Conference Digest*, 1987, pp. 146-147.

KINETIC EFFECTS ON ELECTRON CYCLOTRON EMISSION DURING ELECTRON CYCLOTRON HEATING IN TOKAMAKS

G. Giruzzi

Association EURATOM-FOM, FOM Instituut voor Plasmafysica
"Rijnhuizen", Nieuwegein, The Netherlands

1. Introduction. Plasma heating and current drive in tokamaks by means of high-power electron cyclotron (EC) waves results in generating non-Maxwellian electron distribution functions. These distributions intensely emit at the electron gyrofrequency ω_c and its harmonics because of their high perpendicular energy content. The properties of the radiation emitted by this specific non-Maxwellian system are studied in the present work. The electron distribution is determined by solving the time-dependent bounce-averaged quasilinear/Fokker-Planck equation [1] by means of a 3-D Fokker-Planck code [2]. The computed steady-state distribution function is then used to calculate the emission and transmission spectra for different locations of the receiving antennas, polarizations and harmonics. It results that a detailed analysis of those spectra yields insight in problems like the impact of quasilinear flattening and electron trapping on the form of the steady-state distribution, which are of paramount interest for EC heating and especially for current drive in tokamak reactors. For the illustrative computational examples discussed in the following, typical parameters of the T-10 EC heating experiments were chosen [3], i.e., R = 150 cm , a = 40 cm, $B = B_0/(1+r\cos\chi/R)$, Z = 1, $n_e / n_e(0) = T_e / T_e(0) = 1 - r^2/a^2$, $n_e(0) = 2\times 10^{13}$ cm^{-3} , $T_e(0) = 2$ keV, where a, R are the tokamak radii, B is the magnetic field, r, χ are polar coordinates in the poloidal plane, n_e, T_e are the electron density and temperature, respectively. A wave beam having a cross-section $\sigma \approx 10$ cm^2 and a frequency 84 GHz is considered. The two most attractive scenarios for EC heating are considered, i.e., by an ordinary (o) mode launched from the outboard side and propagating perpendicularly to $\vec{B}$, absorbed at $\omega \approx \omega_c$, and by an extraordinary (x) wave, injected obliquely from the inboard side and absorbed at downshifted frequency ($\omega < \omega_c$). The latter scheme is also representative of current drive experiments.

2. Impact of quasilinear effects on EC emission. As shown earlier [4,5], a strong flattening of the electron distribution in the perpendicular direction is expected during EC heating at high power levels as a consequence of the diffusive nature of the quasilinear operator. This flattening affects the damping of the wave beam itself via two distinct effects: i) decrease of the perpendicular derivative of f, and consequent reduction of the absorption [4] ; ii) increase in the population of mildly superthermal electrons, leading to an enhancement of the absorption [5]. The relative importance of the two effects depends essentially on the velocity range of the absorbing electrons. In order to study the global impact of these quasilinear effects on EC emission and absorption, the case of an o-wave beam, launched from the low-field side of the tokamak in the equatorial plane and propagating perpendicularly to $\vec{B}$ has been considered ($\bar{N}_{\parallel} = 0$). The beam angular width in toroidal direction is $\Delta\psi = 5°$; the values of injected wave power are $P_0 = 2$ and 4 MW; the magnetic field at the plasma centre is $B_0 = 3.04$ T, so that $\omega = \omega_c$ at x = r cos χ = 2 cm. The absorption takes place in the plasma core, mainly for $-2 < x < 2$ cm, i.e., $4 \gtrsim u > 0$, u being the resonant momentum normalized to the thermal one: a large fraction of the wave energy goes to mildly superthermal electrons (u = 1 for x = 1.7 cm). In Fig. 2, level curves of the steady-state distribution function at r = 1 cm (where the power deposition peaks) are shown for $P_0 = 4$ MW. Perpendicular stretching of the electron distribution is evident in this picture, as well as the isotropizing action of pitch-angle scattering. Emission close to the second harmonic of ω_c, polarized in the x-mode and received by an antenna located in the equatorial plane, at the low-field side of the tokamak, is first considered. The theory of EC emission, as well as the definitions of the basic quantities, like optical thickness and radiative temperature, can be found elsewhere [6]. The optical thickness τ_x is shown in Fig. 2. The dashed line represents the Maxwellian optical thickness, which changes very slowly, following the spatial profiles of n_e, T_e and B; on the other hand, curves a) and b), obtained for $P_0 = 4$ and 2 MW, respectively, display a strong variation, consisting in a dip close to $\omega = 2\omega_{c0}$ and a bump at lower frequencies. This structure is closely related to the shape of f (Fig. 1): the dip corresponds to the region of maximum flattening ($2 \lesssim u \lesssim 3$); for $u \gtrsim 3$ ($\omega/\omega_{c0} \lesssim 1.96$) the magnitude of the perpendicular slope starts to increase and the effect of

the enhancement in the tail population becomes dominant: τ_x increases by a large factor. Strong evidence of quasilinear effects can also be found in the spectra of the radiative temperature T_{rx} shown in Fig. 3. In fact, the enhancement in the emission during the heating process takes place exactly in the same frequency range as the dip in τ_x: it is not a manifestation of bulk heating (otherwise it would be symmetric around the position $x_c = 0$), but rather of quasilinear flattening. Note that the bump in τ_x has no counterpart on T_{rx} in Fig. 3, since the plasma is optically thick and the radiation emitted at these frequencies is completely reabsorbed before reaching the low-field-side antenna. The electron population corresponding to that bump can be detected by vertical observation, as shown in Fig. 4. The three spectra display profound differences related to the high-energy part of the electron distribution, i.e., to the bumps in Fig. 2. This completes the demonstration of the sensitivity and flexibility of this diagnostic method for the mildly energetic tails generated by EC heating.

3. Impact of toroidal effects on EC emission. Toroidal effects on the resonance (and resonance width) [2] and the presence of a population of trapped electrons have important consequences on the structure of the steady-state distribution function resulting from the interaction with EC waves, and therefore on the current drive efficiency [1,2]. EC emission is very sensitive to toroidal effects and can be used to investigate their impact on current drive. In order to illustrate this point, wave absorption away from the plasma centre ($r/a \approx 1/2$) of wave beams launched from the high-field side in the equatorial plane, polarized in the x-mode, has been investigated. For a wave power $P_0 = 2$ MW, two cases were considered:

a) $B_0 = 3.7$ T , $\quad \bar{\psi} = \arcsin \bar{N}_{\parallel} = -45°$, $\quad \Delta\psi \approx 10°$;

b) $B_0 = 2.83$ T , $\quad \bar{\psi} = -35°$, $\quad \Delta\psi \approx 7°$.

In both cases, the waves are absorbed by mildly superthermal electrons at $\omega < \omega_c$. In case a), the wave energy is deposited around the position $x = +20$ cm , whereas in case b) it is deposited around $x = -20$ cm, but the parameters are chosen in such a way that absorption takes place for essentially the same local values of ω_c/ω , $N_{\parallel}$ and $\Delta N_{\parallel}$. This procedure allows to isolate the toroidal effects as the only effects responsible for the different kinetic evolution of the electron distribution function in the two cases. The level curves of the steady-state distribution functions in the two cases are shown for $r = 20$ cm in Figs. 5 a,b. The most striking difference between the two figures is the structure of the distribution function in the trapping region, i.e., the region between the two straight lines. This implies large differences in the radiative temperature, as illustrated in Fig. 6 for the x-mode at the second harmonic, observed from the high-field side. The peaks corresponding to case b) are much lower and narrower; in case a) the low-frequency peak is much higher than the high-frequency one: this means that a large contribution to this emission spectrum is due to trapped electrons, which cannot attain the inboard part of magnetic surfaces. An asymmetry of this kind has been observed experimentally during EC heating in T-10 tokamak [7]. A more precise insight into the energy range of the non-Maxwellian tail is provided by vertical observation, as shown in Fig. 7. Since in case a) most of the emission is due to trapped electrons, the corresponding spectrum in case b) is much lower and narrower. This clearly shows the impact of toroidal effects on the generation of superthermal electrons by EC-wave absorption. This effect is so large that it can be detected also for a much lower wave power, e.g., $P_0 = 0.5$ MW. Thus, low-power experiments in smaller tokamaks appear to be quite suitable for an experimental investigation of toroidal effects on the wave-electron interaction process and trapped electron dynamics.

Aknowledgements. Useful discussions with Prof. F. Engelmann are gratefully aknowledged. This work was performed under the Euratom-FOM association agreement, with financial support from ZWO and Euratom.

REFERENCES

[1] KERBEL, G.D., Mc COY, M.G., Phys. Fluids **28** (1985) 3629; O'BRIEN, M.R., et al., Nucl. Fusion **26** (1986) 1625; YOSHIOKA, K., ANTONSEN, T.M., Nucl. Fusion **26** (1986) 839.

[2] GIRUZZI, G., Phys. Fluids, to be published (Euratom-FOM Report 87/049).

[3] ALIKAEV, V.V., et al., Plasma Phys. **29** (1987) 1285 .

[4] FIDONE, I., et al., Phys. Fluids **26** (1983) 3292;
ALIKAEV, V.V., VDOVIN, V.L., Sov. J. Plasma Phys. **9** (1983) 538.

[5] KRIVENSKI, V., et al., Phys. Fluids **30** (1987) 438.

[6] BEKEFI, G., *Radiation Processes in Plasmas* (Wiley, New York, 1986), Chap. 2.

[7] SILLEN, R.M.J., et al., Nucl. Fusion **26** (1986) 303.

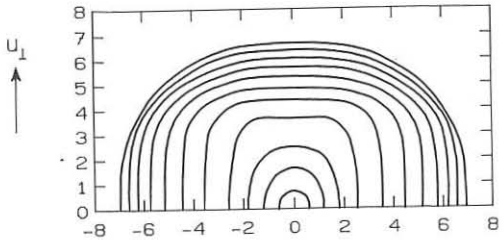

Fig. 1 : Level curves of the steady-state distribution function at r = 1 cm, during EC heating by an o-mode perpendicularly injected from the low-field side; P_0 = 4 MW. Maxwellian distribution would be represented by equally spaced circles.

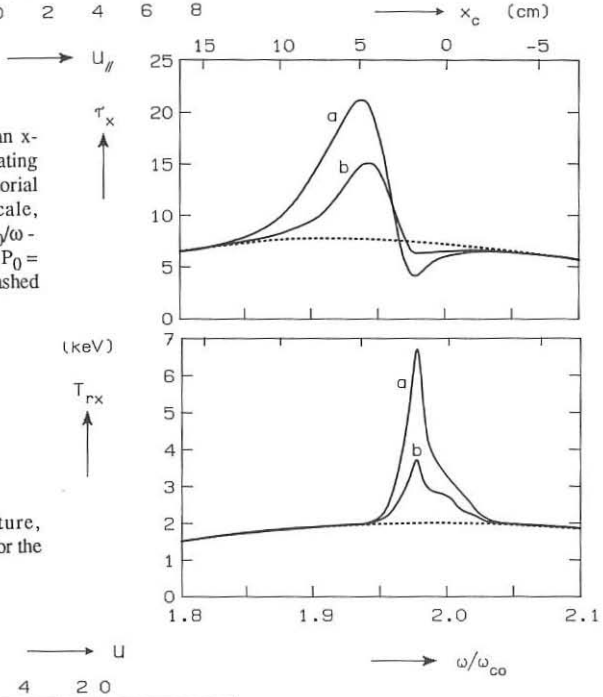

Fig. 2 : Optical thickness of an x-wave, at the 2nd harmonic, propagating perpendicularly to $\vec{B}$ in the equatorial plane, vs. ω/ω_{c0} (lower scale, $\omega_{c0}=\omega_c(r=0)$) and vs. $x_c = R(2\omega_{c0}/\omega - 1)$ (upper scale). P_0 = 4 MW (a), P_0 = 2 MW (b) and Maxwellian case (dashed line).

Fig. 3 :Radiative temperature, observed from the low-field side, for the conditions of Fig. 2.

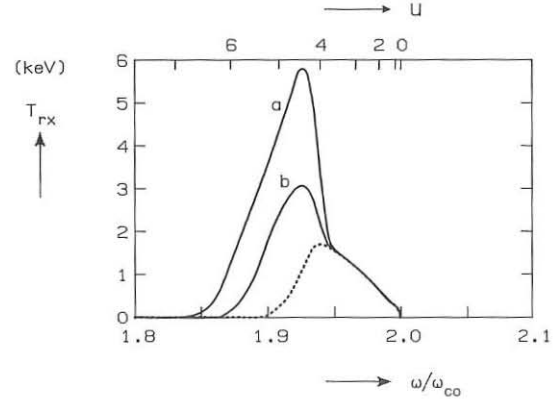

Fig. 4 : Radiative temperature observed from a top location, for the x-mode at the 2nd harmonic, propagating perpendicularly to $\vec{B}$ in the vertical direction, vs. ω/ω_{c0} (lower scale) and vs. $u = [\mu(r=0)]^{1/2}[(2\omega_{c0}/\omega)^2 - 1]^{1/2}$ (upper scale). P_0 = 4 MW (a), P_0 = 2 MW (b) and Maxwellian case (dashed line).

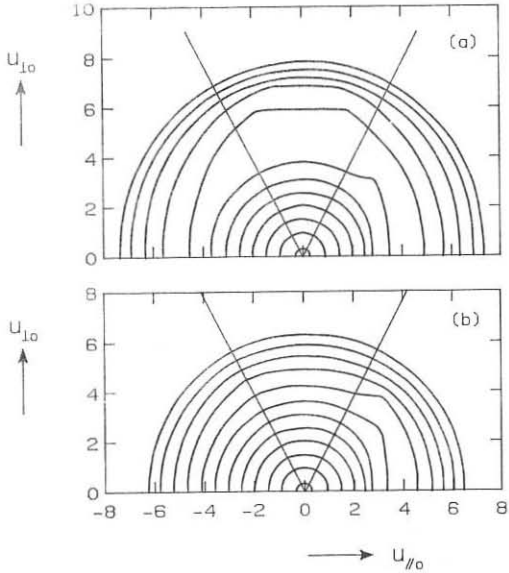

Fig.5 : Level curves of the steady-state distribution function at r = 20 cm, for an x-mode heating case (inside launch) and P_0 = 2 MW.
a) B_0 = 3.7 T, $\bar{\psi}$ = -45°, $\Delta\psi$ = 10° (absorption around x ≈ 20)
b) B_0 = 2.83 T, $\bar{\psi}$ = -35°, $\Delta\psi$ = 7° (absorption around x ≈ -20).

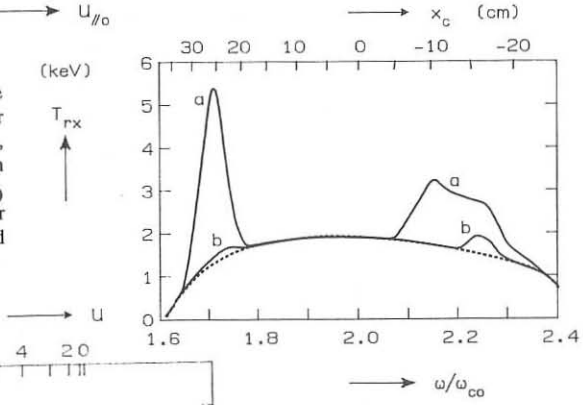

Fig.6 : Radiative temperature observed from the high-field side, for an x-mode at the 2nd harmonic, propagating perpendicularly to $\vec{B}$ in the equatorial plane, vs. ω/ω_{c0} (lower scale) and x_c (upper scale), for the conditions of Fig. 5. Dashed line is the Maxwellian spectrum.

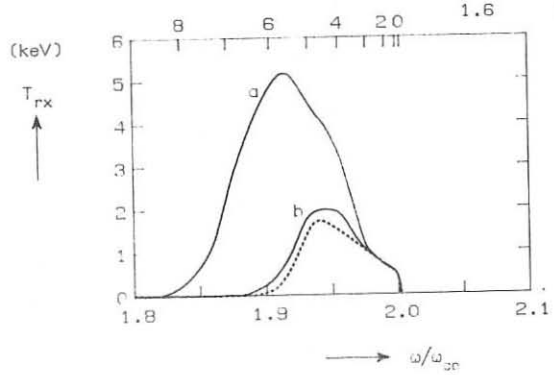

Fig.7 : Radiative temperature observed from a top location, vs. ω/ω_{c0} (lower scale) and vs. $u = [\mu(r=20)]^{1/2}[(2\omega_{c0}/\omega)^2 - 1]^{1/2}$ (upper scale), for the conditions of Fig. 6.

QUASI-LINEAR EVOLUTION OF THE WAVE-DAMPING DURING HIGH POWER ELECTRON CYCLOTRON HEATING

Vladimir Krivenski

Asociación EURATOM/ CIEMAT
CIEMAT, Madrid

Abstract

The early stage of the quasi-linear evolution of the wave-damping during electron cyclotron heating is considered for Alcator C parameters and powers extending from the MW to the GW range. It is shown that for these conditions strong modification of the wave damping occurs, which can be controlled by the wave launching conditions and the wave parameters.

The selectivity of electron cyclotron heating, both in real and in momentum space, makes this heating scheme attractive for temperature control and current drive purposes. The availability in the near future of very high frequency and high power microwave sources makes also realistic to consider its application to the reactor. This perspective raises the question of the plasma behaviour for powers much greater than those considered in today experiments.

The wave absorption is determined by the electron distribution function, which in turn results from the wave-induced diffusion and from the collision and transport processes. So in general the computation of the wave damping requires the solution of the 2D Fokker-Planck equation, including the RF diffusion term, the collision diffusion and slowing-down terms, coupled to the transport code. The various processes determining the wave-absorption have different time-scales and this fact may be exploited to considerably simplify the problem of the wave-damping computation.

Here we study the collisionless stage of the distribution function evolution by solving the 2D relativistic quasi-linear equation. Since the effect of collisions is to stop the quasi-linear flattening of the distribution function in the resonant region of the momentum space, the wave absorption at the time in which collisions become effective,[1]

$$\tau_{eff} \approx \frac{1}{2(5+Z_i)} \left[\frac{p}{(m_e T_e)^{1/2}}\right]^3 ,$$

(where $\tau = t\nu_c$, p, m_e and T_e are the electron momentum, rest mass and temperature, Z_i is the effective ion charge and ν_c the collision frequency) is a good estimate of the steady-state power absorption.[2,3] This is not true for others quantities, as for example the generated current, which evolve on the collisional time scale.

We consider Alcator C tokamak parameters, T_e=1 keV and ordinary mode injection from the low magnetic field side. In Fig.1 we present the absorbed power fraction vs. distance, for t = 0 ,6 13 ,20 τ_c , where τ_c = 0.004 ms is the collision time; the injection angle is 70° with respect to the magnetic field, the electron density $n_e = 10^{14}$ cm^{-3} and the power 10 MW. Fig. 1 shows that the quasi-linear flattening results in the degradation of the wave damping. In this case the effect is not dramatic since in a few collision times the quasi-linear deformation will be stopped by the Coulomb collisions. However we observe that for increasing power the quasi-linear evolution is faster, since t' = t P/P' , where t and t' are two different times at which the distribution function is the same, for powers P and P' respectively.

For example for the parameters of the FEL experiment,[4] i.e., for a power of 5 GW , injection normal to the magnetic field and $n_e = 5\times10^{14}$ cm^{-3} , the evolution of the wave damping is very fast, as shown by Fig.2, where the imaginary part of the wave-damping is plotted vs. time at x = 2.6 cm (chain-dotted line) and x = 2.1 cm (dashed line). In Fig.3 the absorbed power fraction is shown for two different halfwidth, $\Delta N_{||}$,of the wave-spectrum, which we assume to be gaussian at the plasma bord (the solid and chain-dotted lines correspond to $\Delta N_{||}$ = sin (6°), the dashed and dotted lines correspond to $\Delta N_{||}$ = sin (3°), at t=0 and t=7x10^{-7} ms respectively). This calculation shows qualitative agreement with previous results[5] and indicates that in a time shorter than the FEL pulse, 5x10^{-6} ms , the wave absorption will vanish. It should be

observed that this result is at the limit of validity of the quasi-linear theory and should be considered with caution.

The main features of the quasi-linear modification of the wave-damping can be obtained from the simple relations

$$\frac{\partial k''_{\perp}}{\partial \tau} \propto \left[\frac{\mu}{8} \left(\frac{p}{m_e c} \right)^2 - \frac{\omega_c}{\omega} - \frac{1}{\mu \left(\Delta N_{\parallel} \right)^2} \right] ,$$

valid for the ordinary mode and $N_{\parallel}=0$, or by

$$\frac{\partial k''_{\perp}}{\partial \tau} \propto \operatorname{sgn}\left(\frac{\omega_c}{\omega} - 1 \right) \times \left\{ \left[\frac{1}{|N_{\parallel}|} - \frac{\frac{\omega_c}{\omega}}{\left[N_{\parallel}^2 - 1 + \left(\frac{\omega_c}{\omega} \right)^2 \right]^{1/2}} \right] \left(\frac{p}{m_e c} \right)^2 - \frac{2\left(1 - N_{\parallel}^2 \right)^2}{\mu^2 |N_{\parallel}| \left(\Delta N_{\parallel} \right)^2} \right\},$$

valid for the extraordinary mode and $\mu \, | N_{\parallel} |2 \ll 1$, where

$$\mu = \frac{m_e c^2}{T_e} .$$

These relations show that the wave parameters may be choosen as to control the quasi-linear modification of the wave-damping and the shift of the absorption region in the plasma. This kind of control is of great relevance for electron cyclotron current drive studies.

1 N.J. Fisch and A.H. Boozer, Phys. Rev. Lett. **45** 720 (1980).

2 I.Fidone, R.L.Meyer, and G.Granata, Phys. Fluids **26**, 3292 (1983).

3 V.Krivenski,I.Fidone, G.Giruzzi, R.L.Meyer, and L.F.Ziebell, Phys.Fluids **30**, 438 (1987).

4 K.I.Thomassen et al., Free-Electron Laser Experiment in Alcator-C (U.S. GPO, Washington, D.C., 1986).

5 W.M.Nevins, T.D. Rognlien, and B.I. Cohen, Phys. Rev. Lett., **59** 60 (1987).

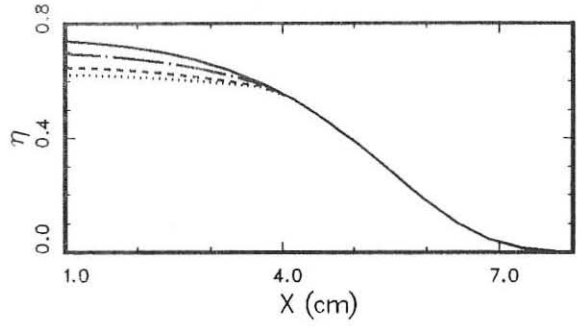

Fig. 1

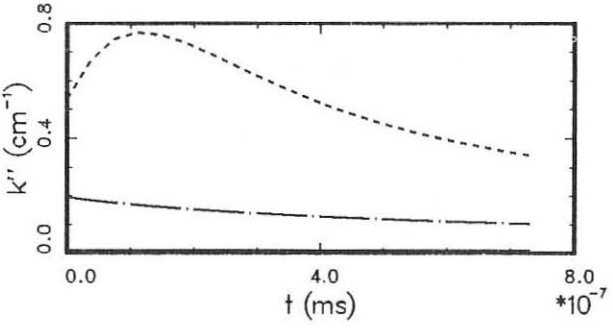

Fig. 2

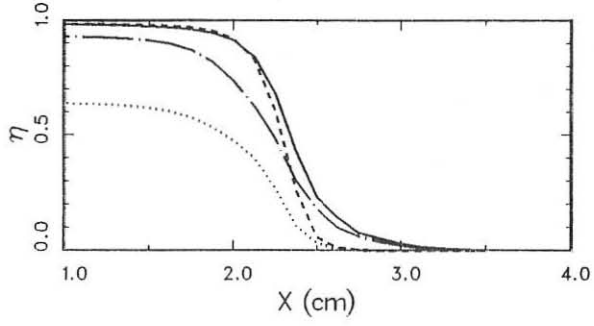

Fig. 3

SECOND ELECTRON CYCLOTRON HARMONIC ABSORPTION IN THE PRESENCE OF A SUPERTHERMAL TAIL

S.Pešić

Institute for Research in Physics, Institute "Boris Kidrič"-Vinča,
P.O.B. 522, 11001 Belgrade, Yugoslavia

The electron cyclotron wave absorption may increase the population of superthermal electrons and form a superthermal tail in the distribution of electron velocities parallel to the magnetic field /1,2/. The evolution of the superthermal tail is determined by a large number of effects: interparticle collisions, pitch angle scattering, magnetic trapping, inductive and RF electron acceleration, etc. Therefore, it appears necessary to examine the wave absorption for a class of model distributions which possess the main envisaged nonthermal features of the expected distributions. In the present paper we investigate the wave plasma interaction near the second harmonic of the electron cyclotron frequency in the presence of current-carrying as well as non-drifting superthermal tail. Only monotonically decreasing superthermal tails obtained by adding a low-density weakly relativistic drifting Maxwellian distribution to an anisotropic (or isotropic) weakly relativistic Maxwellian bulk are considered. So, the assumed model distributions have the following general form,

$$f(v_\perp, v_{/\!/}) = (1-\eta)\pi^{-3/2} v_{b\perp}^2 v_{b/\!/} \exp\{-v_\perp^2/v_{b\perp}^2 - v_{/\!/}^2/v_{b/\!/}^2\}$$

$$+ \eta\, \pi^{-3/2} v_{s\perp}^2 v_{s/\!/} \exp\{-v_\perp^2/v_{s\perp}^2 - (v_{/\!/}-u)^2/v_{s/\!/}^2\}. \qquad (1)$$

The set of three parameters (η, v_s, u) characterize the superthermal deviation of the distribution from a Maxwellian bulk; in general $\eta << 1$.

Starting from the general expression for the dielectric tensor and carrying out the corresponding momentum space integration within the weakly relativistic approximation, we have expressed the tensor components in terms of the function $F_q(n)$. In thermal plasma the function $F_q(n)$ reduces to the relativistic (Shkarofsky) plasma dispersion function /3/ while in presence of thermal anisotropy it goes to the corresponding expression obtained in /4/. In the numerical analysis of the propagation and spatial damping of both, the extraordinary (X) and ordinary (O) mode the finite Larmor radius effects are retained up to the second order in λ. The plasma equilibrium is represented by a parabolic electron density, a $(1-x^2/a^2)^{3/2}$-profile for the bulk and tail electron temperatures and the drift velocity, and by $B=B(0)\vec{e}_z/(1+x/A)$ with $x=r\cos\phi/a$, $\phi=0$ or $\phi=\pi$, $A=3$, for the magnetic field dependence. The parallel component of the wave refractive index is assumed to be real and determined by the direction of the wave vector of the incident electromagnetic waves at the plasma-vacuum interface, $N_{//}=\cos\theta_i$.

Generally, the electromagnetic waves are absorbed by low-velocity electrons ($v_{//}=\mathcal{O}(v_t)$) in thermal plasma /5/. For increasing the electron temperature and/or the ratio of the plasma radius and the vacuum wavelength i.e., k_0a, the region of maximum power deposition moves toward the wings of the thermal absorption profile involving electrons with somewhat larger parallel velocities. Similarly, the presence of a superthermal tail favours the absorption at large electron velocities. The absorption profile has a double- or single-peaked structure which depends on the parameters (n, v_s, u), v_b, k_0a as well as on the launch angle θ_i. As the fraction of electrons in the drifting tail increases the non-thermal contribution to the absorption increases and for large k_0a-values the absorption profile gradually transforms into a pronounced single peak. The previous discussion is illustrated by Fig. 1. in which the

power deposition P' in velocity space is shown for the X-mode launced from the low-field side and $\omega_p^2(0)/\omega_c^2(0)=1.4$, $\theta_i=70^0$, $c/v_b(0)=8$, $c/v_s(0)=16$, $u/v_s=1$ and several values of the fraction of electrons in the tail. Here, and in Figs. 2-3, we took a driving frequency equal to the second harmonic of the "central" electron cyclotron frequency, $\omega=2\omega_c(0)$, and a k_0a-value which is typical for the present large-size devices, $k_0a=5\times10^3$. It should be noted that $v_{//}/v_b$ is related to the dimensionless space coordinate through the relativistic resonance condition, $v_{//}/c=\{2N_{//}\,\omega_c/\omega-(N_{//}^2-1+4\omega_c^2/\omega^2)^{1/2}\}(1-N_{//}^2)^{-1}$. As one can see the power deposition tends to pile up at parallel velocity which is somewhat larger than the drift velocity that is, at $v_{//}\cong1.17u$. Thus, the wave energy is entirely absorbed by the superthermal component. Note that for fixed values of the parameters (η, v_s, u), v_b and $N_{//}$, the relative contribution of the superthermal component to the power deposition decreases as the plasma size or more precisely, k_0a is decreased. For wave launching from the high-field side the position of the maximum power deposition is only slightly displaced from that of the thermal ($\eta=0$) profile. When the fraction of superthermal electrons is kept constant, the increase of the drift velocity leads to a displacement of the power deposition region toward larger parallel velocities. This conclusion can be further verified in Fig. 2. where the power deposition in velocity space for wave launching from the low-field side, and $\eta=0.05$, $u/v_s=0.1$ and $u/v_s=0.5$, is represented. For comparison the corresponding power deposition profile for thermal plasma is also shown. Note that for $u/v_s=0.5$ the power deposition takes place just below the high-frequency boundary of the thermal absorption profile. Wave absorption in presence of both, the thermal anisotropy and drift motion, is presented in Fig. 3. where we show the power deposition profiles in velocity space for X-modes launched from the low and high-field side. In contrast with the previously discussed profiles, in this case the superthermal features are embedded in the bulk one.

References

1. C.F.Karney and N.J.Fisch, Phys. Fluids 22,1817(1979).
2. I.Fidone, G.Granata and R.L.Meyer, Plasma Phys. 22,261(1980).
3. I.P.Shkarofsky, Phys. Fluids 9,561(1966).
4. S.T.Tsai et al., Phys. Fluids 24,2186(1981).
5. S.Pešić, Phys. Fluids 31,115(1988).

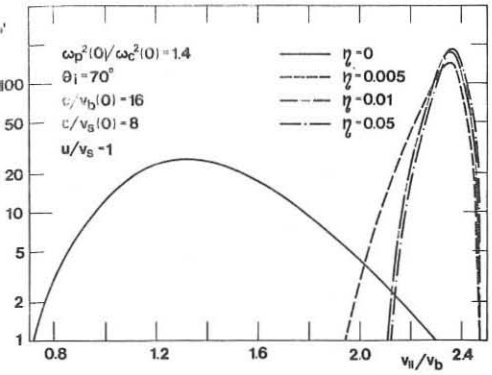

Fig. 1. Power deposition versus $v_{//}/v_b$.

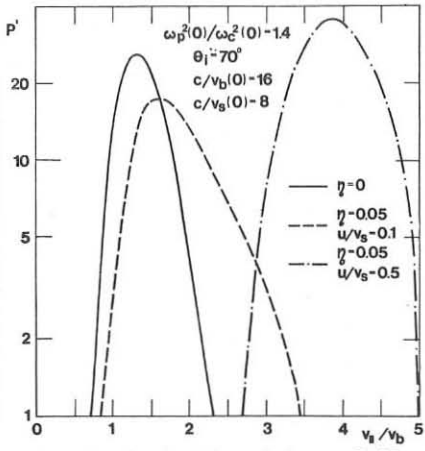

Fig. 2. As in Fig. 1 for η=0.05.

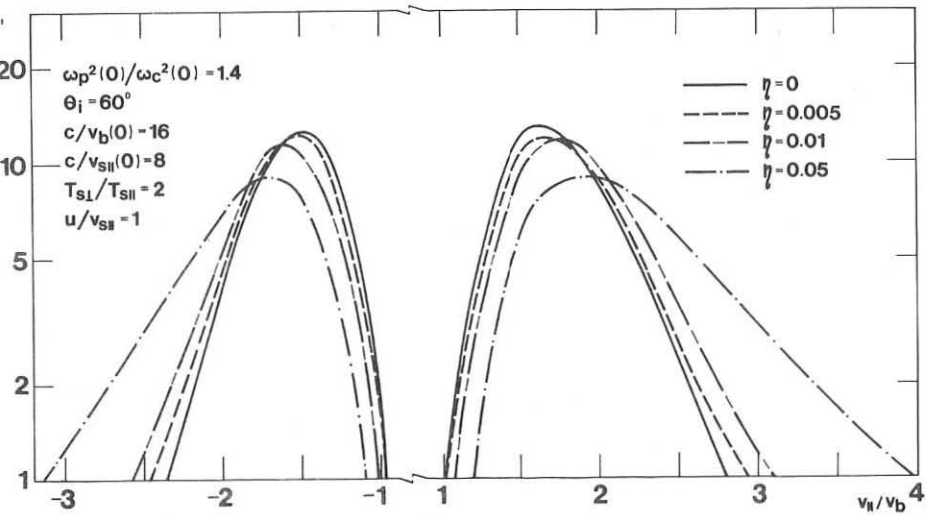

Fig. 3. Power deposition profiles in presence of thermal anisotropy.

QUASI ELECTROSTATIC BRANCH OF X-MODE: A THEORETICAL STUDY

F. Castejón and C. Alejaldre

Asociacion EURATOM / CIEMAT, 28040 Madrid, SPAIN

The dispersion relation for a Vlasov plasma, taking into account relativistic and first order finite Larmor radius effects, becomes a 3rd degree equation on $N_\perp^2$. It admits three solutions, i.e., the ordinary wave branch and two branches of the extraordinary wave: An electromagnetic mode and a quasi-electrostatic mode of propagation, the latter being only briefly considered in the literature (1,2). In this paper we have thoroughly studied such a branch near fundamental and second harmonics, starting from the dielectric tensor calculation presented in (3), valid for a weakly relativistic maxwellian plasma and taking into account first order finite Larmor radius effects. We consider the usual local reference system which has its z-axis parallel to the magnetic field and the wave vector lies on the x-z plane. For quasi-perpendicular propagation, the electrostatic branch will be characterized by $E_x >> E_y, E_z$, and the electromagnetic one by $Ey \geq E_x$.

Robinson shows in (1) that, once the magnetic field and the propagation angle are fixed , the parameter which governs the topology of the two X-mode branches is $\Delta=n/T$ (or $\Delta=n/\langle p^2\rangle$ for non-maxwellian distributions). Therefore from the point of view of the mode topology , rising the temperature is equivalent to lowering the density.

FIRST HARMONIC

The topology of the dispersion relation of the two branches is essentially different in both harmonics. For very low densities, the upper hybrid resonance , $\omega_h^2=\omega_p^2+\omega_c^2$, very close to the cyclotron resonance ω_c , strongly influences the branch distribution near this resonance . Figure 1 shows the upper hybrid resonance, in which the squared refractive index of the two branches of X-mode are complex conjugate, and the electronic cyclotron resonance . For devices with high field gradient , such that the two resonances are very close in the physical space, tunnelling is possible and the upper hybrid resonance is then reachable from the low field side, making mode coupling viable. As the density rises the two resonances are more and more detached and no conversion to the quasi-electrostatic branch is possible from the low field side. Therefore it could be used as a heating method for the starting of the device.

Figure 2 shows that when the density rises, the quasi-electrostatic branch gets uncoupled and there is no possibility of reaching it using optical launching.

In figures 1b and 2b it is shown the polarization of both branches in the two

situations. Notice the gradual conversion of electromagnetic X-mode into the electrostatic one.

Figures 1a,1b

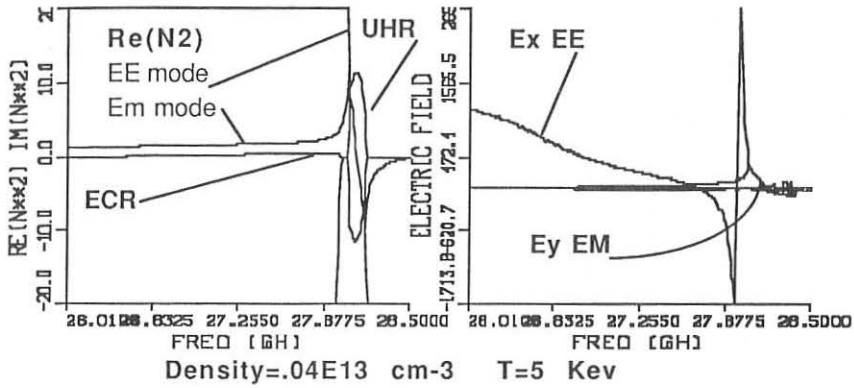

Figures 2a,2b

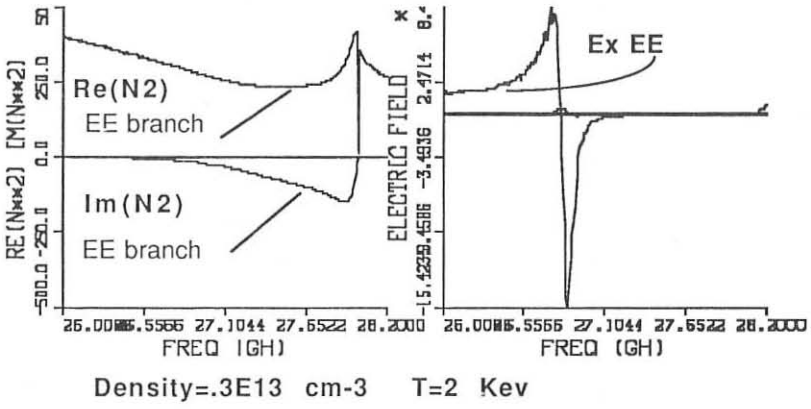

SECOND HARMONIC

In the neighborhood of the second harmonic there are also two possible situations, depending on the value of the parameter Δ. They can be seen in figures 3,4.

In the first situation, both branches exist. The electromagnetic branch can propagate from low and high field sides. The quasi-electrostatic branch could be a very attractive heating method because it is strongly damped. However it cannot be optically

launched, hence its propagation is only possible by mode conversion. From figure 3 it is seen that the possibility of mode coupling is theoretically possible although this linear theory cannot predict its happenning.

The second situation is clearer. The electromagnetic branch of X-mode can propagate from low and high field sides. From low field side it reaches the cut-off and no

Figures 3a,3b

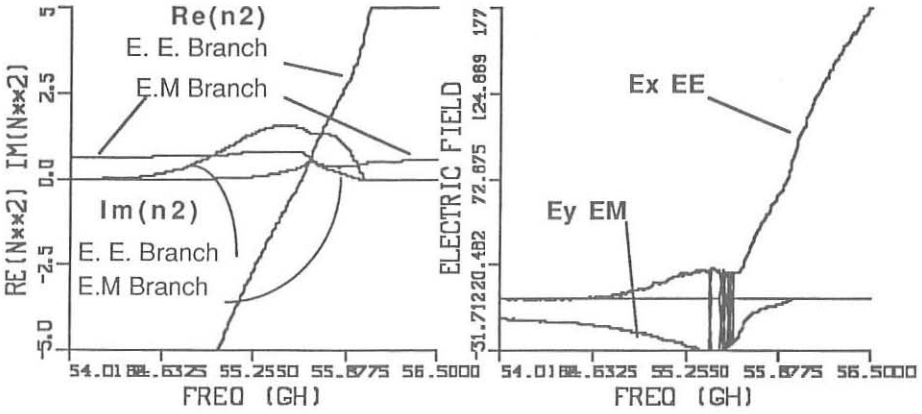

Density=1.E13 cm-3 T=1 Kev

Figures 4a,4b

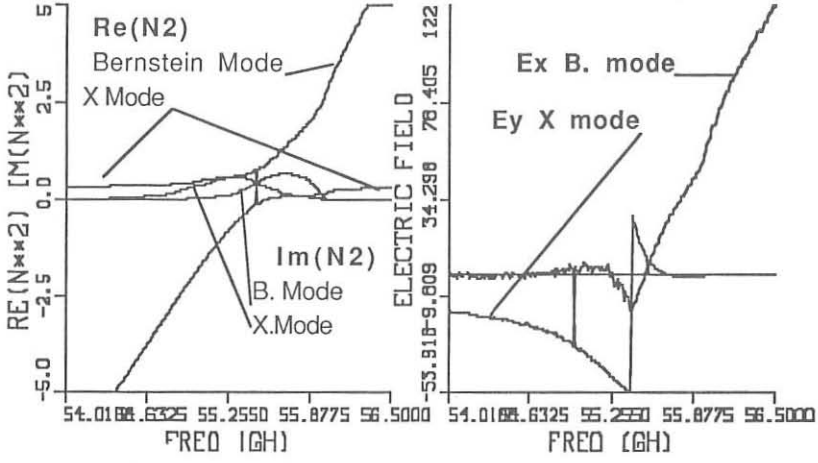

Density=1.5E13 cm-3 T=1 Kev

mode coupling is possible. But when it is launched from high field side it becomes a Bernstein mode which is strongly damped.

See in figures 3b,4b the wave polarization properties for these two situations.

THE INFLUENCE OF $N_{||}$

Up to now, we have studied perpendicular propagation only. Figure 5 shows the $N_{||}$ dependence for the second harmonic. It is shown that the critical value of Δ for changing the branch topology rises with $N_{||}$. When the propagation angle separates from 90 deg., for fixed Δ, the branch topology changes from a situation corresponding to high Δ to that corresponding to low values of Δ.

Figures 5a,5b

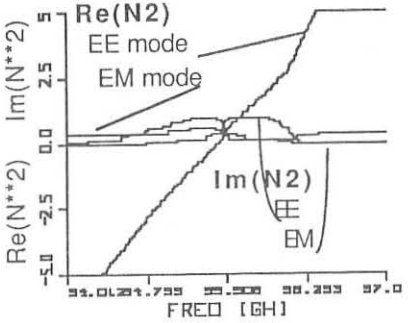

Ang=85 Den=1.5 T=1 Kev

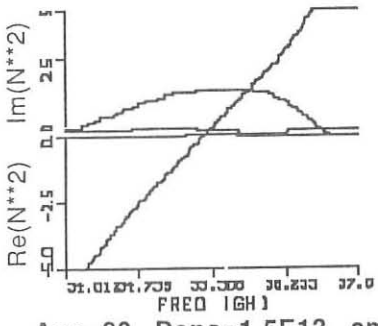

Ang=80 Dens=1.5E13 cm-3
T=1

---

(1) P. A. Robinson. Plasma Physics, 35, part 2, p. 187 (1986)
(2) M. Bornatici, F. Engelman, C. Maroli, V. Petrillo. Plasma Physics, 23, p.89 (1981)
(3) V. Krivenski, A. Orefice. Plasma Physics, 30,p. 125 (1983)

ABSORPTION AND PROPAGATION OF ECH PULSES IN THE PRESENCE OF STRONGLY DISTORTED ELECTRON DISTRIBUTIONS

Roberto Pozzoli

Dipartimento di Fisica, Università di Milano, Milano, Italy

and

Istituto di Fisica del Plasma, CNR, EUR-ENEA-CNR Ass., Milano, Italy

Introduction

With reference to the case of a pulsed free-electron-laser (FEL) radiation in the Microwave Tokamak Experiment (MTX), it has been shown that, in the so called strongly nonlinear regime, most of the injected RF power can be deposited into the plasma through a mechanism of expansion and collapse of the trapped region in phase space, as the electrons stream across the microwave beam /1-2/. This results in a strong distortion (with respect to the initial Maxwellian) of the electron distribution function, achieved on the 10^{-9} sec. time scale. Collisions should then repristinate the Maxwellian bulk on the 10^{-5} sec time scale, during the interval (2×10^{-4} sec) between successive FEL pulses. However, modification of the suprathermal electron distribution can persist longer and affect the EC wave dynamics of the subsequent pulses. This is indeed the case of the stochastic heating regime /1-3-4/, where the formation of a very energetic electron tail is expected. Therefore, the problem arises of the investigation of the behaviour of such strongly modified functions when the driven force due to the FEL radiation is no more present. As a first step, we simulate

the effects of the FEL power absorption by means of a suitable model for the electron distribution and analyze the corresponding linear properties of the plasma. In particular, we consider here the case of EC waves, limiting the analysis, for simplicity, to the ordinary mode in perpendicular propagation. A crude description can be given considering the electron population splitted in a thermal bulk and in a component characterized by perpendicular energies around a typical value ε_0 larger than the thermal energy of the bulk. This should describe the overall characteristics resulting from the numerical investigation of Ref.1. Therefore, we put : $f = f_M + f_1$ where $f_M = C \exp(-u^2\mu/2)$ represents the Maxwellian bulk, and choose for f_1 a cylindrical Maxwellian : $f_1 = C_1 \exp\left\{-\left[(u_\perp - u_0)^2 + u_{\parallel}^2\right]\mu/2\right\}$. In these expressions $u=p/mc$, $\mu = mc^2/T$. An anisotropic temperature can be easily included.

Analysis of the absorption

Taking f as the unperturbed distribution function, from the relativistic linear dispersion relation we obtain the following expression for the imaginary part of the refractive index for the OM in perpendicular propagation:

$$N_i = N_{iM}(1+\delta)^{-1}\left[1 + \alpha(\varepsilon)\,\delta\,\tau^{5/2}\,a^{-5}\,I(a,\epsilon)\,\exp\left\{-\epsilon\left[a^2(1-\tau^{-1})+1\right]\right\}\right] \qquad (1)$$

where N_{iM} refers to the Maxwellian with density $n=n_M+n_1$ and temperature T, $\delta = n_1/n_M$, $\tau = \mu_1/\mu$, $\epsilon = u_c^2\mu_1/2$, $a^2 = (Y^2-1)/u_c^2$, $Y = \Omega/\omega$. The functions $I(a,\varepsilon)$ and $\alpha(\varepsilon)$ are given by:

$$I(a,\varepsilon) = \int_0^a dt\; t^2\,(t-1)\,(a^2 - t^2)^{1/2}\,\exp(2\epsilon t) \qquad (2)$$

$$\alpha(\varepsilon) = 15\left[(2\pi\varepsilon)^{1/2}(1+\mathrm{erf}(\varepsilon^{1/2})) + \exp(-\varepsilon) - 2\right]^{-1} \qquad (3)$$

The function I controls the sign of the contribution to N due to the displaced electron population.

Results

The behaviour of N_i is shown in Fig.1 as a function of the coordinate $z=(Y-1)\mu$, which represents the ratio between the energy of resonant electrons and the thermal energy of the bulk and is proportional to the radial space coordinate. The curve **a** refers to the Maxwellian; curves **b**, **c**, **d** refer to the expression (1) with the same value of ϵ and different τ's. To stress the occurence of regions of negative N_i, high values $\epsilon = 16$ and $\delta = 1$ have been chosen. We can observe the approximate invariance of N_i with respect to $z\tau$. When the region of negative N_i is sufficiently wide, the radiation coming from it can cross the plasma, toward the low field side, without attenuation, or even with a small enhancement. This can be seen from Fig.2, where the optical depth as a function of z is represented for the same cases as in Fig. 1.

References

/1/ T.D. Rognlien et al., 'Heating and current drive with strong ECH pulses', IAEA Technical Committee Meeting on RF Heating and Current Drive, Moscow 1987.

/2/ W.M. Nevins, T.D. Rognlien, B.I. Cohen, Phys. Rev. Lett. **59**, 60 (87)

/3/ C.R. Menyuk et al., Phys. Rev. Lett. **58**, 2071 (1987)

/4/ E. Villalon, W.J. Burke, Phys. Fluids **30**, 3695 (1987)

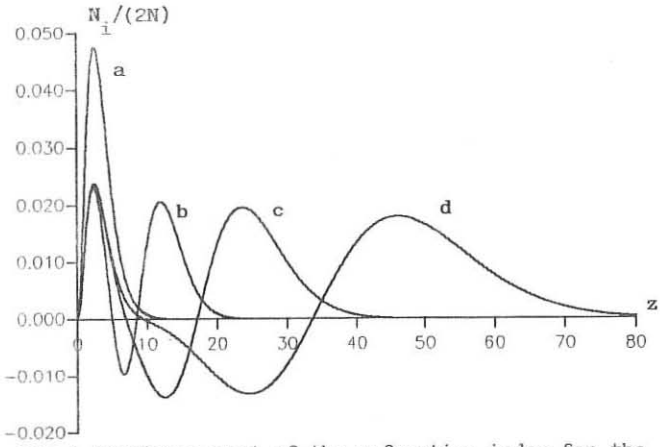

Fig.1 Imaginary part of the refractive index for the OM in perpendicular propagation, versus $z=(Y-1)\mu$. Curve **a** refers to the Maxwellian. Curves **b**, **c**, **d** refer to Exp. (1) with γ = 2, 1, 0.5, respectively. The other parameters are δ = 1, ϵ = 16, T = 1 keV.

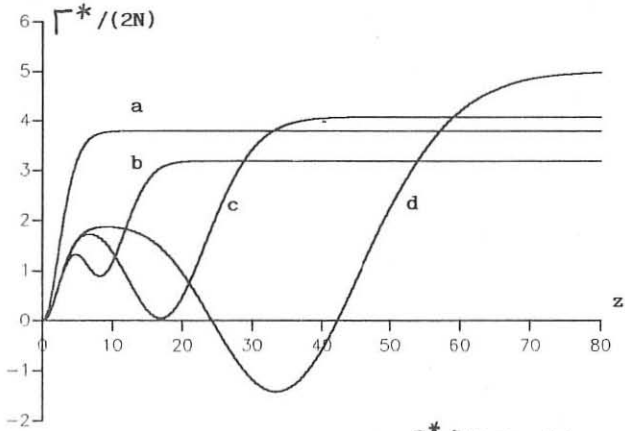

Fig.2 Normalized optical depth $\Gamma^* = \Gamma/(\omega R_o/c)$ where $\Gamma = \int k_i \, dR$, versus z, for the cases of Fig. 1. The values are in units of 10^{-4}.

DISPERSION AND ABSORPTION OF ELECTRON CYCLOTRON WAVES IN ANISOTROPIC, RELATIVISTIC PLASMAS

F. Moser and E. Räuchle

Institut für Plasmaforschung der Universität Stuttgart
7000 Stuttgart 80, Pfaffenwaldring 31
Fed. Rep. of Germany

Abstract

The dispersion and absorption of electromagnetic waves in homogeneous, anisotropic, weakly relativistic, magnetized plasmas are investigated theoretically. Electron distribution functions with anisotropic temperatures and drift motions of the electrons parallel to the magnetic field are considered. Relativistic kinetic theory is used to calculate the dielectric tensor for these conditions and for oblique propagation. Phase velocity, damping and polarization of the electromagnetic waves are calculated for conditions which are of interest for electron cyclotron heating near the electron cyclotron harmonics.

1) Introduction

The study of the propagation of electromagnetic waves in magnetized plasmas with frequencies close to the electron cyclotron frequency or its harmonics is of great interest in recent fusion physics especially for heating plasmas by these waves. The plasma dielectric tensor is a quantity of fundamental importance for the theoretical investigations of electromagnetic wave propagation in plasmas for various regions of the temperature. General expressions in terms of the distribution functions of the charged particles may be found in the literature [1], [2], [3], [4].

In this work we use the dielectric tensor due to Shkarofsky [2], Tsai et al. [4] and Wu et al. [5] for weakly relativistic, magnetized, anisotropic plasmas considering further drift motions of the electrons parallel to the magnetic field. It is assumed that the plasma is homogeneous and that the electrons are weakly relativistic.

2) The dielectric tensor

In the further investigation the electrons are considered only. The dielectric tensor ε_{ij} can be written in the form

$$\varepsilon_{ij} = \delta_{ij} + \chi_{ij}, \tag{1}$$

where χ_{ij} is the tensor of susceptibility.

For an electron distribution function of the form

$$F(p_\perp, p_\parallel) = \frac{1}{\pi^{3/2} \alpha_\parallel \alpha_\perp^2 m_e^3} \exp\left(- \frac{(p_\parallel - p_0)^2}{m_e^2 \alpha_\parallel^2} - \frac{p_\perp^2}{m_e^2 \alpha_\perp^2} \right) \tag{2}$$

Tsai et al. [4] showed that within the weakly relativistic approximation the tensor χ_{ij} results in

$$\chi_{ij} = -i \cdot \frac{4\omega_p^2 c^2}{\omega^2 \cdot \kappa_{\parallel}^2} \cdot \exp(-V^2) \sum_{n=-\infty}^{+\infty} \int_{\tau=0}^{\infty} d\tau \frac{e^{-\lambda} \cdot I_n(\lambda)}{(1-i\tau)^{1/2}(1-i\mu\tau)^{1/2}} \cdot \exp\left[\frac{(V-i\kappa_{\parallel}\tau)^2}{(1-i\tau)} + i\frac{\kappa_{\parallel}^2 c^2 \tau}{\omega^2}\left[\frac{n\omega_{ce}}{\omega}\right]\right] \quad (3)$$

ω_p and ω_{ce} are the electron plasma and cyclotron frequency, $\kappa_{\parallel} = 2v_t^2/\omega$, $v_t=(kT_e/m_e)^{1/2}$ is the electron thermal velocity, $V=p_o/m_o\alpha_{\parallel}$ represents the electron drift motion parallel to the magnetic field, m_o is the electron rest mass, $\tau = (\alpha_{\parallel}^2/2c^2)\omega t$, $h = (k_{\parallel}\cdot\alpha_{\parallel}\cdot c^2)/\omega\alpha_{\parallel}^2$, $\lambda = (k_{\perp}^2\alpha_{\perp}^2/2\omega_{ce}^2)/(1-i\mu\tau)$, $\mu = T_{e\perp}/T_{e\parallel}$, κ is the wave number and ω the frequency of the electromagnetic wave, the indices $\perp$ and $\parallel$ refer to the direction perpendicular and parallel to the applied, constant magnetic field. The matrix M_{ij} is given in [4] and [5].

For the case $|\lambda| \ll 1$, e.g. $\lambda_{\perp} \gg 2\pi r_{Le}$ and using a two series expansion of the integrand in (3) one gets the general expression for χ_{ij} which is given in formula (5) of [8].

The integrals in (3) of the general form:

$$F_{q+\frac{p}{2}}(z) = \int_{\tau=0}^{\infty} \frac{\exp(iz\tau)}{(1-i\tau)^{q+\frac{p}{2}}} \cdot d\tau \quad (4)$$

are Dnestrovskii functions [6] which are a special case of the more general Shkarofsky functions which are discussed in [2], [7] and [9].

These Shkarofsky functions can be expressed by the well known plasma dispersion function $Z(iz^{1/2})$ as pointed out by Shkarofsky [2] or Wu et al. [5] according to the formula:

$$-i\,F_s(z) = \sum_{n=0}^{s-3/2} (-z)^n \cdot \frac{\Gamma(s-1-n)}{\Gamma(s)} + \frac{\pi^{1/2}}{\Gamma(s)} \cdot (-z)^{s-3/2} \cdot \left[iz^{1/2} \cdot Z(iz^{1/2})\right], \quad (5)$$

where $\Gamma(s)$ is the Gamma Function. The analytic character of these relativistic plasma dispersion functions therefore is also well known for the whole complex plane as discussed in detail by Robinson [9].

The tensor elements ε_{ij} are calculated for the following two cases:

a) For the fundamental mode $\omega = \omega_{ce}$ ($\bar{\omega}_{ce} = \frac{\omega_{ce}}{\omega} = 1$) with electron drifts and temperature anisotropy the ε-tensor is:

$$\varepsilon_{ij} = \delta_{ij} + \bar{\chi}_{ij} + \chi_{ij}^{(c)}, \quad (6)$$

where $\bar{\chi}_{ij}$ is calculated from (3) for n = -1 and $n_{ij}^{(c)}$ is due to Wu et al. [5] or Wong et al. [10].

b) For the higher harmonics $\omega = n \cdot \omega_{ce}$ ($\bar{\omega}_{ce} = 1/n$ with $n \geq 2$) the tensor elements ε_{ij} are determined. There is e.g. for $\mu = 1$ and $V = 0$:

$$\varepsilon_{12} = i \frac{\bar{\omega}_p^2 \bar{\omega}_{ce}}{(1-\bar{\omega}_{ce}^2)} + \bar{\omega}_p^{-2} \bar{\mu} \frac{n^2 \lambda_1^{n-1}}{2^n n!} \cdot \left[\bar{F}_{n+3/2}(\bar{z}_n) + h^2 \cdot \left(\bar{F}_{n+5/2}(\bar{z}_n) - 2\bar{F}_{n+3/2}(\bar{z}_n) + \bar{F}_{n+1/2}(\bar{z}_n) \right) \right] \quad (7)$$

with

$$\bar{\mu} = \frac{1}{v_{te}^2}, \quad \bar{\omega}_p = \frac{\omega_p}{\omega}, \quad h = \frac{k_{\parallel} c^2}{\omega \alpha}, \quad \lambda_1 = \frac{k_\perp^2 \alpha^2}{2\omega_{ce}^2}, \quad \bar{z}_n = \bar{\mu} \cdot (1 - n \cdot \bar{\omega}_{ce}), \quad \alpha^2 = 2V_t^2,$$

3) Numerical solution

The dispersion relation Det $|\Lambda_{ij}| = 0$ (8)

with

$$\Lambda_{ij} = n^2 \cdot (\bar{k}_i \bar{k}_j - \delta_{ij}) + \varepsilon_{ij}(k, \omega) \quad (9)$$

$$\left(\bar{k}_i = \frac{k_i}{|k|} \right)$$

is solved numerically using a method of complex residual calculation in the root finding code. Some typical results e.g. the influence of the propagation angle Θ, of the frequency $\bar{\omega}_{ce}$ or the drift velocity $\bar{v}_{eoz}$ on the index of refraction and on the polarization are shown in the figures 1 to 3.

Figure captions

Fig. 1: Damping rate $n_i = \mathrm{Im}(n)$ of the ordinary wave ($\omega = \omega_{ce}$) versus the electron-drift velocity $\bar{v}_{eoz} = v_{eoz}/c$ and angle propagation Θ. (parameters: $\bar{\omega}_{ce} = 1$, $\bar{\omega}_{pe}^2 = 0{,}8$, $T_{e_\perp} = T_{e_\parallel} = 1$ keV).

Fig. 2: Refraction index $n = (n_r, n_i)$ and polarization $|E_x|$, $|E_z|$ of the ordinary wave versus the frequency $\bar{\omega}_{ce} = \omega_{ce}/\omega$ for perpendicular propagation ($\Theta = 90°$). (plasma parameters as in Fig. 1 and $\bar{v}_{eoz} = 0$).

Fig. 3: Refraction index $n = (n_r, n_i)$ and polarization $|E_x|$, $|E_z|$ of the second harmonic of the ordinary wave versus the frequency $\bar{\omega}_{ce} = \omega_{ce}/\omega$ for perpendicular propagation ($\Theta = 90°$). (parameters as in Fig. 1 and $\bar{v}_{eoz} = 0$).

References

[1] B.A. Trubnikow in Plasma Physics and the Problems of Controlled Thermonuclear Reactions, edited by M.A. Leontovich (Pergamon, New York, 1959), Vol. III, p. 122.
[2] I.P. Shkarofsky, Phys. Fluids 9, (1966) 561.
[3] M. Bornatici et al., Nucl. Fusion 23, (1983) 1153.
[4] S.T. Tsai et al., Phys. Fluids 24, (1981) 2186.
[5] C.S. Wu et al., Phys. Fluids 24, (1981) 2191.
[6] Y.N. Dnestrovskii et al., Sov. Phys.-Techn. Phys. 8, Nr.8, (1964) 691.
[7] I.P. Shkarofsky, J. Plasma Physics 35, (1986) 319.
[8] F. Moser et al., Proc. 14th Europ. Conf. on Contr. Fus. and Plasma Physics, Madrid, 1987, Vol III, 964.
[9] P.A. Robinson, J. Math. Phys. 27, (1986) 1206.
[10] H.K. Wong et al., J. Plasma Physics 28, (1982) 503.

Fig. 1

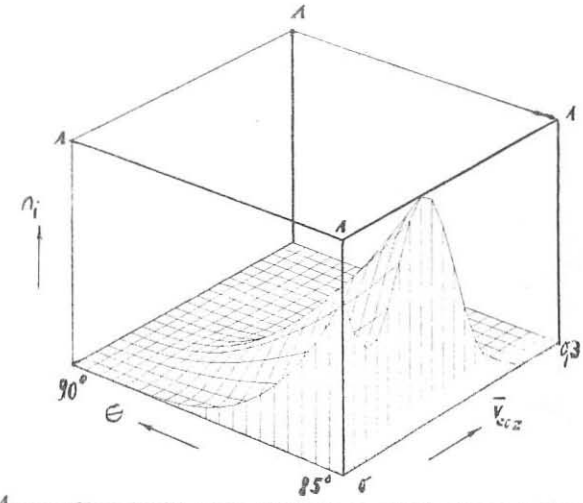

Fig. 2

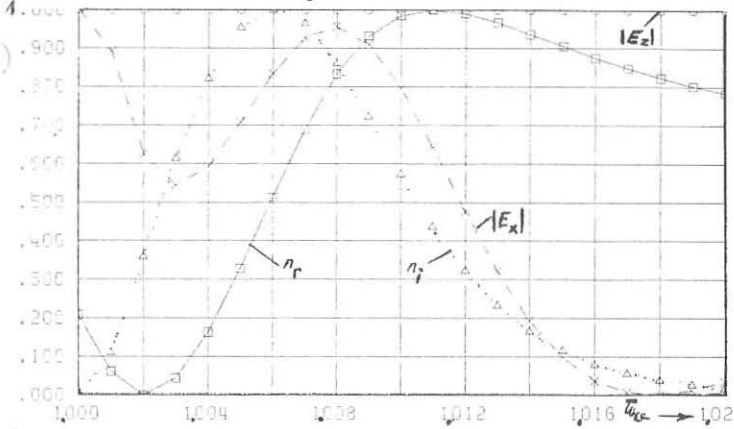

Fig. 3

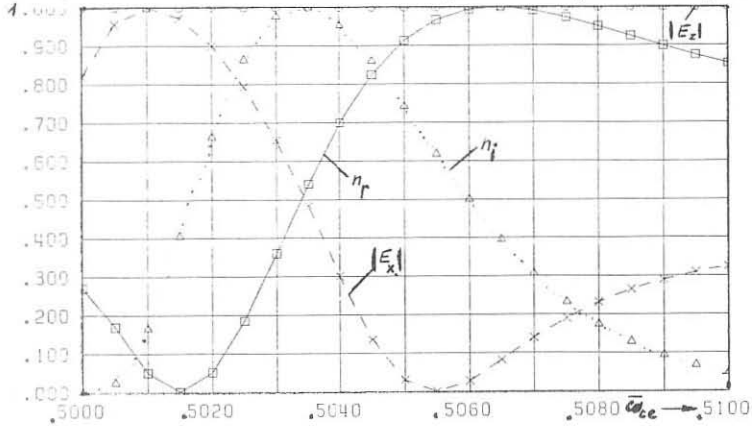

First Author Index